DETERMINATION
of
INTRINSIC MATERIAL FLAMMABILITY PROPERTIES
from
MATERIAL TESTS
assisted by
NUMERICAL MODELLING

THOMAS STEINHAUS

DOCTOR *of* PHILOSOPHY

THE UNIVERSITY *of* EDINBURGH

2009

DECLARATION

This thesis and the research described and reported herein has been completed solely by Thomas Steinhaus under the supervision of Professor Jose L. Torero and Dr. Stephen Welch. Where other sources are quoted, full references are given.

Thomas Steinhaus

ABSTRACT

Computational Fluid Dynamics (CFD) codes are being increasingly used in the field of fire safety engineering. They provide, amongst other things, velocity, species and heat flux distributions throughout the computational domain. The various sub-models associated with these have been developed sufficiently to reduce the errors below 10%-15%, and work continues on reducing these errors yet further. However, the uncertainties introduced by using material properties as an input for these models are considerably larger than those from the other sub-models, yet little work is being done to improve these.

Most of the data for these material properties comes from traditional (standard) tests. It is known that these properties are not intrinsic, but are test-specific. Thus, it can be expected that the errors incurred when using these in computations can be significant. Research has been held back by a lack of understanding of the basic factors that determine material flammability. The term “flammability” is currently used to encompass a number of definitions and “properties” that are linked to standardised test methodologies. In almost all cases, the quantitative manifestations of “flammability” are a combination of material properties and environmental conditions associated with the particular test method from which they were derived but are not always representative of parameters linked intrinsically with the tested material. The result is that even the best-defined parameters associated with flammability cannot be successfully introduced into fire models to predict ignition or fire growth.

The aim of this work is to develop a new approach to the interpretation of standard flammability tests in order to derive the (intrinsic) material properties; specifically, those properties controlling ignition. This approach combines solid phase and gas modelling together with standard tests using computational fluid dynamics (CFD), mass fraction of flammable gases and lean flammability limits (LFL). The back boundary condition is also better defined by introducing a heat sink with a high thermal conductivity and a temperature dependant convective heat transfer coefficient. The intrinsic material properties can then be used to rank materials based

on their susceptibility to ignition and, furthermore, can be used as input data for fire models.

Experiments in a standard test apparatus (FPA) were performed and the resulting data fitted to a complex pyrolysis model to estimate the (intrinsic) material properties. With these properties, it should be possible to model the heating process, pyrolysis, ignition and related material behaviour for any adequately defined heating scenario. This was achieved, within bounds, during validation of the approach in the Cone Calorimeter and under ramped heating conditions in the Fire Propagation Apparatus (FPA).

This work demonstrates that standard flammability and material tests have been proven inadequate for the purpose of obtaining the “intrinsic” material properties required for pyrolysis models. A significant step has been made towards the development of a technique to obtain these material properties using test apparatuses, and to predict ignition of the tested materials under any heating scenario.

This work has successfully demonstrated the ability to predict the driving force (in-depth temperature distribution) in the ignition process. The results obtained are very promising and serve to demonstrate the feasibility of the methodology. The essential outcomes are the “lessons learnt”, which themselves are of great importance to the understanding and further development of this technique. One of these lessons is that complex modelling in conjunction with current standard flammability test cannot currently provide all required parameters. The uncertainty of the results is significantly reduced when using independently determined parameters in the model. The intrinsic values of the material properties depend significantly on the accuracy of the model and precision of the data.

ACKNOWLEDGEMENTS

Based on the elusive comments of good friends of mine (thanks Catherine(F) and Darren (UK)), the support of other friends (Frédéric (B), Hermann(NL), Sujit (IND) etc.), and family (Barbara, Doris, Frank, Maria), I ultimately decided to embark on the endeavour to temporarily or perhaps forever turn my back on the "real" world and engage myself in research and my φιλοσοφία1.

José (PE), who has become over the years a close friend, enabled me to pursue my φιλία[2] at the BRE Centre for fire Safety Engineering at the University of Edinburgh, a place of research and study that has become, due to his contribution, renown in the field, also acting as my "Doktorvater". Without him, many things would have been different. …… Many thanks!

Human nature has it, that when tackling great challenges, picking up additional ones seem to be just a matter of completing the great scheme of things. Being woken by a subtle poke or voice, and welcomed with a huge and friendly smile and gentle voice, thanks Emma and Lara, after a long and exhausting study night in conjunction with a very short period of sleep, is the most amazing thing one can experience. The beauty of such moments - close up view of their hands and the total happiness in their faces - is "Priceless". These easily balance out the inherent challenges of parenthood and beyond. The person that enabled me to pursue my φιλοσοφία[1] and experience my στοργή[3] for Lara and Emma is Maria. There have been many challenges during this intense phase of our lives; I am so grateful for the role she played in overcoming these challenges. Thank you for everything.

---

[1] Philosophia (φιλοσοφία), love for wisdom

[2] Philia (φιλία), which means friendship in modern Greek, a dispassionate virtuous love, was a concept developed by Aristotle. In ancient texts, philos denoted a general type of love, used for love between family, between friends, a desire or enjoyment of an activity, as well as between lovers.

[3] Storge (στοργή) means "affection" in ancient and modern Greek; it is natural affection, like that felt by parents for offspring.

Part of research has it that one is required to look for solutions, not solely within but also outside the box. For this, the environment in Edinburgh was perfect, with its links and brilliant researchers from all around the world and their different approaches to life and work such as the:

- caring god mother, who can turn one's mood with a simple hug,
- peaceful brother of incredible inscrutability, a very interesting friend and kind being that lives in a parallel world,
- remarkable analyst, who glides smoothly around the world,
- relaxed sleeper, who when awake is highly productive,
- un-refused, an unprecedented jester, an artist of his kind,
- mathematical minded industrial engineer, who lives in permanent communication,
- fearless (mushroom) explorer, a very interesting character that takes unusual routes,
- small space friend, who cares for all living beings,
- great organiser, with a prominent understanding,
- divine guide, a silent water that runs deep,
- highly efficient and reflective miller, a baby of my daughters,
- majesty's sand-devil, a cheesy giver and taker with a million questions, the other baby of my daughters,
- gracious artist, who adds another dimension to basic sensing,
- elected ascender, with a gifted connection,
- unbelievable good spotter, who can adapt to almost anything in life,
- moral stranger, an enlightened disciple touched by the son of god,
- pessimist, a great analyst who has achieved so many things,
- restless, a conversationalist with a fascinating musical mind,
- alien, who addresses almost anything from an unexpected, sometimes awkward, angle,
- unnoticed, who accomplishes almost anything by approaching it without fear,
- incredible manager, with amazing clear priorities,

- untypical cosmonaut, who is very still but a very interesting being that does not allow anybody to come close,

…… thank you very much for your input and friendship.

Furthermore, many thanks go to Chris Lautenberger, the key developer of “gpyro”, who provided exceptional assistance getting the program to run on our cluster and tailored it to suit my work. Thanks also to Stephen Welch my second supervisor for his assistant during the project.

This work was funded by FM Global and the European Union under their 6th Framework Program. In that respect, I would also acknowledge the support of the PREDFIRE NANO Team and recognize John de Ris, Mohammed Khan, Stephen Ogden as well as the Rest of the FM Global. The latter were very welcoming and helpful during my stay at their research campus.

TABLE OF CONTENTS

LIST OF FIGURES

NOMENCLATURE

Roman Letters

Variable	Description	Units
a	Absorptivity	-
A	pre-exponential factor	1/s
B	mass transfer numbers	
Bi	Biot number	
c_p	specific heat capacity	J/kg·K
C	pre-exponential factor (polynomial)	1/s
Da	Damköhler	
E	activation energy	J/mol
g	Gravity	
h	heat transfer coefficient	$W/m^2 \cdot K$
h_c	Convective heat trancver coeficient	
H	Heat	J/g
k	Thermal conductivity	W/m·K
$Kcat_i$	Autocatalysis constant	
L	Thickness of the sample	m
ΔL	linear thermal expansion	
m	Mass	kg
$\dot{m}''$	Mass flow rate per unit area	$kg/m^2 \cdot s$
$\dot{m}'''$	Mass flow rate per unit volume	$kg/m^3 \cdot s$
MW	Molecular weight	kg/mol
n	Number of moles	-
Nu	Nusselt Number	
p	Pressure	$kg/m \cdot s^2$
$\dot{q}''$	Heat flux per unit area	W/m^2
$\dot{q}'''$	Heat flux per unit area	W/m^2
r	Pilot location	M
R	ideal gas constant	J/mol·K
Ra	Reynolds number	
t	Time	S
T	Temperature	K
$\vec{u}$	Velocity vector	m/s
v	Velocity	m/s
V	Volume	m^3
x	Depth	N
Y	Mass fraction	g/g

Greek Symbols

Variable	Description	Units
α	absorptivity	-
α_D	diffusivity	m/s^2
α_l	linear expansion coefficient	
α_{TD}	Thermal diffusivity	
ε	emissivity	
ε	With subscript represents the specific depth	m
γ	volumetric expansion coefficient	
$\overline{k_S \rho_S c_{p,S}}$	Thermal inertia	
$\dot{\omega}$	reaction rate	1/s
$\dot{\omega}'''$	gasification rate per unit volume	$kg/s \cdot m^3$
χ	Permeability (fuel)	
σ	Stefan–Boltzmann constant	$W/m^2 \cdot K^4$
ρ	density	g/m^3
μ	viscosity	kg/m·s

Symbols and abbreviations

Variable	Description
CFD	Computational Fluid Dynamics
CR_i	Competing fraction of step i in the total mass loss
DMA	Dynamic Mechanical Analysis
DSC	Differential Scanning Calorimetry
DTA	Differential Thermal Analysis
EGA	Advanced Gas Analysis
FPA	Fire Propagation Apparatus [1]
FR	Fire retardant
FR_i	Share of step i in the total mass loss
HRR	Heat Release Rate
ipd	independent parameter determination
IR_i	Share of step i in the total mass loss of the independent reaction
LIFT	Lateral Ignition and Flame spread Test apparatus [2]
LFL	Lean Flammability Limit
LOI	Limiting Oxygen Index
NC	Nanocomposite
UFL	Upper or Rich Flammability Limit
TGA	Thermo Gravimetric Analysis
PA6	Polyamide 6, Perlon, Nylon and Dederon
PMMA	poly(methyl methacrylate)
RMS	Root Mean Square
TMA	Thermomechanical Analysis
TMDSC	Temperature Modulated Differential Scanning Calorimetry
TRH	Total Released Heat

Exponentials

Variable	Description	Units
m	constant	-
n	constant	-

Subscripts

Variable	Description
air	Air
B	Backing
c	Combustion
CH	Char
char	Characteristic
CND	Conduction
cr	Critical
CV	Convective
ex	Extinction
EXT	External
f	Fusion
F	Flammable gasses
g	Glass transition
G	Gas phase
GEN	Generation
glo	Global
ig	Ignition
m	Melting
min	Minimum
N	Back end of the solid
O	Oxygen
P	Pyrolysat, pyrolysis
R	Frame of reference
RAD	Radiation
S	Solid phase
surf	Surface
T	Thermal wave
tot	Total
0	Initial

1 INTRODUCTION

The development of Computational Fluid Dynamics (CFD) codes in the field of Fire Safety Engineering has resulted in the ability to predict velocity, species and heat flux distributions with a resolution equivalent to detailed experimental measurements. Although it is true that the accuracy of species and heat-flux distributions depend on the adequacy of combustion and radiation models, they are sufficiently developed to reduce errors to the order of 10%-15% [3, 4]. Significant work is currently ongoing to reduce these errors further. The material properties included in these models can introduce much larger errors however, yet little work is being done in the area of material flammability beyond the use of standard test methods.

Most of the data included in CFD fire models comes from traditional (standard) tests. These tests were generally developed when fire models were much less advanced and they relied on simple observations and measurements to estimate material properties. Properties such as the thermal inertia, defined by the the thermal conductivity (k), density (ρ), and specific heat (cp) are not intrinsic to the material but are a combination of material characteristics and the environmental conditions of the test [5]. In the past there have been attempts to address this problem by making the environmental conditions of the test similar to those of a fire [6]. Despite this, estimation of these properties has been difficult and the errors introduced when using them in computations remain significant [7].

Research into material flammability has been hampered by a lack of appreciation of the basic factors that determine the ignition, flame spread, burning processes and extinction [8, 9]. Indeed, links have not been established between fundamental flammability parameters and physical manifestations such as flame geometry, flame height and the composition of combustion products. Furthermore, the term “flammability”, as it is currently used, encompasses a number of definitions and “properties” that are linked to standardized test methodologies but do not always represent parameters that are intrinsically linked to a material. In almost all cases, the quantitative manifestations of “flammability” remain a combination of material

properties and environmental conditions associated with the particular test method used. The consequence of this is that even the best-defined parameters associated with flammability cannot be directly introduced into fire models to predict the growth of a fire.

Currently standard analysis of flammability tests only provides "mixed properties" i.e. The analyses rely on assumptions, e.g. about the flow within the tests, to analyse the results and to extract properties. These properties are limited by the assumptions (e.g. on the flow) and this is why they are "mixed" in nature. In other words, they include some features of the material and some of the flow. This approach has always been necessary because the gas phase could not be resolved completely. Therefore, simplifications have been imposed and then the results analysed with simplified analytical formulations. This is the case in the analysis of tests using the Lateral Ignition and Flame Spread Test (LIFT) apparatus [2], the Cone Calorimeter (Cone) [10] and the Fire Propagation Apparatus (FPA) [1].

The goal in this project is to develop a novel approach to the interpretation of flammability tests such that (intrinsic) material properties controlling ignition may be derived. These properties may then be used to rank materials based on their susceptibility to ignite, but most importantly, can be introduced into fire models.

The current trend in the field is to optimise parameters by fitting the complex models to specific experimental results by means of sophisticated optimization techniques. The optimization process results in ranges of possible values for all parameters stipulated. While success has been reported [11, 12], these optimization processes are limited by the models whose parameters they optimize. It is therefore important to note that even for the most complex models that are available today, some simplifying assumptions have been made.

As progressive as this approach might be, the challenge lies in the determination of the “intrinsic” material properties and not the “global” material properties. Mathematically, an indefinite number of sets of parameters can be found that may equally well represent the known outcome. The challenge is to determine which sets

are physically possible and which sets can be used to model with reasonable accuracy a wide range of conditions that go beyond those of the optimisation test.

This work undertakes the task to:

1. Identify the driving parameters for solid ignition (chapter 2).
2. Independently determine as many material and environmental properties as possible, and provide a robust methodology to obtain them (chapter 3).
3. Estimate the “intrinsic” material properties (using a novel approach) (chapter 5).
4. Compare the “intrinsic” material properties with independently determined properties (chapter 5).
5. Validate obtained material properties, by comparing their result to test data utilizing a different heating scheme (chapter 7).

Throughout this work when referring to material properties, the word “intrinsic” relates to material properties that are wholly independent of any other material properties or environmental condition. When referring to material properties, the word “global” is used to relate to material properties that are mixed in nature. This mixture can be due to the assumptions and simplifications made as part of the process used to determine the property. These can include environmental conditions, represent only one solution of a curve fit or be caused by other factors.

2 IGNITION PROCESS OF SOLIDS

This chapter highlights the driving parameters for solid ignition and describes the parameters that are retrievable by other means, in order to determine (chapters 3 and 5) whether the parameters obtained by fitting the complex models to specific experimental results, by means of sophisticated optimization techniques, are providing “intrinsic” or “global” material properties.

When a solid material, initially at ambient temperature, is subject to an external source of energy, the temperature of the exposed surface starts to increase. This moment will be defined as the onset of the process leading to ignition t=0. A series of physical and chemical processes are initiated as the energy reaches the surface of the material.

Without loss of generality and for simplicity, the ignition process is described in a one-dimensional form with coordinate, x. Only one surface of the material is heated and the origin, x=0, is located at the exposed surface of the material. This frame of reference moves with a velocity v_r as the fuel is consumed and the surface regresses or expands. v_r takes a positive value for regression and a negative one for expansion. For some materials, regression rates are very small and can be neglected, but this is not assumed at this stage. A schematic of a generic solid material undergoing heating is presented in Figure 1. Figure 1 also shows all the different variables that evolve through the heating process. These variables will be described in detail later.

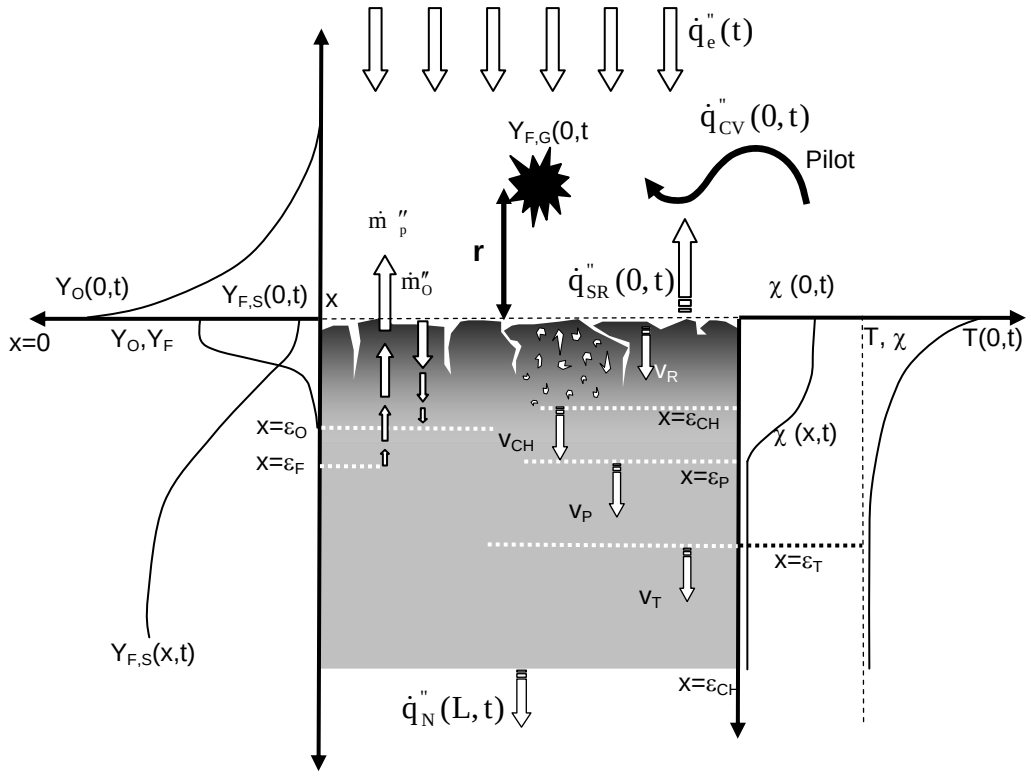

Figure 1 Schematic of the different processes occurring as a material undergoes degradation prior to ignition induced by an external source of heat.

For simplicity, all processes involved are divided in two groups, those associated with the solid phase and those with the gas phase. The solid phase treatment will lead to a description of the production of gas phase fuel ($\dot{m}''_p$) and the gas phase analysis focuses on how the ensemble of gaseous fuel and oxidizer lead to a flame. The solid phase is described first (section 2.1), then the boundary conditions between both phases is established (section 2.2). Finally, a description of the gas phase is given (section 2.3).

2.1 The Solid Phase

The temperature of the solid, initially at ambient (T_0), increases as the heat is transferred to the surface of the material. The highest temperatures are achieved close to the surface, but energy transfer in-depth results in an increase in temperature of a significant part of the solid. Therefore, the temperature varies with depth and time. Thus, temperature needs to be represented as a function of both variables, T(x,t). Figure 1 shows a generic representation of the temperature distribution at a particular

instant in time, t. The evolution of the temperature is defined by an energy balance in the control volumes between both surfaces of the solid (x=0 and x=L). The surfaces will define the heat transfer in/out of the solid fuel or mathematically, the boundary conditions. It is important to note, that if other dimensions were to be considered, similar boundary conditions would have to be established at each surface of the material.

2.1.1 Pyrolysis Process

The process by which the solid transforms into gas phase fuel is called pyrolysis. This is the chemical degradation of a substance invoked by a heating process. Typical mechanisms of thermal decomposition of polymers, for example, are: random-chain scission, end-chain scission, chain-stripping and cross-linking [13]. Pyrolysis tends to be an endothermic process generally controlled by many chemical reactions (sometimes hundreds) which are highly dependant on temperature.

Often pyrolysis reaction rates are described by an Arrhenius type function. Svante August Arrhenius suggested in the late 1800s that the rates of many reactions vary with temperature in such a way that

$$k = A \cdot e^{-\frac{E}{R \cdot T}} \qquad (1)$$

where “k” is the rate constant [14]. The Arrhenius equation is based on collision theory, which assumes that molecules must collide with both the correct orientation and with sufficient kinetic energy if the reactants are to be converted into products. The rate of a reaction is expressed in terms of a rate constant multiplied by a function of concentrations of reactants. The rate constant contains information related to the collision frequency, which determines the rate of a reaction. When the rate constant is given by the Arrhenius equation (1), “E” is the activation energy [kJ/mol]. This is defined as the energy that must be overcome in order for a chemical reaction to occur. For molecules that undergo collision, the exponential is related to the number of molecular collisions that have the required energy to induce reaction. The pre-exponential factor “A” is the frequency factor or pre-exponential factor also given in inverse seconds [1/s], which is related to the frequency of collisions. “R” is the ideal

gas constant with a value of 8.314 [J $mol^{-1}K^{-1}$] and "T" the temperature in degrees kelvin. The constants "E" and "A" are characteristic of each individual chemical reaction. If the natural logarithm of both sides of Equation (1) is taken, "$-\frac{E}{R}$" represents the slope and "ln A" the intercept of a linear relationship.

The process of pyrolysis can be extremely complex and, depending on the fuel and heating characteristics, can follow distinctively different paths. These paths can be a combination of numerous reactions that can be sequential or compete against each other. Furthermore, the chemical pathways can be strongly influenced by the presence (or absence) of oxygen, this is accounted for in equations (2).

$$\dot{\omega} = A Y_O{}^m Y_S{}^n e^{-\frac{E}{R \cdot T}} \tag{2}$$

In this equation, $\dot{\omega}$ is the reaction rate which is generally defined in units of inverse seconds [1/s]. Only when this si multiplied by the fuel density does it gives a gasification rate per unit volume ($\dot{\omega}'''$ [kg/s.m^3]). In equations (2) Y_O and Y_S are generic representations of the oxygen and solid fuel mass fractions participating in the solid degradation and "m" and "n" are constants, otherwise it has the same form as equation (1). It is important to note, that while degradation of some fuels will show dependency on the oxygen concentration, many others will not [15, 16]. In those cases, "m" is assumed to be zero.

Though the Arrhenius function is often used because it describes the temperature dependant reaction processes remarkably well, it is nowadays best seen as an empirical relationship [17]. For completeness, it is noted that the reaction rate could also be described by other simple expressions like polynomials such as:

$$\dot{\omega} = C Y_O{}^m Y_S{}^n \left(\frac{T}{T_0} \right)^b \tag{3}$$

where "C" is a constant that replaces "A" of the previous equation.

The chemical pathways leading to the pyrolysis of most solid fuels of interest in fire science are fundamentally incomplete as much as the constants associated to the equations that will serve to quantify the rate of each reaction step. Many studies have

produced reduced chemical mechanisms for the pyrolysis of different solids [11, 12, 18]. A similar procedure to that presented in references [11, 12] is followed here (see section 3.2).

Thermo-Gravimetric Analysis (TGA) has been used to establish reduced chemical reaction mechanisms as well as the associated constants [19]. As an example, a reduced kinetic mechanism for polyurethane (PU) can be found in reference [11]. The authors propose a four-step mechanism of the form:

Step i

1	PU	$\rightarrow$	$\nu_{\beta,\mathrm{p}}\ \beta\text{-PU} + \nu_{\mathrm{g,p}}\ Gas$
2	β-PU	$\rightarrow$	$\nu_{\mathrm{c,p}\beta}\ \mathrm{Char} + \nu_{\mathrm{g,p}}\ Gas$
3	$\mathrm{PU} + \nu_{\mathrm{O_2,0}}\ \mathrm{O_2}$	$\rightarrow$	$\nu_{\mathrm{c,0}}\ \mathrm{Char} + \nu_{\mathrm{g,0}}\ Gas$
	$\beta\text{-PU} + \nu_{\mathrm{O2,0}\beta}\ \mathrm{O_2}$	$\rightarrow$	$\nu_{\mathrm{c,0}\beta}\ \mathrm{Char} + \nu_{\mathrm{g,0}\beta}\ Gas$
4	$\mathrm{Char} + \nu_{\mathrm{O2,c}}\ \mathrm{O_2}$	$\rightarrow$	$\nu_{\mathrm{r,c}}\ \mathrm{Residue} + \nu_{\mathrm{g,c}}\ Gas$

where the reaction rate for each step ($\dot{\omega}$) is presented by an expression of the form of Equation (2). The first two steps encompass purely thermal degradation, while the last two steps include oxidation. Two intermediate products are formed from the initial degradation of the polyurethane, β-PU and Char. While the terms ‘Gas’ and “Residue” represent the gaseous and solid products of the degradation. It is important to note that there are sequential and competing reactions; while steps 1 and 2 are sequential, step 3 competes with both previous steps. The authors use independent TGA data [20] to obtain all twelve constants thus establishing a complete model for the degradation of polyurethane.

It is important to note that during the ignition process the presence of oxygen close to the surface will result in surface oxidation reactions. Once the flame is established, the region above the fuel is deprived of oxygen by the combustion reaction and all oxidative steps will cease to participate.

Despite the generalised use of TGA data, there is increasing recognition that pyrolysis reaction pathways are sensitive to the heating rate. The basic nature of

TGA studies requires heating rates of the order of 1 to 20 [ºC/min] which is generally an order of magnitude slower than the heating rates typical of fires. Therefore, the constants have to be validated for all the heating rates available, or preferably, obtained using multiple heating rates in that range to account for heating rate errors.

Recent studies such as Lautenberger et al. [12] have established methodologies that use standard test methods and advanced optimization techniques to establish reduced reaction schemes and their associated constants. Although these procedures permit exposure of the materials to heating rates typical of fires and obtain comprehensive sets of constants, they require a detailed analysis of the transport processes within the fuel. In this study, these methods will not be used to obtain kinetic constants but to establish parameters controlling heat and mass transfer.

2.1.2 The Production of Gaseous Fuel

Before flaming ignition can occur, fuel needs to be produced in the gas phase. Solid materials that are not susceptible to spontaneous ignition will show very little evidence of chemical reactions at ambient temperatures, thus can be deemed as inert. The reaction rates associated with the pyrolysis can be considered negligible and therefore, the material will not undergo any transformation. As the temperature increases, the reaction rates increase and the solid fuel starts changing. Given the temperature distribution within the material, the rates of decomposition are a function of “x,” with larger production of pyrolysates close to the surface and lower production in-depth.

Local production of fuel is not the only important variable. The gas phase fuel produced might be the result of a combination of pyrolysis and oxidation reactions, thus its composition might include large quantities of fully oxidized compounds such as carbon dioxide (CO_2), partially oxidized gases such as carbon monoxide (CO) and other molecules that can have all levels of partial oxidation. Therefore, together with the reaction rates, the mass fraction of inert gases needs to be subtracted leaving the remaining reactive gases. As an example, Kashiwagi and Nambu [21] studied the degradation products of cellulose paper showing that there is a significant presence

of inert gases like water vapour, fully oxidized gases such as (CO_2), partially oxidized products like CO and fuel such as CH_4 and H_2.

The mass fraction of flammable gases present in the local products of degradation will be described here by means of a single variable, $Y_{F,S}(x,t)$, which represents a global contribution of all compounds that can be oxidized further. Figure 1 represents $Y_{F,S}(x,t)$ as an increasing function with a minimum at the surface $Y_{F,S}(0,t)$. This is based on the assumption that where there is a higher presence of oxygen there is a higher level of oxidation. The fuel mass fraction can be obtained using TGA data in conjunction with an infrared spectrophotometer or mass spectrometer. Its results can be combined into a single parameter (mass fraction of flammable gases) that includes all compounds that are susceptible to further oxidation. For details, see section 3.3.

Oxygen can migrate inside a fuel resulting also in an in-depth distribution $Y_{O,S}(x,t)$ that reaches ambient values at the surface $Y_{O,S}(0,t)$. In-depth oxygen and fuel diffusion is controlled by the structure of the solid. Some materials are highly permeable and allow unrestricted transport of species into and out of the solid. For other materials, oxidation will occur only very close to the surface, if so can potentially be neglected. The permeability of the fuel can be a function of many variables including the degradation and consumption of the material. This has received very little attention in the fire literature. In the absence of a well defined permeability function, a simple variable associated with the fuel permeability ($\chi(x,t)$) will be introduced here and assumed to describe the fraction of the fuel produced that can flow through the solid material in a generic manner. It is noted that ($\chi(x,t)$) is not strictly a permeability function (as per Darcy's law [22]) but a combination of permeability, porosity and any fractures within the material. No appropriate way is known to extract this property from the conducted analysis therefore this parameter will need to be determined as part of the analysis using the optimisation technique.

Oxygen and fuel concentrations in the solid will be controlled by the local permeability and by production/consumption rates thus, indirectly, by the temperature distribution ($T(x,t)$). This necessitates independent treatment, and consequently, two independent variables, $\varepsilon_F(t)$ and $\varepsilon_O(t)$, emerge. The former

represents the region where fuel is being produced, while the latter represents the region where oxygen is present in significant quantities. Given that a simple fuel mass fraction at the surface will be obtained empirically, this consideration is not relevant for the present study.

If all the reactions occurring are represented in an Arrhenius form (equation (2)), then the local mass production ($\dot{m}'''_P(x,t)$) can be summarised into a function of the form:

$$\dot{m}'''_P(x,t) = Y_{F,S}(0,t)\sum_{i=1}^{i=N} A_i \cdot Y_O^{m_i}(x,t) \cdot Y_S^{n_i}(x,t) \cdot e^{-\frac{E}{R\cdot T(x,t)}} \qquad (4)$$

where the summation is not truly a sum of all the different "N" reaction steps but is a global combination of them that includes sequential and competitive reactions.

To obtain the total fuel production at the surface per unit area ($\dot{m}''_P(0,t)$) it is necessary to integrate equation (3) across the entire depth including the permeability function described above. It is important to note that fuel produced in-depth does not necessarily reach the surface and, in many cases, pressure increases within the fuel structure can be observed. The effects of permeability and pressure are combined in a complex manner to define the flow within the porous medium. This remains an unresolved problem, thus the use of a simple variable such as χ is justified.

Integrating equation (4) we obtain the following expression:

$$\dot{m}''_P(0,t) = \chi \cdot Y_{F,s}(0) \cdot \int_0^L \sum_{i=1}^{i=N} A_i \cdot Y_O^{m_i}(x,t) \cdot Y_S^{n_i}(x,t) \cdot e^{-\frac{E_i}{R\cdot T(x,t)}}\, dx \qquad (5)$$

Assuming that any production of fuel is negligible for $x>\varepsilon_F$ then the boundaries of integration can be changed to:

$$\dot{m}''_P(0,t) = \chi \cdot Y_{F,s}(0) \cdot \int_0^{\varepsilon_F} \sum_{i=1}^{i=N} A_i \cdot Y_O^{m_i}(x,t) \cdot Y_S^{n_i}(x,t) \cdot e^{-\frac{E}{R\cdot T(x,t)}}\, dx \qquad (6)$$

where the chemical reactions are left in a generic form, while recognizing that the reactions occurring between $\varepsilon_O<x<\varepsilon_F$ might differ significantly from those occurring between $0<x<\varepsilon_F$ due to the absence of oxygen.

This generic presentation of a single permeability function and a global fuel concentration does not merit the detailed tracking of the oxygen concentration within the fuel. In this case, it is simpler to estimate the oxygen concentration to be ambient in the char region ($\chi \rightarrow 1$) and define ε_O by the attainment of the initial decomposition temperature. The ambient oxygen concentration will be that of air for ignition and zero once the fuel is burning. This leads to equation (7)):

$$\dot{m}''_P(0,t) = \chi \cdot Y_{F,s}(0) \cdot \int_0^{\varepsilon_F(T)} \sum_{i=1}^{i=N} A_i \cdot Y_O^{m_i}(0) \cdot Y_S^{n_i}(x,t) \cdot e^{-\frac{E_i}{R \cdot T(x,t)}} \, dx \qquad (7)$$

To summarize, the production of fuel is controlled by the following parameters:

Parameter	Description	Units
$T(x,t)$	Temperature	K
$Y_S(x,t)$	Local fuel concentration	g/g
$Y_O(0)$	Local oxygen concentration (char)	g/g
$Y_{F,s}(0)$	Residual fuel fraction	g/g
χ	Permeability function	
$\varepsilon_O(T)$	Oxygen penetration depth	m
$\varepsilon_F(t)$	Reactive depth	m
A_i	Pre-exponential factor	s^{-1}
m_i	Exponential constant	
n_i	Exponential constant	
E_i	Activation energy	J/mol

Table 1 Fuel production is controlled parameter

2.1.3 Charring

For the purpose of ignition of a solid fuel, the process of charring has an impact on both heat and mass transport, and therefore needs to be briefly addressed. A general summary of the chemical processes leading to charring can be obtained from Cullis and Hirschler [13] for polymers, and in the case of wood, from Drysdale [23], thus will not be described here. Instead, an explanation is given concerning the influence of charring on ignition and burning rate.

For charring materials, pyrolysis leads to the production of gaseous fuel (pyrolysat) and a residual solid phase char. The char is commonly a carbonaceous solid that can be further decomposed. This secondary decomposition can also be complete, leading to an inert ash or to a secondary char that can be further decomposed in single or

multiple steps. Non-charring materials decompose leaving no residue behind. Here it will be assumed that the char will not oxidize further, allowing for the definition of an empirical char thickness.

From the perspective of ignition, the exposed surface represents the boundary between the gas and the solid. This boundary moves as the material is completely removed. The rate at which the surface moves is the regression rate (v_R). For charring and non-charring materials, this is the boundary where complete consumption of the fuel is achieved. Furthermore, if during the charring process the material intumesces (swells), v_R takes a negative value. For many of the materials considered here this is the case. Although regression rates can be very different between charring and non-charring materials, at the surface the main difference between the two material types is the temperatures that can be achieved. Carbonaceous chars can reach much higher temperatures, leading in many cases to vigorous oxidation (surface glowing) that can be the catalyst for gas phase ignition. This is part of the gas phase discussion. Regarding the production of fuel, the differences appear mostly in-depth where heat transfer through the char controls temperature and fuel production is effected by an overall permeability function. The effects of permeability were described above and temperature effects on fuel production are discussed in the context of the calculation of the temperature distributions.

2.1.4 The Thermal Depth (ε_T)

When a heat flux is applied to the solid surface, the heat travels into the solid fuel. Initially only a very small volume is affected, but as the thermal wave travels through the material, a larger and larger fraction of the solid is heated. The velocity of this thermal wave is represented in Figure 1 by $v_T(t)$. $v_T(t)$ is a function of time because it will decrease as the thermal wave moves away from the heating source and towards the cold back surface. The region that has been heated is quantified by the characteristic length $\varepsilon_T(t)$. It is important to note that since temperature is a continuous function, $\varepsilon_T(t)$ has to be arbitrarily defined simply as the end of the heated region. There is no exact mathematical definition for this length but physically, it

equates to the temperature approaching ambient ($T \approx T_0$) or the gradient of the temperature approaching zero ($dT/dx \approx 0$). The proximity that the temperature or the gradient has to achieve when approaching these targets depends on the precision required in the analysis.

The length scale $\varepsilon_T(t)$ is extremely important because it characterizes solids into different groups. This breakdown enables the simplification of the energy equation and the generation of simple analytical expressions for the temperature distribution. This is of importance in the formulation of simplified solutions. For the purpose of ignition, solid fuels are classified in:

Semi-Infinite Solid ($L > \varepsilon_T$): If the thermal wave is far from the end of the sample, the heat coming from the exposed surface has still not migrated to the back end. The temperature at the back end is ambient (T_0) and there are no heat losses through this surface. The thickness of the sample is no longer a relevant quantity and therefore the fuel can be treated as a semi-infinite solid ($L \rightarrow \infty$). Materials do not show semi-infinite solid behaviour indefinitely, and as time progresses the thermal wave will eventually reach the end of the sample. In many cases, materials will behave as semi-infinite solids for the period of interest, in which case the assumption of $L \rightarrow \infty$ is valid. The boundary condition for the energy equation becomes:

$$x = L \rightarrow \infty \qquad \begin{aligned} \dot{q}''_N(\infty, t) &= 0 \\ T &= T_0 \end{aligned} \qquad (8)$$

Thermally-Thick and Thermally-Thin Solid ($\varepsilon_T \geq L$): If the thermal wave reaches the end of the sample, heat losses at the back end need to be quantified. The thickness of the sample, L, becomes a relevant dimension of the problem and a boundary condition for x=L needs to be defined. This case can be divided into two different cases, thermally-thick and thermally-thin. A solid can be defined as thermally-thick if a significant thermal gradient exists within the solid through the period of ignition. In contrast, in a thermally-thin solid the gradient is negligible for most of the time before ignition. A simple criterion based on the Biot number (Bi) is generally used to establish if a material is thermally-thin or thick. The Biot number is defined as Bi=hL/k, where "h" is a global heat transfer coefficient [W/m^2K] and "k"

is the thermal conductivity [W/mK]. If Bi<<1 then temperature gradients inside the solid are negligible, while if the Biot number is not much smaller than unity then temperature gradients need to be considered. While this is an important distinction for the energy equation, it does not have an effect on the boundary condition at x=L, so if $\varepsilon_T \geq L$ then the boundary condition is defined as:

x=L
$$-k\frac{dT}{dx}\bigg|_{x=L} = \dot{q}''_N(L,t) \qquad (9)$$

where $\dot{q}''_N(L,t)$ will be left as a generic heat loss term at the rear surface of the solid fuel.

Once the material has ignited, the thermal wave will continue to progress and all materials will progress from being semi-infinite solids to thermally-thick and in many cases even to thermally-thin.

2.1.5 The Pyrolysis (ε_P) and Charring Depths (ε_{CH})

Within the region where the temperature has increased above ambient significant chemical activity can occur. This chemical activity leads to the production of fuel at a rate specified by equations of the type of (2) or (3). The depth at which the chemistry can be assumed to be significant is commonly defined as a pyrolysis depth (ε_P) which propagates at a velocity v_P. As with the thermal depth, there is no mathematical function that describes the location of the pyrolysis front, $x=\varepsilon_P$ because the reaction equations are also continuous functions. Nevertheless, if the assumption is made that pyrolysis reactions have high activation energy then the transition between the zones of significant and negligible reactivity can be considered as being abrupt [24]. This permits the definition of critical parameters that may be considered to define the onset of pyrolysis. The most common parameter is a pyrolysis temperature, T_P, below which the solid fuel may be considered inert. It is important to note that the pyrolysis temperature is not a true physical parameter but a simple way to track the onset of high activation chemical reactions.

As described above, for $x>\varepsilon_P$ the solid may be considered inert, thus thermal properties can be defined as those of the original solid fuel. The thermal properties relevant to ignition are given in Table 2.

Parameter	Description	Units
$\rho(T(x,t))$	Density	kg/m^3
$k(T(x,t))$	Thermal conductivity	W/mK
$c_p(T(x,t))$	Specific heat capacity	J/kgK

Table 2 Thermal properties relevant to ignition

The process of pyrolysis can lead directly to gasification with no residue (non-charring) or to a carbonaceous residue (charring). Figure 1 shows the case of a charring material where a second front for charring ($x=\varepsilon_{CH}$) is formed behind the pyrolysis front. The charring front will propagate at a velocity v_{CH} and will leave behind a residue that will have a new set of properties that are potentially very different to those of the fuel.

The evolution of these properties with temperature for common materials can be found in most heat transfer books [25]. The values obtained for the materials in this work and/or how they could be determined, are presented in sections 3.5, 3.6 and 3.7.

For $x<\varepsilon_P$ the chemical reactions have initiated the decomposition of the material. In this part of the material, the relevant properties remain largely the same. Nevertheless, pyrolysis introduces further changes that can affect the material properties. The gasification of the fuel and its transport towards the surface could potentially affect the density, while any potential voids will force the redefinition of the thermal conductivity and specific heat to account for the presence of at least two phases. Here it will be assumed that there are only two distinct phases and that the property change occurs at ε_P.

2.1.6 Pyrolysis, Melting and the Evaporation of Water

The term heat of pyrolysis is commonly used to describe the endothermic gasification of solid fuels. Here the term will be substituted by heat of reaction ($\Delta H_{P,i}$). An analysis of DSC curves allows the heat of pyrolysis (or reaction in the

solid phase) to be established for all the different steps of the reduced chemistry as discussed in section 2.1.1. Having determined the reaction rates from TGA data (section 2.1.1), a simple heat transfer model can be constructed for the heat exchange in a DSC. By fitting the heat transfer model to the DSC experimental results, the different values of $\Delta H_{P,i}$ can be obtained. Details on how this was performed in this work can be found in section 3.8.

Melting or water evaporation has not been considered until now. These two processes are endothermic phase changes that can have a significant effect on the temperature distribution within the solid. Numerous models have been built in the past to describe the heat sinks associated with melting [26, 27] and several studies have attempted to quantify the impact of melting on practical situations such as dripping [28, 29].

Phase changes are generally incorporated into the energy equation as heat sinks where some rate function is defined to describe the conversion from one phase to the other. The simplest procedure is to assign a critical temperature to the phase change and a heat of melting or evaporation (ΔH_m see section 3.4). Once the fuel or water reaches this temperature, it is converted to the high temperature phase. The phase change process is generally assumed infinitely fast and, therefore, the rate is defined by the available energy reaching the location where the phase change occurs. All the energy is then used for the phase change and consequently, the thermal wave can only proceed once the transition has been completed. This approach is inappropriate if the available energy is very low, in which case thermodynamic equilibrium equations will define the rate of vaporization or melting.

It shall be noted, that the term boiling is often used in the same context. It is a phase transition that vaporizes a liquid rapidly and occurs when the vapour pressure of the liquid is equal to the pressure imposed on the liquid by the environmental pressure.

Given that phase change is fundamentally an additional heat sink that will have to be incorporated to the energy equation in an arbitrary manner, it is justifiable to exclude the detailed treatment of this subject. The change of phase will be treated by a single heat of melting term (ΔH_m) that will include the presence of any water vapour.

2.1.7 The Temperature Distribution

As explained in section 2.1.2, in order to determine the fuel production it is necessary to define the evolution of the temperature inside the solid fuel. This can be achieved by defining a comprehensive energy equation. Figure 2 represents a typical control volume for $x<\varepsilon_P$ where all the main heat transfer mechanisms are incorporated.

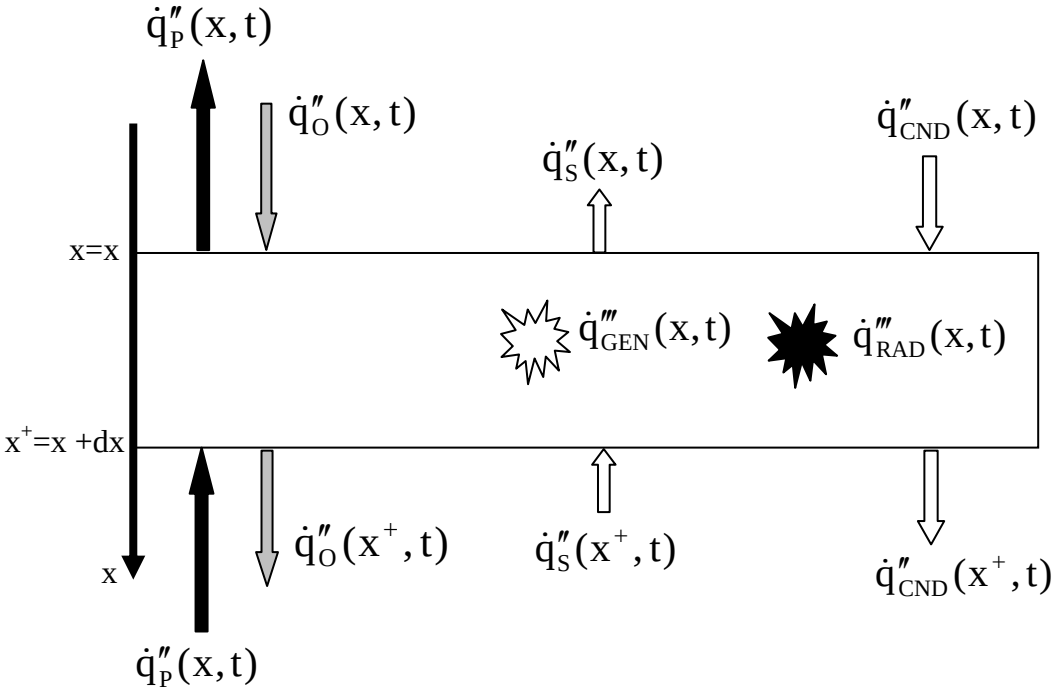

Figure 2 Typical control volume for $x<\varepsilon_P$ showing the main heat transfer mechanisms.

For the purposes of this description, the coordinate system will be anchored to the regressing surface, thus "x" will move with a velocity v_R. A mass flow of fuel will therefore cross the control volume presented in Figure 2 carrying energy in and out ($\dot{q}''_S$). The gaseous products of pyrolysis and oxygen diffusion will also carry energy in and out of the control volume ($\dot{q}''_P, \dot{q}''_O$ respectively) and the generic expression for the mass flow of these gases ($\dot{m}''_P, \dot{m}''_O$) incorporates the regression rate. Heat is conducted in and out of the control volume ($\dot{q}''_{CND}$) and for generality, in-depth radiative absorption is allowed ($\dot{q}'''_{RAD}$). Since for $x<\varepsilon_P$ the temperature is sufficiently

high to allow for chemical reactions, all heat sources and sinks associated to all chemistry need to be included ($\dot{q}'''_{GEN}$). Table 3 summarizes all terms incorporated in Figure 2.

Estimation of the net heat transfer will lead to a change in the energy accumulated within the control volume. The following expression summarizes the energy balance:

$$\begin{aligned}\frac{\partial E_{CV}}{\partial t} = \; & \left[\dot{q}''_S(x^+,t) + \dot{q}''_P(x^+,t) + \dot{q}''_O(x,t) + \dot{q}''_{CND}(x,t)\right] - \\ & \left[\dot{q}''_O(x+,t) + \dot{q}''_{CND}(x+,t) + \dot{q}''_S(x,t) + \dot{q}''_P(x,t)\right] + \\ & \dot{q}'''_{RAD}(x,t)\,dx + \dot{q}'''_{GEN}(x,t)\,dx\end{aligned} \tag{10}$$

where $E_{CV} = \rho_S(x,t)\cdot c_{p,S}(x,t)\cdot T(x,t)\,dx$, which after appropriate substitutions results in the general energy equation for the control volume.

$$\begin{aligned}\frac{\partial\left[\rho_S\cdot c_{p,S}\cdot T\right]}{\partial t} = \; & \frac{\partial}{\partial x}\left[k_S\frac{\partial T}{\partial x}\right] + \frac{\partial\left[\dot{m}''_P\cdot c_{p,P,P}\cdot T_P\right]}{\partial x} - \frac{\partial\left[\dot{m}''_O\cdot c_{p,P,O}\cdot T_O\right]}{\partial x} + \\ & \frac{\partial\left[\rho_S\cdot v_R\cdot c_{p,S}\cdot T\right]}{\partial x} + \dot{q}'''_{RAD} + \\ & \sum_{i=1}^{i=N}\Delta H_{P,i}\cdot\rho_S\cdot\left[A_i\cdot Y_O^{m_i}\cdot Y_S^{n_i}\cdot e^{-\frac{E_i}{RT}}\right]\end{aligned} \tag{11}$$

(7)

The heat sinks associated with melting are excluded from appearing in an explicit form in equation (11) since they can be incorporated as one of the terms in the summation.

Description	In	Out	Formulation
Energy transported by gaseous fuel traversing the control volume	$\dot{q}''_P(x^+,t)$		$\dot{m}''_p(x^+,t)\cdot c_{p,P,P}(x^+,t)\cdot T_P(x^+,t)$
		$\dot{q}''_P(x,t)$	$\dot{m}''_p(x,t)\cdot c_{p,P,P}(x,t)\cdot T_P(x,t)$
Energy transported by oxygen traversing the control volume		$\dot{q}''_O(x^+,t)$	$\dot{m}''_O(x^+,t)\cdot c_{p,P,O}(x^+,t)\cdot T_O(x^+,t)$
	$\dot{q}''_O(x,t)$		$\dot{m}''_O(x,t)\cdot c_{p,P,O}(x,t)\cdot T_O(x,t)$
Energy transported by solid	$\dot{q}''_S(x^+,t)$		$\rho_S(x^+,t)\cdot v_R(t)\cdot c_{p,S}(x^+,t)\cdot T(x^+,t)$
		$\dot{q}''_S(x,t)$	$\rho_S(x,t)\cdot v_R(t)\cdot c_{p,S}(x,t)\cdot T(x,t)$

Description	In	Out	Formulation
fuel traversing the control volume			
Heat conduction	$\dot{q}''_{CND}(x,t)$		$-k_S \left.\frac{dT}{dx}\right\|_{x=x}$
		$\dot{q}''_{CND}(x^+,t)$	$-k_S \left.\frac{dT}{dx}\right\|_{x=x^+}$
Radiative absorption	$\dot{q}'''_{RAD}(x,t).dx$		$\dot{q}'''_{RAD}(x,t).dx$
Chemical energy (generation /sink)	$\dot{q}'''_{GEN}(x,t).dx$		$\sum_{i=1}^{i=N} \Delta H_{P,i} \cdot \rho_S(x,t) \cdot \left[A_i \cdot Y_O^{m_i}(x,t) \cdot Y_F^{n_i}(x,t) \cdot e^{-\frac{E_i}{RT(x,t)}} \right]$

Table 3 Summary of all energy transport within a generic control volume for $x<\varepsilon_P$.

$\Delta H_{P,i}$ is the net heat resulting from each individual chemical reaction. The net heat will be endothermic for most pyrolysis processes and exothermic for oxidative reactions. The summation is not truly a summation but, as explained earlier, is the overall set of chemical reactions where some could be sequential and others competing.

Given the differential nature of the equation, all variables are assumed functions of "x" and "t" so these dependencies are no longer indicated. Many of the terms are left in a generic form and are not quantified here. Their quantification is complex, thus a more detailed discussion will be provided later in those cases where it is necessary.

The solution to equation (11) will provide the evolution of the temperature distribution along the sample as a function of time (T(x,t)). This solution can then be incorporated in equation (7) to establish the fuel production rate. It is important to note that thermal equilibrium between phases has not been assumed, thus there are three different temperatures in equation (11), T, T_P and T_O. Expressions similar to equation (11) are defined for each phase and have to be solved simultaneously. The boundary condition is the exchange of heat between phases. This is generally done using empirical correlations for heat transfer in porous media e.g. [30]. The alternative approach is to demonstrate thermal equilibrium between the phases (heat

transfer is much faster than mass transfer within the pores), in which case all temperatures are the same and only equation (11) has to be solved. This assumption is made for the materials considered here.

To summarize, and in addition to the variables established in sections 2.1.2 and 2.1.5, the temperature distribution is controlled by the following variables:

Parameter	Description	Units
$k_S(x,t)$	Thermal conductivity	W/m·K
$c_p(x,t)$	Specific heat	J/kg·K
$\rho_S(x,t)$	Density of the solid	g/m^3
$v_R(t)$	Regression rate	m/s
$\dot{m}''_P$	Mass flow (pyrolysate)	$g/m^2 \cdot s$
$\dot{m}''_O$	Mass flow (oxygen)	$g/m^2 \cdot s$
T_P	Temperature of the gas phase	K
α_S (x,t)	Radiative properties of the solid (absorptivity)	-
$\Delta H_{P,i}$	Heat of reaction	J/g
$\Delta H_{m,i}$	Heat of phase change	J/g

Table 4 Additional temperature distribution controlling variables

2.2 The Surface Boundary Conditions (x=0 and x=L)

Figure 1 shows all the different modes of heat transfer through the surface control volumes. In theory, control volumes at x=0 and x=L can be represented in a generic manner that makes them identical. In practise, this is generally not the case because materials tend to have an exposed face and one that is in contact with some backing. The backing will generally be defined as a conductive boundary condition while the open face will be defined as a convective/radiative one. Here the exposed face will be defined as an open boundary, thus $\dot{q}''_N(0,t)$ will include convection and radiation, while the back face, $\dot{q}''_N(L,t)$, will be attached to a substrate and thus will be defined as an impermeable conductive boundary condition.

Figure 3 shows the open boundary condition (x=0) at a specific point in time. The different components are mainly those described in section 2.1.5 leading to a very

similar expression for the energy balance as that previously presented. So at the x=0 surface:

$$\frac{\partial E_{CV}(0,t)}{\partial t} = \left[\dot{q}''_S(\varepsilon,t) + \dot{q}''_P(\varepsilon,t) + \dot{q}''_O(0,t)\right] - \left[\begin{matrix}\dot{q}''_O(\varepsilon,t) + \dot{q}''_{CND}(\varepsilon,t) + \dot{q}''_S(0,t) + \\ \dot{q}''_P(0,t) + \dot{q}''_{SR}(0,t) + \dot{q}''_{CV}(0,t)\end{matrix}\right] + \dot{q}'''_{RAD}(x,t)\cdot\varepsilon + \dot{q}'''_{GEN}(x,t)\cdot\varepsilon \quad (12)$$

where the terms that have not yet been defined are described in Table 5. Absorption of radiation within the surface control volume is represented as $\dot{q}''_{RAD}(0,t)\cdot\varepsilon = \dot{q}''_{EXT}(0,t) - \dot{q}''_{EXT}(\varepsilon,t)$ to remain consistent with the notation used previously.

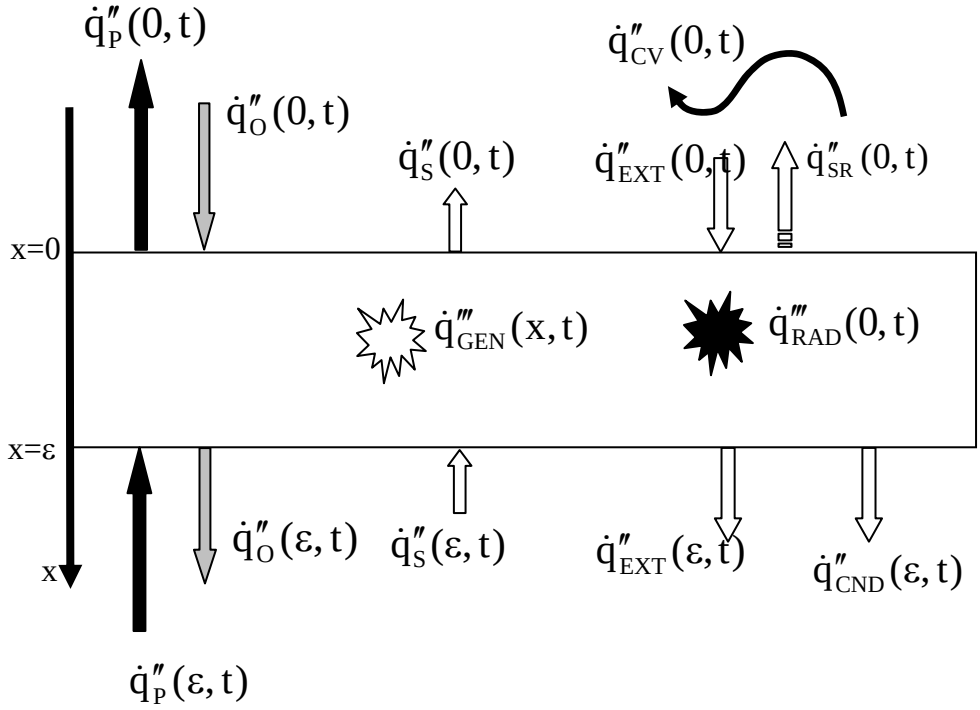

Figure 3 Boundary control volume for x=0 showing the main heat transfer mechanisms.

For the boundary control volume, the characteristic thickness ε tends towards zero, which eliminates all energy transported by mass flow, radiation absorption and energy generation. The final expression for the exposed boundary condition is, therefore:

$$0 = k_S \left.\frac{\partial T}{\partial x}\right|_{x=0^+} - \varepsilon_S(0,t)\cdot\sigma(T^4(0,t) - T_0^4) - h_{CV}(t)\cdot(T(0,t) - T_0) \qquad (13)$$

A similar treatment can be followed with the back end boundary condition (x=L). In this study, the back surface is assumed to be in direct contact with another solid. Mass transfer, convection and radiative losses to the environment are therefore neglected. The boundary condition will only include conductive terms and may be described as:

$$0 = -k_S \left.\frac{\partial T}{\partial x}\right|_{x=L^-} + k_B \left.\frac{\partial T_B}{\partial x}\right|_{x=L^+} \qquad (14)$$

where k_B is a global thermal conductivity of the backing material, which could include the thermal resistance between the two solids. In most cases, the contact between the solids is not perfect, leaving air gaps or requiring adhesives, in these cases it is important to define the thermal conductivity in a manner that includes the contact resistance. The variable T_B is the temperature of the backing solid. This temperature is calculated using an additional energy balance equation of the form of equation (11). If k_B is very small, the backing can be assumed an insulator and the boundary condition can be reduced to have no losses at the back. This eliminates the need to solve a second energy equation for T_B.

Description	In	Out	Formulation
Radiation from the exposed surface to the environment		$\dot{q}''_{SR}(0,t)$	$\varepsilon_S(0,t)\cdot\sigma(T^4(0,t) - T_0^4)$
Convective losses from the surface		$\dot{q}''_{CV}(0,t)$	$h_c(T(0,t) - T_0)$
External radiative heat-flux	$\dot{q}''_{EXT}(0,t)$		$\dot{q}''_{EXT}(0,t)$

Table 5 Summary of all energy transport within the surface control volume. Only terms not presented in Table 3 are described here.

The Stefan-Boltzmann constant (σ) is 5.670 x 10-8 W/m^2K^4, $\varepsilon_s(0,t)$ is the surface emissivity and h_c is the convective heat transfer coefficient. For illustration purposes, two different approaches are used to describe radiation, absorption is allowed to happen in-depth, while emission is treated as a surface process. The spectral

emissivity and absorptivity of the material will define the most appropriate treatment for each specific case.

To summarise, and in addition to the variables established in sections 2.1.2, 2.1.5 and 2.1.7, the temperature distribution is controlled by the following variables:

Parameter	Description	Units
$k_B(x,t)$	Global thermal conductivity of the backing material	W/m·K
$T_B(x,t)$	Temperature of the backing material	K
$\varepsilon_S(x,t)$	Emissivity of the solid	-
$h_c(t)$	Convective heat transfer coefficient	$W/m^2 \cdot K$
T_0	Ambient temperature	K

Table 6 Additional temperature distribution controlling variables (surface boundary)

The convective heat transfer coefficient can be obtained from the literature [31] or by deducting it from tests e.g. with an inert solid heated at a constant heat flux (see section 3.9).

Two different approaches can be taken when dealing with the back end boundary condition. The back end can be insulated allowing the assumption that $k_B \rightarrow 0$ in equation (14) or a material of known thermal conductivity may be used, the greater the thermal conductivity the more precise the estimation of equation (14).

2.3 The Gas Phase

The sequence of events leading to the ignition of a gas phase flame is described in this section. It is assumed that gaseous fuel emerges from the solid following the description provided in section 2.1.

After the onset of pyrolysis, gas begins to emerge from the fuel surface, initially in very small quantities, but as ε_F and T(x,t) increase, equation (7) shows that the fuel mass flux will increase. The emerging fuel will encounter the ambient oxidizer and will eventually produce a flammable mixture. Given that fuel is migrating into the

oxidizer flow, the definition of a flammable mixture is not a simple one. In standard test methods, the ambient flow is fairly well defined, for example:

- mixed convection generated by a horizontal heated surface and the extraction system in the cone calorimeter [10]
- natural convection resulting from a vertical heated surface in the LIFT apparatus [2]
- forced convection over the fuel surface (horizontal or vertical) in the FM Global Fire Propagation Apparatus [1].

The convective heat transfer coefficients evaluated for the FPA and cone calorimeter are presented in Figure 27.

In real fires, flow fields are defined by the flames themselves and by the geometry of the environment (obstacles, fuel geometry, etc.) with the possibility of complex flow patterns. The only mechanisms to establish the fuel distribution within the gas phase are detailed measurements or modelling. Nevertheless, from a phenomenological perspective, what is required to achieve ignition is the production of a flammable condition in at least one location in the gas phase.

A flammable mixture occurs when the fuel concentration in a gas mixture is between the Lower (or Lean) Flammability Limit (LFL) and the Upper (or Rich) Flammability Limit (UFL). Although the LFL and UFL are apparatus dependent measurements, it is clear that the precision required for flaming ignition of solids does not require a more general description of flammability.

2.3.1 Auto-Ignition

Once a flammable mixture is obtained, this mixture needs to increase in temperature until a combustion reaction can occur. This process is described in great detail by Fernandez-Pello [32], who cites a series of experiments by Niioka [33] where ignition was studied using a stagnation point flow over a solid fuel surface. In these experiments, the heat to initiate the combustion reaction was provided by a hot flow impinging on a fuel surface that acted as a heat sink. Niioka [33] identified an

induction time and a pyrolysis time. The pyrolysis time corresponds to the time required to attain a flammable mixture while the induction time is the time for the mixture to reach a temperature at which ignition can occur. For the specific configuration tested, it was found that the pyrolysis time decreased with the flow velocity (enhanced heat transfer to the fuel surface) while the induction time increased (reduced residence time in the gas phase). Although these observations may not be universally applicable, they serve to illustrate the process of auto-ignition. Fernandez-Pello [32] describes Niioka's conclusions graphically by means of a schematic, which is simplified and presented in Figure 4.

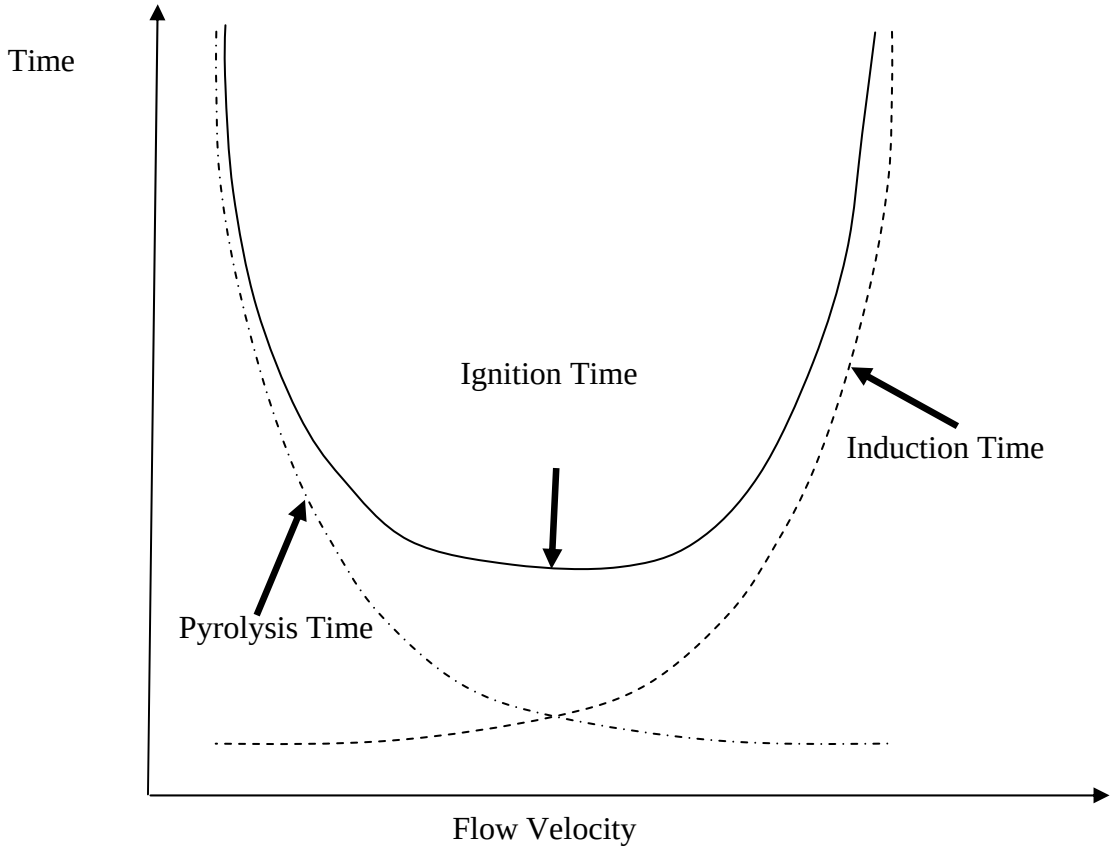

Figure 4 Schematic of the characteristic times involved in the ignition of a flat plate subject to a hot stagnation point flow. This schematic is based on the work by Niioka [33] and adapted from Fernandez-Pello [32].

Figure 4 shows how the summation of the pyrolysis and induction times leads to an ignition time.

In auto-ignition, no hot spot exists that serves as an initiation point for the reaction. Thus, the mixture has to absorb sufficient energy to reach ignition. The exact amount of energy required for ignition can be associated to a Damköhler number [24]. The Damköhler number corresponds to the ratio between the local residence and chemical time. The chemical time represents the necessary time for the reaction chemistry to occur, which is expressed as the inverse of the reaction rate. Combustion reactions can be described by expressions such as equation (2). Thus, the temperature of the reactants directly influences the chemical time; the higher the temperature, the greater the reaction rates and the shorter the chemical time. The residence time is a measure of the strain (or dissipation rates) or the time the reactants remain together at a specific location. Thus, it is directly related to the velocity field; the faster the flow or the velocity gradients, the shorter the residence time. If the chemical times are shorter than the residence times, the reaction has sufficient time to proceed and a flame can exist. A critical Damköhler number for ignition can then be established, above which a combustion reaction can proceed [24]. In the schematic presented in Figure 4, critical Damköhler numbers are attained at both sides of the ignition curve, thereby preventing ignition. This is probably the most precise way to describe ignition but it requires the full resolution of the flow and temperature fields as well as comprehensive knowledge of the kinetic constants associated with the combustion reaction. While the flow field can be resolved by means of Computational Fluid Dynamics (CFD), the chemistry of most fire related fuels remains uncertain. Qualitative assessment of the Damköhler number for ignition has only been achieved for a few very well defined experimental conditions such as stagnation flows [11, 33, 34] or boundary layers [35]. Other alternative representations of the ignition conditions that are based on the same fundamental approach have been discussed by Quintiere [36] and by Gray and Lee [37].

An important aspect of the ignition process that remains, to some extent, unresolved is the origin of the heat that is necessary for the gaseous fuel to reach the critical Damköhler number. If the air flow is hot, as in Niioka’s experiments [33], then the energy will come from the oxidizer and the problem is immensely simplified. If the oxidizer is cold and there is an external radiative heat source, then the solid and gas will heat at different rates. The solid will absorb heat and its surface temperature will

change following equation (11), while the gas will absorb heat based on its absorptivity and dissipate it in a manner governed by the flow field. The absorptivity of the gas is a strong function of the fuel type and concentration. Knowledge of absorptivity therefore also requires detailed knowledge of the flow field. The two possible outcomes are that the gas phase heats faster than the solid phase or vice versa. In the former case, ignition will occur away from the fuel surface since the fuel will act as a heat sink for the gas. In the latter case, ignition will occur closer to the fuel surface since the fuel acts as a heat source. This latter scenario is common with charring materials where oxidation of the char contributes to an increase of the surface temperature [38].

It is clear that auto-ignition is a complex process, which fully involves interactions of the solid and gas phases. To characterize auto-ignition of solid fuels, it is necessary to establish well-defined experimental conditions and simplifications to the analysis. Scatter in the reported data for auto ignition is commonplace, as data obtained from different experimental conditions and using a specific analysis will generally not be compatible with other data that have been obtained from a different experiment or deduced by means of an alternative analysis.

Data on auto-ignition is generally reported as Auto-Ignition Temperatures (AIT), which corresponds to a recorded temperature at the instant ignition is first observed. A summary of much of the data available is presented in [6] together with a series of references of relevant papers and textbooks [39, 40]. Given the complexity of the processes leading to auto-ignition, these values can only be taken as reference values that are a direct function of the specific test conditions. Generally, significant discrepancy is found in the literature; reported Auto-Ignition Temperatures can vary by more than 150^{o}C for the same material. The greatest discrepancies tend to be found when the orientation of the solid fuel is varied and the fluid mechanics and heat transfer are significantly altered [6]. Auto-Ignition Temperatures are most consistent for gaseous mixtures and liquid fuels where tests are conducted in enclosed vessels where the fuel has been fully evaporated.

2.3.2 Piloted Ignition

As discussed previously, the process of auto-ignition is extremely difficult to describe in a quantitative manner, even in simple experimental configurations, therefore it is not practical to rely on auto-ignition to describe the susceptibility of solid materials to ignite. A mechanism to simplify the process is to include a pilot flame or a hot spot. Since in most ignition scenarios, there will be a region of high temperature, this is a practical experimental simplification based on reality. The presence of a pilot strongly simplifies the gas phase processes and reduces the influence of environmental variables. While characterization of the flow field is still required to establish the presence of a flammable mixture, it is no longer necessary to resolve heat transfer between phases or to define the absorption of energy by the gas. In the presence of a pilot, ignition may be assumed to occur at the instant where a flammable mixture (LFL) is attained at the location of the pilot.

Currently, all standard test methods that attempt the description of the ignitability of solids use some form of a pilot. In some cases, the pilot is a large flame [2] while in others it is either a small pilot flame [1] or a high energy spark [10]. All methods have their advantages and disadvantages. Sparks produce only local heating and consequently have less of a tendency to influence the solid phase by acting as a heat source. Nevertheless, given their small volume, ignition is strongly influenced by the spark location. The flow field has to establish a flammable mixture at the exact location of the pilot. In contrast, large pilot flames have a tendency to supply heat to the fuel surface, but cover a large volume, and are therefore less sensitive to the flow field. Due to its practical relevance, all tests used in this project include a pilot; the FPA uses a small pilot flame and the Cone Calorimeter uses a spark. As a result, CFD tools have been used to define the fuel concentration distribution in the gas phase.

To attain the LFL at the pilot location, it is necessary to resolve the momentum and mass transport equations simultaneously. This can be done using the surface boundary conditions explained above. Figure 1 shows an arbitrary distribution of the fuel concentration external to the sample, $Y_{F,G}$. A similar representation could be

made for the oxygen concentration ($Y_{O,G}$). The characteristic equation that describes the flow field is as follows:

$$\rho_{air}\frac{\partial \vec{u}}{\partial t} = -\nabla p + \rho_{air}\cdot\vec{g} + \mu_{air}\nabla^2\vec{u} \quad (15)$$

where $\vec{u}$ is the velocity field, ρ_{air} the density of the air, p the pressure field, $\vec{g}$ the gravity vector and μ_0 the viscosity of the air. Temperature dependencies of the properties have been omitted for simplification, assuming that air is the main constituent and it will remain close to ambient temperature. Conservation of fuel and oxygen concentrations can then be defined by:

$$\rho_{air}\frac{\partial Y_{F,G}}{\partial t} = \rho_{air}\cdot\alpha_{D,F,O}\cdot\nabla^2 Y_{F,G} \quad (16)$$

$$\rho_{air}\frac{\partial Y_{O,G}}{\partial t} = \rho_{air}\cdot\alpha_{D,F,O}\cdot\nabla^2 Y_{O,G} \quad (17)$$

where species transport is assumed to be non-reactive and the source/sink has been omitted. This is an adequate assumption for pure mixing. To obtain the solution of equations (15), (16), and (17) it is necessary to add the variables shown in Table 7 to those established in sections 2.1.2, 2.1.5, 2.1.7 and 2.2.

Parameter	Description	Units
ρ_{air}	Density of air	g/m^3
$\vec{u}$	Velocity field	m/s
p	Pressure field	$kg/m\cdot s^2$
μ_{air}	Viscosity of air	kg/m·s
$\alpha_{D,F,air}$	Diffusivity of fuel in air	m/s^2
r	Pilot location	m

Table 7 Additional temperature distribution controlling variables (gas phase)

At this point, there is no need to specify a critical Damköhler number for ignition because of the presence of the pilot, although to be absolutely rigorous, this assumes that the flow conditions are such that blow-off of the flame kernel does not occur, thus the pilot will allow a flame to be established across the flammable mixture.

All the properties presented in Table 7 can be found in the databases of different CFD models. Properties such as density are defined using the ideal gas law while others such as viscosity or diffusivity are described by empirical laws.

Equations (15), (16) and (17) are generally solved using CFD codes. Equations (7) and (13) correspond to the boundary conditions necessary to properly include the solid phase.

2.3.3 "Flash Point" and "Fire Point"

Once ignition has been achieved, a flame can propagate through the regions where a flammable mixture is present, consuming the reactants. Independent of the flow field, it is most likely that a flammable mixture will be established close to the solid fuel surface. The pyrolysis rates at the instant when the flame is established will determine if a flame can continue to exist or if the combustion reaction will cease after the gas phase mixture is consumed. The feedback from the flame will enhance pyrolysis but, usually, the relatively large thermal inertia of the solid will result in a slow response. It is therefore necessary for pyrolysis rates to be sufficient even in the absence of the flame heat feedback. If pyrolysis rates are not sufficient, the flame will extinguish and continuous pyrolysis will lead once again to the formation of a flammable mixture and subsequent re-ignition. This manifests itself as a sequence of flashes that precede the establishment of a persistent flame over the combustible solid. This process is identical to the "flash point" generally associated with liquid fuels and for solid fuels has been described in detail by Atreya [38].

The transition between the "flash point" ignition and the established flame, which is also termed the "fire point" in an analogy with liquid fuels, deserves special attention. The flow field and the supply of fuel define the characteristics of the diffusion flame established on a solid fuel surface. The rate at which both reactants reach the flame zone defines the flame temperature and thus the characteristic chemical time. If the amount of fuel reaching the flame is small, then the flame temperature will be low and the chemical time will be long. As described above, the flow field defines the residence time. In this situation, a second critical Damköhler number appears, but this time is one of extinction. This concept has been described many times explicitly in the combustion literature [25] but only implicitly in the fire literature. There are few studies where a critical extinction Damköhler number has been presented to describe the "fire point". All these cases concern idealised flow

fields that allow a direct correlation between fuel production and flame temperature to be established [34, 35]. In most discussions, simplifications have been made that lead to simpler parameters, which can serve as surrogates for the Damköhler number. Williams [41] discusses a critical gas phase temperature below which extinction will occur. If the residence time remains unchanged, then extinction is only associated to the chemical time, thus can be directly linked to a critical gas phase temperature. It can also be argued that extinction is much more sensitive to temperature than to flow. Only radical changes in the residence time need to be addressed making this criterion a robust one. A more practical surrogate to the Damköhler number is a critical fuel mass flux criterion. Under specific testing conditions, the flow field will remain invariable. In this case, the attainment of a critical mass flux of fuel will be the single parameter defining the flame temperature and the associated Damköhler number [42]. Furthermore, under more restrictive conditions the critical mass flux can be associated to a critical solid phase temperature [43]. Drysdale [23] and Beyler [44] provide a detailed description of the classic approaches to this subject while Quintiere and Rangwala address some of the more current studies [45]. Thus in summary, the only added variable required to model the "fire point" will be the critical Damköhler number for extinction ($Da_{ex,cr}$) or any equivalent way to represent the extinction condition. As mentioned above, other criteria can be used to establish the extinction condition that are partially equivalent to the critical Damköhler number. Such criteria are a critical mass transfer numbers (B_{cr}) [35, 46], critical mass fluxes [23, 42, 44] or critical temperatures (T_{cr}) [23, 36, 41, 43, 45].

The sequence of events relating "flash" and "fire" points is not trivial because they represent distinctively different processes. For piloted ignition, the "flash point" only requires a flammable mixture. The "fire point" on the other hand requires the rate of fuel supply to be sufficient to achieve a chemical time shorter than the residence time. Thus, a number of different scenarios can be observed that, in many cases, can affect the consistency of different ignition studies. A simple example can be used to illustrate the sensitivity of ignition to different variables and the importance of detailed observations to the validity of conclusions and comparisons. In this example, pilot location is used to make this point. However, a similar analysis could be made with heat flux, oxygen concentration or flow field.

If the pilot is very close to the fuel surface then a flammable mixture would be achieved at the pilot location soon after the onset of pyrolysis. In this case, fuel supply would be far from that required to sustain a flame. A significant delay would exist between flash and fire points where several flashes would occur. If the pilot were at a greater distance from the fuel surface, it would take longer to attain a flammable mixture. Consequently, at the instant of the first flash, the fuel supply would have increased and a smaller number of flashes would occur before the flame became fully established. Further separation of the pilot from the fuel surface might result in the flammable mixture being attained at the pilot location at the same time, as the fuel supply would be sufficient to sustain a flame. In this case, the "fire point" would correspond with the first flash. A further increase in the distance between pilot and fuel would not change the physical manifestation but would continue to delay ignition. In this case, ignition would not represent the flash or fire points.

2.3.4 The Heat of Combustion (ΔH_c)

Once the material has ignited, the result is an exothermic reaction in the gas phase that leads to self-sustained burning of the fuel. This exothermic reaction will be represented by expressions similar to those in equation (2) that in the gas phase could include several hundred different reaction steps. Unless extinction is of interest, the chemistry is vigorous and its representation is not relevant as a description of the flammability of a material. Traditional tests methods will globalise the combustion chemistry into a single parameter such as the Limiting Oxygen Index (LOI). These tests can never provide a material property that is independent of the specific scenario of the test.

In contrast, CFD models have the capability of resolving the combustion chemistry. Nevertheless, extensive computational times and difficulty in identifying the kinetic constants make this approach impractical.

For the purposes of this study, the gas phase chemistry is summarised as a single flammability parameter, which is the heat of combustion (ΔH_c). A global heat of combustion can be determined in many ways, from a bomb calorimeter to the Cone

Calorimeter. Given the similarity of the gas phase process of a fire with the Cone Calorimeter and the FPA, this later approach will be used in this work. The specifics of how to determine these parameters, and the results for the materials analysed are presented in section 3.11.

2.4 Simplifications and Standardisation

To predict flaming ignition of a solid fuel, it is necessary to solve equations (2) to (17). A number of authors have attempted the solution to these equations for a number of materials and in some cases further complexity has been added [47, 48]. Extensive reviews of these modelling efforts can be found in references [16, 49-52]. In most cases, some simplifications have been necessary. In general, the critical limitations of these models are associated to the inadequate definition of many of the relevant variables and parameters listed in the previous sections. Nevertheless, the analysis above proposes a methodology to extract all the different variables necessary. This methodology is detailed in nature, but some simplifications remain. Other simplified analysis methodologies, which provide a series of global properties rather than intrinsic properties obtained from detailed testing as described above, are also presented in this section.

As mentioned previously, the current trend is to optimise parameters by fitting the complex models to specific experimental results by means of sophisticated optimisation techniques. The optimisation process gives ranges of possible values for all parameters stipulated. The results have then been extrapolated to other experimental conditions. While success has been reported [11, 12], these optimization processes are only as good as the models whose parameters they optimise. It is therefore important to note that even in the most complex models, some simplifying assumptions have been made.

This section takes the equations presented in previous sections and proposes simplifications. These simplifications, will lead to models commonly used in the analysis of standard test methods evaluating the (flaming) ignition of solid fuels.

2.4.1 The Inert Solid Assumption

The assumption that the solid remains inert until ignition is probably the most far reaching of all the proposed simplifications. This assumption allows the energy equation to be dramatically simplified. Despite the far-reaching implications of this assumption, there is very limited work that assesses its validity.

The only explicit studies found that discuss the importance of this assumption are those by Cordova et al. [53], Dakka et al. [54] and Beaulieu and Dembsey [55]. In the first two studies, transparent poly(methyl methacrylate) (PMMA) was used. In the latter work, the detailed analysis is completed with black PMMA, however a number of other materials serve to confirm the conclusions. Despite the bias towards PMMA, the discussion is appropriate here to illustrate the potential errors associated to this simplification.

Figure 5 presents characteristic ignition delay times (t_{ig}) and pyrolysis delay times (t_P) for PMMA. The ignition delay time was recorded as the first flash while the pyrolysis delay time as the moment when the fuel initiates its endothermic degradation. The onset of pyrolysis was characterized by means of mass loss measurements, flow visualization and IR-Thermography. These results show that for these particular experiments there is a significant difference between the “flash point” and the onset of pyrolysis (up to 100%). The assumption therefore, that the fuel remains inert until ignition, may not be justified.

The breakdown of the inert solid heating assumption is further discussed by Beaulieu and Dembsey [55] who show that an analysis following this approximation will lead to shorter ignition delay times for realistic heat fluxes. The biggest errors were observed at the higher heat fluxes. Their tests were completed on a comprehensive array of materials and with heat fluxes up to 200 kW/m^2.

Despite these experimental results, this assumption still remains the backbone of all standard test method analyses for ignition [1, 2, 10]. If this approach is followed and the regression rate is assumed negligible, $v_R \approx 0$, equation (11) is reduced to:

$$\frac{\partial\left(\rho_S \cdot c_{p,S} \cdot T\right)}{\partial t} = -\frac{\partial}{\partial x}\left(-k_S \frac{\partial T}{\partial x}\right) + \dot{q}'''_{RAD} \tag{18}$$

In addition, the boundary conditions to:

$$x=0 \qquad 0 = k_S \left.\frac{\partial T}{\partial x}\right|_{x=0^+} - \varepsilon_S(0,t) \cdot \sigma \cdot \left(T^4(0,t) - T_0^4\right) - h_{CV}(t) \cdot \left(T(0,t) - T_0\right) \tag{19}$$

$$x=L \qquad 0 = -k_S \left.\frac{\partial T}{\partial x}\right|_{x=L^-} + k_B \left.\frac{\partial T_B}{\partial x}\right|_{x=L^+} \tag{20}$$

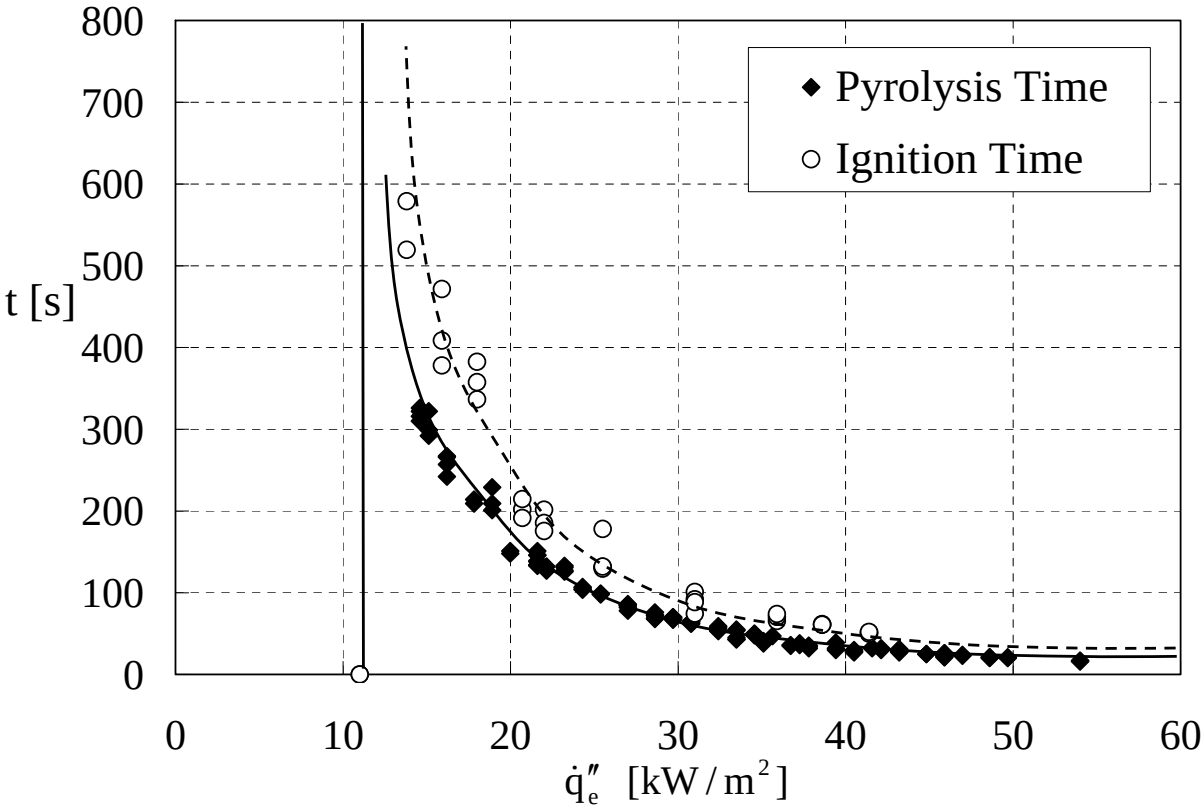

Figure 5 Characteristic ignition delay times (t_{ig}) and times to the onset of pyrolysis (t_P) for PMMA and a wide range of external heat fluxes extracted from reference [54]. Onset of pyrolysis or ignition did not occur below 11 kW/m^2.

2.4.2 Absorption of Radiation and Global Properties

The other major simplifications that are commonly accepted are to assume that most of the incident heat flux is absorbed at the surface ($\alpha(t)\approx 1$), and that the thermal properties of the solid can be considered invariant ($\rho_S(x,t)\approx \overline{\rho}_S$, $c_{p,S}(x,t) \approx \overline{c}_{p,S}$, and

$k_S(x,t) \approx \bar{k}_S$). These assumptions further simplify equation (18) because they allow the neglection of in-depth radiative absorption. The thermal properties can then be extracted from the differential terms and external radiation appears in the exposed boundary condition:

$$\bar{\rho}_S \cdot \bar{c}_{p,S} \frac{\partial T}{\partial t} = \bar{k}_S \frac{\partial^2 T}{\partial x^2} \tag{21}$$

x=0 $$0 = \bar{k}_S \left.\frac{\partial T}{\partial x}\right|_{x=0^+} + \dot{q}''_e - \sigma \cdot \left(T^4(0,t) - T_0^4\right) - h_{CV}(t) \cdot \left(T(0,t) - T_0\right) \tag{22}$$

x=L $$0 = -\bar{k}_S \left.\frac{\partial T}{\partial x}\right|_{x=L^-} + \bar{k}_B \left.\frac{\partial T_B}{\partial x}\right|_{x=L^+} \tag{23}$$

There is little true justification in the literature to support these assumptions. Nevertheless, they are of practical use since for many fire related materials the absorptivity (or emissivity) will approach unity [54]. In the case of testing, the material surface can be treated with a coating that has these properties [1]. Furthermore, thermal properties vary with temperature, but a global set of properties can be established to provide a good fit to ignition data. An example of a comprehensive assessment of the impact of variable thermal properties is provided by Steinhaus [5].

2.4.3 The Boundary Conditions

To standardise the ignition process it is important to provide a controlled environment. This allows test results to be consistent between laboratories and different users of the standard. With this aim, standard test methods provide clear definition of the environmental conditions, thermal characteristics of the backing material and pilot location [1, 2, 10]. Equations (15), (16) and (17) do not have to be solved to obtain the fuel concentration at the pilot location. Instead, the impact of the gas phase on the results is ignored. This is done on the basis that flow conditions are

the same between tests thus their impact on the transport of fuel and oxidizer to the pilot is the same.

Standardisation of the flow conditions has a significant effect on the meaning of the results. The thermal properties associated to the analysis are no longer the true thermal properties of the material but global properties that are a combination of the solid and the standardised gas phase conditions. This is of critical importance because, as a product of standardisation, test results can be compared among themselves if the same method is used. Nevertheless, they cannot be extrapolated to conditions different to those of the test. This applies to other standard tests or to real fire conditions. Cordova et al. [53] provides a graphical assessment of the effect of varying the flow conditions on the resulting thermal properties showing that small variations in the flow field can result in drastic variations of the resultant thermal properties.

It is common to apply ignition data from standard tests to fire models and it is only recently that CFD models such as the Fire Dynamics Simulator (Version 5) allow realistic representations of the solid phase that include “true” thermal properties [56]. It is important to note that any extrapolations are not necessarily correct; nevertheless, they must be done with great care to guarantee either that the effect of the environment on the thermal properties can be neglected or that an appropriate correction is provided.

Different test methods use different flow fields and consequently, values for the convective heat transfer coefficient vary with the authors. A commonly cited value is 15 W/m^2K. Furthermore, it is common to linearise surface radiation to define a single total heat transfer coefficient ($h_{tot} \approx 45$ W/m^2K).

Most test methods define the backing material as a good insulator ($\overline{k}_B \to 0$), neglecting heat losses through the back end of the sample. Finally, characteristic ignition delay times can be considered much shorter than the time required for the thermal wave to travel through the sample. Consequently, $L > \varepsilon_T$ and the solid is generally assumed as semi-infinite.

This last set of simplifications is not necessary, as a simple numerical solution can be obtained without linearising surface radiation or assuming a semi-infinite solid. Many studies have attempted to establish the impact of these simplifications by means of numerical solutions that relax these assumptions. The most recent of these papers is by Mowrer [57]. If surface radiation is described by means of constant heat transfer coefficient, then a correction is necessary to account for the growth of this coefficient as the surface temperature increases. Mowrer [57] showed that a correction to the global thermal properties could be made to account for this effect.

The back end boundary condition is a more difficult problem. For low heat fluxes the thermal wave reaches the end of the sample, $L < \varepsilon_T$, before ignition occurs and heat is exchanged between the sample and the insulating material. Quantification of this heat exchange can be done numerically, as indicated in section 2.2. This is however not a simple process as it is necessary to describe properly the different components associated with the way the arrangement of the sample during tests. The alternative solution of providing a well defined insulating boundary and neglecting back end losses has been preferred and detailed analyses have been conducted to characterize the physical arrangements of the sample and insulating material. Among the most comprehensive of these studies is presented in reference [58].

If all these assumptions are made, equations (21), (22) and (23) can be reduced to:

$$\bar{\rho}_S \cdot \bar{c}_{p,S} \frac{\partial T}{\partial t} = \bar{k}_S \frac{\partial^2 T}{\partial x^2} \tag{24}$$

x=0 $$0 = \bar{k}_S \left.\frac{\partial T}{\partial x}\right|_{x=0^+} + \dot{q}''_{EXT} - h_{tot} \cdot \left(T(0,t) - T_0\right) \tag{25}$$

x=L $$0 = -\bar{k}_S \left.\frac{\partial T}{\partial x}\right|_{x=L^-} \tag{26}$$

2.4.4 The Ignition Condition

It is assumed that the solid is inert until ignition, and that the gas phase can be summarised into a single total heat transfer coefficient (h_{tot}). This is tantamount to

the assumption that ignition will occur at the onset of pyrolysis and that these processes can be simply characterised by the attainment of a characteristic surface temperature that is commonly labelled the ignition temperature, T_{ig}. If the sample is suddenly exposed to an external heat flux, then the time delay between exposure and ignition is named the ignition delay time, t_{ig} [2]. These two parameters represent then the entire process of ignition.

A final link can be made to establish a critical ignition condition. If the ignition delay time is infinitely long, there will be no temperature gradients within the solid. The surface heat losses will then be equivalent to the heat input. This represents the minimum heat flux required to achieve T_{ig}, and thus flaming ignition of the solid fuel. This heat flux is named the minimum heat flux for ignition, $\dot{q}''_{min,ig}$. Since surface temperatures are more difficult to measure than heat fluxes, the minimum heat flux for ignition can be used to establish the ignition temperature. Equation (25) can then be re-written to:

$$T_{ig} = T_0 + \frac{\dot{q}''_{min,ig}}{h_T} \tag{27}$$

The assumption that no temperature gradients exist in the solid can lead to errors in the calculation of T_{ig}. To establish a relationship between external heat fluxes and surface temperature that includes in-depth heat transfer, a sample can be allowed to reach thermal equilibrium and the surface temperature recorded. The obtained relationship represents a more accurate representation of equation (27). It can be used to extract ignition temperatures from measured heat fluxes. A graphic representation of this relationship can be found in reference [2].

Again, minimum heat flux for ignition and ignition temperature are not material properties but a combination of the material and the specific environmental conditions associated to the test [53]. Extrapolation to realistic scenarios and fire models has to be done with much care.

2.4.5 The Solution

Imposing a constant external heat flux ($\dot{q}''_{EXT}$=constant) and using all the above assumptions allows for an analytical solution to equation (24). This solution establishes the evolution of the solid temperature as a function of time. This solution can be found in any heat transfer book [25] but was first postulated for the flaming ignition of a solid fuel by Quintiere [59] and incorporated in ASTM E-1321 [2]. More detailed discussion of methodologies and nomenclature can be found in the description of the standard tests [1, 10].

The solution for T(x,t) is given by:

$$T(x,t) - T_0 = \frac{\dot{q}''_{EXT}}{(h_{tot})}\left[\operatorname{erfc}\left(\frac{x}{\sqrt{4\overline{\alpha}_{TD} t}} \right) - e^{\frac{(h_{tot})}{\sqrt{\alpha_{TD}}\sqrt{\overline{k}_S\overline{\rho}_S\overline{c}_{p,S}}}x + \frac{(h_{tot})^2}{\overline{k}_S\overline{\rho}_S\overline{c}_{p,S}}t} \operatorname{erfc}\left(\frac{(h_{tot})}{\sqrt{\overline{k}_S\overline{\rho}_S\overline{c}_{p,S}}} t^{\frac{1}{2}} + \frac{x}{\sqrt{4\overline{\alpha}_{TD} t}} \right) \right] \quad (28)$$

where $\overline{\alpha}_{TD}$=$k_S/\rho_S C_S$ is the global thermal diffusivity and "erfc" is the complement to the error function. To obtain the surface temperature (T_s), x is set equal to 0 and T = T(0,t) = T_s. Therefore, equation (28) simplifies to:

$$T_s = T_0 + \frac{\dot{q}''_{EXT}}{(h_{tot})}\left[1 - e^{\left(\frac{(h_{tot})^2}{\overline{k}_S\overline{\rho}_S\overline{c}_{p,S}} \right) t} \operatorname{erfc}\left(\frac{(h_{tot})}{\sqrt{\overline{k}_S\overline{\rho}_S\overline{c}_{p,S}}} t^{\frac{1}{2}} \right) \right] \quad (29)$$

from equation (29),

$$\overline{T} = \frac{\dot{q}''_{EXT}}{(h_{tot})} \quad (30)$$

can be defined as a characteristic temperature and,

$$t_{char} = \frac{\overline{k}_S\overline{\rho}_S\overline{c}_{p,S}}{(h_{tot})^2} \quad (31)$$

is defined as a characteristic time. Equation (29) is the general solution to the surface temperature at all levels of incident heat flux. To obtain the ignition delay time (t_{ig}) the surface temperature (T_s) is substituted by T_{ig} and equation (29) can be rewritten as:

$$T_{ig} = T_0 + \overline{T}\left[1 - e^{\frac{t_{ig}}{t_{char}}} \operatorname{erfc}\left(\left(\frac{t_{ig}}{t_{char}}\right)^{\frac{1}{2}}\right)\right] \tag{32}$$

To avoid the complex form of the error function, simplified solutions have been proposed in the literature [59, 60]. In order to solve for the ignition delay time (t_{ig}) a first order Taylor series expansion of equation (32) has been conducted. The range of validity of this expansion is limited, thus it cannot be used over a large range of incident heat fluxes and the domain has to be divided into a minimum of two regions.

The first domain corresponds to high incident heat fluxes where the ignition temperature (T_{ig}) is attained very quickly ($t_{ig} << t_{char}$). Application of the first order Taylor Series Expansion to equation (32) around $t_{ig} / t_{char} \to 0$ yields the following formulation for the ignition delay time (t_{ig}):

$$\frac{1}{\sqrt{t_{ig}}} = \frac{2}{\sqrt{\pi}\sqrt{\overline{k}_S \overline{\rho}_S \overline{c}_{p,S}}} \frac{\dot{q}''_{EXT}}{\left(T_{ig} - T_0\right)} \tag{33}$$

As can be seen from equation (33), the short time solution for the ignition delay time (t_{ig}) is independent of the total heat transfer coefficient term (h_T). Thus the ignition delay time (t_{ig}) is only a function of the external heat flux ($\dot{q}''_e$), the global properties ($\overline{k}_S$, $\overline{\rho}_S$, $\overline{c}_{p,S}$) of the solid fuel, and the ignition temperature (T_{ig}).

For low incident heat fluxes $t_{ig} \geq t_{char}$, the Taylor series expansion is made around $t_{ig} / t_{char} \to \infty$, where the first order approximation yields:

$$\frac{1}{\sqrt{t_{ig}}} = \frac{h_{tot}\sqrt{\pi}}{\sqrt{\overline{k}_S \overline{\rho}_S \overline{c}_{p,S}}}\left[1 - \frac{h_{tot}\left(T_{ig} - T_\infty\right)}{\dot{q}''_{EXT}}\right] \tag{34}$$

Equations (33) and (35) establish the relationship between ignition delay time and external heat flux. It is convenient to express the ignition delay time data, presented in Figure 7, as $1/\sqrt{t_{ig}}$, where T_{ig} is obtained from the experimental minimum heat flux for ignition and equation (27). A plot demonstrating this is presented in Figure 6. Substituting T_{ig} in equation (33) allows the product of the three thermal properties

($\overline{k_S\rho_S c_{p,S}}$) to be extracted as a single experimental parameter. This parameter represents the global material properties controlling flaming ignition of solid fuels that can be considered semi-infinite. Quintiere terms this product the thermal inertia [59].

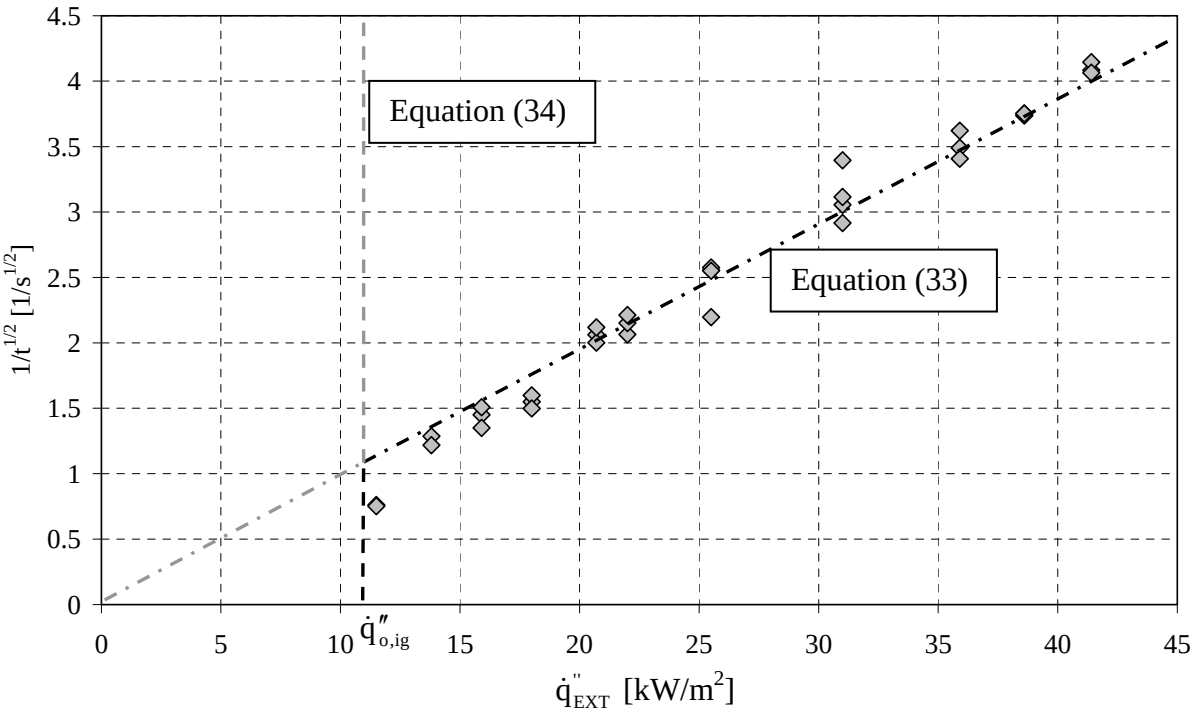

Figure 6 Ignition delay time ($1/t_{ig}^{-0.5}$) for different external heat fluxes using PMMA as a solid fuel. Data extracted from reference [54].

When describing ignition propensity of solid fuels, it is customary to summarise the description of the materials based on only two parameters: the ignition temperature, (T_{ig}), and the thermal inertia ($\overline{k_S\rho_S c_{p,S}}$). Several tables have been produced in the past with comprehensive lists of materials typical of fires. An example are the tables compiled by Quintiere [59]. A list of these global properties for all materials studied is presented in section 6.3.

3 INDEPENDENT PARAMETER DETERMINATION

It is crucial to know the actual material and environmental properties that play a major role in order to determine correctly the material properties for a complex solid heating/ignition model by optimisation. This chapter does this and determines as many of these parameters as possible. They describe physical, observable and/or measurable parameters as depicted in chapter 2.

In the determination of these parameters, special care should be given to the accuracy of these properties. The same material with the same brand name can have different material properties, if they stem from different suppliers or they are produced in a slightly different way from the same supplier. It is therefore, essential to obtain the material parameter based on exactly the same material. Mixing and matching parameters from the various sources can potentially lead to misleading results. To avoid any unnecessary errors stemming from the material composition and structure it was decided to use some of the materials and test results from the PREDFIRE-NANO project [61].

The overall aim of this project is to develop a tool for the prediction of large-scale burning behaviour of polymer nanocomposites using intrinsic property data extracted from small-scale measurements. Participating in that research group of the PREDFIRE-NANO project were material suppliers, plastic manufacturer, testing laboratories and research facilities. The test materials were well described and consistency between the batches was guaranteed. Consequently, the results of the conducted tests (TGA, TGA-EGA and DSC) can thus be considered reliable.

3.1 Materials

Four different materials were tested as part of this work. Their base material is Polyamide 6 (PA6). There were two different additives used: flame retardant (Exolit OP1311) and a nanocomposite (Cloisite 30B). Hereafter, the name and composition used will be as presented in Table 8.

Material	PA6 [%]	PA6+FR [%]	PA6+NC [%]	PA6+NC+FR [%]
PA6	100	95	82	77
Flame Retardant (Exolit OP1311)	0	0	18	18
Nanocomposite (Cloisite 30B)	0	5	0	5

Table 8 Test material compositions

Polyamide 6 (PA6), also known under its trademark names Perlon and Nylon 6, is formed by ring-opening polymerization. Polyamide 6 begins as pure caprolactam. As caprolactam has 6 carbon atoms, it has been given the name Polyamide 6.

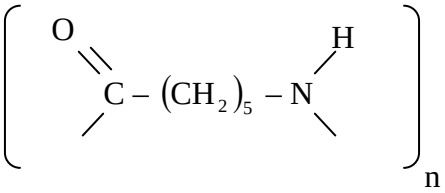

Exolit OP1311 (FR), is as defined in the product data sheet from the producer, Clariant, a non-halogenated flame retardant based on organic phosphinates. It achieves its flame retardant effect through intumescence (a swelling process). The thermoplastic polymer containing Exolit OP 1311 generates a foam and cross links on exposure to a flame and forms a stable char at the surface acting as a barrier. The protective layer provides a heat insulation effect, reduces oxygen access and prevents dripping of molten polymer.

Cloisite® 30B (NC) is, according to the manufacturer (Southern Clay Products), an additive that consist of a natural montmorillonite modified with a quaternary ammonium salt.

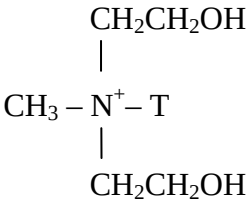

It is said to:

- reinforce the thermoplastics by enhancing flexural and tensile modulus while lowering coefficient of linear thermal expansion,
- improve the gas barrier properties of thermoplastic systems,
- enhance the formation of a surface char and flame retardance,
- improve the physical properties of some unique application areas,
- improve the properties of injection molded pieces, of flexible and rigid packaging such as films, bottles, trays, and blister packs, and of electronics plastics such as wire and cable coatings.

3.2 Determine the reduced chemical reaction parameters

Polymer degradation is in general a complex phenomenon [62]. It is difficult to precisely determine the nature of the chemistry which occurs during the thermal decomposition. The products of degradation encompass multiple decomposition processes, which depend on factors such as temperature, atmosphere, chemical structure, sample thickness, melt viscosity, etc. Describing this fully has proved to be difficult, especially when increasing the complexity such as when fire retardants are at work. To shed light into the complexity, the degradation products of Poly(imino(l-oxohexamethylene), or Nylon 6 / PA6, as determined by Düssel at al. [52] are presented below:

- Cyclic monomer,
- acetonitrile,
- HCN,
- NH, 3
- acrylonitrile,
- 3-cyanopropene,
- 4-cyanobutadiene,
- 4-cyano-1-butene,
- 5-cyano-1, 3pentadiene,
- 4-pentenal, 5-cyano-1-pentene,
- 3,5-hexadienal, 5-isocyanato- 1-pentene,
- linear dimmer

In many cases, a reduced treatment of the chemical reaction is sufficient. For this study it has been decided that the determination of the reduced chemical reaction mechanism shall be sufficient. These can be determined by Thermogravimetric Analysis (TGA). TGA is an analytical method in which the mass change of a sample is measured as a function of the temperature and time, where the mass change of a solid probe is observed during a known heating or cooling process. The most common application of this is the heating process with a constant heating rate. Changes in the mass can have the following causes:

- physical processes such as phase transformation,
- chemical decomposition (breakup of a chemical compounds into elements or smaller compounds),
- and chemical reaction mass loss and increase.

From the changes in the mass, one can derive the reduced chemical reaction mechanisms or determine the composition of the test specimen. Here, we will focus on the former. More information about TGA can be obtained from the literature [19, 63].

It is possible to initially postulate a one-step reaction mechanism (Table 9) for a material with a specific reaction type (Table 10) using the TGA data available from the PREDFIRE-NANO project. This project provided mass loss and mass loss rate plots as a function of temperature and, therefore, of time. This can be done for the various materials and for the various constant heating rates (usually 1,2,5,10 and 20 [K/min]).

Reaction Step Type	Reaction Steps
1	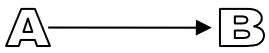
2	
3	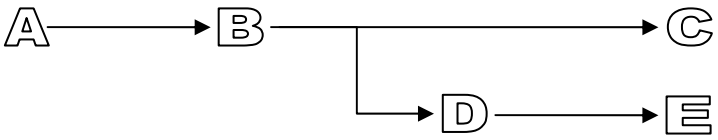
4	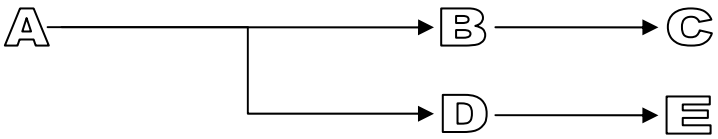

Table 9 Used reactions steps

Following the analogy of equation (2) this can be rewritten as:

$$\dot{\omega} = A \cdot e^{-\frac{E}{R \cdot T}} \cdot Y_O{}^m \cdot Y_S{}^n = k(T) \cdot f(e,p) \tag{35}$$

where “k” is the rate coefficient and “f” one of the functions of Table 10.

If the TGA data cannot be reproduced, then a two-step mechanism or a different reaction type is proposed. The number of steps is increased and/or a different reaction type is used until the TGA plots can be reproduced accurately. This process is followed for both the inert degradation (Figure 7) and oxidative degradation (Figure 8) to obtain the minimum number of steps that are adequate to reproduce the gasification process. Selection of the right initial parameters to arrive at a working model is not trivial and a science in itself.

To assist in this process the researchers of the PREDFIRE-NANO project [61] used the Netzsch Thermokinetics Software [64]. Part of the reaction parameter determination process is the estimation of the model-free activation energy according to Friedman Analysis[65], Ozawa-Flynn-Wall Analysis [66, 67] and/or ASTM E698 Analysis. Based activation energy estimation a multivariate nonlinear regression is

applied using a 6th-degree Ruge-Kutta process in a modified Marquadt procedure to solve a system of differential equations.

Table 11 and Table 12 present a compilation of the data for the materials studied where validity had to be achieved with the same numbers for all the recorded heating rates. Figure 9 and Figure 10 depict how the reduced reaction schemes fit the TGA data for pure PA6. The graphs for the other PA6 based materials can be found in Appendix A.1.

Code	f(e,p)	Reaction Type
Acceleratory		
Pn	$n \cdot p^{\frac{1-n}{n}}$	Power law
E1	p	Exponential law
Sigmoid		
An	$n \cdot e \cdot \left(-\ln(e)\right)^{\frac{n-1}{n}}$	n-dimensional nucleation/nucleus growth according to Avrami/Erofeev (sigmoid)
Bna	$e^n \cdot p^a$	expanded Prout-Tompkins equation (na) (sigmoid)
Deceleratory		
R2	$2 \cdot e^{\frac{1}{2}}$	Geometrical, contracting area
R3	$3 \cdot e^{\frac{1}{3}}$	Geometrical, contracting volume
D1	$\frac{0.5}{p}$	one-dimensional diffusion
D2	$-\frac{1}{\ln(e)}$	two-dimensional diffusion
D3	$1.5 \cdot e^{\frac{1}{3}} \cdot \left(e^{\frac{1}{3}} - 1\right)$	three-dimensions diffusion (Jander's)
D4	$\frac{1.5}{e^{\frac{1}{3}} - 1}$	three-dimensional diffusion (Ginstling-Brounstein)
Fn	e^n	nth-order reaction
Catalytic		
Cn-X	$e^n \cdot (1 + Kcat \cdot X)$	nth-order reaction with autocatalysis through the reactants, X X = a product in the complex model, frequently X = p.

e = concentration of the reactant (1-p); p = concentration of the product

Table 10 used reaction types [63, 68]

As described in the PREDIFIRE-NANO analysis [61] the tested PA6 based materials in N_2 has only one weight loss step. The addition of nanoclay (NC) does not significantly modify the temperature of the weight loss rate peak. On the other hand,

the addition of the flame retardant (FR) introduces a secondary weight loss rate peak at lower temperature. The combination of FR and NC shifts the second peak of weight loss rate to a lower temperature with respect to PA6. Therefore, under nitrogen the n^{th} order reaction type (Fn) was used to fit the experimental curves. This was done using a one-step or a two-step model, depending on the formulation.

Tha PREDFIRE-NANO analysis [61] states for the tested PA6 based materials in Air that:

- the thermal degradation of PA6 occurs in a two-step process,
- the first step corresponding to a weight loss of 89 wt-% and can be assigned to the release of NH_3, H_2O, CO_2 and caprolactam as main product,
- the second step corresponds to the decomposition in air of the char formed during the first step,
- and that the presence of nanoparticles does not modify the thermal stability of PA6, which is a statement that is not generally accepted.

The flame-retarded formulations present three main steps of degradation. In the two first steps of degradation, the materials are less thermally stable than PA6 but then for the third step, a much higher residue is maintained for both intumescent formulations with and without clay. It seems that more carbonaceous residue is formed during the earlier stage of degradation and that the decomposition of the formed residue in air is slower than for pure PA6. The incorporation of nanoparticles in PA6+NC formulation improves the char formation. At the same temperature, 10% more weight is maintained than for PA6+NC. It can thus be stated, that the degradation of PA6 materials in air implies complex reaction routes. It should be noted that only the main reactions have been considered. For PA6 and PA6+NC materials, a model containing two competitive reactions (4) has been chosen. The dependence of the residue formed from the heating rate means that the model which provided the best fit were an n^{th} order autocatalysis reaction (Cn-X) for the first step and for the others an Avrami- Erofeev reaction (An). For PA6+FR and PA6+NC+FR

materials, the degradation occurs in the first step. In this step, the residues are independent from the heating rate contrary to the final residue. Consequently, model (3) was chosen. The first step corresponds to an n^{th} order autocatalysis reaction (CN-X), and the others to an n^{th} order Avrami- Erofeev reaction.

Name	Reaction Step Mechanism	Step i	Reaction Type	$lg(A_i)$	E_i	n_i	FR_i
PA6	1	1	Fn	13.3	212	1.15	
PA6+FR	2	1	Fn	15.8	201	2.96	0.177
		2	Fn	13.1	205	1.09	
PA6+NC	1	1	Fn	13.5	211	1.05	
PA6+NC+FR	2	1	Fn	12.3	164	2.80	0.211
		2	Fn	14.3	219	1.16	

Table 11 Kinetic properties for the different materials studied in N_2

Name	Reaction Step Mechanism	Step i	Type	$lg(A_i)$	E_i	n_i	$lg(Kcat)_i$	FR_i	CR_i
PA6	4	1	Cn -X	11.4	1800	1.17	-4.98	0.443	1.01
		2	An	11.0	1800	1.43			
		3	An	1.67	66.3	0.773		0.193	0.961
		4	An	6.05	132	0.813			
PA6+FR	3	1	Cn -X	7.51	114	2.50	0.216	0.314	
		2	An	13.7	213	0.944			0.996
		3	An	4.77	96.7	1.13		0.160	0.968
		4	An	5.76	135	0.874			
PA6+NC	4	1	Cn -X	13.8	208	1.53	-1.84	0.273	0.994
		2	An	9.30	156	1.62			
		3	An	0.04	47.1	0.862		0.397	1.00
		4	An	8.36	171	0.779			
PA6+NC+FR	3	1	Cn -X	8.08	119	2.52	0.140	0.274	
		2	An	16.9	253	0.682			0.997
		3	An	5.88	108	0.796		0.165	0.980
		4	An	5.71	135	1.01			

Table 12 Kinetic properties for the different materials studied in Air

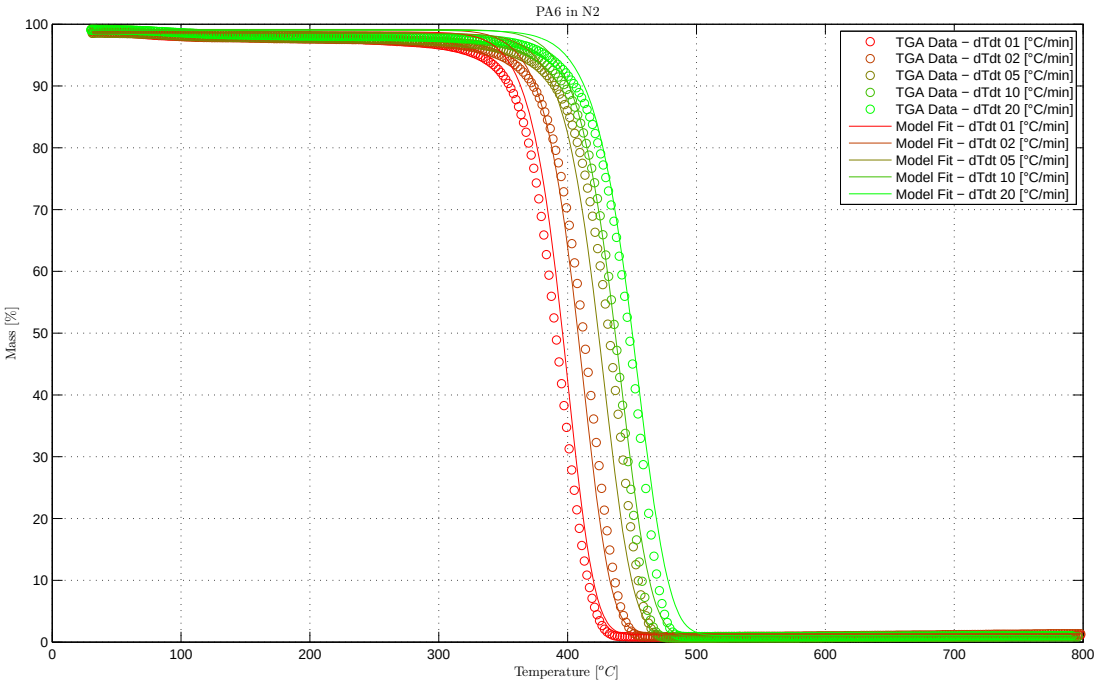

Figure 7 TGA Mass data and reduced reaction schemes fits for PA6 in inert atmosphere (N_2)

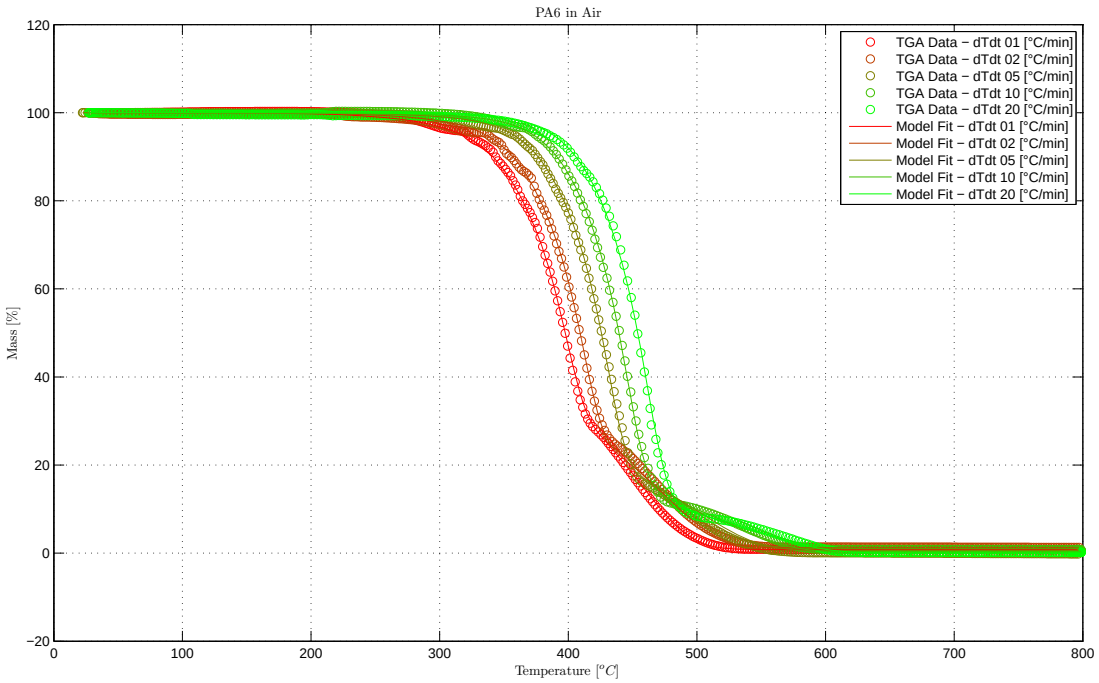

Figure 8 TGA Mass data and reduced reaction schemes fits for PA6 in air

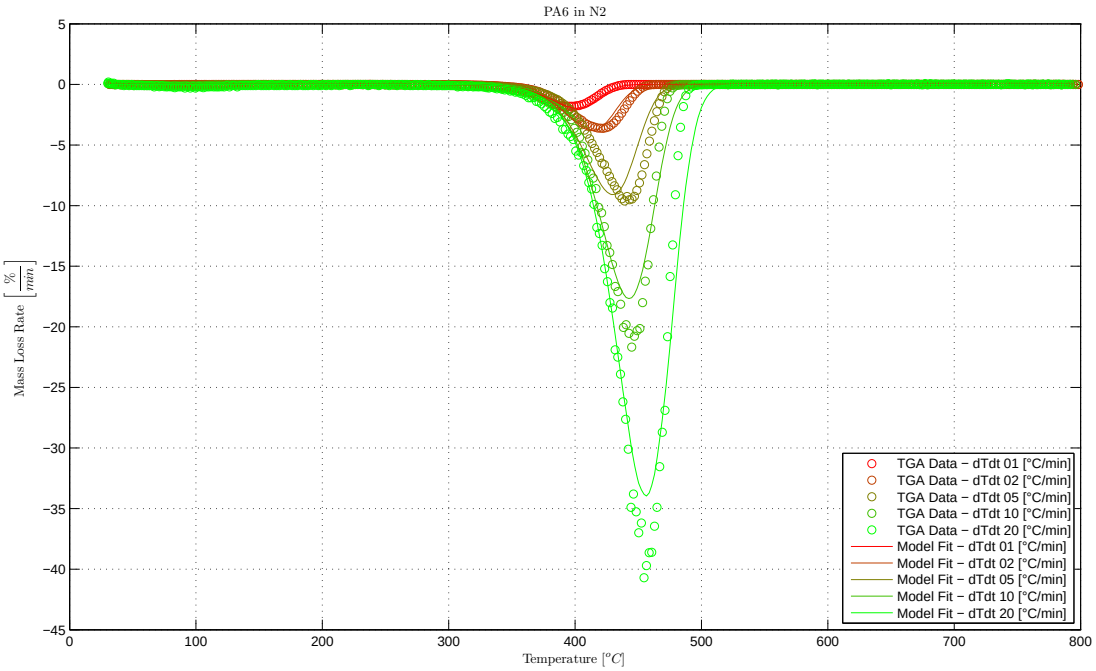

Figure 9 TGA MLR data and reduced reaction schemes fits for PA6 in inert atmosphere (N_2)

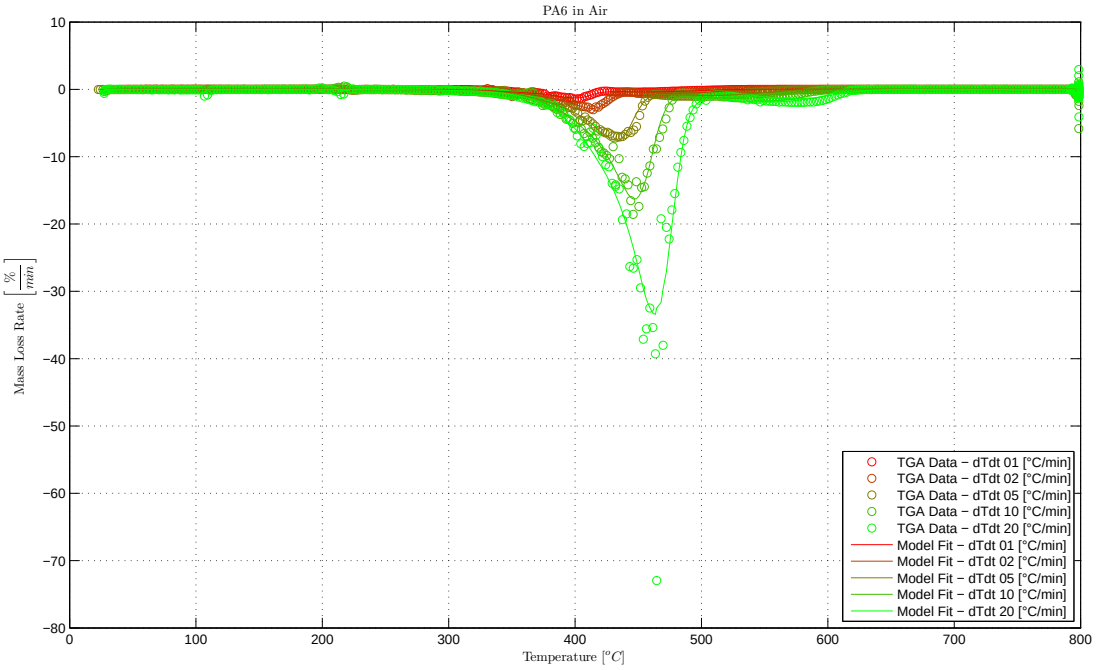

Figure 10 TGA MLR data and reduced reaction schemes fits for PA6 in air

3.3 Mass fraction of flammable gases $Y_{F,S}(x,t)$ from TGA-EGA

Section 2.1.2 highlighted the importance of the gaseous fuel produced as part of the ignition process. To obtain the mass fraction of flammable gases present in the local products of degradation, TGA-EGA is used. The TGA provides the mass loss, while

the EGA determines the concentrations of all compounds emerging from the degradation. This enables reconstruction of the degradation compounds. The variable, $Y_{F,S}(0,t)$, represents a global contribution of all compounds that can be further oxidized. This is the same form of analysis as described in section 3.2 (TGA). However, it has been modified to simultaneously conduct an Evolved Gas Analysis (EGA) of the exhaust gases. For the analysis this allows to use the time and temperature dependant mass and mass loss data obtained from the TGA together with the gas concentrations of the exhaust gasses, measured by the EGA. By converting volumetric gas concentrations of CO_2 and CO with the ideal gas law Equation (36) into mass rates ($\dot{m}_{CO_2}, \dot{m}_{CO}$), one is able to subtract these from the mass loss rate of the sample ($\dot{m}_s$).

$$p \cdot V = n \cdot R \cdot T = \frac{m}{MW} \cdot R \cdot T \tag{36}$$

$$p \cdot \dot{V} = \dot{n} \cdot R \cdot T = \frac{\dot{m}}{MW} \cdot R \cdot T \tag{37}$$

This leads to the mass generation rate of flammable gases ($\dot{m}_F$) in form of equation (38) or (39) depending whether it is decided that CO would or would not significantly contribute to a combustion process (see Figure 11).

$$\dot{m}_{F_{(CO_2)}} = \dot{m}_s - \dot{m}_{CO_2} \tag{38}$$

$$\dot{m}_{F_{(CO_2,CO)}} = \dot{m}_s - \dot{m}_{CO_2} - \dot{m}_{CO} \tag{39}$$

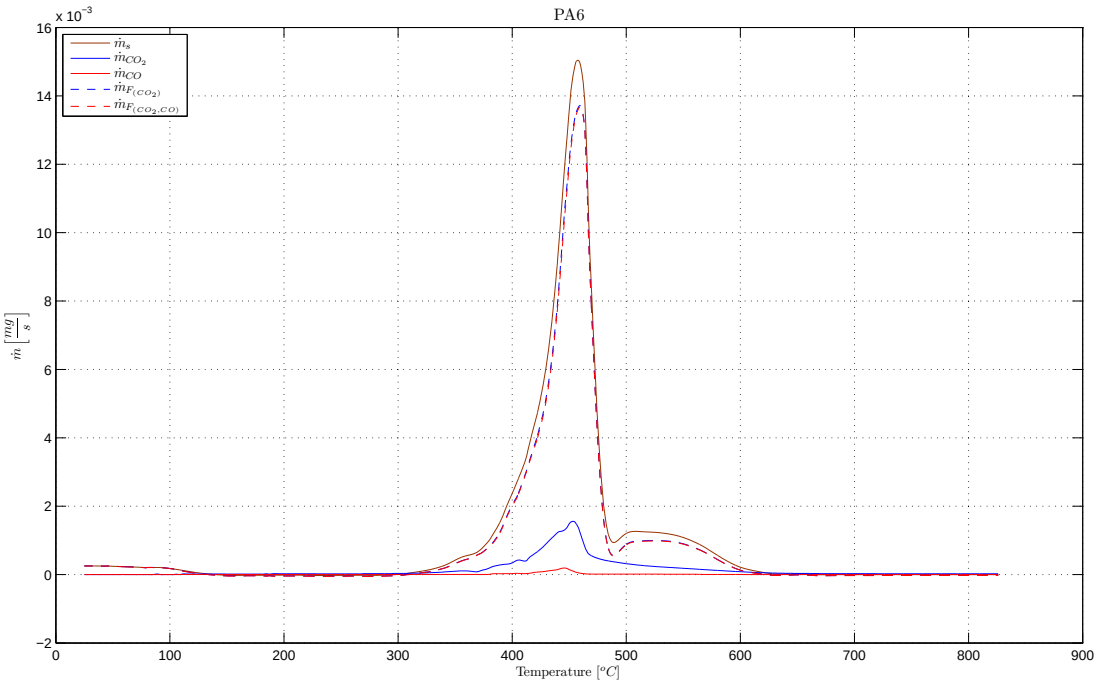

Figure 11 TGA-EGA Mass Rates of PA6

Dividing these by the mass loss rate of the sample (equation (40) and (41)) one obtains the mass fraction of flammable gases $Y_{F,S}(0,t)$ which, to recapitulate, includes all compounds that are susceptible to further oxidation.

$$Y_{F,S}(0,t)_{(CO_2)} = \frac{\dot{m}_{F_{(CO_2)}}}{\dot{m}_s} \tag{40}$$

$$Y_{F,S}(0,t)_{(CO_2,CO)} = \frac{\dot{m}_{F_{(CO_2,CO)}}}{\dot{m}_s} \tag{41}$$

A graphical representation of this for PA6 is presented in Figure 12. Figure 12 only presents data for the 200-600 ºC temperature range. This range corresponds to the main reaction zone. The data outside this range is unusable, as it is compromised by the small amount of mass produced, which gives a very small signal to noise ratio, thus unusable data (see Figure 11).

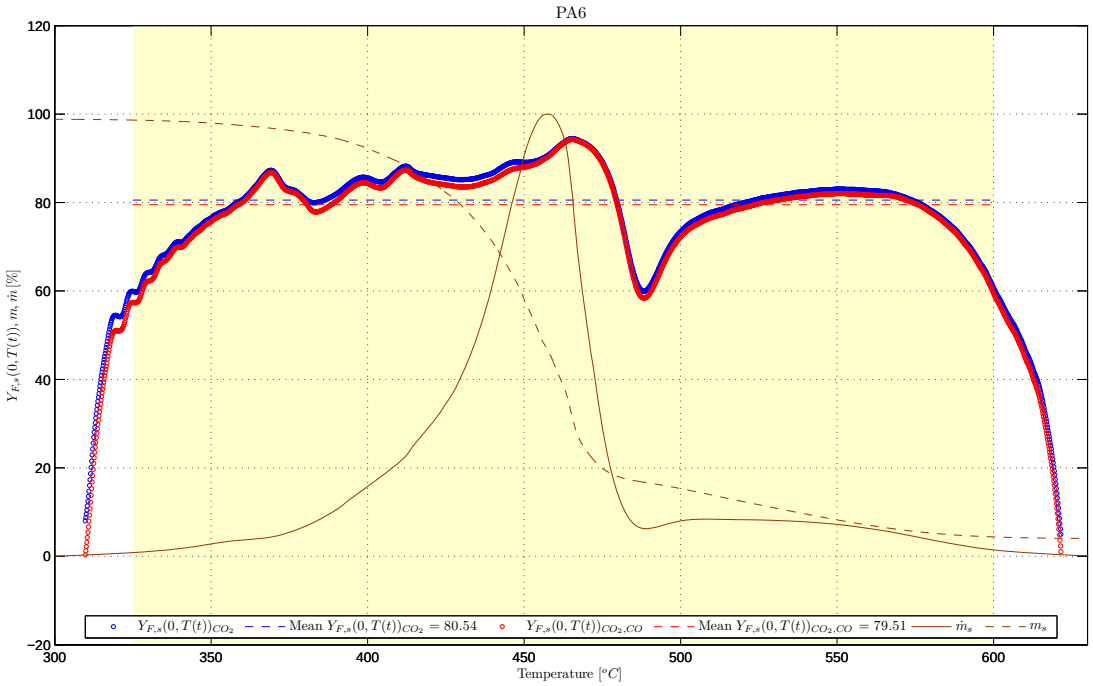

Figure 12 Mass fraction of flammable gases $Y_{F,S}(0,t)$ for PA6

From Figure 12 (which represents the situation for PA6) or from the graphs of the other materials presented in Appendix A.2, it is possible to conclude, that there is no big difference between the cases with and without CO and that the mass fraction of flammable gases is fairly constant for a large temperature range.

A material specific generic lookup table can be generated from these results in order to utilise the mass fraction of flammable gases $Y_{F,S}(0,t)$ for an ignition analysis. To enable further simplification, a constant mass fraction of flammable gases can be assumed and used for modelling. Table 13 presents an average value obtained from the experiments ($Y_F(0)$). It will be assumed that, while the amount of gas phase fuel increases in time, the mass fraction of effective fuel will rapidly attain a steady state value similar to that of the one obtained during Thermogravimetric-Analysis. The results for the materials studied are presented in Table 13.

Material	**$Y_{F,S}(0)_{(CO2)}$**	**$Y_{F,S}(0)_{(CO2,CO)}$**
	[%]	[%]
PA6	80.5	79.5
PA6+FR	86.2	84.8
PA6+NC	76.3	75.0
PA6+NC+FR	86.9	86.0

Table 13 Constant fuel mass fractions for the different materials studied.

Experimental data similar to that presented in Figure 11 and Figure 12, for the other materials, is also presented in Appendix A.2.

It should be noted, that this work focuses on the explanation of a methodology and, though many data set were studied, only one set has been presented in full.

3.4 Phase transition (T_m, T_g, ΔH_f, ΔH_c)

For the thermophysical analysis, it is of interest to know when the thermophysical material properties and behaviour change as highlighted in section 2.1.4, 2.1.5, 3.5, 3.6 and 3.7. Phase transition is a process that has the characteristic of taking a given medium with given properties and transforming some, or all, of that medium into a new medium with new properties. This occurs either at a specific temperature or over a temperature range. Furthermore, it is vital to know whether heat is generated or consumed during the process. This is discussed in section 2.1.6.

As they are heated, aliphatic polyamides, such as PA6 [69], change from glassy, via soft/rubbery to a liquid state, before they pyrolyse. They can be separated, in terms of temperature, by the glass transition temperature (T_g), and melting temperature (T_m). A detailed explanation of these phenomena and how to obtain them can be found in the literature [19, 63, 70]. In brief, the glass transition temperature is the temperature range that separates the value above which amorphous (non-crystalline) materials are fluid or rubbery and below which they are immobile and rigid, simply frozen in a disordered, non-crystalline state. The temperature range assigned to the melting separates the state above which amorphous materials are fluid and below which they are rubbery or solid. The glass transition temperature can be determined by methods such as Differential Scanning Calorimetry (DSC) [71, 72], Thermomechanical Analysis (TMA) [73, 74] or Dynamic Mechanical Analysis (DMA) [75] and the melting temperature by methods such as DSC [76] and Differential Thermal Analysis (DTA) [77].

In this study, T_g and T_m are obtained form ordinary Differential Scanning Calorimetry. Figure 13 shows the DSC scans (under nitrogen: 50mL/min, heating

rate: 10°C /min, sample size ~5mg) for the different PA6 based materials that were obtained as part of the PREDFIRE-NANO project [61].

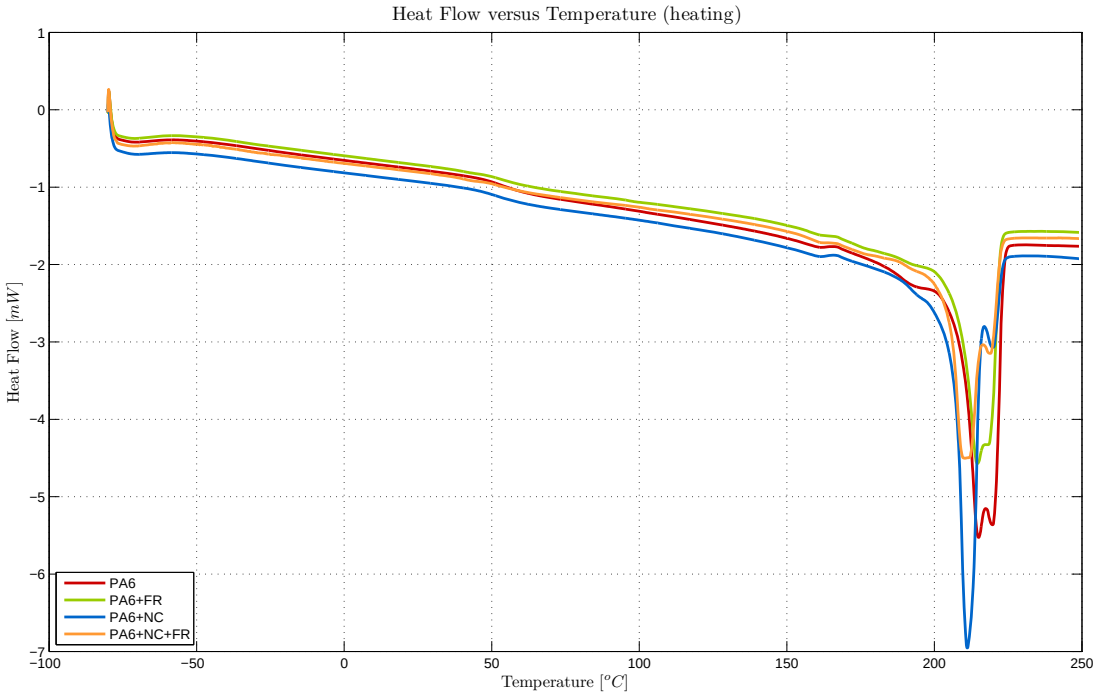

Figure 13 DSC heating scan for PA6 based materials

DSC is a thermal analysis where the difference in the amount of heat that is required (as a function of temperature) to keep the temperature of a sample and a reference during a heating, cooling and/or isothermal process at the same temperature. It is of interest how much more or less heat is required to flow to the sample compared to the reference to maintain both at the same temperature. Whether it is more or less depends on whether the process is exothermic or endothermic. This enables the study of the (transitions) processes that require or produce energy such as melting, glass transitions, or a range of more complex events such as exothermic decompositions. Furthermore, it provides the researcher with a quantitative measure of these phenomena and at which temperature they occur. More details can be obtained from [19, 78].

The glass transition manifests itself as a discontinuity (step) of the recorded DSC signal. This is also described as a second-order transition (second-order derivative of the Gibbs free energy equation with respect to temperature) [19] and is due to a change in heat capacity. Figure 14 shows the temperature region around the glass

transition for PA6 and its 1st and 2nd derivative. The same graph for the other materials can be found in Appendix A.2.

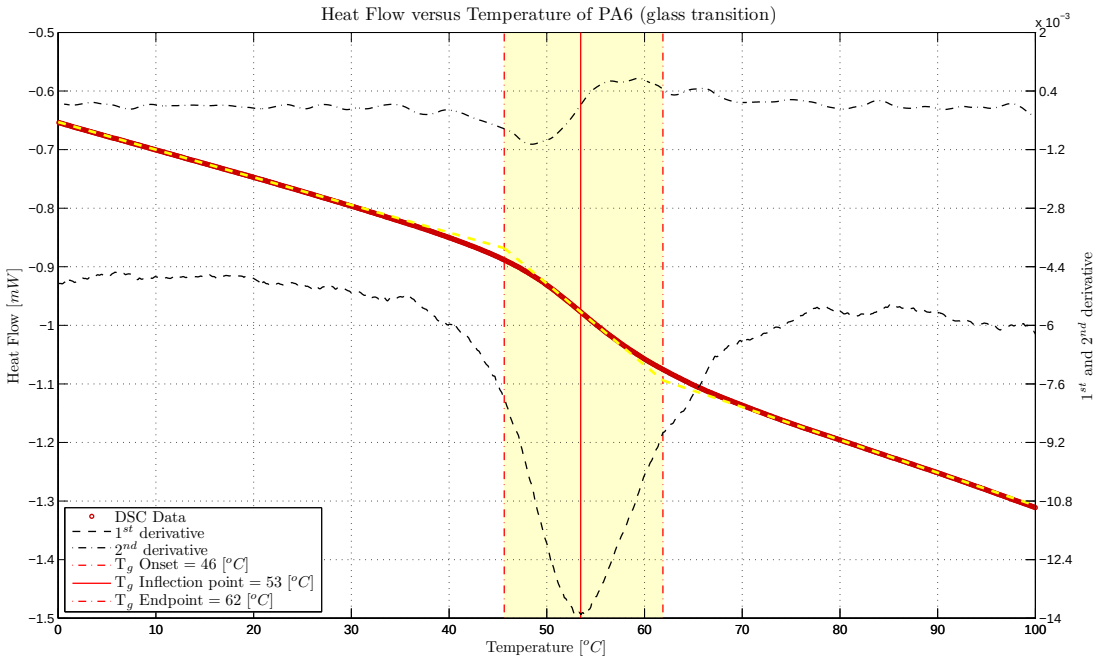

Figure 14 Heat Flow versus Temperature of PA6 in the temperature region of the glass transition

Gabbott [19] and others [78] have noted that the glass transition is not a single point and occurs over a temperature region rather then a single point. Nevertheless, usually just one value is given. Further confusion is caused by the fact that there are different methods and definitions to determine that point. Since it might be interesting for the analysis, three temperatures are presented here which denote the borders and a notional middle point as depicted in Figure 14 and Table 14. The calculated glass transition temperatures are:

1. “Onset”: Thus the intersection of the tangents from the line before the step and the slope of the step

2. “Inflection point”: The inflection point of the step and

3. “Endpoint”: The intersection of the tangents from the slope of the step and line behind the step.

Material	**T_g**		
	Onset	Inflection Point	End point
	[ºC]	[ºC]	[ºC]
PA6	46	53	62
PA6+FR	45	53	61
PA6+NC	43	52	61
PA6+NC+FR	45	51	59

Table 14 Glass transition temperatures of PA6 based Materials

The glass transition temperatures of the material analysed falls within the range of glass transition values found in the literature [62, 79-82]. The temperatures of Table 14 indicate, when a property change can be expected, and their corresponding behaviour with temperature. This process does not produce or consume heat.

Melting appears as a peak in the recorded DSC signal. It is also described as a first-order transition and is a process that results in the phase change of a substance from a solid to a liquid. Melting has a discontinuous step in the first-order derivative of the Gibbs free energy equation. Consequently, the first derivative of the enthalpy curve results in a peak caused by the melting transition. It is an endothermic process whereby the sample absorbs energy. Integration of the peak gives the heat of fusion (ΔH_f), also known as the heat of melting (ΔH_m) [19]. Figure 15 shows the temperature region where melting occurs for PA6 and its corresponding first and second derivatives from which multiple events can be better distinguished than from raw data. This is important, since PA6 is a polymer that can crystallize in two different forms (α- and γ-form) [69, 83]. These two crystalline forms therefore, are likely to melt at different points in temperature (and time). The graphs for the other PA6 based materials can be found in Appendix A.3.

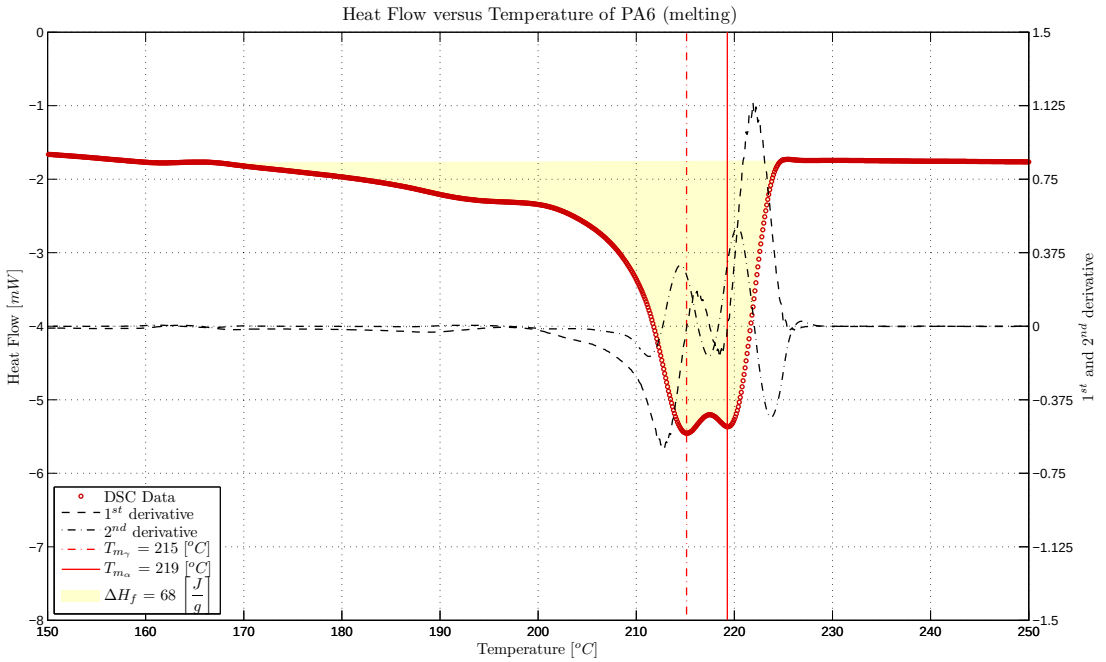

Figure 15 Heat Flow versus Temperature of PA6 around the melting region

For the glass transition temperature, the melting process happens over a range. It is therefore, advantageous to know its onset, peak/mean and its endpoint. For single crystals, the onset is commonly used as the single distinguishing parameter [19]. For materials such as PA6, that contain multiple crystals, the melting process is broad and gradual. Trying to obtain an onset temperature is difficult and possibly meaningless because the melting process is so broad and gradual. The temperature at the maximum peak or, if distinguishable, multiple peaks (melting of the α- and γ-form crystal) is the most meaningful of these indicators. This is presented in Figure 15 and Table 15. These temperatures indicate when a property change can be expected, how their behaviour changes with temperature. The highlighted area represents the range where melting takes place. This also depicts the heat of fusion (ΔH_f). The obtained melting points and heat of fusion for the base material (PA6) correspond well to values found in the literature [62, 79, 84].

The heat of fusion (ΔH_f) is reduced when nanocomposites or flame-retardants are introduced to the base material. The lowest value of heat of fusion is obtained when both additives are present. This observation does not correspond with the findings from literature. Ammala et al. [85] reports that Nylon MXD6 with nanocomposites (Cloister 30B - the same nanocomposites as used in this work) shows a slightly

higher glass transition temperature, melting temperature and heat of fusion values as the base material. The opposite behaviour is observed for the materials in this analysis. This could be due to the different base material, though nothing conclusive is known.

Material	**T_m**		**ΔH_f**
	[ºC]	[ºC]	[J/g]
	γ	α	
PA6	215	219	68
PA6+FR	215	218	53
PA6+NC	211	219	65
PA6+NC+FR	211	219	51

Table 15 State distinguishing Temperatures of PA6 based Materials

Cooling of the material is not of direct interest to this work since the interest lies solely at the heating process. Nevertheless, it might be of interest whether or not the materials analysed here crystallise, which they clearly do as per Figure 16.

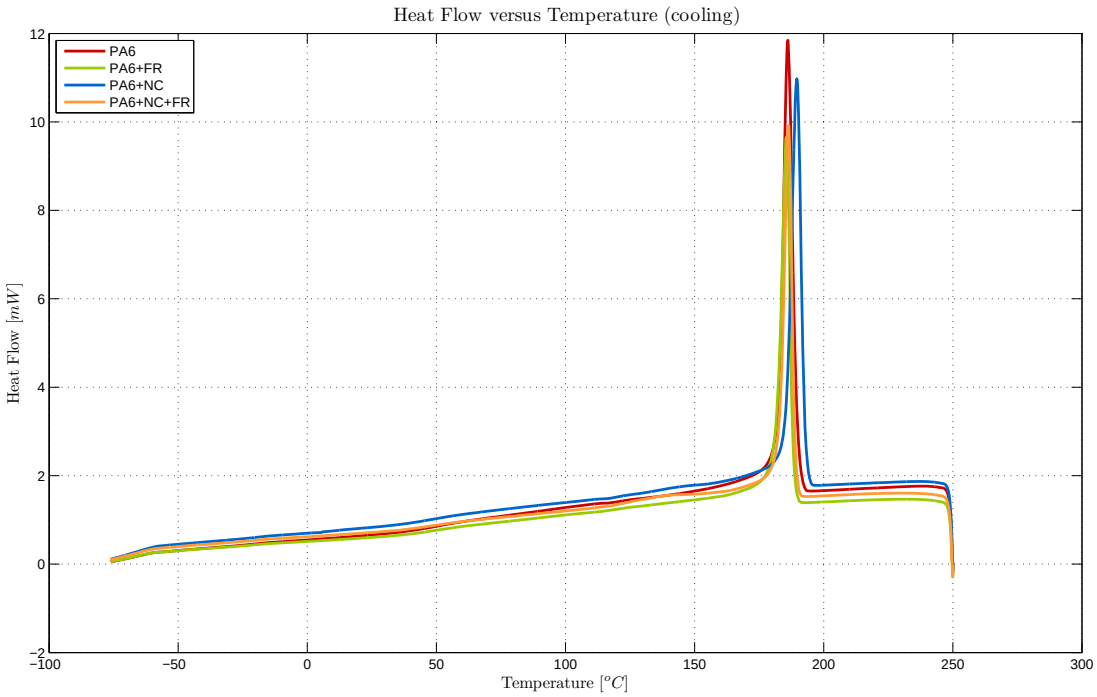

Figure 16 DSC cooling scan for PA6 based materials

Further information about the crystallisation temperatures or the heat of crystallisation (ΔH_c) can be found in Appendix A.4.

3.5 Specific Heat capacity (c_p)

Mathematically describing the ignition process of solids requires knowledge of their temperature dependant specific heat capacity as mentioned section 2.1.5. To obtain quality and retain simplicity, literature [19, 78, 86] suggests it is best to use Temperature Modulated Differential Scanning Calorimetry (TMDSC) to obtain the specific heat capacity (c_p). This was also what the researchers of the PREDFIRE_NANO project concluded.

TMDSC is a modification of DSC that overcomes some of its inherent limits. The conventional heating programme is modulated by some form of perturbation (usually by applying a sinusoidal temperature over a constant temperature rate) and the resulting heat flow signal is then analysed to deconvolute the response to the perturbation from the response to the underlying heating programme. This technique enables separation the heat flow into its reversing (thermodynamic or heat capacity related) and non-reversing (kinetic) components. This provides additional information and improves the quality of the data obtained [19, 78, 86-88].

The reversible heat capacity signal obtained during the Temperature Modulated Differential Scanning Calorimetry corresponds to the specific heat (c_p). Figure 17 shows the resulting TMDSC scans and the specific heat capacities versus temperature (under nitrogen, heating rate: 2°C /min, sample size ~10mg). Each of these results is for the different PA6 based materials that were tested as part of the PREDFIRE-NANO project [61].

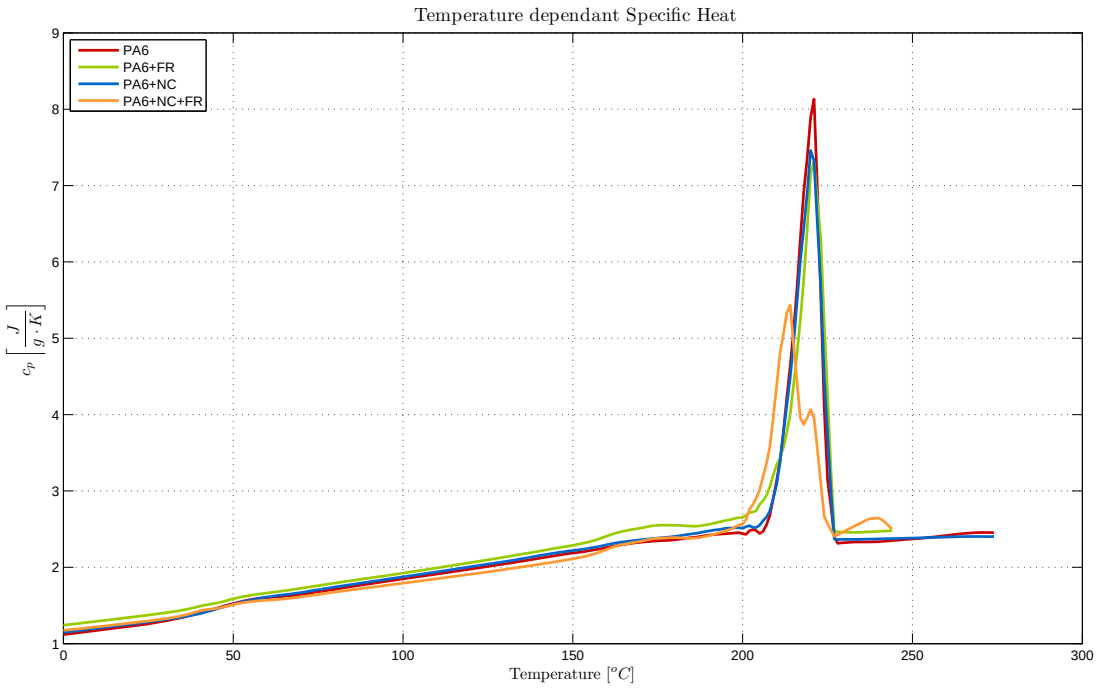

Figure 17 Specific heat capacity signal obtained from TMDSC for the PA6 based materials

When using these graphs to obtain the specific heat capacity (c_p) at a specific temperature, it is important to note that the clearly protruding peaks correspond to the discontinuity of the heat capacity during the melting process. These have no significance for the specific heat capacity (c_p) itself.

A comparison of Table 17 with values found in a review paper [89], shows that they are in good agreement (Figure 18) in terms of the order of magnitude and slope. The difference between the results stem from the fact that the molecular weight used in the literature (113 [kg/mol]) [89] is not likely to be the actual molecular weight of the PA6 analysed in this study. Other references e.g. [90] used different molecular weights (e.g. 131.2 [kg/mol]) and produce results that are significantly closer to the findings of the TMDSC measurements of Figure 18. For reference, these data points will be plotted on each graph for the different materials tested.

As mentioned previously, the glass transition can be described as a second-order transition (second-order derivative of the Gibbs free energy equation with respect to temperature), which is caused by a (sudden) change in specific heat capacity. This change should theoretically manifest itself in a change in specific heat capacity slope. Melting, on the other hand, manifests itself as a discontinuity (step) in the first-order

derivative of the Gibbs free energy equation and a corresponding step in the specific heat capacity (c_p). For the later analysis, Figure 18 for PA6, and the other data plots of appendix A.5, contains linear root mean square (rms) data fits for the glassy, soft and liquid sate of PA6, where the last data point of the glassy state falls on the first data point of the soft state.

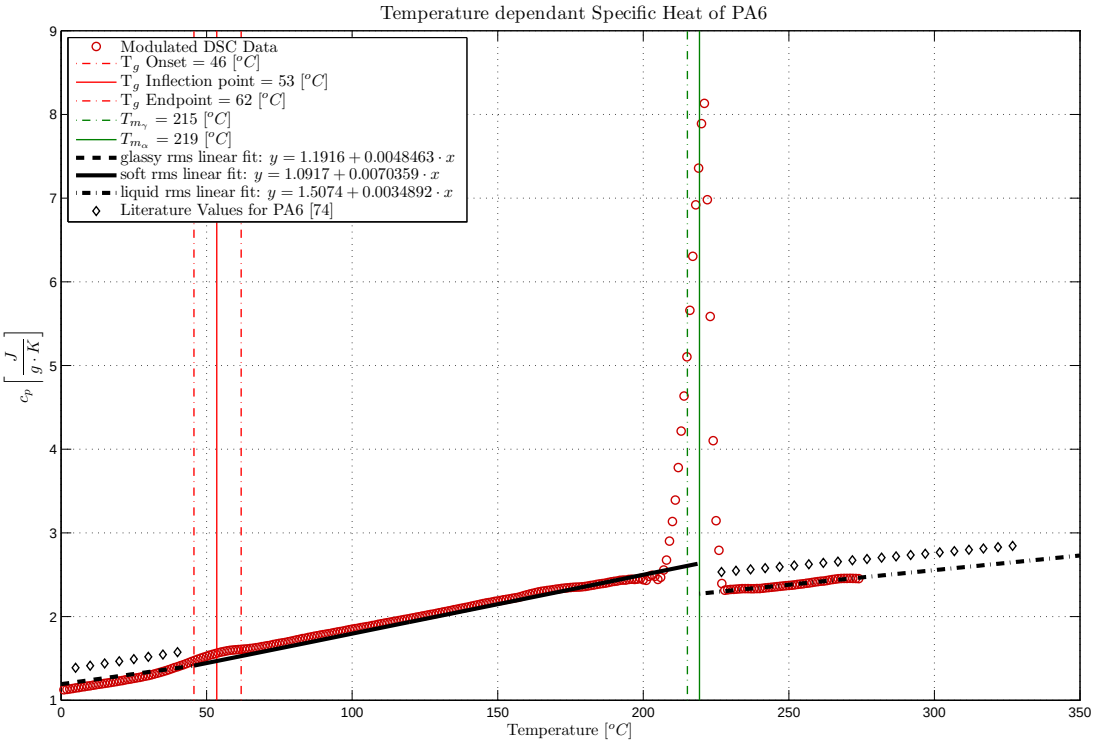

Figure 18 Specific heat capacity (c_p) versus temperature of PA6

3.6 Density (ρ)

Modelling the ignition process of solids requires knowledge of the dependence of density on temperature (as mentioned section 2.1.5). The ambient densities of the materials analysed in this study are listed in Table 16. These are measured densities rather than literature values, and represent the basis for the determination of the temperature dependant values.

Material	weight	thickness	width	depth	density
@ 20°C	[g]	[mm]	[mm]	[mm]	[g/cm^3]
PA6	67.8	6.21	99.0	99.0	1.114
PA6+FR	69.8	5.95	98.9	98.8	1.201
PA6+NC	68.2	6	99.2	99.2	1.156
PA6+NC+FR	70.7	6.02	99.1	99.1	1.196

Table 16 Densities at 20°C

Unfortunately, the change in the density (ρ) as a function of temperature was not analysed with sufficient detail as part of the PREDFIRE-NANO project [61] to have a complete set of such data. This fact, together with limited amount of materials, was unfortunate, since density resembles is one of the basic intrinsic material properties.

For the base material PA6 this is less of a problem, since some information is available from the literature [26], see Figure 19. In combination with the measured density at ambient temperature (Table 16), a reasonably accurate density temperature curve can be estimated. For this estimation to be made, the assumption that the density does not have a step change must be made.

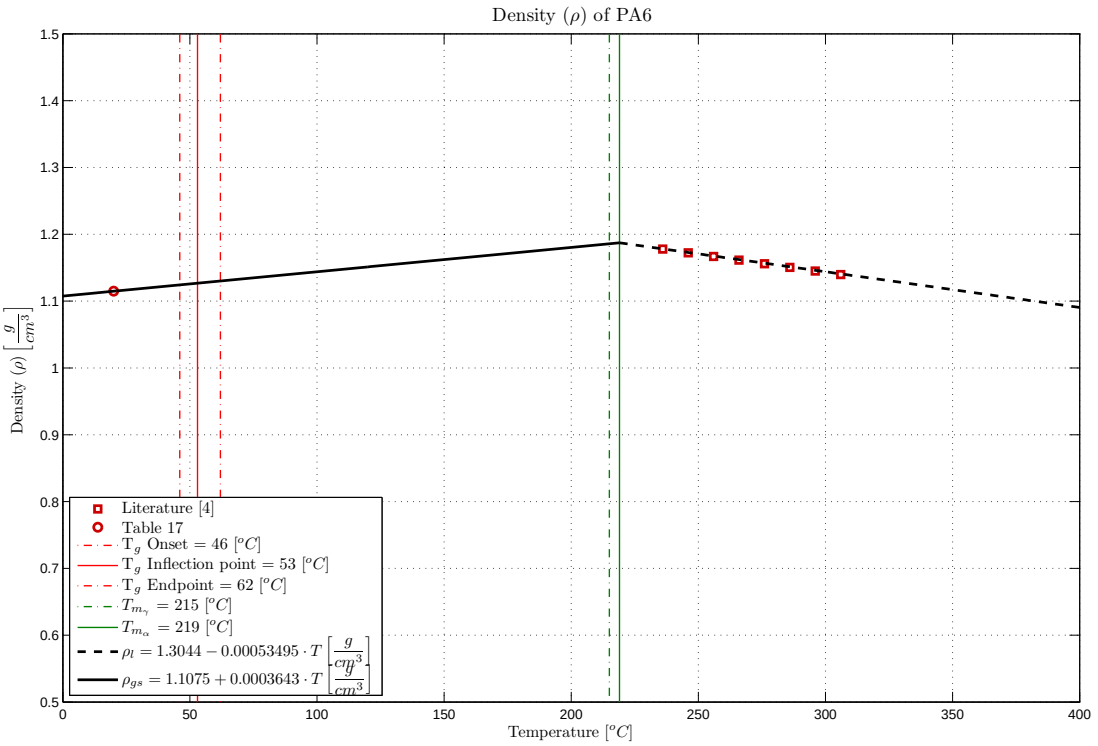

Figure 19 Density versus temperature of PA6

The temperature dependant expansion factor is commonly used to determine the temperature dependant density. Such data was, for the PA6 materials in this study only available for those with flame-retardants and was obtained using a rheometer. It seems, that the parties involved in the PREDFIRE-NANO project [61] focused more on the determination of the temperature dependant expansion of a forming

intumescent then on obtaining all intrinsic material properties, to which the density clearly belongs.

From the change in the linear thermal expansion (ΔL) as a function of the change in temperature (ΔT) one can calculate the materials' temperature dependant density using the following correlations:

$$\rho = \frac{\rho_0}{1+\gamma \cdot \Delta T}\,[91] \tag{42}$$

$$\alpha_l = \frac{\Delta L}{L_0 \cdot \Delta T}\,[91] \tag{43}$$

$$\gamma \approx 3 \cdot \alpha_l\,[91] \tag{44}$$

where L_0 is the starting length of the test specimen, ρ_0 is the starting density and γ is the volumetric expansion coefficient. The volumetric expansion coefficient is about 3 times the linear expansion coefficient (α_l) assuming that the material is isotropic. The linear thermal expansion (ΔL) as well as the density (ρ) as a function of temperature is presented for PA6+FR in Figure 20. The graphs for the PA6+NC+FR can be found in Appendix A.6.

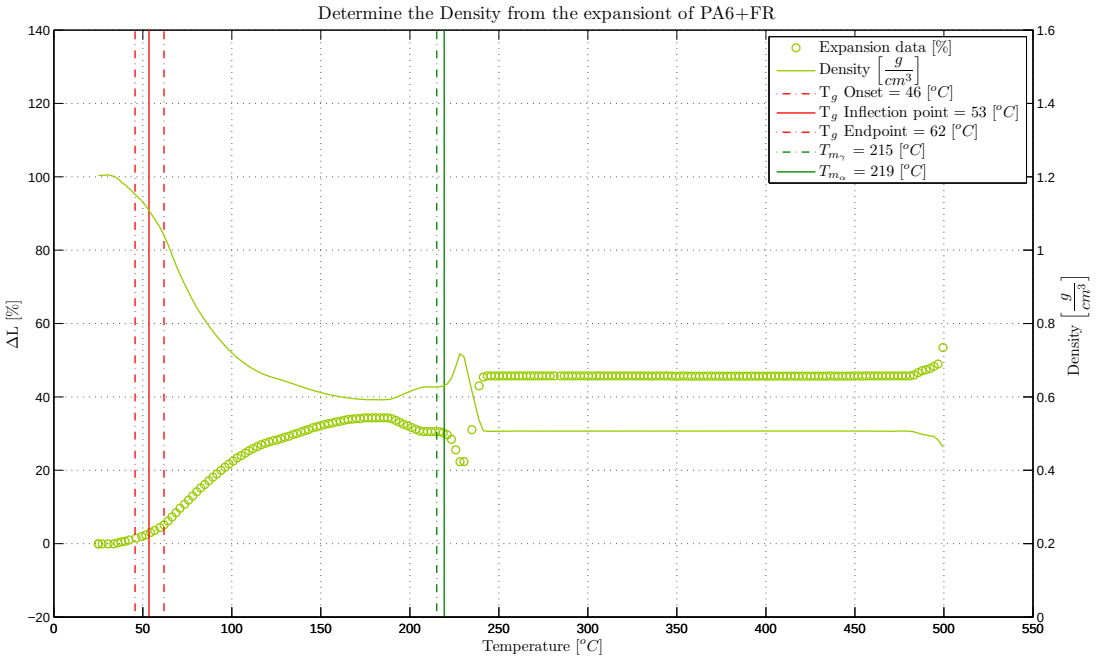

Figure 20 Density versus temperature of PA6+FR

3.7 Thermal conductivity (k)

Thermal conductivity (k) is one of the key intrinsic material properties (section 2.1.4 and 2.1.5). Despite this, it has not yet been obtained as part of the PREDFIRE-NANO project [61]. As expressed in section 2.1.5 the thermal conductivity is a function of the temperature. It would have been most valuable, therefore, to obtain this as a function of temperature. The only available instrument however, was a "guarded heat flow meter" from Dynatech (TCHM-LT C-Matic). It provided only an average thermal conductivity between ~60 and 100°C. This instrument was used to provide some baseline values for the thermal conductivity of the materials of interest as depicted in Table 17. The measured value for the base material (PA6) falls within the range of the thermal conductivity reported in the literature [26, 92]. This, to some extent, validates the measurement.

Material	Thermal conductivity
between ~60 & 100°C	[W/mK]
PA6	0.2825
PA6+FR	0.2474
PA6+NC	0.2900
PA6+NC+FR	0.2984

Table 17 Thermal conductivity between ~60 and 100 C

The literature suggests [26] that, as the temperature rises, the thermal conductivity of amorphous materials increases gradually in the glassy region and decreases slowly or remain constant in the rubbery region. Since the measurement covers the whole range of glassy and rubbery regions, these measurements will be classified as global equivalents to a temperature dependent thermal conductivity.

3.8 Heat(s) of pyrolysis (ΔH_P)

The importance of the heat of pyrolysis/reaction for the ignition process of solids was highlighted in section 2.1.6. The heat associated with the endothermic decomposition reaction (referred to in this work as the heat of pyrolysis, (ΔH_P)) can be obtained from DSC analysis equivalent to the determination of the heat of fusion (ΔH_m) in section 3.4. When interested in modelling pyrolysis one is not only interested in the total heat of pyrolysis thus the total area under the peak(s), but the heat of pyrolysis

($\Delta H_{P,i}$) for the various reactions steps. As per Table 11 and Table 12, the pyrolysis is modelled as a series of reactions. These reactions show as endothermic peaks when conducting a DSC analysis. If there is a single step, then the integral over the peak defines the heat of pyrolysis. If there are multiple steps, then each peak defines the heat of pyrolysis of an individual step. Given the reaction steps as per Table 11 and Table 12, the heats of pyrolysis for the different materials can be determined from DSC analysis.

Unfortunately, the attempt to obtain the heat of pyrolysis ($\Delta H_{P,i}$) can go no further than this point. The available DSC data from the PREDFIRE-NANO project [61] stopped just after melting at temperatures of around 250 °C. The pyrolysis reaction, however, as presented in section 3.2 started above this temperature.

Usually with the known reaction rates from TGA data (section 2.1.1) a simple heat transfer model can be constructed for the heat exchange in a DSC. By fitting the heat transfer model to the DSC experimental results, the different values of $\Delta H_{P,i}$ can be obtained. Unfortunately, this could not be completed here.

What could be done with the available data was to determine when (in temperature) endothermic peaks could be expected to occure. The first derivative of the relative mass of PA6 in N_2 and Air for the TGA data is presented in Figure 21 and Figure 22 together with the points in temperature when the reaction appears to be most vigorous and is thus at its peak. These are simply indicators where the reaction might take place.

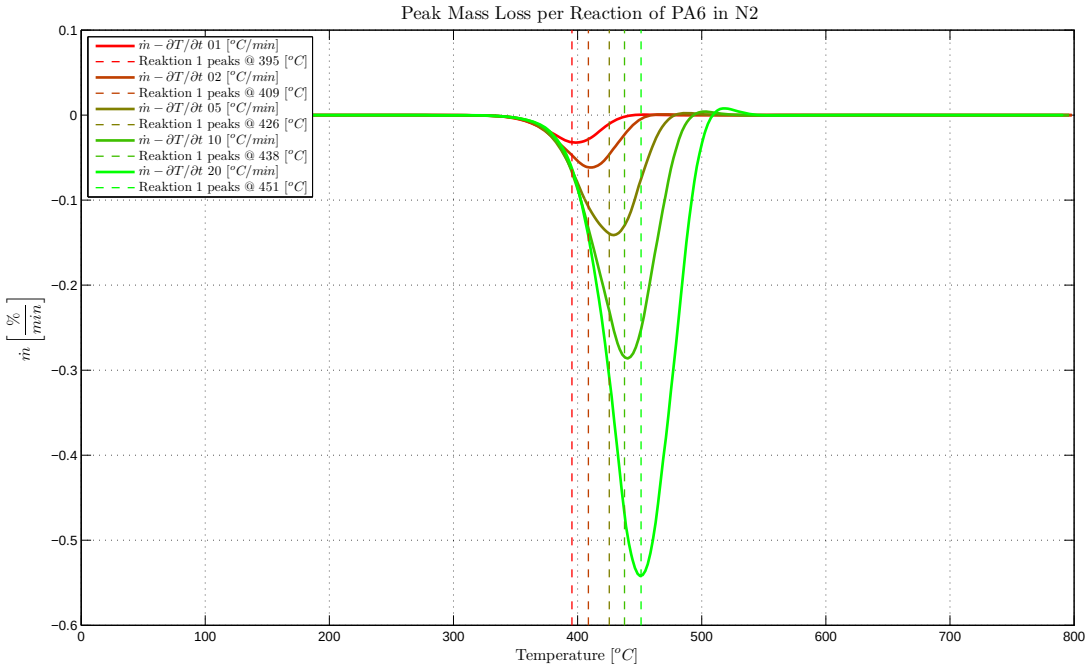

Figure 21 Temperature when the reaction seams to be most vigorous PA6 in N_2

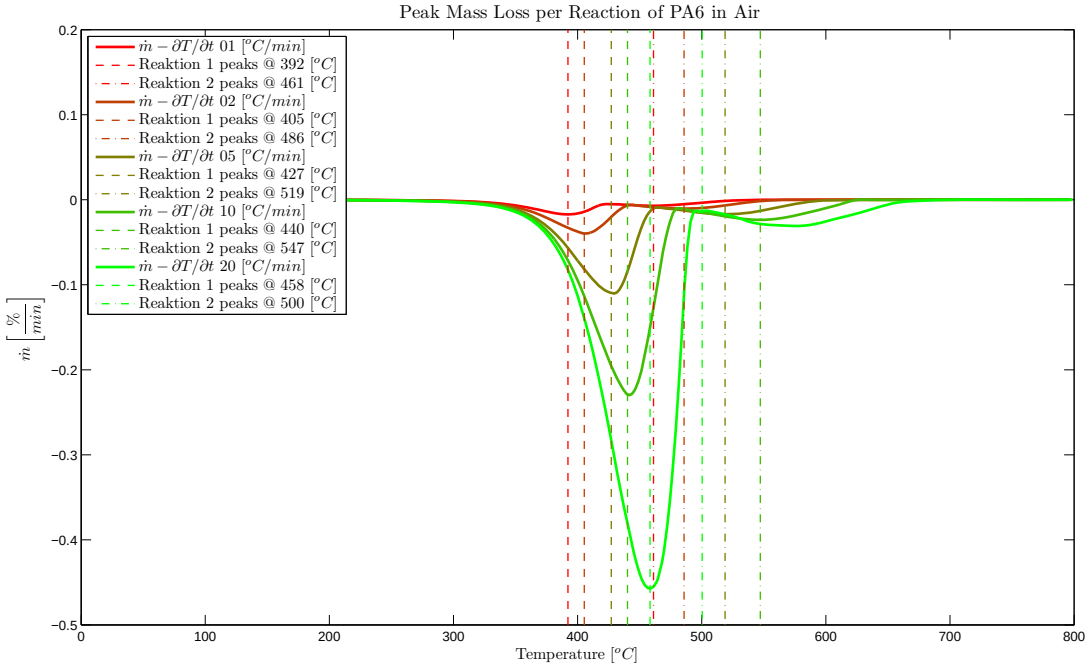

Figure 22 Temperature when the reaction seams to be most vigorous PA6 in air

3.9 Convective heat transfer coefficient (h_c)

The involvement of the convective heat transfer coefficient in the ignition process of solids has been put into context in section 2.2. It was determined using an inert solid (aluminium block) heated at various, but constant, heat fluxes. By fixing the heat

flux and monitoring the temperature evolution within the solid, the convective heat transfer coefficient for the Cone Calorimeter [10] and the FPA [1] is being established, by deploying the tes setup as depicted in Figure 23.

To solve this inverse mathematical problem, one has to, if one wants to arrive at a temperature dependant heat transfer coefficient (h_c), use the results of the test described in Figure 23. The in-depth temperature measurements over time must be analysed using the one-dimensional heat diffusion equation (45). Assuming that it is valid for the specific case, it states:

$$\rho \cdot c_p \cdot \frac{\partial T}{\partial t} = \frac{\partial}{\partial x}\left(k \frac{\partial T}{\partial x} \right) \tag{45}$$

where ρ is the density, c_p is the heat capacity, $\partial T/\partial t$ is the change in temperature over time, k is the thermal conductivity, $\partial T/\partial x$ is the change in temperature over depth x, and $\partial/\partial x$ is the divergence.

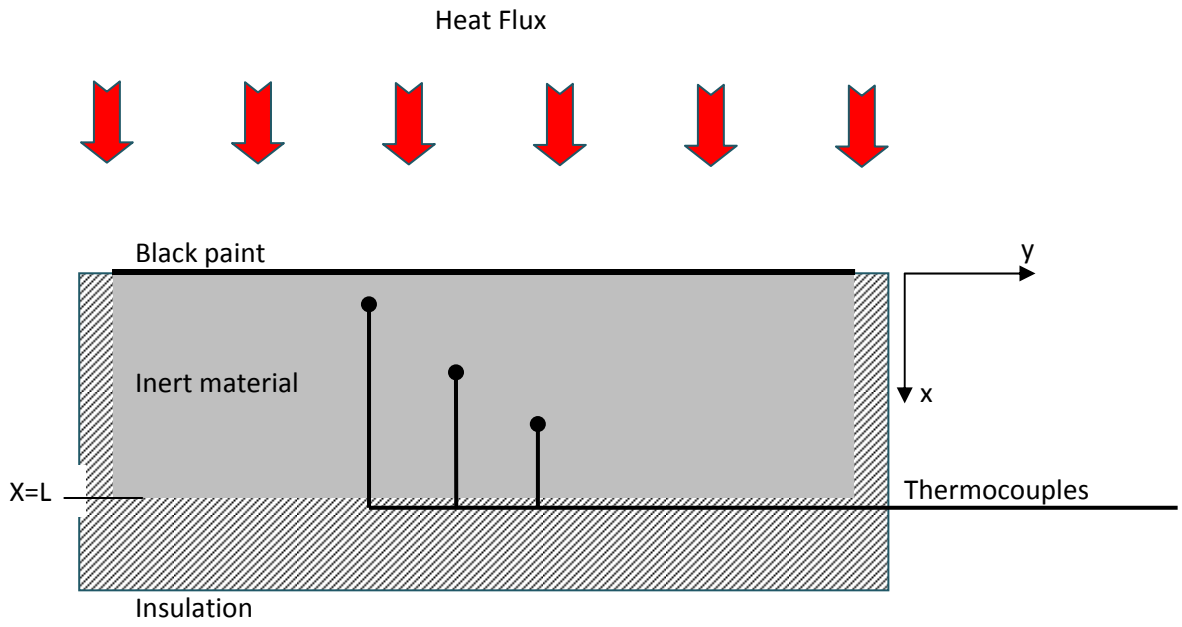

Figure 23 Test setup to determine the convective heat transfer coefficient (h_c)

Equation (45) is a partial differential equation, which usually has multiple solutions and requires, for a definite answer, additional conditions e.g. boundary and initial conditions. The boundary condition at x=0 has, for the setup in Figure 23, the following form:

$$x=0 \qquad -k\cdot\left.\frac{\partial T}{\partial t}\right|_{x=0} = a\cdot q_{EXT} - \varepsilon\cdot\sigma\cdot\left(T_{(x=0,t)}^4 - T_a^4\right) - h_{CV}\left(T_{(x=0,t)} - T_a\right) \qquad (46)$$

where “a” is the absorptivity, ε is the emissivity, k the thermal conductivity of the aluminium block, σ is the Stefan–Boltzmann constant, and h_c the to determine convective heat transfer coefficient, which is to be determined. In this equation, T_a is the ambient temperature and q_{EXT} the incident heat flux. Equation (46) deviates slightly from equation (13) because it incorporates surface instead of in depth absorptivity.

The boundary condition at x=L, when assuming the well-insulated (adiabatic) case, has the following form:

$$x=L \qquad -k\cdot\left.\frac{\partial T}{\partial t}\right|_{x=L} = 0 \qquad (47)$$

The large ratio between the thermal conductivity of aluminium and the insulation guarantees the precision of the above boundary condition. The initial condition is:

$$t=0 \qquad T(x, t=0) = T_a \qquad (48)$$

Knowledge of the temperature dependant properties for the used aluminium:

$$\text{Density:} \qquad \rho = 2762 - 0.1864\cdot T \qquad (49)$$

$$\text{Specific Heat:} \qquad c_p = 705 + 0.6375\cdot T \qquad (50)$$

$$\text{Thermal Conductivity:} \qquad k = 135.2266 + 0.145\cdot T \qquad (51)$$

and the absorptivity ($a = 0.95$) and emissivity ($\varepsilon = 0.86$) of the black paint, together with the incident heat flux (q_i) to which the test specimen was exposed to, result in only one remaining parameter: the convective heat transfer coefficient (h_{CV}). Now it is possible to numerically fit the one dimensional heat transfer model by minimising the Root Mean Square (RMS) of the temperature difference between the measured values and the calculated values of the model using equation (52).

$$z = \sqrt{\frac{1}{o}\cdot\sum_{k=1}^{o}\frac{1}{n}\cdot\sum_{j=1}^{n}\frac{1}{m}\cdot\sum_{i=1}^{m}\left(T_{Model_{i,j,k}} - T_{Tests_{i,j,k}}\right)^2} \qquad (52)$$

where “m” is the number of temperature data point to compare “n” is the number of depths where the temperature was measured, and “o” is the number of heat flux

cases. Various heat flux cases and various depths were used to arrive at a robust solution. This is important when it is considered that the accuracy and values of a test could possibly be slightly different due to, for example, operating and measurement errors. These could lead, for a single data fit, to a mathematically sound but physically wrong answer. The mathematical model, however, is valid for all these cases. The solution, therefore, should best fit all the cases and not just one.

Since the convective heat transfer coefficient (h_c) is a function of the surface temperature [25], equation (53) is introduced to account for it. For the given cases of the Cone Calorimeter [10] and the FPA [1] it can be assumed that it is composed of a quasi-steady state forced flow term (stemming from the extraction and/or the induced flow field of the apparatus), as well as a temperature dependant term (stemming from a hot horizontal plate (test specimen) induced natural convection).

$$h_{CV} = h_{CV,a} + h_{CV,b} \cdot (T - T_{ambient})^{1/4} \tag{53}$$

For the specific case of a hot horizontal plate heat transfer correlations [25] suggest a ¼ power dependency of the Nusselt on the Rayleigh number. The Rayleigh number is proportional to a characteristic temperature difference that, will here be taken as the temperature difference between the surface and ambient.

$$h_{CV,b} = f_1(Nu) = f_2(Ra^{1/4}) = f_3(\Delta T^{1/4}) \tag{54}$$

The method that was chosen to determine the two remaining parameters for best fit was a genetic algorithm [93]. This was used to find the global minimum and Newton's method [94] for the local minimum. Using a generic algorithm for this case, where the task is to find the best model to data fit for two parameters, is exaggerating. This will become useful, when determining the intrinsic/global material properties of a more complex model as done later. It provides insight into the specific challenges of this kind of problems (solve inverse problems).

Surprisingly, whichever minimisation method chosen, the temperature curves of the tests and model could, initially, not be well fitted (Figure 24). Broadening the search to include the parameters for the density (ρ), thermal conductivity (k) and specific

heat (c_p) did not improve the fit, and nor did changing the temperature dependant convective heat transfer correlation.

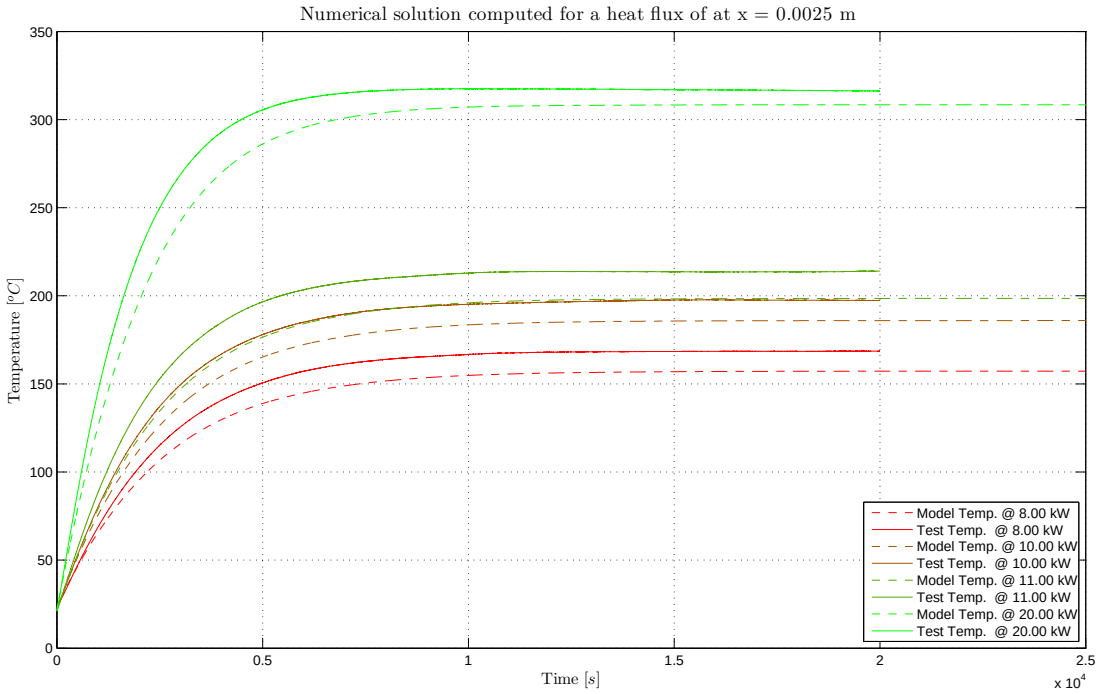

Figure 24 Initial bad model to data fit

In a final attempt the search area was broadened to also include the major input parameter, the incident heat fluxes (q_{EXT}), but with very narrow bounds ±1 kW of the heat flux it was set to. The optimisation algorithm was therefore seeking a best-fit solution of three parameters: the two convective heat transfer parameters, and the incident heat flux. This resulted in a good fit and lead to the conclusion that the reading from the heat flux meter did not correspond with the actual values. Deviations from the actual values of the used heat flux meter type have been reported in the literature [95, 96], in a Schmidt-Boelter (thermopile) total heat flux meter. It was not expected that this measurement would be of such significance. Particularly as it is part of the standard test procedure of the Cone Calorimeter [10] and the FPA [1], both of which are intended to create reproducible test conditions. In this case, the heat flux measurements are taken before the actual test. The measurement surface of the heat flux meter is required to fall within the same plane as the exposed surface of the specimen to be tested. This test setup is prone to errors, but technical and procedural steps specified in the standards should eliminate these. When extra care

was taken in the test setup, and measurements were taken to insure that the radiative environmental conditions had reached steady state (waiting for >10 min before reading the values of the heat flux meter) the situation dramatically improved. The improvement can bee seen in Figure 25 and Figure 26. The plots for the other measured depth are presented in appendix A.8.

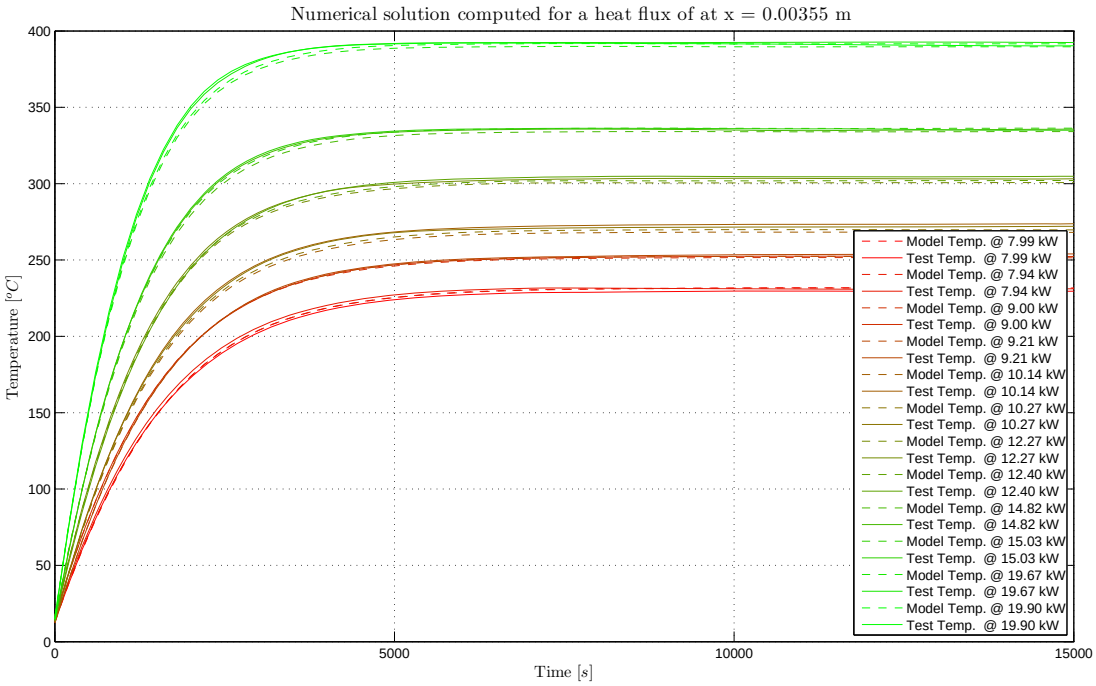

Figure 25 Model to Test data fit in the FPA for various heat fluxes at a depth of x=0.00355 [m]

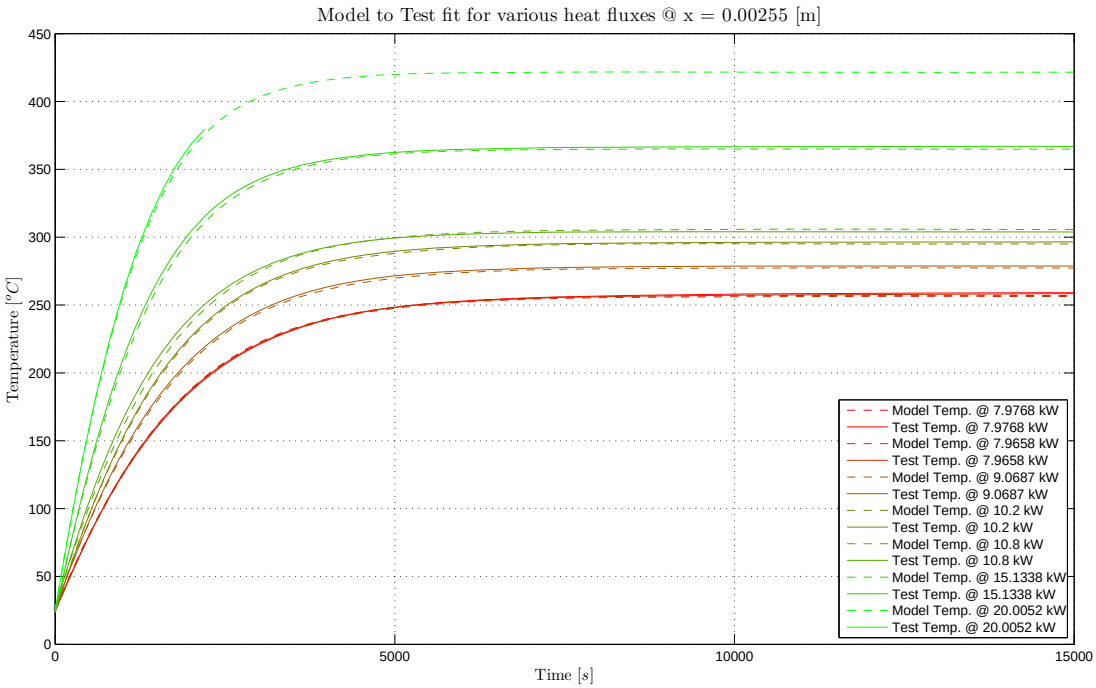

Figure 26 Model to Test data fit in the Cone for various heat fluxes at a depth of x=0.00255 [m]

Good agreement between the model and the test data is a necessity when attempting to determine (with the method described in this section) the convective heat transfer coefficient (h_{CV}). The results as depicted in Figure 27 fall in the same range as the values reported in the literature [31, 97, 98]. They are, however, specific for the environmental conditions and setup of the test setup. Thus, Figure 27 and their corresponding correlations, do not generally apply to all Cone Calorimeters [10] and the FPAs [1]. The values may be very similar, but they remain test setup specific.

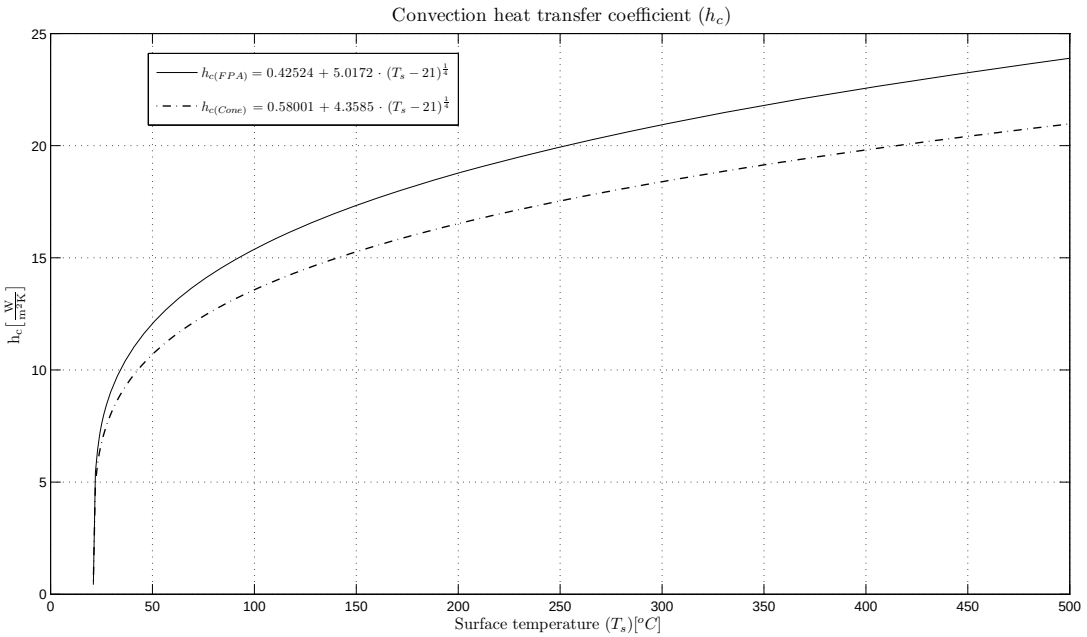

Figure 27 Convective heat transfer coefficient h_{CV} (T)

The solution of this very basic problem has provided a tremendous insight into inverse problems and, by extrapolation, into the inverse problem of chapter 5. Particularly, the importance of using the correct incident heat flux (q_{EXT}) to fit the model with the test data has been revealed.

From the good agreement finally obtained, it can be further concluded that the usual assumption of a constant incident heat flux (q_{EXT}) throughout the tests of the Cone Calorimeter [10] and the FPA [1] is, for the accuracies obtained here, no valid.

3.10 Determining the worst ignition scenario for fire applications

For the present study, the complexity of the ignition process (charring and intumescing materials) did not allow the effective differentiation between “flash” and “fire” point. Consequently, the first manifestation of ignition was taken to be the “flash” point. As a result, there was no need for the definition of a critical Damköhler number (section 2.3.3). Instead, CFD models were used with equation (7) as boundary condition to establish the LFL for the materials tested. This represents, under the given circumstances of a fire scenario, the worst-case scenario. For fire safety, knowledge of the air/fuel mixture (LFL) of the product of a test specimen that

can ignite is of more importance then knowing when it will be able to sustain a flame.

The procedure followed includes the modelling of the heating process (solid phase and gas phase) and the production of fuel. The fuel distribution in the gas phase is established at the time to ignition providing a fuel concentration at the pilot location; this is termed the Lean Flammability Limit (LFL). The time to ignition and the corresponding mass loss rate were ($\dot{m}_{ig}$) established from the tests for both the Cone Calorimeter [10] and the FPA [1]. Figure 28 and Figure 29 show the mean values and errors for each of the materials using the data obtained from the Cone Calorimeter and FPA respectively. The total hydrocarbon to inert ratio or the mass fraction of flammable gasses (Y_F) originating from the sample surface was established previously and is presented in section 3.3 (Table 13). Steady state CFD calculations (appendix A.10) lead to the fuel concentration at the pilot location. For this, the environmental properties of the two test apparatuses such as velocity of the extraction system or forced flow field are required. From this the LFL is obtained.

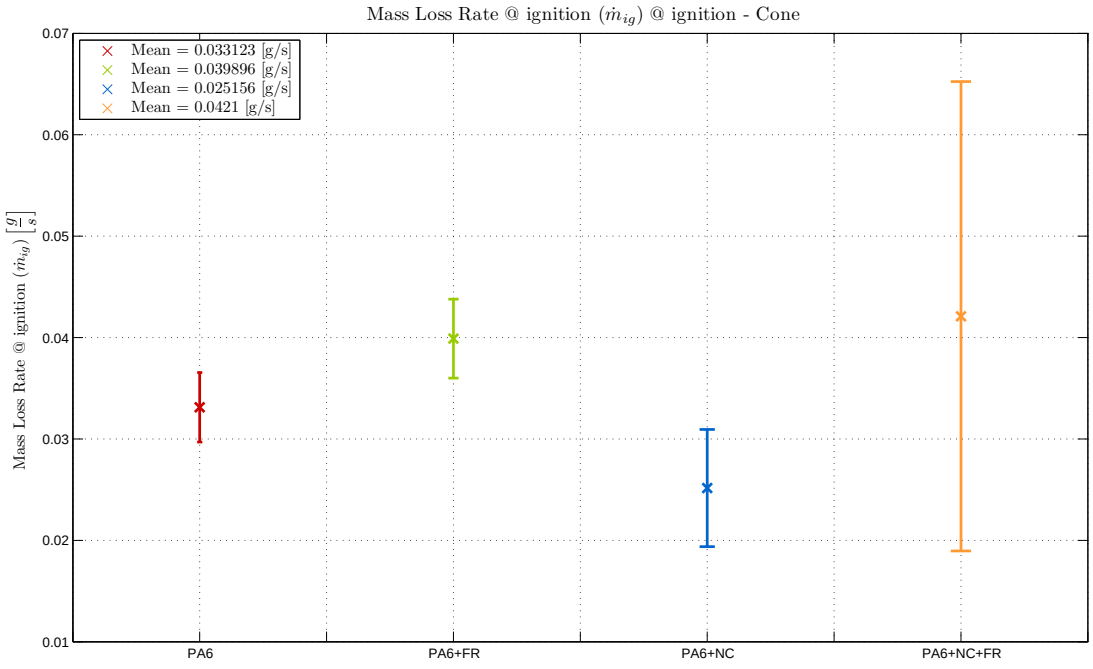

Figure 28 Mass Loss Rates at ignition for the different materials in the Cone

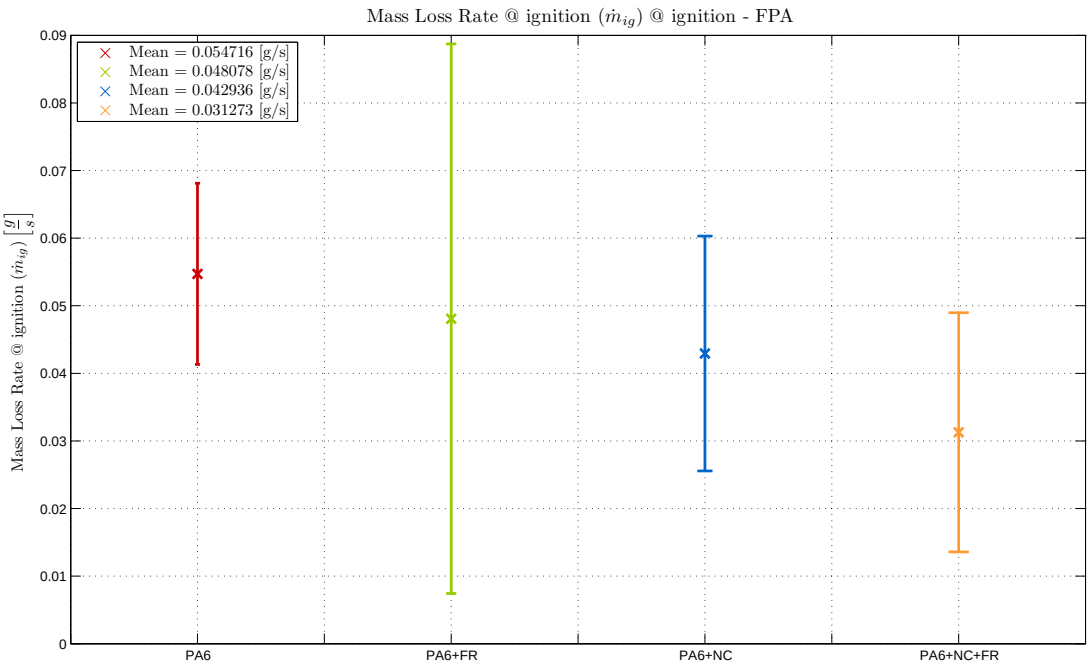

Figure 29 Mass Loss Rates at ignition for the different materials in the FPA

The lookup table or graph (Figure 30 and Figure 31) can be used to obtain the LFL without having to run another CFD calculation for the specific (new) case. This was created using several CFD simulations for the different mass fractions of flammable gasses (Y_F) and mass loss rates ($\dot{m}_p$).

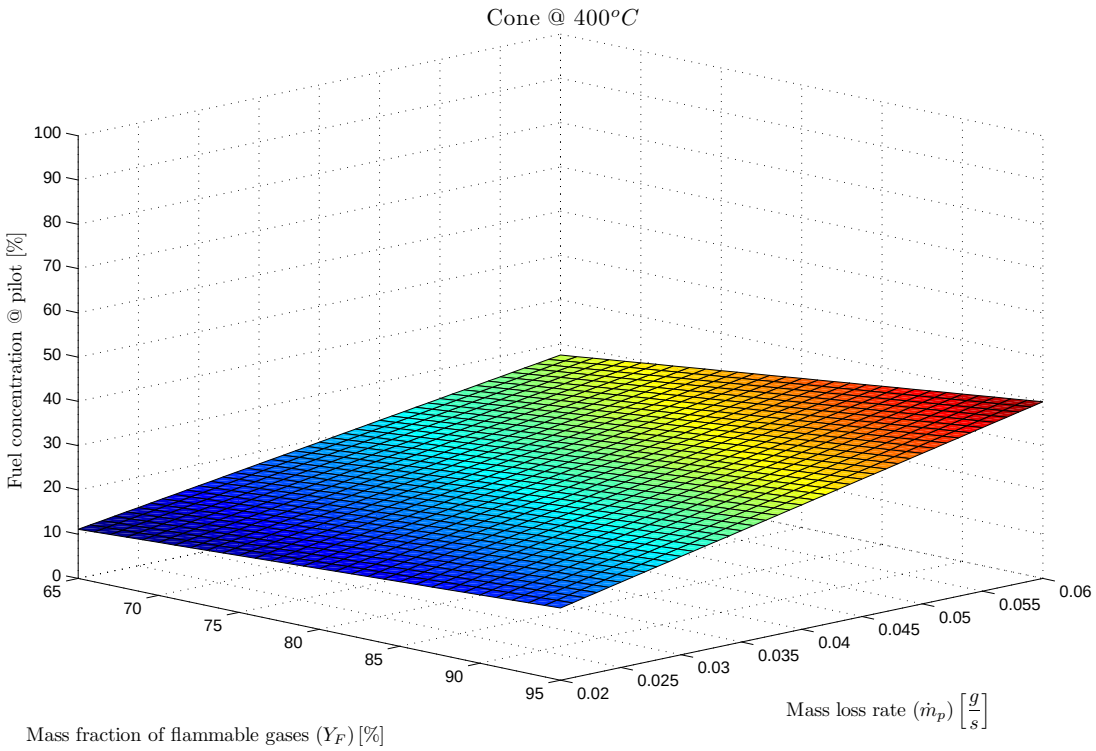

Figure 30 LFL lookup graph for the Cone Calorimeter

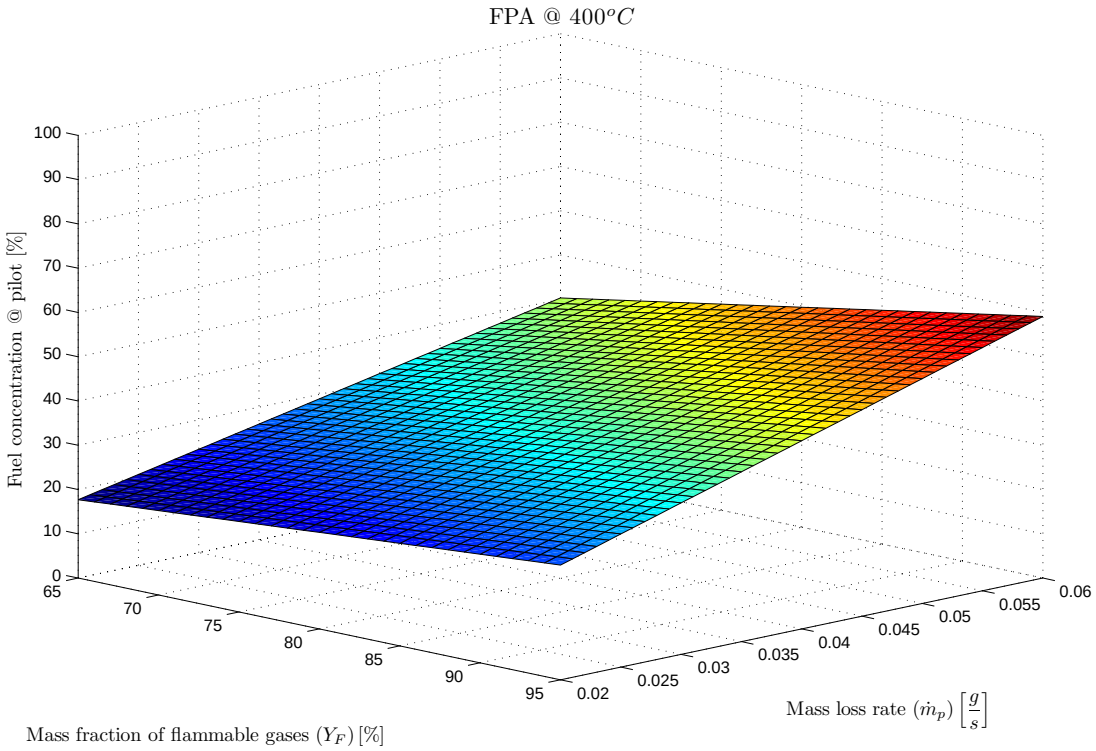

Figure 31 LFL lookup graph for the FPA

To establish and estimate the robustness for the process, the LFL's for the different heat fluxes and test apparatuses were plotted as a function of the heat flux. Figure 32 shows such a plot for the materials tested in this study.

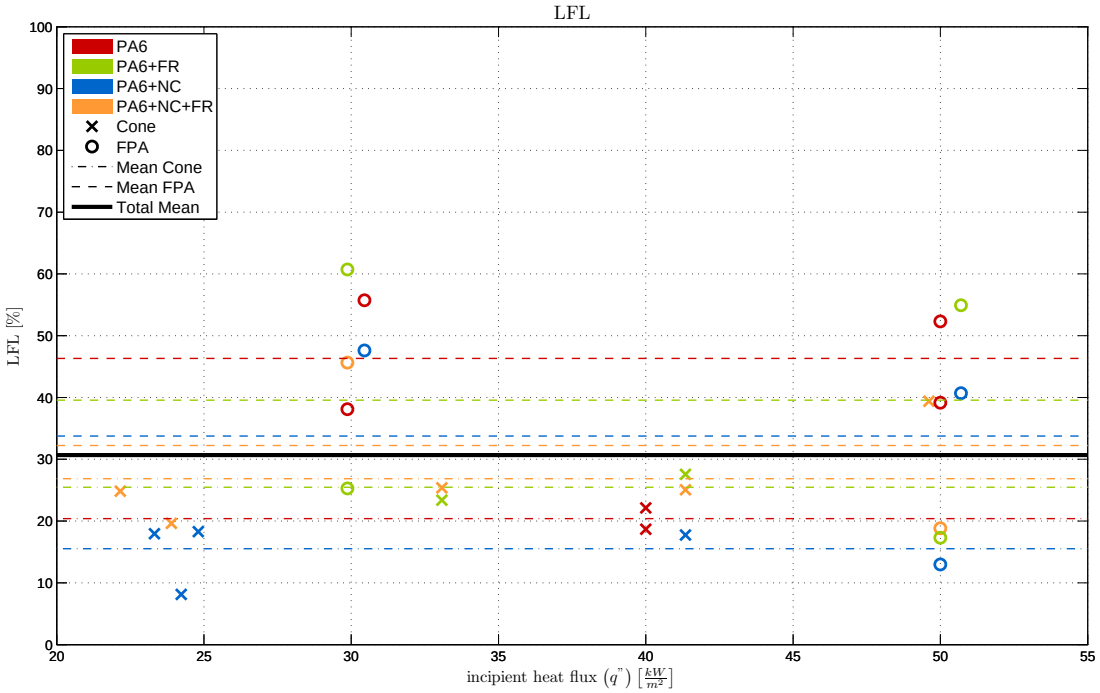

Figure 32 LFL as a function of the external heat flux for PA6

Despite the big scatter, the results are promising. The scatter is not unreasonable, considering the limited amount of samples, the broad range of heat fluxes and the accuracy of the mass loss readings of the used test apparatus (Cone and FPA) before ignition (Figure 28, Figure 29 and section 6.1). The results appear to indicate that there is no correlation between the different sample types. The overall LFL is approximately ±10% standard deviation for the cone and ±20% standard deviation for the FPA. Given that the same base material was used (PA6), it can therefore be established that the nanocomposites and fire retardants do not play a significant role in the combustion process. To establish the validity of this assumption, a more detailed study with more samples and a more accurate mass loss measuring device is required.

It is important to note that the Cone and FPA show different values. This difference may originate from the different ignition protocols. Table 18 contains the representative values that have been obtained for all fuels studied for each test

apparatus. The LFL values from the Cone Calorimeter tests are lower then the average while the FPA values are higher.

Material	LFL (Cone Calorimeter)	LFL (FPA)
PA6	20	46
PA6+FR	25	40
PA6+NF	16	34
PA6+FR+NF	27	32

Table 18 LFL for the different materials studied.

3.11 The Heat of Combustion (ΔH_c)

The heat of combustion (ΔH_c) is the energy that is released when one unit of fuel undergoes complete combustion and where the H_2O in the combustion products is in its gaseous state. The relationship between this and the ignition process of solids is discussed in section 2.3.4. The heat of combustion can either be estimated from chemistry, or determined from tests (usually using the bomb calorimeter). Oxygen consumption or carbon dioxide generation calorimetry can also be used.

The Cone Calorimeter [10] and FPA [1], though different apparatus, both provide heat release rates (HRR) [kW/s]. The heat release rate can be obtained from oxygen consumption or carbon dioxide generation calorimetry. When dividing the HRR by the mass loss rate or burning rate ($\dot{m}_P$) [g/s] one arrives at the heat of combustion (ΔH_c) [kW/kg]. It should be noted that the mass loss rate is also a measured value. Given the heat of combustion, the HRR can be described by:

$$HRR = \Delta H_C \cdot \dot{m}''_P \cdot A_{surf} = \Delta H_C \cdot \dot{m}_P \tag{55}$$

where A_{surf} [m^2] is the surface area of the sample. By re-arranging the equation, the heat of combustion (ΔH_c) can be obtained:

$$\Delta H_C = \frac{HRR}{A_{surf} \cdot \dot{m}''_P} = \frac{HRR}{\dot{m}_P} \tag{56}$$

Figure 33 and Figure 34 show typical heat release rate (HRR) and mass loss rate ($\dot{m}_P$) graphs for PA6. The graphs for the other materials are presented in Appendix A.10.

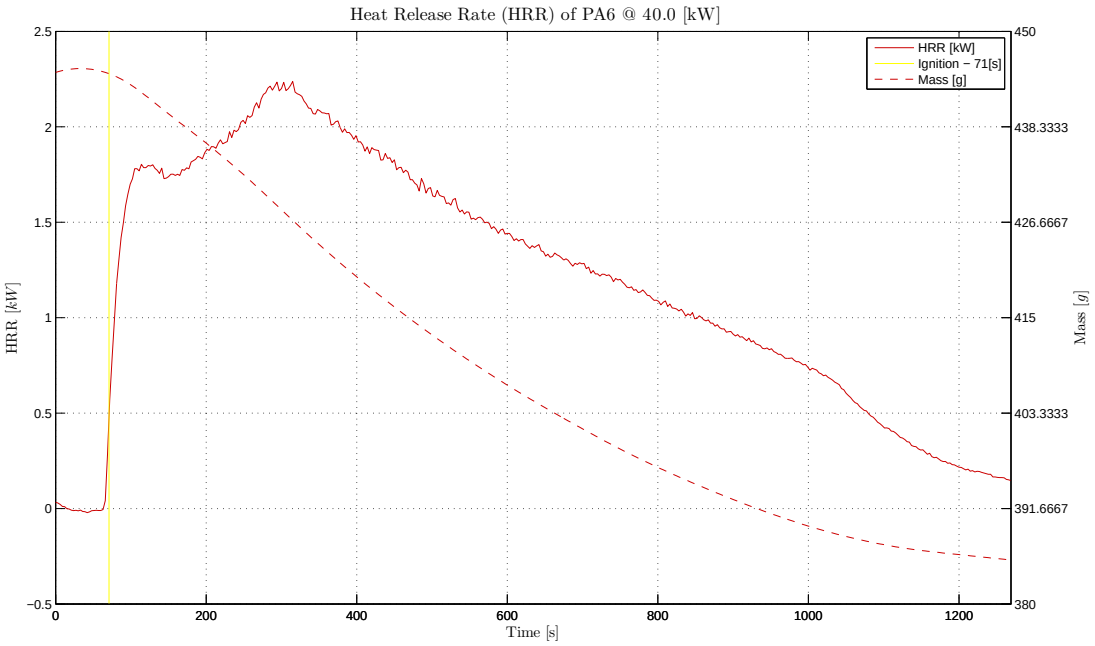

Figure 33 Cone: HRR and Mass versus Time of PA6

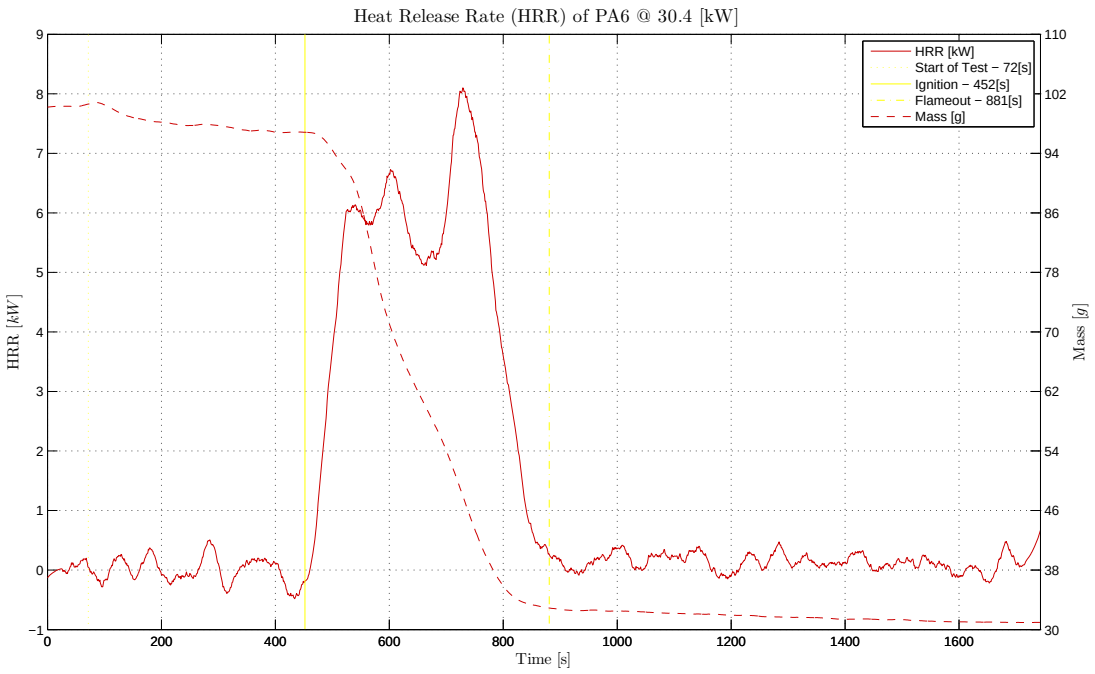

Figure 34 FPA: HRR and Mass versus Time of PA6

The heat release rate (HRR) and mass loss rate ($\dot{m}_p$) as obtained from the Cone Calorimeter and FPA are a function of time (Figure 33 and Figure 34). Thus, is also the heat of combustion (ΔH_c) as per equation (56). Due to the incomplete combustion processes, the resulting heat of combustion (ΔH_c) does not always allow a simple extraction of a constant or average heat of combustion (e.g. start and end of the

combustion process). The aim is to determine the heat of combustion (ΔH_c) and the corresponding energy released as heat when a unit of the material undergoes complete combustion with oxygen. Thus, engineering judgement is sometimes required to determine the constant heat of combustion. The resulting heat of combustion (ΔH_c) graphs are presented as an example in Figure 35 and Figure 36. These are both for the material PA6. The figures for the other materials can be found in Appendix A.

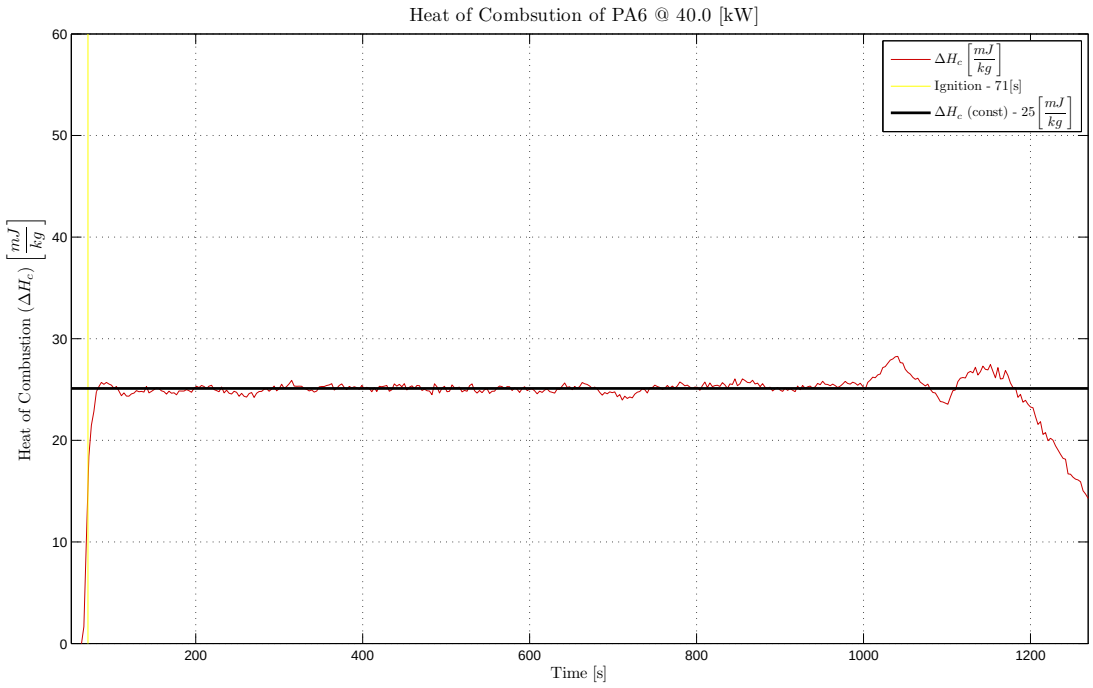

Figure 35 Cone: Heat of Combustion versus Time of PA6

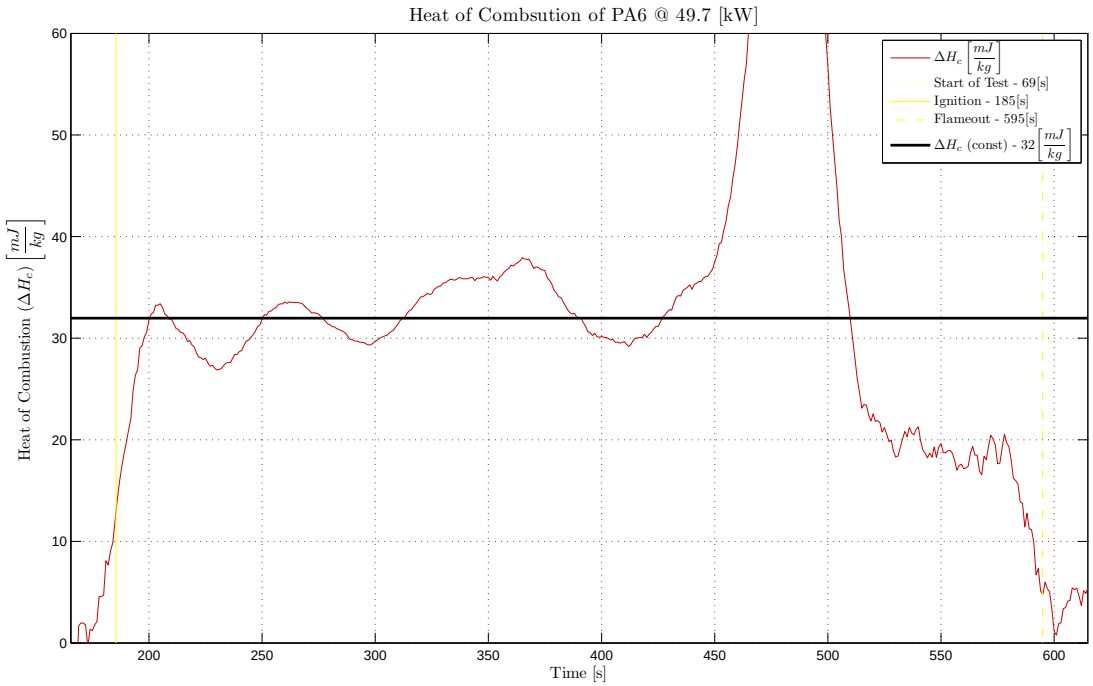

Figure 36 FPA: Heat of Combustion versus Time of PA6

Table 19 presents the extracted mean value and standard deviations for the Cone and FPA.

Material	**ΔH_C** [MJ/kg] (Cone)		**ΔH_C** [MJ/kg] (FPA)	
	Mean	Standard Deviation	Mean	Standard Deviation
PA6	25	±3	31	±3
PA6 + FR	26	±3	29	±2
PA6 + NC	26	±3	30	±2
PA6 + NC + FR	24	±7	30	±6

Table 19 Heat of combustion for the different materials studied.

Literature [31] states that for pure PA6 a range between 28-29.6 MJ/kg is usual. This corresponds reasonably well with the data found from the Cone Calorimeter and FPA.

4 PARAMETER SUMMARY

The goal of chapter 3 was to determine as many of the parameters that are necessary to describe the heating/ignition process of a solid as possible. The parameters that could and those that could not be determined are summarised in Table 20. This table is based on Table 1, Table 2, Table 4, Table 6 and Table 7 of chapter 2. The last column of this table provides information on whether these parameters:

- are calculated as part of a model (Calculated),
- are commonly known (Given), thus can be obtained from the literature,
- represent specific ambient conditions (Ambient) that can be measured or assumed,
- can be determined as laid out in chapter 3 (section Ref.),
- or are true unknowns (Unknown) that require determination by some other method.

Parameter	Description	Units	Where this parameter can be obtained from:
$T(x,t)$	Temperature	K	Calculated
$Y_S(x,t)$	Local fuel concentration	g/g	Calculated
$Y_O(0)$	Local oxygen concentration (char)	g/g	Ambient
$Y_{F,s}(0)$	Residual fuel fraction	g/g	section 3.3
χ	Permeability function		Unknown
$\varepsilon_O(T)$	Oxygen penetration depth	m	Unknown
$\varepsilon_F(t)$	Reactive depth	m	Unknown
A_i	Pre-exponential factor	s^{-1}	section 3.2
m_i	Exponential constant		section 3.2
n_i	Exponential constant		section 3.2
E_i	Activation energy	J/mol	section 3.2
$\rho(T(x,t))$	Density	kg/m^3	section 3.6
$k(T(x,t))$	Thermal conductivity	W/mK	section 3.7
$c_p(T(x,t))$	Specific heat capacity	J/kgK	section 3.5
$k_S(x,t)$	Thermal conductivity	W/m·K	section 3.7
$c_p(x,t)$	Specific heat	J/kg·K	section 3.5
$\rho_S(x,t)$	Density of the solid	g/m^3	section 3.6
$v_R(t)$	Regression rate	m/s	Calculated
$\dot{m}''_p$	Mass flow (pyrolysate)	$g/m^2 \cdot s$	Calculated
$\dot{m}''_O$	Mass flow (oxygen)	$g/m^2 \cdot s$	Calculated

Parameter	Description	Units	Where this parameter can be obtained from:
T_P	Temperature of the gas phase	K	Calculated
α_S (x,t)	Radiative properties of the solid (absorptivity)	-	Calculated
$\Delta H_{P,i}$	Heat of reaction	J/g	section 3.8
$\Delta H_{m,i}$	Heat of phase change	J/g	section 3.4
$k_B(x,t)$	Global thermal conductivity of the backing material	W/m·K	Given (Literature)
$T_B(x,t)$	Temperature of the backing material	K	Calculated
$\varepsilon_S(x,t)$	Emissivity of the solid	-	Calculated
$h_c(t)$	Convective heat transfer coefficient	$W/m^2 \cdot K$	section 3.9.
T_0	Ambient temperature	K	Ambient
ρ_{air}	Density of air	g/m^3	Given (Literature)
$\vec{u}$	Velocity field	m/s	Calculated by CFD
p	Pressure field	$kg/m \cdot s^2$	Calculated by CFD
μ_{air}	Viscosity of air	kg/m·s	Given (Literature)
$\alpha_{D,F,air}$	Diffusivity of fuel in air	m/s^2	Calculated by CFD
r	Pilot location	m	Given (Literature) Cone/FPA [1, 3]

Table 20 Summary of parameters from chapter 2 and 3

5 PARAMETER DETERMINATION BY MODEL TO DATA FITTING

This chapter shall determine whether the parameters obtained by fitting a complex model to experimental results by means of sophisticated optimization techniques can provide material properties. It will also determine whether they are “intrinsic” or “global” material properties. As mentioned previously, not all of the parameters that are necessary for a description of the heating/ignition process of a solid (chapter 2) can readily be obtained from independent measurements.

5.1 Test Data

When a solid material is subject to an external source of energy, its temperature rises: the instant that a material is exposed to an external source can be defined as the onset of the ignition process. It initiates a series of physical and chemical phenomena that lead to ignition.

Reproduction of this heating process with a model, such as the one described in section 5.2, is the overall goal in the field. Preferably, the aim is to do this with intrinsic material properties. However, the values of the governing parameters of a specific material are rarely known. Knowledge of the values of these parameters can be obtained by solving this problem in an inverse manner. To obtain these parameters, an appropriate experimental data set is required. This data set can be used to fit the complex models to specific experimental results, using sophisticated optimisation techniques. For the specific case, the temperature distribution in space and time of a material subjected to an external heat source is the driving force that initiates the consecutive phenomena. These phenomena depend on the intrinsic material properties and test setup thus, can be used for this purpose (section 5.1.1). Another measurable effect of the heating process that leads to burning is that the sample will loose mass as it pyrolysis. This creates volatiles that eventually ignite. Consequently, the mass loss was also taken into consideration (section 5.1.3).

5.1.1 Setup

The introduction states that the goal of this work is to develop a novel approach to determine the “intrinsic” material flammability properties using (standard) flammability tests. The used apparatuses were the Fire Propagation Apparatus (FPA) [1] and Cone Calorimeter (Cone) [10]. While the former was mainly used in the determination of the “intrinsic” material flammability properties, the later was used for verification purposes. The Fire Propagation Apparatus (FPA) as described in ASTM E2058-03 [1] that was used for these tests was designed and delivered by FTT (Fire Testing Technology). The used Cone Calorimeter (Cone) as described in ASTM E-1354-03 [10] was designed and delivered by Stanton Redcroft. The tests were conducted according to the mentioned standards, where a test specimen is exposed to a constant heat flux that heats up the sample until piloted ignition occurs. With these apparatuses the ignition time, mass loss and combustion products (CO, CO_2 and O_2) are measured. After the tests, the data is analysed to obtain the required information such as the heat release rate or heat of combustion. More details can be found in the standards of each apparatus.

For this work, the standard sample/sample-holder setup was replaced with the arrangement depicted in Figure 37 and Figure 38. The collected data extended the required area of interest for this work. All collected data not falling in the period between heat exposure and ignition have therefore been disregarded. Figure 37 and Figure 38 show the sample/sample-holder setup with thermocouples. This setup allowed the in-depth temperature readings to be gathered. A similar arrangement was used for the mass loss measurements. The only difference was that the thermocouples were not in place for the mass loss measurements. This was obviously necessary not to disturb the mass readings.

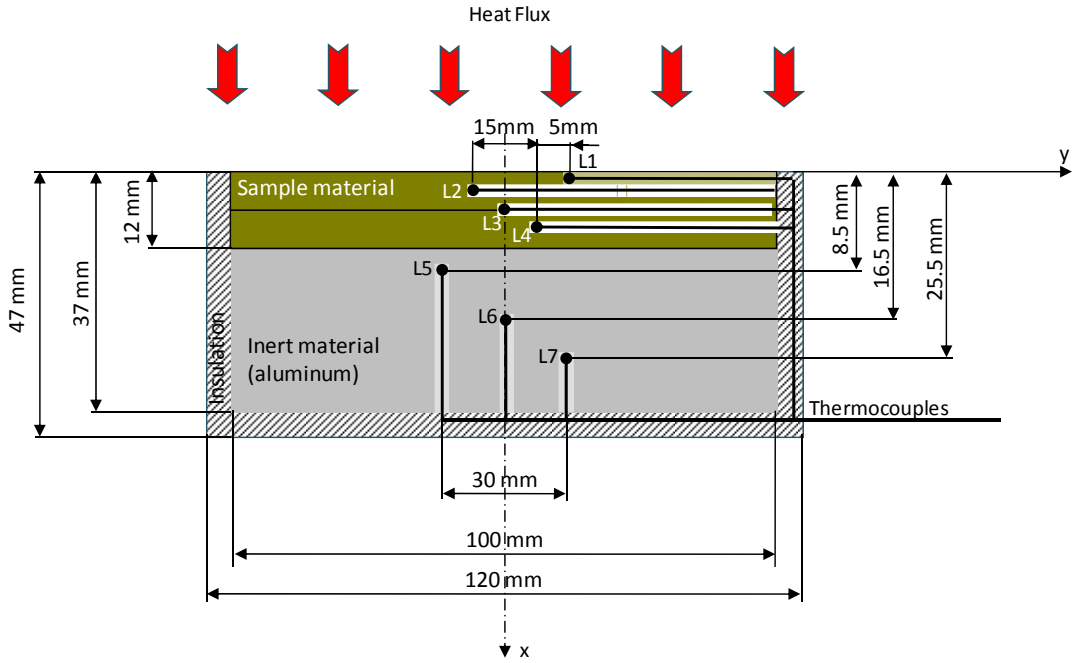

Figure 37 Sample and holder setup with in depth thermocouples (front)

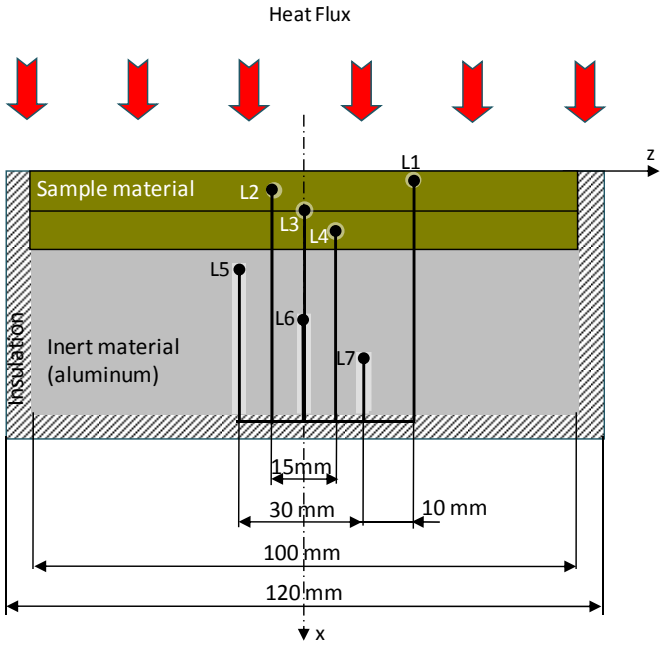

Figure 38 Sample and holder setup with in depth thermocouples (side)

Holes were drilled into the sample and the aluminium block using a 3 mm drill bit to allow thermocouple placement. To reduce potential errors in the thermocouple temperature readings the holes in the test samples were drilled lateral to the main

heat flow. However, in the aluminium block they were drilled with the main direction of the heat flow for convenience, as depicted in Figure 37 and Figure 38.

The thermocouples were made out of KX type (nickel-chromium) thermocouple wire, with fibreglass insulation with a 0.2 mm strand diameter and overall external dimensions of 2 x 3 mm. The beaded ends at the location of measurement, were created by welding and were approximately 1 mm in diameter. This thermocouple type are deemed to give accurate readings within the range of -180°C to 1350°C [99]. Each thermocouple was cut to the required length and its electrical continuity tested before it was placed in the sample or aluminium block. To record the temperature, an Agilent 34980A data logger with one 40-channel multiplexer 34921A module was used. This had a built-in reference temperature.

The sample and aluminium block was insulated with a 10 mm thick layer of "Rockwool" and the arrangement was secured with aluminium tape.

5.1.2 In-Depth Temperature

Ideally, to capture the effect of the thermophysical properties of a material the temperature data would have been measured with high spatial resolution. This would have been particularly useful for materials with a low thermal conductivity. However, in-depth thermocouples are difficult to place and a coarser resolution had to be accepted. A setup as specified in Figure 37 and Figure 38 has been used in the FPA to obtain the in depth temperature distribution within the test specimen. The experiments conducted have been limited to solely address the heating process in the FPA. This is intentional. In chapter 7, a similar test setup is used for the Cone from which temperature data in space and time has been obtained. This temperature data is not used in an attempt to obtain the, as yet, unknown intrinsic material properties. Instead, it is used to validate the applicability of the model on a different experimental setup (different flow conditions, different infrared radiation etc.).

The test setup shown in Figure 37 and Figure 38 shows three in-depth thermocouples evenly distributed throughout the sample. An additional thermocouple is located as close as possible to the surface. Due to the difficulty placing the thermocouples at

various depths, the need arose to glue two samples (of height 6 mm) together. At the interface between the sample and the inert material (aluminium block), a highly conductive paste was used. The usual application of this paste is to guarantee heat transfer between a processor of a computer and its heat sink. Within the aluminium block, three further temperature readings were taken. This allows the losses to the back to be defined (section 2.2). The test setup described a one-dimensional treatment of the problem. Given the limited number of samples available for the in depth temperature distribution, the focus rested on obtaining at least two in-depth temperature measurements at two different heat fluxes.

Figure 39 and Figure 40 show, for PA6, an example of the in depth temperature measurements; the graphs for the other PA6 based materials can be found in Appendix B.1. . From these graphs, it is clear that the temperature of some of the thermocouples at location (L1 and L2) increase more rapidly then the rest. It was determined that this phenomenon usually takes place around the melting temperature (≈220°C). Observations during the tests confirm that these thermocouples are being displaced from their original position. When emerging from the sample they heat up faster as they are directly exposed to the incident radiation. Any temperature readings above the melting temperature are disregarded in these cases.

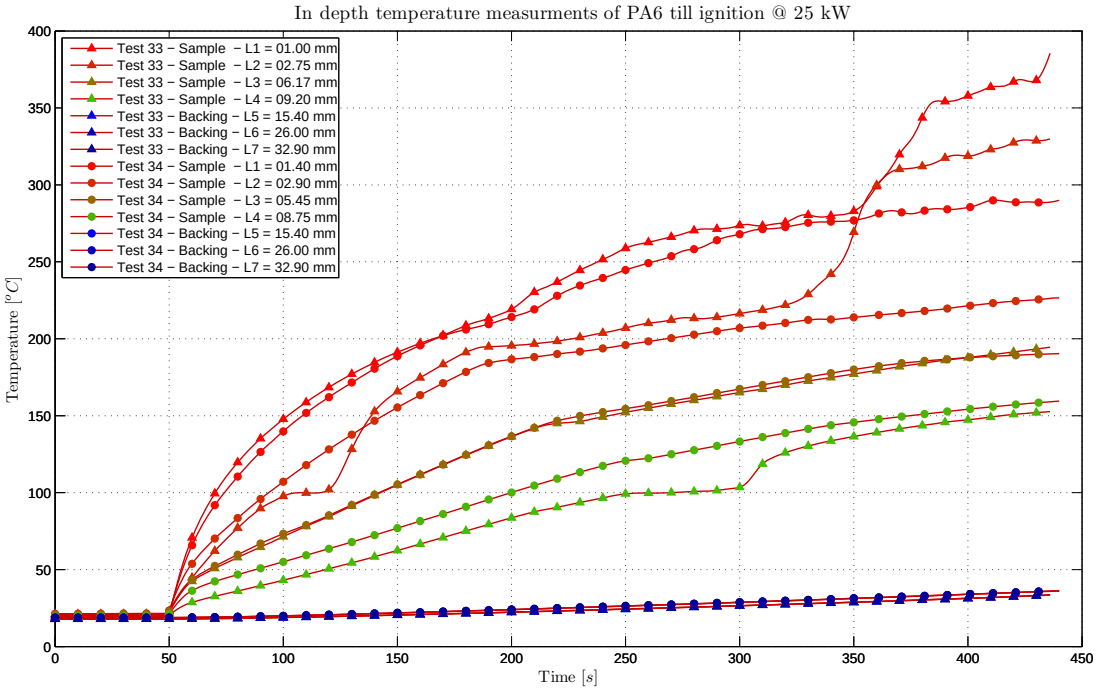

Figure 39 In-depth temperature data of PA6 exposed to a radiative heat flux of 25 kW in the FPA

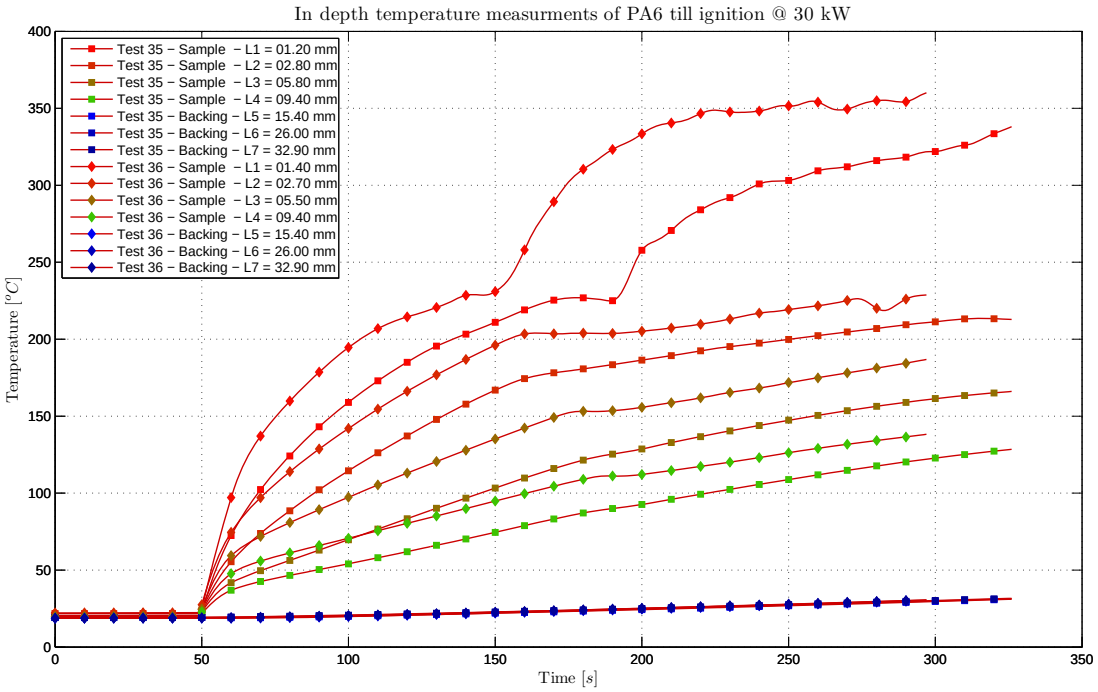

Figure 40 In-depth temperature data of PA6 exposed to a radiative heat flux of 30 kW in the FPA

On each figure (Figure 39, Figure 40 as well as the equivalent figures in Appendix B.1), every marker shape represents a different test. Their rough location is represented by the thermocouple locations L1 to L4 inside the sample, and L5 to L7 in the backing as shown in Figure 37 and Figure 38. For visualisation, the markers

gradually change their colour from red to green inside the sample and from light blue to dark blue in the backing. This is in accordance to their distance from the surface. As can also be seen from the graphs, the samples were exposed to the respective heat flux 50 seconds into the recordings.

5.1.3 Mass Loss Data

The collection of the mass loss data during the setup, as described in Figure 37, and conducted in the FPA is prone to significant errors. This is due to the cabling of the thermocouples. Ideally, a wireless solution would have been used, but due to space and resource limitations, the mass loss data had to be obtained from a different set of experiments. Standard calorimetry measurements of the FPA [1] that were conducted in a manner similar to the setup of Figure 37 and Figure 38 (without the thermocouples) provided the mass loss for the required period between the start of the test and ignition. The similarity of the test setup assured that the data could be used simultaneously in solving the inverse problem described in the following sections.

Two representative mass loss and mass loss rates of PA6 are presented here (Figure 41 and Figure 42). Graphs for the other tests of PA6 and the other materials are presented in Appendix B.2. The figures show the mass data points for each experiment and a least square spline approximation [100]. The later was chosen to be able to obtain a smooth but reasonable representation of the mass loss rate. At the start of the test, a step change can often be observed. The origin of this fluctuation is the lowering of the shield in the FPA. This was eliminated by reducing the weight of the first four data points of each test in the least square spline approximation. Overall, the mass loss up to ignition had substantial fluctuations from one tests to the other, but were reasonable as shown in Figure 41, Figure 42 and in Appendix B.2. The mass loss rate, however, showed significant fluctuations not shown on these figures. These can be assumed by looking at the fluctuations in the mass data.

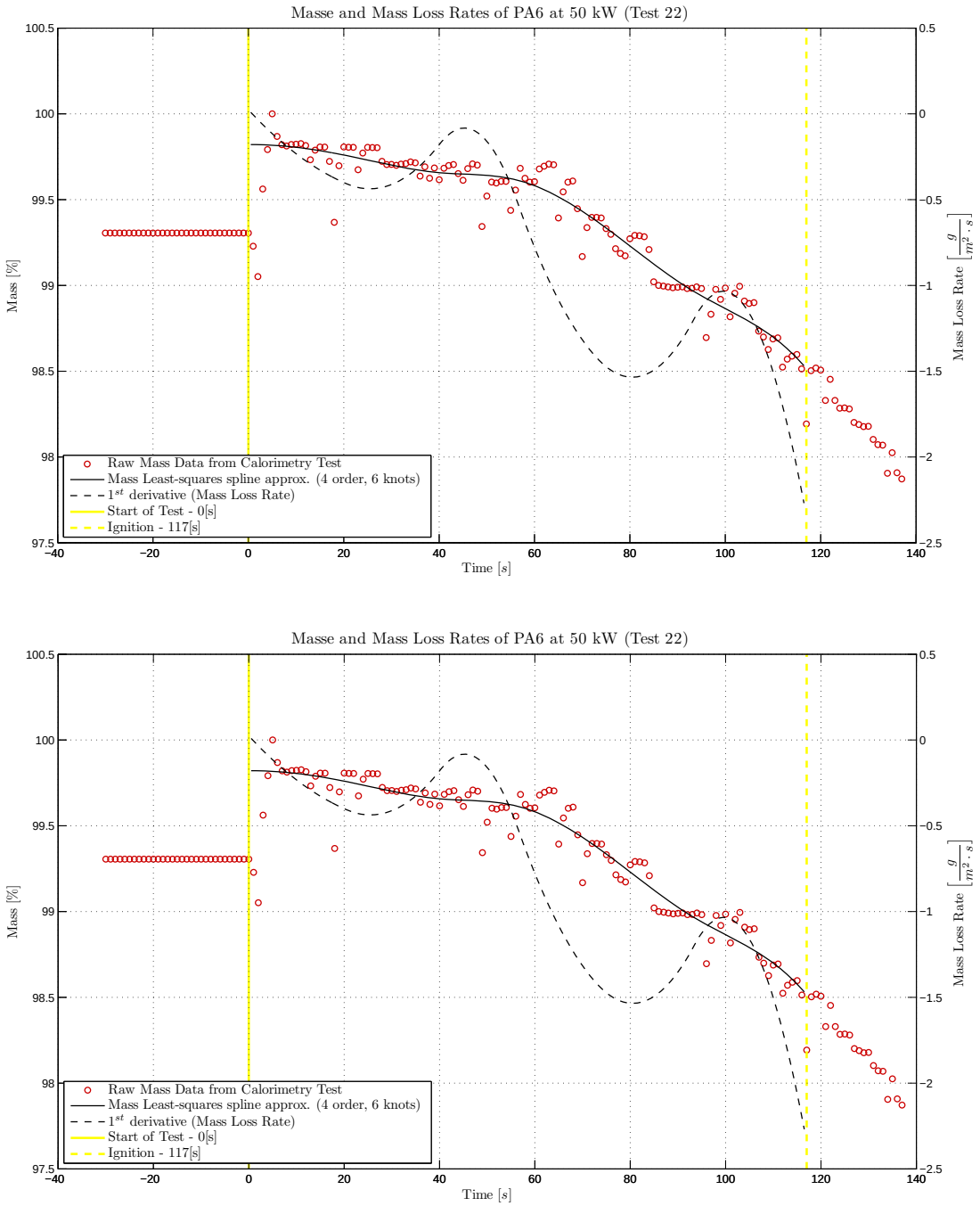

Masse and Mass Loss Rates of PA6 at 50 kW (Test 22)
Mass [%]
Mass Loss Rate $\left[\frac{g}{m^2 \cdot s}\right]$
Time $[s]$
Raw Mass Data from Calorimetry Test
Mass Least-squares spline approx. (4 order, 6 knots)
1^{st} derivative (Mass Loss Rate)
Start of Test - 0[s]
Ignition - 117[s]

Figure 41 Mass and mass loss rate of PA6 (Test 22)

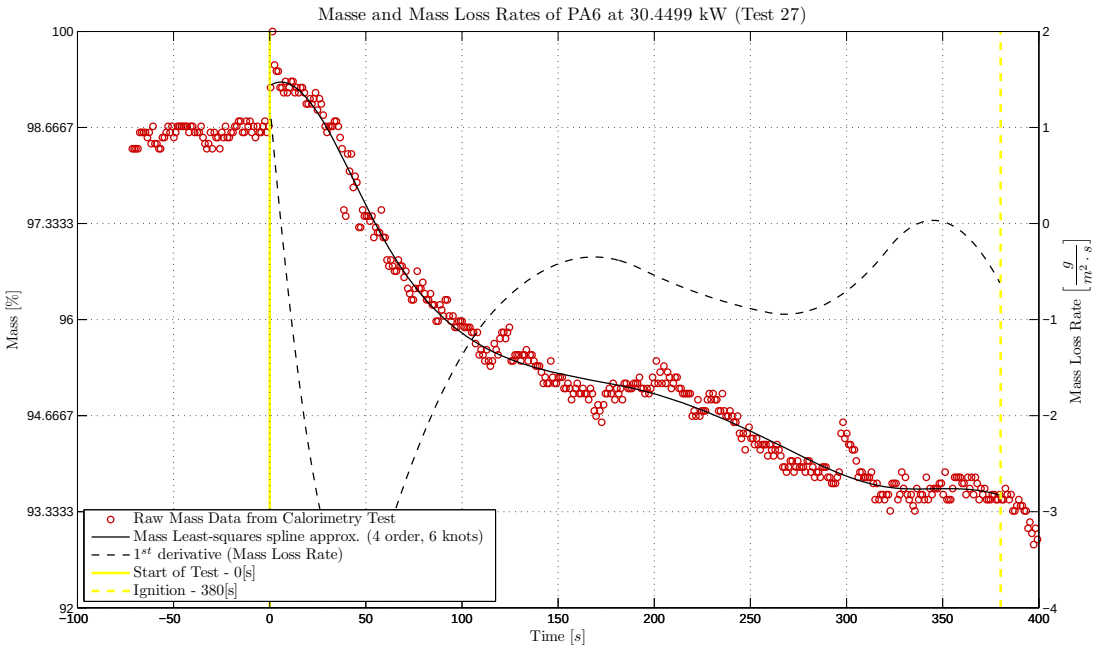

Figure 42 Mass and mass loss rate of PA6 (Test 27)

5.2 Model used

Given the task, it was decided to either develop an in-house model, that incorporated the essential physical phenomena of the ignition process of the investigated materials (polymer that possibility chars and could intumesce due to fire retardants, etc.) or to use a public available code.

Due to:

- the complexity of the task (which is a project of its own),
- the public availability,
- not knowing what to expect,
- and the representation of the expected physical phenomena,

the program “gpyro” was used.

Gpyro is a computer model that describes the thermal response of solid materials exposed to external heating, including thermo-oxidative pyrolysis of the condensed phase. This code can be obtained from [101]. It simulates the pyrolysis of thermoplastics and charring solids, intumescing coatings, and smolder in porous media. The main core of the model is extended by a material property estimation

program called “gpyro_propest”. This program can be used to help estimate the required material properties from experimental data. Gpyro was originally developed at UC Berkeley. The model was first fully presented by Lautenberger [102].

Although gpyro is significantly more complex than the approach discussed in chapter 2, the basic equations and parameters are the same, just expressed in a different manner. To illustrate this: the model specifics, equations and its parameters as provided in the Technical Reference [103] are summarised below.

Gpyro is one-dimensional model. It is designed to accommodate for volume change (shrinkage or swelling). This is accomplished by assuming that the bulk density is a property of a condensed phase species and that each grid cell is permeable to gaseous mass transfer but is impermeable to condensed phase mass transfer. Gpyro solves the conservation equations (see Table 21) for gaseous and condensed phase mass, species, and energy as well as gas phase momentum separately. It is able to cater for an arbitrary number of gas phase and condensed phase species, each having its own thermophysical properties. Any number of heterogeneous (solid/gas) or homogeneous (gas/gas) reactions can be specified. It allows for an in–depth radiation absorption and radiation transport across pores. Melting is modelled using a localised increase (Gaussian peak) in the apparent specific heat capacity. Volatiles generated inside the solid can escape to the ambient either with or without resistance to the flow. In case of the former, the pressure distribution in the solid is calculated. This is used to calculate the resultant flow of volatiles according to Darcy’s law.

Condensed phase conservation	
Mass	$\frac{\left(\bar{\rho}\Delta z\right)_P - \left(\bar{\rho}\Delta z\right)_P^\circ}{\Delta t} = -\left(\dot{\omega}_{fg}'''\Delta z\right)_P$
Species	$\frac{\left(\bar{\rho}Y_i\Delta z\right)_P - \left(\bar{\rho}Y_i\Delta z\right)_P^\circ}{\Delta t} = \left(\dot{\omega}_{fi}'''\Delta z\right)_P - \left(\dot{\omega}_{di}'''\Delta z\right)_P$
Energy	$\frac{\left(\bar{\rho}\bar{h}\Delta z\right)_P - \left(\bar{\rho}\bar{h}\Delta z\right)_P^\circ}{\Delta t} = -\dot{q}''\Big\|_b + \dot{q}''\Big\|_t - \left(\dot{Q}_{s-g}'''\Delta z\right)_P + \left(\dot{Q}_s'''\Delta z\right)_P - \left(\frac{\partial \dot{q}_r''}{\partial z}\Delta z\right)_P + \sum_{i=1}^{M}\left(\left(\dot{\omega}_{fi}''' - \dot{\omega}_{di}'''\right)h_i\Delta z\right)_P$
Gas phase conservation	

Mass	$\frac{\left(\rho_g \overline{\psi} \Delta z\right)_P - \left(\rho_g \overline{\psi} \Delta z\right)_P^\circ}{\Delta t} + \dot{m}''\big\|_b - \dot{m}''\big\|_t = \left(\dot{\omega}'''_{fg} \Delta z\right)_P$
Species	$\frac{\left(\rho_g \overline{\psi} Y_j \Delta z\right)_P - \left(\rho_g \overline{\psi} Y_j \Delta z\right)_P^\circ}{\Delta t} + \dot{m}'' Y_j\big\|_b - \dot{m}'' Y_j\big\|_t =$ $- \dot{j}''_j\big\|_b + \dot{j}''_j\big\|_t + \left(\dot{\omega}'''_{fj} \Delta z\right)_P - \left(\dot{\omega}'''_{dj} \Delta z\right)_P$
Energy	$\dot{q}''_g + \sum_{j=1}^{N} \dot{j}''_j h_{g,j} = -\frac{\overline{\psi} k_g}{c_{pg}} \frac{\partial h_g}{\partial z} + \sum_{j=1}^{N} \left(\overline{\psi} \left(\frac{k_g}{c_{pg}} - \rho_g D_j \right) h_{g,j} \frac{\partial Y_j}{\partial z} \right)$
Momentum	$\dot{m}''\big\|_b = -\left(\frac{\overline{K}}{\nu}\right)_b \frac{\partial P}{\partial z}\Big\|_b$ $\dot{m}''\big\|_t = -\left(\frac{\overline{K}}{\nu}\right)_t \frac{\partial P}{\partial z}\Big\|_t$

Letters

c	Specific heat capacity (J/kg–K)
h	Enthalpy (J/kg)
k	Thermal conductivity (W/m–K)
K	Permeability (m^2)
$\dot{m}''$	Mass flux (kg/m^2–s)
M	Number of condensed phase species
N	Number of gaseous species
P	Pressure (Pa)
$\dot{q}''$	Heat flux (W/m^2); $\dot{q}''$ is conductive, $\dot{q}''_r$ is radiative, $\dot{q}''_e$ is external radiative
$\dot{Q}'''$	Volumetric rate of heat release or absorption (W/m^3)
Δt	Time step (s)
Y	Mass fraction (–)
δz	Distance from center of grid one grid cell to center of adjacent grid cell (m)
Δz	Size (height) of grid cell (m)

Greek symbols

ν	Viscosity (m^2–s)
ρ	Density (kg/m^3)
ψ	Porosity (–)
$\dot{\omega}'''$	Volumetric reaction rate (kg/m^3–s)

Subscripts

b	Baseline or bottom (interface value)
d	Destruction or datum
f	Formation
g	Gaseous, gas phase, or gasification
i	Condensed phase species i
j	Gaseous species j
P	Point P
s	Solid phase (really, condensed phase)
t	Top (interface value

Superscripts

$\overline{(\ )}$	Weighted or averaged
°	Value at present time

Table 21 gpyro: governing equations as per the Technical Reference [90]

Table 21 briefly summarises the model specifics. In section 2.1.7, the heat transfer was examined with one governing energy conservation equations. Gpyro solves the mass species and energy conservation equations separately. However, they essentially perform the same task.

Due to: the specifics of the model, its key features, and capabilities the parameters used might slightly differ from the ones described in chapter 2. However, they are essentially the same. To demonstrate this, the key parameters and definitions are presented in the following table (Table 22).

Description	Equation*
Bulk Density	
The condensed phase is composed of a distinct amount of species, thus the $\overline{\rho}$ is the weighted bulk density, ρ_i is the bulk density of condensed phase species i and X_i is the volume fraction of condensed phase species i.	$$\overline{\rho} = \sum_{i=1}^{M} X_i \rho_i$$
The bulk density is assumed to vary with temperature, where $\rho_{0,i}$ and $n_{\rho,i}$ are user–specified parameters and T_r is a user–specified reference temperature	$$\rho_i(T) = \rho_{0,i}\left(\frac{T}{T_r}\right)^{n_{\rho,i}}$$
Bulk porosity	
The bulk porosity ($\overline{\psi}$) is a "property" of each condensed phase species thus their porosity ψ_i. $\rho_{s0,i}$ is a user-specified constant corresponding to the density of solid nonporous species i at a particular temperature, and $\rho_i(T)$ is the bulk density of species i.	$$\overline{\psi} = \sum X_i \psi_i = \sum X_i\left(1 - \frac{\rho_i(T)}{\rho_{s0,i}}\right)$$
Effective thermal conductivity	
The averaged effective thermal conductivity $(\overline{k})$ is weighted by condensed phase volume fractions X_i. The effective thermal conductivity of each condensed phase species is broken into a solid ($k_{s,i}$) and a radiative ($k_{r,i}$) component. The temperature dependancy of $k_{s,i}$ is prepresented by $k_{0,i}$ and $n_{k,i}$ which are user-specified parameters and T_r is a user–specified reference temperature. $k_{r,i}$ is attributed to radiation heat transfer across pores, where the parameter γ_i controls the radiative contribution to the effective thermal conductivity.	$$\overline{k} = \sum_{i=1}^{M} X_i k_i$$ $$k_i(T) = k_{s,i}(T) + k_{r,i}(T)$$ $$k_i(T) = k_{0,i}\left(\frac{T}{T_r}\right)^{n_{k,i}} + \gamma_i \sigma T^3$$
Apparent specific heat capacity	
The temperature–dependent specific heat capacity of species i is assumed to be the sum of a "baseline" specific heat ($c_{b,i}$) and the apparent increase in the specific heat capacity due to the latent heat of melting ($c_{m,i}$). The specific heat is assumed to vary with temperature, where $c_{0,i}$ and $n_{c,i}$ are user–specified parameters and T_r is a user–specified	$$c_i(T) = c_{b,i}(T) + c_{m,i}(T)$$ $$c_{b,i}(T) = c_{0,i}\left(\frac{T}{T_r}\right)^{n_{c,i}}$$ $$c_{m,i}(T) = \frac{\Delta H_{m,i}}{\sqrt{2\pi\sigma_{m,i}^2}} \exp\left(-\frac{(T - T_{m,i})^2}{2\sigma_{m,i}^2}\right)$$

Description	Equation*
reference temperature. The latent heat of melting (ΔH_m) is assumed to be distributed via a Gaussian peak centered at T_m, the melting temperature.	
Radiative properties	
The bulk radiative properties are composed the emissivity (ε_i) and radiative absorption coefficient (κ_i) of each condensed-phase species. Emissivity controls the fraction of the incident radiation absorbed at the surface and the fraction of the blackbody emissive power of the surface that is radiated away. The radiative absorption coefficient controls the depth over which incident thermal radiation is attenuated.	$\bar{\varepsilon} = \sum_{i=1}^{M} X_i \varepsilon_i$ $\bar{\kappa} = \sum_{i=1}^{M} X_i \kappa_i$
Permeability	
The weighted permeability is calculated on a volume basis	$\bar{K} = \sum_{i=1}^{M} X_i K_i$
Gas density and molecular weight	
The gas-phase density is calculated from the ideal gas law, where R is the universal gas constant, and $\bar{M}$ is calculated from the local volume fractions of all gaseous species.	$\rho_g = \frac{P\bar{M}}{RT_g}$ $\bar{M} = \sum_{j=1}^{N} X_j M_j$
Gaseous specific heat capacity and enthalpy	
It is assumed that all gaseous species have equal specific heat capacities that are independent of temperature. As with the condensed phase enthalpy, the gas phase sensible enthalpy is weighted by mass, where c_{pg} denotes the gaseous specific heat capacity.	$\bar{h}_g = \sum_{j=1}^{N} Y_j h_{g,j} = c_{pg}\left(T_g - T_d\right)$
Gaseous mass diffusivity, thermal conductivity, and viscosity	
Gaseous diffusion coefficients are calculated from Chapman–Enskog theory. It is a binary diffusion coefficient for species *A* diffusing into species *B*. M_A and M_B are the molar masses, σ_{AB} is a weighted collision diameter of species *A* and *B*, k_b is the Boltzmann constant, and ε_{AB} is the maximum energy of attraction between molecules *A* and *B*. It is assumed that all gaseous species have the same diffusivity ($D_{AB} = D$), taken as that of oxygen	$D_{AB} = 0.018829 \frac{\sqrt{T^3\left(\frac{1}{M_A} + \frac{1}{M_B}\right)}}{P\sigma_{AB}^2 \Omega_{D,AB}}$ $k_g \approx \rho_g D c_{pg}$ $\nu \approx D$

Description	Equation*
into the background species. Prandtl, Schmidt, and Lewis numbers are (Pr = Sc = 1). This allows for considerable simplification of the gas phase energy equation.	

Table 22 Sumamry of the properties and defintions of the Technical Reference [90] of gpyro

* *One might find unexplained parameters in the equations of Table 22. This is because it represents only a brief summary of the properties and their definitions. The focus lies on the important parameter in respect to chapter 2. For detailed information and extra clarification, please consult the Technical Reference [90].*

The remaining terms of the governing equations of gpyro (Table 21) that have not yet been addressed are the source terms attributed to reactions. As given in Technical Reference [90], gpyro considers two types of reactions (Table 23), one of which is heterogeneous (solid/gas) and the other homogeneous (gas-gas). Under heterogeneous reaction, it is understood that they involve the destruction of a condensed phase species to form gases and/or additional condensed phase species. While a homogeneous gas phase, reaction involves only gases.

Heterogeneous reaction stoichiometry

A condensed phase reaction is denoted by the index k. The total number of condensed phase reactions is designated K. The stoichiometry of gas phase reactions is expressed using the molar ν, with the important difference that the ν coefficients are given on a mass basis. A_k denotes the condensed phase reactant species and B_k denotes the condensed phase product species. The composition of the gases consumed and produced by a heterogeneous reaction is controlled by the parameters $\nu'_{j,k}$ and $\nu''_{j,k}$. Here $\nu'_{j,k}$ is the net mass of gaseous species j consumed by reaction k, and $\nu''_{j,k}$ is the net mass of gaseous species j produced by reaction k per unit mass of A_k consumed.

$$1\,\text{kg}\,A_k + \sum_{j=1}^{N} \nu'_{j,k}\ \text{kg gas j} \rightarrow \nu_{B,k}\ \text{kg}\,B_k + \sum_{j=1}^{N} \nu''_{j,k}\ \text{kg gas j}$$

Homogeneous gas phase reactions
A gas phase reaction is denoted by the index ℓ. The total number of gas phase reactions is designated L. Each homogeneous gas phase reaction ℓ converts two gas phase reactants (A_ℓ and B_ℓ) to gaseous products. The stoichiometry of homogeneous gas phase reactions is expressed here on a mass basis. $y_{g,j,\ell}$ is the net mass of gaseous species j produced/consumed by reaction ℓ per unit mass of gaseous species A_ℓ. $$1\,\text{kg}\ A_\ell - y_{g,B_\ell,\ell}\ \text{kg}\ B_\ell \rightarrow \sum_{j=1}^{N} \max\left(y_{g,j,\ell},0\right)\text{kg gas}\ j$$

Table 23 gpyro: reaction types as per Technical Reference [90]

The rate at which these reactions occur are quantified via the commonly used Arrhenius type functions of the temperature as described in Equation (2). This is modified to cater for possible volume change.

From the above summary of the model, it becomes clear that this is a significant more complex approach then the one described in chapter 2. Due to its specifics, in addressing each potential species, it has a significant higher number of parameters to define. This, however, does not significantly change the conclusions of chapter 4.

5.3 Parameter allocation

This section serves to tailor and summaries the parameters determined in chapter 3 so that they can be used in gpyro either to limit the search space, or to use them directly as known parameters in the model. Due to the complexity of the model, the heating behaviour of a vast amount of different materials can be modelled. This requires a substantial number of input parameters, as specified and explained in [102-104]. This section will not attempt to provide an in detail overview of all the used input parameters, but will provide the applicable ones in concurrence with the assumptions stated in chapter 2 and the parameter found chapter 3. For the reminder, the default values as stated in the user guide [104] have been used. Table 24-Table 28 describes in brief the parameter that will be further specified at the end of this section.

Case properties		
Symbol	**Units**	**Description**
q_e	W/m^2	*Incident heat flux*
h_{c0}	W/m^2-K	*Convective heat transfer coefficient,* at the exposed surface.
n_{hc}	-	*Exponent of the heat transfer coefficient*
δ_0	m	*Initial thickness in z-direction*
n_{cell}	-	*Number of computational cells that span this thickness in z-direction*
Y_∞	g/g	*Ambient gaseous mass fraction*

Table 24 The essential case properties of gpyro for the problem to be solved

Initial conditions and layer setup properties		
Symbol	**Units**	**Description**
n_{layers}	-	*Number of layers*
z_1	m	*Layer start location* in the z-direction
z_2	m	*Layer stop location* in the z-direction
h_{cr}	-	*Inverse contact resistance* or *back boundary heat transfer coefficient* in z-direction
T_0	K	*Initial temperature* of the specific layer
Y_{i0}	-	*Initial mass fraction* in the layer

Table 25 The essential initial conditions and layer setup properties of gpyro for the problem to be solved

Solid/liquid properties		
Symbol	**Units**	**Description**
k_{0z}	W/m-K	*Thermal conductivity* at reference temperature
n_{kz}	-	*Thermal conductivity exponent* with which the specific heat is calculated at a different temperature, when "0" k_{0z} becomes constant
ρ_0	kg/m^3	*Density* at reference temperature
n_ρ	-	*Density exponent* with which the specific heat is calculated at a different temperature, when "0" ρ_0 becomes constant
c_0	J/kg-K	*Specific heat capacity* at reference temperature
n_c	-	*Specific heat capacity exponent* with which the specific heat is calculated at a different temperature, when "0" n_c becomes constant
ε	-	*Emissivity*; controls the fraction of the incident radiation absorbed at the surface
κ	m^{-1}	*Radiation absorption coefficient*; controls the depth over which incident thermal radiation is attenuated when $> 10^6\ m^{-1}$ then only surface absorption.
γ	m	Controls radiation heat transfer across pores, when "0" this radiation heat transfer is omitted
T_m	K	*Melting temperature*, unattainable high values (5000) ensure that melting does not take place
ΔH_m	J/kg	latent heat of melting if T_m is reached.
σ_m^2	K^2	Width of effective melt c_p, controls Gaussian "width" of the

Solid/liquid properties		
Symbol	**Units**	**Description**
		Gaussian specific heat capacity peak attributed to the latent heat of melting
K_z	m^2	*Permeability ,* has an effect if the pressure solver is invoked
ρ_{s0}	kg/m^3	*Density of solid nonporous species*, has an effect if the porosity is being solved

Table 26 The essential solid properties of gpyro for the problem to be solved

Condensed-phase reactions properties		
Symbol	**Units**	**Description**
Z	s^{-1}	*Pre-exponential factor*
E	kJ/mol	*Activation energy*
ΔH_{vol}	J/kg	Heat of volatilization, heat of vaporization or *heat of pyrolysis*; it is the amount of heat required to volatilize unit mass of the condensed phase reactant
χ	-	*Parameter affecting swelling*, closer to "0" means more swelling, and closer to "1" means more volatilization
n	-	*Reaction order*
n_{O_2}	-	Reaction order in O_2 concentration; it is an exponent that controls the oxygen dependency.
$i_{kineticmodel}$	-	*Index of kinetic model* as per [104]
i_{O_2} rxn	-	Index affecting oxygen reaction order. If "0" then $(1-Y_{O_2})^{n_{O_2}}$ otherwise $(Y_{O_2})^{n_{O_2}}$
K_{cat}	-	*Autocatalysis factor*, it defines the contribution of the autocatalysis
i_{cat}	-	Index of the condensed-phase species that is responsible for the catalytic behaviour

Table 27 The essential condensed-phase reaction properties of gpyro for the problem to be solved

Gas-phase thermophysical properties		
Symbol	**Units**	**Description**
Name		*Gaseous species name*
Y	g/g	*Initial gas-phase mass fraction*
M	g/mol	*Molecular weight of each species*

Table 28 The essential gas-phase thermophysical properties of gpyro for the problem to be solved

The general test setup parameters used are presented hereafter with a brief explanation why they were chosen, followed by the values and search ranges for PA6. The values and search ranges for the other materials can be found in Appendix B.2.

Initial conditions and layer setup of the sample layer			
Symbol	**Units**	**Value**	**Explanation**
n_{layers}	-	1	The samples themselves represent the first layer
z_1	m	0	The samples consist of 2 glued together 6mm thick samples starting at z = 0 mm.
z_2	m	0.012	
h_{cr}	-	100	Estimated from literature [105] according to which 100 represents a tipical contact resistance of a polymer
T_0	K	294	Initial temperature is ambient temperature defined as 21°C.
$Y_{i0,1}$	-	1	Links this material with its properties at material property location 1

Table 29 Used values for the sampler layer

Initial conditions and layer setup of the aluminium block			
Symbol	**Units**	**Value**	**Explanation**
n_{layers}	-	2	The aluminium block represent the second layer
z_1	m	0.012	The aluminium block is 25.5 mm thick
z_2	m	0.0375	
h_{cr}	-	10	The back boundary of the samples is defined by the temperature distribution and the thermophysical properties of the aluminium block, thus the losses are. The losses to the back of the sample are irrelevant as long as the temperature model curve fits the real data.
T_0	K	294	Initial temperature is ambient temperature defined as 21°C.
$Y_{i0,6}$	-	6	Links this material with its properties at material property location 6

Table 30 Used values for the backing layer (aluminium block)

Gas-phase thermophysical properties			
Symbol	**Units**	**Value**	**Explanation**
Name	*Oxygen (O2)*		Ambient Air
Y	g/g	*0.23*	
M	g/mol	*32*	
Name	*Nitorgen (N2)*		
Y	g/g	*0.77*	
M	g/mol	*28*	
Name	*Fuel (Propane)*		Since no detailed information is available in respect to what the exact gaseous species are, that are being produced one has to revert to a best suitable representation. This information is rarely known, especially when using a reduced chemical reaction mechanism. In this work the release gasses shall be represented by a ratio of propane (resembling the released total hydrocarbons) and an inert (resembling the released no reacting products). The ratios for the different materials when reacting are taken as presented in Table 13 of section 3.3. Due to this the model requires to specify numbers for the molecular weigt and mass ration even though combustion has not yet taken place.
Y	g/g	*0*	
M	g/mol	*44*	
Name	*Inert (Nitrogen)*		
Y	g/g	*0*	
M	g/mol	*28*	

Table 31 Used values for the gas-phase thermophysical properties and initial mass fractions

The backing (aluminium) was present for all tests. Its material properties, therefore, are presented in the following Table 32. The reason an aluminium block was used was to quantify the losses to the back (back boundary condition at the sample).

Solid properties of the aluminium block			
Symbol	**Units**	**Value**	**Explanation**
k_{0z}	W/m-K	179.98 (177.88)	The maximum difference of the thermal conductivity as per section 3.9 of the recorded temperature range (21 and 50 °C section 5.1) is ±1.17% which is neglectable therefore the mean was chosen
n_{kz}	-	0	
ρ_0	kg/m^3	2704 (2707)	The maximum difference of the density as per section 3.9 of the recorded temperature range (21 and 50 °C section 5.1) is ±0.1% which is neglectable therefore the mean was chosen
n_ρ	-	0	
c_0	J/kg-K	901.8 (892.5)	The maximum difference of the specific heat capacity as per section 3.9 of the recorded temperature range (21 and 50 °C section 5.1) is ±1% which is neglectable therefore the mean was chosen
n_c	-	0	
ε	-	0.5	Even though neglectable due to the small effect of the temperature difference between the ambient and the back surface via the $\Delta T^{1/4}$ dependency. Just in case

Solid properties of the aluminium block			
Symbol	**Units**	**Value**	**Explanation**
			"0.5" was chosen due to the matt back surface of the aluminium block and in connection with the experiences gained during the tests described in section 5.1
κ	m^{-1}	$9 \cdot 10^{-9}$	The aluminium block is not being exposed to the external heat flux, thus it is irrelevant what the radiation absorption coefficient is. To insure that the model has all the parameters needed value > 10^6 m^{-1} is selected that indicates only surface absorption, which is for aluminum a reasonable assumption anyway.
γ	m	0	The aluminium block is not being exposed to the external heat flux, thus the radiation heat transfer across it pores is irrelevant. "0" indicates to ignore it just in case.
T_m	K	5000	The aluminium does not melt during time of exposure.
ΔH_m	J/kg	0	
σ_m^2	K^2	1	
K_z	m^2	$1 \cdot 10^{-10}$	The overpressure is approximately inversely proportional to the permeability. Thus for a peak overpressure of 10 Pa the permeability becomes $1 \cdot 10^{-10}$ m^2. The here assumed value is merely estimated.
ρ_{s0}	kg/m^3	2704 (2707)	The aluminium block is considered as non-porous thus the density of solid nonporous species (ρ_{s0}) equals (ρ_0).

Table 32 Used values for the backing layer (aluminium block)

As an example, the case for PA6 is described here while all the other cases (PA6+FR, PA6+NC as well as PA6+NC+FR) are presented in Appendix B.2.

Material specific input data (PA6)

For the determination of the (intrinsic or global) material properties, four different tests have been analysed. Two of these have been conducted at a heat flux (q_e) of 25 kW/m^2 and two at 30 kW/m^2. The overall initial thickness (δ_0) that was taken into consideration for the analysis of these tests was the 37.5 mm combined thickness of the tested sample and the aluminium block with a cell number (n_{cell}) of 300, resulting in a cell thickness of 0.125 mm. The ambient gaseous mass fraction (Y_∞) was taken to be 23% for O_2 and 77% for N_2. Gpyro handles, as previously described, the input of temperature dependant parameters in a specific way (see Table 22). Therefore, it

was necessary to curve fit the function to the results of section 3.9. This gave the heat transfer coefficient (h_{c0}) and its exponent (n_{hc}) for the FPA of 12.14 W/m^2-K and 0.81 respectively as presented in Appendix B.4.4.

As determined from the TGA analysis in section 3.2 the reduced chemical reaction mechanisms in air of PA6 follow a four-step reaction process as shown in Table 12 and Table 9. From this analysis, it is possible to tell how the material is chemically reacting when heated, even though it being in a reduced manner. An option would be to expand the later conducted parameter search to, also, find the ideal reaction step model, as well as the reaction types. Since obtaining these is in itself very challenging (due to the high level of complexity), it has been opted to directly apply the in section 3.2 determined best reduced chemical reaction mechanism. The kinetic properties for the reaction of PA6 in air (Table 12) serve to keep the search area limited, in order to insure that the model could converge. Attempts with a too large search region ended in endless calculations caused by the pre-exponential and exponential factor being too different. Table 12 provides most of the condensed-phase reactions properties of Table 27. The remaining two parameters for each of the four reactions are the heat of pyrolysis (ΔH_{vol}) and χ, the parameter affecting swelling. Though the first of these parameter was never obtained, as explained in section 3.11, its values are assumed to be in the range of $1 \cdot 10^6$ J/kg. The parameter χ is set to "1" for PA6 since no significant swelling nor charring was observed. As in Equation (4) - (7), and Table 27 the index affecting the oxygen reaction $i_{O_2}\,rxn$ is set to "1".

As in the TGA analysis, four reduced chemical reaction mechanisms were distinguished. This leads us to five different species including the initial/virgin material. For each of these species, the physically possible initial search range of the properties determined in chapter 3 (numbers in brackets "( )") are presented. It is possible to assign temperature dependant values for the thermal conductivity, density and specific heat capacity. This added degree of freedom could conceivably lead to issues of convergence. Since only limited data on the temperature dependency for the thermal conductivity and the density for the temperature range in question was available (see Table 17 and Appendix B.4.3), it was decided to use for the virgin

PA6 the average; thus, $n_{kz} = n_\rho = 0$. Temperature dependant values of the specific heat capacity of the virgin material are being searched or used. Since limited knowledge is available for the intermediate and residue species, their thermal properties shall be assumed constant ($n_{kz} = n_\rho, = n_c = 0$). This is the case except for the virgin material where there is independent data available, as presented in sections 3.5, 3.6 and 3.7. The values of Table 33 are mere educated guesses with the help of the literature [25, 31].

Symbol	**Units**	Virgin	Intermediate 1	Residue 1	Intermediate 1	Residue 2
k_{0z}	W/m-K	0.01-3 (0.283)	0.01-20	0.01-20	0.01-20	0.01-20
ρ_0	kg/m^3	900-1500 (1146)	100-2000	100-2000	100-2000	100-2000
c_0	J/kg-K	100-4500 (1743)	100-4500	100-4500	100-4500	100-4500
n_c		0-1 (0.847)	0	0	0	0

Table 33 PA6: thermal conductivity, density and specific heat capacity

It is assumed that of the differentiated species, only the virgin material (the PA6 itself) undergoes the process of melting. The required parameters for gpyro are obtained from the analysis in sections 3.5, 3.6 and 3.7. From Table 15, the melting temperature (T_m) of 488 K and the latent heat of melting (ΔH_m) of 68000 J/kg can be obtained. A reasonable range between 423 and 523 K and 20,000 and 300,000 J/kg was used when searching for these properties. From Figure 15 it can be assumed that σ_m^2 is in the range between 16 and 225 K^2 while from Figure 154, the best normal distribution fit was reached with 53.9 K^2. This was obtained using the root mean squared error regression analysis.

The remaining parameters considered here, are the ones presented in Table 34. These parameters have not been obtained elsewhere, thus, have to either be assumed or be obtained in a inverse manner. To help narrow down their physically possible values the standard literature of this process has been consulted [25, 31, 102, 104, 106].

Symbol	**Units**	Virgin	Intermediate 1	Residue 1	Intermediate 1	Residue 2
E	-	0.3-0.99	0.3-0.99	0.3-0.99	0.3-0.99	0.3-0.99
K	m^{-1}	10^0-10^6	0^0-10^6	0^0-10^6	0^0-10^6	0^0-10^6
γ	m	0-0.001	0-0.001	0-0.001	0-0.001	0-0.001
K_z	m^2	10^{-20}-10^{-5} ($1.46 \cdot 10^{-12}$)	10^{-20}-10^{-5}	10^{-20}-10^{-5}	10^{-20}-10^{-5}	10^{-20}-10^{-5}
ρ_{s0}	kg/m^3	900-2000	100-2000	100-2000	100-2000	100-2000

Table 34 Used values for the PA6 layer (aluminium block)

5.4 Fitting process

For the fitting process, the available (all) test data of section 5.1 for each material was used simultaneously together with the parameters and bounds of section 5.3. This allowed, the material property estimation program “gpyro_propest” as mentioned in section 5.1 to be executed. The objective was to obtain one set of parameters that simultaneously suited all the available test data and bounds. The program searches for a best model to data fit by means of “generic algorithm” [93]. The strength of this optimisation technique is to find global minima. The obtained results are usually within the right solution area, but require refinement. Ideally, a refinement of the initial results should be done by an optimisation algorithm especially designed to find local minima. This is not part of the currently available gpyro package; therefore, further refinement was reached by manually narrowing down the search bounds, which was not ideal, but suited the purpose.

Gpyro uses “generic algorithm” as an optimisation technique that is ideally suited for parallelisation. This enables the effective parallel execution of the code. This capacity was exploited fully on the computer cluster of the Edinburgh Compute and Data Facility (ECDF). This facility was equipped with an Intel processor based cluster running 64-bit Linux, consisting of 1456 processors.

5.5 Results

This section presents the results of the fitting process and contains graphs comparing the in depth temperature and mass loss test data as a function of time with the results from the model. For the latter, the parameters that provided the best model to data fit were used. These are also presented here.

To assess whether the properties obtained are “intrinsic” or “global” material properties, the results with and without the independently obtained intrinsic material properties are presented side by side (left without (w/o) and right with (w)). This representation was chosen to enable a visual comparison and to allow the reader to get a sense of the quality of the fit. Due to the vast amount of available data and plots, the presentation in this section concentrates on PA6. The examples focus on demonstrating visually best and worst fits. For an enlarged version or the other graphs and tables, for other materials or a different case Appendix B.5 should be consulted.

In the temperature figures (Figure 43 - Figure 46), the lines with the makers represent the test data. The marker-less line represents the model result. Similarly, in the cumulative mass loss figures (Figure 47 - Figure 50) the markers represent the test data while the line represents the model results.

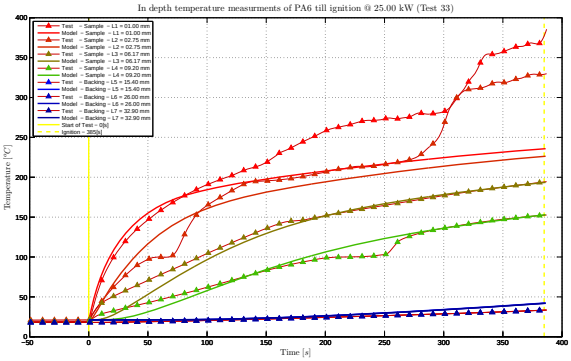

Figure 43 In-depth temp. comp. PA6 w/o; best

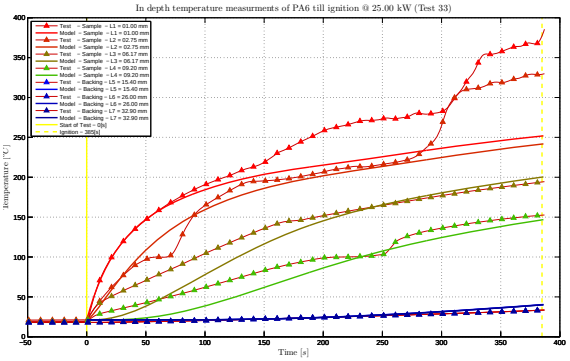

Figure 44 In-depth temp. comp. PA6 w; best

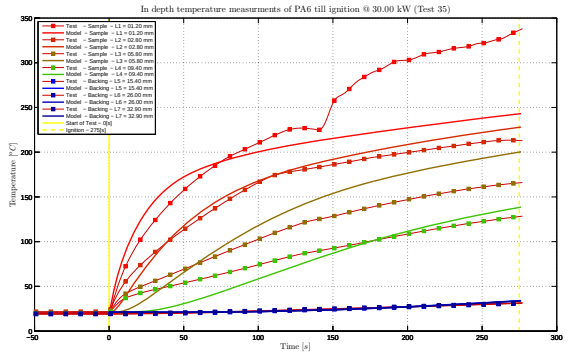

Figure 45 In-depth temp. comp. PA6 w/o; worst

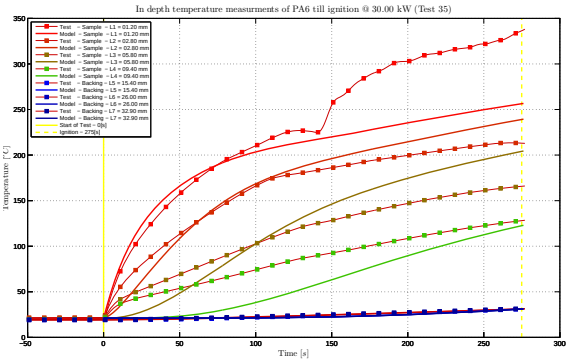

Figure 46 In-depth temp. comp. PA6 w; worst

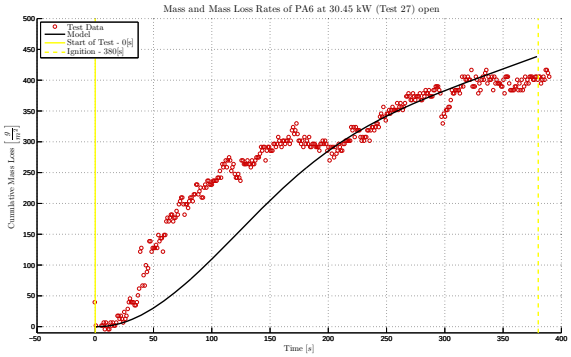

Figure 47 Cum. mass loss comp. PA6 w/o; best

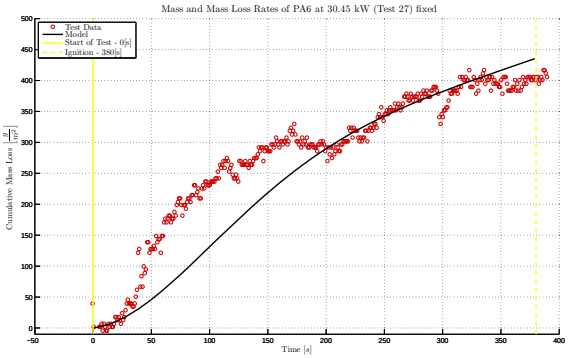

Figure 48 Cum. Mass loss comp. PA6 w; best

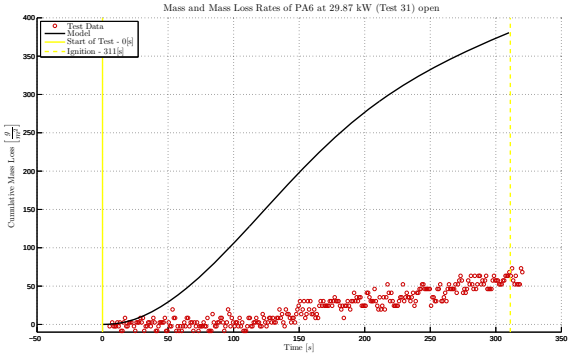

Figure 49 Cum. mass loss comp. PA6 w/o; worst

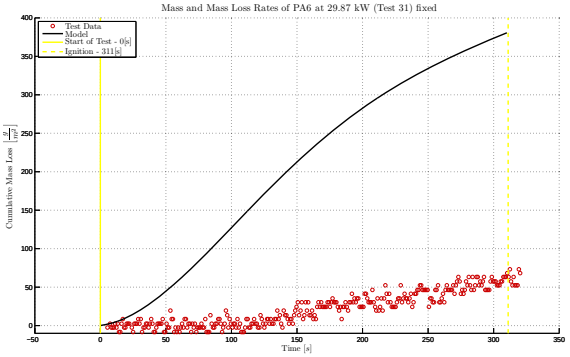

Figure 50 Cum. Mass loss comp. PA6 w; worst

For the results presented in the above graphs, all available data sets have been used. A selection whether they resemble good or bad data sets could not be established due to the small number of tests. Together with the measurement error, scatter can be expected, especially in the case of mass loss. The tests have been conducted under the best possible and repeatable conditions, which might have not been suitable and are subject to improvement, but represented the standard testing procedures for the used apparatuses used.

The main objective is to determine whether this methodology provides promising results that can be further explored in later work. The deviations in the obtained and used test results are apparent. For example, the deviations of the in-depth time temperature curves in the presented heat flux cases of section 5.1.1, are handled in the optimisation process by taking them all equally into account. As the model has to find a solution that satisfies all input data, this can lead to a test to model deviation for each test that is worse than when fitting the parameters to a single test, because it has to find a solution that satisfies all input data. Theoretically, the use of the same materials under the same test conditions should provide the same results, since they have not changed. The aim is to obtain “intrinsic” material properties. Therefore, the interest lies upon parameters that are intrinsic in nature that are not test dependant.

In the above figures, as well as the figures in section B.5, the effect of the independently obtained parameters (idp) has on the fitting results can be seen; they appear to be similar but not precisely the same. This remains true for all the materials tested.

The independently determined parameters (column 4) as in chapter 3 as well as the results from the property estimation with (column 6) and without (column 5) usage of the independently determined parameters are being presented for PA6 in Table 35. Column 2 contains the number to which of the four species, of the four-step reaction, the parameter value belongs. The symbol in column 3, which is explained in section 5.3, associates the parameter value to the type of parameter.

Parameter					
#	Species	Symbol	independently determined parameters (idp)	gpyro_propest fit without idp	gpyro_propest fit with idp
1	1	Z	11.4	11.4	11.4
2	1	E	180	180	180
3	1	ΔH_{vol}		6.24	5.51
4	1	χ		1	1
5	1	n	1.17	1.05	1.17
6	1	n_{O_2}		0.547	2.33
7	1	K_{cat}	-4.98	-4.33	-4.53
8	2	Z	11.1	10.1	11.1
9	2	E	180	180	180
10	2	ΔH_{vol}		5.90	2.39
11	2	χ		1	1
12	2	n	0.697	0.525	0.697
13	2	n_{O_2}		0.0906	0
14	3	Z	1.85	6.10	1.85
15	3	E	66.3	67.7	66.3
16	3	ΔH_{vol}		5.78	6.05
17	3	χ		1	1
18	3	n	1.30	1.19	1.30
19	3	n_{O_2}		0.573	0.852
20	4	Z	6.05	5.99	6.04
21	4	E	132	130	132
22	4	ΔH_{vol}		5.88	7.54
23	4	χ		1	1
24	4	n	1.23	1.10	1.23
25	4	n_{O_2}		1.52	2.14

Parameter					
#	Species	Symbol	independently determined parameters (idp)	gpyro_propest fit without idp	gpyro_propest fit with idp
26	1	k_{0z}	0.283	0.426	0.283
27	2	k_{0z}		6.42	10.6
28	3	k_{0z}		12.3	16.7
29	4	k_{0z}		13.0	12.4
30	5	k_{0z}		16.7	22.7
31	1	ρ_0	1114	1093	1114
32	1	n_ρ		0	0
33	2	ρ_0		679	757
34	3	ρ_0		373	730
35	4	ρ_0		640	567
36	5	ρ_0		489	655
37	1	c_0	1743	1236	1743
38	1	n_c	0.85	1.11	0.85
39	2	c_0		3489	4010
40	3	c_0		2872	3157
41	4	c_0		3147	3625
42	5	c_0		2755	2255
43	1	ε		0.91	0.99
44	2	ε		0.73	0.47
45	3	ε		0.62	0.53
46	4	ε		0.47	0.65
47	5	ε		0.70	0.55
48	1	κ		3.61	3.06
49	2	κ		2.43	0.18
50	3	κ		1.63	2.45

Parameter					
#	Species	Symbol	independently determined parameters (idp)	gpyro_propest fit without idp	gpyro_propest fit with idp
51	4	κ		3.16	2.65
52	5	κ		3.20	4.30
53	1	T_m	488	464	488
54	1	ΔH_m	68000	82046	68000
55	1	σ_m^2	52.9	149	52.9
56	1	γ		0.000509	0.000636
57	2	γ		0.000598	0.000582
58	3	γ		0.000469	0.000475
59	4	γ		0.000636	0.000638
60	5	γ		0.000615	0.000308
61	1	K_z		-12.6	-15.3
62	2	K_z		-15.4	-17.3
63	3	K_z		-18.0	-20.0
64	4	K_z		-10.1	-11.3
65	5	K_z		-11.8	-13.8
66	1	ρ_{s0}		1450	1504
67	2	ρ_{s0}		992	1288
68	3	ρ_{s0}		493	987
69	4	ρ_{s0}		1088	1099
70	5	ρ_{s0}		604	732
71	1	h_{cr}		128	152
72	2	h_{cr}		6.28	7.93

Table 35 Comparison of the resulting parameters for PA6

The results are different, which has partially to do with the optimisation technique used that is designed to find global but not local minima. As such, minor differences are acceptable. Trying to determine the reason(s) for these differences is a risky

endeavour due to the vast amount of influencing parameters. Research beyond the present work would be required to narrow these down. Nevertheless, a first attempt is conducted in the following chapter in the form of a discussion of the obtained results. From the results presented here, and the results in the associated appendix, it is not directly obvious, but the more complex the material is chemically (PA6 → PA6+NC → PA6+FR → PA6+NC+FR), the less “good” the fit between the test and model data became.

While the present results indicate that there is robustness in the parameter outcome, in that many parameters are very similar, it is not clear that the number of known parameters introduced here is sufficient to obtain the correct solution. When introducing independently obtained parameters, the model is generating a solution that is different to the one that optimises all parameters. A further sensitivity analysis should be conducted to establish what the effect of locking further parameters would be. Unfortunately, this is beyond the scope of this study.

6 DISCUSSION OF THE RESULTS

The goal of this study was to develop an approach, which interpreted (standard) flammability tests such that it was possible to derive (intrinsic) material properties controlling ignition. The aim was to derive these properties so that, ultimately, they can then be used to model material behaviour in a real fire.

The full goal has not been reached, as is clear from the results in the previous chapter (chapter 5), and from the following discussion. Nevertheless, a significant step towards the main goal has been achieved. As many parameters as possible have been independently determined for complex but realistic materials. It has been demonstrated that a high degree of consistency can be obtained in the optimisation process. A more comprehensive sensitivity analysis that includes more independent variables will need to be conducted to establish an invariant set of intrinsic properties.

The following sections will analyse the results obtained within the perspective of the desired application.

6.1 Error estimation

When measurements are taken once or only a few times, it is not possible to quantify the error based on statistical analysis. In these cases, one has to rely on the estimation of maximum bounding error. This approach of error estimation will be followed here.

Since the errors in the temperature and mass readings are a function of various independent measurements such as the time, depth of the measurement, and exposed heat flux, the resulting absolute error needs to be calculated based on these systems [107]. This can be done either by use of the error propagation analysis or by determining the absolute maximum error. Since the interest in this work lay in the determination of the maximum error and not in the determination of a compensated value, the latter was chosen.

The absolute maximum error can be obtained using the general Equation (57). As a general equation, this is valid for a system of "n" independent variables of the value "x", where Δx_i represents the accuracy with which that measurement can be taken.

$$\Delta f(x_1, x_2, \ldots, x_n)_{abs.max.} = \sum_{i=1}^{n} \left| \frac{\partial}{\partial x_i} f(x_1, x_2, \ldots, x_n) \right| \cdot \Delta x_i \tag{57}$$

This equation states that the sum of the first derivative of the dependant variables, multiplied by their observation error (for each of the independent variables), represents the absolute maximum error. It is advantageous to have small steps in ∂x_i.

When altering Equation (57) for the measurements of section 5.1 one obtains Equation (58) and (59) respectively. These are the error estimates for temperature (ΔT_{total}) and mass loss (Δm_{total}), where "t" is the time, "x" is the depth, "q" the heat flux.

$$\Delta T_{total\ error} = \left| \frac{\partial T_t}{\partial t} \right| \cdot \Delta t + \left| \frac{\partial T_x}{\partial x} \right| \cdot \Delta x + \left| \frac{\partial T_q}{\partial q} \right| \cdot \Delta q \tag{58}$$

$$\Delta m_{total\ error} = \left| \frac{\partial m_t}{\partial t} \right| \cdot \Delta t + \left| \frac{\partial m_q}{\partial q} \right| \cdot \Delta q \tag{59}$$

While the time and depth derivatives impose no complications in their application to the tests, the heat flux derivatives do. The reason for this is that there are large differences in the time dependant heat flux measurements of the conducted tests. In other words, the temperature and mass difference of two significantly different heat fluxes is only valid up to the point of ignition. Beyond this point, the heat flux exposure of the sample has changed because of the additional heat flux from the flame. Thus, the variables cease to be independent. Additionally the applicability of the heat flux derivative is jeopardized due to the fact that for the two tests, the depths of the thermocouples are different. This is because of the physically different placement of the thermocouples.

From a separate analysis of the sum of the right hand side of Equation (58) (solely including the heat flux induced errors up to ignition and assuming similar locations), it has been found that the main error is caused by the summand that accounts for the in-depth error. One example of this is shown for the various measured depths in

Figure 51 to Figure 57. This source of error could have been expected when dealing with materials that have a low conductivity. In the error analysis the assumed accuracy of the measurements taken are assumed to be Δt of ±0.5 s for the time, Δx of ±1 mm for the depth and Δq of ±0.5 kW for the heat. The heat flux induced error is disregarded in the later representation of the errors since it cannot be properly represented. This is considered reasonable, as its influence is minor compared to the error induced by the in-depth measurement. The error of the temperature measurement devices themselves (type K thermocouples) shall serve as a reference. According to the manufacturer [108] in conjunction with an independently conducted analysis [109] the error of type K thermocouples is below ±2.5 °C. From this information, it can be concluded that the main error is caused by test setup mainly rather then the instrument.

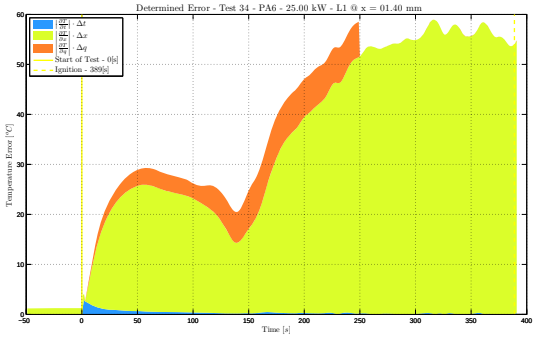

Figure 51 ΔT error - Test 34 - PA6 – x=1.4mm

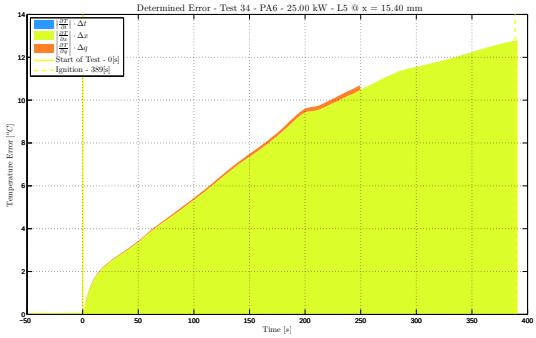

Figure 52 ΔT error - Test 34 - PA6 – x=15.4mm

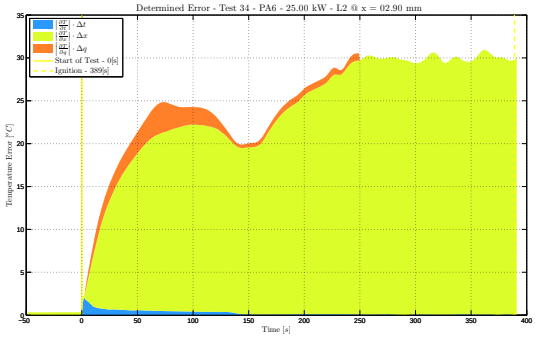

Figure 53 ΔT error - Test 34 - PA6 – x=2.9mm

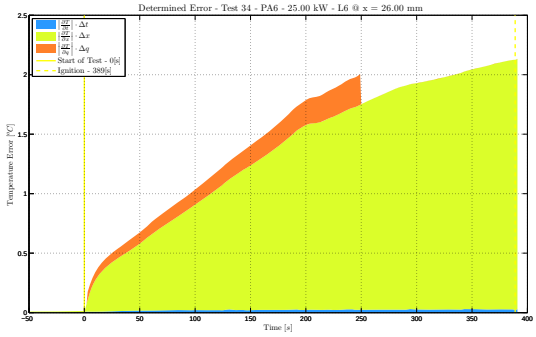

Figure 54 ΔT error - Test 34 - PA6 – x=26mm

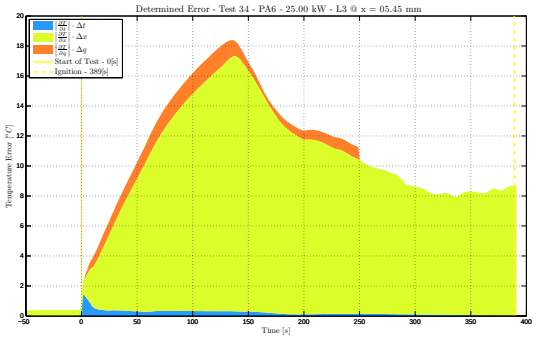

Figure 55 ΔT error - Test 34 - PA6 – x=5.45mm

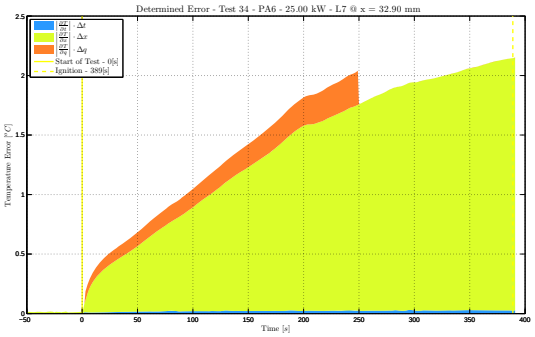

Figure 56 ΔT error - Test 34 - PA6 – x=32.9mm

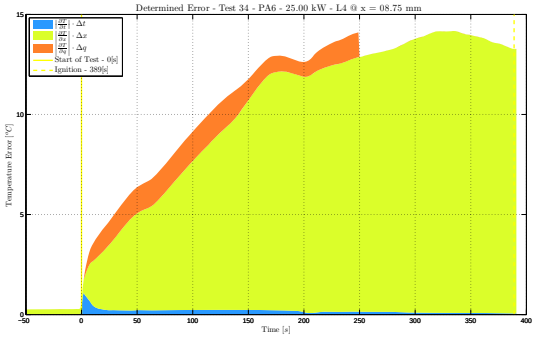

Figure 57 ΔT error - Test 34 - PA6 – x=8.75mm

If the errors determined are applied to the test data in the test-to-model comparison as per section 5.5 (Figure 43 - Figure 46), the quality of the in depth temperature distribution becomes evident. The results are shown in Figure 43 - Figure 46, where the lines with the makers represent the test data while the marker-less line represents the model result. As previously outlined, the unique sample depth is represented by a specific colour. The error bands into which the model solution, for the specific depth, should fall are represented by the same colour, but with a degree of transparency. The presented graphs show the “best” and “worst” results as well as results with (w) or without (w/o) the use of the independently obtained intrinsic material properties.

The model results fall, predominantly, within the error bounds. It must be noted, that the results presented here, have been obtained using all available data sets. A selection, whether they resemble good or bad data sets, could not be established due to the small number of tests. This fact is well represented in the difference of the deviations between the model data and the error bands in the labelled “best” and “worst” cases. The model data for the thermocouples closest to the surface sometimes shows significant deviations from the error band. Their possible

dislocation closer to the surface or even the possibility that they may fully protrude out of the surface will have caused this. The reason for the early deviation of the model from the error band in every graph can only be speculated at. These additional discrepancies will be addressed in section 6.2. Appendix C.1 presents the full set of graphs for all the data. This includes enlarged graphs of Figure 58 to Figure 61, and the other test cases as well as those for the other materials.

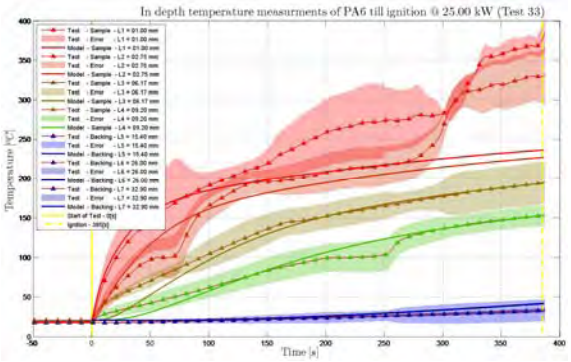

Figure 58 Model fit to PA6 in-depth temp. test data w/o (best)

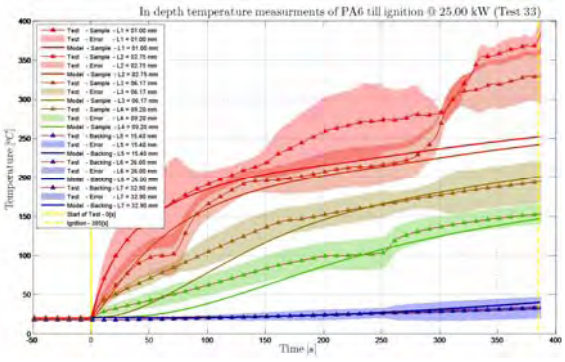

Figure 59 Model fit to PA6 in-depth temp. test data w (best)

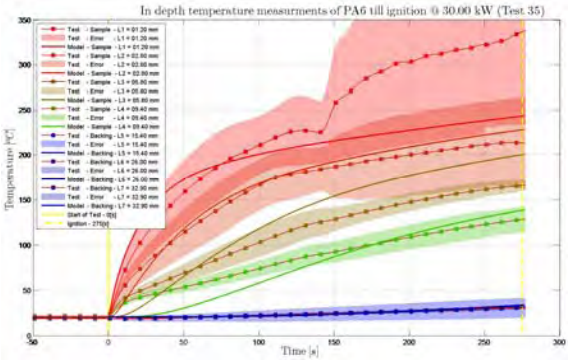

Figure 60 Model fit to PA6 in-depth temp. test data w/o (worst)

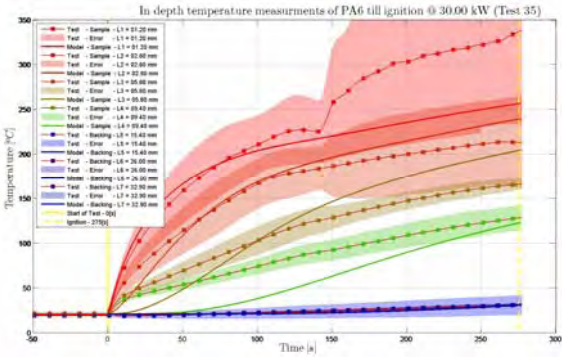

Figure 61 Model fit to PA6 in-depth temp. test data w (worst)

This analysis shows how promising the presented methodology is. Nevertheless, it also reveals, that the techniques can be improved, especially in respect to the accuracy in locating the thermocouples. An improvement in the temperature readings is likely to provide better results. This is because of the closer search bound; however, it could also have an adverse effect.

As with the temperature measurements, the error of the mass loss readings is also determined. To enable this, an analysis of the summation of the right hand side of Equation (59) (solely including the heat flux induced errors up to ignition and

assuming similar locations) is conducted. This analysis shows that the heat flux / test difference induced error are similar to the errors induced by the time difference. It varies from test to test, but is reasonably similar. An example figure is presented in Figure 62 using the reading accuracy of Δt of ±0.5 s for the time and Δq of ±0.5 kW for the heat flux. The sudden change of the heat flux induced errors, between 100 and 150 seconds, is caused by the fact that Δq between analysed tests is too large. In general, both errors are far smaller then the errors observed from the actual conducted mass loss measurements (section 5.1.3). This is also the case for the apparatus induced error of ±1 g or ±100 g/m^2.

It is assumed that due to the potential for a misinterpretation of the heat flux / test difference induced error, it is inadequately represented. Despite the big fluctuation between two tests at a single heat flux, the overall heat flux deviation for the large heat flux step is very small when it is multiplying by the reading accuracy of the heat flux measurement. The accuracy of the mass loss readings of the standard FPA [1] fulfils the requirements for the measurement of the mass loss after ignition. This is because the mass loss is significantly higher after ignition than before ignition. Furthermore, the mass loss measurements in the FPA are influenced by the setup itself due to the effects of the lever principle and friction. Careful evaluation of the absolute maximum error was conducted, and it was found to be around ±2-3 g or ±200-300 g/m^2.

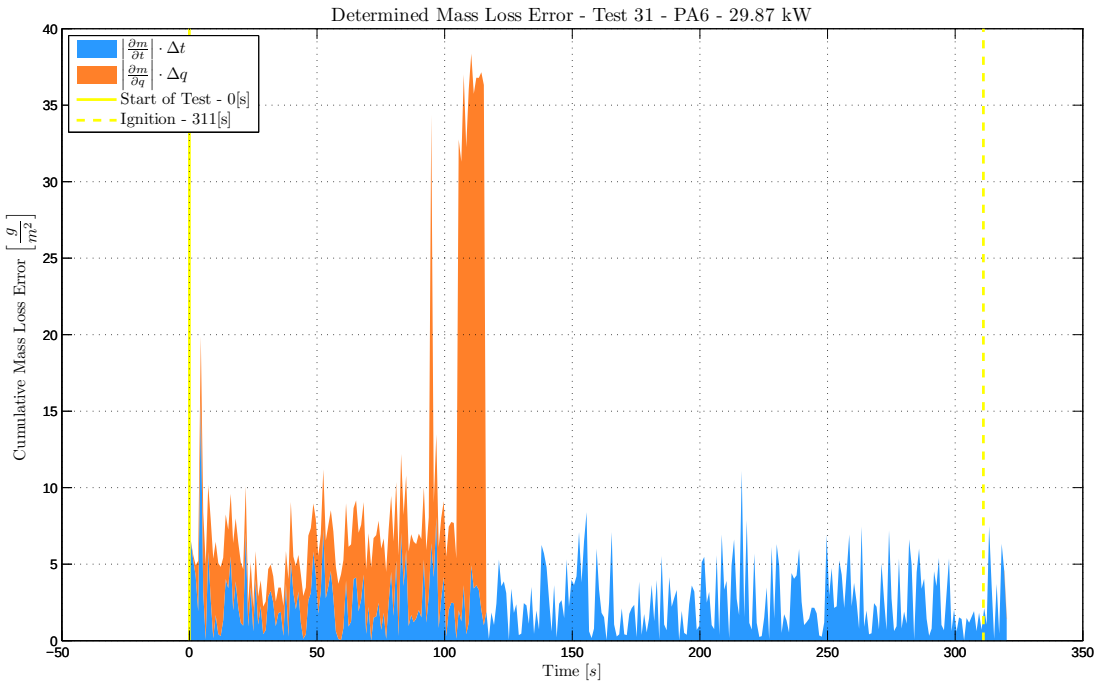

Figure 62 Δm error - Test 31 - PA6

The determined error was applied to the test data in the test-to-model comparison as per section 5.5 (Figure 47 - Figure 50). This allows the quality of the cumulative mass loss to become apparent. An example of this is presented in Figure 63 to Figure 66. These figures show the test data and errors as well as the determined model fit. The data presented in this section are the visually best and worst fit for the case with (w) and without (w/o) the use of the independently obtained intrinsic material properties. The graphs for the other cases and materials can be found in Appendix C.1.

This analysis also shows how promising the presented methodology is. With this methodology, it is possible to calculate the mass loss of an analysed material. However, it only fits to the average test data, since the material properties were obtained to best represent all involved data sets. The results also show that the accuracy and repeatability of the mass loss readings for a given heating case need to be significantly improved. This is likely to provide better results, due to the closer search bound, but could also have an adverse effect.

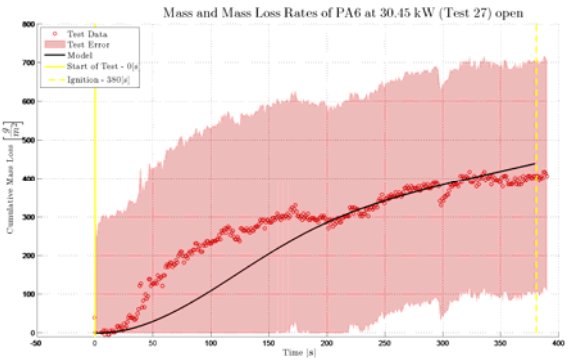

Figure 63 Model fit to PA6 cum. mass loss w/o (best)

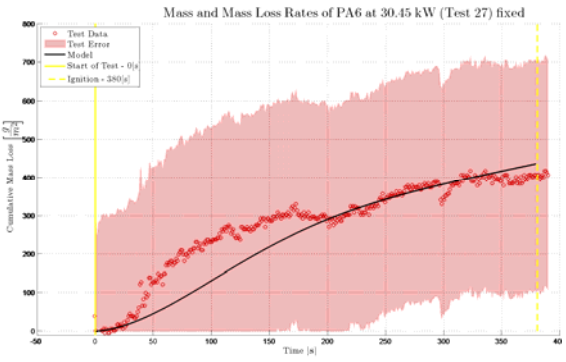

Figure 64 Model fit to PA6 cum. mass loss w/o (best)

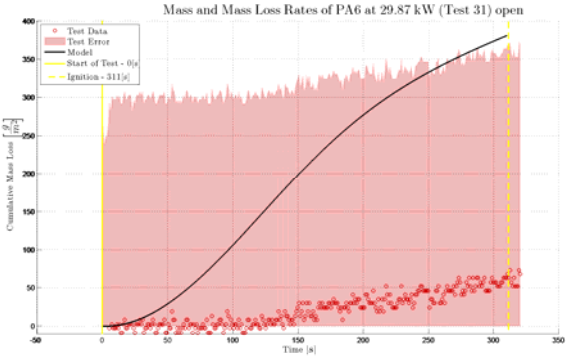

Figure 65 Model fit to PA6 cum. mass loss w (worst)

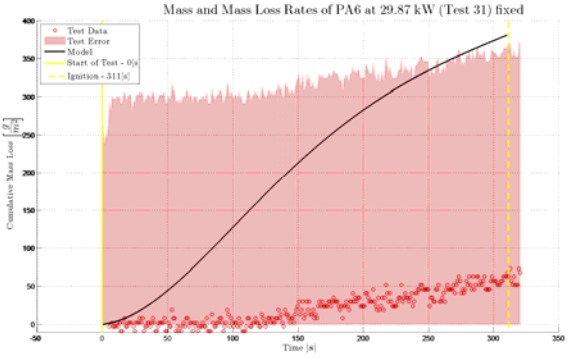

Figure 66 Model fit to PA6 cum. mass loss w (worst)

6.2 Peculiarity of the results

In addition to the critical analysis and peculiarities of the fit mentioned above, further observations shall be presented here. Due to the vast amount of test cases and possible comparisons, the mentioned observations are not an attempt to be fully comprehensive, but represent occurrences that were observed frequently.

Analysis of the in-depth temperature comparison (Figure 58, Figure 61 as well as the corresponding figures in Appendix C.1), it can be observed, that occasionally the two thermocouples at locations closest to the exposed surface (L1 and L2) experience a dramatic increase in temperature. This increase usually begins at around the melting temperature, and is assumed to be caused by relocation of these measurement elements closer to the radiation source possibly even out of the sample. The latter was occasionally observed during the tests.

It can also be observed from the same data that there is a bigger deviation between the model and the test in case of the two readings taken from within the sample furthest away from the exposed surface (L3 and L4) compared to the others. Their final location may have been within either of the glued samples or on the boundary of these samples. The unfortunate necessity of the need to glue two samples in the experimental setup together could easily be the reason for the increased difference of the model to data fit. The difference would be induced by the thermal contact resistance between the samples. Also of note in these figures is their behaviour in the beginning of the test. While the test data appears to show concave behaviour, the model is convex. To explore this further, Figure 67 shows the overall in-depth temperature distribution over time as produced by the model. Figure 68 shows the same data, but with the area of interest magnified. Since this behaviour is observed throughout the test to model comparison, only one case is presented here.

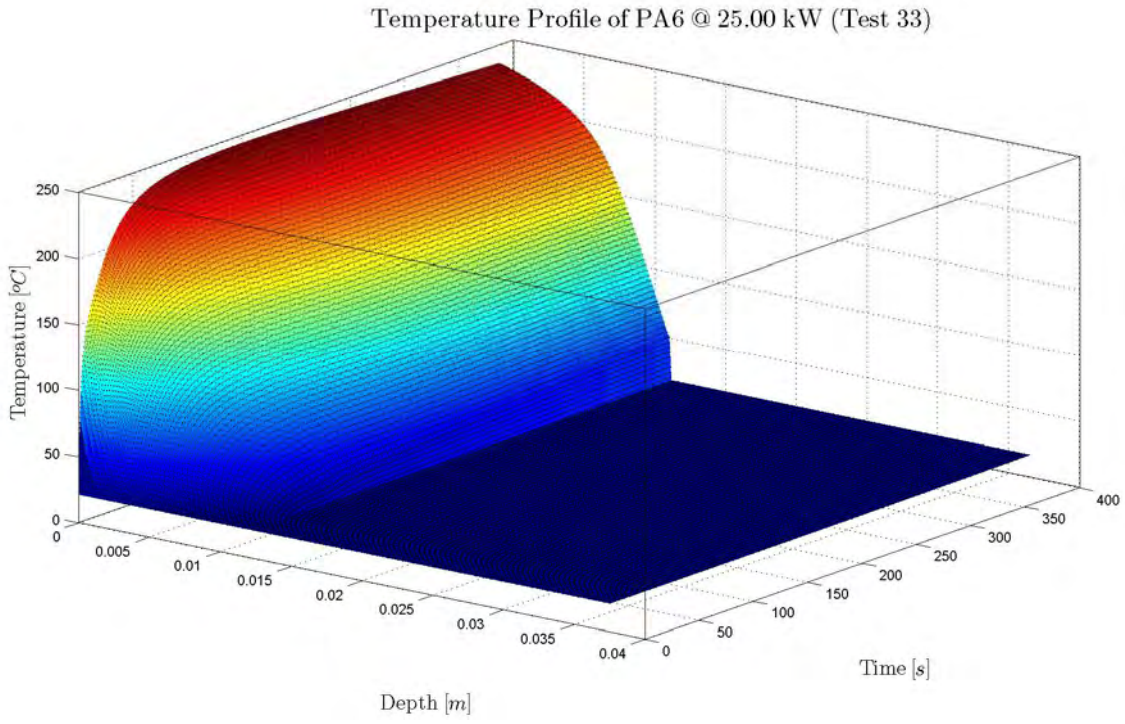

Figure 67 Typical in depth temperature distribution versus time

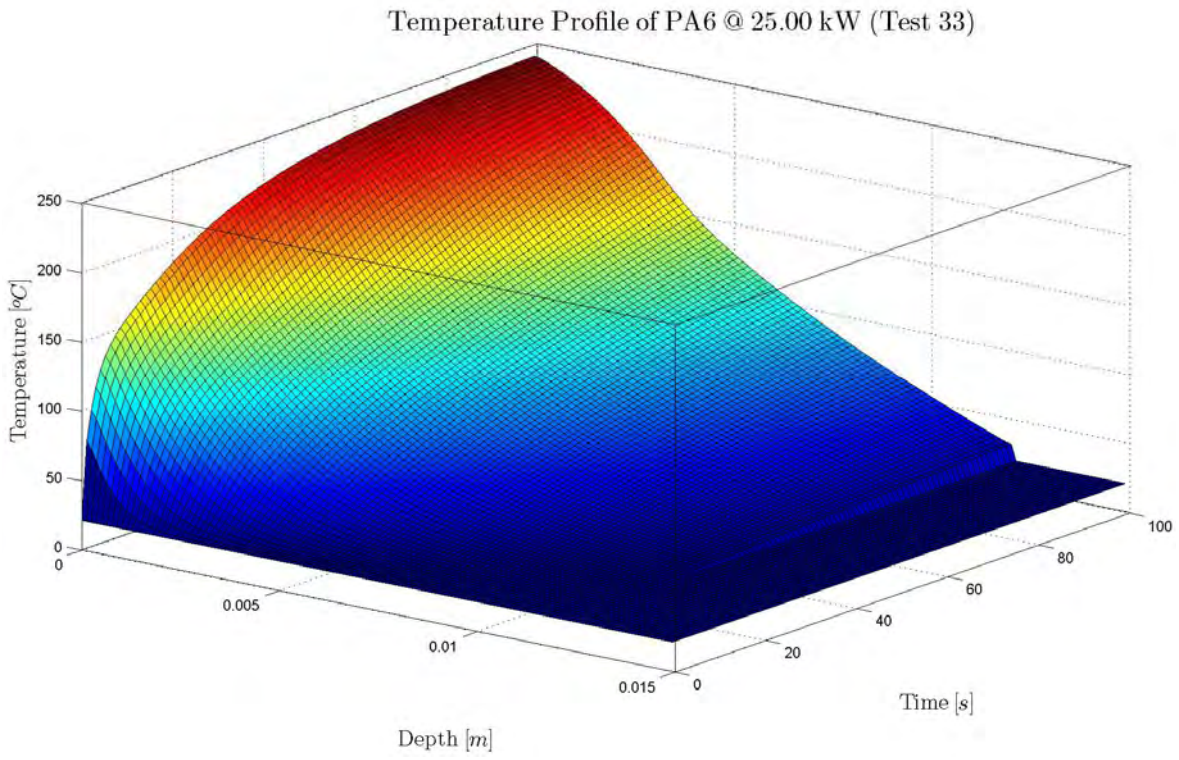

Figure 68 Typical in depth temperature distribution versus time (zoomed in)

No further insight was obtained through analysis of these graphs. The reason for this reoccurring phenomenon remains therefore unknown. The curve should start concave when the rate at which the heat is conducted away into the solid is faster then heat arriving at the surface. It should be convex when this process is dominated by heating, and the rate at which the heat arrives at the surface is bigger then the heat that is being conducted away. This would mean either that cold thermal conductivity is being under-predicted or that the boundary conditions are wrong.

6.3 Result classification towards current flammability tests

Currently flammability tests are used in a manner that only provides "mixed properties". They rely on assumptions about, for example, the flow within the tests to analyse the results and to extract properties. A totally different and new path for obtaining the driving material properties that determine the flammability of a product has been used. The result classification shall be conducted hereafter following an earlier approach [5]. In this approach, the thermal inertia (thus the lump of thermal conductivity, specific heat and density) obtained from standard test procedures are

compared to independently obtained values. For this endeavour, the determinable properties of the simplified approach as laid out in section 2.4 need to be acquired. The required tests were conducted only in the cone calorimeter due to lack of availability of sufficient test samples. It can be argued, that this defeats the purpose of the comparison; however, these tests provide an assessment of the material flammability, and thus, should be globally applicable.

As described in the simplified approach (Section 2.4), one of the pieces of information that must be obtained is the critical heat flux for ignition. This is the lowest thermal insult per unit area capable of initiating a combustion reaction on a given material. It can be obtained [23] either by determining the heat flux capable of producing conditions for piloted ignition after an arbitrary, but experimentally valid, time interval (e.g. 15 minutes [110] or alternatively, it can be found by extrapolating to obtain the minimum value of the imposed heat flux at which ignition is theoretically possible (i.e. $t_{ig}=\infty$). The method of extrapolation has two main variations: extrapolation of the imposed heat flux curve versus time to ignition [59, 111] and correlations based on heat transfer models [112-114].

The latter is commonly obtained by using the test results of the cone calorimeter [10, 115, 116], FPA [1] or the LIFT [2]. Regression fitting a straight line can be used to obtain a slope. To do this, values of the inverse of the square root of time to ignition (t_{ig}) and values for the corresponding incident heat flux (q_i) must be plotted against one another. Extrapolation of this line to the point where it crosses the abscissa allows a heat flux reading to be taken, which is supposed to resemble the critical heat flux for ignition. The result depends significantly on the data points collected and on the definition which data point should be included for this analysis [114, 117]. Nevertheless, it has been shown [118] that this method can provide incorrect results. Therefore, it was decided to obtain the critical heat flux capable of producing the conditions for piloted ignition by exposing each sample to a different heat flux in the cone calorimeter starting with a low heat flux and increasing it until piloted. From a multitude of tests for the various materials, the critical heat fluxes were determined (q_{cr}) as presented in Table 36. From these heat fluxes, the surface ignition

temperatures can be estimated using Equation (32). These are also presented in Table 36.

Material	q_{cr}	T_{ig}
-	[kW/m^2]	[°C]
PA6	20	465
PA6+FR	19.8	462
PA6+NC	23.7	549
PA6+NC+FR	23	532

Table 36 Critical heat flux and estimated ignition temperature

The regression analysis is presented in Figure 69. A straight line, which goes through the origin is plotted through the data points of the inverse of the square root of time to ignition (t_{ig}) and the values for the corresponding incident heat flux (q_i). This figure also shows the results from the model with and without the values of the independently parameter determination (ipd). These are based on the mean mass loss rate at ignition as shown in Figure 29. The time to ignition corresponds, to the point in time when the mean mass loss rate as determined for each tested material and test apparatus in section 3.10 via the LFL. The reason for this analysis was explained in section 2.4.5. In case of PA6 the agreement of the results are not perfect, but are promising. However, at a second glace, the unsteadiness of the results of the model needs to be further examined. This unsteadiness is also present in the analysis of PA6+NC as shown in Appendix C.1 where the differences in the slope are more significant. The model results of PA6+FR and PA6+NC+FR did not provide sufficiently large mass loss rates to resemble ignition.

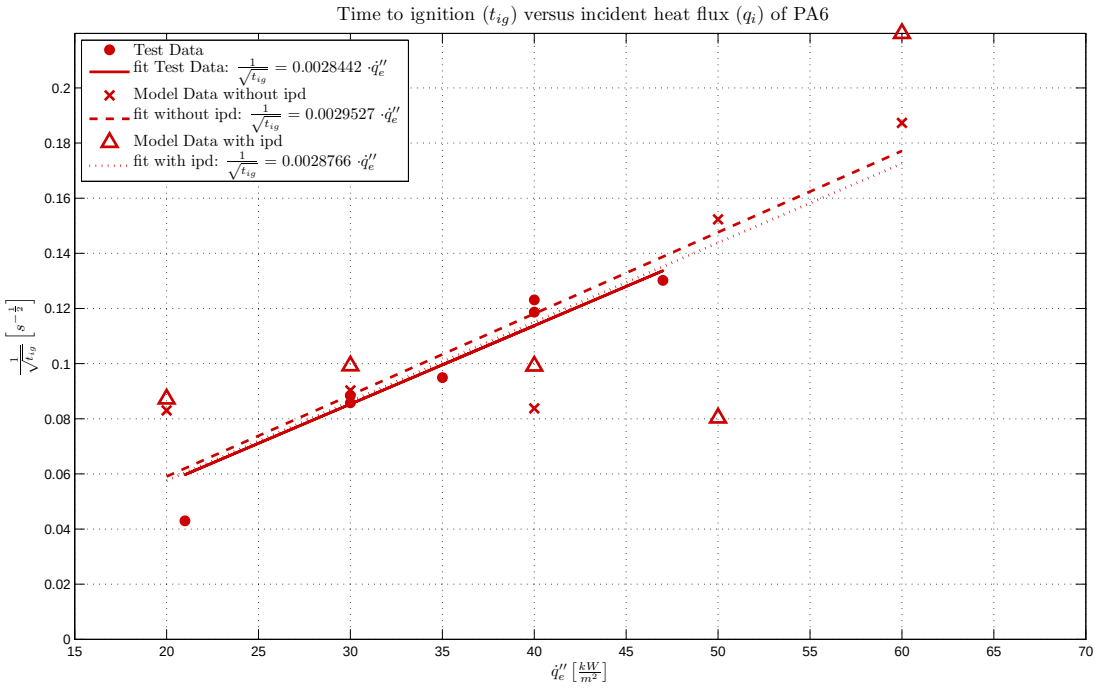

Figure 69 Time to ignition (t_{ig}) versus incident heat flux (q_i) of PA6

In addition to the graphical representation of Figure 69, a numerical comparison is also conducted. By using Equation (33) (which represents the solution of the simplified approached), in the material analysis of standard flammability test apparatuses (Section 2.4), the so-called thermal inertia ($\overline{k_s \rho_s c_s}$) can be obtained from the tests. For this, the slope of a linear fit must be used. How this is done is briefly explained in section 2.4.5. The values of the materials analysed are presented in Table 37 together with the averaged and multiplied thermal conductivity (k), density (ρ) and specific heat (c_p) of the independently determined parameter (idp). The model results using and not using the independently determined parameter are also shown.

Material	$k \cdot \rho \cdot c_p$ from independently determined parameter (idp) chapter 3	Standard flammability tests $\overline{k_s \rho_s c_s}$		$k \cdot \rho \cdot c_p$ from model to data fit without ipd section 5.5		$k \cdot \rho \cdot c_p$ from model to data fit with ipd section 5.5	
			Var. to idp		Var. to idp		Var. to idp
-	$[W^2 \cdot s \cdot m^{-4} \cdot K^{-2}]$	$[W^2 \cdot s \cdot m^{-4} \cdot K^{-2}]$	[%]	$[W^2 \cdot s \cdot m^{-4} \cdot K^{-2}]$	[%]	$[W^2 \cdot s \cdot m^{-4} \cdot K^{-2}]$	[%]
PA6	$7.34 \cdot 10^5$	$7.98 \cdot 10^5$	8.8	$7.41 \cdot 10^5$	1	$7.81 \cdot 10^5$	6
PA6+FR	$6.57 \cdot 10^5$	$4.83 \cdot 10^5$	27	N/A		N/A	
PA6+NC	$7.27 \cdot 10^5$	$5.73 \cdot 10^5$	21	$1.19 \cdot 10^6$	60	$1.79 \cdot 10^6$	122
PA6+NC+FR	$7.91 \cdot 10^5$	$4.43 \cdot 10^5$	44	N/A		N/A	

Table 37 Ignition Data for all materials studies

The per cent variance in Table 37 shows how much the obtained thermal inertia deviates, when compared to the same parameter determined in the independently determined parameter (idp) of chapter 3. When studying the difference, it has to be noted, that they do not represent absolute errors. As three material properties are multiplied, compensation or enhancement of the error can take place. Thus, a higher or lower percentile for any material does not mean that errors are bigger or smaller.

Nevertheless, from this analysis, it has to be said, that the new approach is even further away from the average thermal inertia. This is not surprising considering the lessons learned from this attempt. The large deviations are likely to be caused by the imperfect representation of the mass loss rate in the chosen test apparatus. However, they do not diminish the potential of this attempt; they just represent the state of the current research.

7 USAGE OF THE FOUND PARAMETERS FOR PREDICTION (VALIDATION)

This chapter addresses whether or not the obtained material parameter from chapter 5 can be used, regardless of their intricacy, to ideally predict ignition under a different heating scenario than the one used to determine the material properties. If successful, this would bring the fire safety community a significant step forward. It would close the gap between material testing and fire modelling. A material could be tested in a laboratory and its use and exposure modelled. Whether it is permitted or used would no longer be based on a pass-fail test criterion, but on its performance under a specific scenario and location where it shall be used. This would allow a true material safety evaluation.

An assessment of the predictive capabilities of the model (section 5.1) in conjunction with the obtained material properties of section 5.5 was conducted. The same materials in the same test setup, as described in section 5.1, were exposed to a constant heat flux in the Cone Calorimeter (section 7.1) and a ramped heat flux in the FPA (section 7.2); these were then compared. To go a step further, it would eventually be hoped that it would be possible to predict the ignition time of materials under a random heating scenario from the obtained material properties. This can actually be done with the data acquired so far, how accurate is described hereafter.

Due to material availability, the only two materials investigated here are PA6 and PA6+NC. This is acceptable since the main interest lies in the feasibility itself.

7.1 Constant heat flux in the Cone Calorimeter

In the first (validation) approach, it is determined whether the model in conjunction with the obtained parameters can be used to reproduce the heating process from the exposure of the tested solids up to ignition in a different test apparatus. Using the Cone Calorimeter instead of the FPA leaves the general test setup untouched, but involves changes in the radiation source, flow conditions etc. The details can be determined comparing the relevant standards [1, 10].

Since the test setup modelled is the same, the only change in the model presented in section 5.3 is the top surface boundary condition or to be more specific, the convective heat transfer coefficient. As in the analysis in section 3.9 and Appendix C.3.1, the values for the convective heat transfer coefficient (h_{c0}) and its exponent (n_{hc}) for the Cone Calorimeter are 10.7 W/m^2-K and 0.804.

Figure 70 and Figure 71 show the in-depth temperature of a Cone Calorimeter test for PA6 in comparison with the temperature evolution given by the model. The temperature in the model were determined by using the material properties obtained from the best fitting parameter for each material (chapter 5). Figure 72 and Figure 73 show the cumulative mass loss of a PA6 test in comparison with the mass loss in the model, using the same material properties. The graphs show the in-depth temperature as well as the mass comparison. Here, (w/o) indicates, that the parameters obtained without using the parameters from independent parameter determination were used and (w) indicates that these were used. Enlarged versions of the figures and the results for PA6+NC can be found in Appendix C.3.

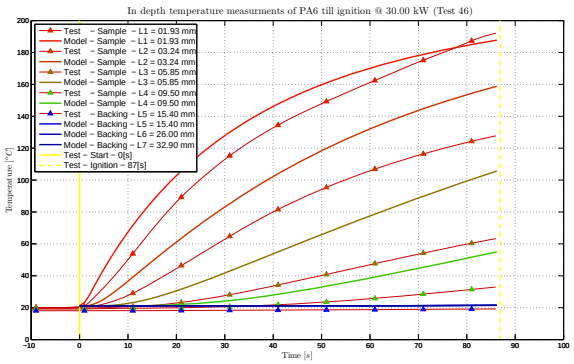

Figure 70 In-depth temp. Cone comp. PA6 w/o

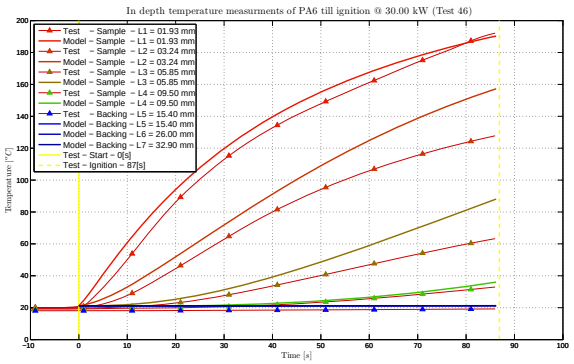

Figure 71 In-depth temp. Cone comp. PA6 w

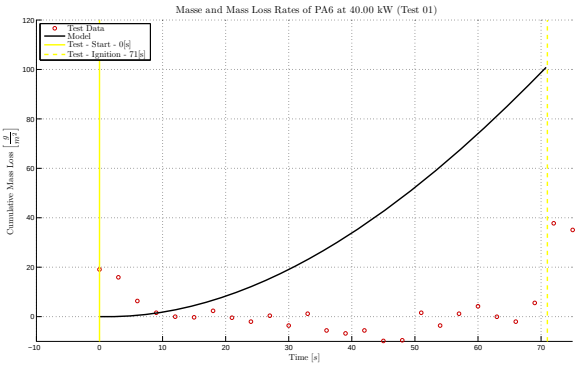

Figure 72 Cum. mass loss Cone comp. PA6 w/o

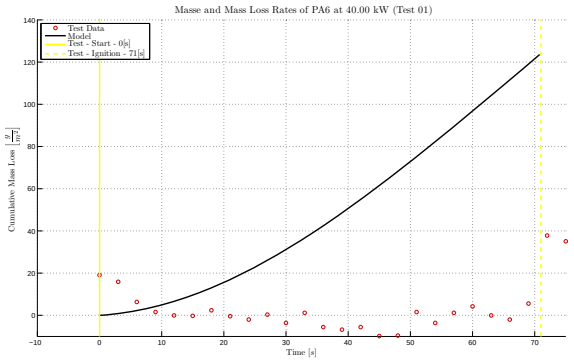

Figure 73 Cum. mass loss Cone comp. PA6 w

From the figures, it is possible to identify that the in-depth temperature could have been reasonably predicted with the found parameters, but not the mass loss. As observed from the error estimation, the initial mass loss data was scattered. Consequently, the obtained parameters, representing some form of average of the available test data, are likely to badly represent the mass loss. It can therefore, be expected that these would provide incorrect answers. This could be the reason for the discrepancies in Figure 72 and Figure 73. However, it seems that the mass loss readings from the cone calorimeter are even less sensitive and accurate before ignition then in the FPA, which is represented by values close to zero.

This is a highly satisfactory outcome; it appears that in the areas where there is reasonably good test data (in-depth temperature), it is possible to predict the materials' behaviour under a different heating scheme. This should encourage researchers to refine this approach.

Irrespective of the differences in the mass loss, an attempt shall be made to determine from the model the time to ignition and compare these with the recorded ignition

times in the cone. Section 3.10 describes a methodology to determine the values of the lean flammability limit (LFL) (Table 18), a semi intrinsic material property. To account for the flow conditions around the Cone Calorimeter, a reverse approach is required. Since the forward approach has already been conducted in that section 3.10 for the FPA and Cone, the correlation table/graph (Figure 30) can be used to directly determine the fuel mass loss required in the Cone Calorimeter. This can be completed using the semi intrinsic material property of the lean flammability limit (LFL) (Table 18). The required mass loss rates for PA6 and PA6+NC have been calculated for the cone to be 0.0539 and 0.0401 g/s respectively. With this required mass loss rate for ignition in the Cone, the ignition time can be estimated as presented in the Table 38.

Material	Heat Flux	Measured ignition time	Modelled ignition time	
			without idp	with idp
-	[kW/m^2]	[s]	[s]	[s]
PA6	21	541	140	130
	30	128-136	123	101
	35	111	116	93
	40	66-71	74	102
	47	59	48	41
PA6+NC	24	636-1048	168	305
	30	147-151	157	262
	41	52	129	247
	50	36	123	200

Table 38 Predicting the ignition of the samples in the Cone Calorimeter for a constant heat flux

It appears that the ignition times can be predicted. However, the model showed good results for only PA6 when not using the independently determined parameter (idp). Given the degree of errors in the mass loss rate data used to determine the material properties, this result is very promising.

7.2 Ramped heat flux in the FPA

In the second (validation) approach, it is determined, whether the model (when used in conjunction with the obtained parameters) can reproduce the heating process of tested solids up to the point of ignition under a different heating scenario. In this case, though, the heating is in the FPA apparatus. Instead of exposing the sample to a

constant heat flux, the heat flux is ramped. The remainder of the setup is left untouched from the original parameter determination tests.

Figure 74 and Figure 75 show the in-depth temperature of a ramped FPA test for PA6. It shows these results in comparison with the temperature evolution of the model as determined by the use of the material properties obtained from the best fitting parameter for each material (chapter 5). Here, (w/o) indicates, that the parameters obtained without using the parameters from independent parameter determination were used while (w) indicates that these were used. Cumulative mass loss for these tests was not obtained due to lack of material availability. The results are not perfect but promising. The model was able to predict the heating within the sample under a very different heating scheme, reasonably well.

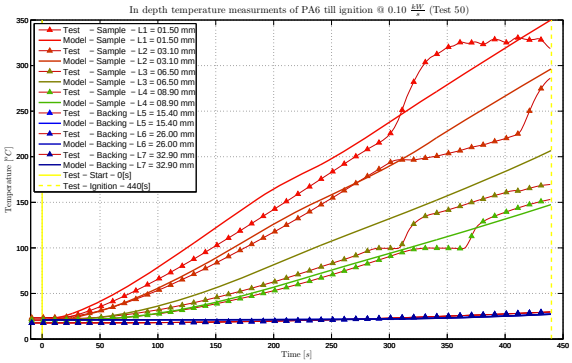

Figure 74 In-depth temp. ramped FPA comp. PA6 w/o

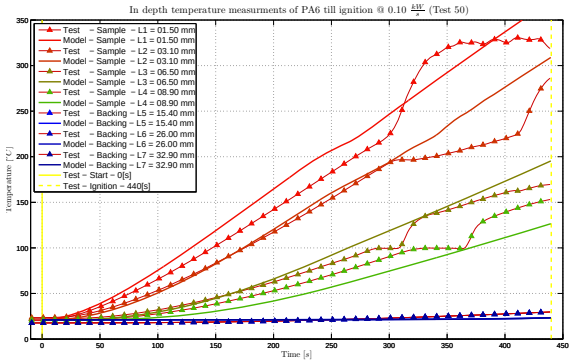

Figure 75 In-depth temp. ramped FPA comp. PA6 w

As in the previous section, irrespective of the problems with the accuracy of the mass loss rate, an attempt shall be made to determine from the model the time to ignition. These will be compared with the recorded ignition times for the ramped heat flux in the FPA. The same methodology was applied as described in the previous section. From table/graph (Figure 31) the required fuel mass loss rate in the FPA can be determined from the semi intrinsic material property, the lean flammability limit (LFL). With this minimum required mass loss rate for ignition, the ignition time can be calculated from the model. The degree of the predictive success can be determined from Table 39.

Material	Heat Flux Ramp	Measured ignition time	Modelled ignition time	
			without idr	with idr
-	[kW/m^2·s]	[s]	[s]	[s]
PA6	0.1	440	203	
PA6+NC	0.1	435-454	231	
	0.2	261-266	164	

Table 39 Predicting the ignition of the samples in the FPA under a ramped heat flux

8 CONCLUSIONS

The main objective of this study was to establish a methodology to predict piloted ignition using a first principles model. The challenge was to obtain the "intrinsic" properties required by the model using detailed material testing and traditional flammability tests. The test data was fitted to the model, by means of sophisticated optimization techniques, which allowed the determination of the properties that could not be measured independently. Reliable determination of all "intrinsic" properties would enable the use of first principle pyrolysis models within more complex fire models.

A few general conclusions can be established from the present study:

- The utilisation of a complex model in conjunction with a simple flammability test does not allow for the determination of all the parameters involved. The uncertainty of the solution and the output is too large given the very limited data and the number of variables involved.
- The introduction of independently determined parameters into the model to reduce the number of searched variables significantly reduces the uncertainty. Nevertheless, it is important to establish a minimum number of independently determined or bounded parameters before achieving this objective. For the present study, this goal was not achieved; several parameters showed unexplainable discrepancies that could not be tested given the constraints of the flammability tests used.
- The "intrinsic" properties are only as accurate as the model used to describe the phenomena, and the precision of the data obtained for the optimisation process. Significant limitations of the models and experiments were established through the course of this study; these will be discussed in more detail below.

To enable the determination of correct boundary conditions, a series of tests were conducted to establish specific parameters associated with the flammability tests. The conclusions of these tests indicate that:

- In this work, the back end boundary condition for each sample is not insulated as defined by the used standards test apparatus. It was deemed that insulation defines an evolving boundary condition that is difficult to quantify. Thus, an alternate option is to introduce a heat sink with a high thermal conductivity (aluminium block). The high thermal conductivity of the material reduces the temperature gradients; thus, monitoring a single temperature of the aluminium block allows the precise definition of the heat losses to the back of the sample.
- The convective heat transfer coefficient on the exposed face is determined by the solution of the inverse conduction problem for an aluminium block. The precision of this analysis proved to be highly dependent on the external heat flux. Thus, a sensitivity analysis that varies the prescribed heat fluxes within small bounds of the measured heat flux must be performed to obtain a good fit.

The independent parameter determination showed that:

- Flammability and material tests are not designed for the purpose of obtaining the "intrinsic" material properties required for pyrolysis models. From the data as well as the analysis, it becomes evident that: the data acquisition, the test setup, as well as the test apparatuses require changes if they are to be used for this purpose. The aim of this study was to define a methodology, and to establish the limitations of current testing practises for attaining the objectives of this methodology. Thus, it is beyond the scope of this study to refine the existing test methods.
- Piloted ignition is intimately linked to the Lean Flammability Limit and, therefore, to the flow field above the sample and to the pilot location. The Lean Flammability Limit is the final criteria required to establish ignition. The determination of the Lean Flammability Limit (LFL) posed significant challenges. Definition of the flow field required CFD modelling of the test. The challenges associated with this type of modelling are not only related to the choice of the turbulence model, but also to the definition of the boundary conditions. The FPA and Cone Calorimeter proved to have boundary conditions that are difficult to define numerically. Furthermore, the unstable nature of the

flow when using horizontal samples makes ignition extremely sensitive to the pilot location.

- Mass loss is an integral parameter that requires great experimental sensitivity to be used for the purpose of this methodology. Though mass loss was used in this study, it was clear that the precision and spatial resolution of in-depth thermocouple measurements provided much more and more precise information. The mass loss readings obtained before ignition are not acceptable, given the results and error analysis. The scales of the standard test apparatuses provide good readings for the period after ignition but are not suitable to capture the mass loss from the initial heat exposure of the samples up to ignition. A refinement of the mass loss readings is required if they are to be used in conjunction with this methodology.
- The precise in depth placement of the thermocouples is of critical importance when dealing with materials having a high thermal conductivity – as it is the case in this study. This importance was confirmed by the results of the measurement as well as from error analysis. An important aspect of these measurements is that some materials melt and are in a liquid state before reaching ignition. This can have an effect on the temperature readings due to a possible relocation of the thermocouples closer or further away from the heat source. Furthermore, shrinkage/swelling behaviour, or charring can affect the location of the thermocouples. Monitoring the location of the thermocouples throughout the experiment would help resolve some of these issues.
- In future studies volumetric changes, such as shrinkage or intumescence of the sample, should be monitored. These have not been included in this study, but both can have a significant effect on the temperature distribution throughout the sample, thus should be quantified.

9 REFERENCES

1. ASTM E2058-03; *Standard Method of Testing fore Measurments of Synthetic Polymer Material Flammability Using the Fire Propagation Apparatus (FPA)*; Philiadelphia; American Society for Testing and Materials; 2003
2. ASTM 1321-97a; *Standard Test Method for Determining Material Ignition and Flame Spread Properties*; Philiadelphia; American Society for Testing and Materials; 1997
3. McGrattan, K.; Hostikka, S.; Floyd, J.; McDermott, R.; Prasad, K.; *Validation*, Fire Dynamics Simulator (Version 5), Technical Reference Guide, 2009, 3,
4. McGrattan, K.; miles, S.; *Modeling Enclosure Fires Using Computational Fluid Dynamics (CFD)*, in: The SFPE Handbook of Fire Protection Engineering, 4th ed.; NFPA, SFPE: Quincy, Massachusetts, 2008.
5. Steinhaus, T.; *Evaluation of the thermophysical properties of poly(methyl methacrylate): a reference material for the development of a flammability test for micro-gravity environments*; Thesis (M S); University of Maryland, College Park, MD, 1999
6. Babrauskas, V.; *Ignition handbook: principles and applications to fire safety engineering, fire investigation, risk management and forensic science*; Fire Science Publishers, Issaquah, WA, 2003, viii, 1116 p.
7. Zhou, Y. Y.; Fernandez-Pello, C.; *An enthalpy-temperature hybrid method for solving phase-change problems and its application to polymer pyrolysis and ignition*, Combustion Theory and Modelling, 2000, 4, (4), 27
8. Tewardson, A.; *Generation of Heat and Gaseous, Liquid, and Solid Products in Fire*, in: The SFPE Handbook of Fire Protection Engineering, 4th ed.; NFPA, SFPE: Quincy, Massachusetts, 2008.
9. Quintiere, J. G.; *Compartment Fire Modelling*, in: The SFPE Handbook of Fire Protection Engineering, 4th ed.; NFPA, SFPE: Quincy, Massachusetts, 2008.
10. ASTM E-1354-03; *Standard Test Method for Heat and Visible Smoke Release Rates for Materials and Products Using an Oxygen Consumption Calorimeter*; Philadelphia; American Society for Testing and Materials; 2003
11. Rein, G.; Lautenberger, C.; Fernandez-Pello, A. C.; Torero, J. L.; Urban, D. L.; *Application of genetic algorithms and thermogravimetry to determine the kinetics of polyurethane foam in smoldering combustion*, Combustion and Flame, 2006, 146, (1-2), 95-108
12. Lautenberger, C.; Rein, G.; Fernandez-Pello, C.; *The application of a genetic algorithm to estimate material properties for fire modeling from bench-scale fire test data*, Fire Safety Journal, 2006, 41, (3), 204-214
13. Cullis, C. F.; Hirschler, M. M.; *The combustion of organic polymers*; Clarendon Press : Oxford University Press, Oxford, 1981, x, 419 p
14. Arrhenius, S.; Zeitschrift für Physikalische Chemie, 1889, 4,
15. Hirata, T.; Kashiwagi, T.; Brown, J. E.; *Thermal and Oxidative-Degradation of Poly(Methyl Methacrylate) - Weight-Loss*, Macromolecules, 1985, 18, (7), 1410-1418

16. Di Blasi, C.; *Modeling and Simulation of Combustion Processes of Charring and Non-Charring Solid Fuels*, *Progress in Energy and Combustion Science*, 1993, 19, 71-104
17. Levenspied, O.; *Chemical Reaction Engineering*; 3rd ed.; John Wiley, New York, 1999, 660
18. Ohlemiller, T. J.; *Modeling of Smoldering Combustion Propagation*, Progress in Energy and Combustion Science, 1985, 11, (4), 277-310
19. Gabbott, P.; *Applications of thermal analysis*; 1st ed.; Blackwell Pub., Ames, Iowa, 2007,
20. Chao, C. Y. H.; Wang, J. H.; *Comparison of the thermal decomposition behavior of a non-fire retarded and a fire retarded flexible polyurethane foam with phosphorus and brominated additives*, Journal of Fire Sciences, 2001, 19, (2), 137-156
21. Kashiwagi, T.; Nambu, H.; *Global Kinetic Constants for Thermal Oxidative-Degradation of a Cellulosic Paper*, Combustion and Flame, 1992, 88, (3-4), 345-368
22. Darcy, H.; *Les Fontaines Publiques de la Ville de Dijon*; Paris, 1856,
23. Drysdale, D.; *An introduction to fire dynamics*; 2nd ed.; J. Wiley, Chichester, 1999, xviii, 451p
24. Williams, F. A.; *Combustion theory : the fundamental theory of chemically reacting flow systems*; 2nd ed ed.; Benjamin/Cummings Pub. Co, Menlo Park, Calif, 1985, xxiii, 680 p
25. Incropera, F. P.; DeWitt, D. P.; Bergman, T. L.; Lavine, A. S.; *Fundamentals of heat and mass transfer*; 6th ed.; John Wiley, Hoboken, NJ, 2007, xxv, 997 p.
26. Mark, J. E.; *Physical properties of polymers handbook*; AIP Press, Woodbury, N.Y., 1996, xv, 723 p.
27. Harrison, I. R.; Runt, J.; *Heat of Fusion of Polymer Crystals: Thermodynamics of melting*, Journal of Macromolecular Science: Physics, 1980, B17, (1), 83-97
28. Chen, H.; *Modeling of polymer melting, drop deformation, and breakup under shear flow*, Polymer Engineering and Science, 2004, 44, (7), 8
29. Butler, K. M., in: 11th International Conference on Fire and AMterials, Interscience Communications Limited, London, England: San Francisco, USA, 2009; pp 341-352.
30. Nield, D. A.; Bejan, A.; *Convection in porous media*; Springer-Verlag, New York, 1992, xvii, 408 p.
31. National Fire Protection Association; Engineers, S. o. F. P.; *SFPE handbook of fire protection engineering*; 3rd ed.; National Fire Protection Association ; Society of Fire Protection Engineers, Quincy, Mass., Bethesda, MD., 2002,
32. Fernandez-Pello, A. C.; *The Solid Phase*, in: Combustion fundamentals of fire, Cox, G., (Ed.) Academic Press: London ; San Diego, 1995; pp 31-100.
33. Niioka, T.; Takahashi, M.; Izumikawa, M.; *Gas-phase ignition of a solid fuel in a hot stagnation point flow*, *18th Symposium on Combustion*, Pittsburgh, 1981, 741-747
34. Delichatsios M. A.; M., D. M.; *Critical Mass Pyrolysis Rates for Extinction in Fires Over Solid Materials*, Fifth Symposium on Fire Safety Science, Melbourne, Australia, 3-7 March, 1997, 153-164

35. Torero, J. L.; Vietoris, T.; Legros, G.; Joulain, P.; *Estimation of a Total Mass Transfer Number from Stand-off Distance of a Spreading Flame, Combustion Science and Technology*, 2002, 174, (11-12), 187-203
36. Quintiere, J. G.; *Fundamentals of fire phenomena*; John Wiley, Chichester, 2006, xix, 439 p.
37. Gray, P.; Lee, P. R.; *Thermal Explosion Theory, Oxidation and Combustion Reviews*, 1967, 2, 3-180
38. Atreya, A.; *Ignition of Fires, Philosophical Transactions of the Royal Society A: Mathematical, Physical, and Engineering Sciences* 1998, 356, 2787-2813
39. Horrocks, A. R.; Gawande, S.; Kandola, B.; Dunn, K. W.; *Recent Advances in Flame Retardancy of Polymeric Materials*; Business Communications Co.; Norwalk, Connecticut, USA, 2000.
40. Backer, S.; Tesoro, G. S.; Toong, T. Y.; Moussa, N. A.; *Textile fabric flammability*; MIT Press, Cambridge, 1976, viii, 385 p.
41. Williams, F. A.; *A Review of Flame Extinction, Fire Safety Journal*, 1981, 3, 163-175
42. Rasbash, D. J.; Drysdale, D. D.; Deepak, D.; *Critical Heat and Mass Transfer at Pilot Ignition and Extinction of a Material, Fire Safety Journal*, 1986, 10, 1-10
43. Thomson, H. E.; Drysdale, D. D.; Beyler, C. L.; *An Experimental Evaluation of Critical Surface Temperature as a Criterion for Piloted Ignition of Solid Fuels, Fire Safety Journal*, 1988, 13, 185-196
44. Beyler, C.; *A Unified Model of Fire Suppression, Journal of Fire Protection Engineering*, 1992, 4, (1), 5-16
45. Quintiere, J. G.; Rangwala, A. S.; *A theory for flame extinction based on flame temperature*, Fire and Materials, 2004, 28, (5), 387-402
46. Roberts, A. F.; Quince, B. W.; *A Limiting Condition for Burning of Flammable Liquids, Combustion and Flame*, 1973, 20, 245-251
47. Lautenberger, C.; Fernandez-Pello, A. C.; *A generalized pyrolysis model for combustible solids*, 5th International Seminar on Fire and Explosion Hazards, Edinburgh, UK, April, 23-27, 2007,
48. Butler, K. M.; *Mixed Layer Model for Pyrolysis of Bubbling Thermoplastic Materials*; NISTIR 6242, National Institute of Standards and Technology; Gaithersburg, MD, October 1998.
49. Kashiwagi, T.; *Polymer Combustion and Flammability-Role of the Condensed Phase, Proceedings of the Combustion Institute*, 1994, 25, 1423-1437
50. Di Blasi, C.; *The state of the art of transport models for charring solid degradation, Polymer International*, 2000, 49, 1133-1146
51. Moghtaderi, B.; *The state-of-the-art in pyrolysis modelling of lignocellulosic solid fuels*, Fire and Materials, 2006, 30, (1), 1-34
52. Lautenberger, C.; Fernandez-Pello, A. C.; *Pyrolysis Modeling, Thermal Decomposition, and Transport Processes in Combustible Solids*, in: *Transport Phenomena in Fires*, Faghri, M.; Sunden, B., (Eds.) WIT Press: 2008.
53. Cordova, J. L.; Walther, D. C.; Torero, J. L.; Fernandez-Pello, A. C.; *Oxidizer Flow Effects on the Flammability of Solid Combustibles, Combustion Science and Technology*, 2001, 164, (1-6), 253-278

54. Dakka, S. M.; Jackson, G. S.; Torero, J. L.; *Mechanisms Controlling the Degradation of Poly(methyl methacrylate) Prior to Piloted Ignition*, *Proceedings of the Combustion Institute*, 2002, 29, 281-287
55. Beaulieu, P. A.; Dembsey, N. A.; *Flammability Characteristics at Applied Heat Flux Levels up to 200 kW/m^2*, *Fire and Materials*, 2007, 32, (2), 61-86
56. McGrattan, K.; Klein, B.; Hostikka, S.; Floyd, J.; *Fire Dynamics Simulator (Version 5), User's Guide*; 1019-5, NIST Special Publication; 2007.
57. Mowrer, F. W.; *An analysis of effective thermal properties of thermally thick materials*, *Fire Safety Journal*, 2005, 40, (5), 395-410
58. deRis, J. L.; Khan, M. M.; *A Sample Holder for Determining Material Properties*, *Fire and Materials*, 2000, 24, 219-226
59. Quintiere, J.; *A Simplified Theory for Generalizing Results from a Radiant Panel Rate of Flame Spread Apparatus*, Fire and Materials, 1981, 5, (2), 52-60
60. Wickman, I. S.; *Theory of Opposed flame Spread*, *Progress in Energy and Combustion Science*, 1993, 18, (6), 553-593
61. *WP2 –Thermal decomposition – Mechanism and intrinsic flammability properties*; Predicting Fire Behaviour of Nanocomposites from Intrinsic Properties; University of Ulster, Bolton institute, CDCMP, ENSCL; p 193.
62. Brandrup, J.; Immergut, E. H.; Grulke, E. A.; *Polymer handbook*; 4th ed.; Wiley, New York, 1999, 2336
63. Brown, M. E.; *Handbook of thermal analysis and calorimetry. Vol. 1, Principles and practice*; Elsevier, Amsterdam ; London, 1998, xxx, 691 p.
64. Netzsch; *User manual Netzsch Thermokinetics Version*; 2001, 12a,
65. Friedman, H. L.; *Kinetics of thermal degradation of char-forming plastics from thermogravimetry - application to a phenolic plastic*, Joiurnal of polymer Science, 1963, C6, 13
66. Ozawa, T.; *A New Method of Analyzing Thermogravimetric Data*, Bulletin of the Chemical Society of Japan, 1965, 38, (11), 6
67. Flynn, J. H.; Wall, L. A.; *A quick, direct method for the determination of activation energy from thermogravimetric data*, Journal of Polymer Science Part B: Polymer Letters, 1965, 4, (5), 6
68. Hatakeyama, T.; Quinn, F. X.; *Thermal analysis : fundamentals and applications to polymer science*; 2nd ed.; Wiley, Chichester ; New York, 1999, viii, 180 p.
69. Fornes, T. D.; Paul, D. R.; *Crystallization behavior of nylon 6 nanocomposites*, Polymer, 2003, 44, (14), 3945-3961
70. Guggenheim, E. A.; *Thermodynamics: an advanced treatment for chemists and physicists*; 8th ed.; North-Holland ; Sole distributors for the U.S.A. and Canada, Elsevier Science Pub. Co., Amsterdam ; New York; New York, N.Y., U.S.A., 1986, xxiv, 390 p.
71. ISO 11357-2:1999; *Plastics -- Differential scanning calorimetry (DSC) -- Part 2: Determination of glass transition temperature*; International Organization for Standardization; 1999
72. ASTM E1356-08; *Standard Test Method for Assignment of the Glass Transition Temperatures by Differential Scanning Calorimetry*; Philadelphia; American Society for Testing and Materials; 2008

73. ASTM E1824-08; *Standard Test Method for Assignment of a Glass Transition Temperature Using Thermomechanical Analysis*; Philadelphia; American Society for Testing and Materials; 2008
74. ISO 11359-2:1999; *Plastics -- Thermomechanical analysis (TMA) -- Part 2: Determination of coefficient of linear thermal expansion and glass transition temperature*; International Organization for Standardization; 1999
75. ASTM E1640-04; *Standard Test Method for Assignment of the Glass Transition Temperature By Dynamic Mechanical Analysis*; Philadelphia; American Society for Testing and Materials; 2004
76. ASTM D3418-03 *Standard Test Method for Transition Temperatures and Enthalpies of Fusion and Crystallization of Polymers by Differential Scanning Calorimetry*; ASTM International; 2003
77. DIN 51004:1994-06; *Thermal analysis; determination of melting temperatures of crystalline materials by differential thermal analysis*; Deutsches Institut für Normung e.V.; 1994
78. Brown, M. E.; *Principles and Practice*; First ed.; Elsevier Science B.V., Amsterdam, 1998, 1, 722
79. Patnaik, P.; Dean, J. A.; *Dean's analytical chemistry handbook*; 2nd ed.; McGraw-Hill, New York, 2004,
80. Cui, X.; Liu, Z.; Yan, D.; *Synthesis and characterization of novel even–odd nylonsnext term based on undecanedioic acid* European Polymer Journal, 2004, 40, (6), 1111-1118
81. Thomas, T. L.; Sivakumar, N.; Gurunathan, L.; Mishra, A. K.; *Fluorescence anisotropy of pyrene incorporated in nylonnext term as a tool to monitor thermal relaxations nylon*, Polymer Testing, 2003, 22, (2), 143-147
82. Sundararaj, U.; Macosko, C. W.; *Reliable Measurements of the Nylon 6 Glass Transition Made Possible by the New Dynamic DSC*, Macromolecules, 1995, 28, (8), 2644-2646
83. Hatfield, G. R.; Glans, J. H.; Hammond, W. B.; *Characterization of structure and morphology in nylon 6 by solid-state carbon-13 and nitrogen-15 NMR*, Macromolecules, 1990, 23, (6), 1654-1658
84. Krištofič, M.; Marcinčin, A.; Ujhelyiová, A.; *The DSC Study of PA 6, Polyamides and Copolyamides*, Journal of Thermal Analysis and Calorimetry, 2000, 60, (2), 357-369
85. Ammala, A.; Pas, S. J.; Lawrence, K. A.; Stark, R.; Webb, R. I.; Hill, A. J.; *Poly(m-xylene adipamide)-montmorillonite nanocomposites: effect of organo-modifier structure on free volume and oxygen barrier properties*, Journal of Materials Chemistry, 2008, 18, (8), 911-916
86. Reading, M.; Hourston, D. J.; *Modulated temperature differential scanning calorimetry : theoretical and practical applications in polymer characterisation*; Springer, Dordrecht, 2006, xiii, 328 p.
87. Reading, M.; Elliott, D.; Hill, V. L.; *A new approach to the calorimetric investigation of physical and chemical transitions*, Journal of Thermal Analysis and Calorimetry, 1993, 40, (3), 949-955
88. Gill, P. S.; Sauerbrunn, S. R.; Reading, M.; *Modulated differential scanning calorimetry* Journal of Thermal Analysis and Calorimetry, 1993, 40, (3), 931-939

89. Gaur, U.; Lau, S.-f.; Wunderlich, B. B.; Wunderlich, B.; *Heat Capacity and Other Thermodynamic Properties of Linear Macromolecules, VIII Polyesters and Polyamides*, Journal of Physical and Chemical Reference Data, 1983, 12, (1), 65-89
90. Gabriel, S.; Maass, T. A.; *Über ε-Amidocapronsäure*, Berichte der deutschen chemischen Gesellschaft, 1899, 32, (1), 1266-1272
91. Kurzweil, P.; Frenzel, B.; Gebhard, F. *Physik Formelsammlung Für Ingenieure und Naturwissenschaftler*.
92. Aharoni, S. M.; *n-Nylons, their synthesis, structure, and properties*; J. Wiley & Sons, Chichester ; New York, 1997, xiv, 598 p.
93. Sivanandam, S. N.; Deepa, S. N.; *Introduction to genetic algorithms*; Springer, Berlin ; New York, 2007, xix, 442 p.
94. Nocedal, J.; Wright, S. J.; *Numerical optimization*; 2nd ed.; Springer, New York, 2006, xxii, 664 p.
95. Bryant, R.; Womeldorf, C.; Johnsson, E.; Ohlemiller, T.; *Radiative heat flux measurement uncertainty*, Fire and Materials, 2003, 27, (5), 209-222
96. Pitts, W. M.; Murthy, A. V.; deRis, J. L.; Filtz, J. R.; Nygard, K.; Smith, D.; Wetterlund, I.; *Round Robin Study of Total Heat Flux Gauge Calibration at Fire Laboratories*, Fire Safety Journal, 2006, 41, (6), 459-475
97. Jiang, F.; Ris, J. L. d.; Khan, M. M.; *Absorption of thermal energy in PMMA by in-depth radiation*, Fire Safety Journal, 2009, 44, (1), 106-112
98. Khan, M. M.; deRis, J. L.; *Device and Method for Measuring Absorbed Heat Flux*, 10th International Conference on Fire and Materials, San Francisco, 29th-31st January, 2007,
99. *TC Guide to Thermocouple and Resistance Thermometry*; TC Ltd., 2004,
100. De Boor, C.; *A practical guide to splines*; Rev. ed.; Springer, New York, 2001, xviii, 346 p.
101. Lautenberger, C. *gpyro: generalized pyrolysis model for combustible solids* http://code.google.com/p/gpyro/
102. Lautenberger, C.; *A Generalized Pyrolysis Model for Combustible Solids*; Ph.D. Dissertation; University of California, Berkeley, 2007
103. Lautenberger, C.; *Technical Reference - gpyro 0.660*; Gpyro - A Generalized Pyrolysis Model for Combustible Solids; University of California; Berkeley, 6. January, 2009.
104. Lautenberger, C.; *Users' Guide - gpyro 0.660*; Gpyro - A Generalized Pyrolysis Model for Combustible Solids University of California; Berkeley, 6. January, 2009.
105. Gibbins, J.; *Thermal Contact Resistance of Polymer Interfaces*; Master Thesis; University of Waterloo, 2006
106. Massey, L. K.; *Permeability properties of plastics and elastomers : a guide to packaging and barrier materials*; 2nd ed.; Plastics Design Library/William Andrew Pub., Norwich, NY, USA, 2003, xiv, 601 p.
107. Bronstein, I. N.; Semendjajew, K. A.; Musiol, G.; Mühlig, H.; *Taschenbuch der Mathematik*; 6 ed.; Harri Deutsch, Frankfurt am Main, 2005, 1242
108. *TC Guide to Thermocouple and Resistance Thermometry*; TC Ltd.; UK, 2004.
109. Reszka, P.; Empis, C. A.; Biteau, H.; Cowlard, A.; Steinhaus, T.; Fletcher, I.; Fuentes, A.; Gillie, M.; Welch, S.; *Experimental Layout and Description of the Building*, in: The Dalmarnock Fire Tests: Experiments and Modelling, Rein,

G.; Abecassis-Empis, C.; Carvel, R., (Eds.) School of Engineering and Electronics, University of Edinburgh: 2007.

110. ISO 5657; *Fire Tests. Reaction to Fire. Ignitability of building products*; Geneva; International Organisation for Standardisation; 1997
111. Sims, D. L.; *On the piloted ignition of wood by radiation*, Combustion and Flame, 1963, 7, 253-261
112. Quintiere, J. G.; Harkleroad, M.; *New Concepts for Measuring Flame Spread Properties*; National Bureau of Standards; 1984.
113. Mikkola, E.; Wichman, I. S.; *On the Thermal Ignition of Combustible Materials*, Fire and Materials, 1989, 14, 87-96
114. Tewarson, A.; Ogden, S. D.; *Fire Behavior of Polymethylmethacrylate*, Combustion and Flame, 1992, 89, 237-259
115. Babrauskas, V.; *From Bunsen burner to heat release rate calorimeter*, in: Heat Release in Fires, Babrauskas, V.; Grayson, S. J., (Eds.) Elsiver Applied Science: Barking, 1992; pp 7-29.
116. Babrauskas, V.; *The Cone Calorimeter*, in: SFPE Handbook of Fire Protection Engineering, 3rd ed.; al., P. J. D. N. e., (Ed.) Society of Fire Protection Engineers: Boston, 2002; pp 3.63-3.81.
117. ANSI 4880; *Evaluating: A) Insulated Wall or Wall & Roof/Ceiling Assemblies B) Plastic Interior Finish Materials C) Plastic Exterior Building Panels D) Wall/Ceiling Coating Systems E) Interior or Exterior Finish Systems*; Norwood; FM Approvals; 2001
118. Long, R. T.; Torero, J. L.; Quintiere, J. G.; Fernandes-Pello, A. C.; *Scale and Transport Considerations on Piloted Ignition of PMMA*, 6th International Symposium on Fire Safety Science, 2000, 567-578

Appendix A: INDEPENDENT PARAMETER DETERMINATION

A.1 Determine the reduced chemical reaction parameters

A.1.1 PA6

A.1.1.1 In inert atmosphere (N_2)

See Figure 7 Mass and Figure 9 for the Mass Loss Rate Data

A.1.1.2 In air

See Figure 8 Mass and Figure 10 for the Mass Loss Rate Data

A.1.2 PA6 + FR

A.1.2.1 In inert atmosphere (N_2)

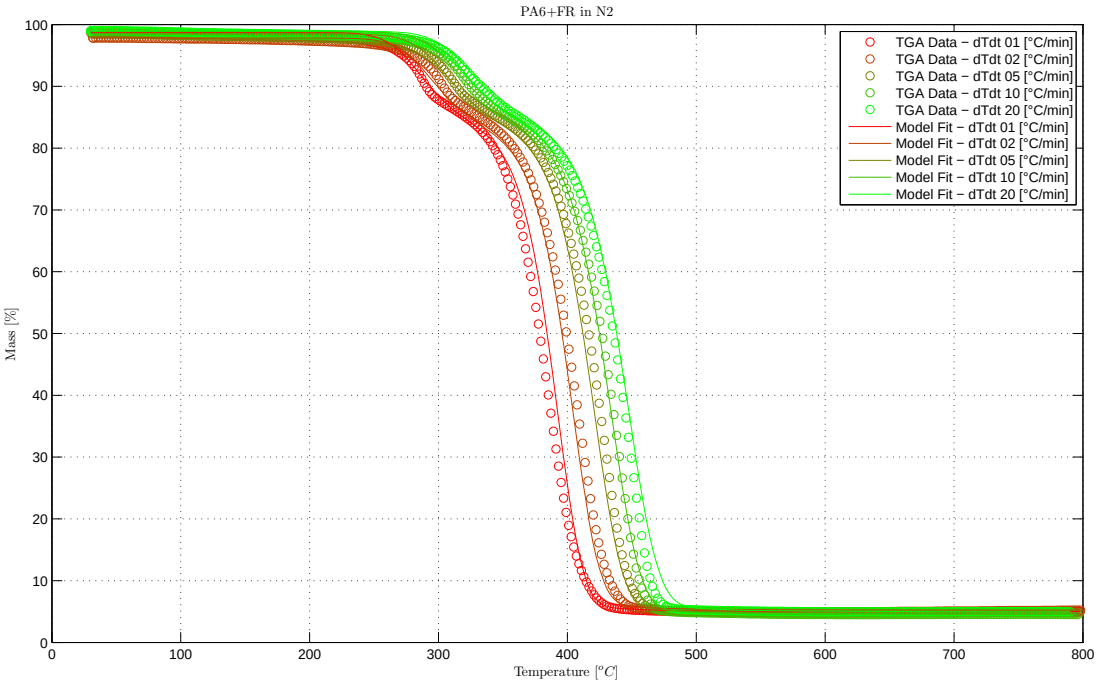

Figure 76 TGA Mass data and reduced reaction schemes fits for PA6+FR in inert atmosphere (N_2)

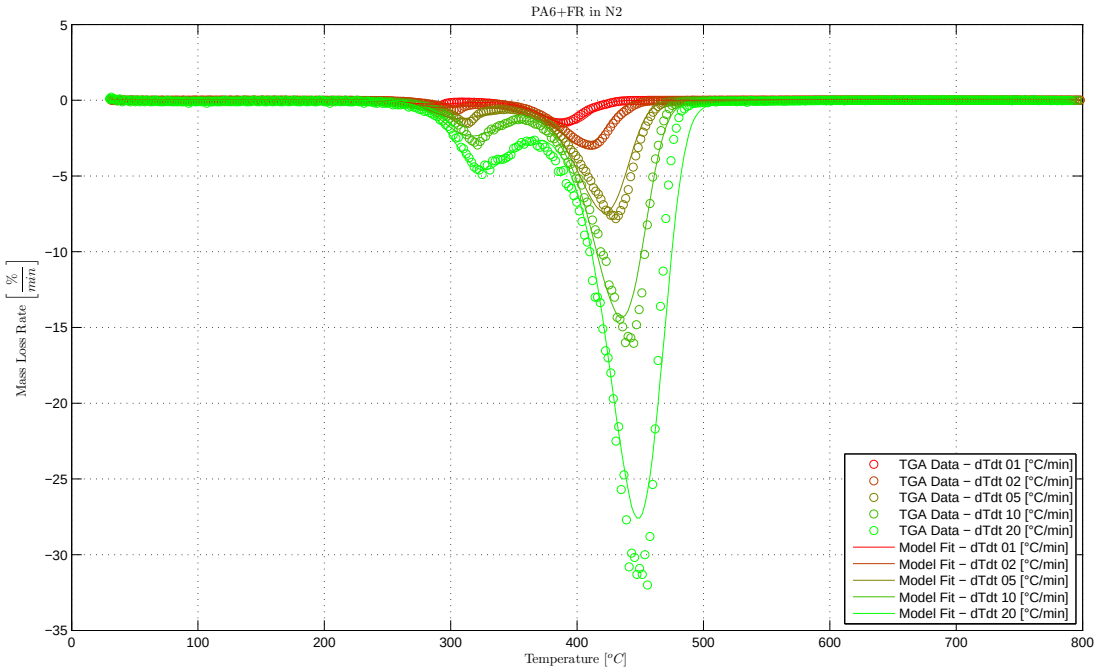

Figure 77 TGA MLR and reduced reaction schemes fits for PA6+FR in inert atmosphere (N_2)

A.1.2.2 In air

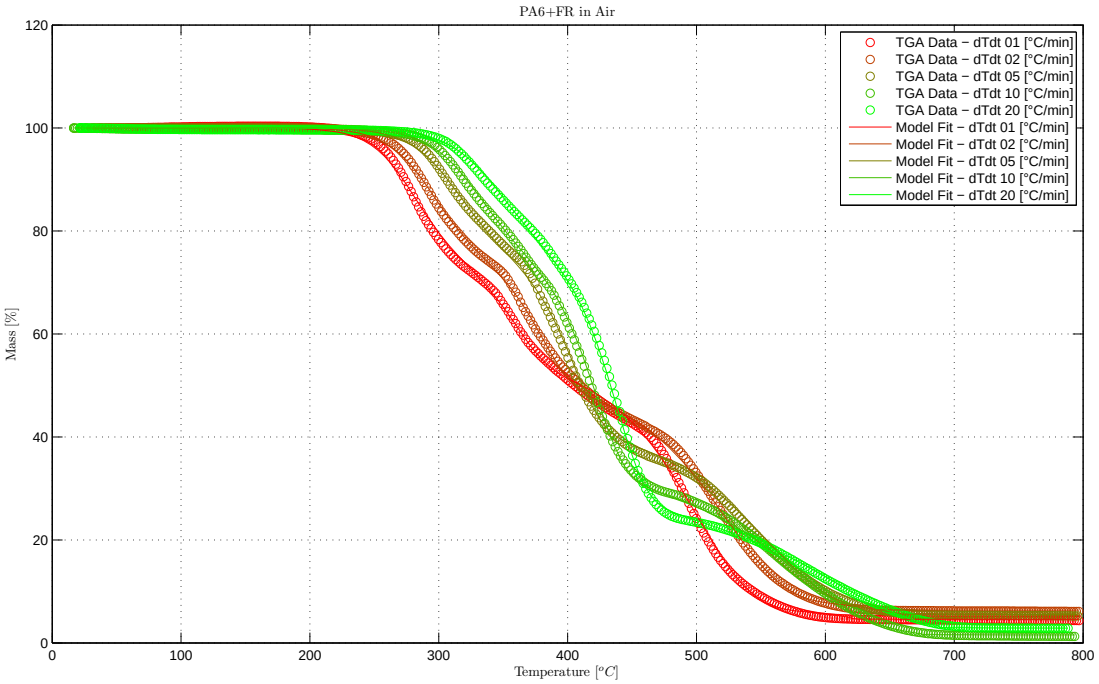

Figure 78 TGA Mass data and reduced reaction schemes fits for PA6+FR in inert atmosphere (N_2)

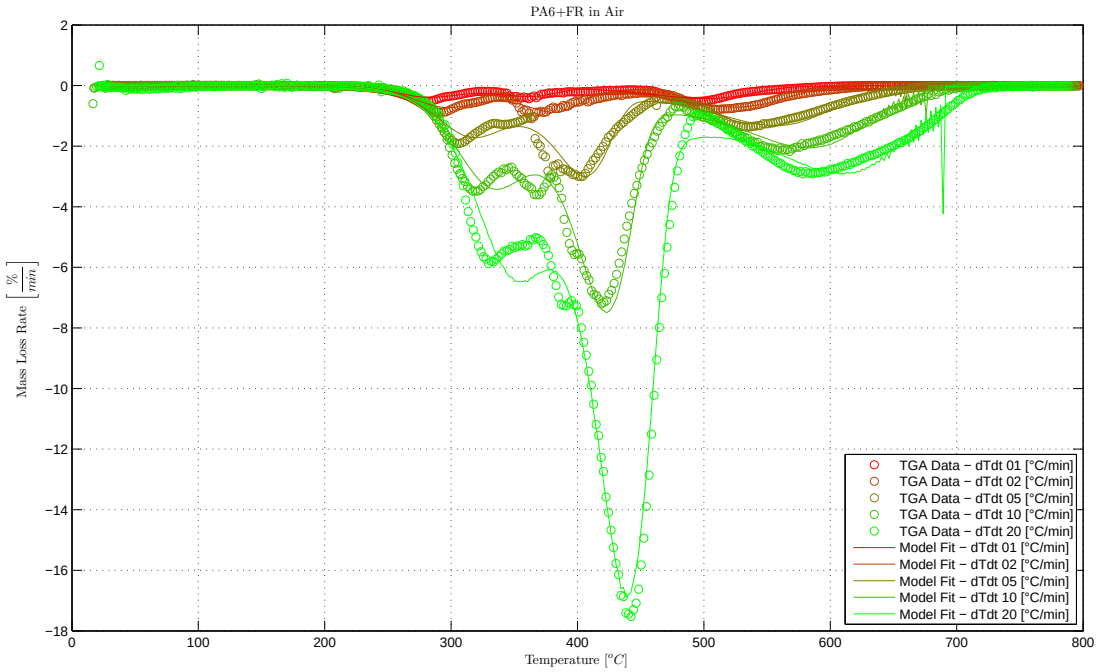

Figure 79 TGA MLR data and reduced reaction schemes fits for PA6+FR in inert atmosphere (N_2)

A.1.3 PA6 + NC

A.1.3.1 In inert atmosphere (N_2)

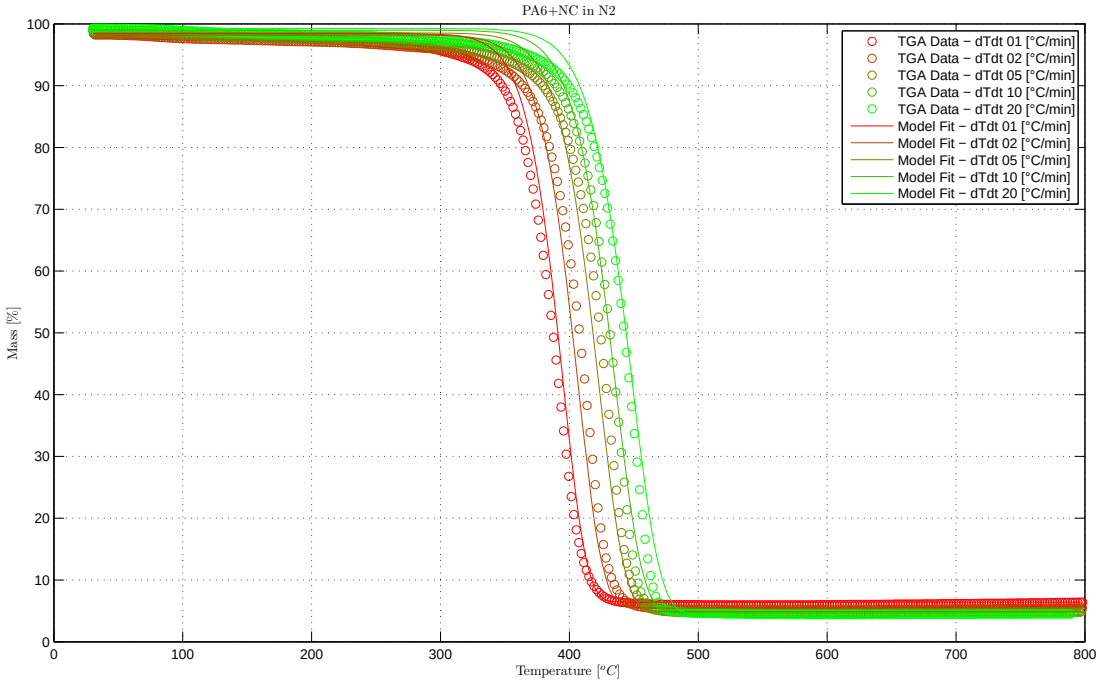

Figure 80 TGA Mass data and reduced reaction schemes fits for PA6+NC in inert atmosphere (N_2)

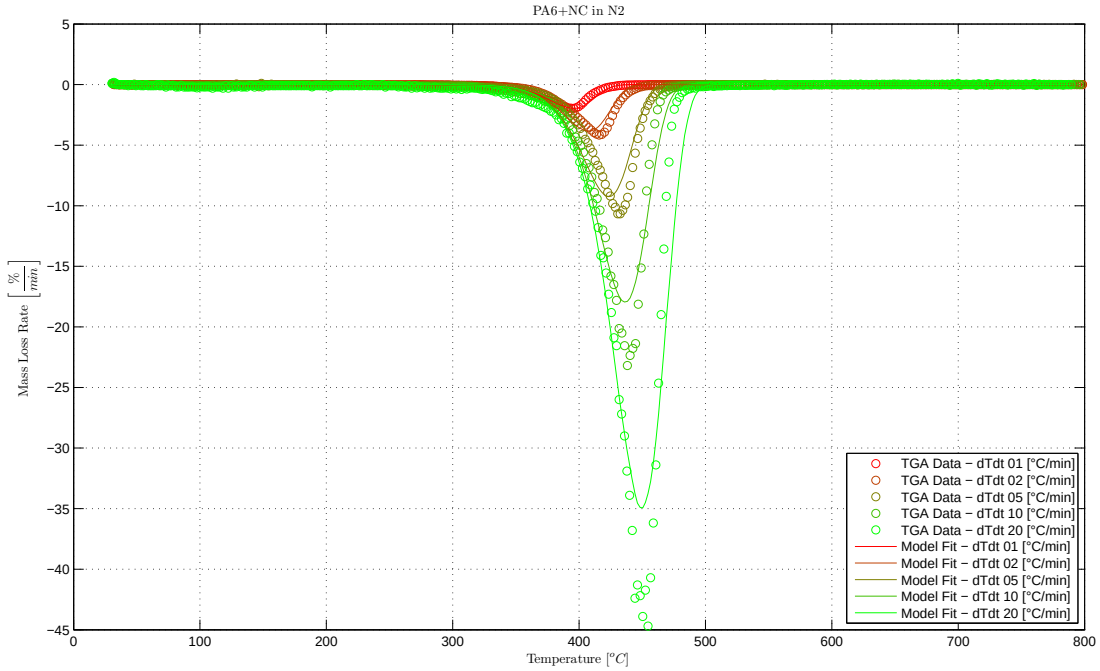

Figure 81 TGA MLR data and reduced reaction schemes fits for PA6+NC in inert atmosphere (N_2)

A.1.3.2 In air

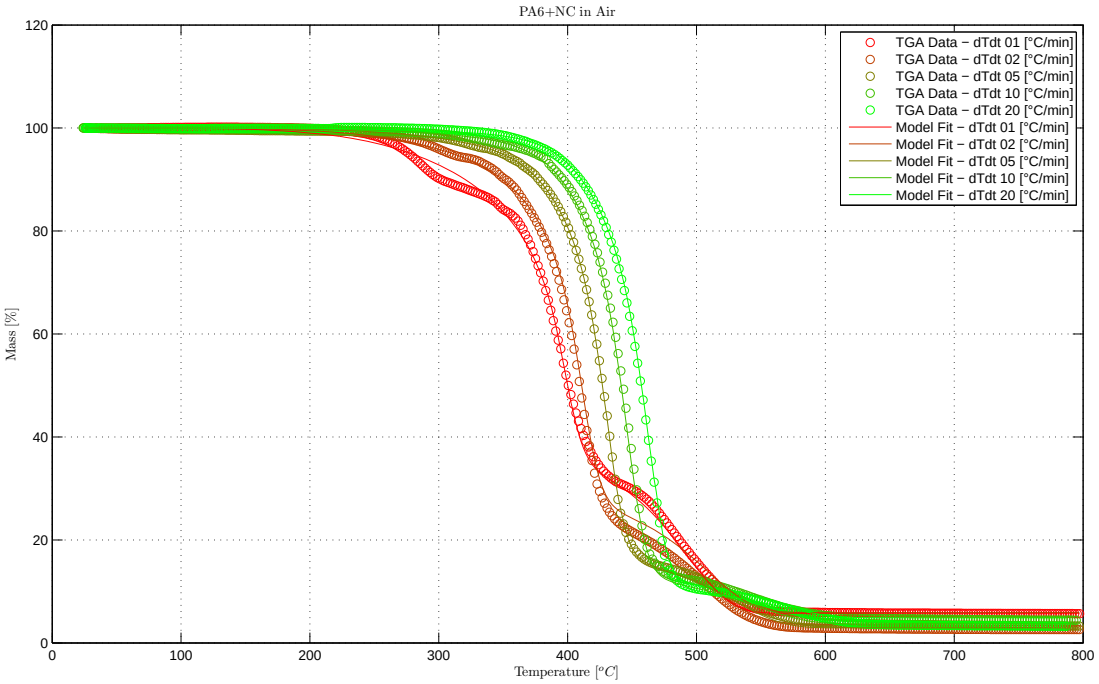

Figure 82 TGA Mass data and reduced reaction schemes fits for PA6+NC in inert atmosphere (N_2)

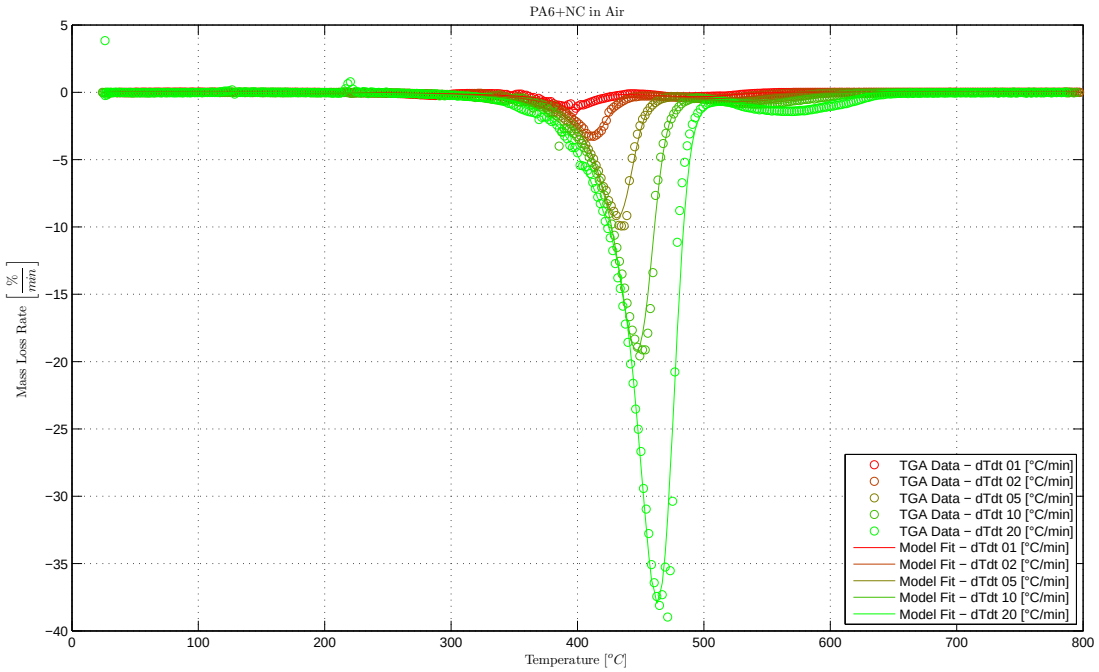

Figure 83 TGA MLR data and reduced reaction schemes fits for PA6+NC in inert atmosphere (N_2)

A.1.4 PA6 + NC + FR

A.1.4.1 In inert atmosphere (N_2)

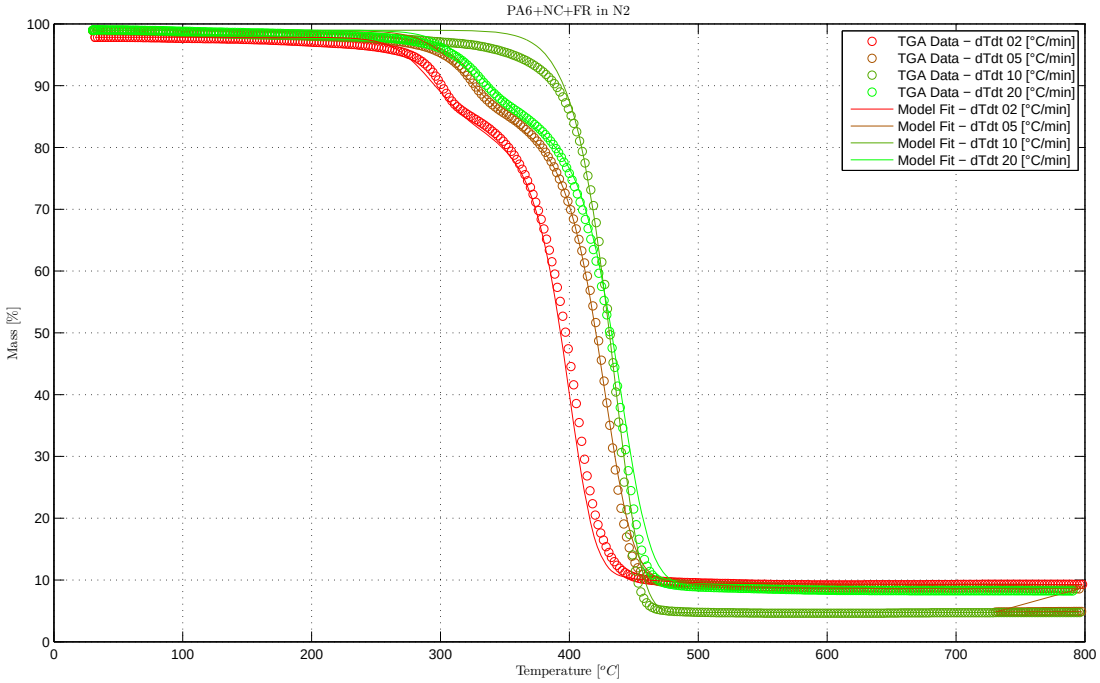

Figure 84 TGA Mass data and reduced reaction schemes fits for PA6+NC+FR in inert atmosphere (N_2)

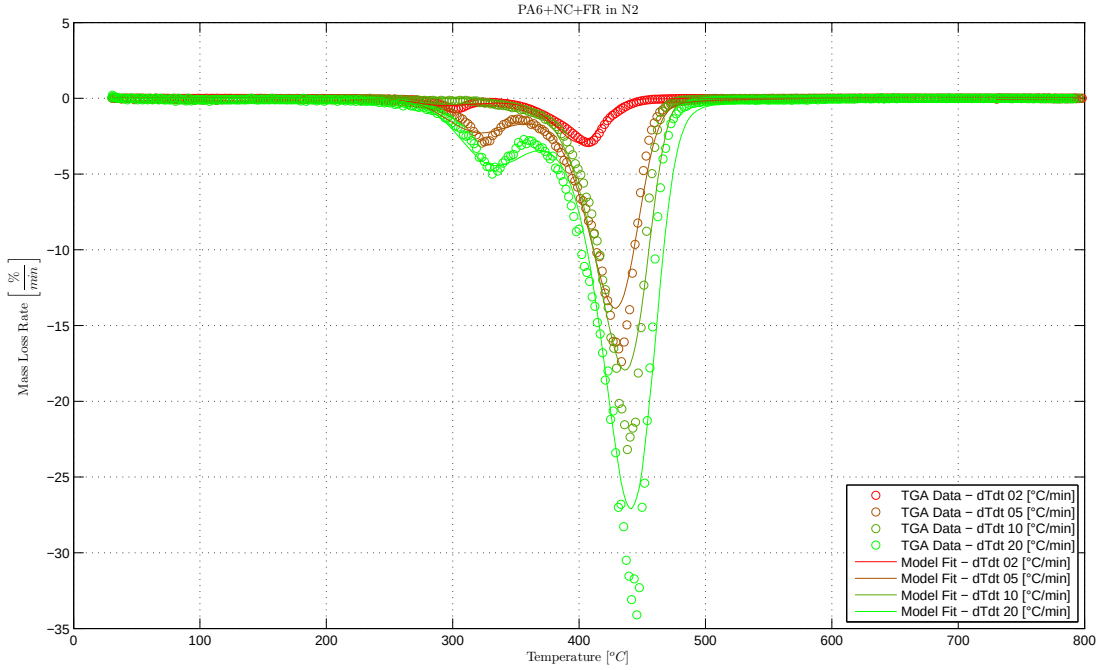

Figure 85 TGA MLR data and reduced reaction schemes fits for PA6+NC+FR in inert atmosphere (N_2)

A.1.4.2 In air

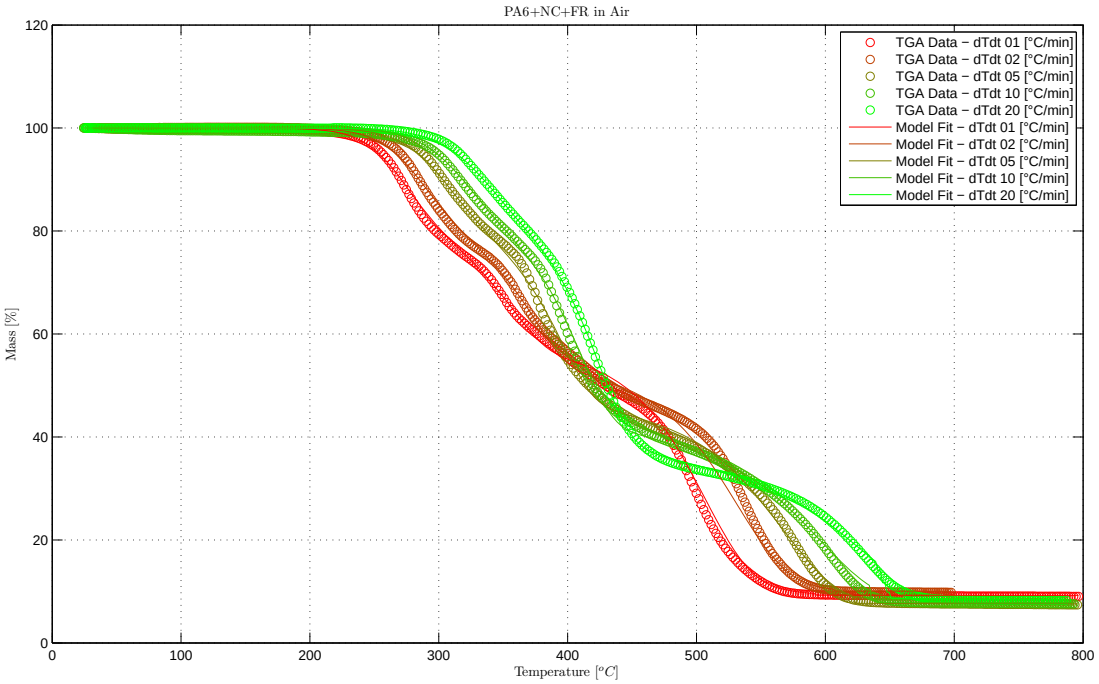

Figure 86 TGA Mass data and reduced reaction schemes fits for PA6+NC+FR in inert atmosphere (N_2)

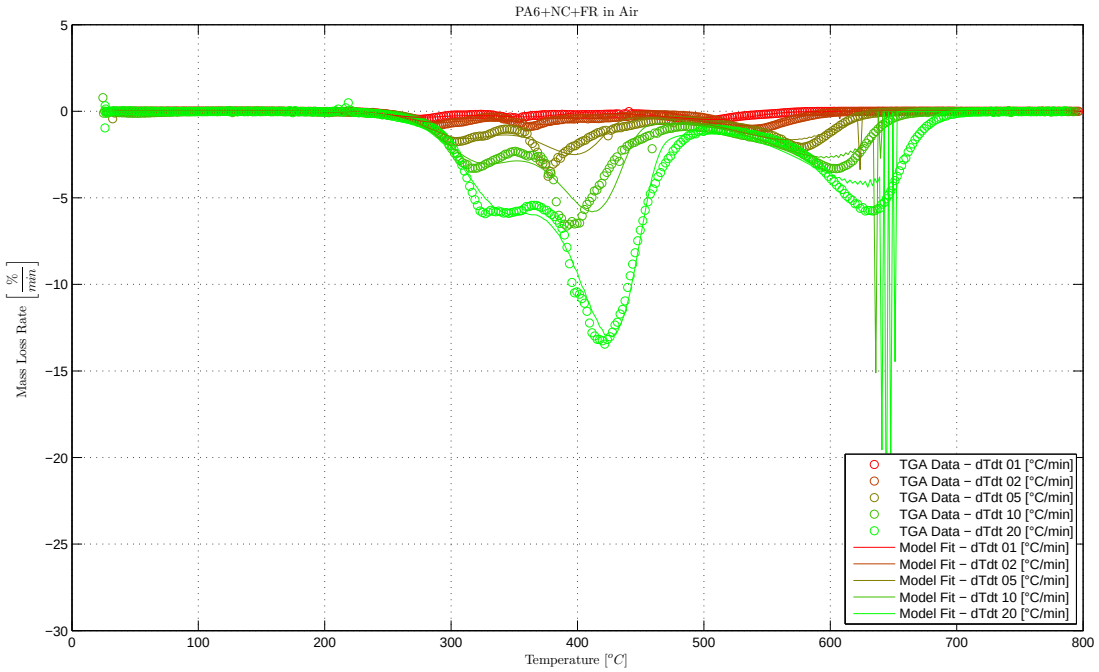

Figure 87 TGA MLR data and reduced reaction schemes fits for PA6+NC+FR in inert atmosphere (N_2)

A.2 Mass fraction of flammable gases YF,S(x,t) from TGA-EGA

A.2.1 PA6

See Figure 11 for TGA-EGA Mass Rates of PA6 and Figure 12 for Mass fraction of flammable gases YF,S(0,t) for PA6.

A.2.2 PA6 + FR

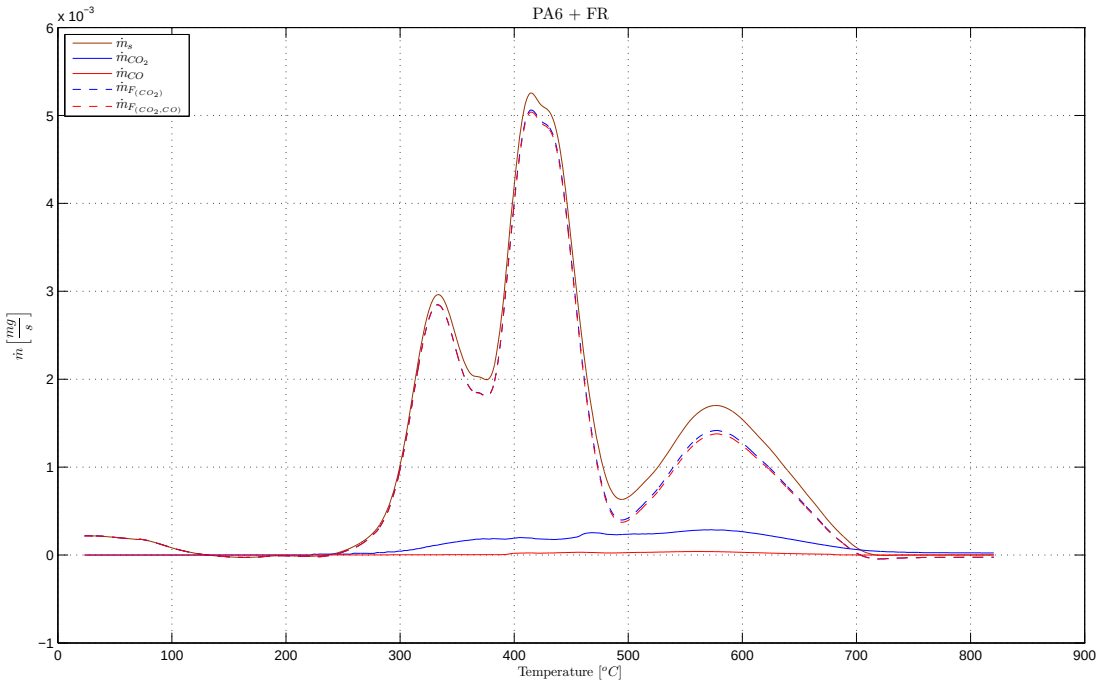

Figure 88 TGA-EGA Mass Rates of PA6+FR

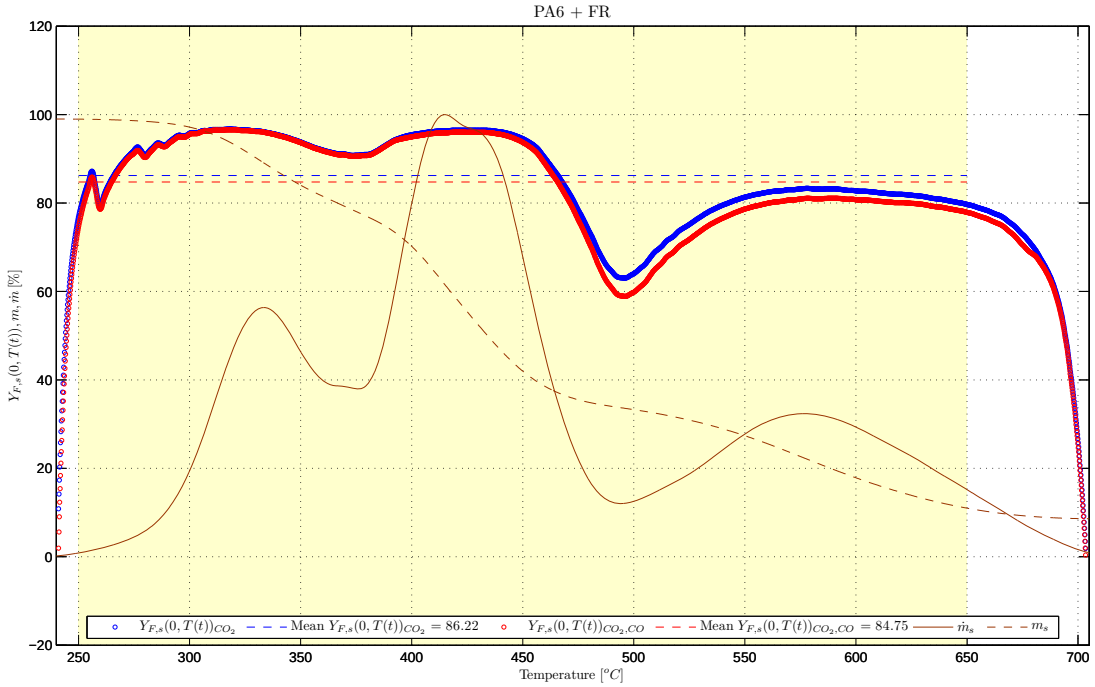

Figure 89 Mass fraction of flammable gases $Y_{F,s}(0,t)$ for PA6+FR

A.2.3 PA6 + NC

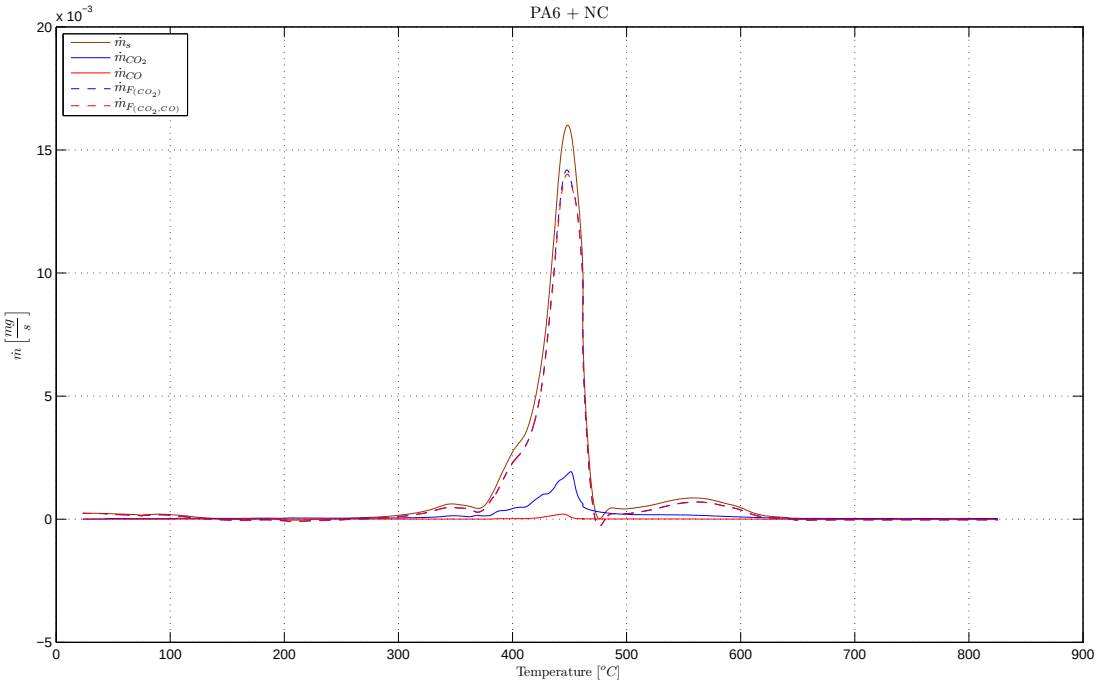

Figure 90 TGA-EGA Mass Rates of PA6+NC

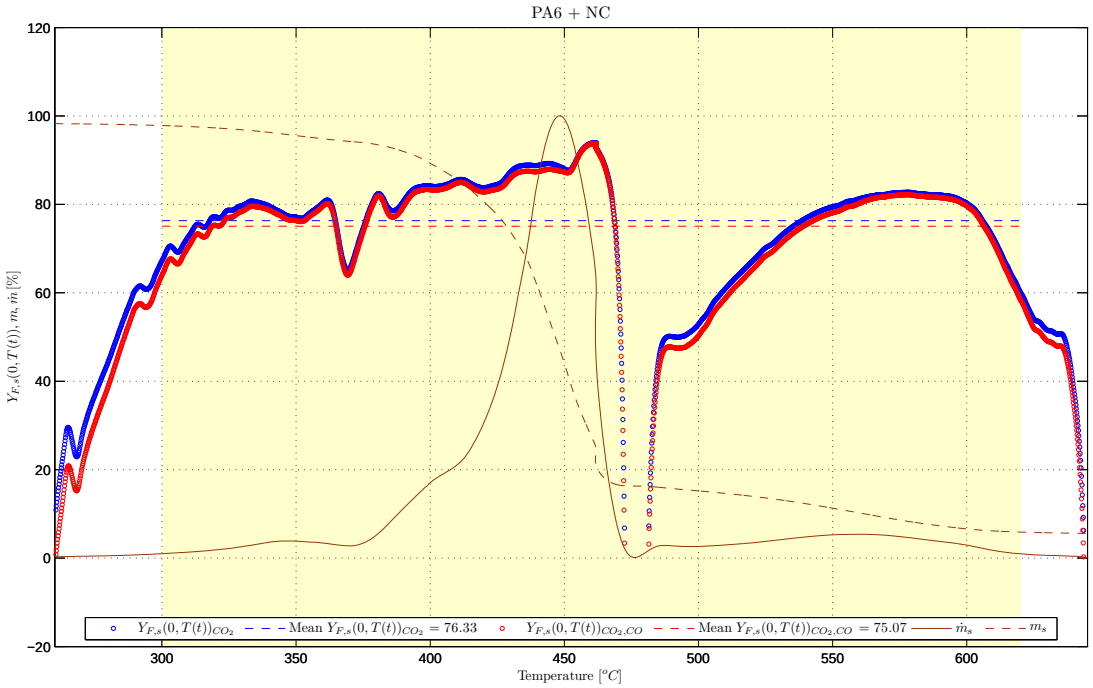

Figure 91 Mass fraction of flammable gases $Y_{F,s}(0,t)$ for PA6+NC

A.2.4 PA6 + NC + FR

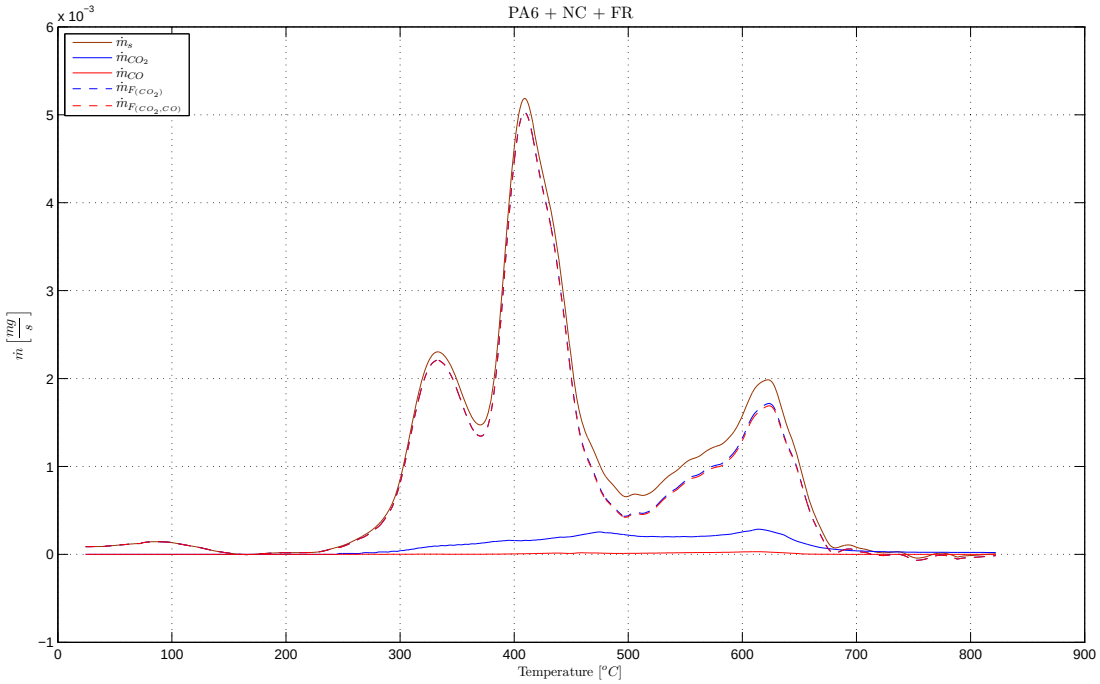

Figure 92 TGA-EGA Mass Rates of PA6+NC+FR

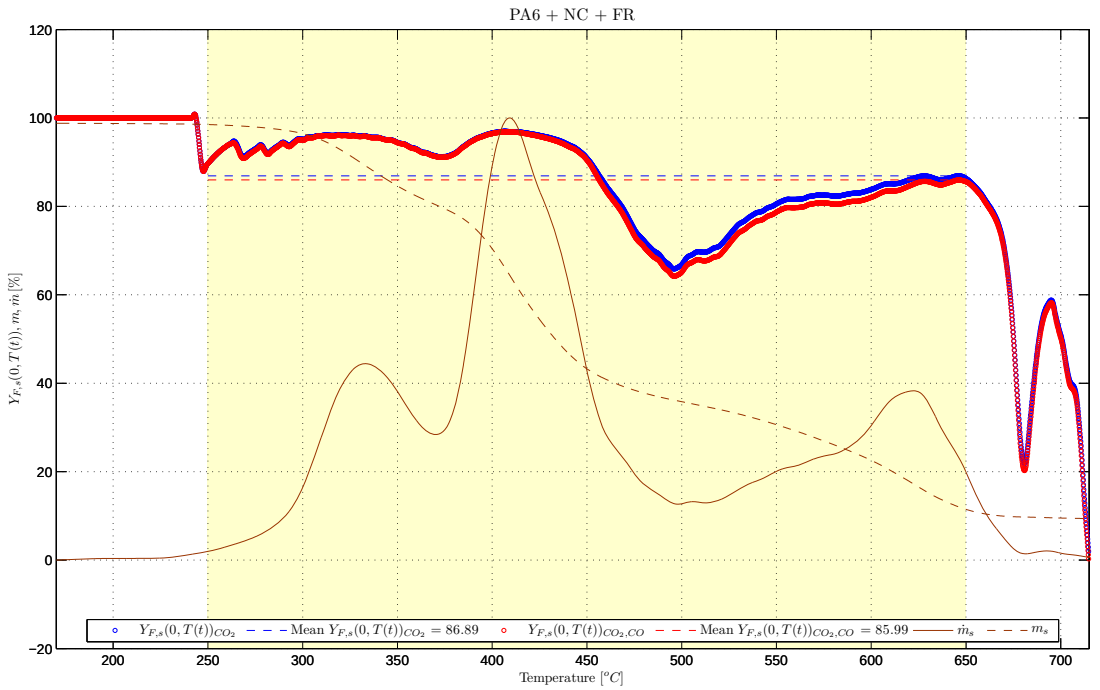

Figure 93 Mass fraction of flammable gases $Y_{F,S}(0,t)$ for PA6+NC+FR

A.3 Glass Transition

A.3.1 PA6

See Figure 14 for the Heat Flow versus Temperature of PA6 in the temperature region of the glass transition.

A.3.2 PA6+FR

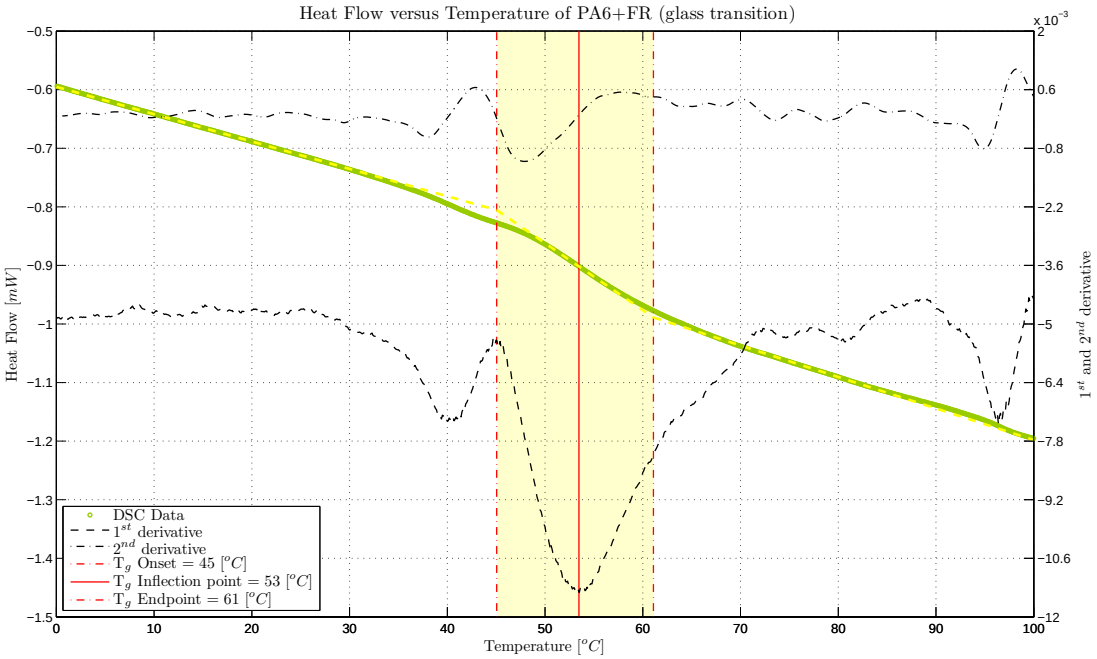

Figure 94 Heat Flow versus Temperature of PA6+FR in the temperature region of the glass transition

A.3.3 PA6+NC

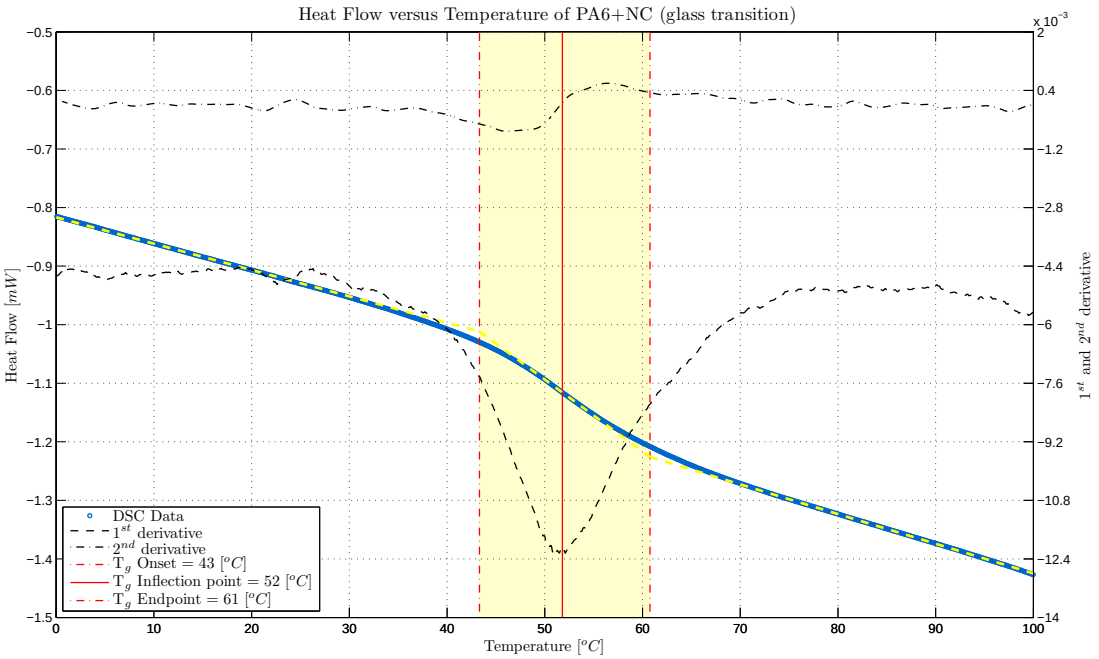

Figure 95 Heat Flow versus Temperature of PA6+NC in the temperature region of the glass transition

A.3.4 PA6+NC+FR

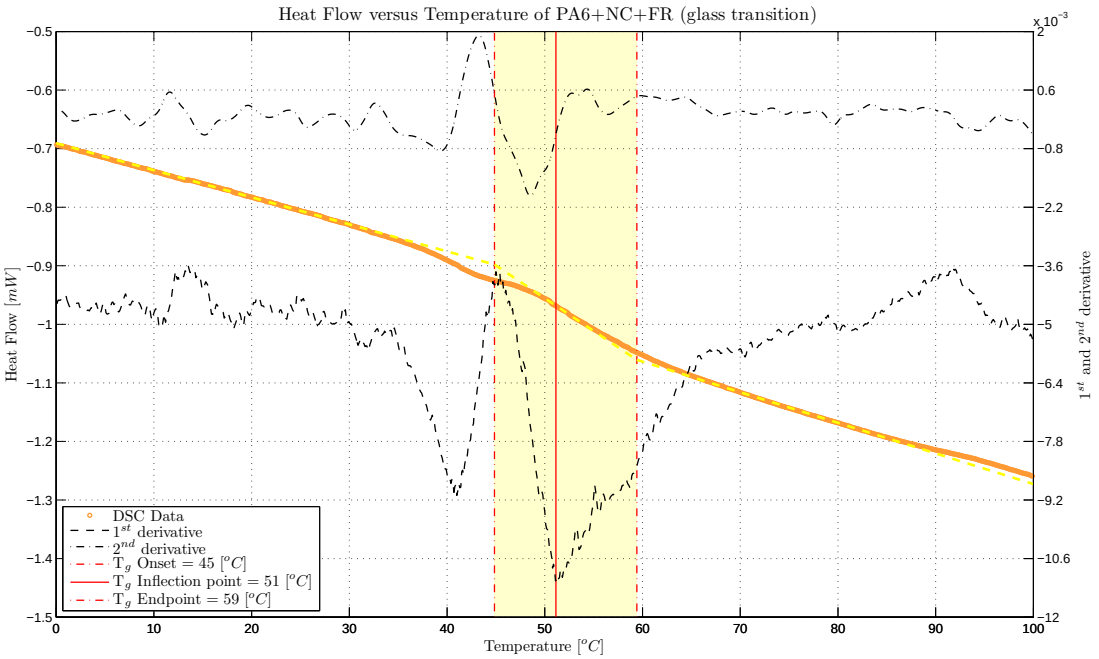

Figure 96 Heat Flow versus Temperature of PA6+NC+FR in the temperature region of the glass transition

A.4 Melting

A.4.1 PA6

See Figure 15 for the Heat Flow versus Temperature of PA6 around the melting region

A.4.2 PA6+FR

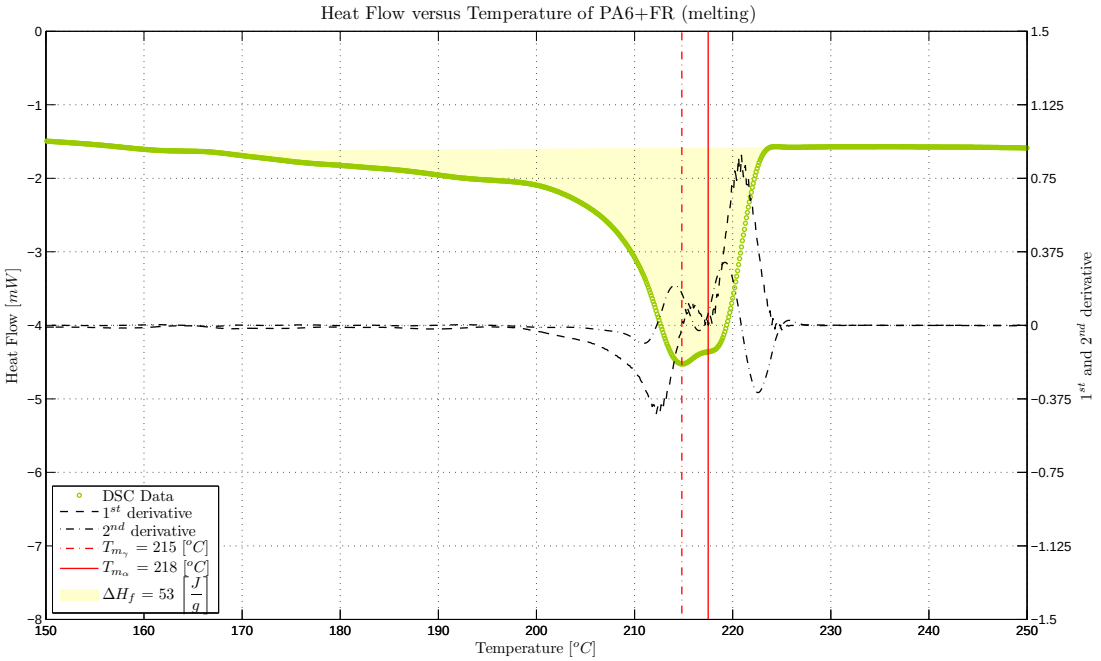

Figure 97 Heat Flow versus Temperature of PA6+FR around the melting region

A.4.3 PA6+NC

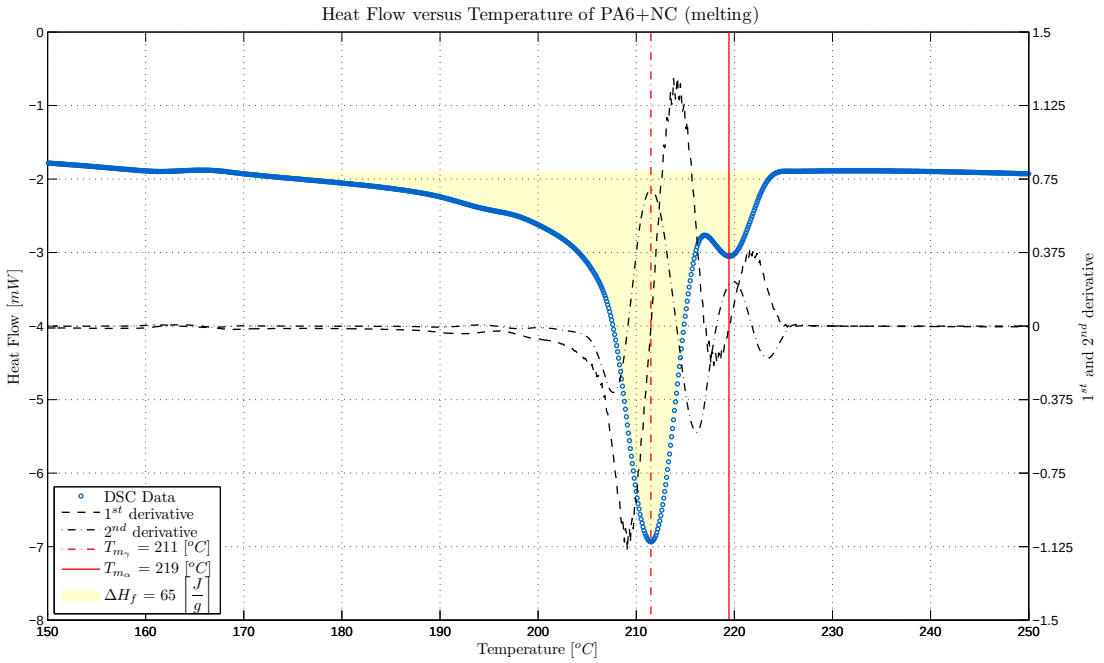

Figure 98 Heat Flow versus Temperature of PA6+NC around the melting region

A.4.4 PA6+NC+FR

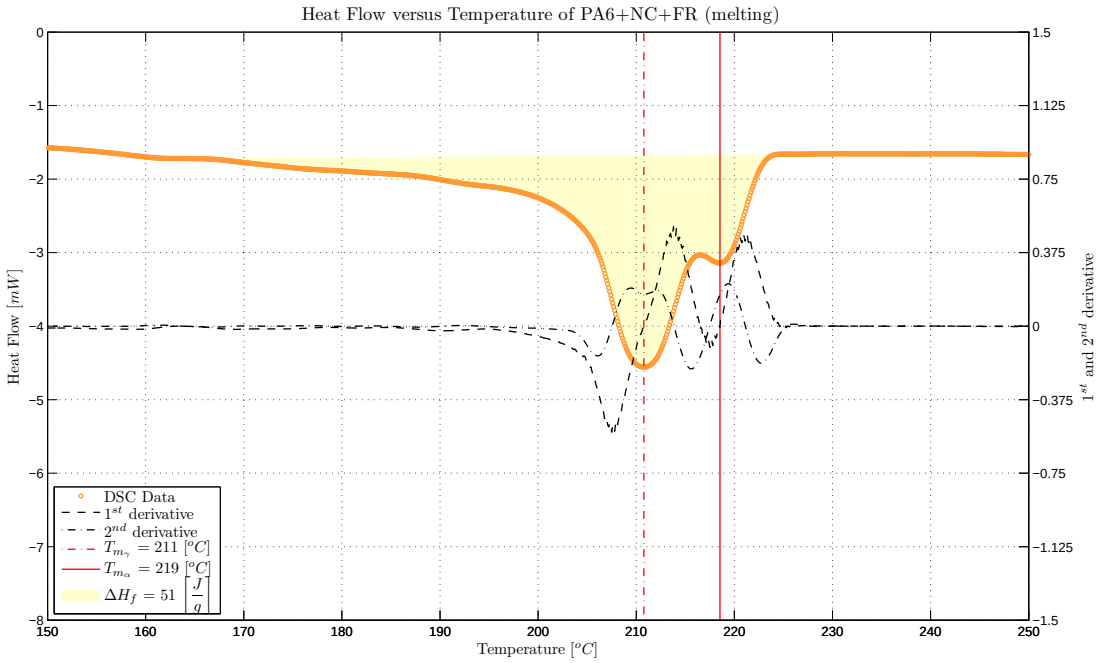

Figure 99 Heat Flow versus Temperature of PA6+NC+FR around the melting region

A.5 Crystallisation

A.5.1 PA6

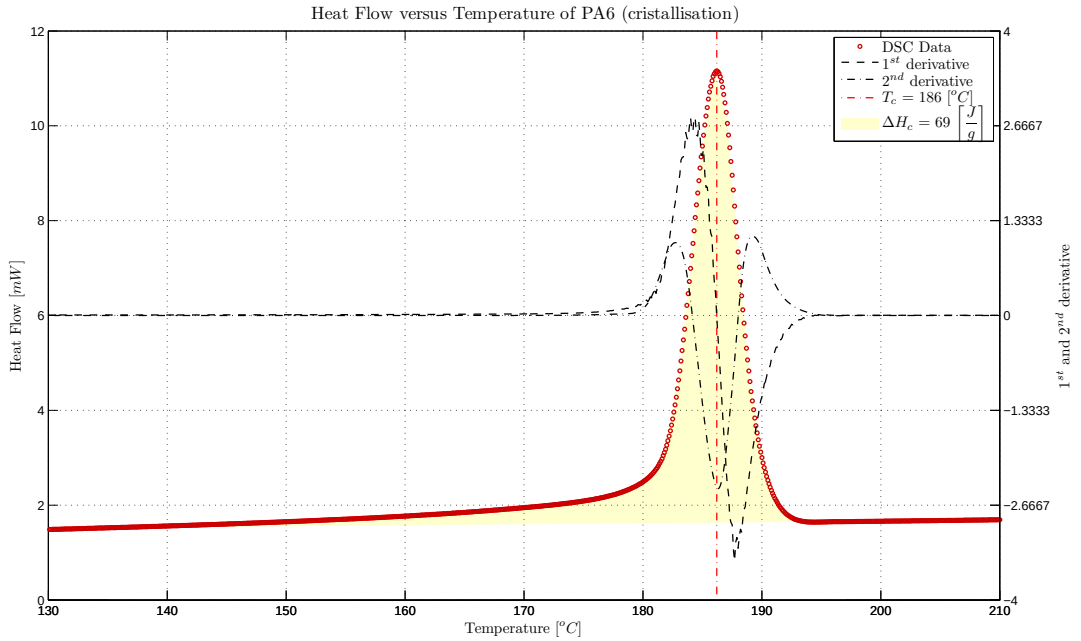

Figure 100 Heat Flow versus Temperature of PA6 around the crystallisation region

A.5.2 PA6+FR

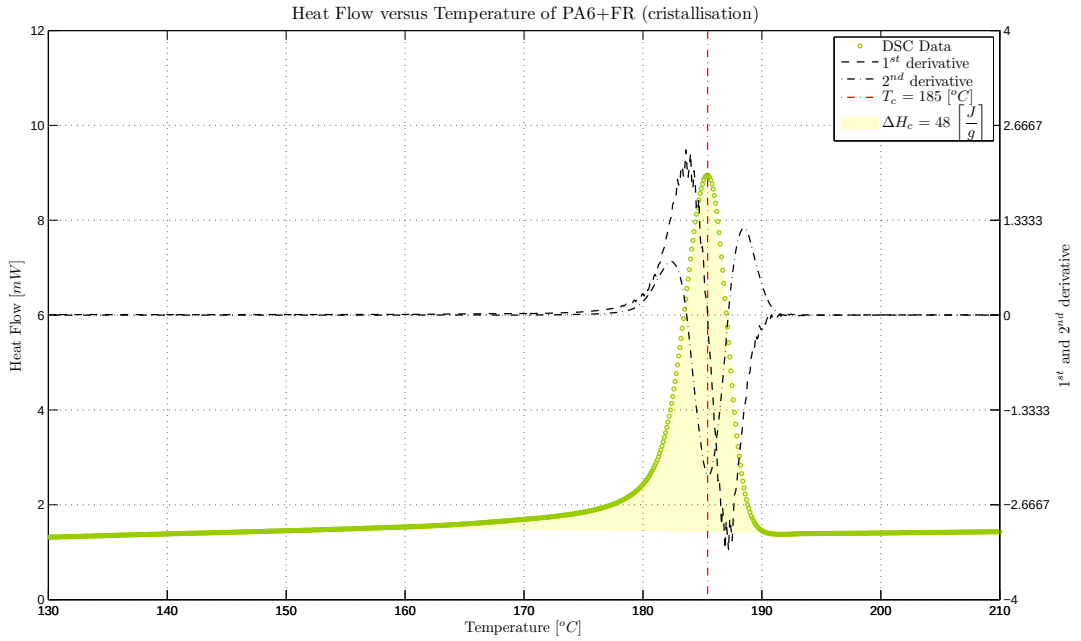

Figure 101 Heat Flow versus Temperature of PA6+FR around the crystallisation region

A.5.3 PA6+NC

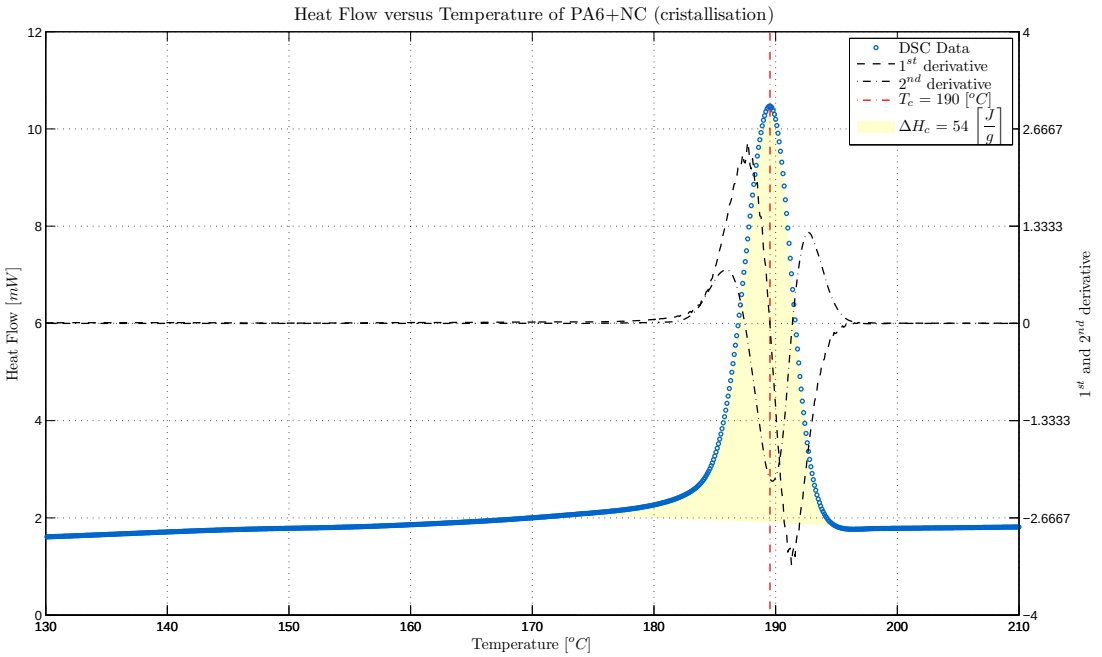

Figure 102 Heat Flow versus Temperature of PA6+NC around the crystallisation region

A.5.4 PA6+NC+FR

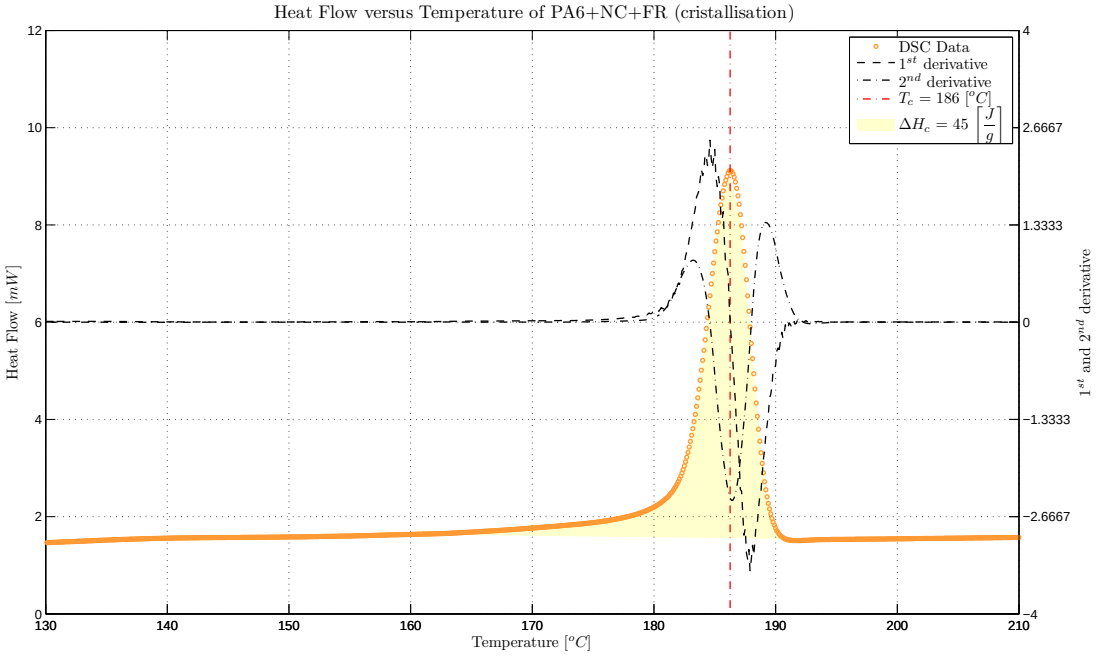

Figure 103 Heat Flow versus Temperature of PA6+NC+FR around the crystallisation region

A.6 Specific heat capacity

A.6.1 PA6

See Figure 18 for the Heat Flow versus Temperature of PA6 around the melting region

A.6.2 PA6+FR

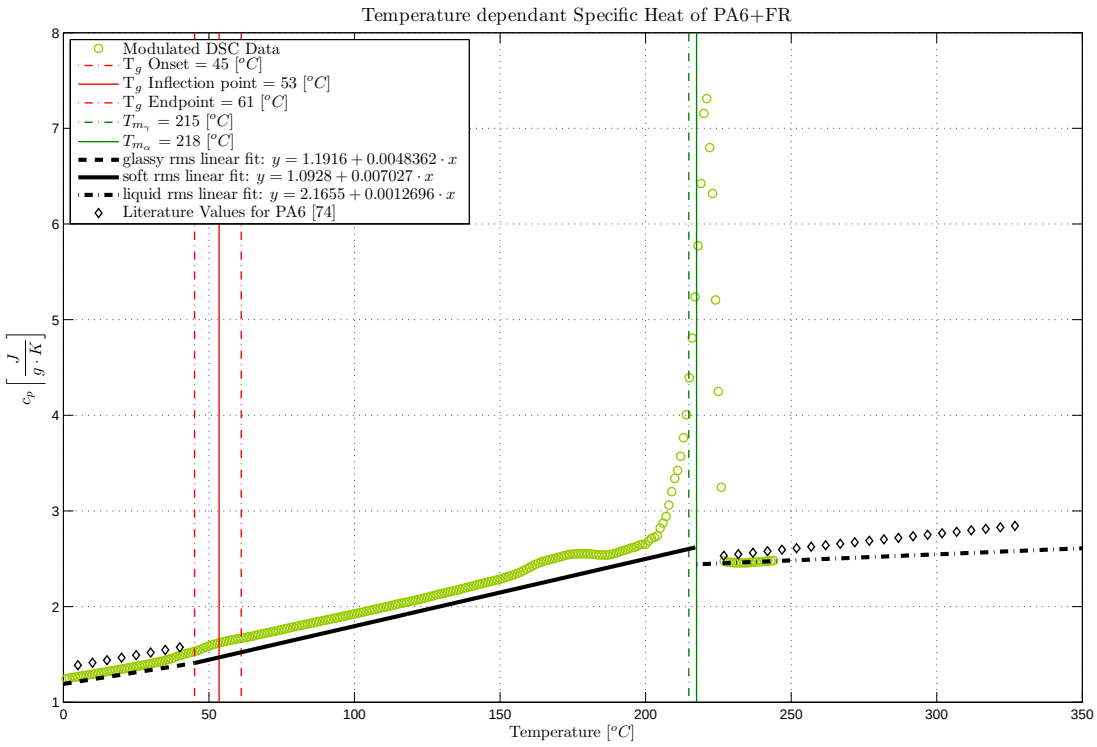

Figure 104 Specific heat capacity (c_p) versus temperature of PA6+FR

A.6.3 PA6+NC

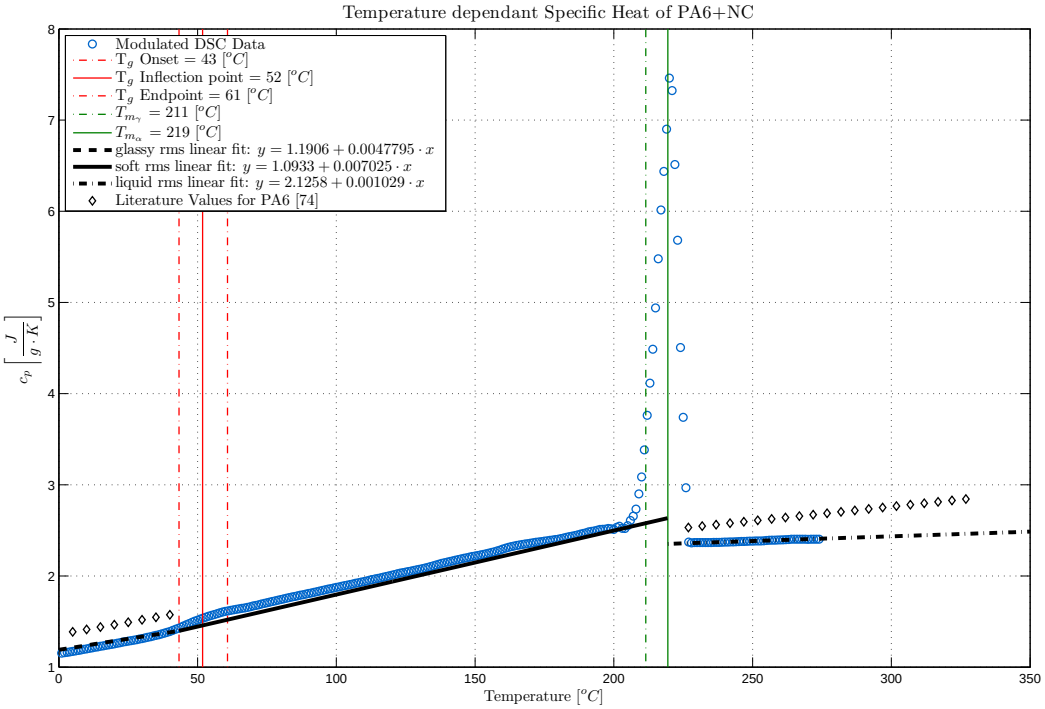

Figure 105 Specific heat capacity (c_p) versus temperature of PA6+NC

A.6.4 PA6+NC+FR

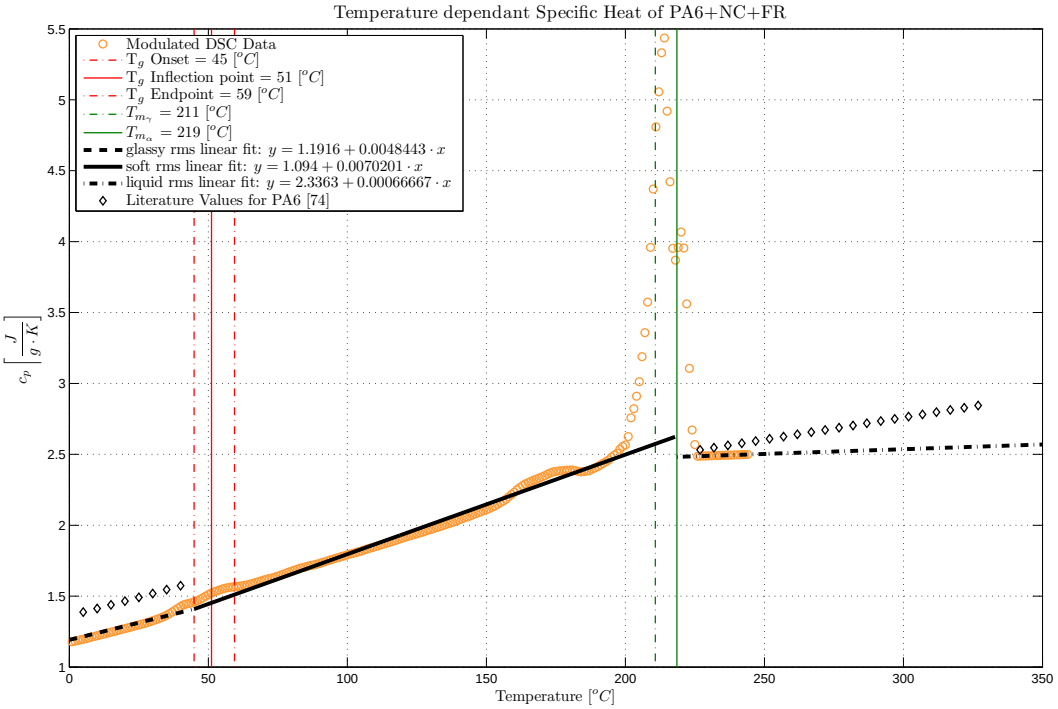

Figure 106 Specific heat capacity (c_p) versus temperature of PA6+NC+FR

A.7 Density

A.7.1 PA6

See Figure 19 for the Density versus Temperature of PA6

A.7.2 PA6+NC

N/A

A.7.3 PA6+FR

See Figure 20 for the Density versus Temperature of PA6+FR

A.7.4 PA6+NC+FR

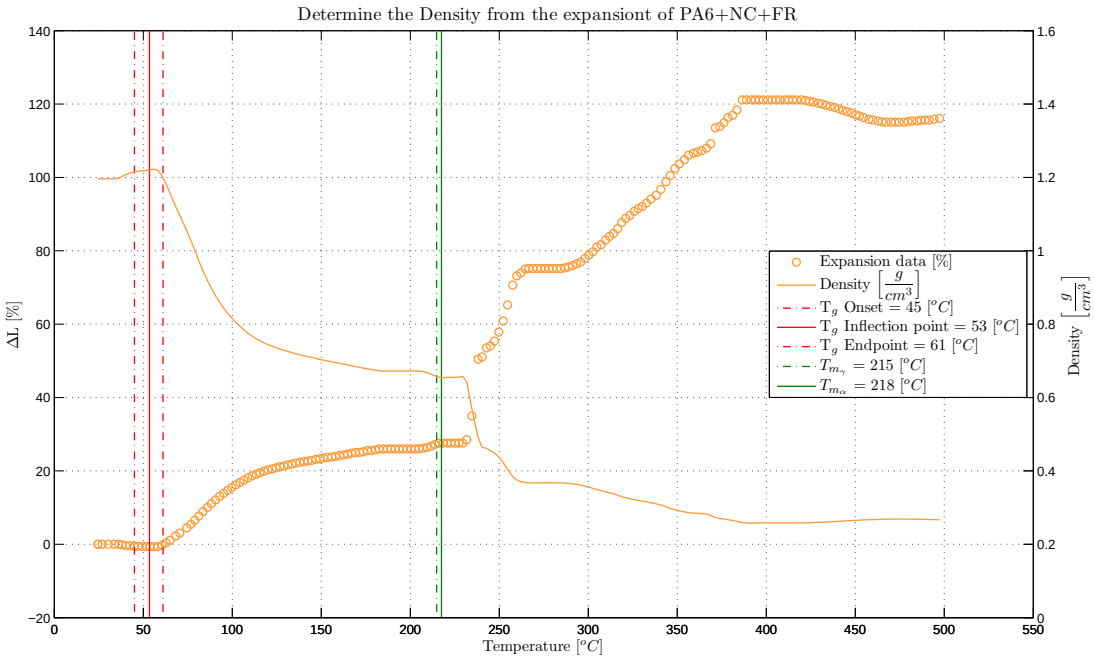

Figure 107 Density versus temperature of PA6+NC+FR

A.8 Temperature when the reaction seams to be most vigorous

A.8.1 PA6

A.8.1.1 In inert atmosphere (N_2)

See Figure 21 for Temperature when the reaction seams to be most vigorous in PA6+FR in N_2

A.8.1.2 In air

See Figure 22 for Temperature when the reaction seams to be most vigorous in PA6+FR in air

A.8.2 PA6+NC

A.8.2.1 In inert atmosphere (N_2)

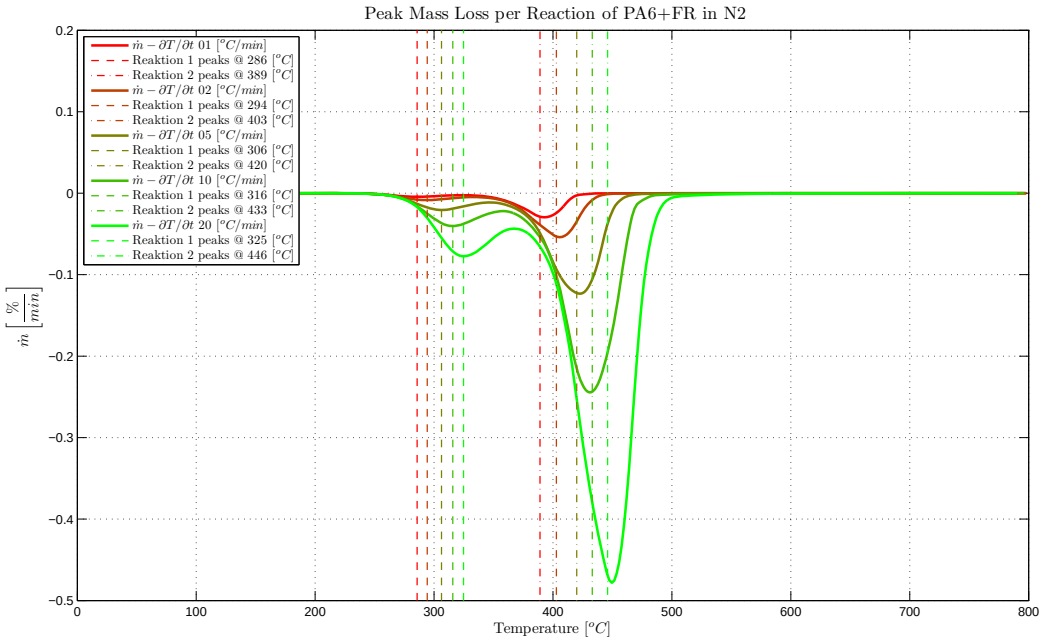

Figure 108 Temperature when the reaction seams to be most vigorous PA6+FR in N_2

A.8.2.2 In air

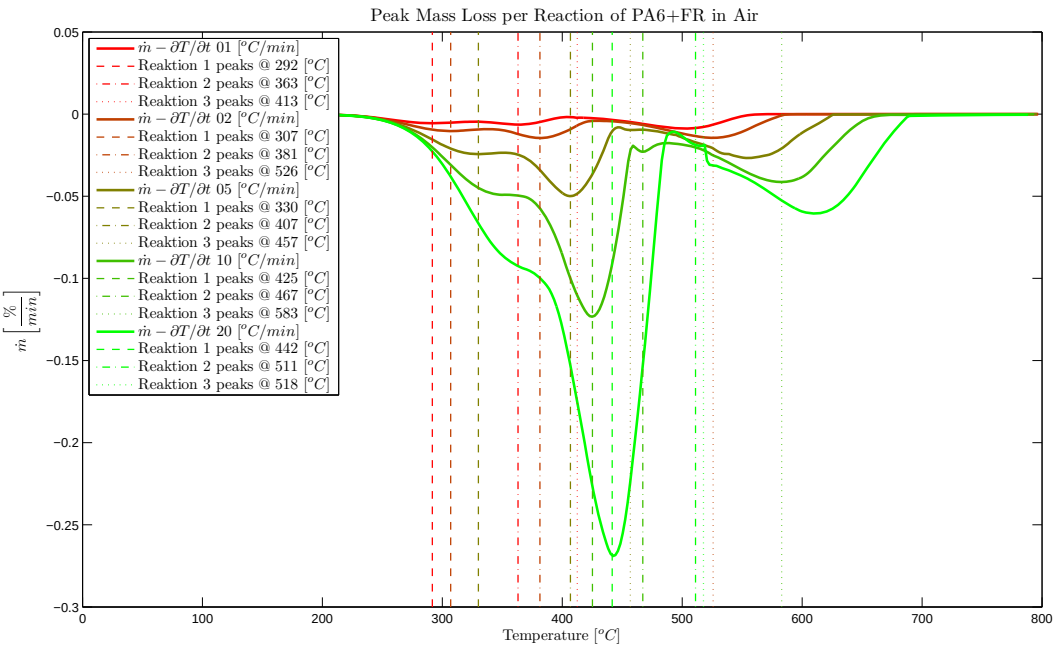

Figure 109 Temperature when the reaction seams to be most vigorous PA6+FR in air

A.8.3 PA6+FR

A.8.3.1 In inert atmosphere (N_2)

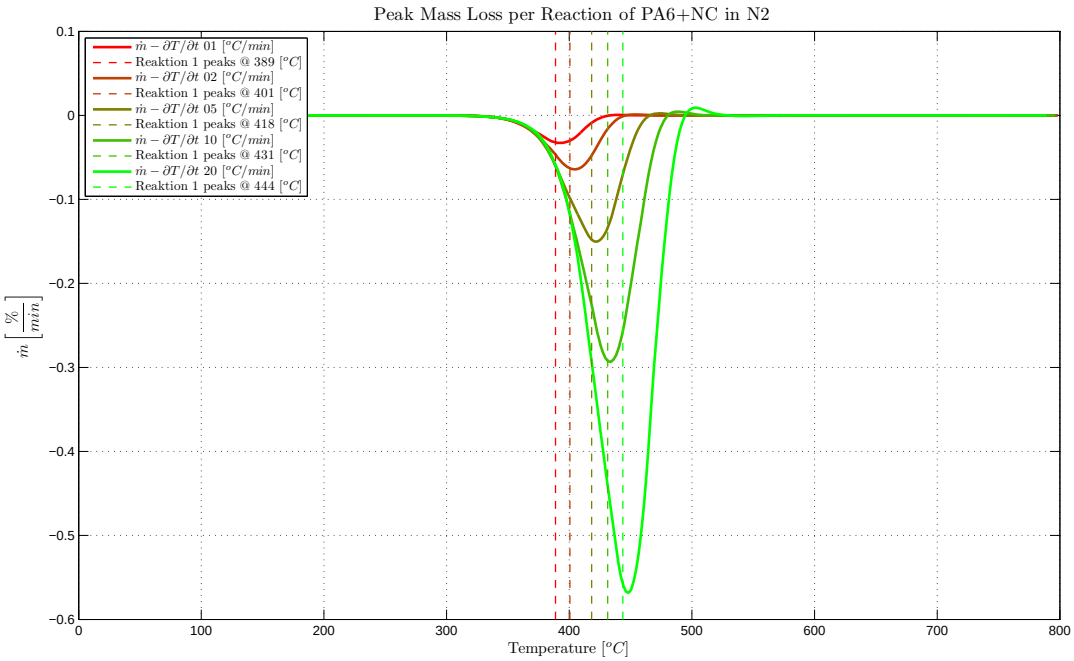

Figure 110 Temperature when the reaction seams to be most vigorous PA6+NC in N_2

A.8.3.2 In air

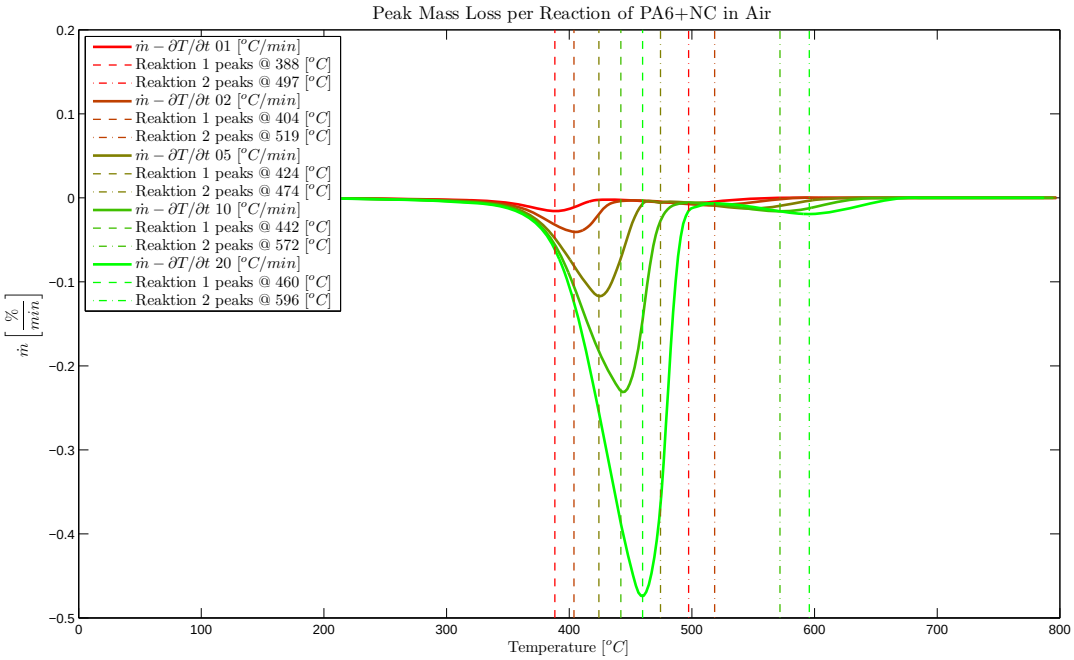

Figure 111 Temperature when the reaction seams to be most vigorous PA6+NC in air

A.8.4 PA6+NC+FR

A.8.4.1 In inert atmosphere (N_2)

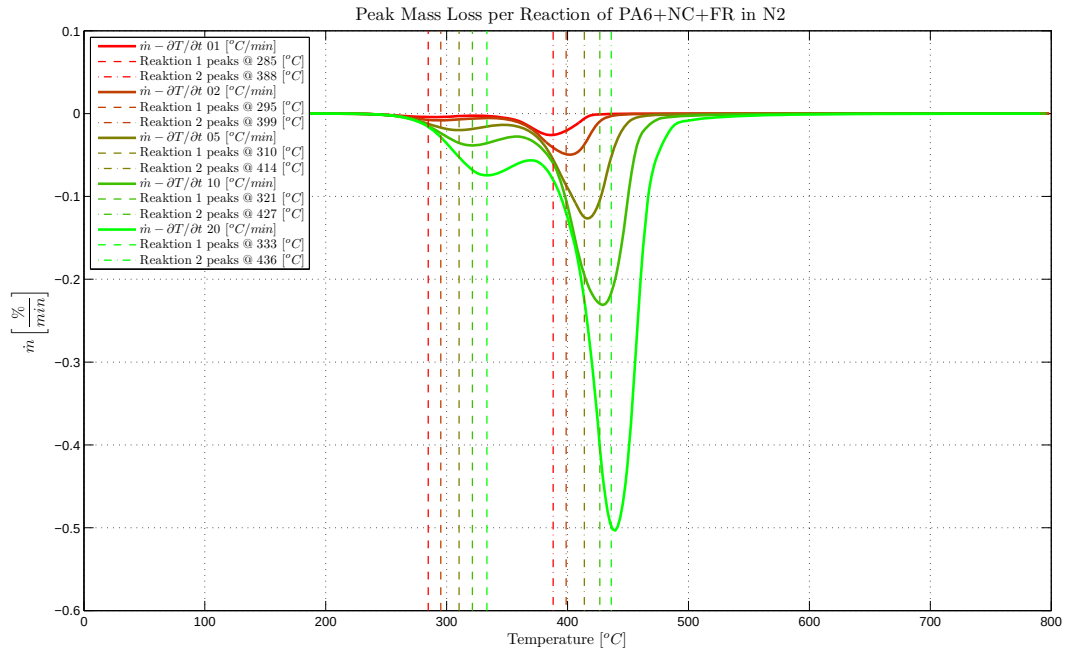

Figure 112 Temperature when the reaction seams to be most vigorous PA6+NC+FR in N_2

A.8.4.2 In air

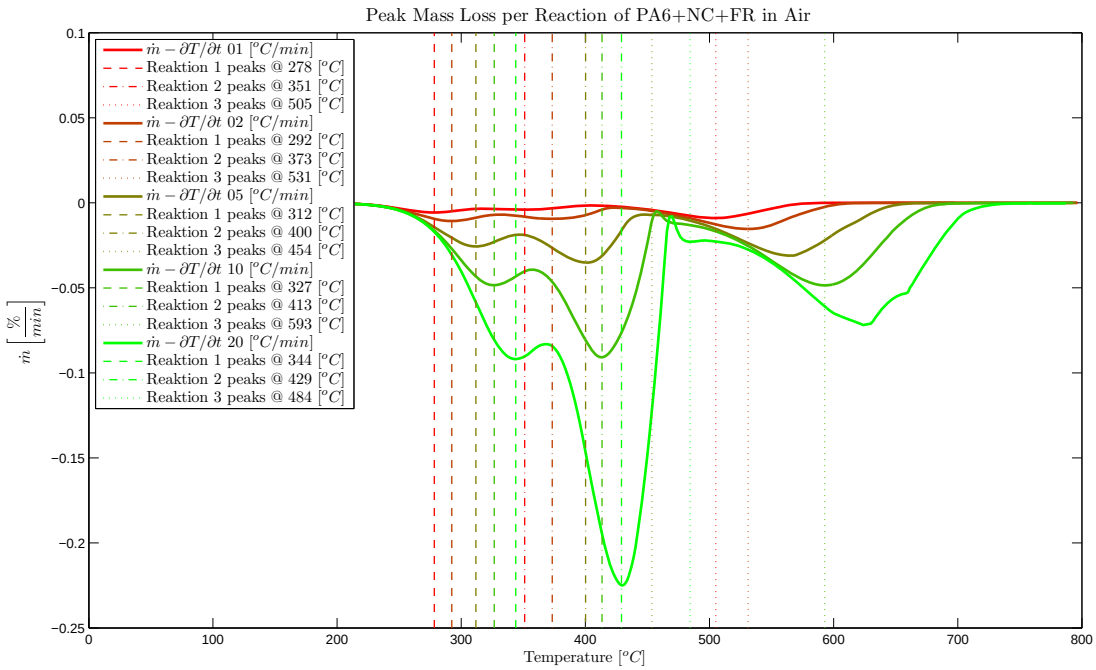

Figure 113 Temperature when the reaction seams to be most vigorous PA6+NC+FR in air

A.9 In depth temperature fits for various heat fluxes between the model and the measured data to determine the convective heat transfer coefficient at an aluminium block

A.9.1 FPA

A.9.1.1 Depth from the surface of the aluminium block of x=0.00355 [m]

See Figure 25 for the model to test data fit for various heat fluxes at a depth of x=0.0 0355 [m]

A.9.1.2 Depth from the surface of the aluminium block of x=0.01355 [m]

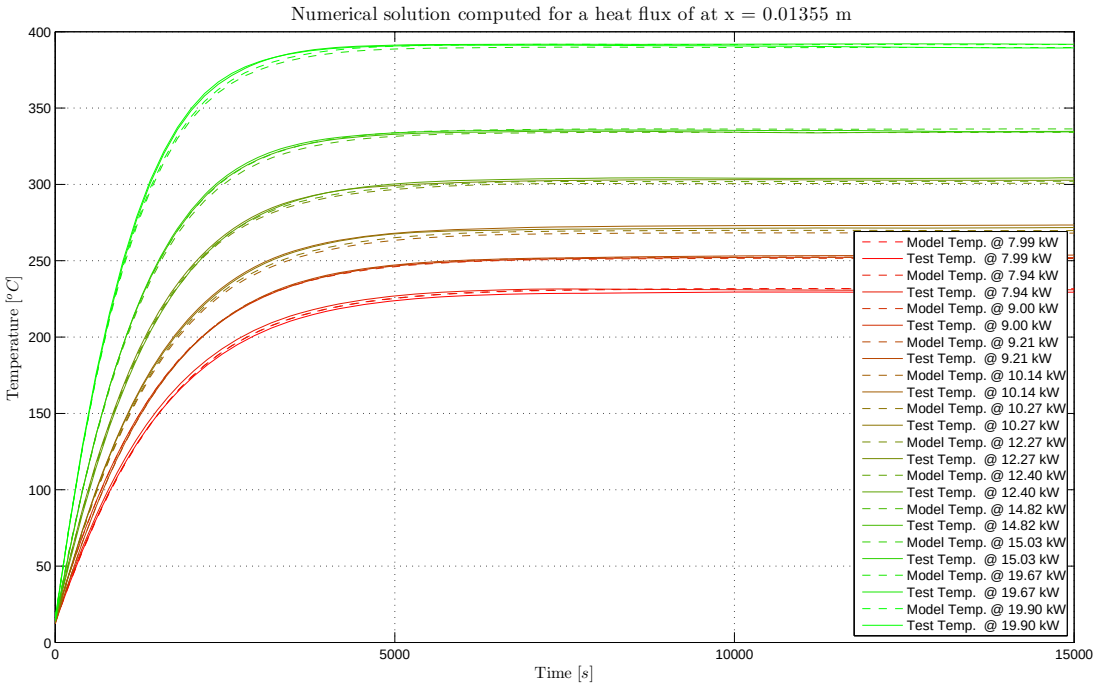

Figure 114 Model to Test data fit in the FPA for various heat fluxes at a depth of x=0.01355 [m]

A.9.1.3 Depth from the surface of the aluminium block of x=0.02155 [m]

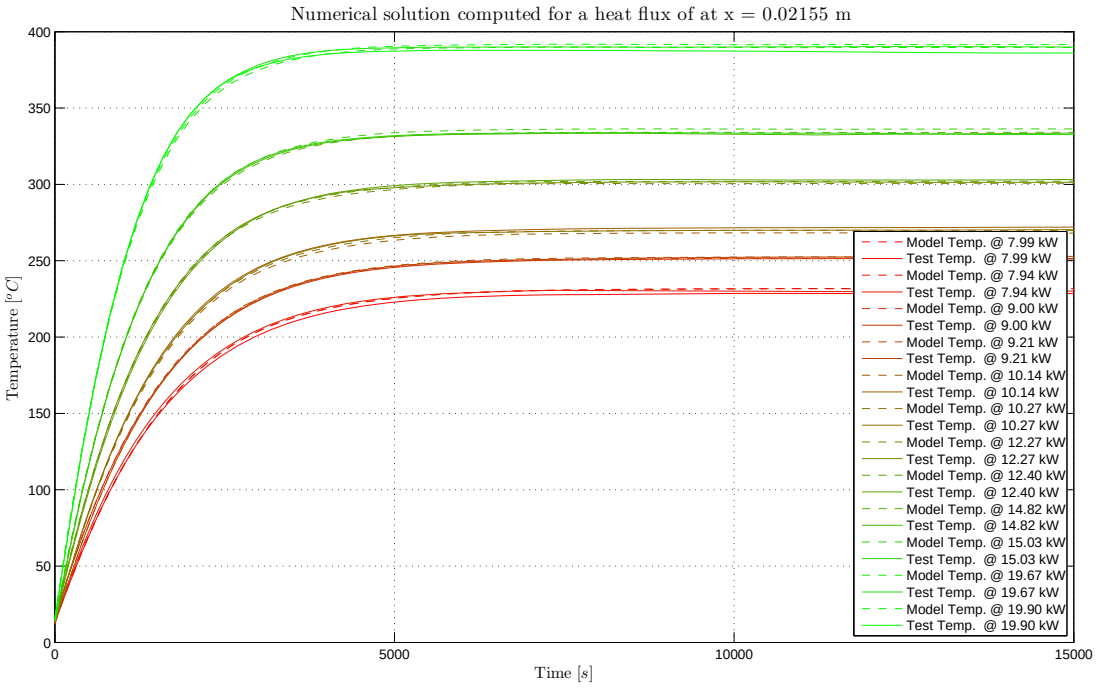

Figure 115 Model to Test data fit in the FPA for various heat fluxes at a depth of x=0.02155 [m]

A.9.1.4 Back side of the aluminium block thus a depth from the surface of the aluminium block of x=0.002555 [m]

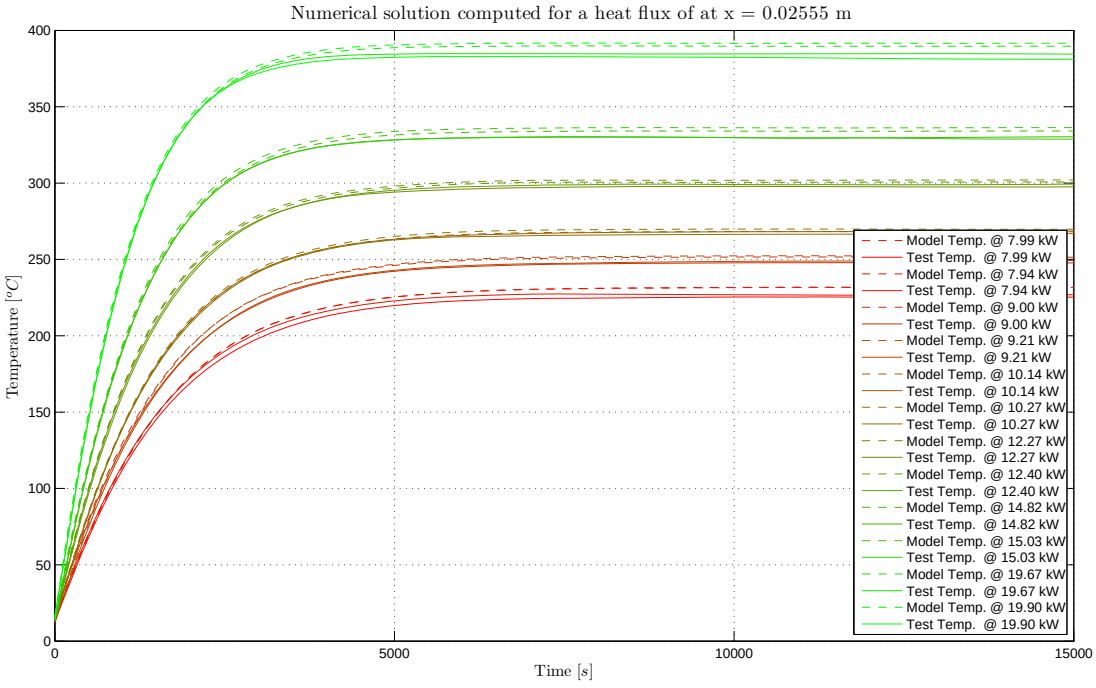

Figure 116 Model to Test data fit in the FPA for various heat fluxes at a depth of x=0.02555 [m]

A.9.2 Cone

A.9.2.1 Depth from the surface of the aluminium block of x=0.00255 [m]

See Figure 26 for the model to test data fit for various heat fluxes at a depth of x=0.0 0255 [m]

A.9.2.2 Depth from the surface of the aluminium block of x=0.01055 [m]

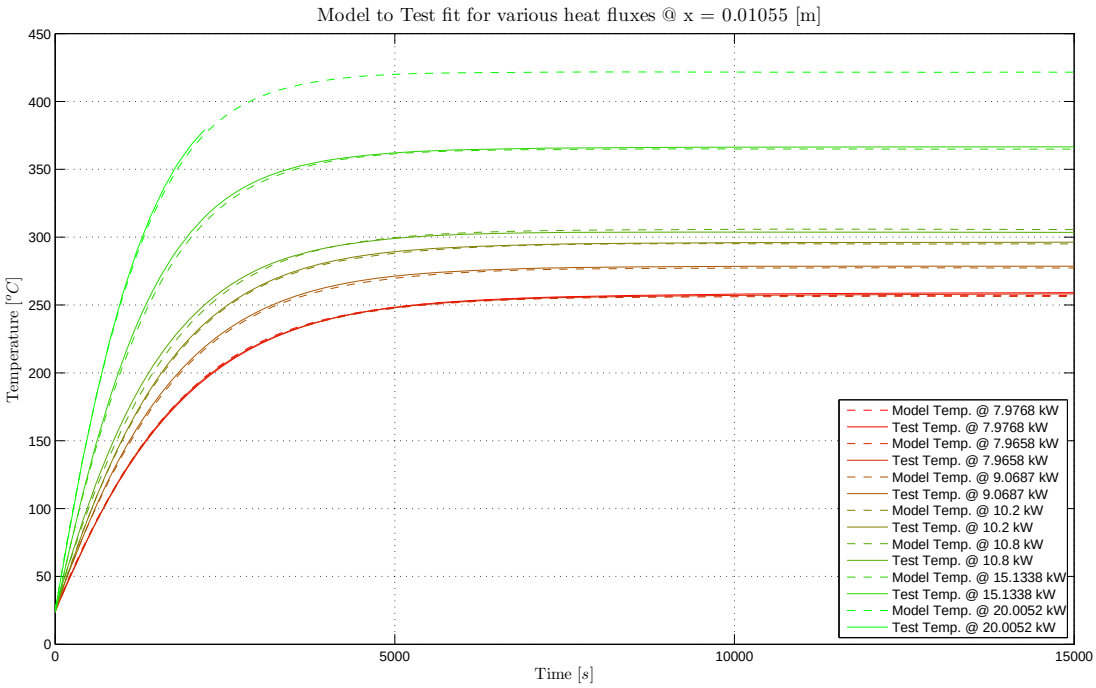

Figure 117 Model to Test data fit in the Cone for various heat fluxes at a depth of x=0.01055 [m]

A.9.2.3 Depth from the surface of the aluminium block of x=0.01955 [m]

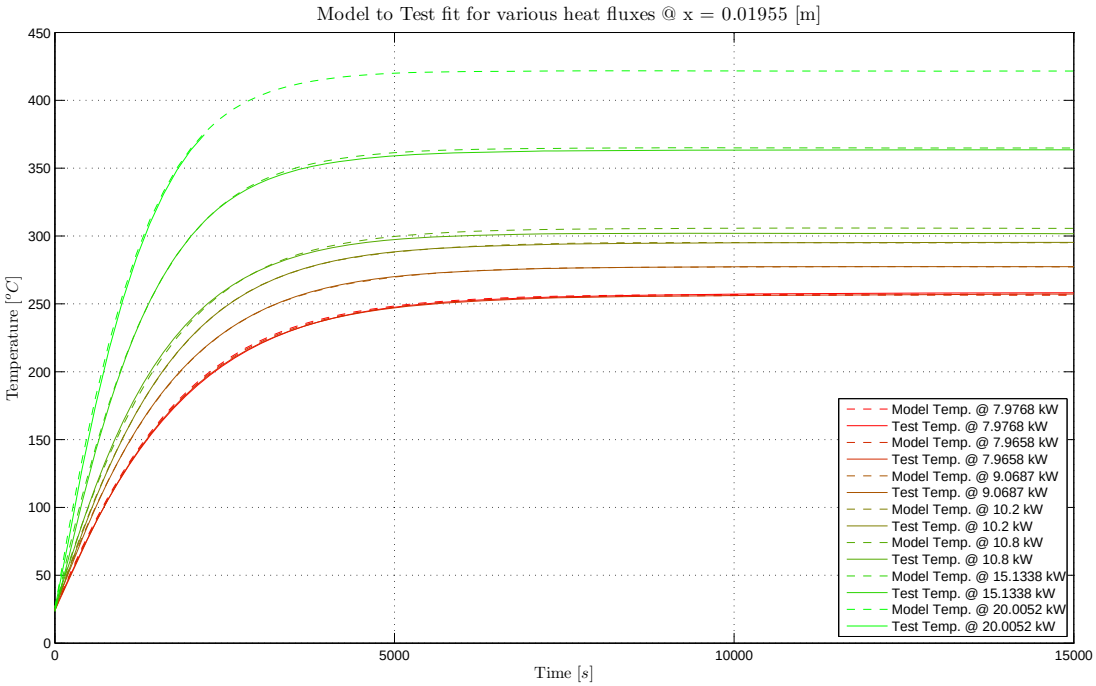

Figure 118 Model to Test data fit in the Cone for various heat fluxes at a depth of x=0.01955 [m]

A.9.2.4 Back side of the aluminium block thus a depth from the surface of the aluminium block of x=0.00244 [m]

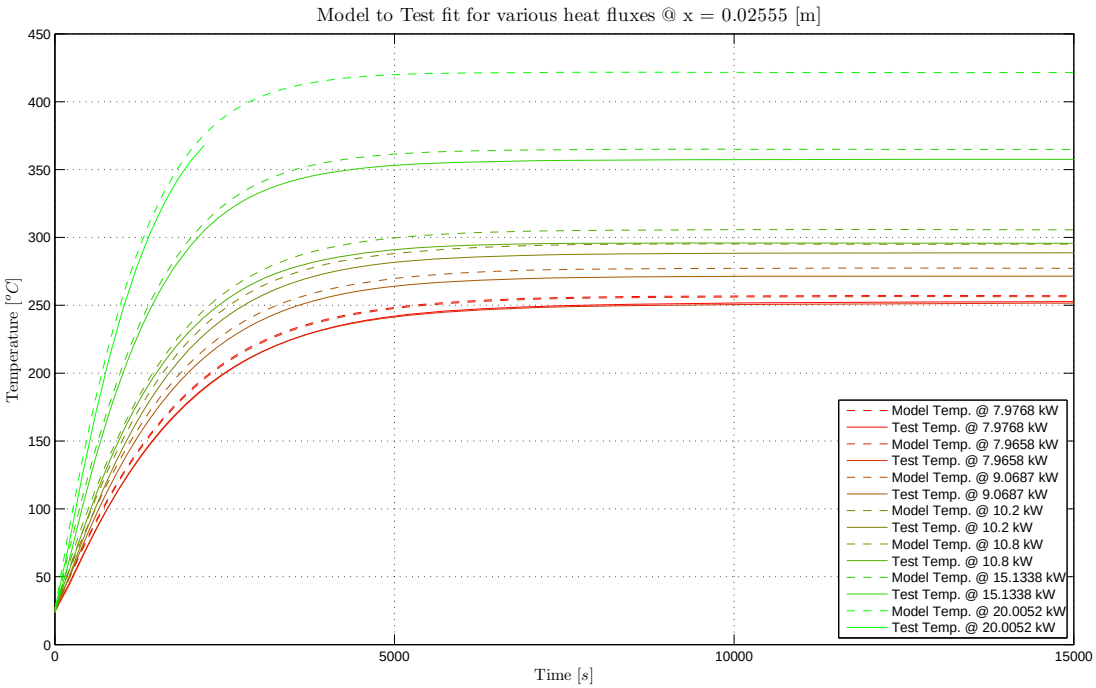

Figure 119 Model to Test data fit in the Cone for various heat fluxes at a depth of x=0.02555 [m]

A.10 CFD

The CFD modelling has been conducted using the commercial CFD code FLUENT. This code has been extensively used for simulating buoyancy induced flows. The turbulent fluctuations of the fluid-dynamic quantities have been modelled by means of Reynolds-averaged Navier-stokes equations (RANS). From the available RANS turbulence models, the k-e model has been applied in this work. The production and the destruction of turbulence kinetic energy, because of the effect of the buoyancy, have also been accounted for. The standard k–ε model is not valid for fluid regions characterized by a low Reynolds number, like locations close to the walls [22]. Thus in these regions the standard wall functions have been used. The boundary conditions, the mesh and the resulting flow field for the Cone and the FPA are described in section A.10.1 and A.10.2 respectively. The steady state simulations were considered to be converged when the scaled residuals were lower than 10-5 with the exception of the energy equation where the maximum allowed value was 10-7. Furthermore, the second order up-wind approximation of convective fluxes was used.

A.10.1 Cone

Presented below are the specifics for the conducted CFD modelling in the Cone, staring with the boundary conditions used, then presenting the mesh (Figure 121) and the resulting flow field (Figure 122).

Boundary Conditions

Boundary 1: Wall

- Adiabatic

Boundary 2: Velocity inlet

- Velocity computed from mass loss rate (section 3.10)
- Temperature is the temperature at pyrolysis
- The mass fraction of the fluid is:

Species	Mass Fraction
O_2	0 %
CO_2	dependant on the sample burnt see section 3.3
N_2	0 %
C_3H_8	dependant on the sample burnt see section 3.3

Boundary 3: Velocity outlet

- Velocity computed from the Cone test setup (exhaust duct velocity ~24 l/min)
- Temperature of the fluid is ambient
- The mass fraction of the fluid is:

Species	Mass Fraction
O_2	23 %
CO_2	0 %
N_2	77 %
C_3H_8	0 %

Boundary 4: Pressure inlet

- Static pressure is assumed to be zero
- Temperature of the fluid is ambient
- The mass fraction of the fluid is:

Species	Mass Fraction
O_2	23 %
CO_2	0 %
N_2	77 %
C_3H_8	0 %

Boundary 5: Cone heater

- Fixed temperature from test setup

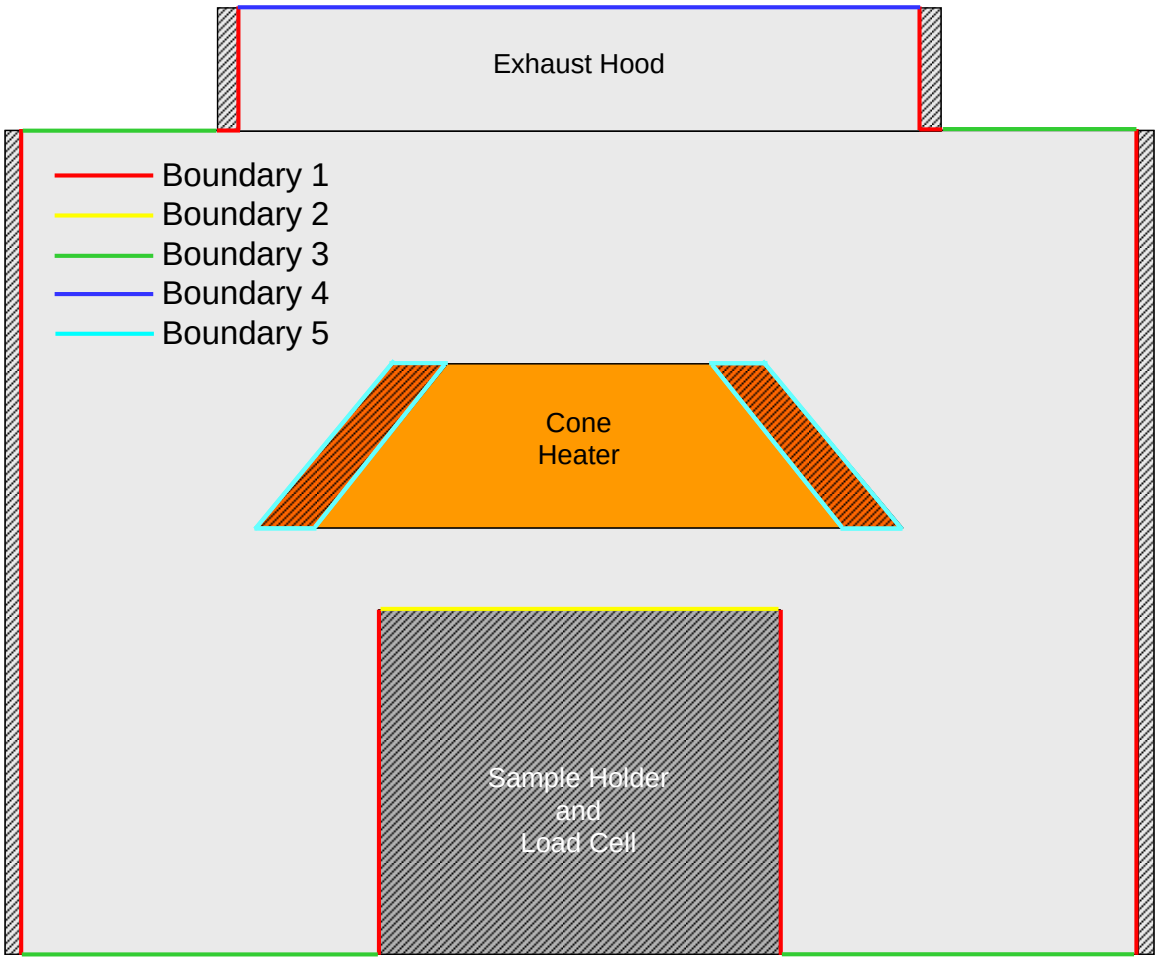

Figure 120 CFD Boundaries Cone

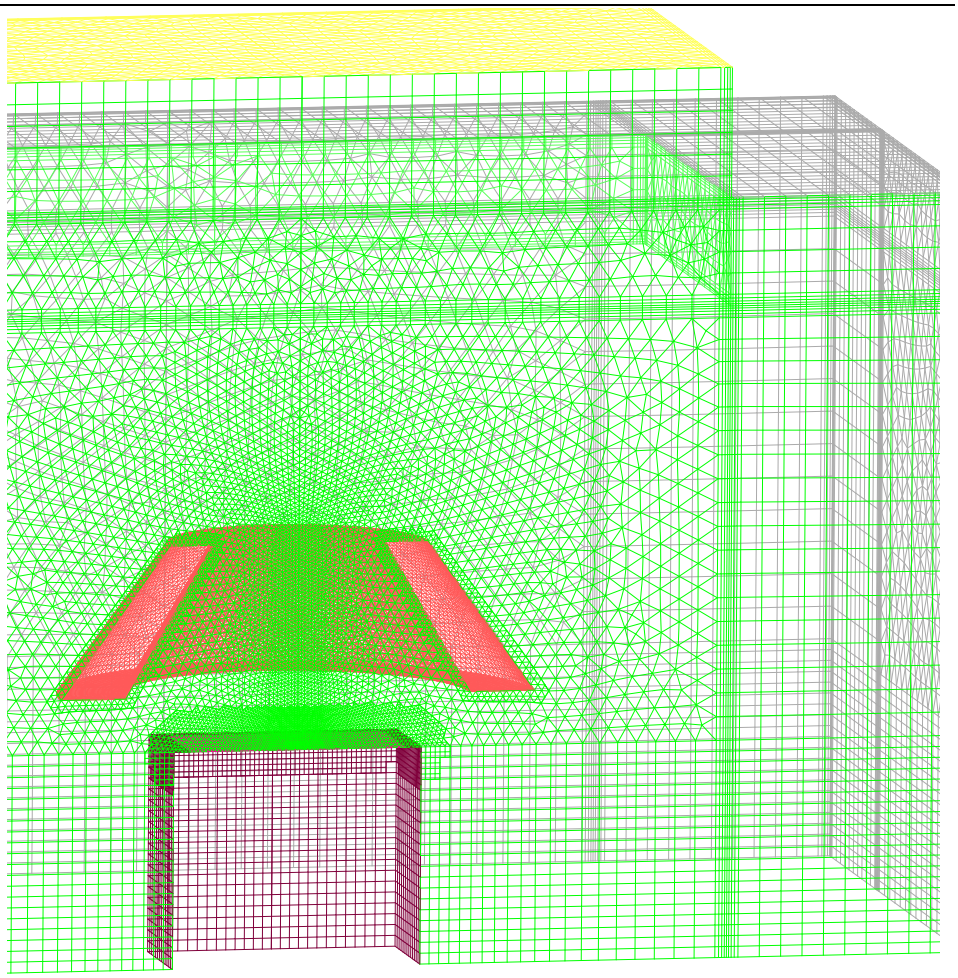

Figure 121 CFD Cone Grid

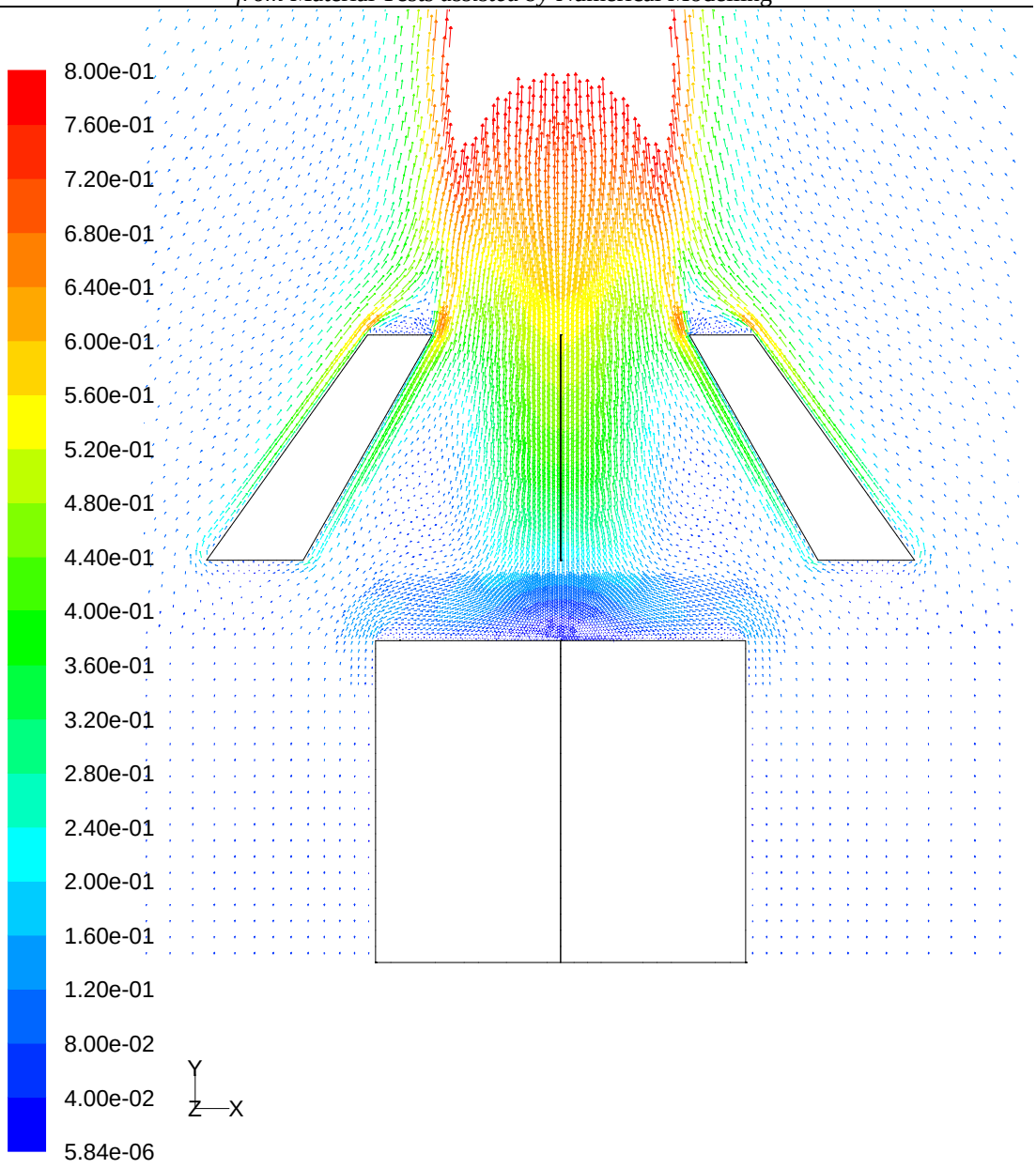

Figure 122 CFD Cone Flow Field [m/s]

A.10.2 FPA

Presented below are the specifics for the conducted CFD modelling in the FPA, staring with the boundary conditions used, then presenting the mesh (Figure 124) and the resulting flow field (Figure 125).

Boundary Conditions

Boundary 1: Wall

- Adiabatic

Boundary 2: Velocity inlet

- Velocity computed from mass loss rate (section 3.10)
- Temperature is the temperature at pyrolysis
- The mass fraction of the fluid is:

Species	Mass Fraction
O_2	0 %
CO_2	dependant on the sample burnt see section 3.3
N_2	0 %
C_3H_8	dependant on the sample burnt see section 3.3

Boundary 3: Velocity inlet

- Velocity provided by the test setup of the FPA
- Temperature of the fluid is ambient
- The mass fraction of the fluid is:

Species	Mass Fraction
O_2	23 %
CO_2	0 %
N_2	77 %
C_3H_8	0 %

Boundary 4: Pressure outlet

- Static pressure is assumed to be zero
- Temperature of the fluid is ambient
- The mass fraction of the fluid is:

Species	Mass Fraction
O_2	23 %
CO_2	0 %
N_2	77 %
C_3H_8	0 %

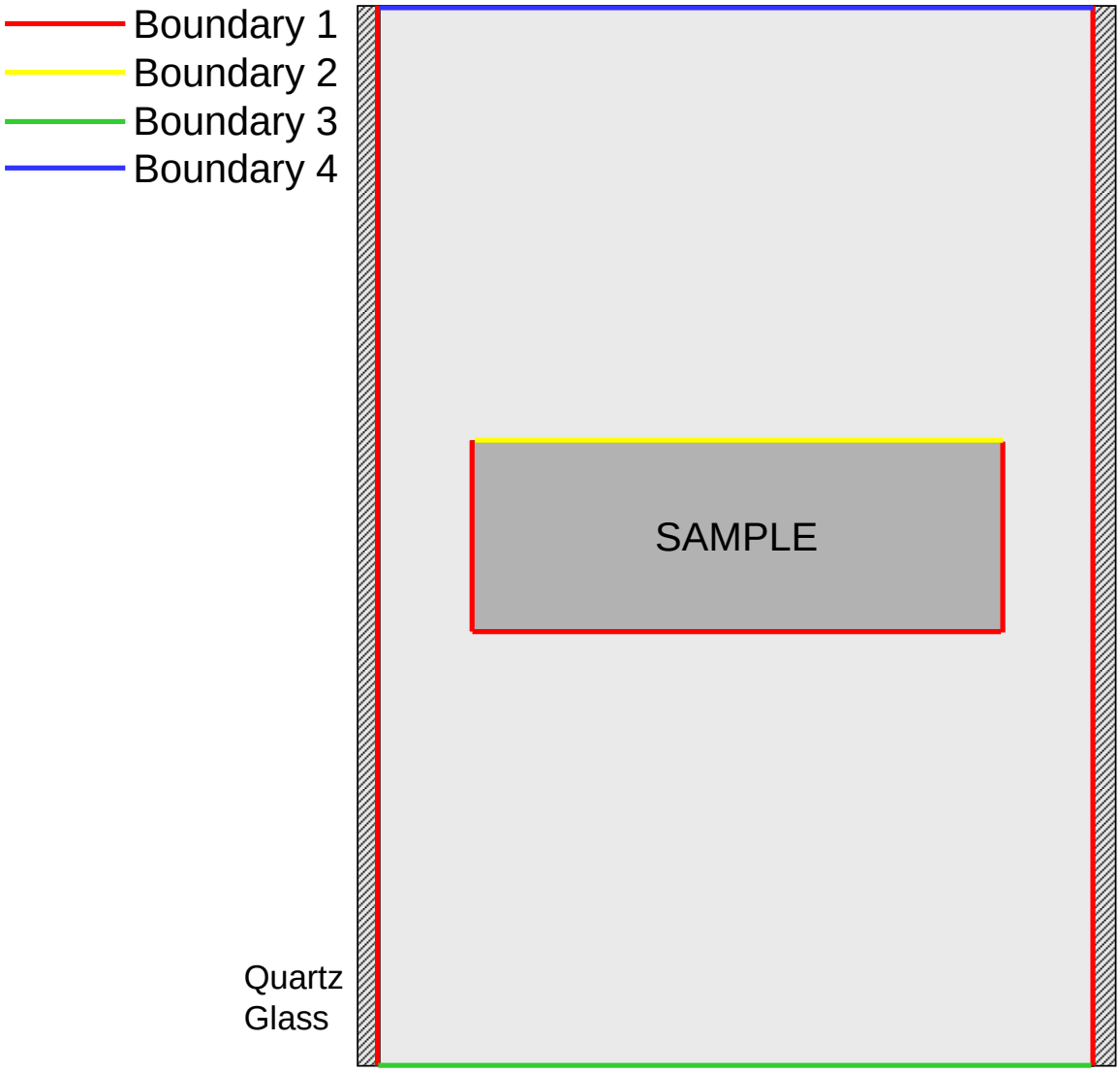

Figure 123 CFD Boundaries FPA

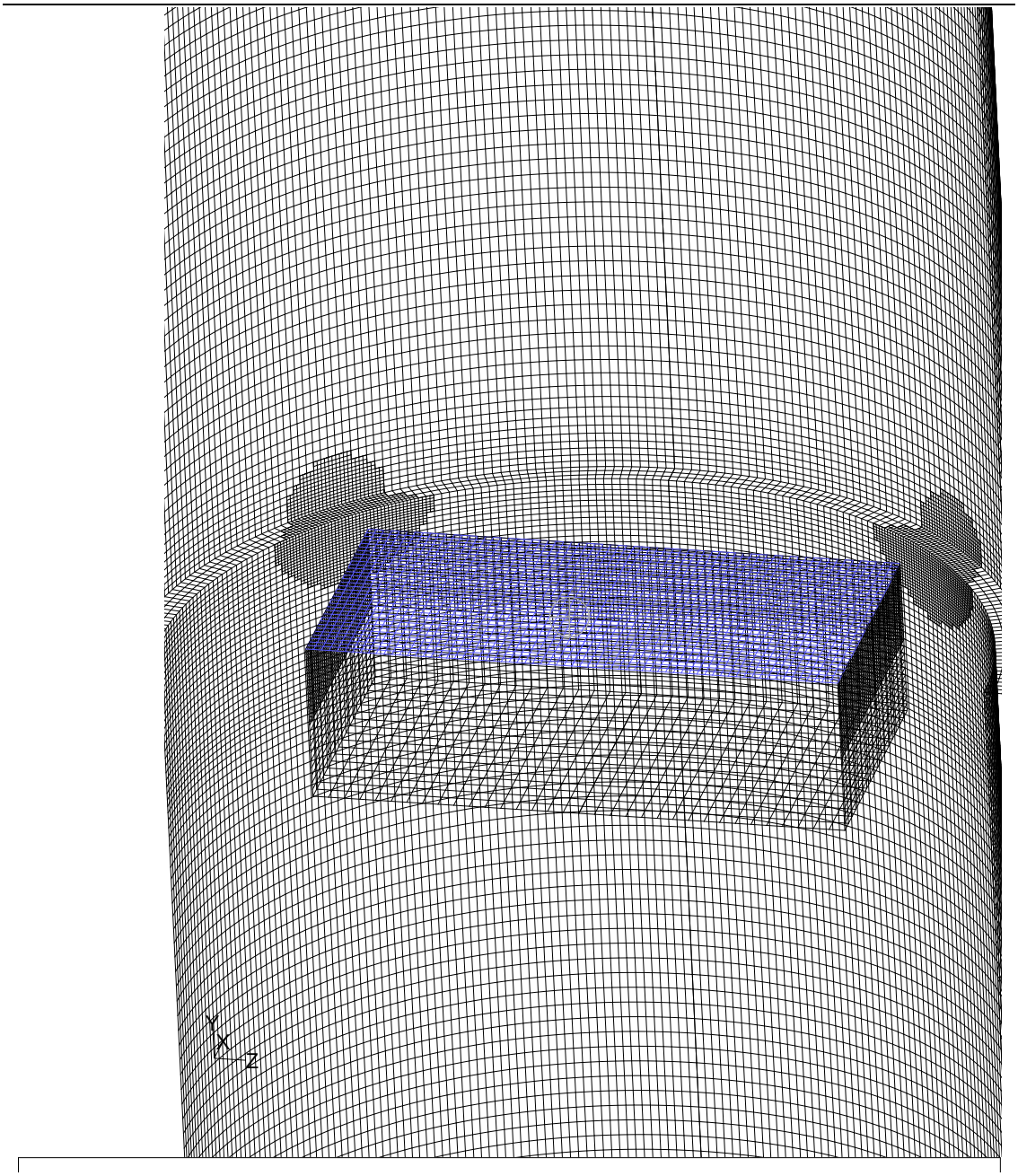

Figure 124 CFD FPA Grid

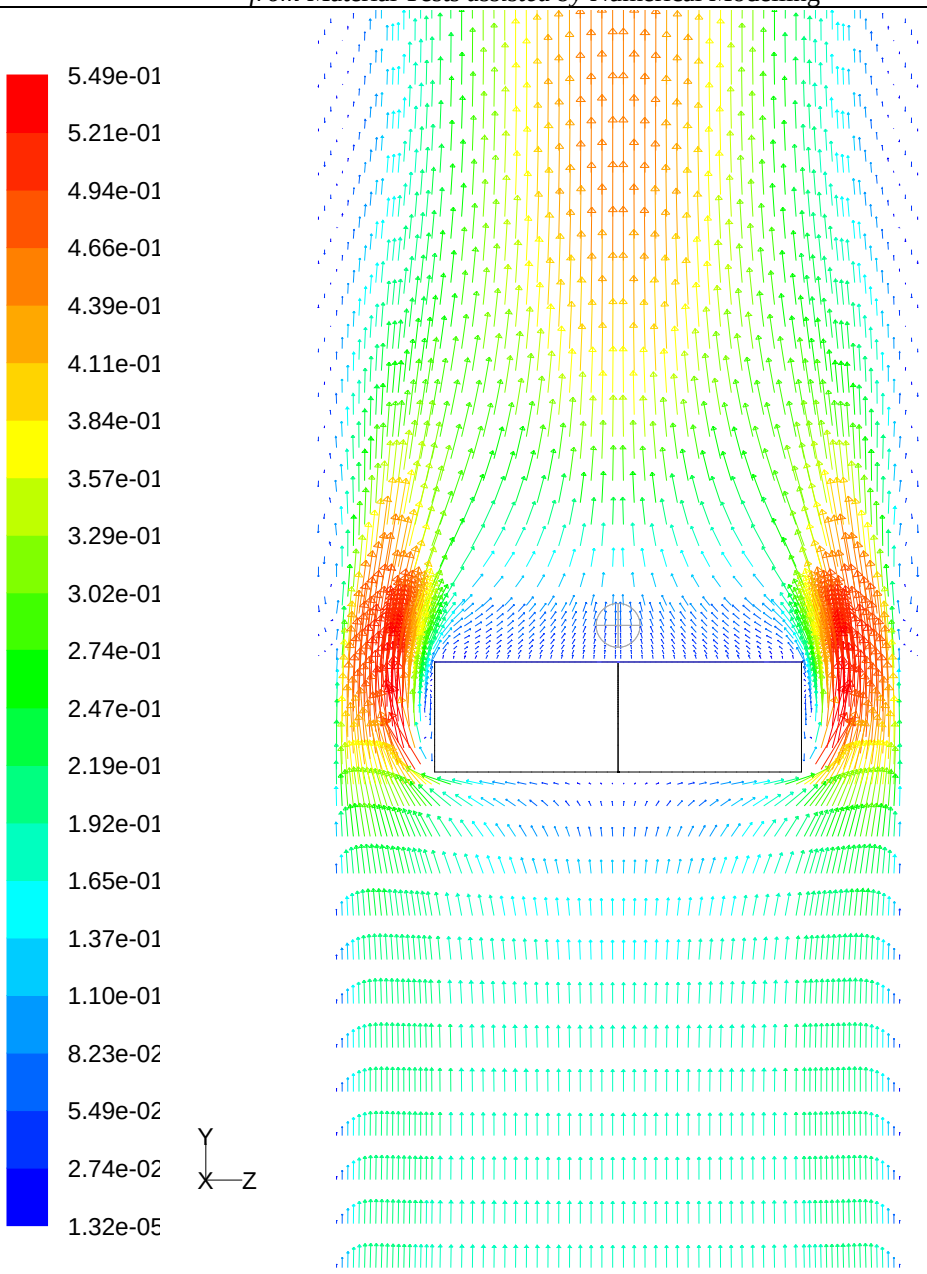

Figure 125 CFD FPA Flow Flied [m/s]

A.11 Exemplary Heat Release Rate (HRR) and Mass Loss Data

A.11.1 PA6

A.11.1.1 Cone Calorimeter

See Figure 33 for Cone: HRR and Mass versus Time of PA6

A.11.1.2 FPA

See Figure 34 for FPA: HRR and Mass versus Time of PA6

A.11.2 PA6+FR

A.11.2.1 Cone Calorimeter

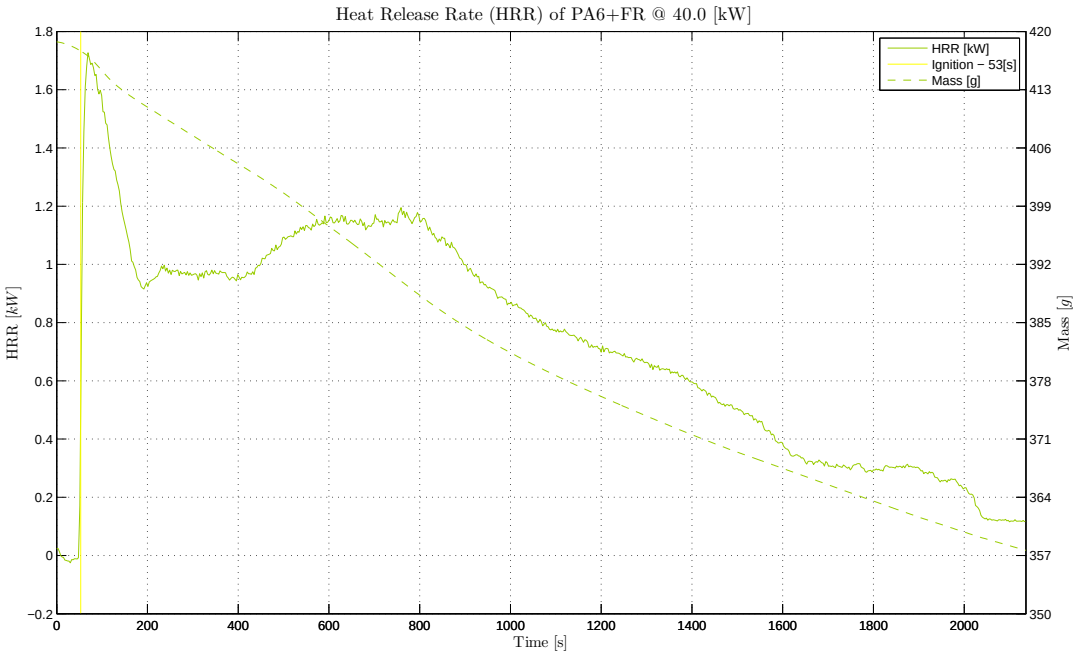

Figure 126 Cone: HRR and Mass versus Time of PA6+FR

A.11.2.2 FPA

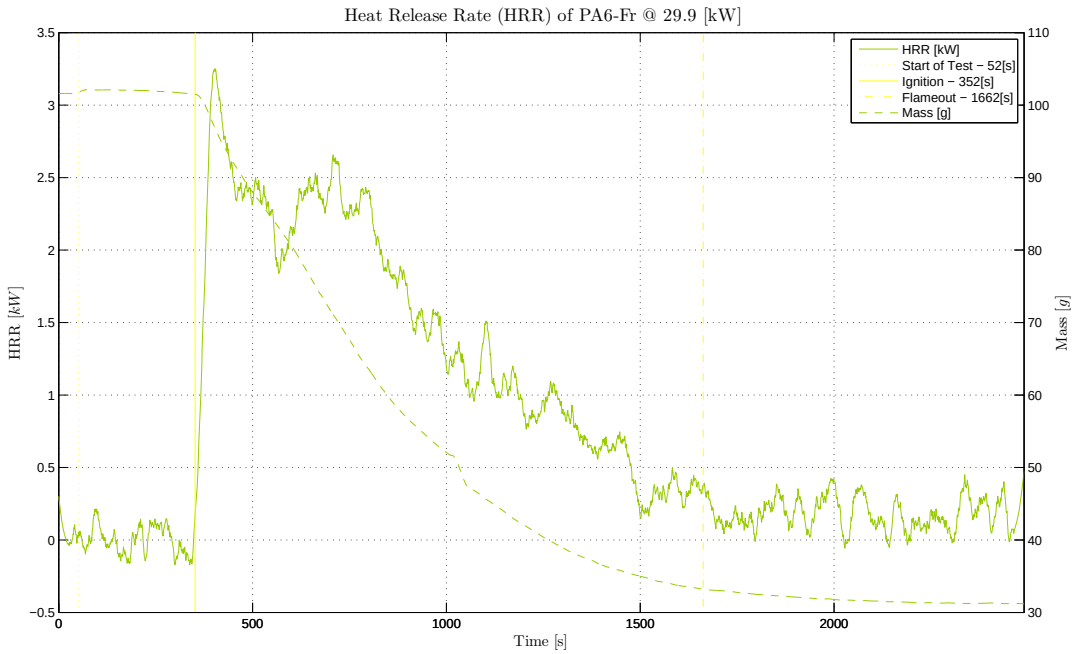

Figure 127 FPA: HRR and Mass versus Time of PA6+FR

A.11.3 PA6+NC

A.11.3.1 Cone Calorimeter

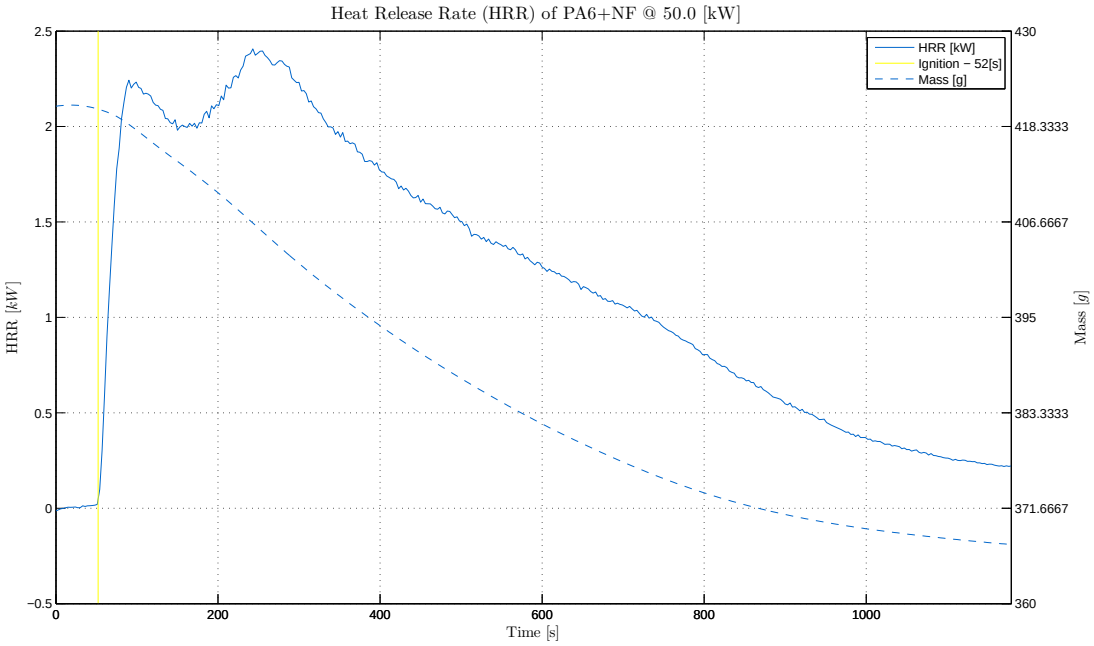

Figure 128 Cone: HRR and Mass versus Time of PA6+NC

A.11.3.2 FPA

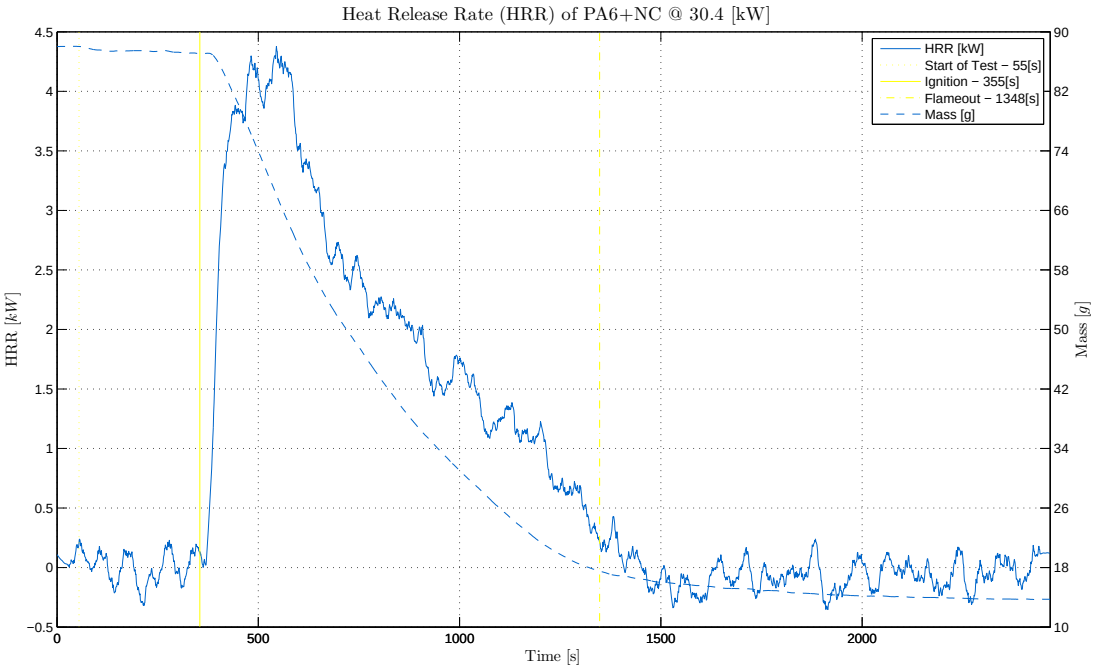

Figure 129 FPA: HRR and Mass versus Time of PA6+NC

A.11.4 PA6+NC+FR

A.11.4.1 Cone Calorimeter

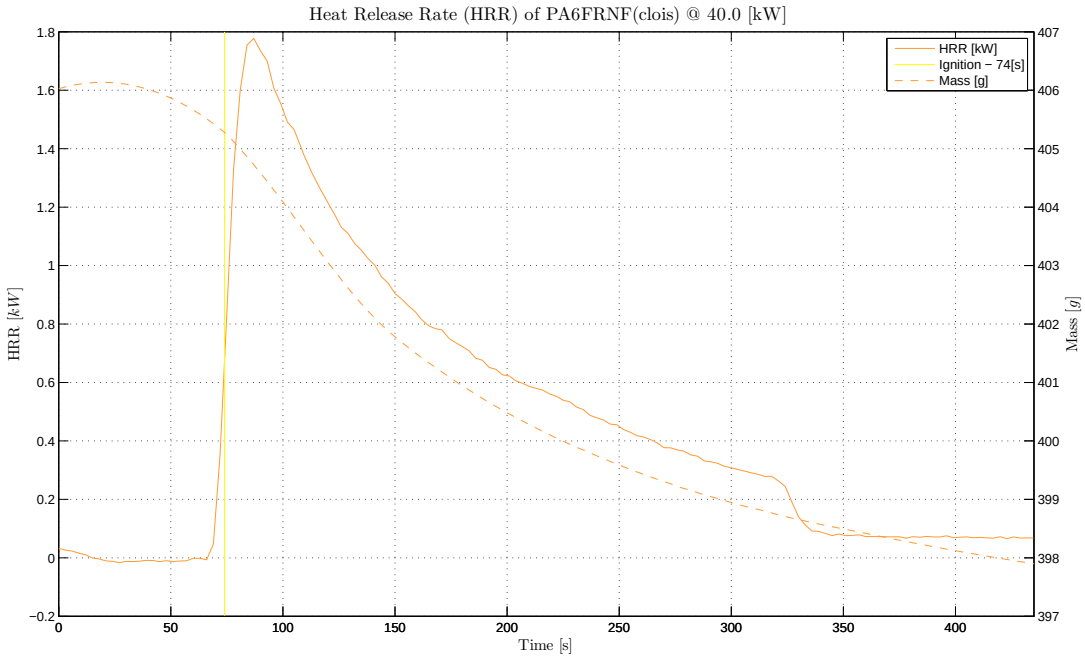

Figure 130 Cone: HRR and Mass versus Time of PA6+NC+FR

A.11.4.2 FPA

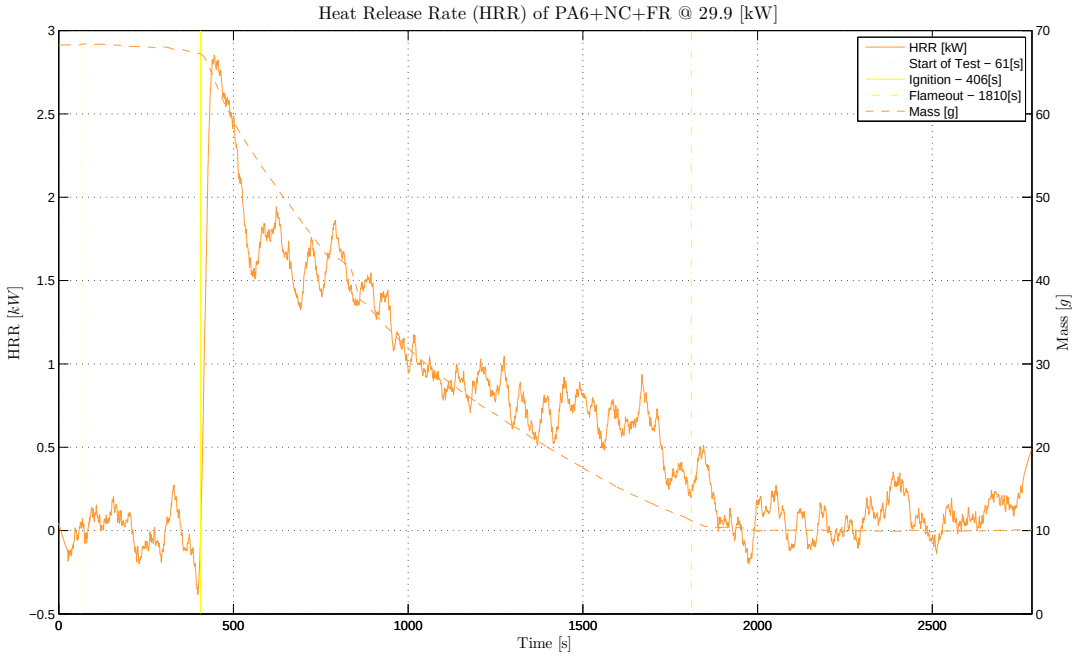

Figure 131 FPA: HRR and Mass versus Time of PA6+NC+FR

A.12 Exemplary Heat of Combustion (ΔH_c)

A.12.1 PA6

A.12.1.1 Cone Calorimeter

See Figure 35 for Cone: Heat of Combustion versus Time of PA6

A.12.1.2 FPA

See Figure 36 for FPA: Heat of Combustion versus Time of PA6

A.12.2 PA6+FR

A.12.2.1 Cone Calorimeter

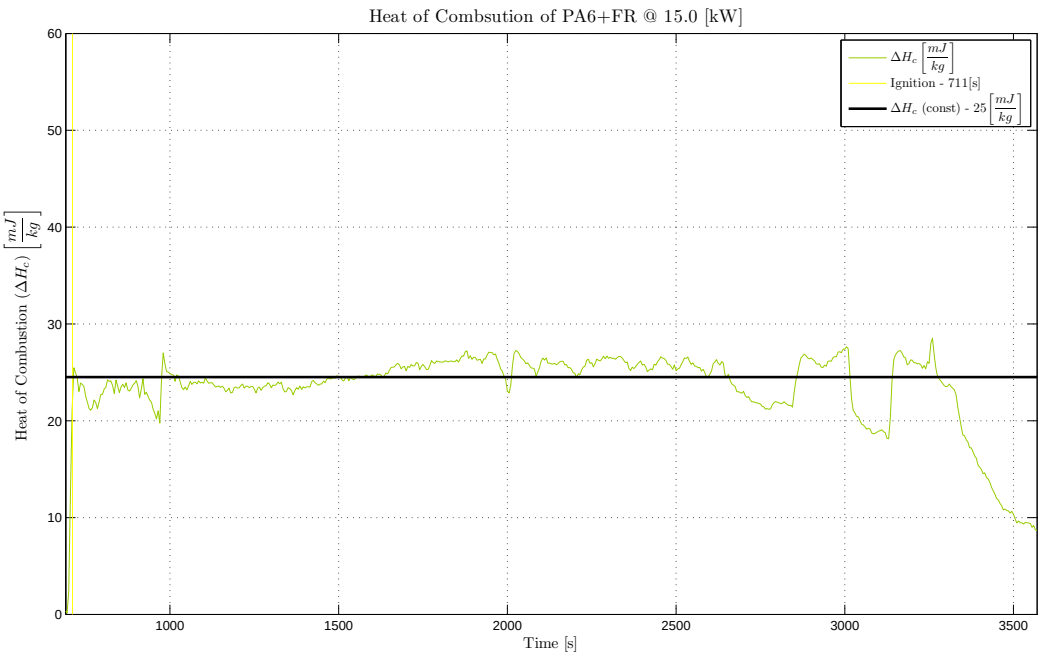

Figure 132 Cone: Heat of Combustion versus Time of PA6+FR at 15kW

A.12.2.2 FPA

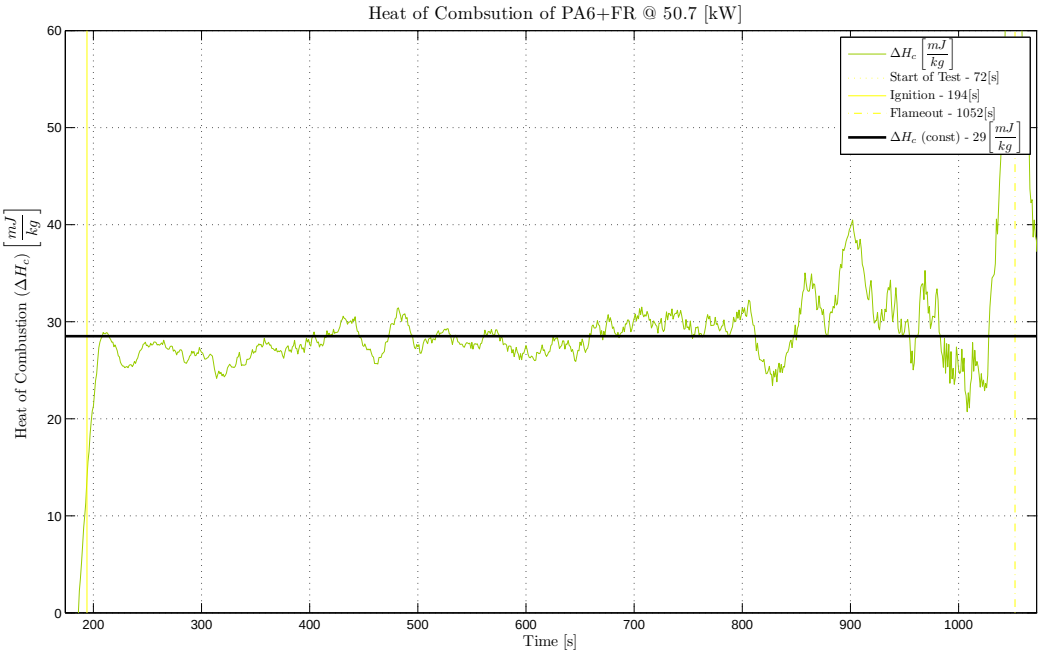

Figure 133 FPA: Heat of Combustion versus Time of PA6+FR at 50kW

A.12.3 PA6+NC

A.12.3.1 Cone Calorimeter

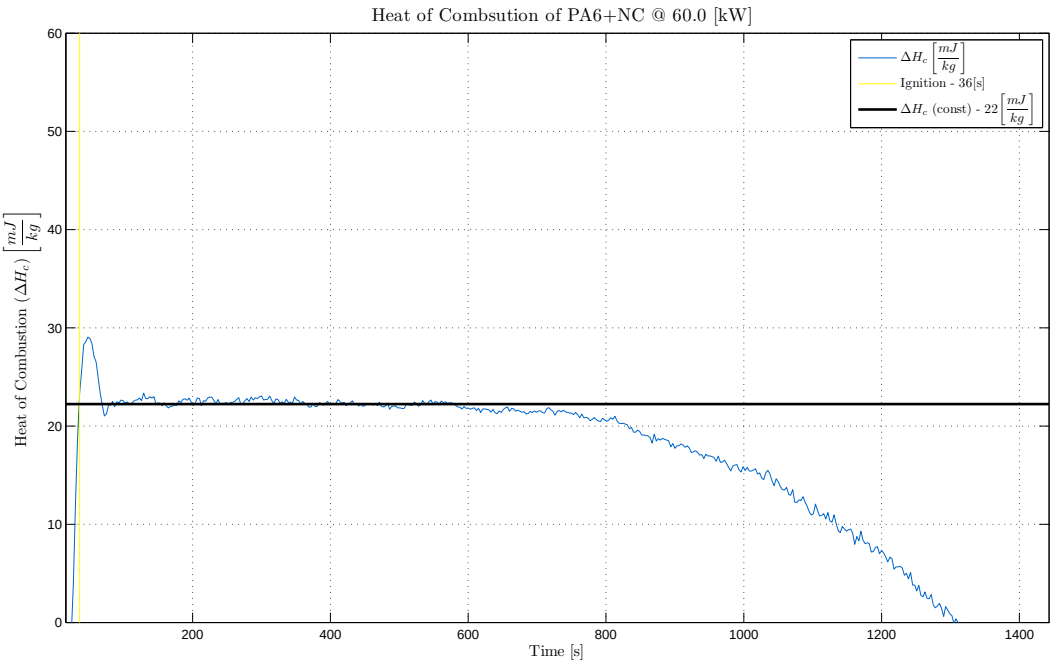

Figure 134 Cone: Heat of Combustion versus Time of PA6+NC at 60kW

A.12.3.2 FPA

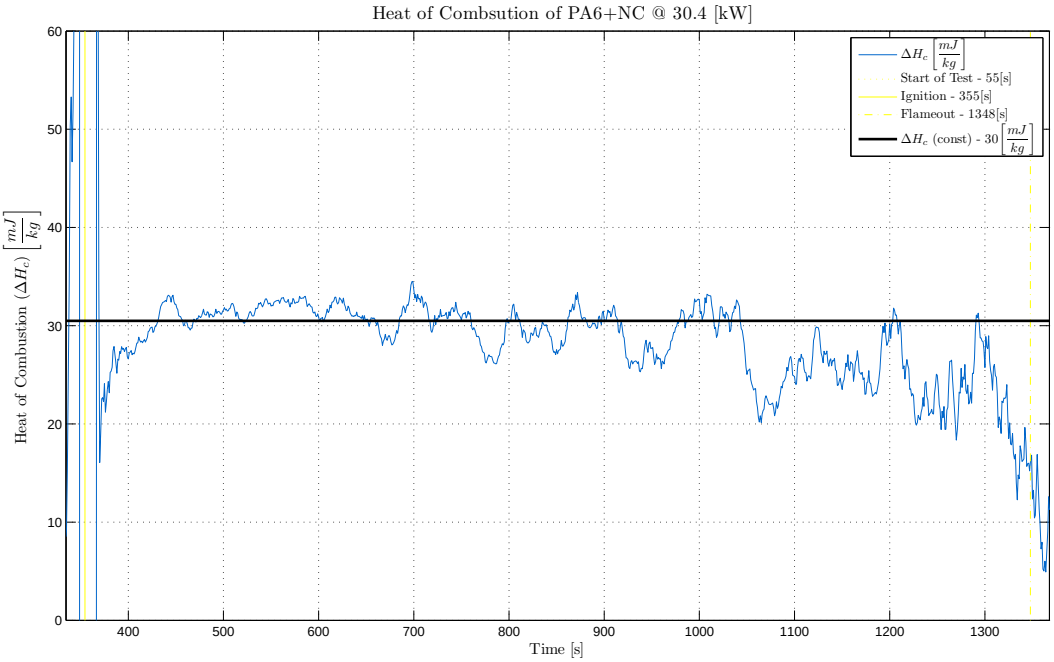

Figure 135 FPA: Heat of Combustion versus Time of PA6+NC at 30kW

A.12.4 PA6+NC+FR

A.12.4.1 Cone Calorimeter

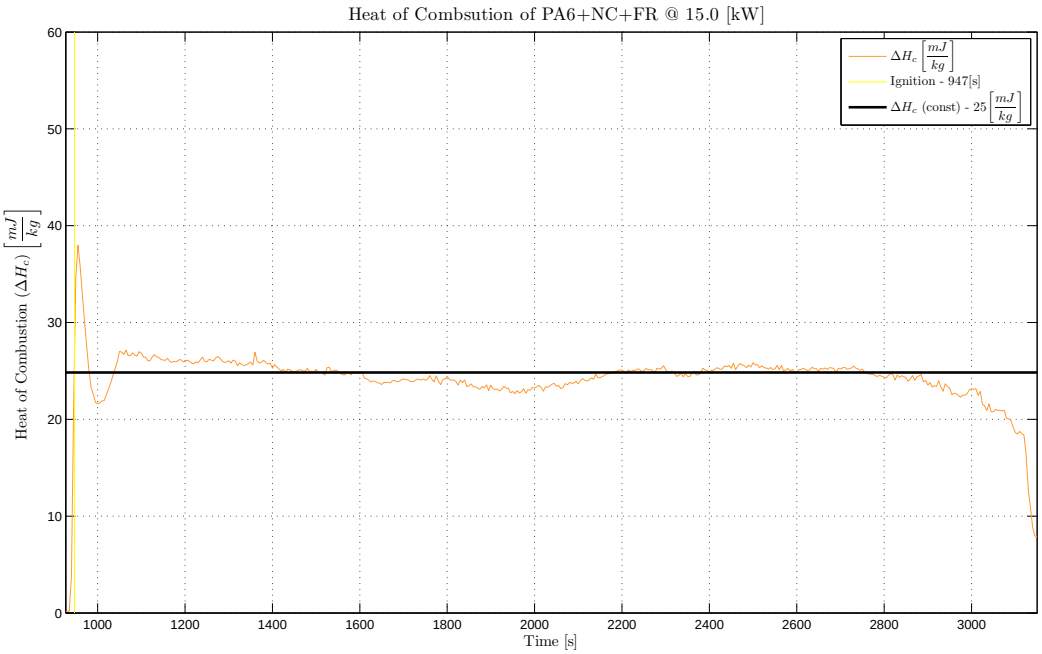

Figure 136 Cone: Heat of Combustion versus Time of PA6+NC+FR at 15kW

A.12.4.2 FPA

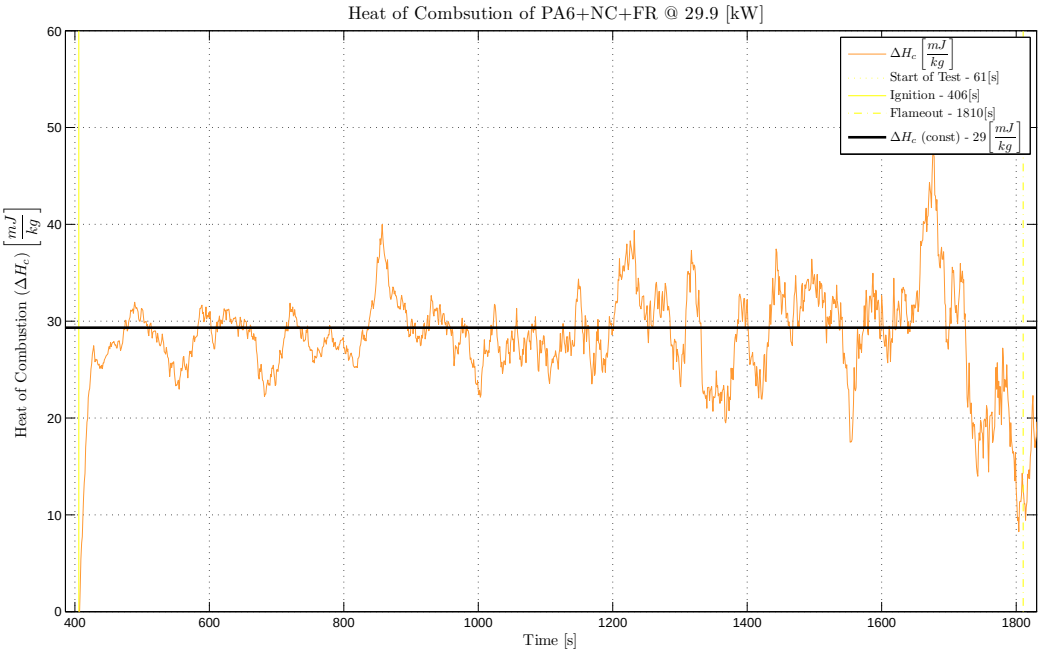

Figure 137 FPA: Heat of Combustion versus Time of PA6+NC+FR at 30kW

Appendix B: PARAMETER DETERMINATION BY MODEL TO DATA FITTING

B.1 In-depth Temperature Data

B.1.1 PA6

See Figure 39 and Figure 40 for in-depth temperature measurements of PA6 at 25 kW and 30 kW respectively.

B.1.2 PA6 + FR

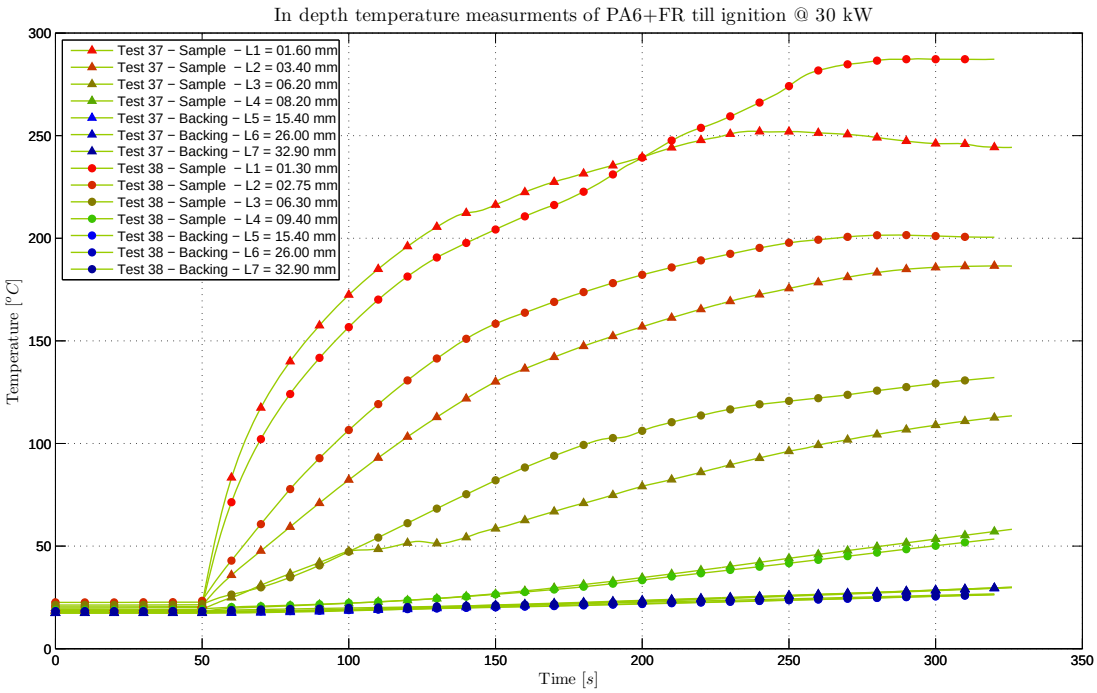

Figure 138 In-depth temperature data of PA6+FR exposed to a radiative heat flux of 30 kW in the FPA

B.1.3 PA6 + NC

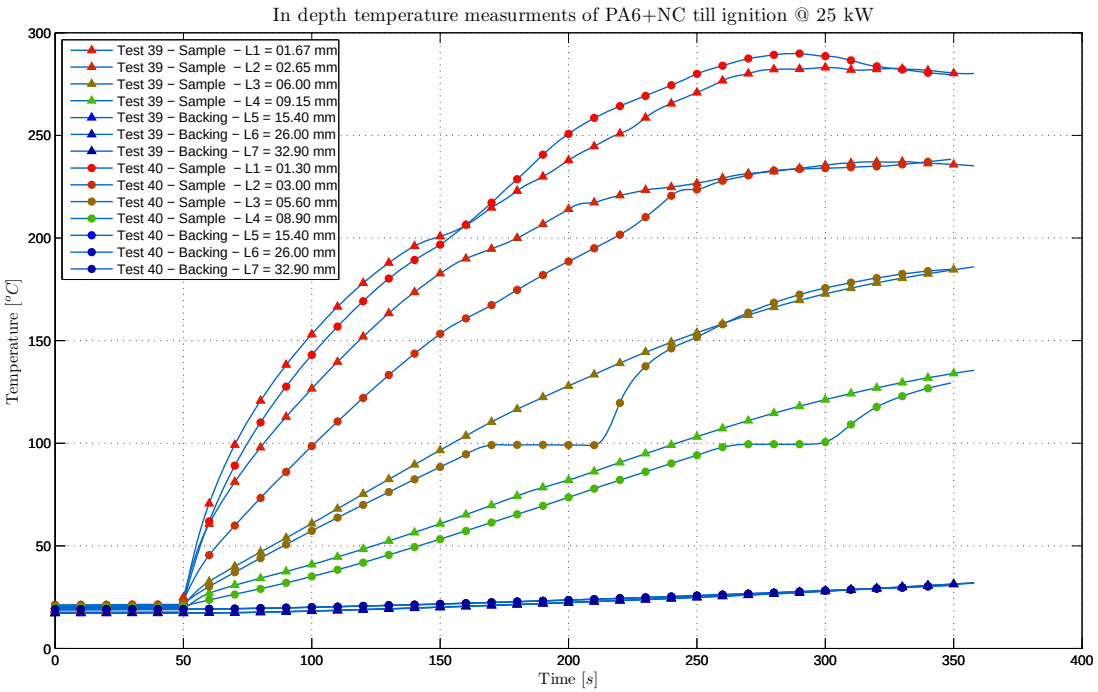

Figure 139 In-depth temperature data of PA6+NC exposed to a radiative heat flux of 25 kW in the FPA

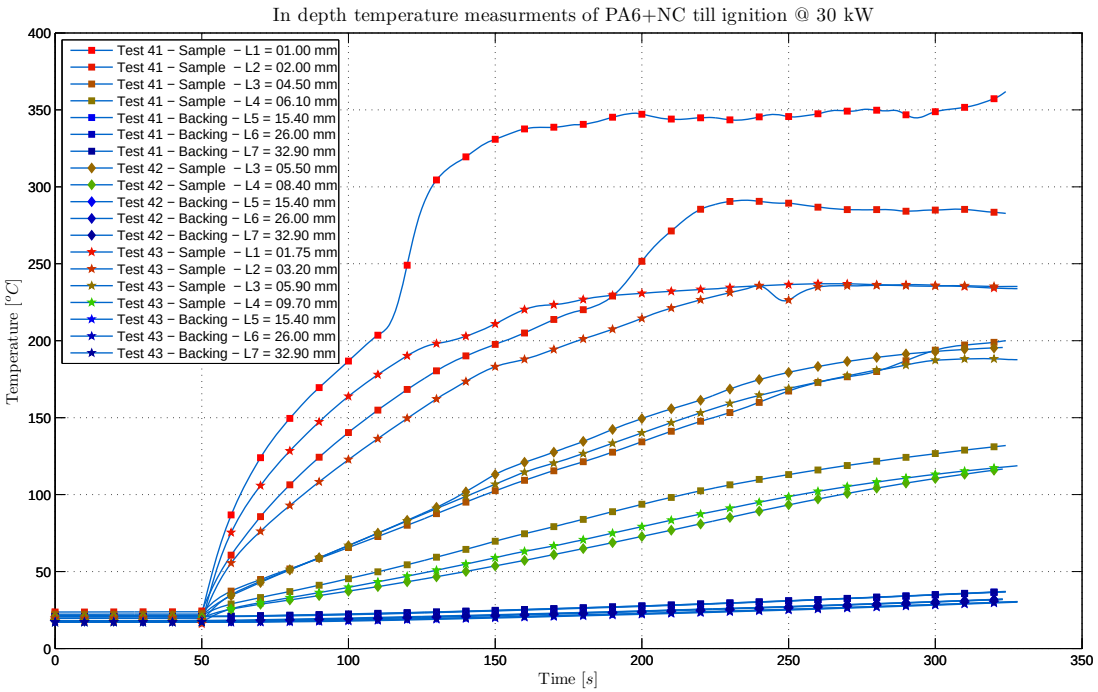

Figure 140 In-depth temperature data of PA6+NC exposed to a radiative heat flux of 30 kW in the FPA

B.1.4 PA6 + NC + FR

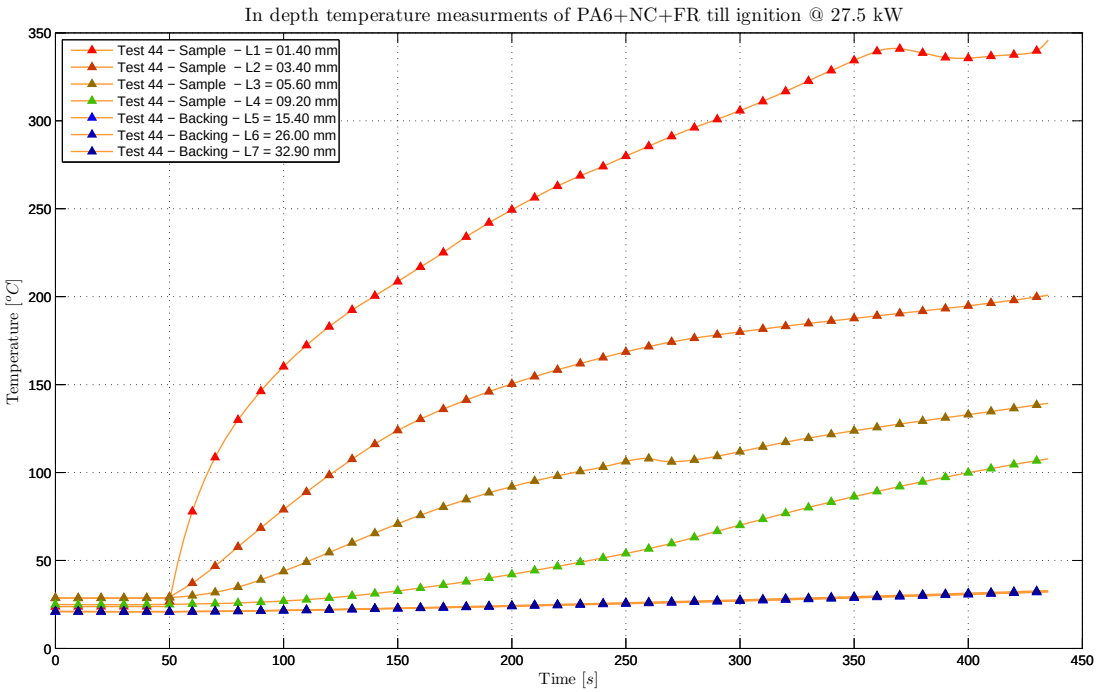

Figure 141 In-depth temperature data of PA6+NC+FR exposed to a radiative heat flux of 27.5 kW in the FPA

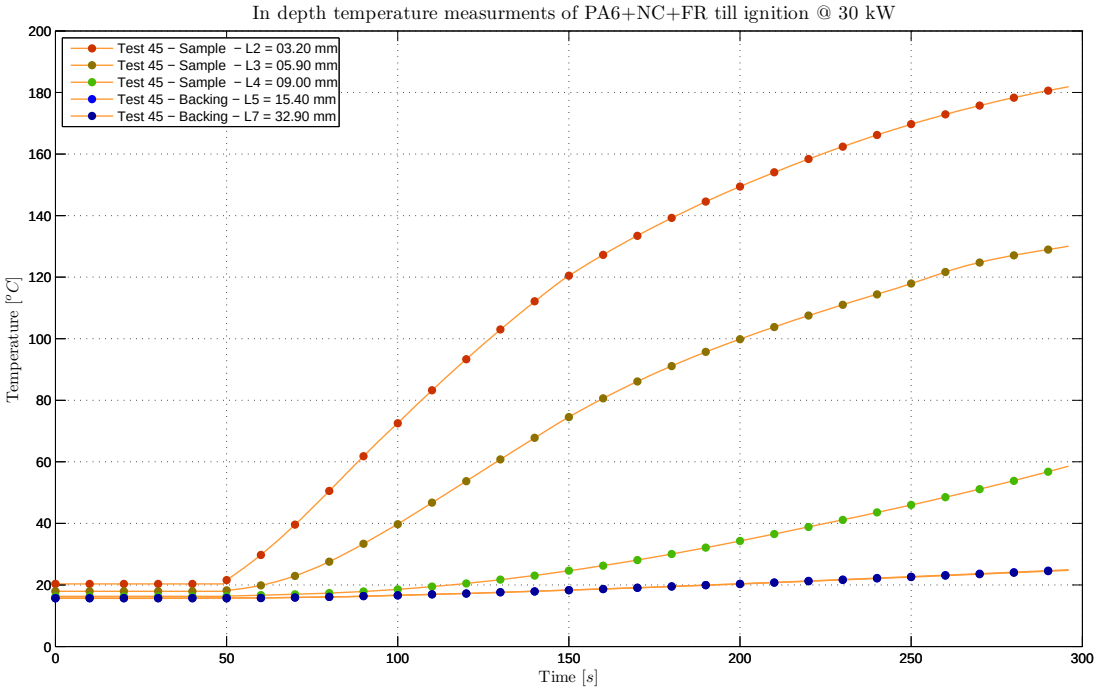

Figure 142 In-depth temperature data of PA6+NC+FR exposed to a radiative heat flux of 30 kW in the FPA

B.2 Mass Loss Data

B.2.1 PA6

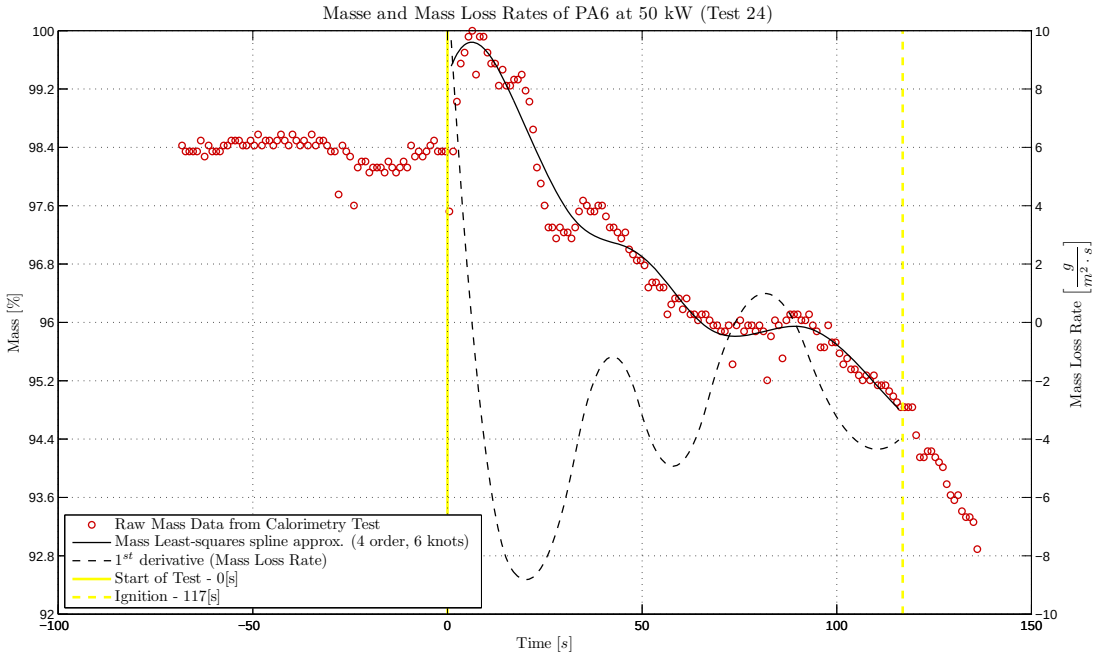

Figure 143 Mass and mass loss rate of PA6 (Test 24)

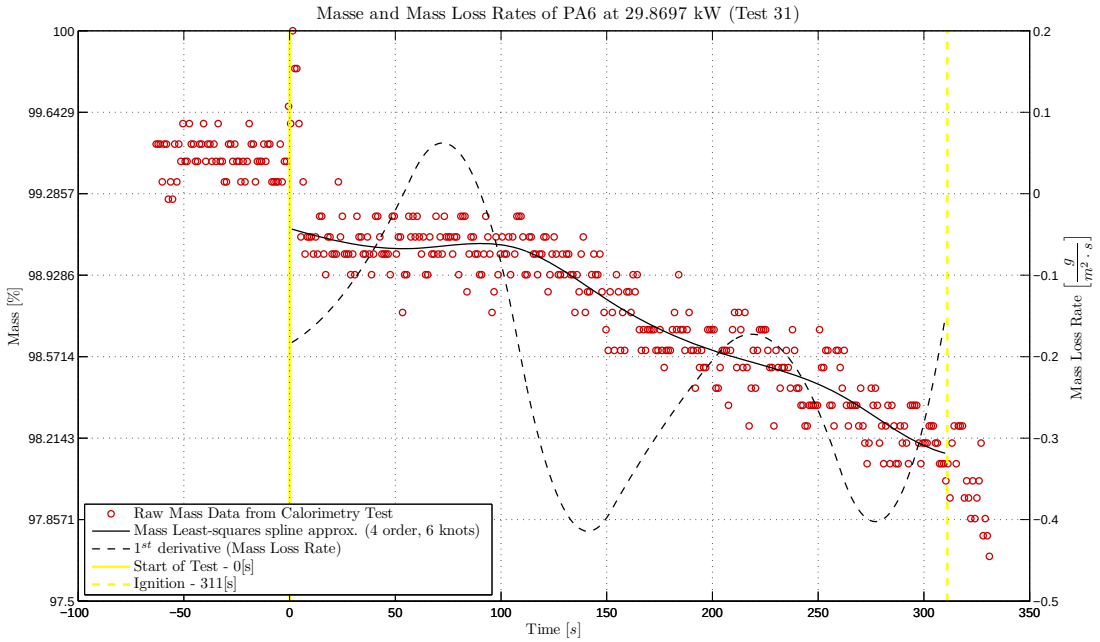

Figure 144 Mass and mass loss rate of PA6 (Test 31)

B.2.2 PA6+FR

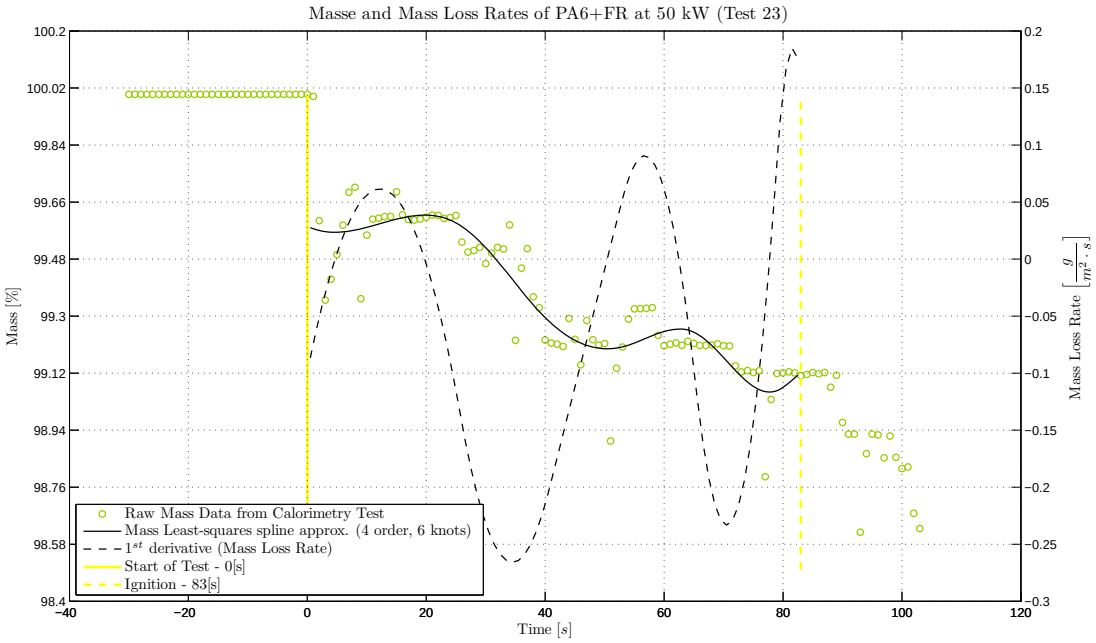

Figure 145 Mass and mass loss rate of PA6+FR (Test 25)

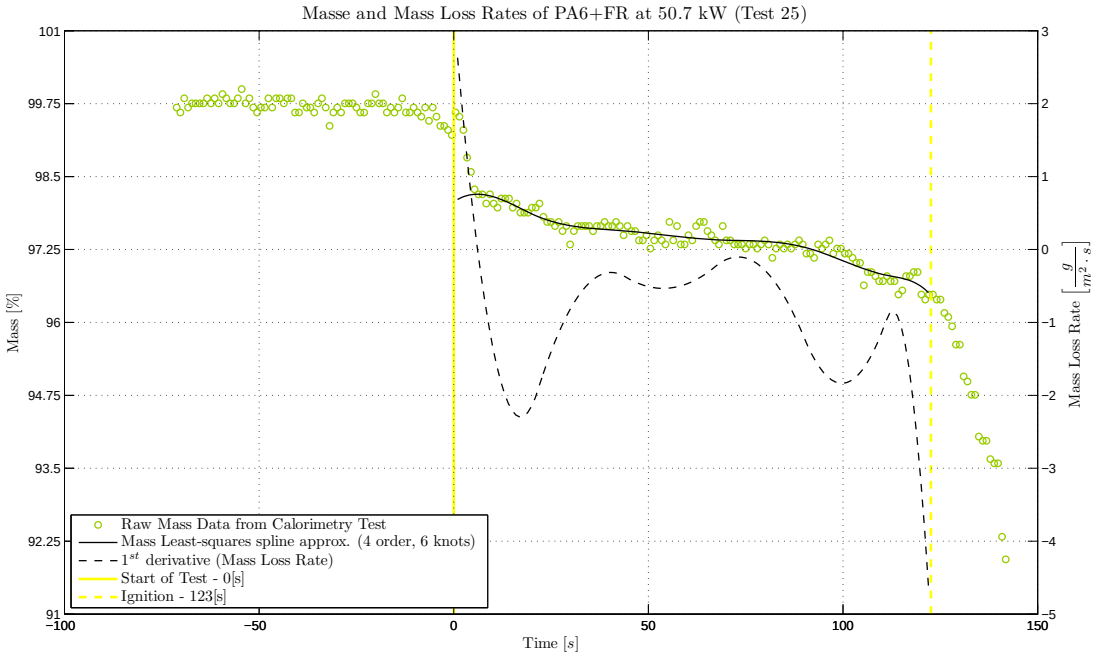

Figure 146 Mass and mass loss rate of PA6+FR (Test 25)

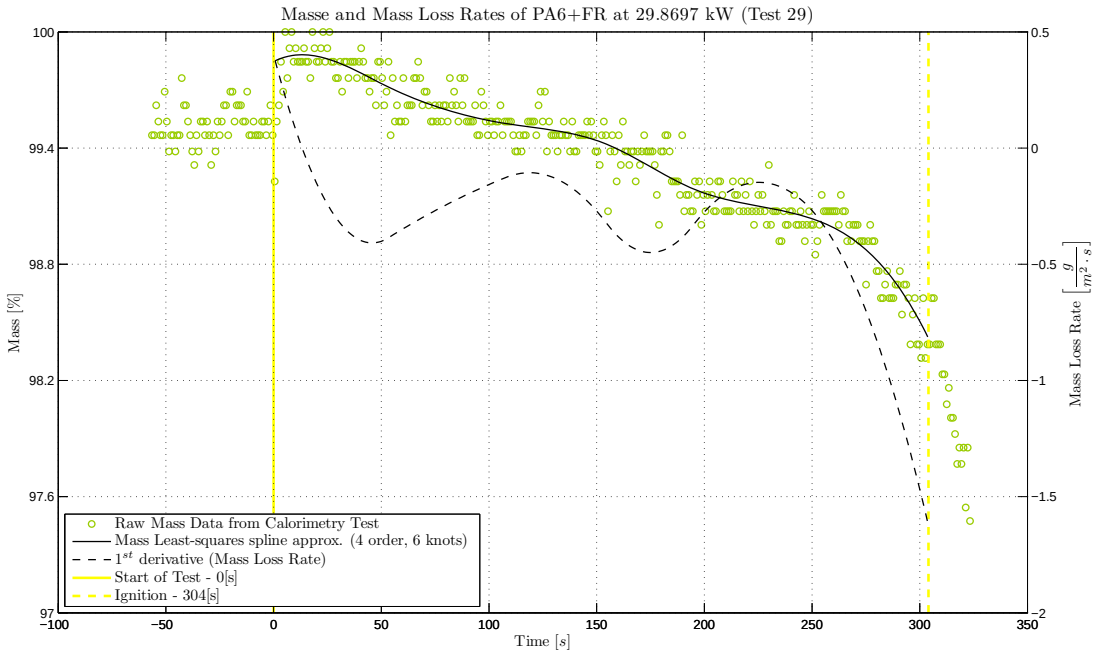

Figure 147 Mass and mass loss rate of PA6+FR (Test 29)

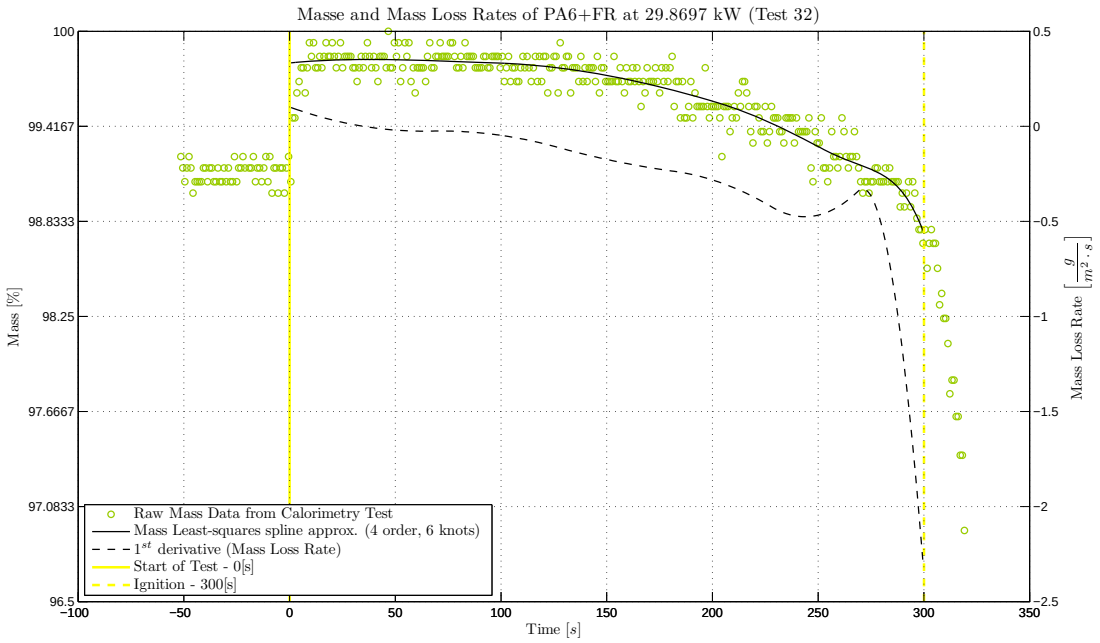

Figure 148 Mass and mass loss rate of PA6+FR (Test 32)

B.2.3 PA6+NC

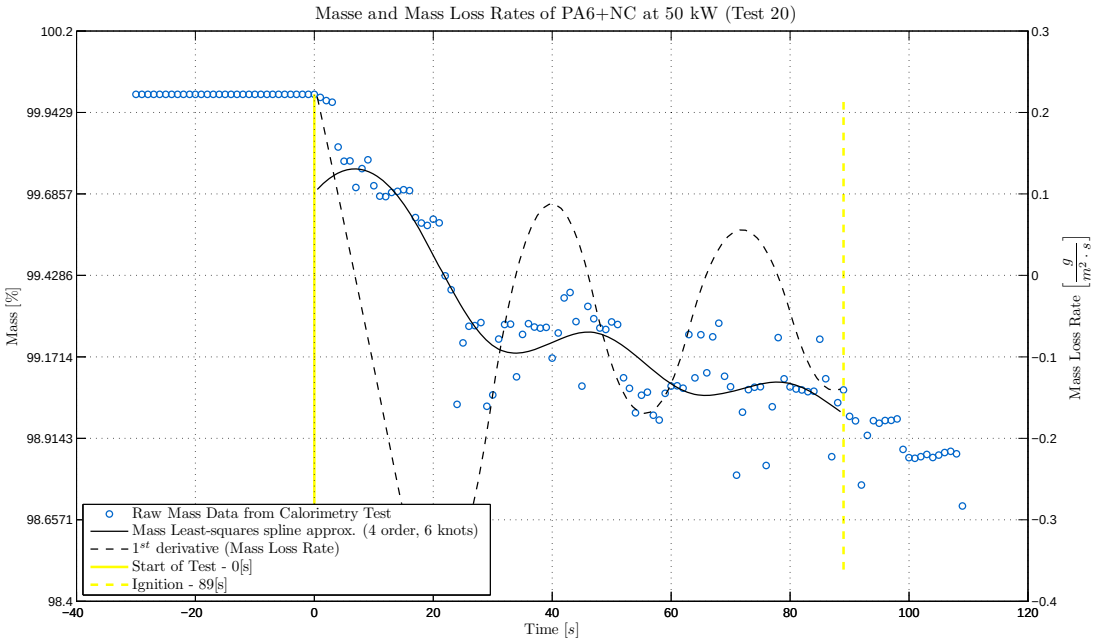

Figure 149 Mass and mass loss rate of PA6+NC (Test 20)

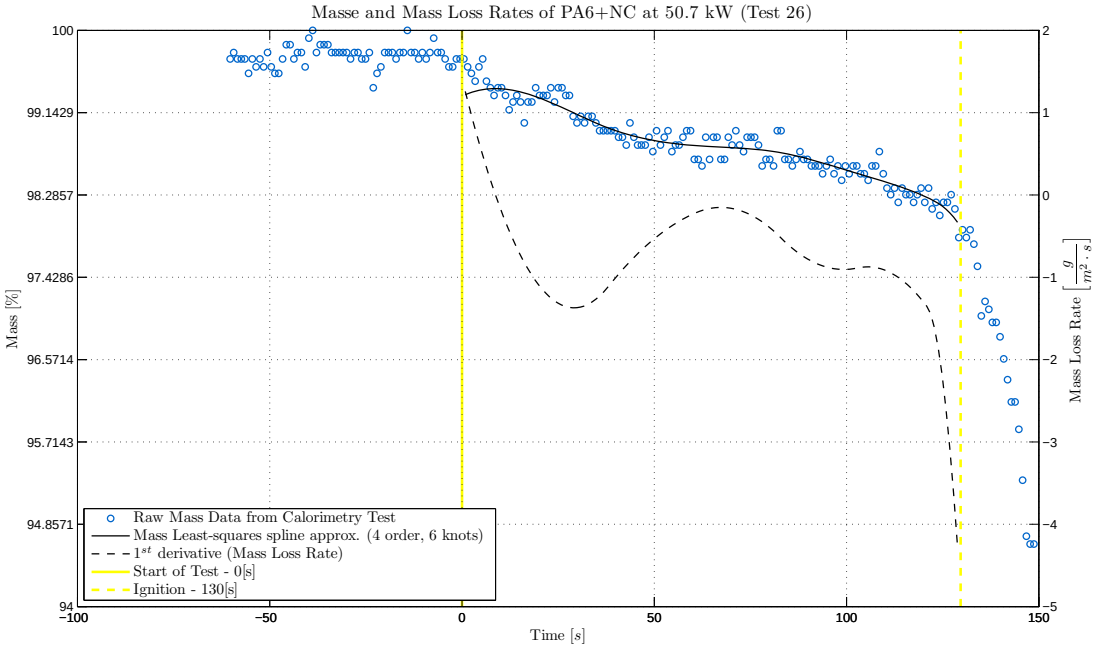

Figure 150 Mass and mass loss rate of PA6+NC (Test 26)

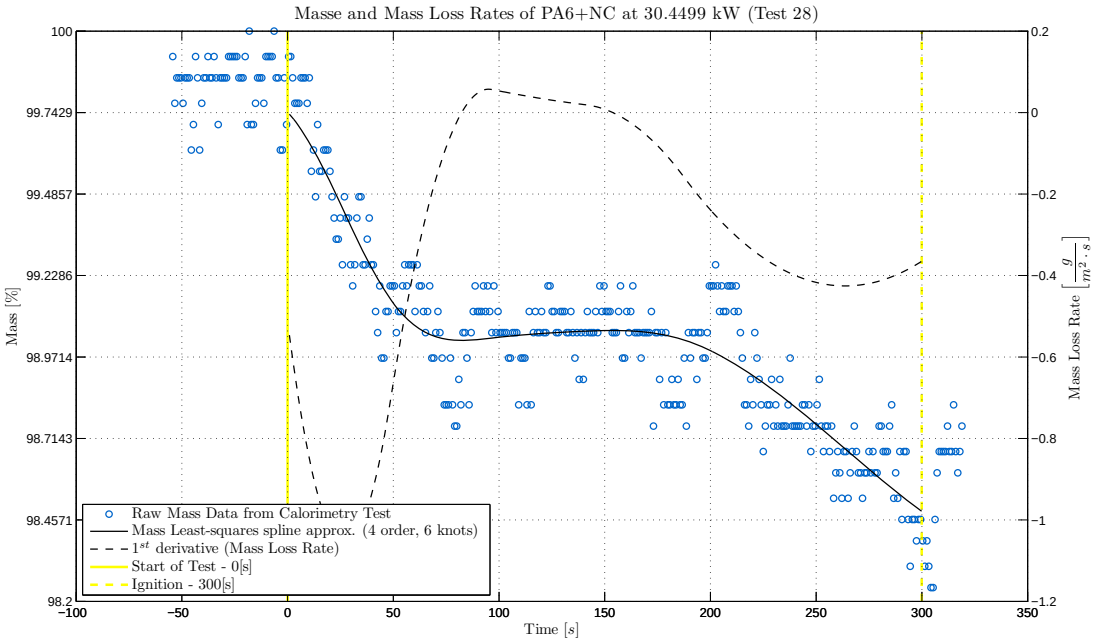

Figure 151 Mass and mass loss rate of PA6+NC (Test 28)

B.2.4 PA6+NC+FR

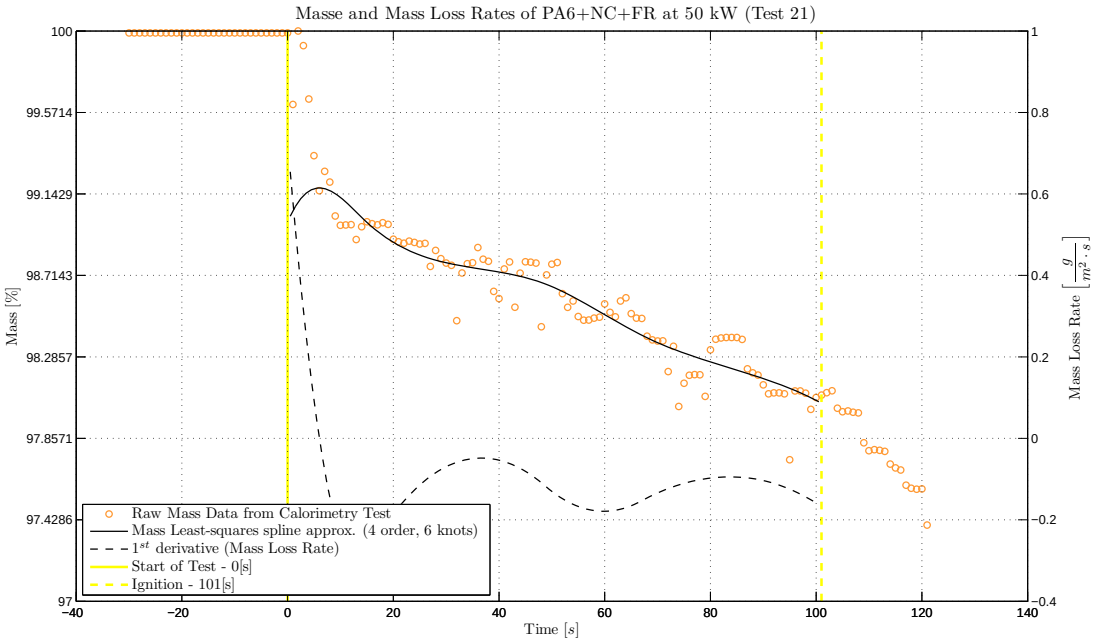

Figure 152 Mass and mass loss rate of PA6+NC+FR (Test 21)

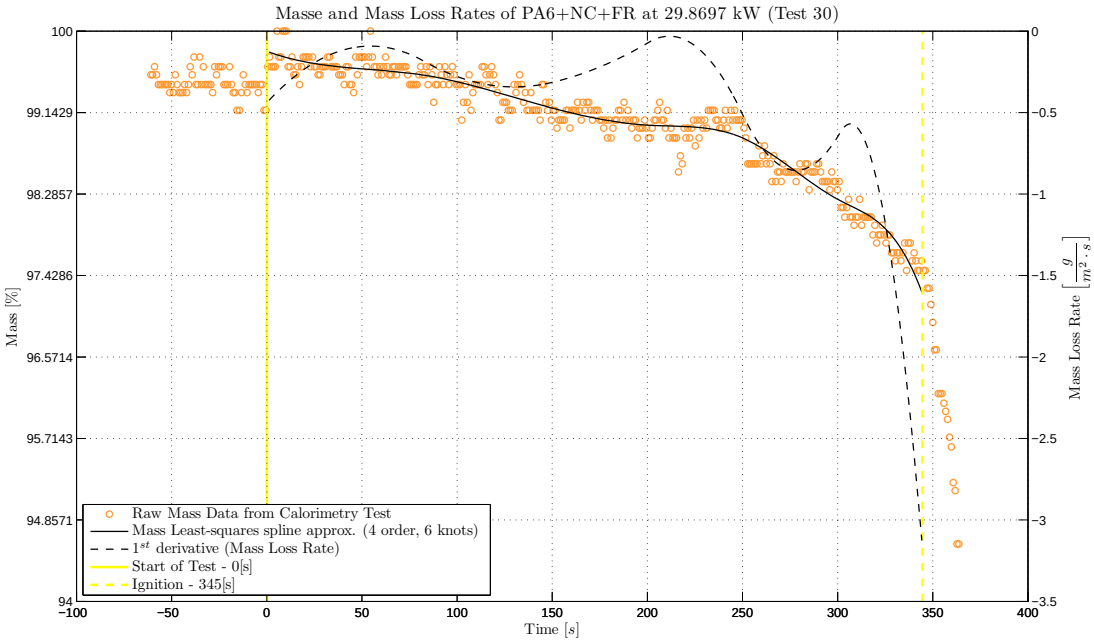

Figure 153 Mass and mass loss rate of PA6+NC+FR (Test 30)

B.3 Material specific search range stipulation

B.3.1 PA6

See the end of section 5.3.

B.3.2 PA6+FR

For the determination of the (intrinsic or global) material properties of this material only two, due to material limitations, different tests have been analysed. Both at a heat flux (q_e) of 30 kW/m^2. The overall initial thickness (δ_0) that was taken into consideration for the analysis of these tests was the 37.5 mm combined thickness of the tested sample and the aluminium block with a cell number (n_{cell}) of 300 , resulting in a cell thickness of 0.125 mm. The ambient gaseous mass fraction (Y_∞) was taken to be 23% for O_2 and 77% for N_2. Gpyro handles, as previously described, the input of temperature dependant parameters in a specific way (see Table 22). Therefore, it was necessary to curve fit the function to the results of section 3.9. This gave the heat transfer coefficient (h_{c0}) and its exponent (n_{hc}) the FPA of 12.14 W/m^2-K and 0.81 respectively as presented in Appendix B.4.4.

As determined from the TGA analysis in section 3.2, the reduced chemical reaction mechanisms in air of PA6+FR follow a four-step reaction process shown in Table 12 and Table 9. From this analysis, it is possible to tell how the material is chemically reacting when heated, even though it being in a reduced manner. An option would be to expand the later conducted parameter search to, also, find the ideal reaction step model, as well as the reaction types. Since obtaining these is in itself very challenging (due to the high level of complexity), it has been opted to directly apply the in section 3.2 determined best reduced chemical reaction mechanism. The kinetic properties for the reaction of PA6+NC in air (Table 12) serve to keep the search area limited, in order to insure that the model could converge. Attempts with a too large search region ended in endless calculations caused by the pre-exponential and exponential factor being too different. Table 12 provides most of the condensed-phase reactions properties of Table 27. The remaining two parameters for each of the

four reactions are the heat of pyrolysis (ΔH_{vol}) and χ, the parameter affecting swelling. Though the first of these parameter was never obtained, as explained in section 3.11, its values are assumed to be in the range of $1 \cdot 10^6$ J/kg. Though the first of these parameter was never obtained, as explained in section 3.11 its assumed values are in the range of $1 \cdot 10^6$ J/kg. Figure 20 in comparing with Figure 76 and Figure 77, show that swelling occurred before the reduced chemical reaction mechanisms was taking place. Therefore, it was assumed that swelling only occurred for the virgin material. From observations, it is clear that PA6+FR swells, therefore the search boundary was set between 0 and 1 indicating that. As in equations (4) - (7), and Table 27 the index affecting the oxygen reaction $i_{O_2}\,rxn$ is set to "1".

As in the TGA analysis, four reduced chemical reaction mechanisms were distinguished. This leads us to five different species including the initial/virgin material. For each of these species, the physically possible initial search range of the properties determined in chapter 3 (numbers in brackets "( )") are presented. It is possible to assign temperature dependant values for the thermal conductivity, density and specific heat capacity. This added degree of freedom could conceivably lead to issues of convergence. Since only limited data on the temperature dependency for the thermal conductivity and the density for the temperature range in question was available (see Table 17 and Appendix B.4.3), it was decided to use for PA6+FR the average for the thermal conductivity for the temperature range in question of the virgin material ($n_{kz} = 0$). Temperature dependant values of the specific heat capacity and the density of the virgin material are being searched for or used. Since limited knowledge is available for the intermediate and residue species their thermal properties shall be assumed constant ($n_{kz} = n_\rho, = n_c = 0$). This is the case except for the virgin material where there is independent data available, as presented in section sections 3.5, 3.6 and 3.7. The values of Table 40 are mere educated guesses with the help of the literature [25, 31].

Symbol	**Units**	Virgin	Intermediate 1	Residue 1	Intermediate 1	Residue 2
k_{0z}	W/m-K	0.01-3 (0.247)	0.01-20	0.01-20	0.01-20	0.01-20
ρ_0	kg/m^3	900-1500 (1111)	100-2000	100-2000	100-2000	100-2000
n_ρ	-	-2-0 (-1.22)	0	0	0	0
c_0	J/kg-K	100-4500 (1515)	100-4500	100-4500	100-4500	100-4500
n_c	-	0.769	0	0	0	0

Table 40 PA6+FR: thermal conductivity, density and specific heat capacity

It is assumed that of the differentiated species only the virgin material (the PA6+FR itself) undergoes the process of melting. The required parameters for gpyro are obtained from the analysis in section sections 3.5, 3.6 and 3.7. From Table 15, the melting temperature (T_m) of 488 K and the latent heat of melting (ΔH_m) of 53000 J/kg can be obtained. A reasonable range between 423 and 523 K and 20,000 and 300,000 J/kg was used when searching for these properties. From Figure 97 it can be assumed that σ_m^2 is in the range between 16 and 225 K^2 while from Figure 155, the best normal distribution fit was reached with 52 K^2, using the root mean squared error regression analysis.

The remaining parameters considered here, are the ones presented in Table 41. These parameters have not been obtained elsewhere, thus, have to either be assumed or be obtained in an inverse manner. To help narrow down their physically possible values, the standard literature of this process has been consulted [25, 31, 102, 104, 106].

Symbol	**Units**	Virgin	Intermediate 1	Residue 1	Intermediate 1	Residue 2
E	-	0.3-0.99	0.3-0.99	0.3-0.99	0.3-0.99	0.3-0.99
K	m^{-1}	0^0-10^6	0^0-10^6	0^0-10^6	0^0-10^6	0^0-10^6
γ	m	0-0.001	0-0.001	0-0.001	0-0.001	0-0.001
K_z	m^2	10^{-20}-10^{-5} ($1.46\cdot10^{-12}$)	10^{-20}-10^{-5}	10^{-20}-10^{-5}	10^{-20}-10^{-5}	10^{-20}-10^{-5}
ρ_{s0}	kg/m^3	900-2000	100-2000	100-2000	100-2000	100-2000

Table 41 Used values for the PA6+FR layer

B.3.3 PA6+NC

For the determination of the (intrinsic or global) material properties five different tests have been analysed. Two of which have been conducted at a heat flux (q_e) of

25 kW/m^2 and three at 30 kW/m^2. The overall initial thickness (δ_0) that was taken into consideration for the analysis of these tests was the 37.5 mm combined thickness of the tested sample and the aluminium block with a cell number (n_{cell}) of 300, resulting in a cell thickness of 0.125 mm. The ambient gaseous mass fraction (Y_∞) was taken to be 23% for O_2 and 77% for N_2. Gpyro handles, as previously described, the input of temperature dependant parameters in a specific way (see Table 22). Therefore, it was necessary to curve fit the function to the results of section 3.9. This gave the heat transfer coefficient (h_{c0}) and its exponent (n_{hc}) for the FPA of 12.14 W/m^2-K and 0.81 respectively as presented in Appendix B.4.4.

As determined from the TGA analysis in section 3.2 the reduced chemical reaction mechanisms in air of PA6 follow a four-step reaction process as shown in Table 12 and Table 9. From this analysis, it is possible to tell how the material is chemically reacting when heated, even though it being in a reduced manner. An option would be to expand the later conducted parameter search to, also, find the ideal reaction step model, as well as the reaction types. Since obtaining these is in itself very challenging (due to the high level of complexity), it has been opted to directly apply the in section 3.2 determined best reduced chemical reaction mechanism. The kinetic properties for the reaction of PA6 in air (Table 12) serve to keep the search area limited, in order to insure that the model could converge. Attempts with a too large search region ended in endless calculations caused by the pre-exponential and exponential factor being too different. Table 12 provides most of the condensed-phase reactions properties of Table 27. The remaining two parameters for each of the four reactions are the heat of pyrolysis (ΔH_{vol}) and χ, the parameter affecting swelling. Though the first of these parameter was never obtained, as explained in section 3.11, its values are assumed to be in the range of $1 \cdot 10^6$ J/kg. The parameter χ is set to “1” for PA6+NC, since no significant swelling or charring was observed. As in equations (4) - (7), and Table 27 the index affecting the oxygen reaction $i_{O_2}\,rxn$ is set to “1”.

As in the TGA analysis, four reduced chemical reaction mechanisms were distinguished. This leads us to five different species including the initial/virgin material. For each of these species, the physically possible initial search range of the

properties determined in chapter 3 (numbers in brackets "( )") are presented. It is possible to assign temperature dependant values for the thermal conductivity, density and specific heat capacity. This added degree of freedom could conceivably lead to issues of convergence. Since only limited data on the temperature dependency for the thermal conductivity and the density for the temperature range in question was available (see Table 17 and Appendix B.4.3), it was opted to use for PA6+NC the average for the thermal conductivity and the density for the temperature range in question of the virgin material ($n_{kz} = n_\rho, = 0$). Temperature dependant values of the specific heat capacity of the virgin material are being searched for or used. Since limited knowledge is available for the intermediate and residue species their thermal properties shall be assumed constant ($n_{kz} = n_\rho, = n_c = 0$). This is the case except for the virgin material where there is independent data available, as presented in sections section 3.5, 3.6 and 3.7. The values of Table 42 are mere educated guesses with the help of the literature [25, 31].

Symbol	**Units**	Virgin	Intermediate 1	Residue 1	Intermediate 1	Residue 2
k_{0z}	W/m-K	0.01-3 (0.290)	0.01-20	0.01-20	0.01-20	0.01-20
ρ_0	kg/m^3	900-1500 (1156)	100-2000	100-2000	100-2000	100-2000
c_0	J/kg-K	100-4500 (1528)	100-4500	100-4500	100-4500	100-4500
n_c	-	0-1 (0.716)	0	0	0	0

Table 42 PA6+NC: thermal conductivity, density and specific heat capacity

It is assumed that of the differentiated species, only the virgin material (the PA6+NC itself) undergoes the process of melting. The required parameters for gpyro are obtained from the analysis in sections 3.5, 3.6 and 3.7. From Table 15, the melting temperature (T_m) of 484 K and the latent heat of melting (ΔH_m) of 65000 J/kg can be obtained. A reasonable range between 423 and 523 K and 20,000 and 300,000 J/kg was used when searching for these properties. From Figure 98 it can be assume that σ_m^2 is in the range between 16 and 225 K^2 while from Figure 156, the best normal distribution fit was reached with 40 K^2. This was obtained using the root mean squared error regression analysis.

The remaining parameters considered here, are the ones presented in Table 43. These parameters have not been obtained elsewhere thus have to either be assumed or be obtained in a inverse manner. To help narrow down their physically possible values, the standard literature of this process has been consulted [25, 31, 102, 104, 106].

Symbol	**Units**	Virgin	Intermediate 1	Residue 1	Intermediate 1	Residue 2
E	-	0.3-0.99	0.3-0.99	0.3-0.99	0.3-0.99	0.3-0.99
K	m^{-1}	10^0-10^6	0^0-10^6	0^0-10^6	0^0-10^6	0^0-10^6
γ	m	0-0.001	0-0.001	0-0.001	0-0.001	0-0.001
K_z	m^2	10^{-5}-10^{-20} ($1.46 \cdot 10^{-12}$)	10^{-5}-10^{-20}	10^{-5}-10^{-20}	10^{-5}-10^{-20}	10^{-5}-10^{-20}
ρ_{s0}	kg/m^3	900-2000	100-2000	100-2000	100-2000	100-2000

Table 43 Used values for the PA6+NC layer

B.3.4 PA6+NC+FR

For the determination of the (intrinsic or global) material properties of this material only two, due to material limitations, different tests have been analysed one at a heat flux (q_e) of 27.5 kW/m^2 and the other at 30 kW/m^2. The overall initial thickness (δ_0) that was taken into consideration for the analysis of these tests was the 37.5 mm combined thickness of the tested sample and the aluminium block with a cell number (n_{cell}) of 300, resulting in a cell thickness of 0.125 mm. The ambient gaseous mass fraction (Y_∞) was taken to be 23% for O_2 and 77% for N_2. Gpyro handles, as previously described, the input of temperature dependant parameters in a specific way (see Table 22). Therefore, it was necessary to curve fit the function to the results of section 3.9. This gave the heat transfer coefficient (h_{c0}) and its exponent (n_{hc}) for the FPA of 12.14 W/m^2-K and 0.81 respectively as presented in Appendix B.4.4.

As determined from the TGA analysis in section 3.2 the reduced chemical reaction mechanisms in air of PA6 follow a four-step reaction process as shown in Table 12 and Table 9. From this analysis, it is possible to tell how the material is chemically reacting when heated, even though it being in a reduced manner. An option would be to expand the later conducted parameter search to, also, find the ideal reaction step model, as well as the reaction types. Since obtaining these is in itself very challenging (due to the high level of complexity), it has been opted to directly apply the in section 3.2 determined best reduced chemical reaction mechanism. The kinetic

properties for the reaction of PA6 in air (Table 12) serve to keep the search area limited, in order to insure that the model could converge. Attempts with a too large search region ended in endless calculations caused by the pre-exponential and exponential factor being too different. Table 12 provides most of the condensed-phase reactions properties of Table 27. The remaining two parameters for each of the four reactions are the heat of pyrolysis (ΔH_{vol}) and χ, the parameter affecting swelling. Though the first of these parameter was never obtained, as explained in section 3.11, its values are assumed to be in the range of $1 \cdot 10^6$ J/kg. Looking at . Figure 20 in comparing with Figure 76 and Figure 77, show that swelling occurred before the reduced chemical reaction mechanisms was taking place. Therefore, it was assumed that swelling only occurred for the virgin material. From observations, it is clear that PA6+NC+FR swells, therefore the search boundary was set between 0 and 1 indicating that. As in equation (4) - (7), and Table 27 the index affecting the oxygen reaction $i_{O_2}\,rxn$ is set to "1".

As in the TGA analysis, four reduced chemical reaction mechanisms were distinguished. This leads us to five different species including the initial/virgin material. For each of these species, the physically possible initial search range of the properties determined in chapter 3 (numbers in brackets "( )") are presented. It is possible to assign temperature dependant values for the thermal conductivity, density and specific heat capacity. This added degree of freedom could conceivably lead to issues of convergence. Since only limited data on the temperature dependency for the thermal conductivity and the density for the temperature range in question was available (see Table 17 and Appendix B.4.3), it was depicted to use for PA6+FR the average for the thermal conductivity for the temperature range in question of the virgin material ($n_{kz} = 0$). Temperature dependant values of the specific heat capacity and the density of the virgin are being searched for or used. Since limited knowledge is available for the intermediate and residue species their thermal properties shall be assumed constant ($n_{kz} = n_\rho, = n_c = 0$). This is the case except for the virgin material where there is independent data available, as presented in sections 3.5, 3.6 and 3.7. The values of Table 44 are mere educated guesses with the help of the literature [25, 31].

Symbol	Units	Virgin	Intermediate 1	Residue 1	Intermediate 1	Residue 2
k_{0z}	W/m-K	0.01-3 (0.298)	0.01-20	0.01-20	0.01-20	0.01-20
ρ_0	kg/m^3	900-1500 (1376.9)	100-2000	100-2000	100-2000	100-2000
n_ρ	-	-5-0 (-1.88)	0	0	0	0
c_0	J/kg-K	100-4500 (1519.1)	100-4500	100-4500	100-4500	100-4500
n_c	-	0.770	0	0	0	0

Table 44 PA6+NC+FR: thermal conductivity, density and specific heat capacity

It is assumed that of the differentiated species only the virgin material (the PA6+NC+FR itself) undergoes the process of melting. The required parameters for gpyro are obtained from the analysis in sections 3.5, 3.6 and 3.7. From Table 15, the melting temperature (T_m) of 484 K and the latent heat of melting (ΔH_m) of 51000 J/kg can be obtained. A reasonable range between 423 and 523 K and 20,000 and 300,000 J/kg was used when searching for these properties. From Figure 99 it can be assume that σ_m^2 is in the range between 16 and 225 K^2 while from Figure 157, the best normal distribution fit was reached with 62 K^2. This was obtained using the root mean squared error regression analysis.

The remaining parameters considered here, are the ones presented in Table 45. These parameters have not been obtained elsewhere thus have to either be assumed or be obtained in a inverse manner. To help narrow down their physically possible values, the standard literature of this process has been consulted [25, 31, 102, 104, 106].

Symbol	Units	Virgin	Intermediate 1	Residue 1	Intermediate 1	Residue 2
ε	-	0.3-0.99	0.3-0.99	0.3-0.99	0.3-0.99	0.3-0.99
κ	m^{-1}	10^0-10^6	0^0-10^6	0^0-10^6	0^0-10^6	0^0-10^6
γ	m	0-0.001	0-0.0010	0-0.001	0-0.001	0-0.001
K_z	m^2	10^{-20}-10^{-5} ($1.46\cdot10^{-12}$)	10^{-20}-10^{-5}	10^{-20}-10^{-5}	10^{-20}-10^{-5}	10^{-20}-10^{-5}
ρ_{s0}	kg/m^3	900-2000	100-2000	100-2000	100-2000	100-2000

Table 45 Used values for the PA6+NC+FR layer

B.4 Data preparation to suite required model input

B.4.1 Fitting a Normal Distribution to the Heat of Fusion peak to the various materials

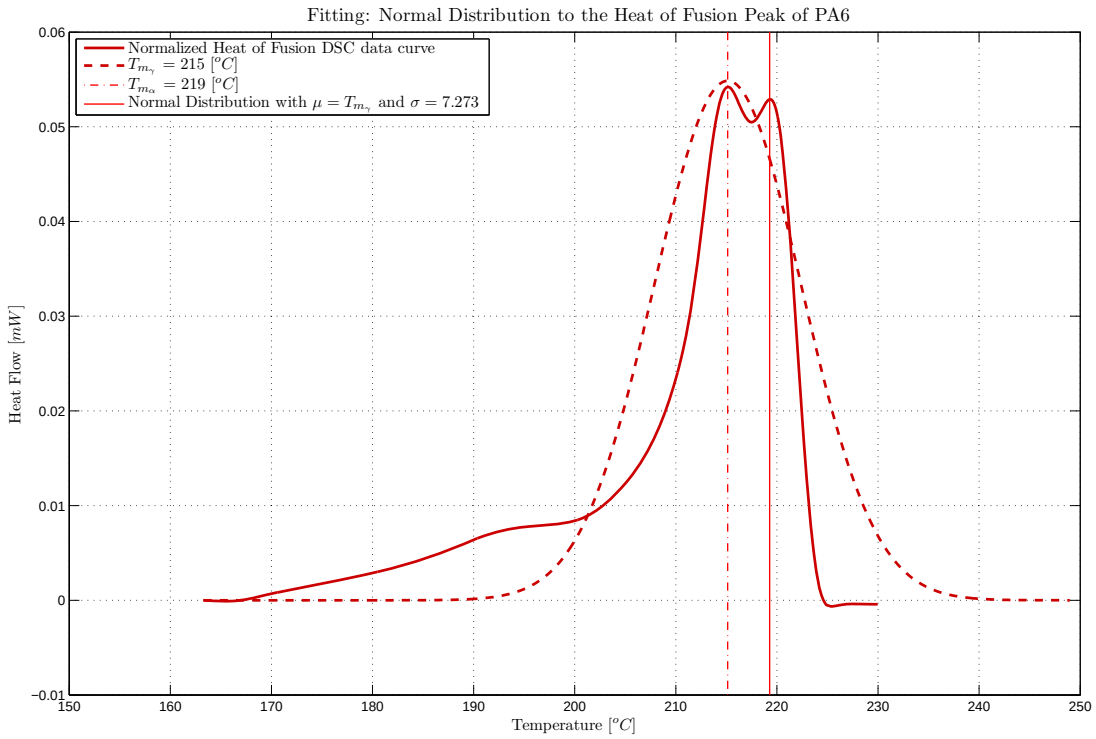

Figure 154 Fitting: Normal Distribution to the Heat of Formation Peak of PA6

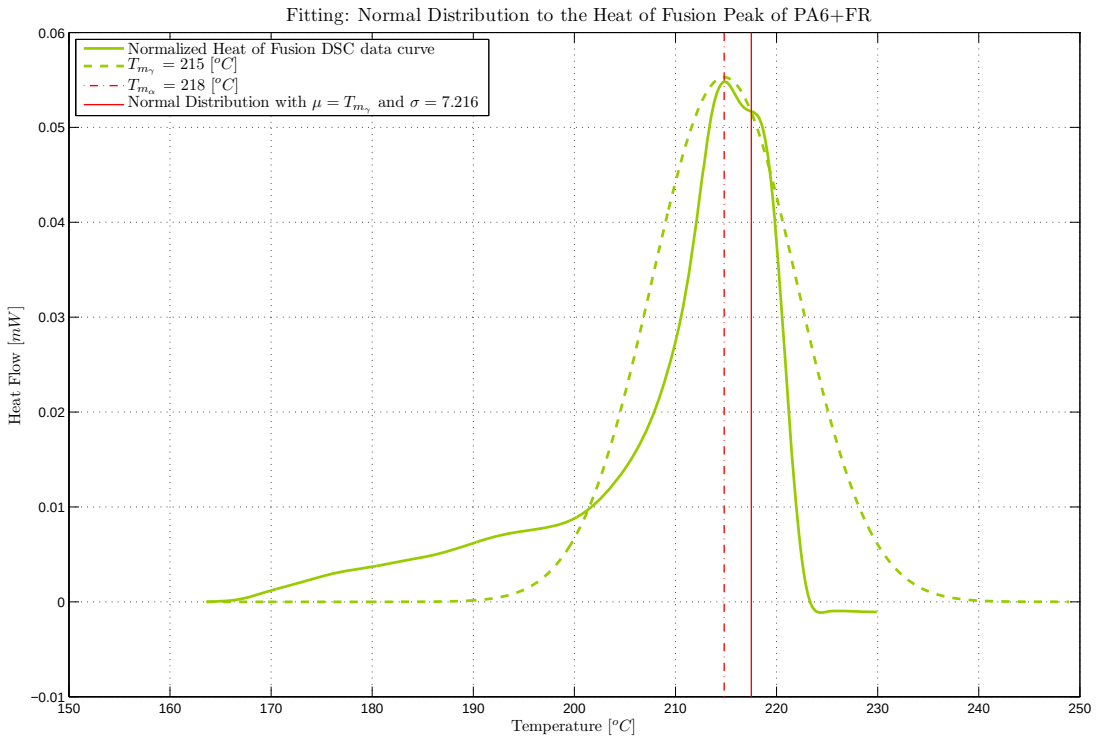

Figure 155 Fitting: Normal Distribution to the Heat of Formation Peak of PA6+FR

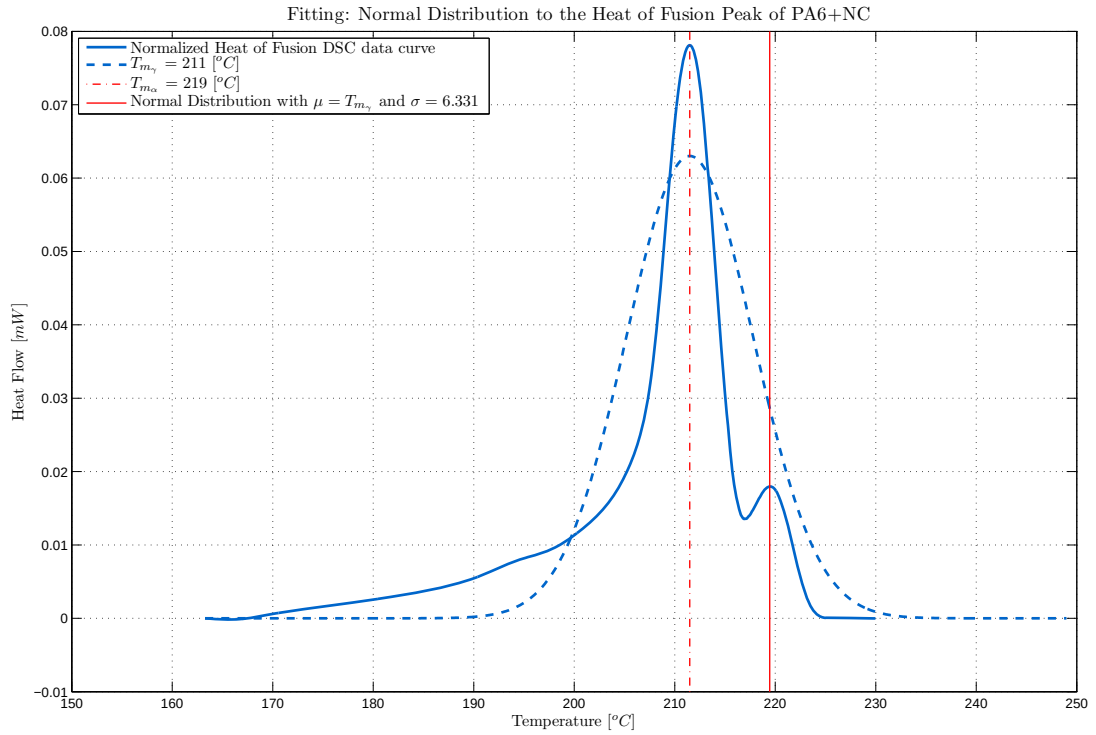

Figure 156 Fitting: Normal Distribution to the Heat of Formation Peak of PA6+NC

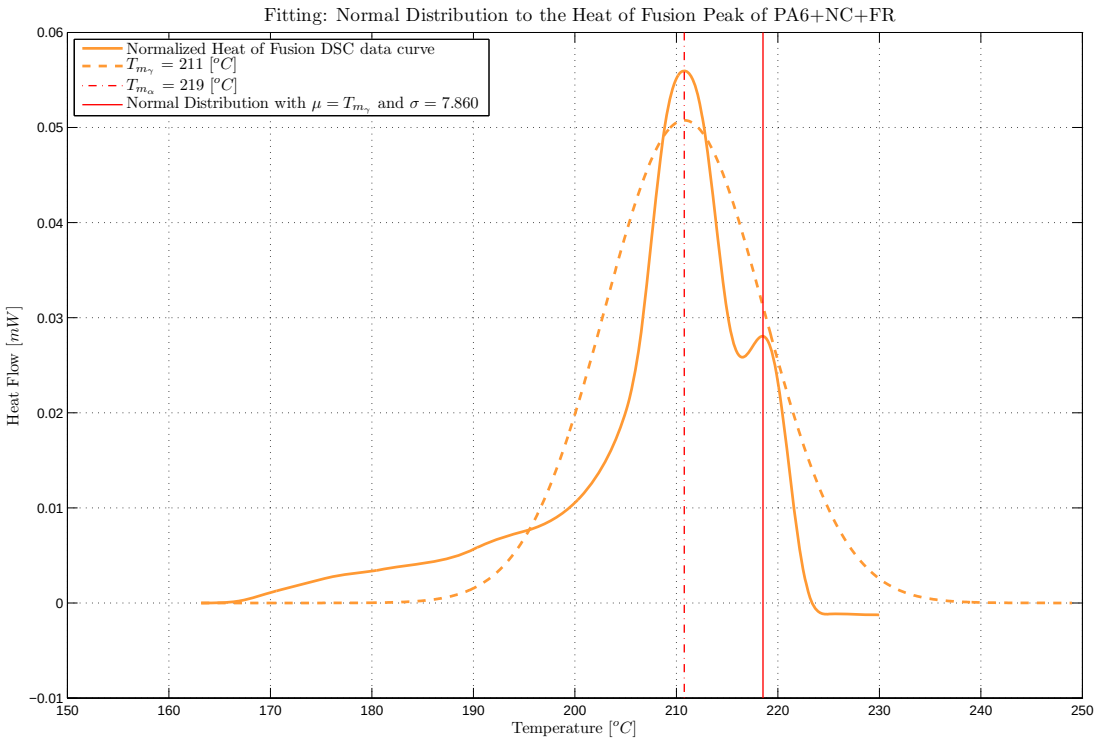

Figure 157 Fitting: Normal Distribution to the Heat of Formation Peak of PA6+NC+FR

B.4.2 Determining the temperature dependant parameter of the specific heat capacity for gpyro

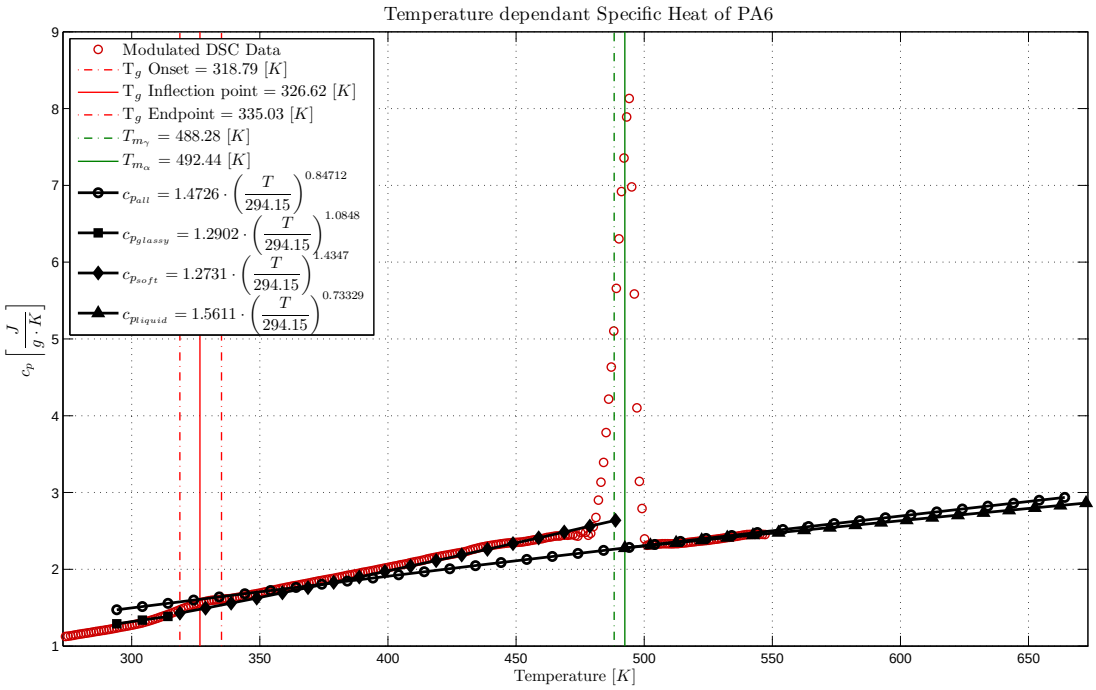

Figure 158 c_p of PA6 for gpyro

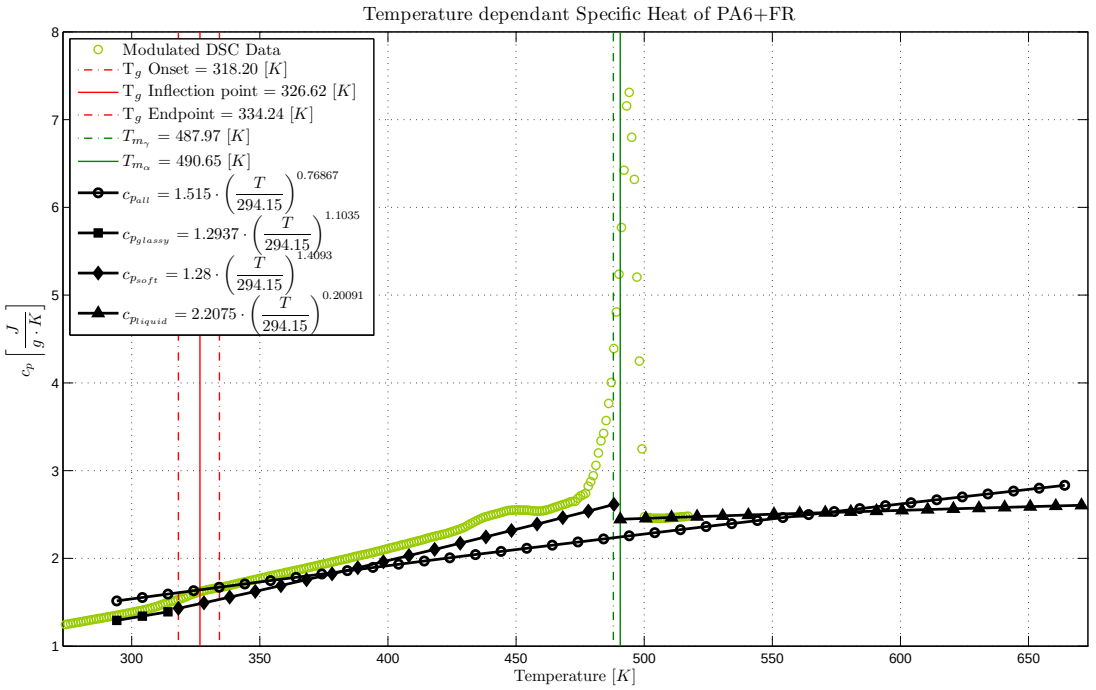

Figure 159 c_p of PA6+FR for gpyro

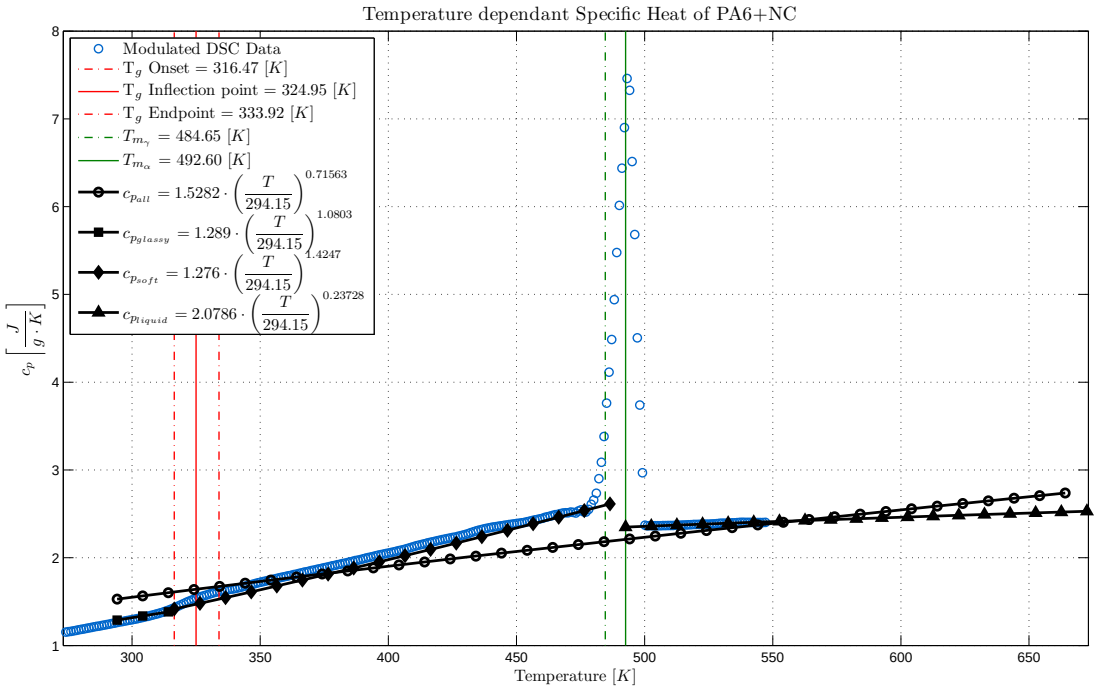

Figure 160 c_p of PA6+NC for gpyro

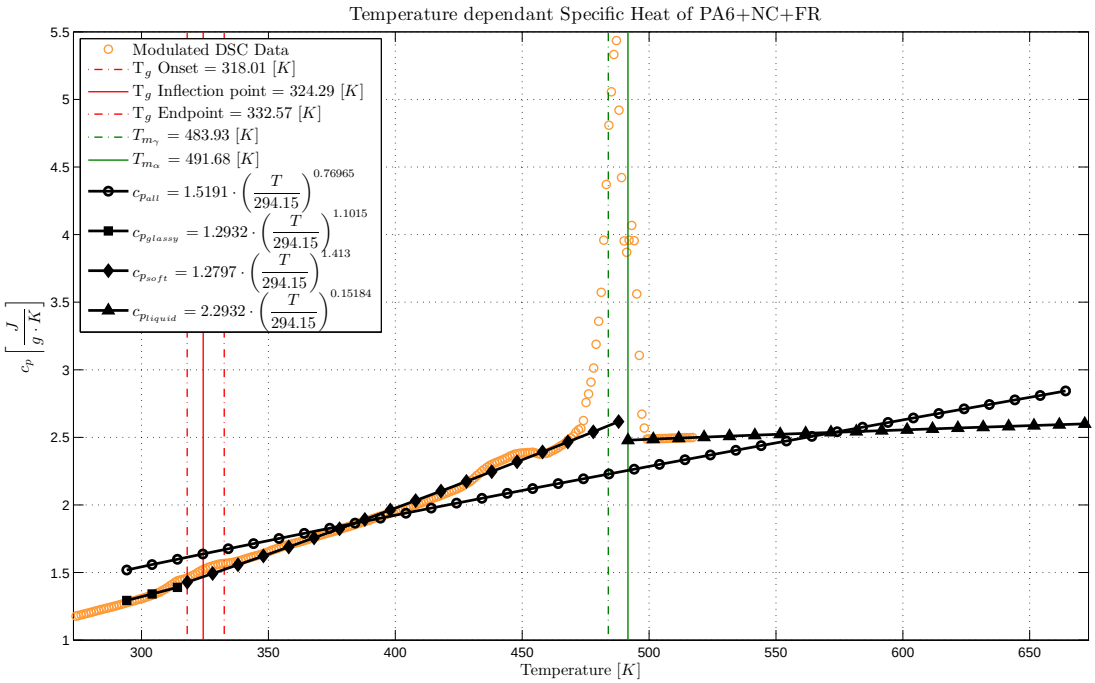

Figure 161 c_p of PA6+NC+FR for gpyro

B.4.3 Determining the temperature dependant parameter of the density for gpyro

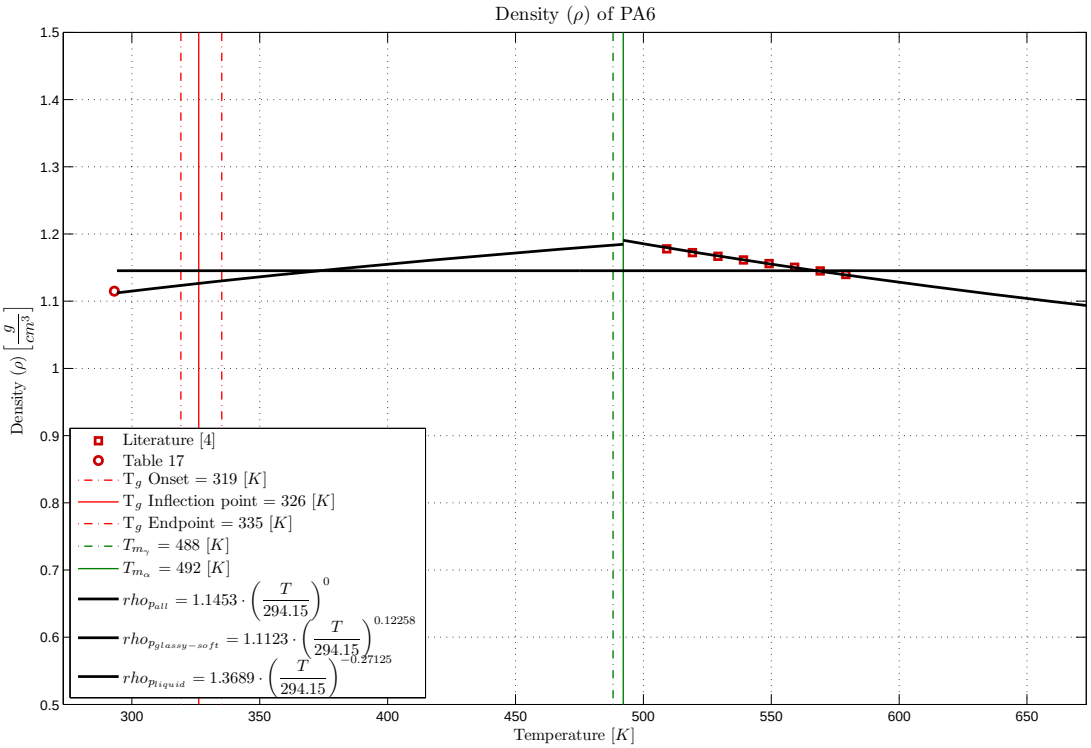

Figure 162 ρ of PA6 for gpyro

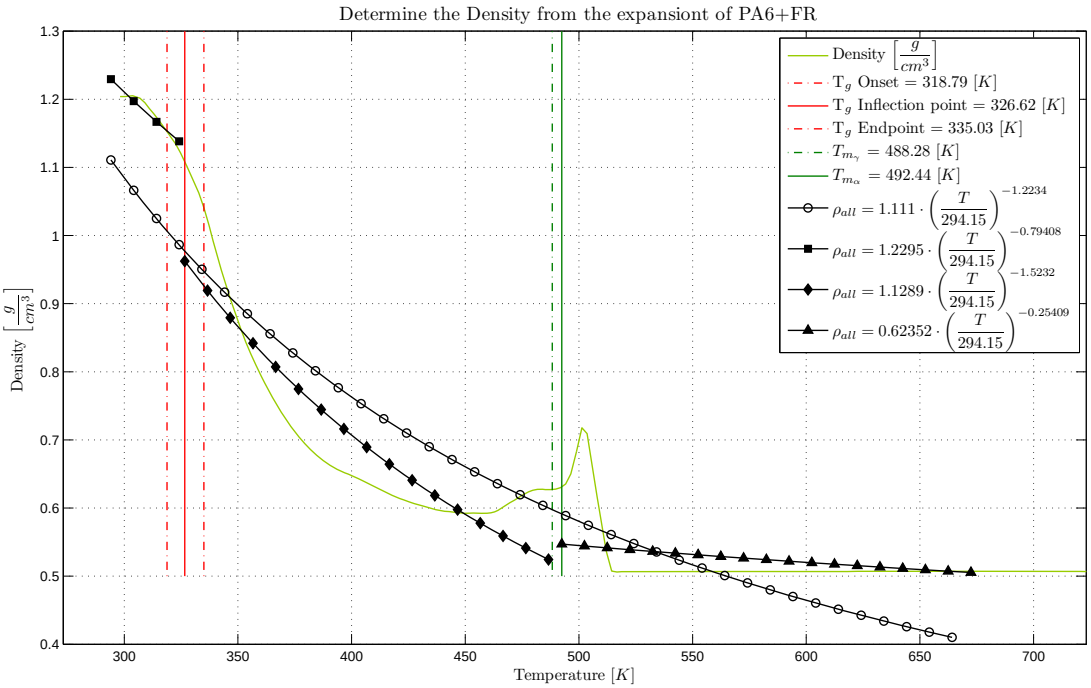

Figure 163 ρ of PA6+FR for gpyro

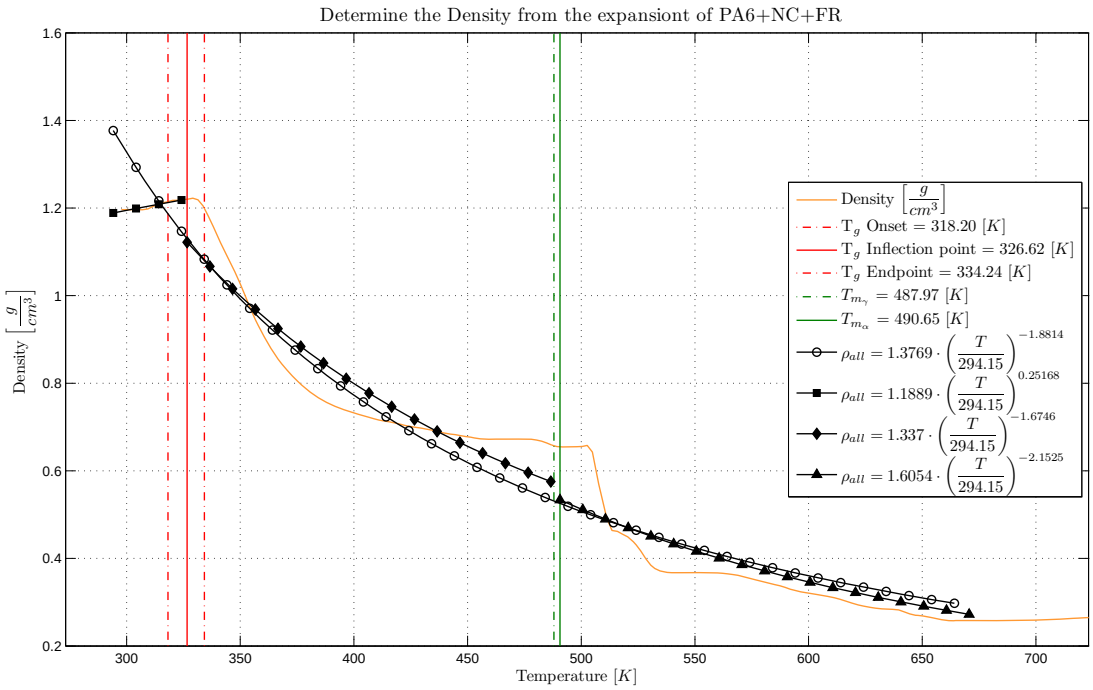

Figure 164 ρ of PA6+NC+FR for gpyro

B.4.4 Determining the temperature dependant parameter of the convective heat transfer coefficient for gpyro

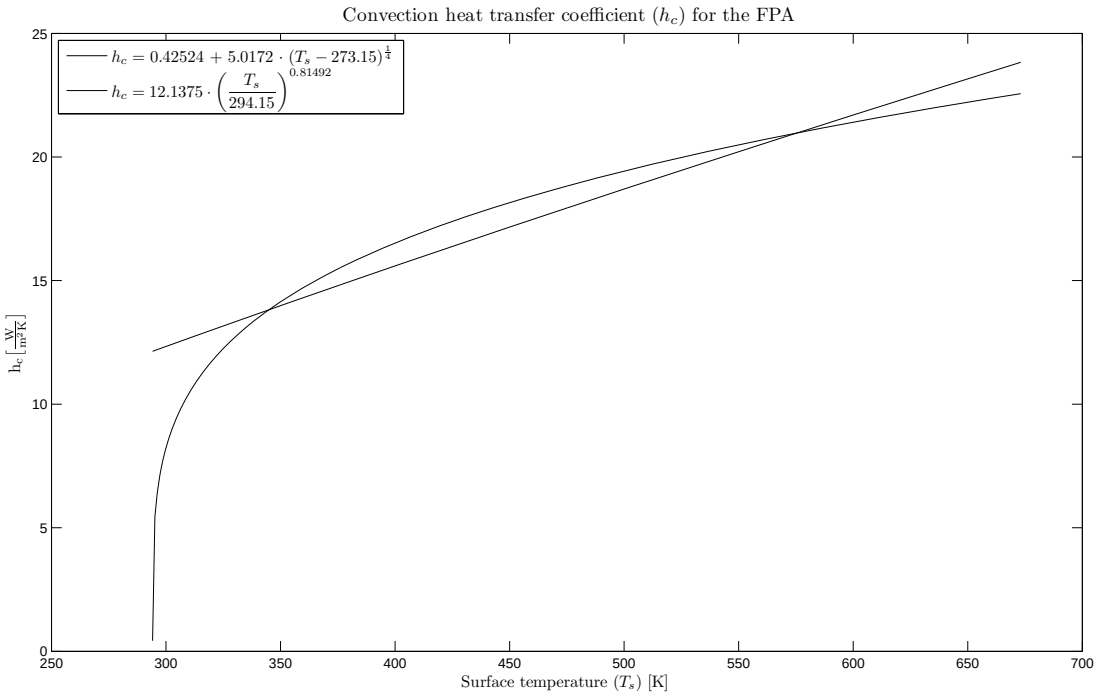

Figure 165 gpyro temperature dependant: convective heat transfer coefficient h_c (T) for the FPA

B.5 Results

B.5.1 PA6

B.5.1.1 In-depth temperature fit

Without the independently obtained intrinsic material properties

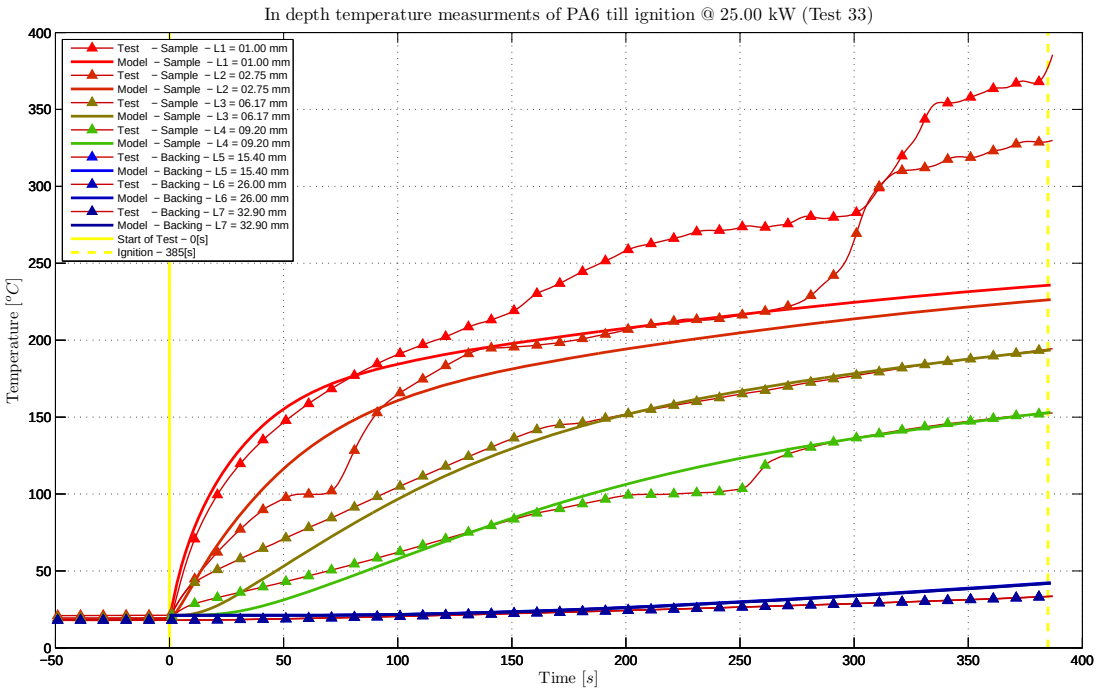

Figure 166 In-depth temperature “Test to Model” comparison of PA6 *without* the independently obtained intrinsic material properties (Test 33)

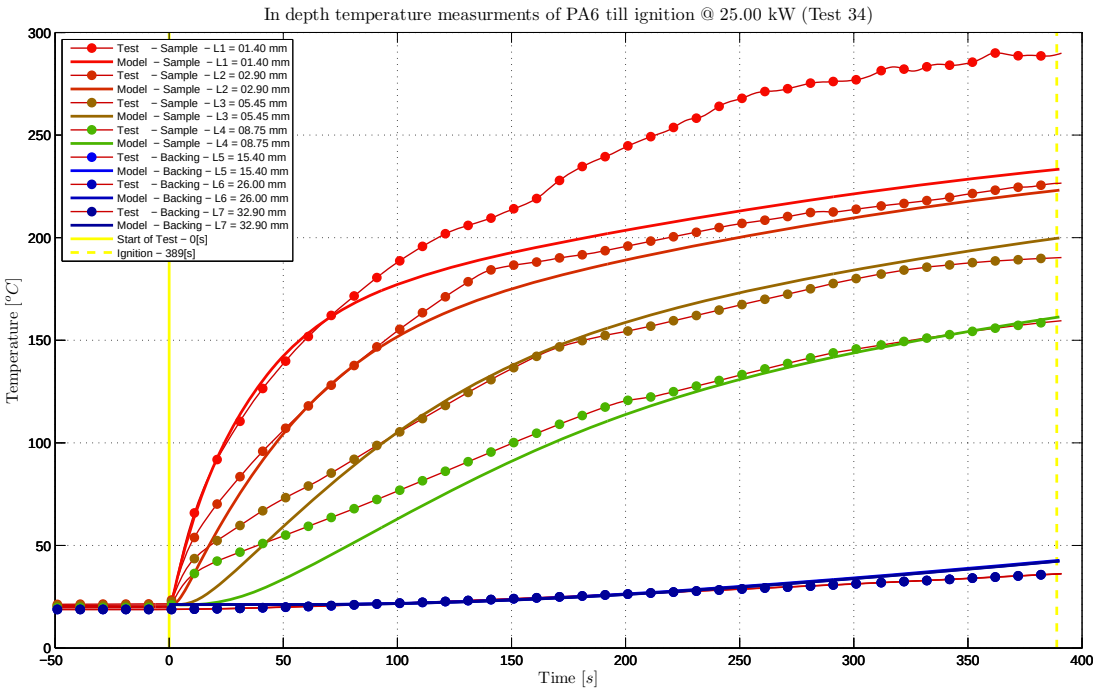

Figure 167 In-depth temperature "Test to Model" comparison of PA6 *without* the independently obtained intrinsic material properties (Test 34)

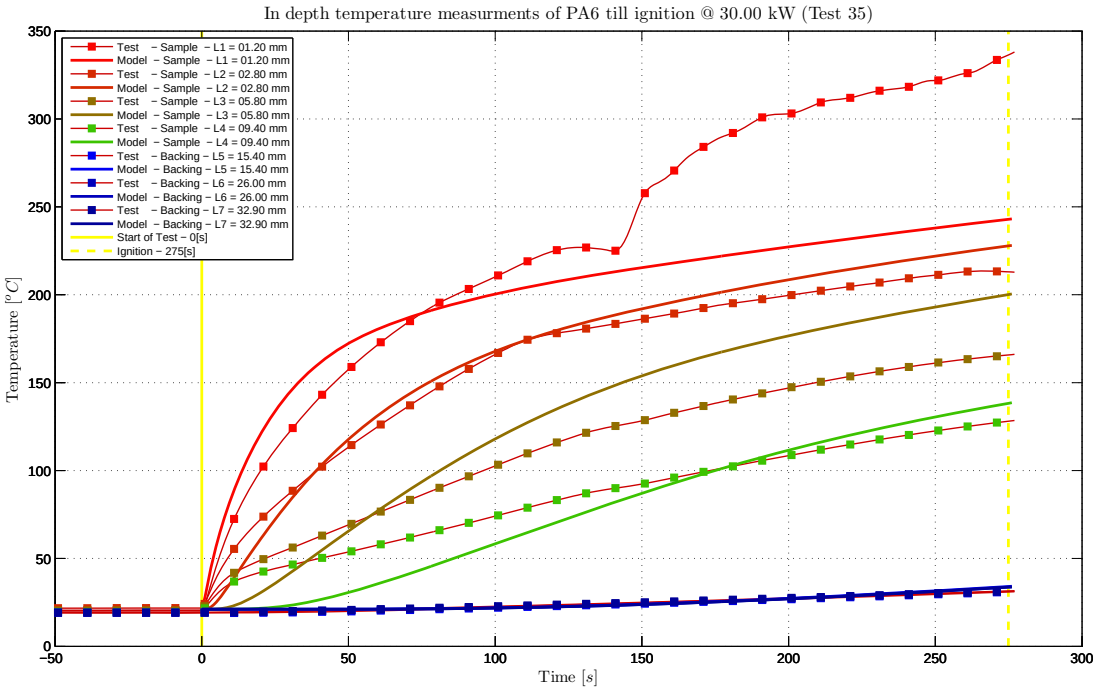

Figure 168 In-depth temperature "Test to Model" comparison of PA6 *without* the independently obtained intrinsic material properties (Test 35)

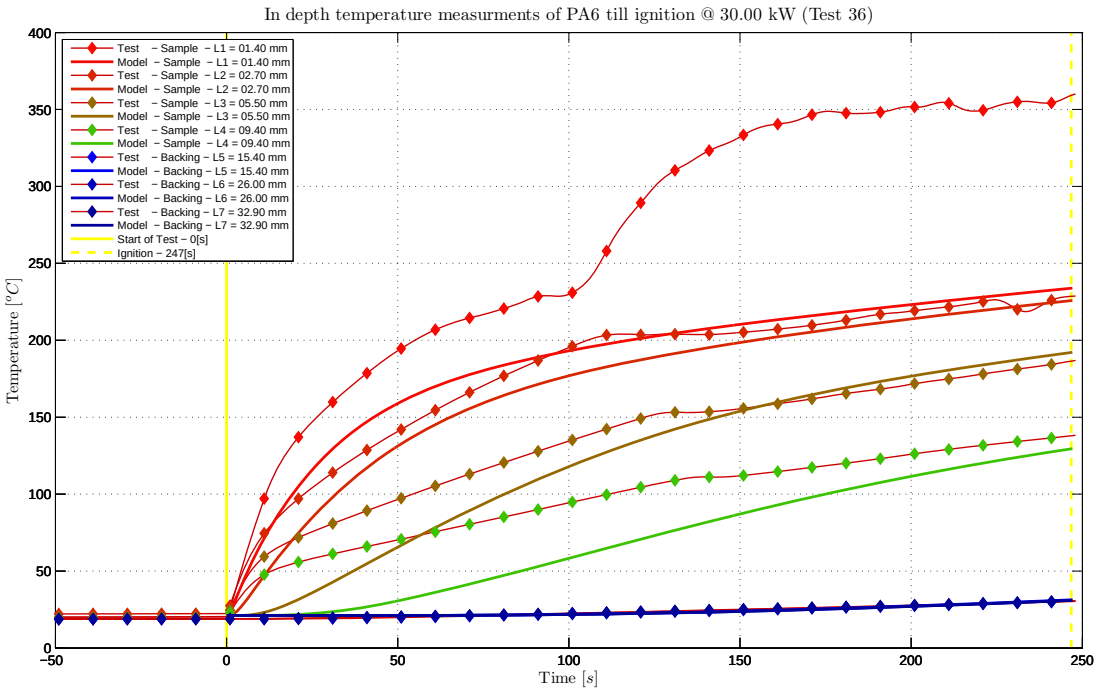

Figure 169 In-depth temperature "Test to Model" comparison of PA6 *without* the independently obtained intrinsic material properties (Test 36)

With the independently obtained intrinsic material properties

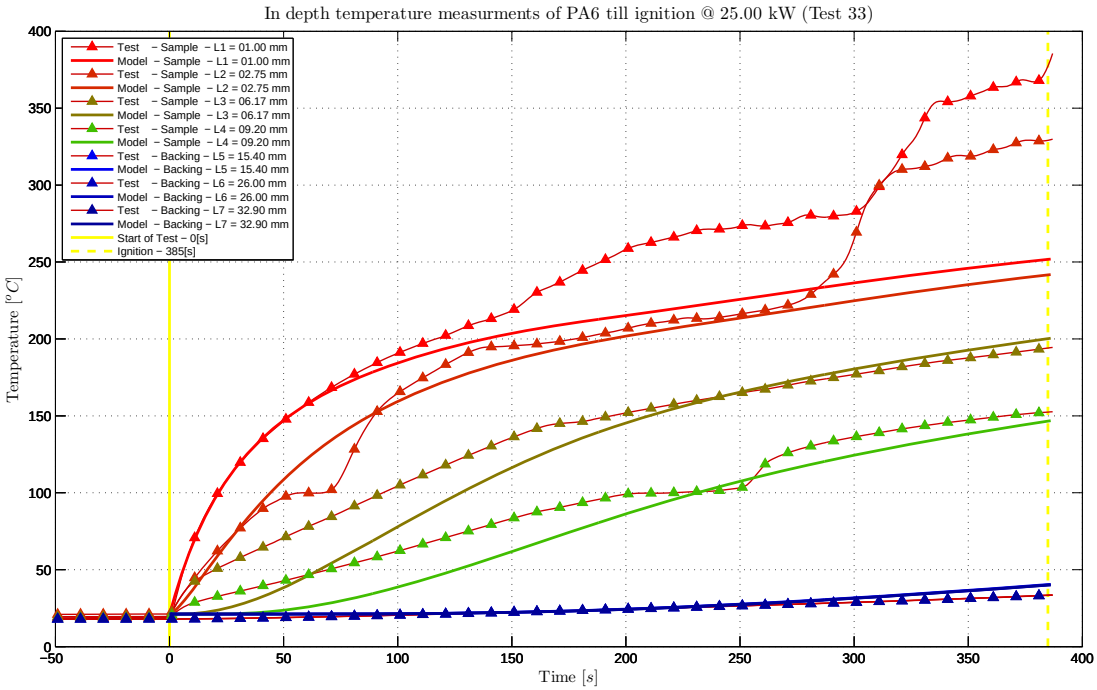

Figure 170 In-depth temperature "Test to Model" comparison of PA6 *with* the independently obtained intrinsic material properties (Test 33)

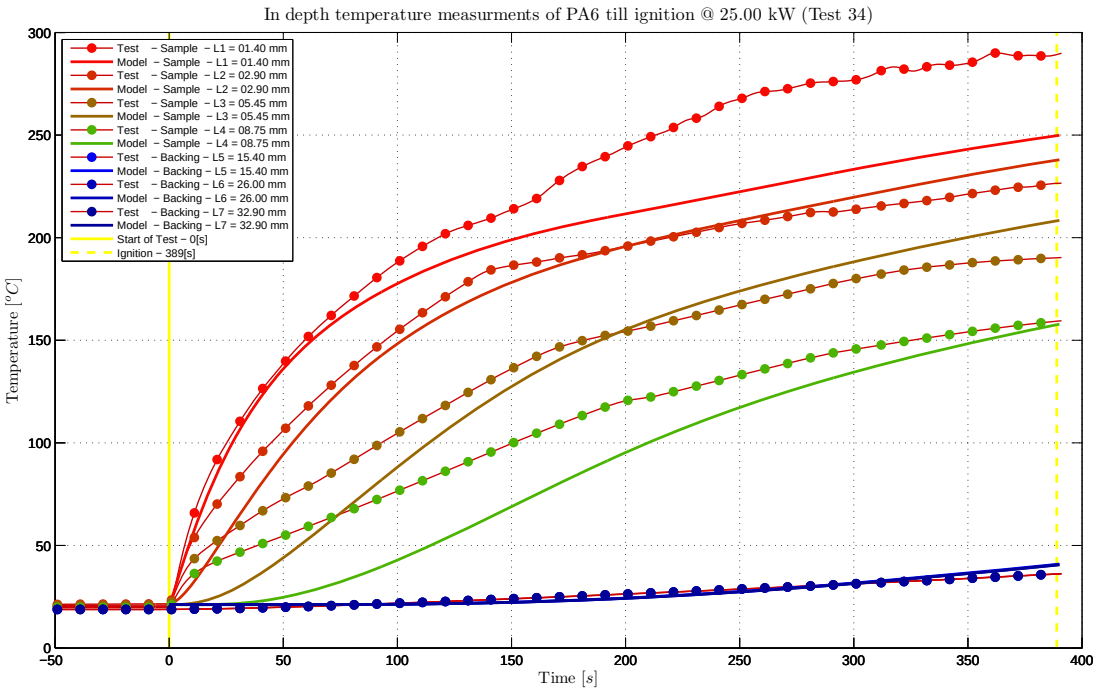

Figure 171 In-depth temperature "Test to Model" comparison of PA6 *with* the independently obtained intrinsic material properties (Test 34)

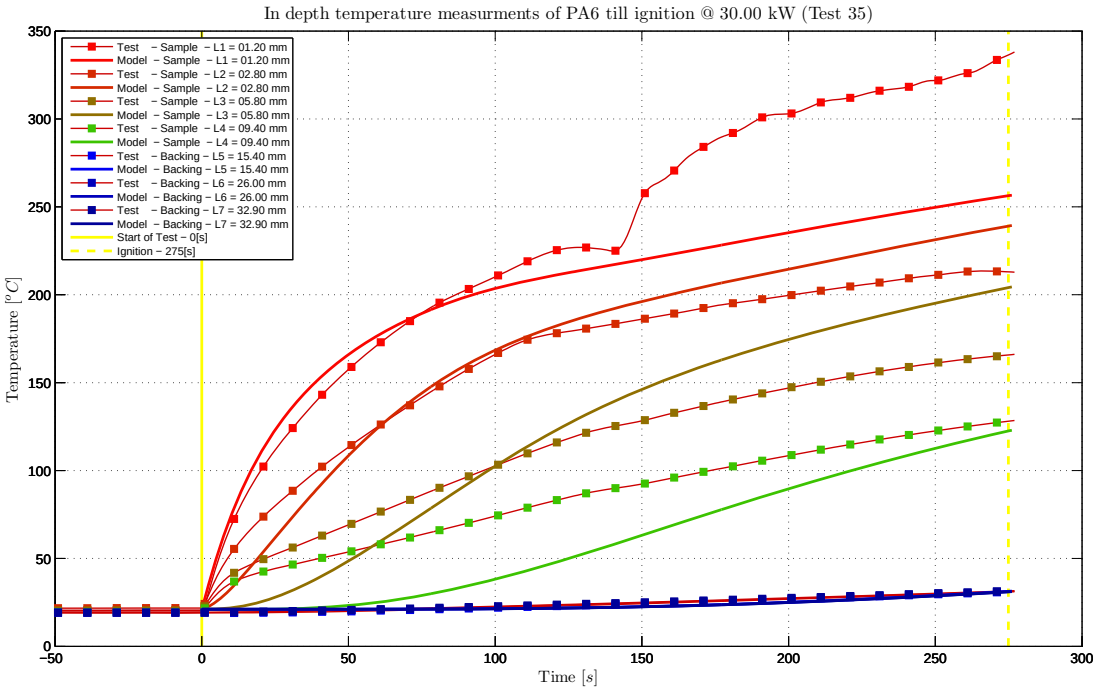

Figure 172 In-depth temperature "Test to Model" comparison of PA6 *with* the independently obtained intrinsic material properties (Test 35)

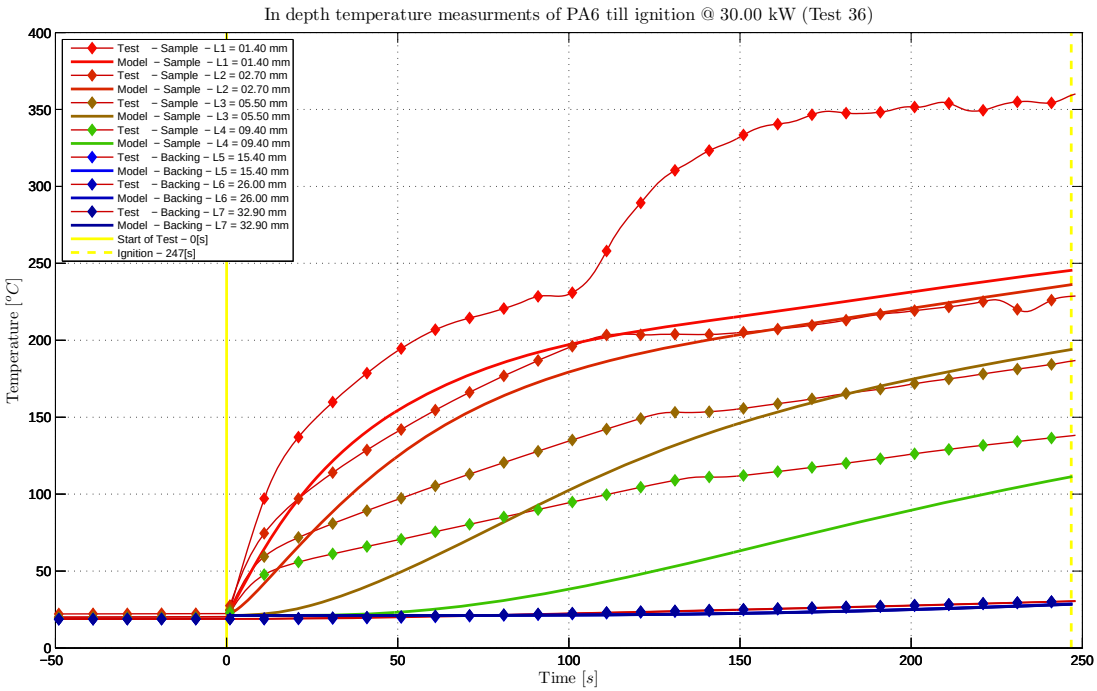

Figure 173 In-depth temperature "Test to Model" comparison of PA6 *with* the independently obtained intrinsic material properties (Test 36)

B.5.1.2 Mass loss fit

Without the independently obtained intrinsic material properties

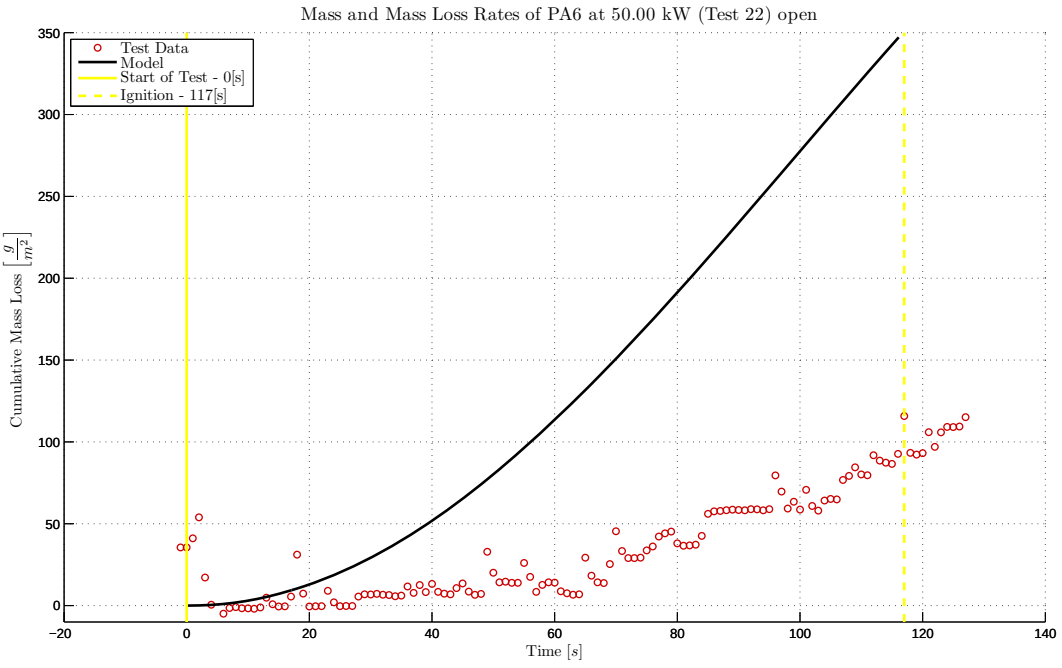

Figure 174 Cumulative mass loss "Test to Model" comparison of PA6 *without* the independently obtained intrinsic material properties (Test 22)

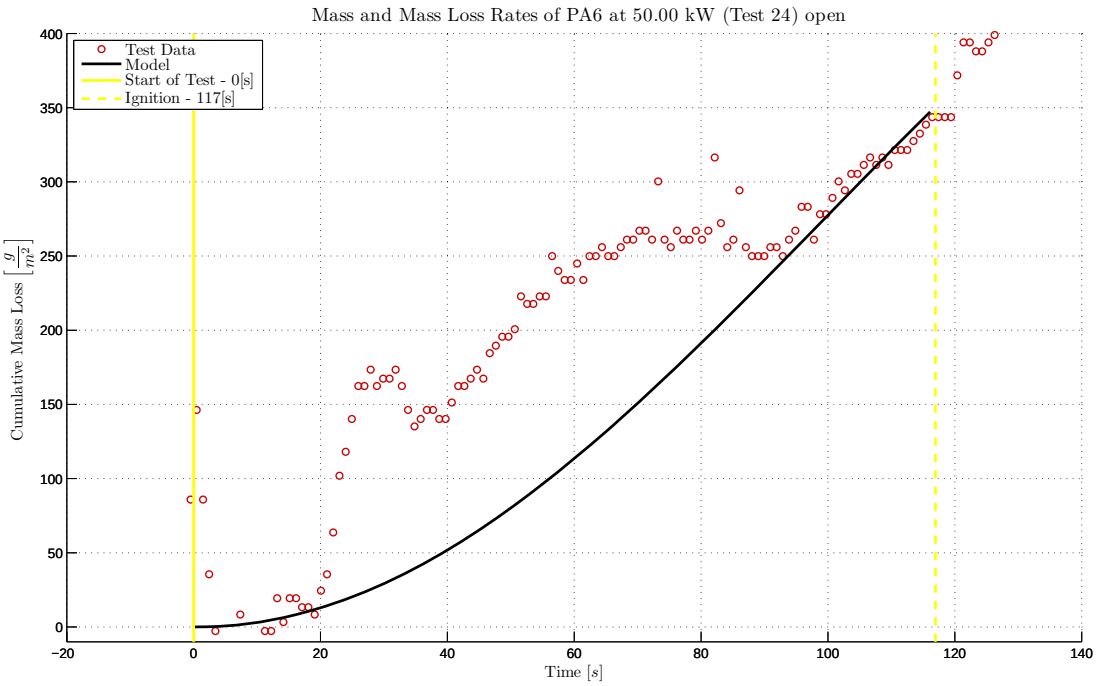

Figure 175 Cumulative mass loss "Test to Model" comparison of PA6 *without* the independently obtained intrinsic material properties (Test 24)

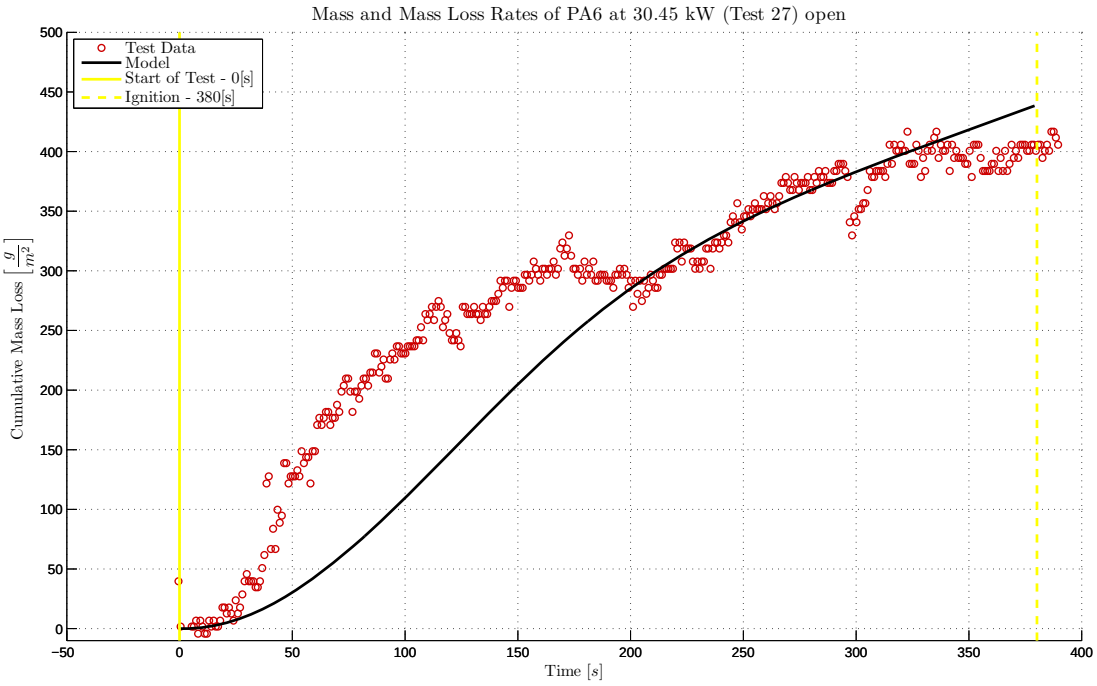

Figure 176 Cumulative mass loss "Test to Model" comparison of PA6 *without* the independently obtained intrinsic material properties (Test 27)

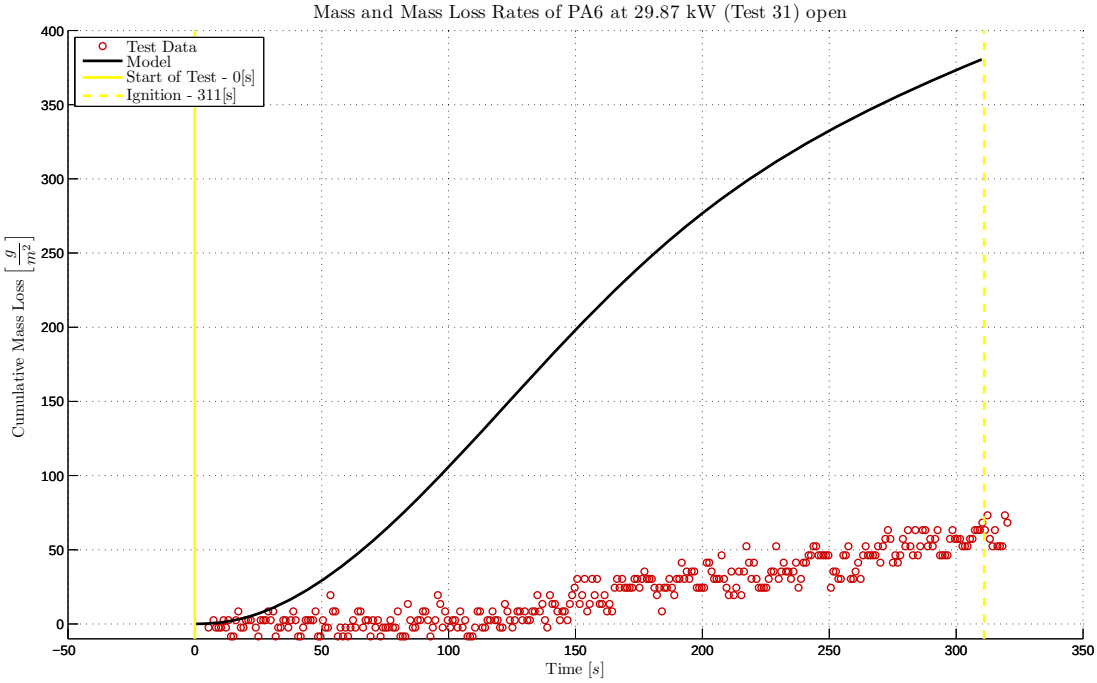

Figure 177 Cumulative mass loss "Test to Model" comparison of PA6 *without* the independently obtained intrinsic material properties (Test 31)

With the independently obtained intrinsic material properties

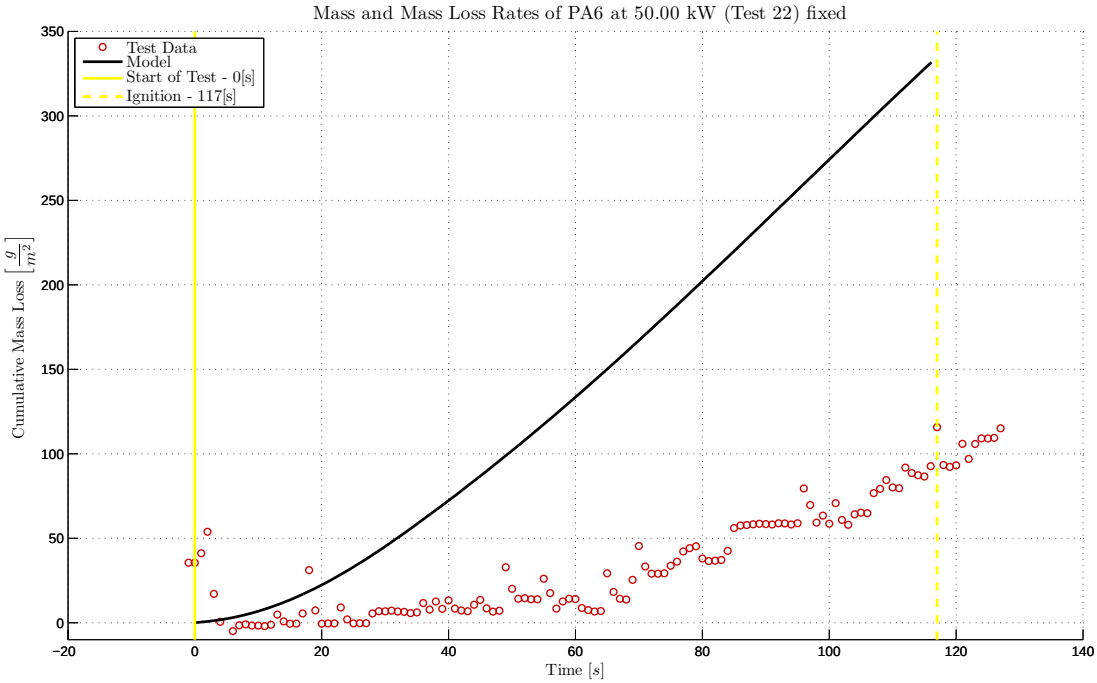

Figure 178 Cumulative mass loss "Test to Model" comparison of PA6 *with* the independently obtained intrinsic material properties (Test 22)

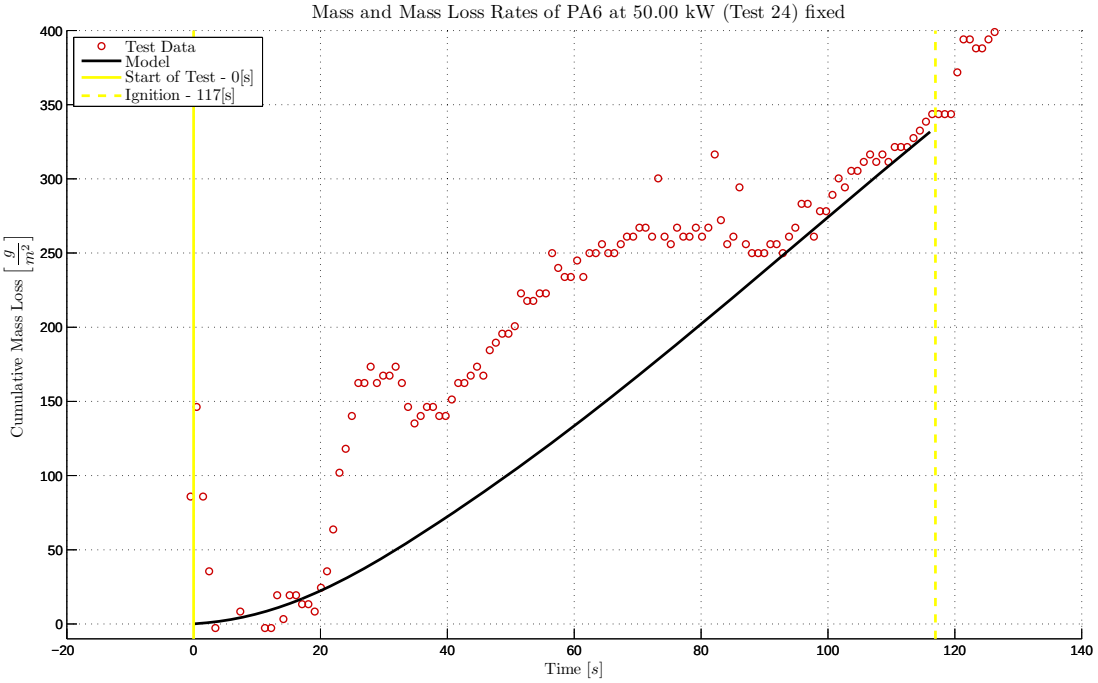

Figure 179 Cumulative mass loss "Test to Model" comparison of PA6 *with* the independently obtained intrinsic material properties (Test 24)

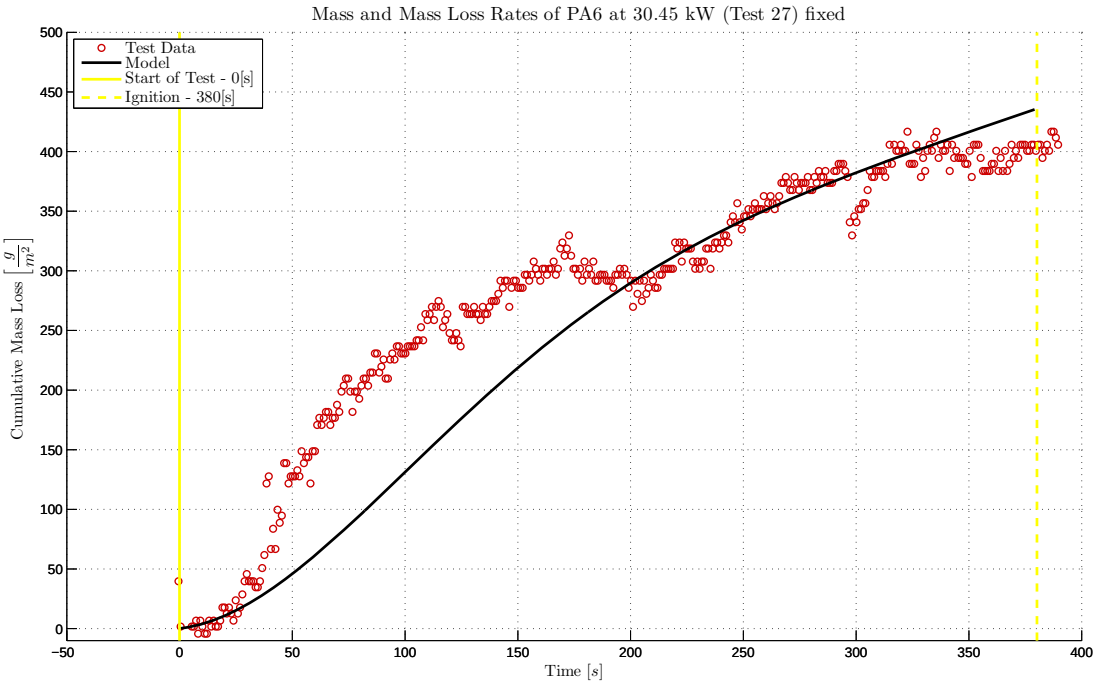

Figure 180 Cumulative mass loss "Test to Model" comparison of PA6 *with* the independently obtained intrinsic material properties (Test 27)

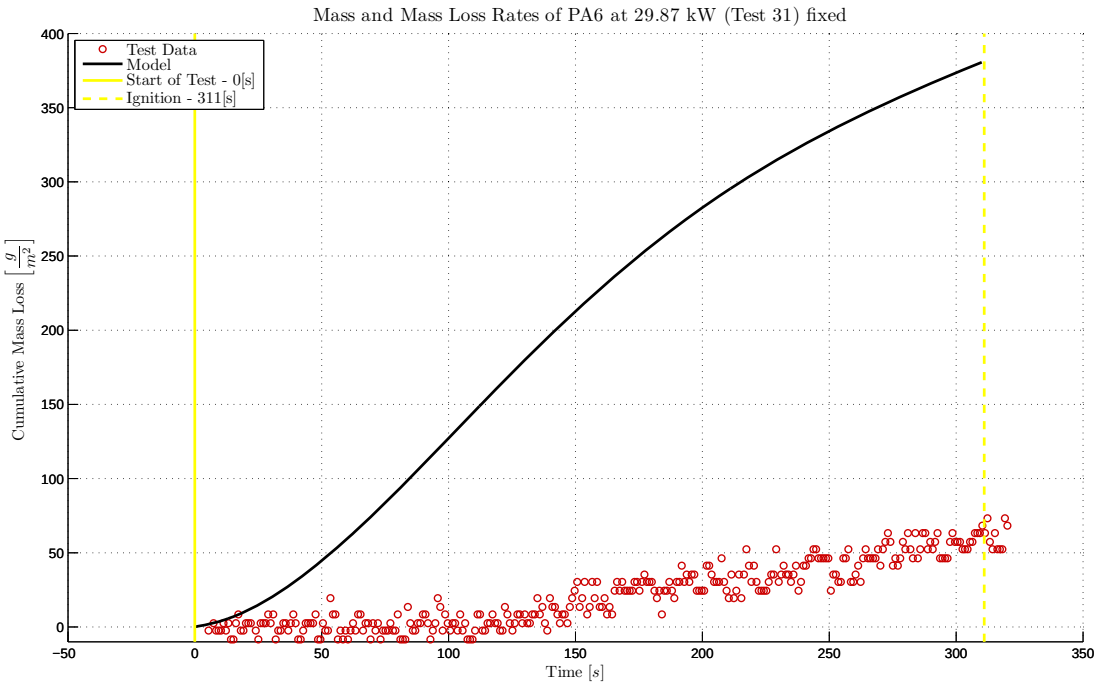

Figure 181 Cumulative mass loss "Test to Model" comparison of PA6 *with* the independently obtained intrinsic material properties (Test 31)

B.5.1.3 Side by side property comparison

Please consult Table 35 in section 5.5.

B.5.2 PA6+FR

B.5.2.1 In-depth temperature fit

Without the independently obtained intrinsic material properties

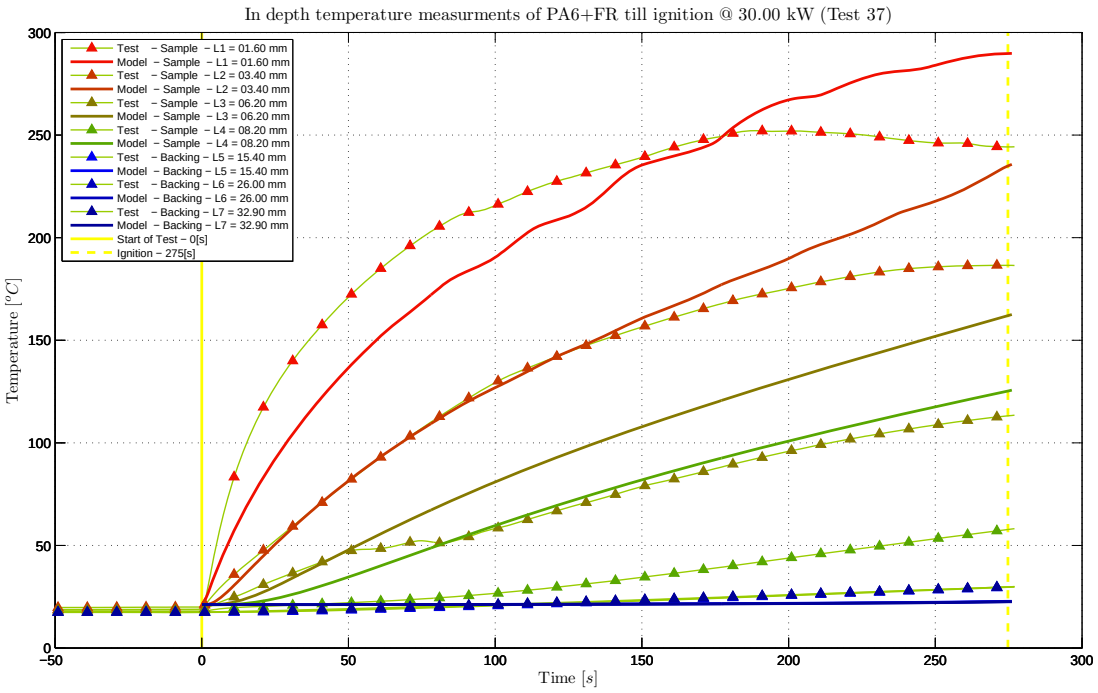

Figure 182 In-depth temperature "Test to Model" comparison of PA6+FR *without* the independently obtained intrinsic material properties (Test 37)

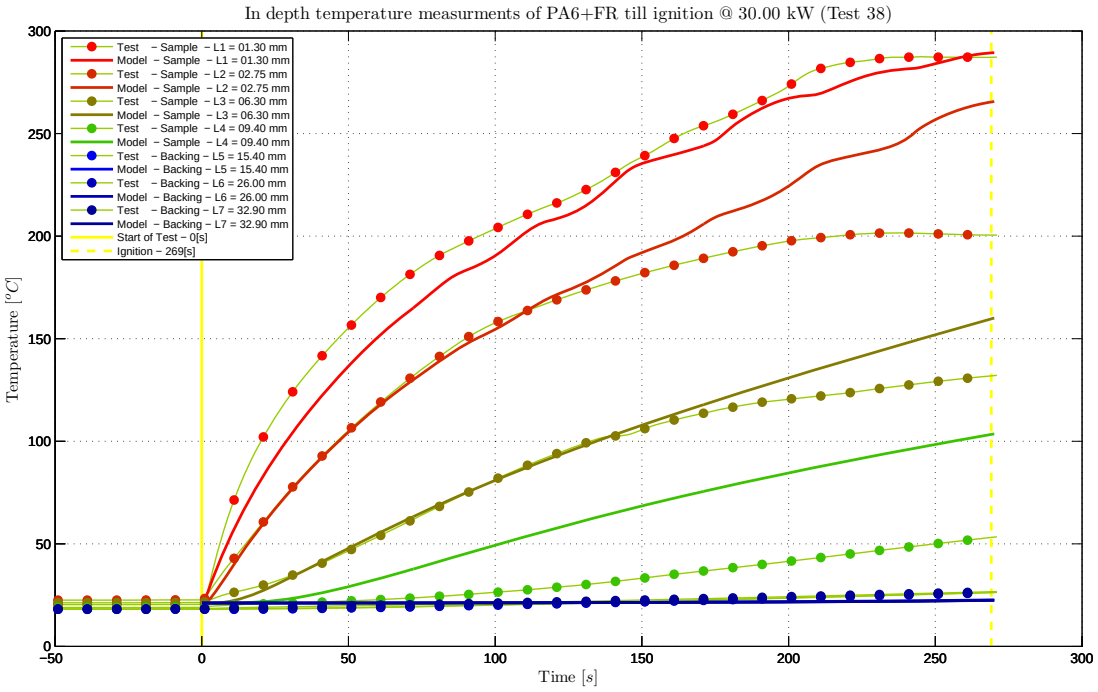

Figure 183 In-depth temperature "Test to Model" comparison of PA6+FR *without* the independently obtained intrinsic material properties (Test 38)

With the independently obtained intrinsic material properties

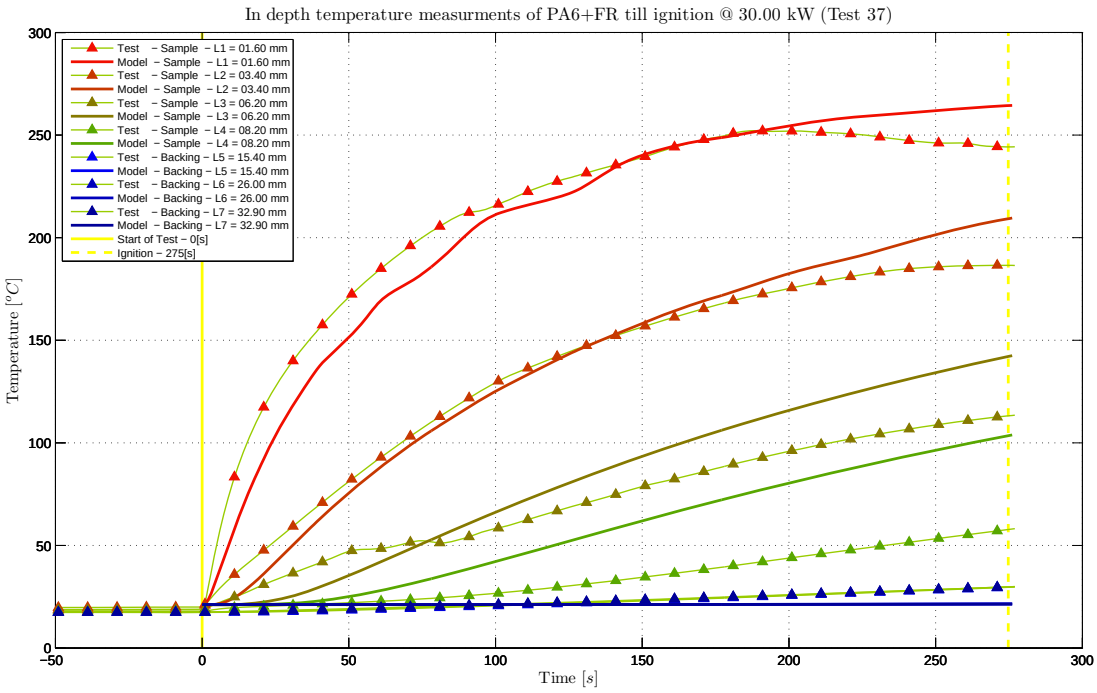

Figure 184 In-depth temperature "Test to Model" comparison of PA6+FR *with* the independently obtained intrinsic material properties (Test 37)

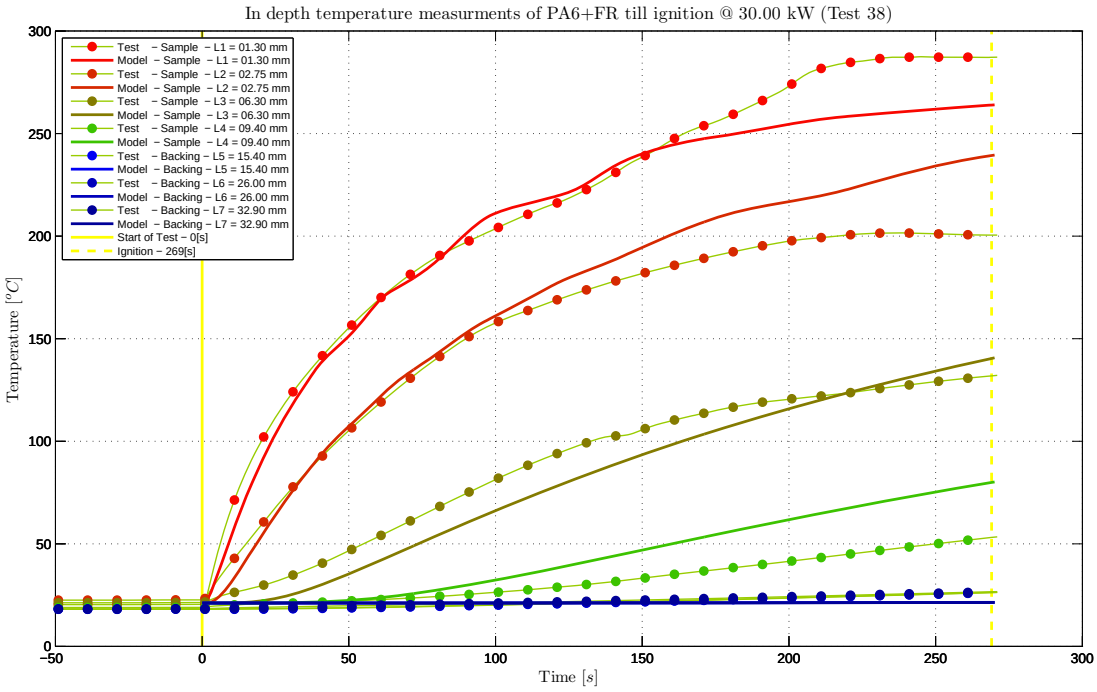

Figure 185 In-depth temperature "Test to Model" comparison of PA6+FR *with* the independently obtained intrinsic material properties (Test 38)

B.5.2.2 Mass loss fit

Without the independently obtained intrinsic material properties

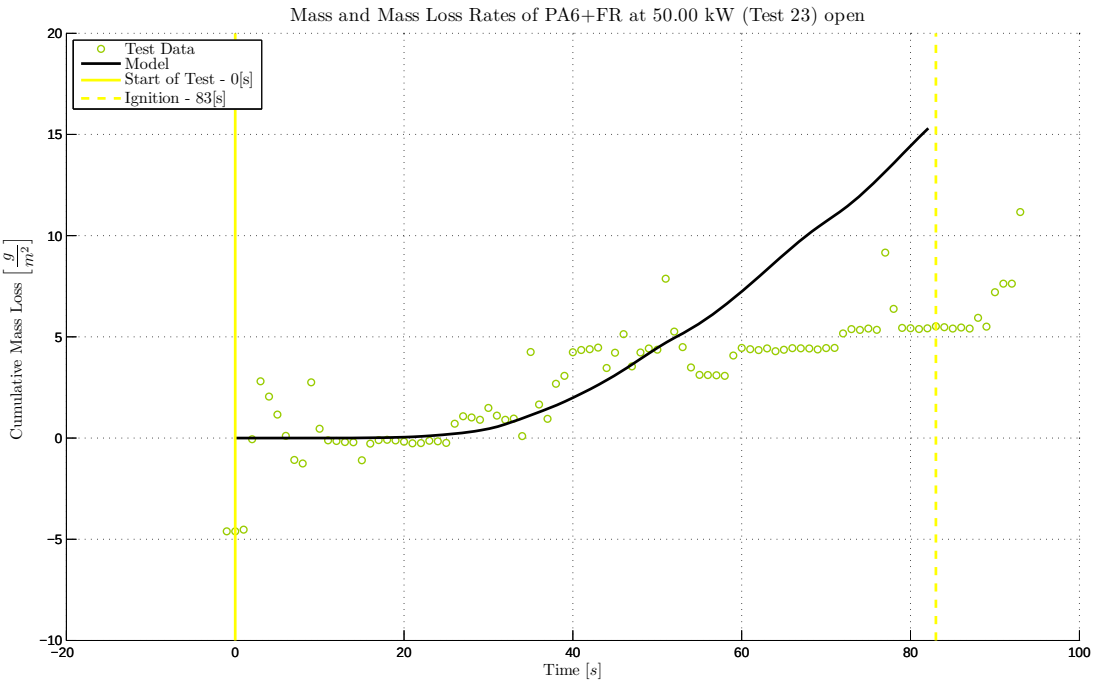

Figure 186 Cumulative mass loss "Test to Model" comparison of PA6+FR *without* the independently obtained intrinsic material properties (Test 23)

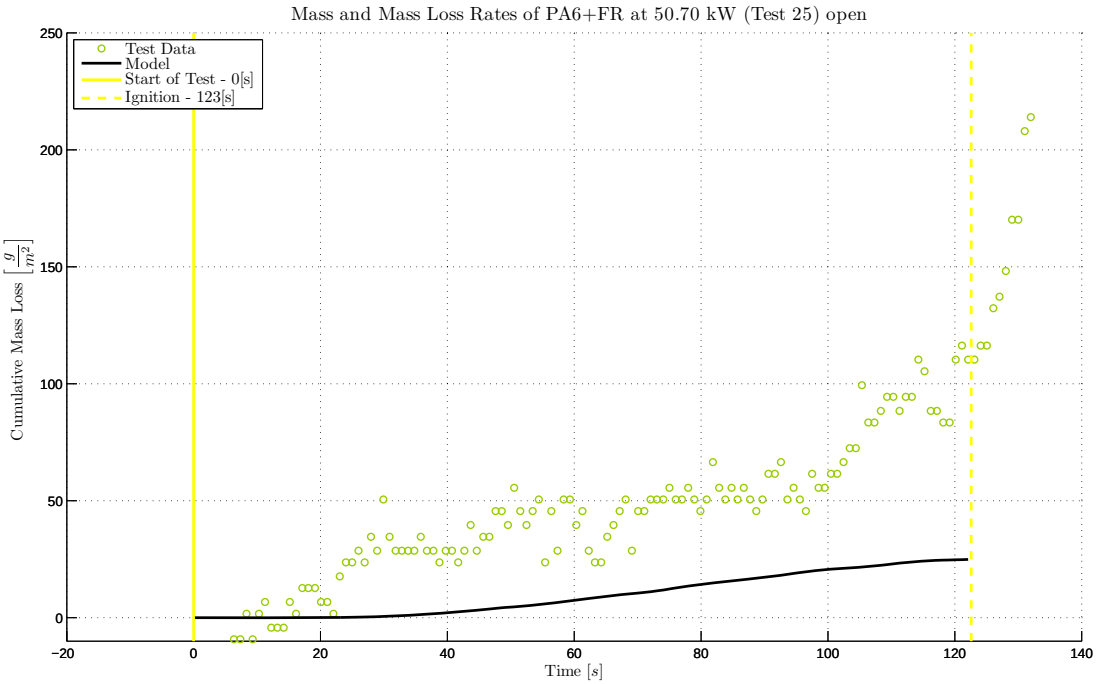

Figure 187 Cumulative mass loss "Test to Model" comparison of PA6+FR *without* the independently obtained intrinsic material properties (Test 25)

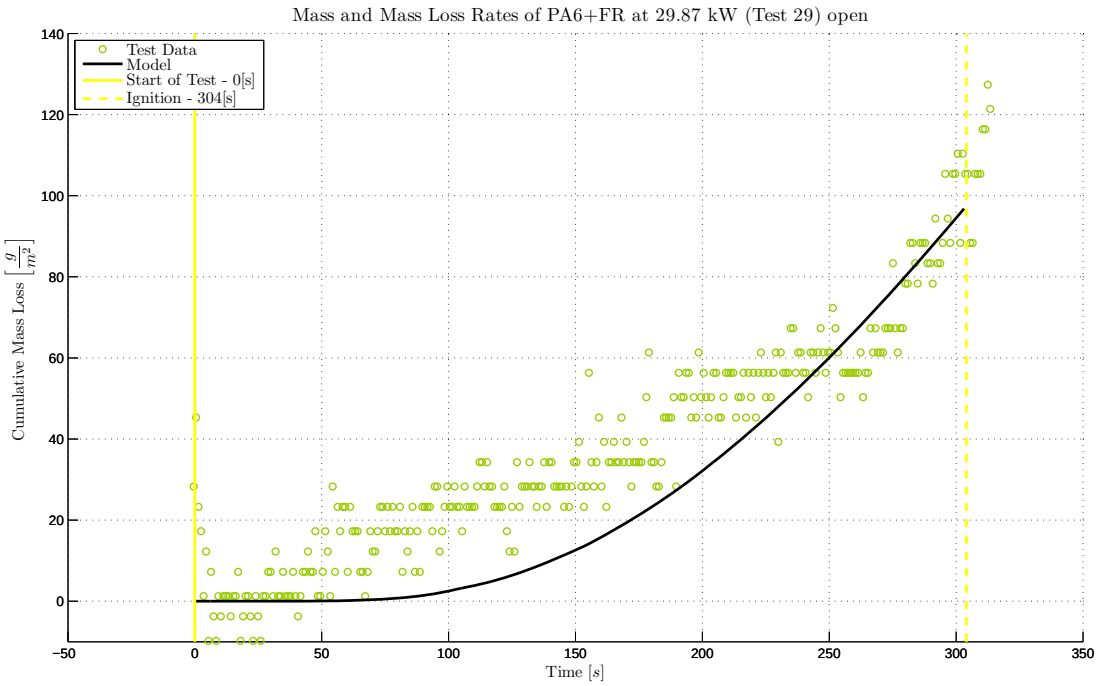

Figure 188 Cumulative mass loss "Test to Model" comparison of PA6+FR *without* the independently obtained intrinsic material properties (Test 29)

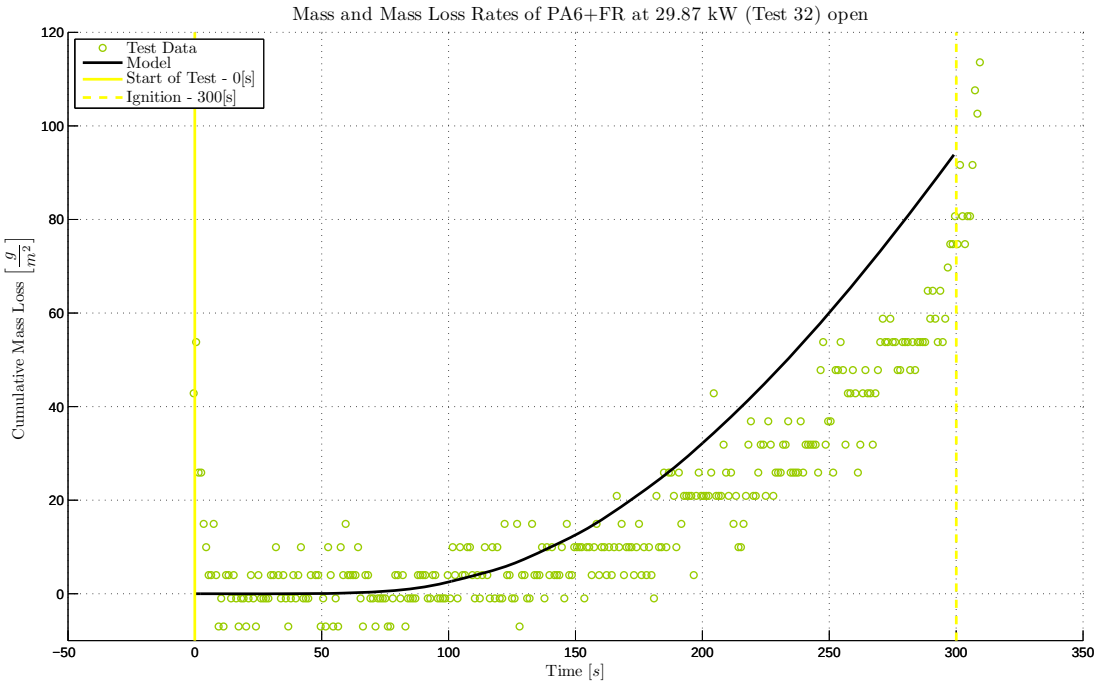

Figure 189 Cumulative mass loss "Test to Model" comparison of PA6+FR *without* the independently obtained intrinsic material properties (Test 32)

With the independently obtained intrinsic material properties

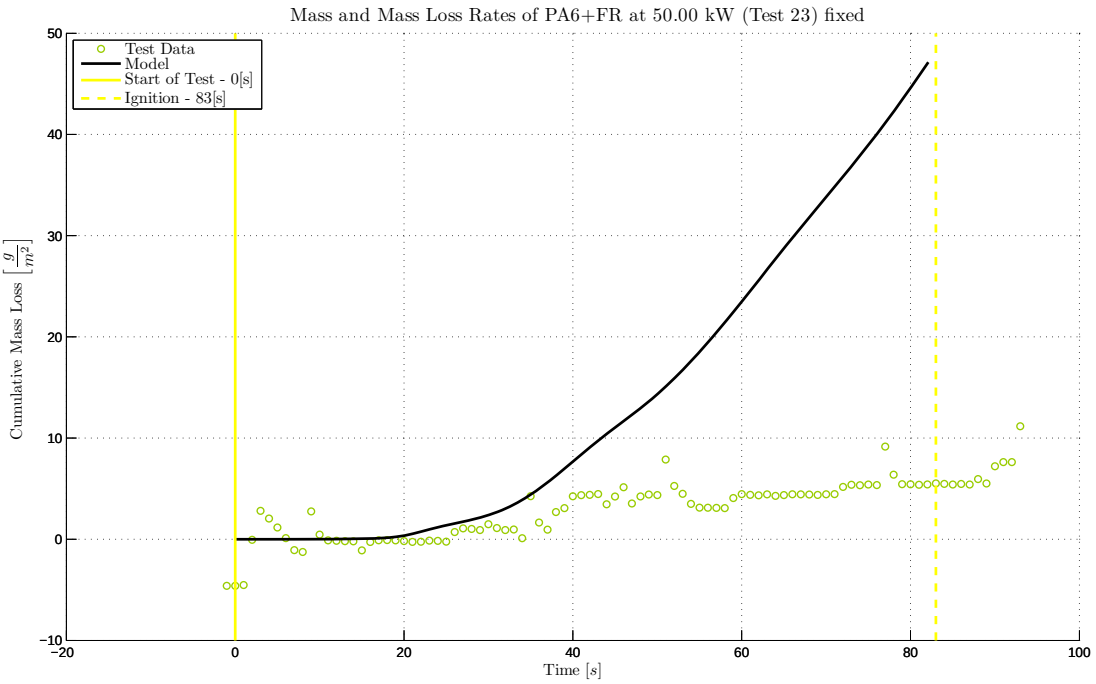

Figure 190 Cumulative mass loss "Test to Model" comparison of PA6+FR *with* the independently obtained intrinsic material properties (Test 23)

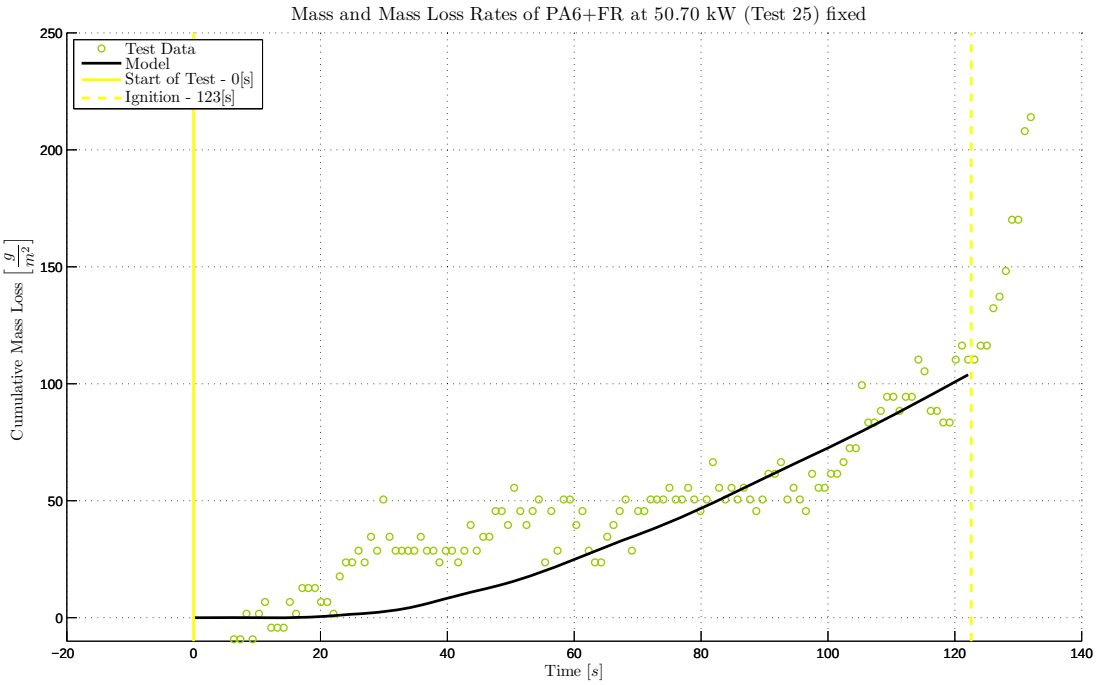

Figure 191 Cumulative mass loss "Test to Model" comparison of PA6+FR *with* the independently obtained intrinsic material properties (Test 25)

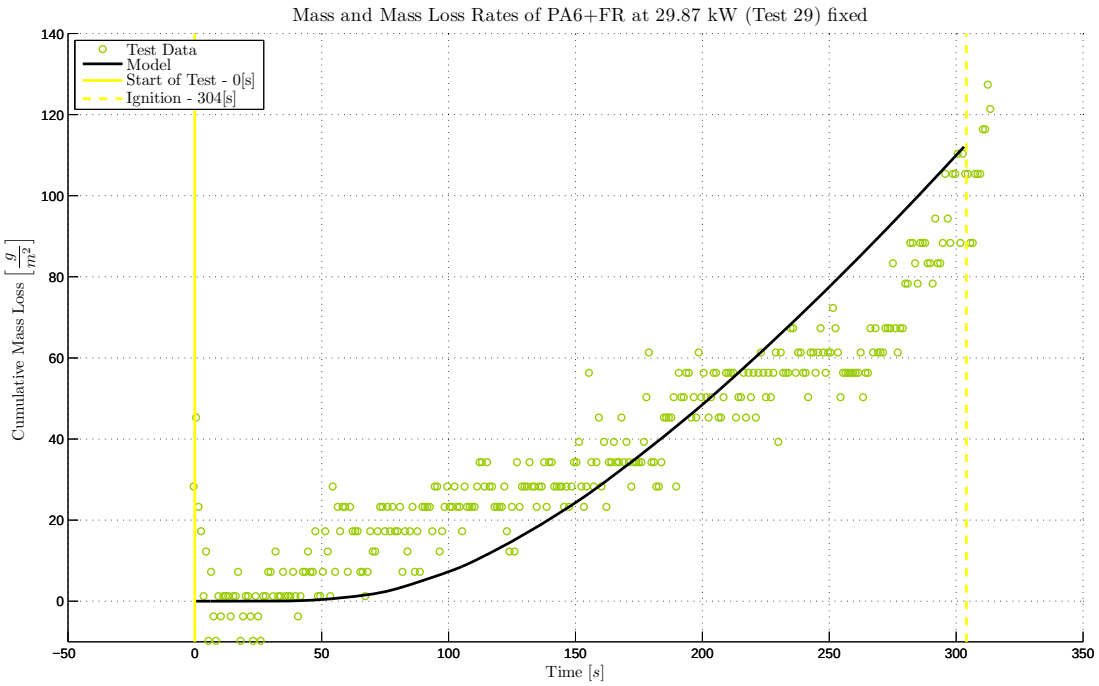

Figure 192 Cumulative mass loss "Test to Model" comparison of PA6+FR *with* the independently obtained intrinsic material properties (Test 29)

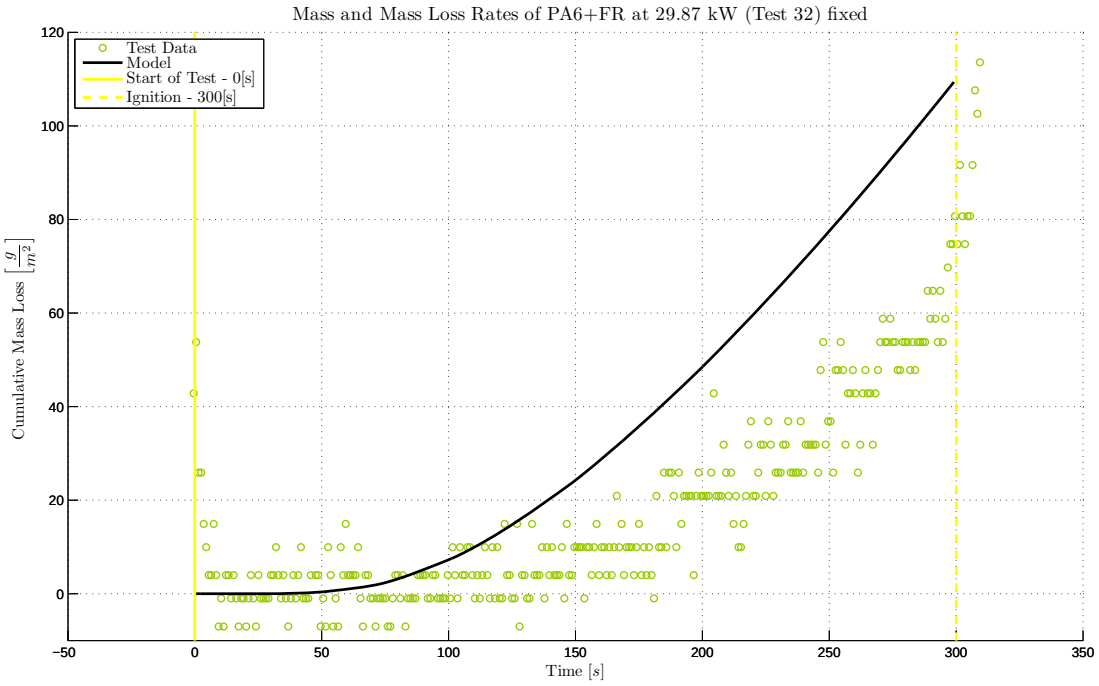

Figure 193 Cumulative mass loss "Test to Model" comparison of PA6+FR *with* the independently obtained intrinsic material properties (Test 32)

B.5.2.3 Side by side property comparison

Parameter					
#	Species	Symbol	Independently determined	gpyro_propest fit without independently determined	gpyro_propest fit with independently determined
1	1	Z	7.48	7.80	7.48
2	1	E	113	111	113
3	1	ΔH_{vol}		6.27	7.13
4	1	χ		0.798	0.866
5	1	n	2.52	2.45	2.52
6	1	n_{O_2}		0.0011	0
7	1	K_{cat}	0.19	2.06	0.19
8	2	Z	13.7	13.2	13.7
9	2	E	215	211	215
10	2	ΔH_{vol}		7.54	9.11
11	2	χ		0.877	0.840
12	2	n	1.04	1.18	1.04
13	2	n_{O_2}		0.901	3.691
14	3	Z	4.16	5.03	4.16
15	3	E	89	86	89
16	3	ΔH_{vol}		4.49	5.87
17	3	χ		0.798	0.864
18	3	n	0.816	0.990	0.816
19	3	n_{O_2}		0.75	3.76
20	4	Z	5.67	5.71	5.67
21	4	E	133	130	133
22	4	ΔH_{vol}		7.34	8.32
23	4	χ		0.949	0.859
24	4	n	1.13	1.27	1.13
25	4	n_{O_2}		0.97	1.84
26	1	k_{0z}	0.25	0.73	0.25
27	2	k_{0z}		13.68	11.04
28	3	k_{0z}		23.58	16.29
29	4	k_{0z}		3.66	15.85
30	5	k_{0z}		17.70	7.23
31	1	ρ_0	1111	12303	1111
32	1	n_ρ		-1.73	-0.19
33	2	ρ_0	823	348	235
34	3	ρ_0	18	842	387
35	4	ρ_0	640	616	900
36	5	ρ_0	59	593	458
37	1	c_0	1515	1611	1515

Parameter					
#	Species	Symbol	Independently determined	gpyro_propest fit without independently determined	gpyro_propest fit with independently determined
38	1	n_c	0.77	0.13	0.77
39	2	c_0		109	1885
40	3	c_0		1009	1428
41	4	c_0		3787	3127
42	5	c_0		1752	2224
43	1	ε		0.88	0.91
44	2	ε		0.80	0.90
45	3	ε		0.78	0.74
46	4	ε		0.70	0.64
47	5	ε		0.36	0.59
48	1	κ		3.47	3.75
49	2	κ		5.18	3.40
50	3	κ		0.78	2.97
51	4	κ		4.72	2.53
52	5	κ		2.37	2.15
53	1	T_m	488	512	488
54	1	ΔH_m	53000	22923	53000
55	1	σ_m^2	52	23	52
56	1	γ		0.000630	0.000468
57	2	γ		0.000759	0.000319
58	3	γ		0.000843	0.000385
59	4	γ		0.000277	0.000362
60	5	γ		0.0000179	0.000462
61	1	K_z		-5.59	-8.44
62	2	K_z		-5.31	-8.07
63	3	K_z		-12.78	-11.68
64	4	K_z		-10.80	-14.64
65	5	K_z		-18.63	-13.97
66	1	ρ_{s0}		1566	1636
67	2	ρ_{s0}		827	786
68	3	ρ_{s0}		527	1054
69	4	ρ_{s0}		1258	1190
70	5	ρ_{s0}		168	798
71	1	h_{cr}		78.6	60.6
72	2	h_{cr}		5.4	6.71

Table 46 Comparison of the resulting parameters for PA6+FR

B.5.3 PA6+NC

B.5.3.1 In-depth temperature fit

Without the independently obtained intrinsic material properties

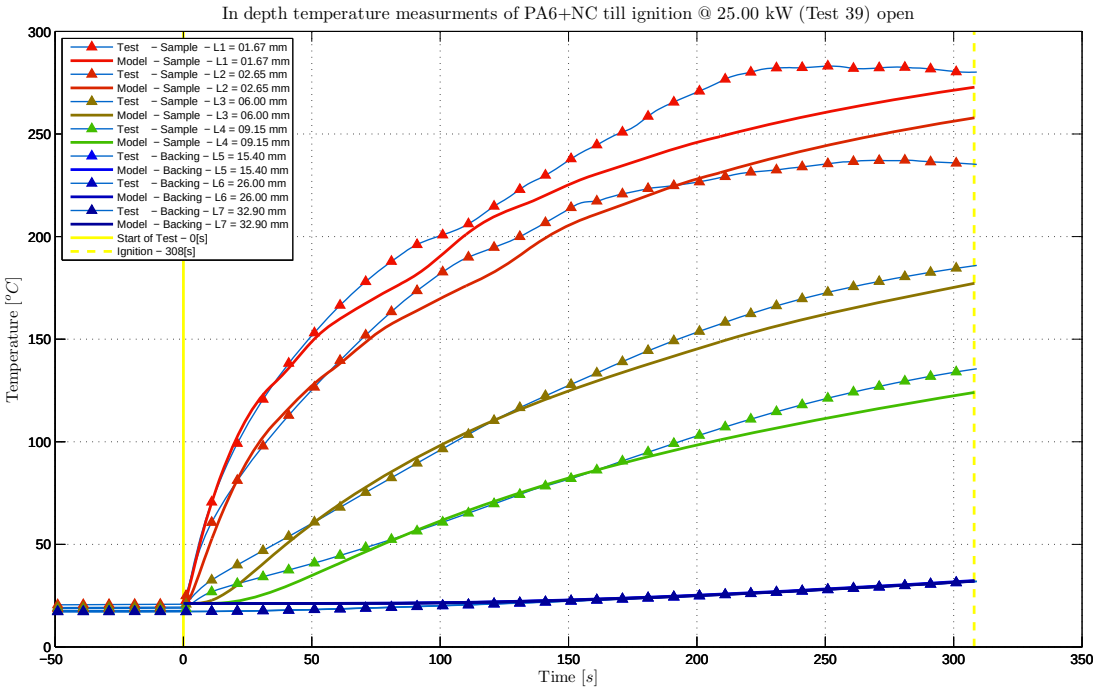

Figure 194 In-depth temperature “Test to Model” comparison of PA6+NC *without* the independently obtained intrinsic material properties (Test 39)

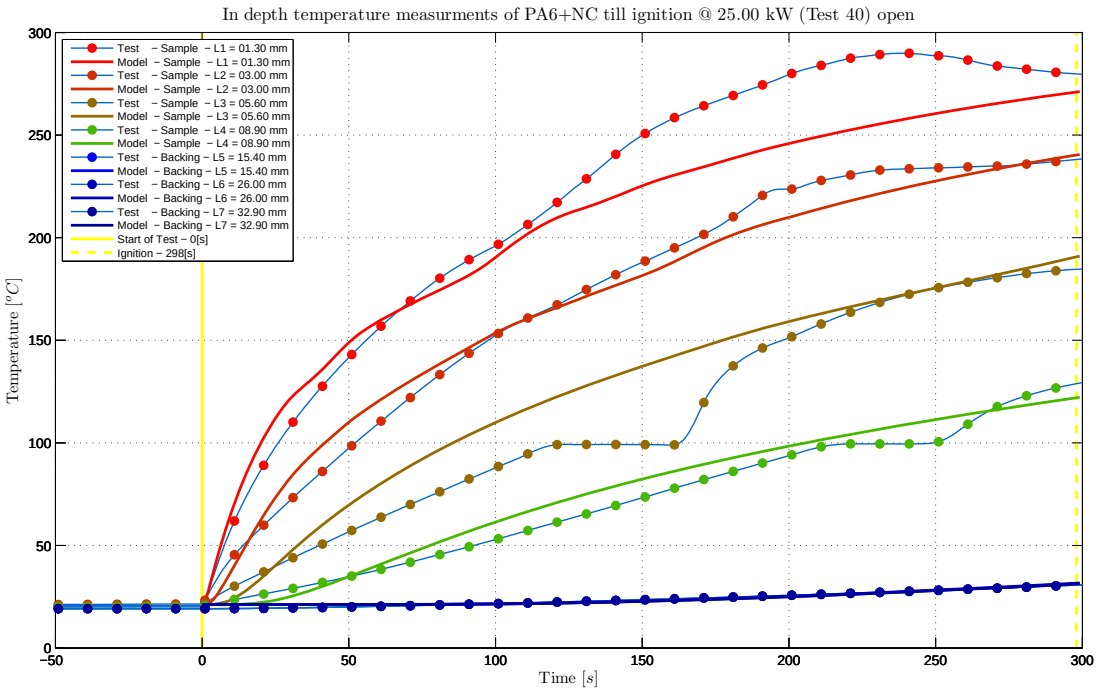

Figure 195 In-depth temperature "Test to Model" comparison of PA6+NC *without* the independently obtained intrinsic material properties (Test 40)

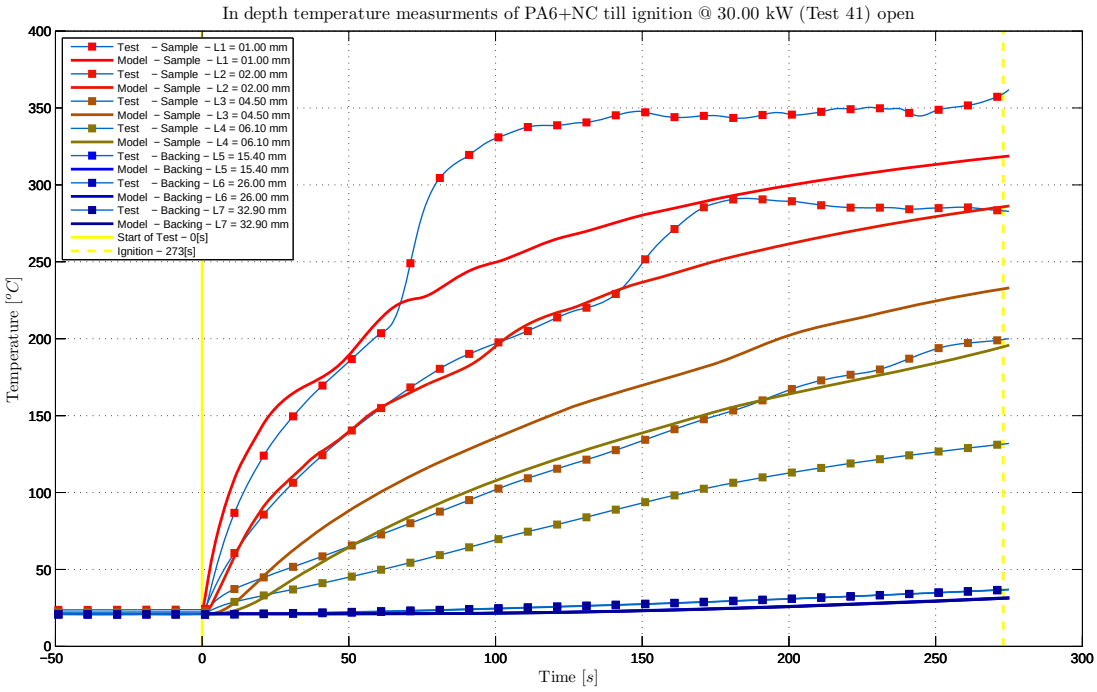

Figure 196 In-depth temperature "Test to Model" comparison of PA6+NC *without* the independently obtained intrinsic material properties (Test 41)

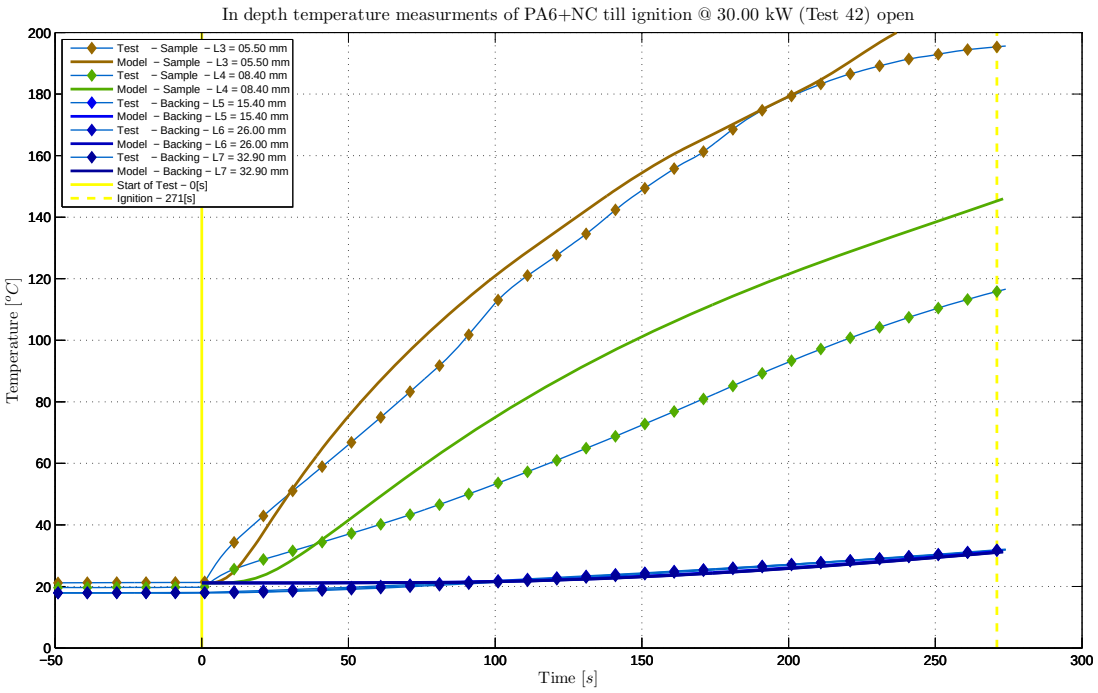

Figure 197 In-depth temperature "Test to Model" comparison of PA6+NC *without* the independently obtained intrinsic material properties (Test 42)

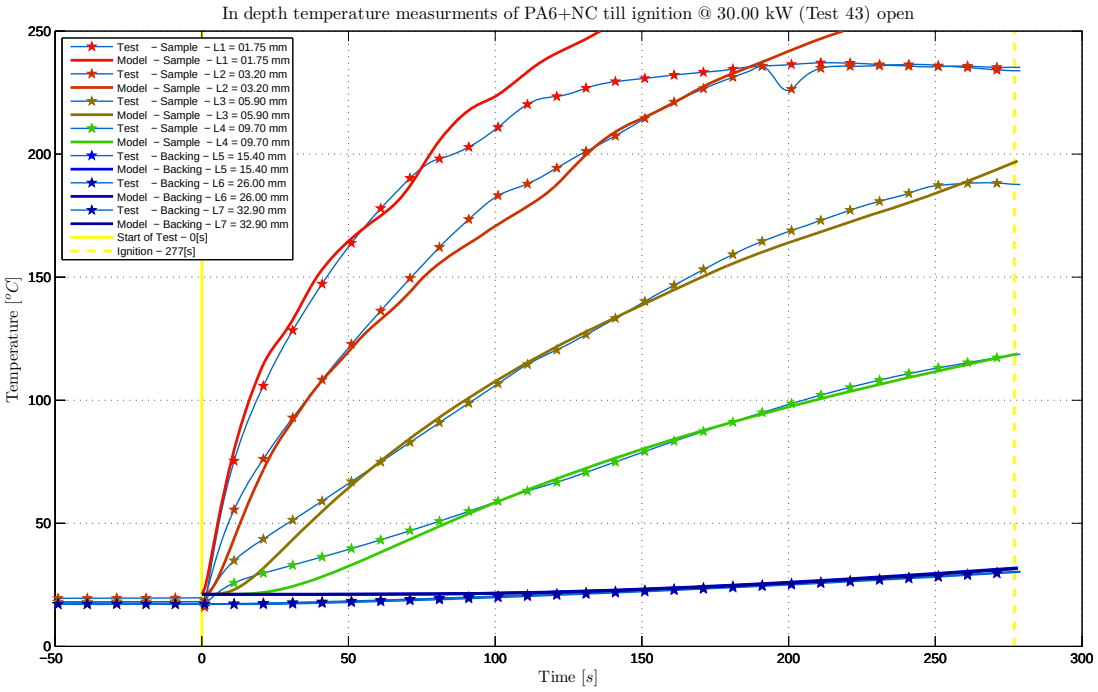

Figure 198 In-depth temperature "Test to Model" comparison of PA6+NC *without* the independently obtained intrinsic material properties (Test 43)

With the independently obtained intrinsic material properties

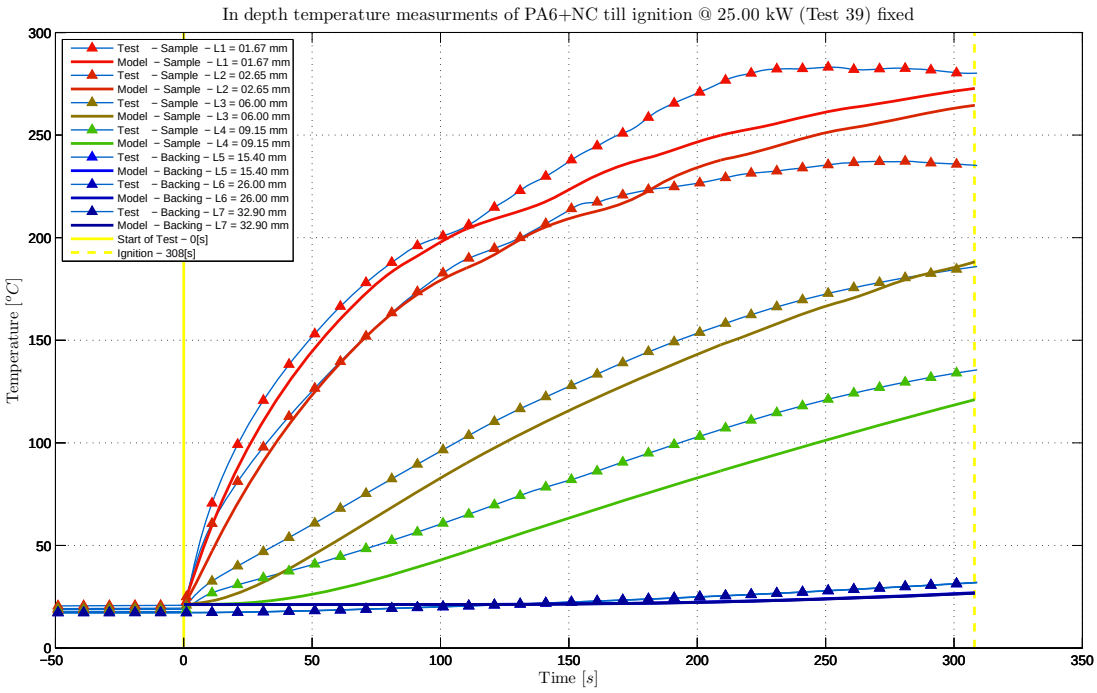

Figure 199 In-depth temperature "Test to Model" comparison of PA6+NC *with* the independently obtained intrinsic material properties (Test 39)

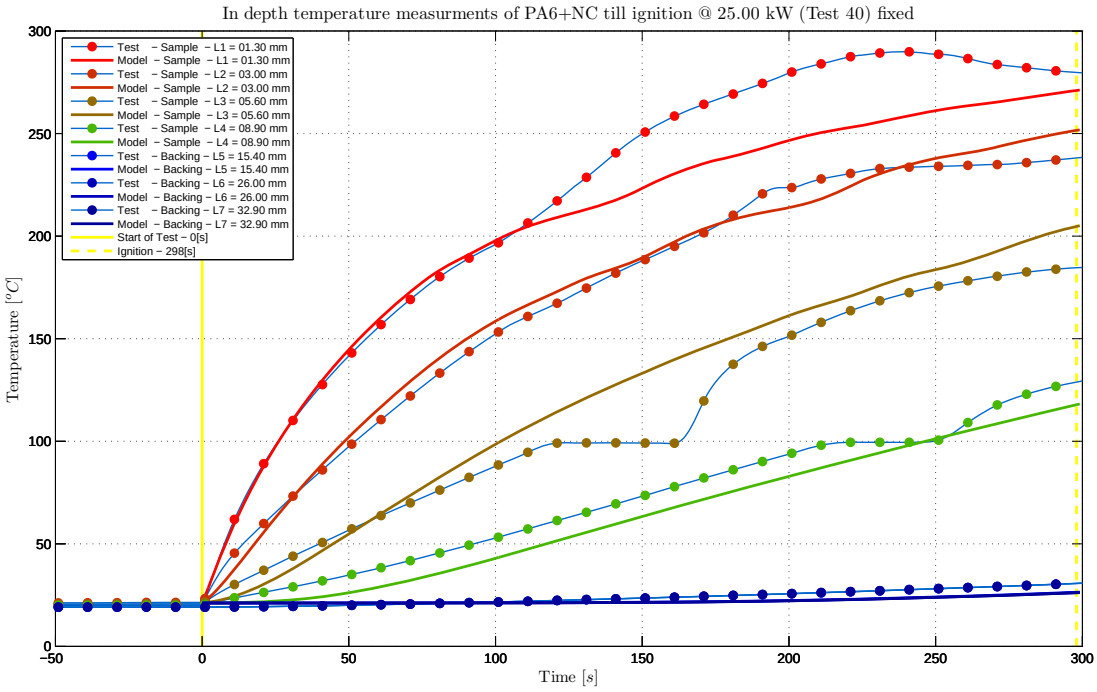

Figure 200 In-depth temperature "Test to Model" comparison of PA6+NC *with* the independently obtained intrinsic material properties (Test 40)

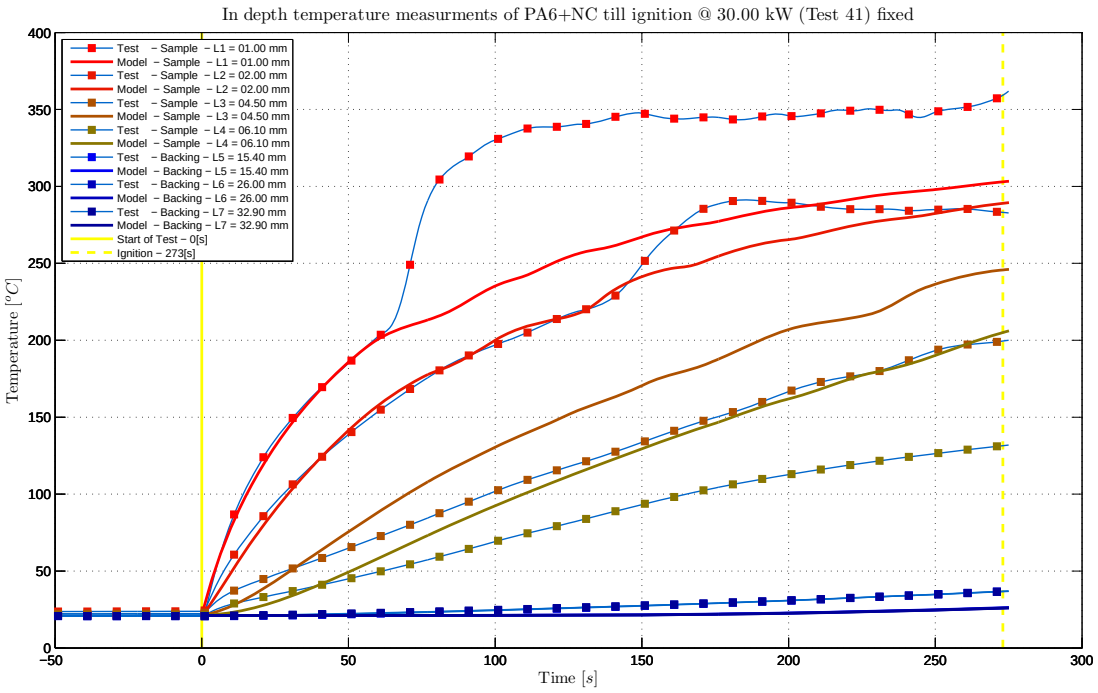

Figure 201 In-depth temperature "Test to Model" comparison of PA6+NC *with* the independently obtained intrinsic material properties (Test 41)

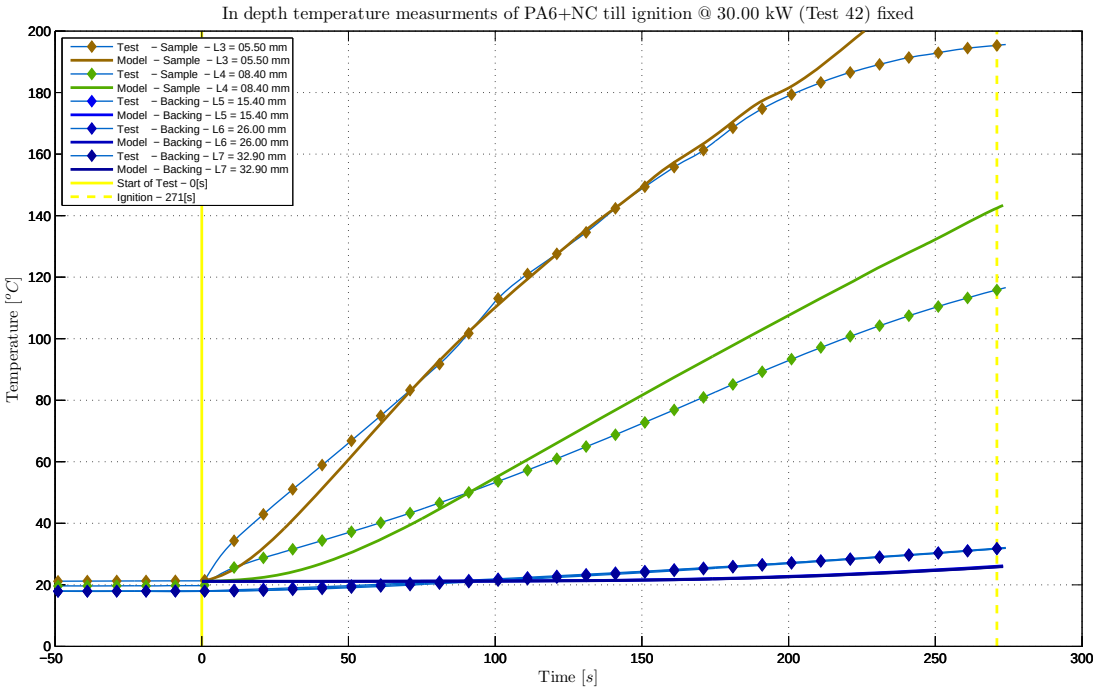

Figure 202 In-depth temperature "Test to Model" comparison of PA6+NC *with* the independently obtained intrinsic material properties (Test 42)

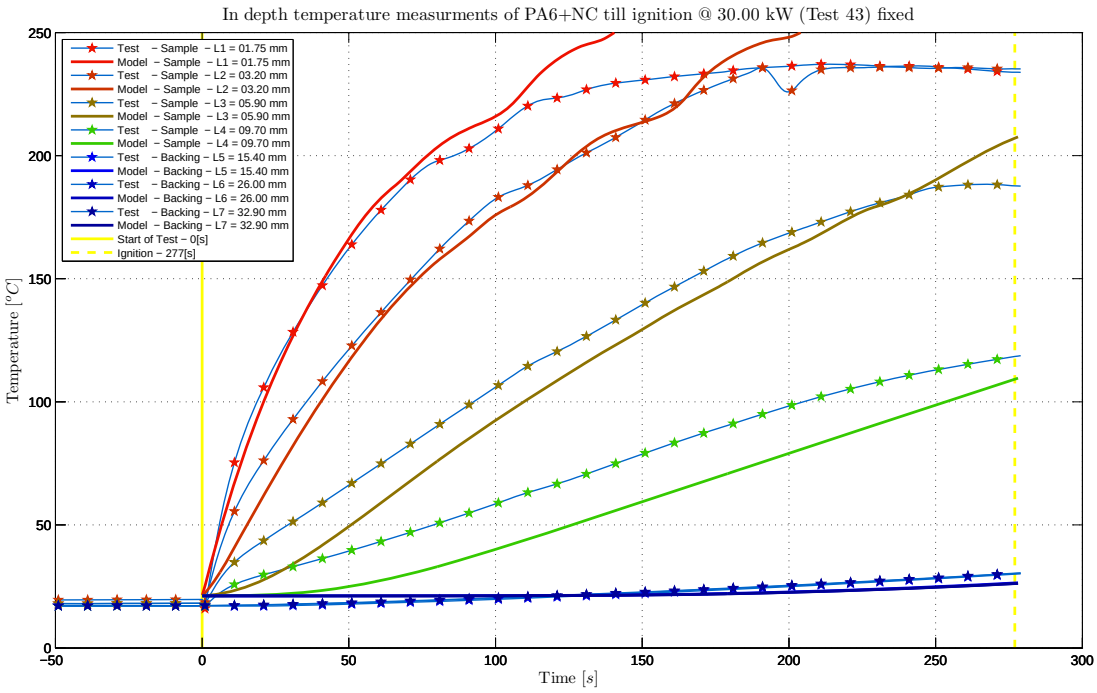

Figure 203 In-depth temperature "Test to Model" comparison of PA6+NC *with* the independently obtained intrinsic material properties (Test 43)

B.5.3.2 Mass loss fit

Without the independently obtained intrinsic material properties

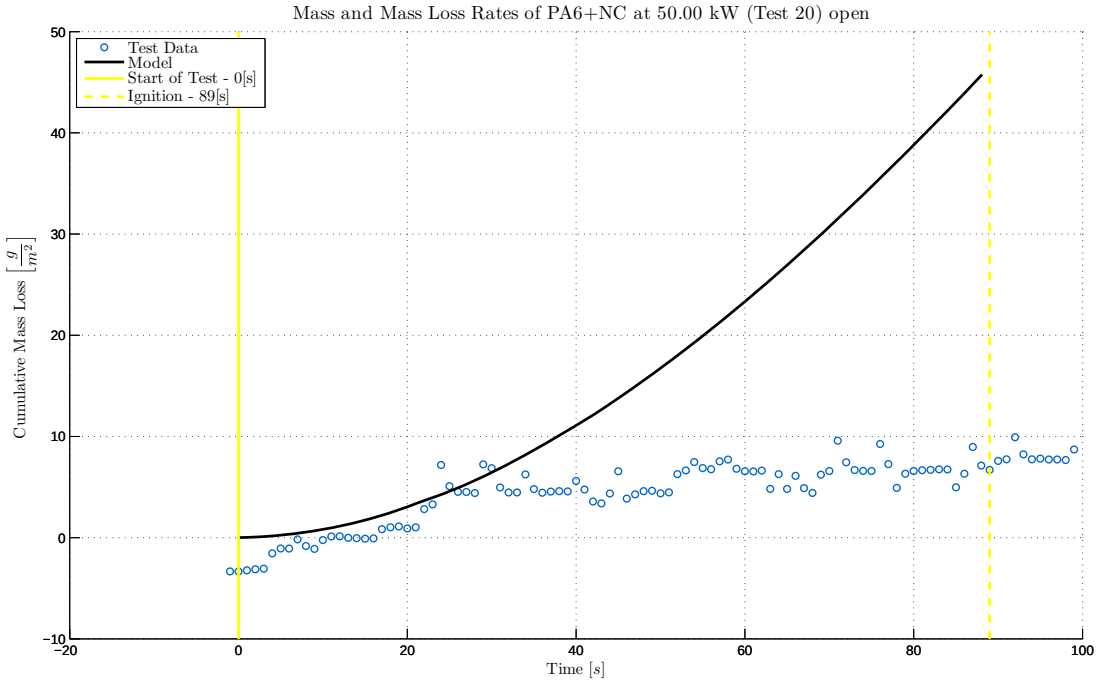

Figure 204 Cumulative mass loss "Test to Model" comparison of PA6+NC *without* the independently obtained intrinsic material properties (Test 20)

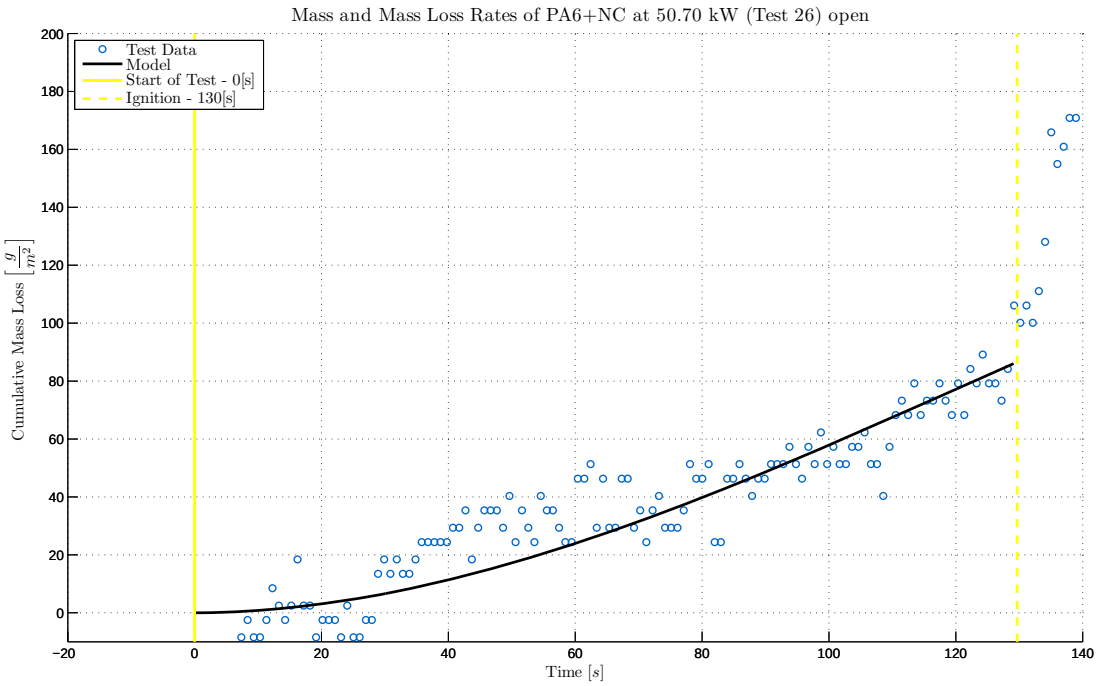

Figure 205 Cumulative mass loss "Test to Model" comparison of PA6+NC *without* the independently obtained intrinsic material properties (Test 26)

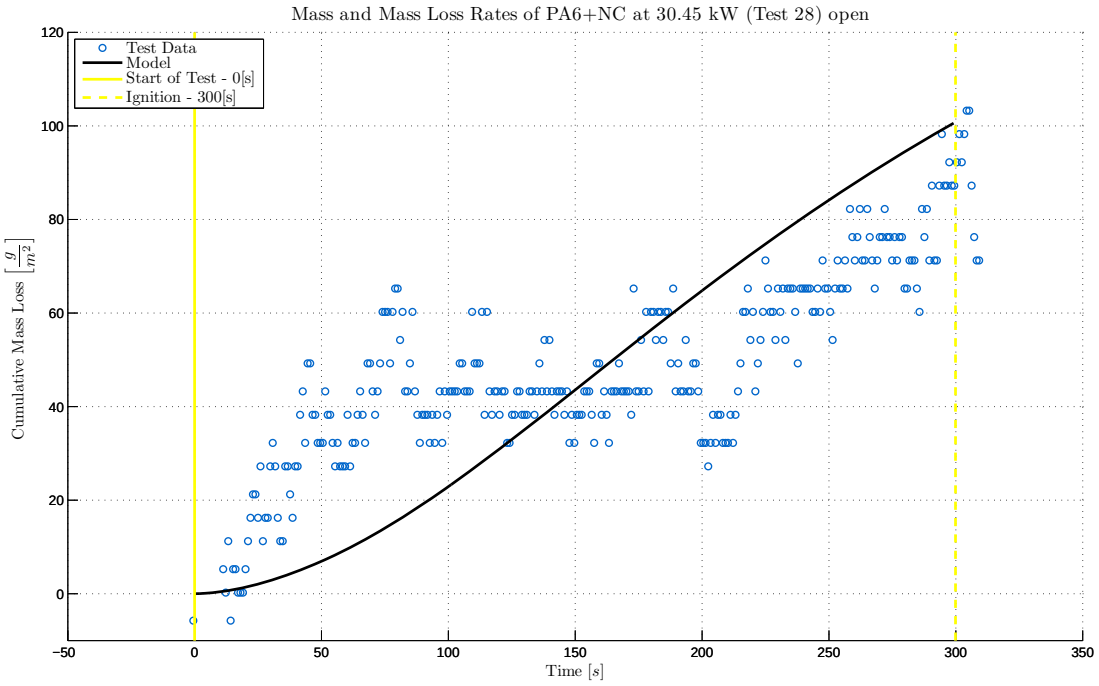

Figure 206 Cumulative mass loss "Test to Model" comparison of PA6+NC *without* the independently obtained intrinsic material properties (Test 28)

With the independently obtained intrinsic material properties

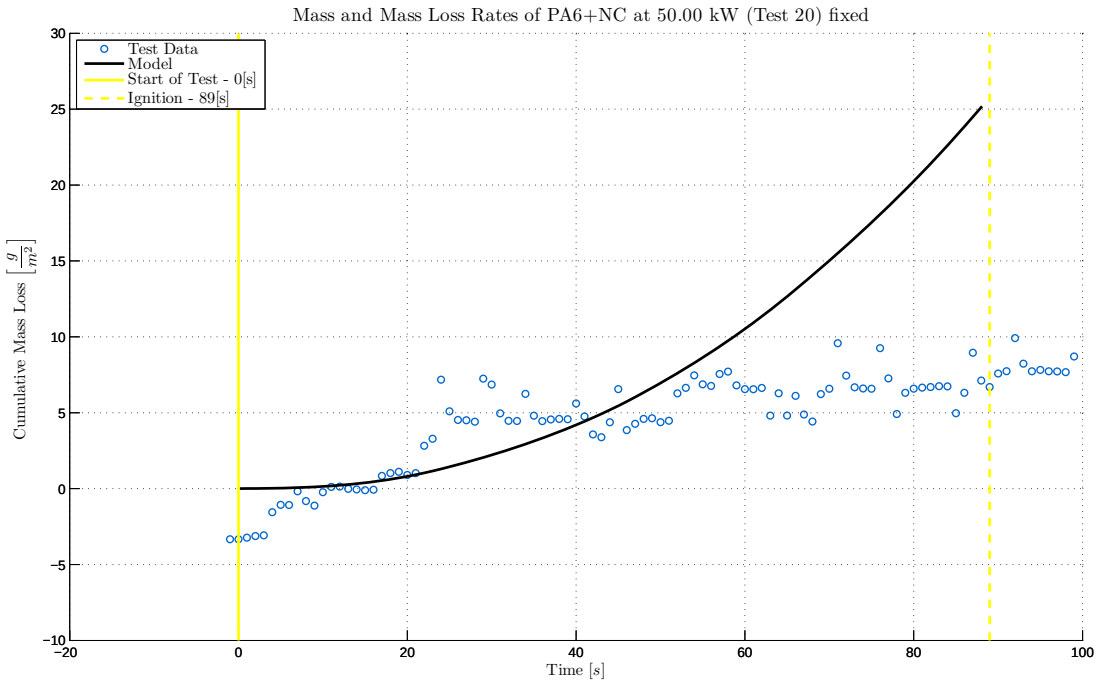

Figure 207 Cumulative mass loss "Test to Model" comparison of PA6+NC *with* the independently obtained intrinsic material properties (Test 20)

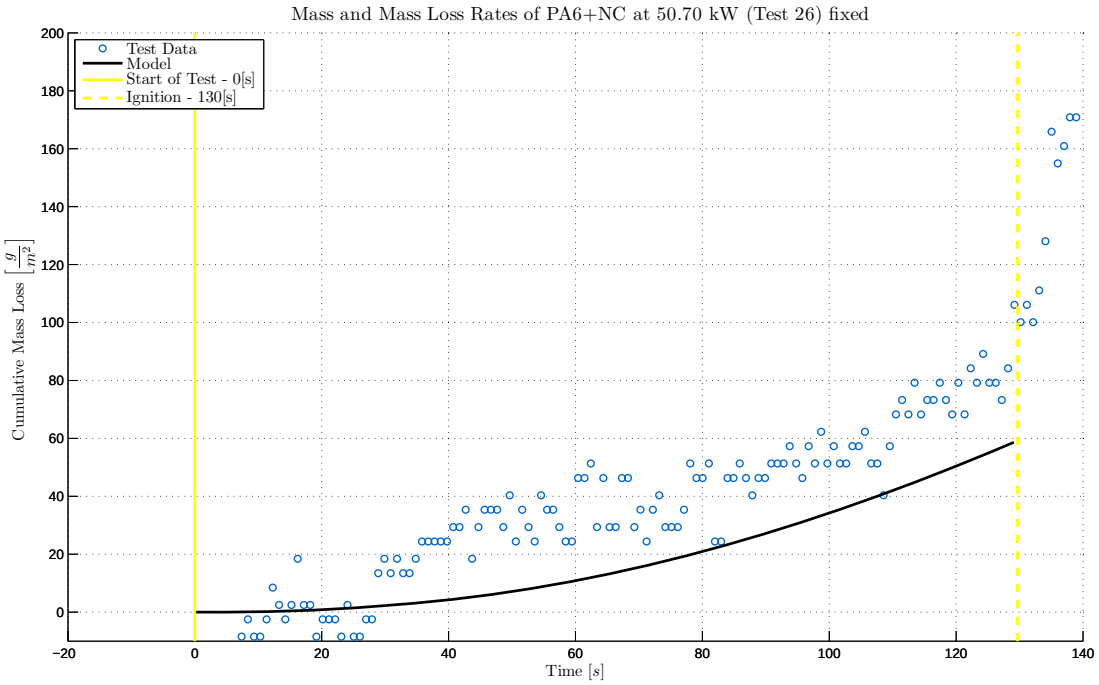

Figure 208 Cumulative mass loss "Test to Model" comparison of PA6+NC *with* the independently obtained intrinsic material properties (Test 26)

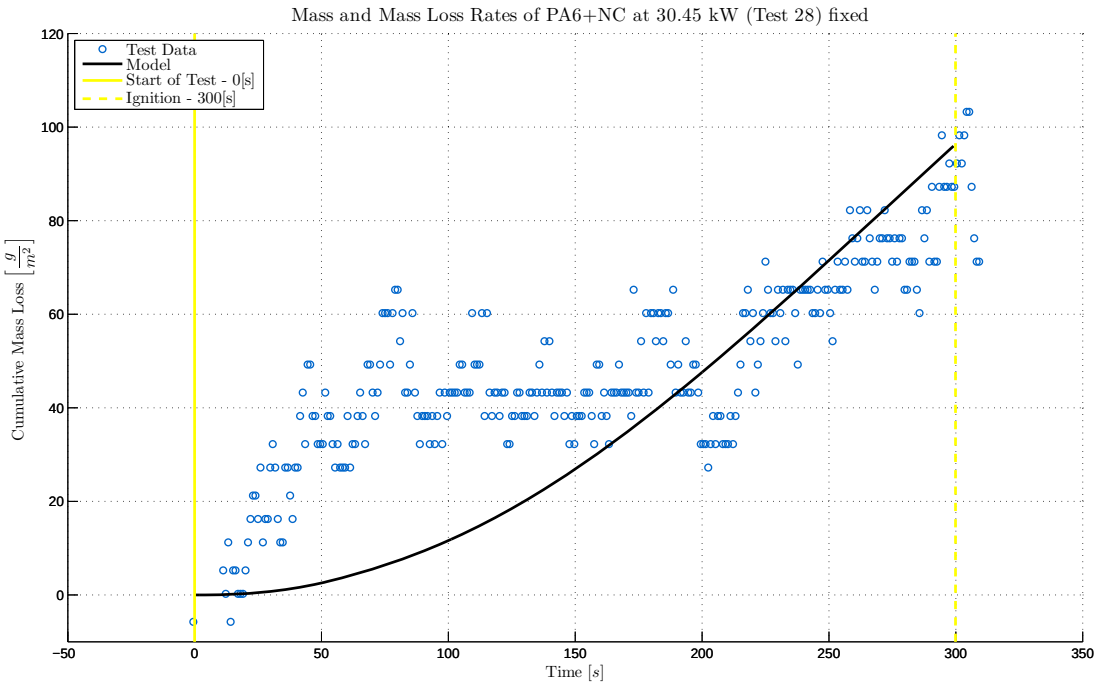

Figure 209 Cumulative mass loss “Test to Model” comparison of PA6+NC *with* the independently obtained intrinsic material properties (Test 28)

B.5.3.3 Side by side property comparison

Parameter					
#	Species	Symbol	Independently determined	gpyro_propest fit without independently determined	gpyro_propest fit with independently determined
1	1	Z	13.8	133	13.8
2	1	E	208	211	208
3	1	ΔH_{vol}		3.90	3.73
4	1	χ		1	1
5	1	n	1.53	1.51	1.53
6	1	n_{O_2}		3.03	3.61
7	1	K_{cat}	-1.84	-2.03	-1.84
8	2	Z	9.31	8.71	9.31
9	2	E	156	154	156
10	2	ΔH_{vol}		4.32	4.08
11	2	χ		1	1
12	2	n	0.616	0.508	0.616
13	2	n_{O_2}		2.82	2.58
14	3	Z	1.65	1.52	1.65
15	3	E	47	44	47
16	3	ΔH_{vol}		4.89	5.24
17	3	χ		1	1
18	3	n	1.16	1.17	1.16
19	3	n_{O_2}		0.579	0.342
20	4	Z	8.37	8.62	8.37
21	4	E	171	169	171
22	4	ΔH_{vol}		6.04	6.33
23	4	χ		1	1
24	4	n	1.28	1.37	1.28
25	4	n_{O_2}		2.08	2.29
26	1	k_{0z}	0.290	0.4	0.3
27	2	k_{0z}		13.7	22.5
28	3	k_{0z}		14.3	18.7
29	4	k_{0z}		7.3	18.4
30	5	k_{0z}		10.2	12.5
31	1	ρ_0	1156	1208	1156
32	1	n_ρ		0	0
33	2	ρ_0	809	566	820
34	3	ρ_0	52	982	115
35	4	ρ_0	712	502	729
36	5	ρ_0	18	774	64
37	1	c_0	1528	966	1528

Parameter					
#	Species	Symbol	Independently determined	gpyro_propest fit without independently determined	gpyro_propest fit with independently determined
38	1	n_c	0.72	0.31	0.72
39	2	c_0		2003	2144
40	3	c_0		1968	1320
41	4	c_0		1816	1717
42	5	c_0		2249	1801
43	1	ε		0.88	0.98
44	2	ε		0.70	0.69
45	3	ε		0.54	0.83
46	4	ε		0.63	0.82
47	5	ε		0.83	0.58
48	1	κ		3.67	2.89
49	2	κ		3.30	4.26
50	3	κ		3.84	2.95
51	4	κ		3.69	2.95
52	5	κ		4.13	4.69
53	1	T_m	484	442	484
54	1	ΔH_m	65000	89703	65000
55	1	σ_m^2	40	125	40
56	1	γ		0.000555	0.000530
57	2	γ		0.000535	0.000659
58	3	γ		0.000489	0.000568
59	4	γ		0.000555	0.000618
60	5	γ		0.000663	0.000910
61	1	K_z		-12.6	-11.7
62	2	K_z		-11.64	-10.7
63	3	K_z		-13.1	-12.6
64	4	K_z		-12.2	-13.4
65	5	K_z		-12.7	-12.6
66	1	ρ_{s0}		1718	1418
67	2	ρ_{s0}		863	1075
68	3	ρ_{s0}		1081	231
69	4	ρ_{s0}		1018	998
70	5	ρ_{s0}		1120	148
71	1	h_{cr}		123	126
72	2	h_{cr}		6	7

Table 47 Comparison of the resulting parameters for PA6+NC

B.5.4 PA6+NC+FR

B.5.4.1 In-depth temperature fit

Without the independently obtained intrinsic material properties

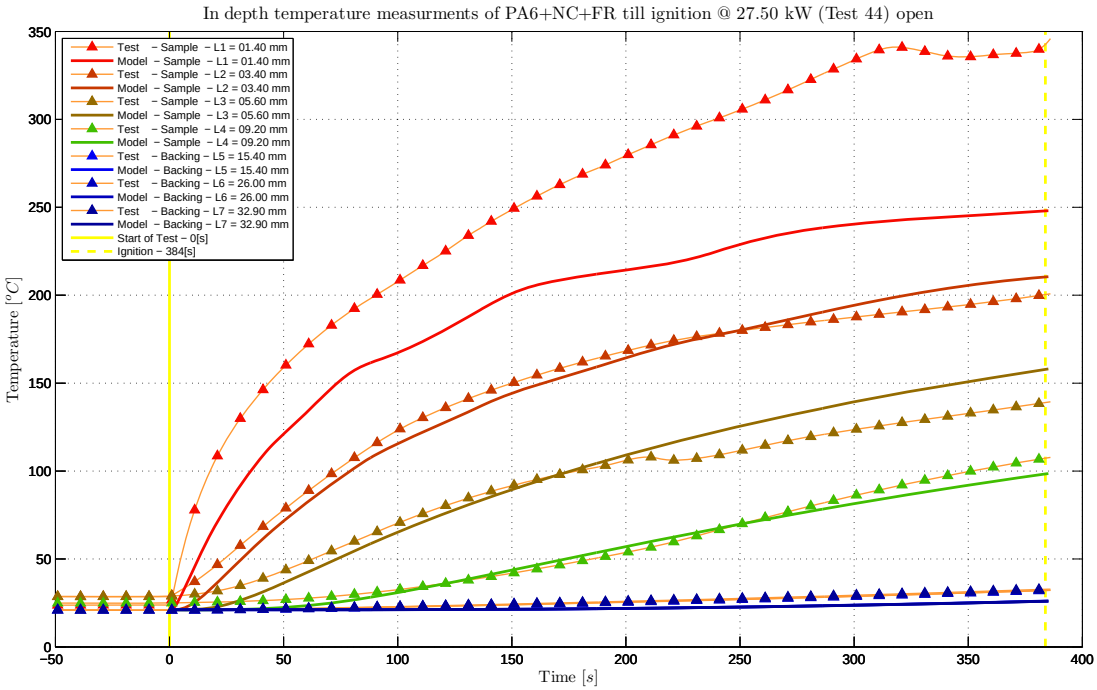

Figure 210 In-depth temperature “Test to Model” comparison of PA6+NC+FR *without* the independently obtained intrinsic material properties (Test 44)

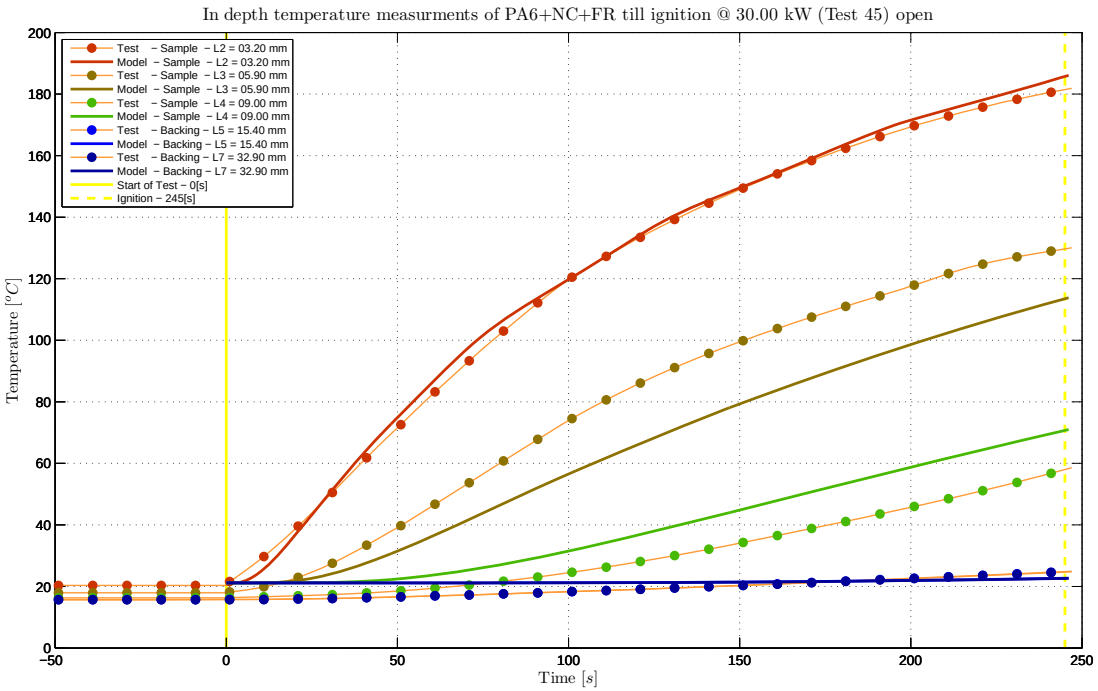

Figure 211 In-depth temperature "Test to Model" comparison of PA6+NC+FR *without* the independently obtained intrinsic material properties (Test 45)

With the independently obtained intrinsic material properties

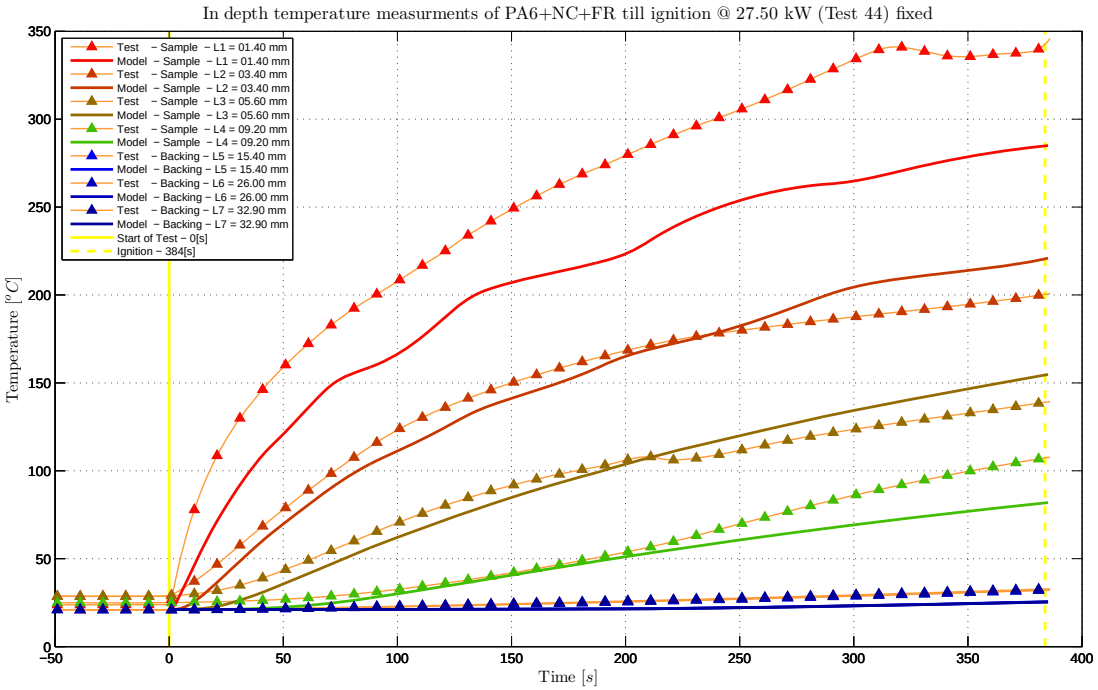

Figure 212 In-depth temperature "Test to Model" comparison of PA6+NC+FR *with* the independently obtained intrinsic material properties (Test 44)

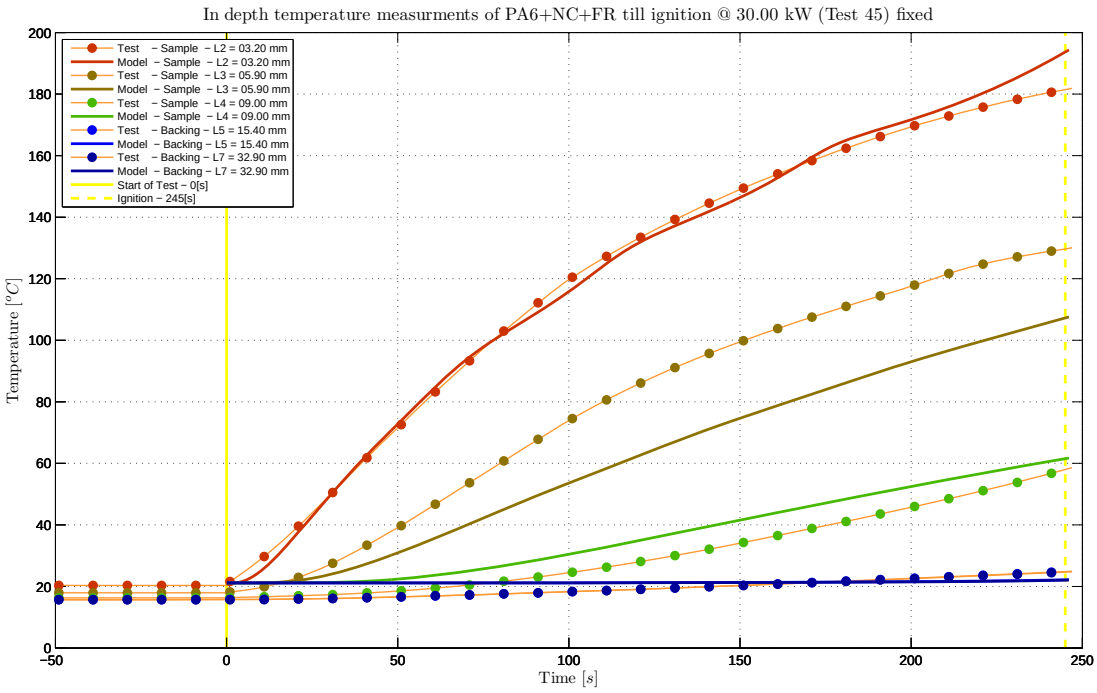

Figure 213 In-depth temperature "Test to Model" comparison of PA6+NC+FR *with* the

B.5.4.2 Mass loss fit

Without the independently obtained intrinsic material properties

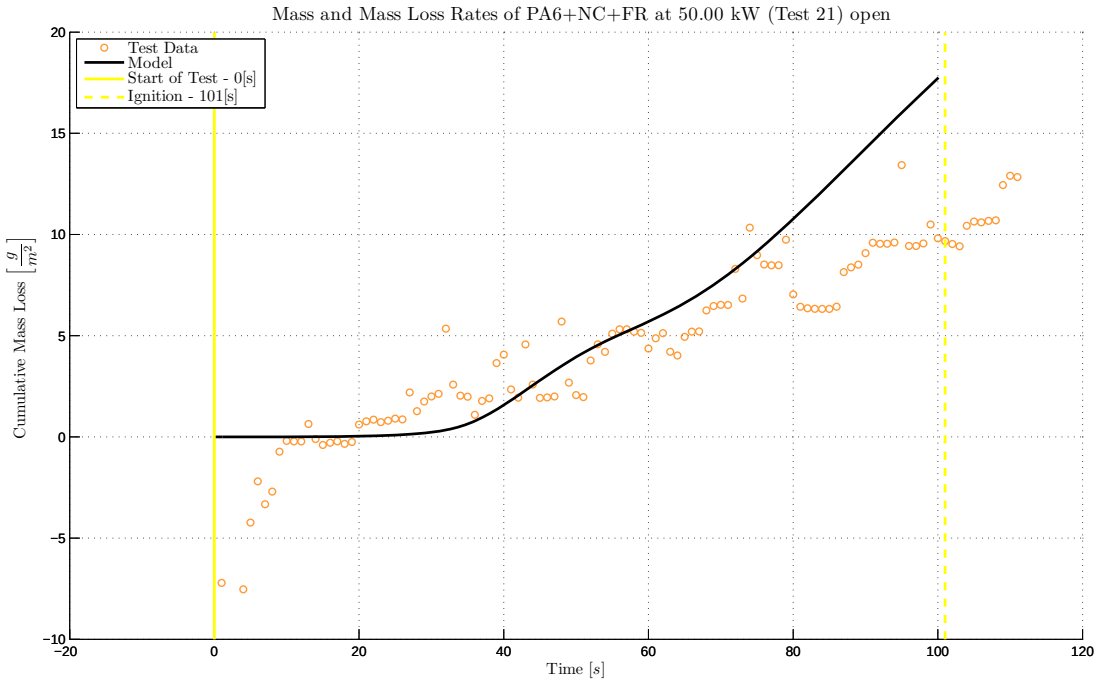

Figure 214 Cumulative mass loss "Test to Model" comparison of PA6+NC+FR *without* the independently obtained intrinsic material properties (Test 21)

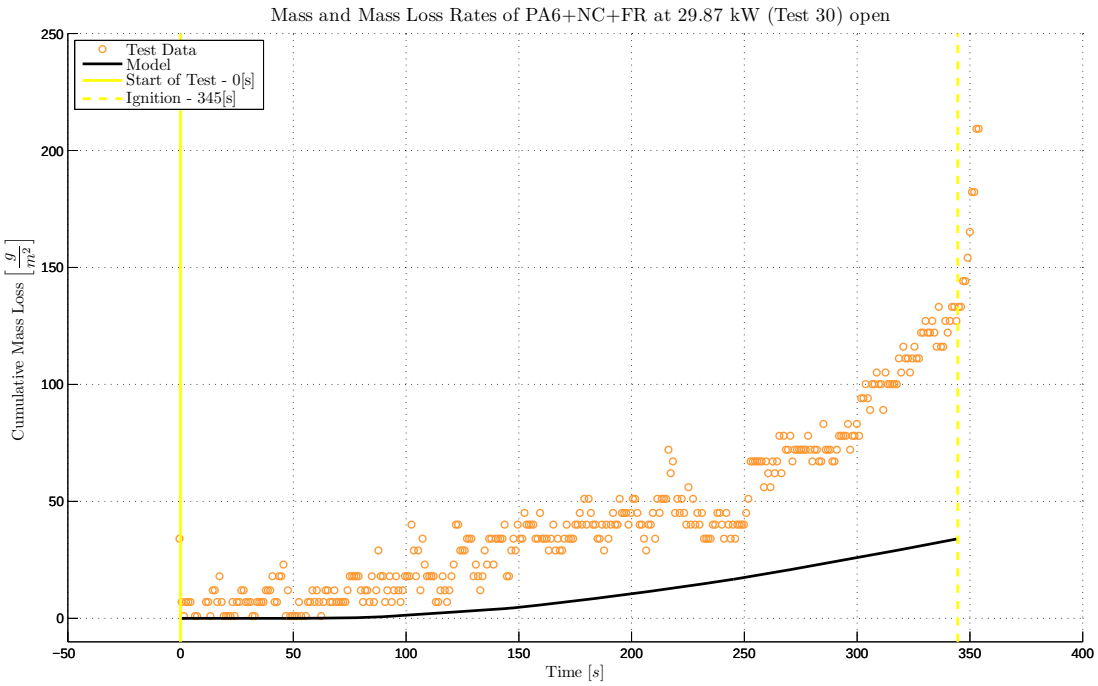

Figure 215 Cumulative mass loss "Test to Model" comparison of PA6+NC +FR *without* the independently obtained intrinsic material properties (Test 30)

With the independently obtained intrinsic material properties

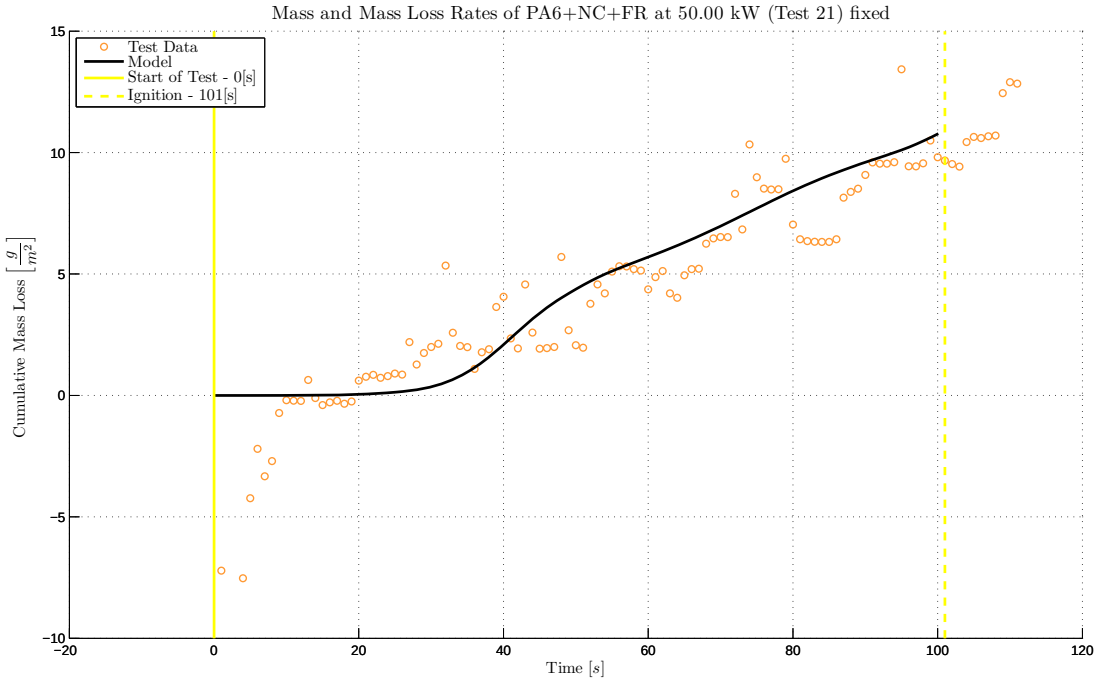

Figure 216 Cumulative mass loss "Test to Model" comparison of PA6+NC +FR *with* the independently obtained intrinsic material properties (Test 21)

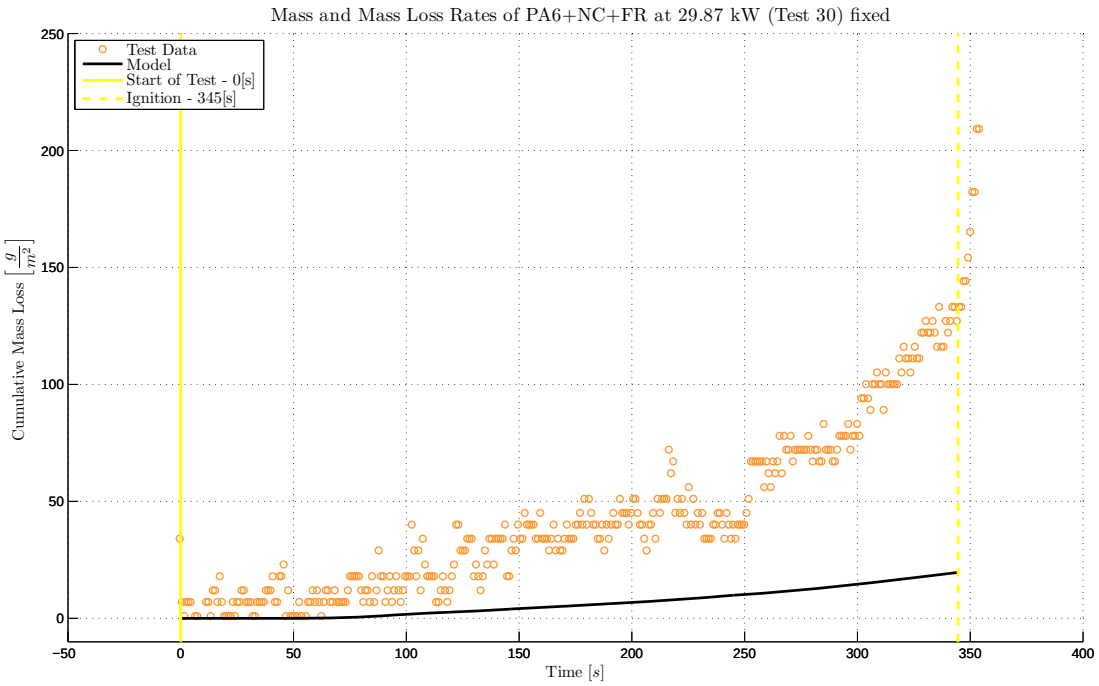

Figure 217 Cumulative mass loss "Test to Model" comparison of PA6+NC +FR *with* the independently obtained intrinsic material properties (Test 30)

B.5.4.3 Side by side property comparison

Parameter					
#	Species	Symbol	Independently determined	gpyro_propest fit without independently determined	gpyro_propest fit with independently determined
1	1	Z	8.09	7.83	8.09
2	1	E	119	126	119
3	1	ΔH_{vol}		7.70	7.16
4	1	χ		0.719	0.861
5	1	n	2.52	2.33	2.52
6	1	n_{O_2}		0.23	0.42
7	1	K_{cat}	0.14	-1.13	0.14
8	2	Z	17	17	17
9	2	E	253	258	253
10	2	ΔH_{vol}		6.61	3.74
11	2	χ		0.85	0.88
12	2	n	1.47	1.50	1.47
13	2	n_{O_2}		0.59	2.08
14	3	Z	5.89	6.20	5.89
15	3	E	108	108	108
16	3	ΔH_{vol}		5.92	6.87
17	3	χ		0.885	0.891

Parameter					
#	Species	Symbol	Independently determined	gpyro_propest fit without independently determined	gpyro_propest fit with independently determined
18	3	n	1.26	1.50	1.26
19	3	n_{O_2}		2.76	1.82
20	4	Z	5.71	6.15	5.71
21	4	E	135	140	135
22	4	ΔH_{vol}		6.60	5.52
23	4	χ		0.872	0.791
24	4	n	0.99	0.95	0.99
25	4	n_{O_2}		4.30	2.17
26	1	k_{0z}	0.298	0.180	0.30
27	2	k_{0z}		1.63	15.52
28	3	k_{0z}		16.38	16.82
29	4	k_{0z}		10.61	25.27
30	5	k_{0z}		20.80	25.61
31	1	ρ_0	1377	1310	1377
32	1	n_ρ		-0.33	-0.76
33	2	ρ_0	857	818	469
34	3	ρ_0	105	78	461
35	4	ρ_0	690	639	664
36	5	ρ_0	87	43	444
37	1	c_0	1519	102	1519
38	1	n_c	0.77	0.46	0.77
39	2	c_0		629	2761
40	3	c_0		2141	2749
41	4	c_0		1761	2639
42	5	c_0		1639	2648
43	1	ε		0.61	0.87
44	2	ε		0.35	0.65
45	3	ε		0.86	0.80
46	4	ε		0.56	0.51
47	5	ε		0.77	0.56
48	1	κ		3.24	3.65
49	2	κ		0.70	3.94
50	3	κ		1.89	2.16
51	4	κ		4.41	4.74
52	5	κ		4.34	0
53	1	T_m	484	479	484
54	1	ΔH_m	51000	134974	51000
55	1	σ_m^2	62	208	62
56	1	γ		0.000694	0.000377
57	2	γ		0.000670	0.000582

Parameter					
#	Species	Symbol	Independently determined	gpyro_propest fit without independently determined	gpyro_propest fit with independently determined
58	3	γ		0.000925	0.000340
59	4	γ		0.000680	0.000469
60	5	γ		0.000048	0.000227
61	1	K_z		-7.3	-12.0
62	2	K_z		-14.6	-6.2
63	3	K_z		-6.6	-11.4
64	4	K_z		-16.6	-13.1
65	5	K_z		-16.2	-11.4
66	1	ρ_{s0}		1549	1671
67	2	ρ_{s0}		1009	1149
68	3	ρ_{s0}		261	1208
69	4	ρ_{s0}		838	1054
70	5	ρ_{s0}		264	863
71	1	h_{cr}		69	142
72	2	h_{cr}		7	9

Table 48 Comparison of the resulting parameters for PA6+NC+FR

Appendix C: DISCUSSION

C.1 Error estimation

C.1.1 PA6

C.1.1.1 In-depth temperature

Without the independently obtained intrinsic material properties

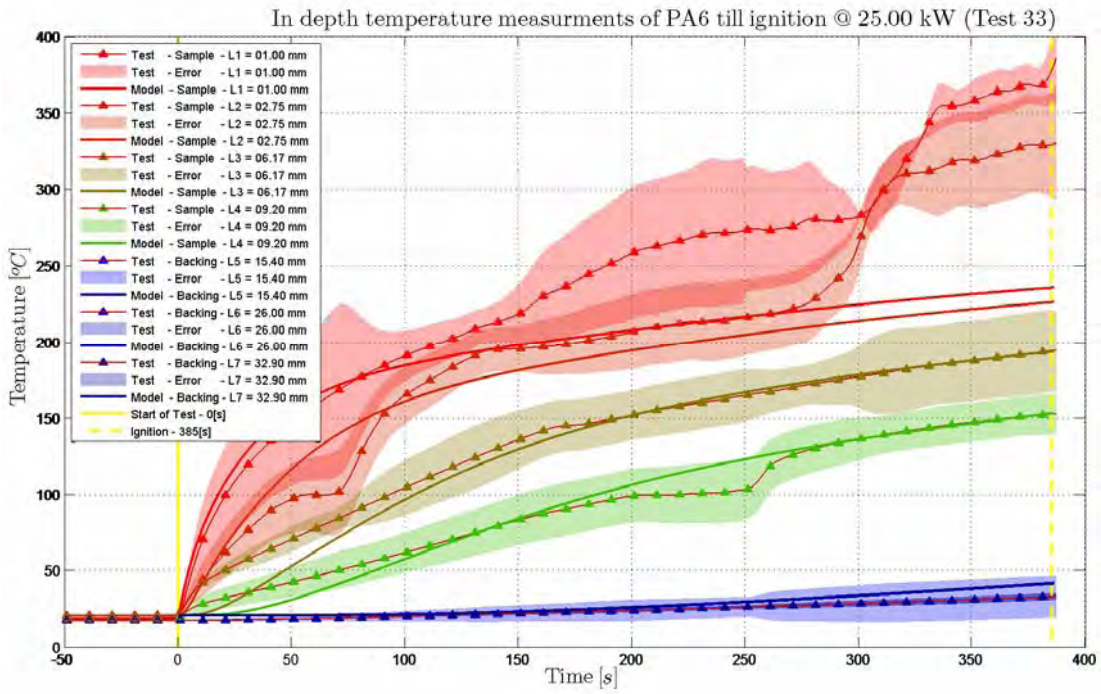

Figure 218 In-depth temperature “Test to Model” error comparison of PA6 *without* the independently obtained intrinsic material properties (Test 33)

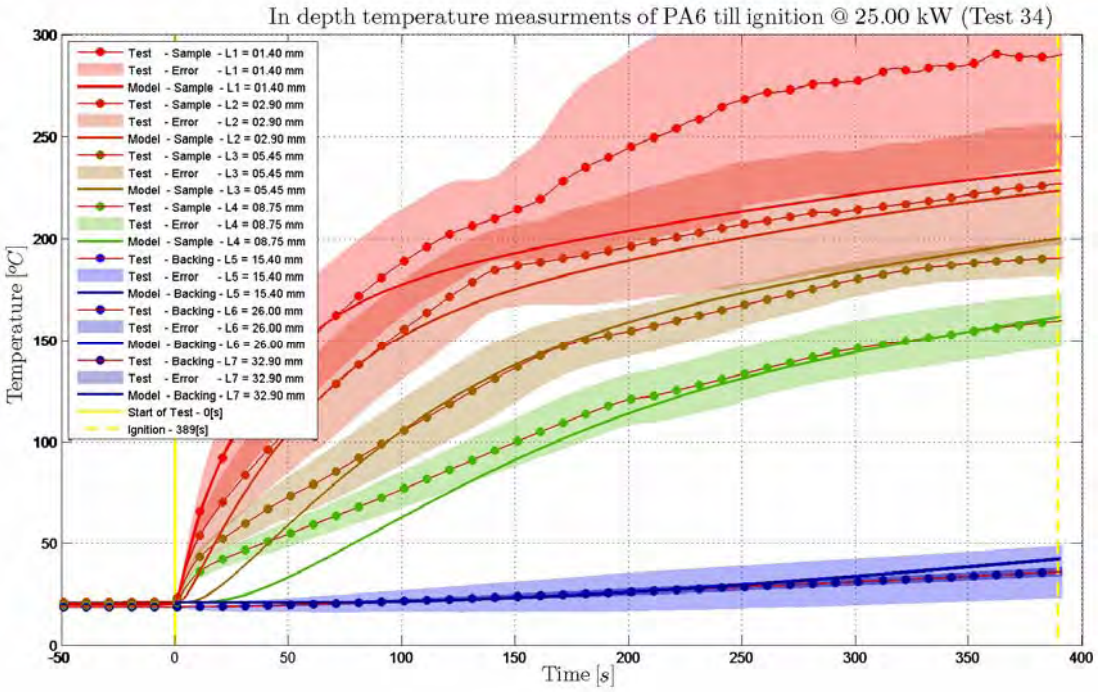

Figure 219 In-depth temperature "Test to Model" error comparison of PA6 *without* the independently obtained intrinsic material properties (Test 34)

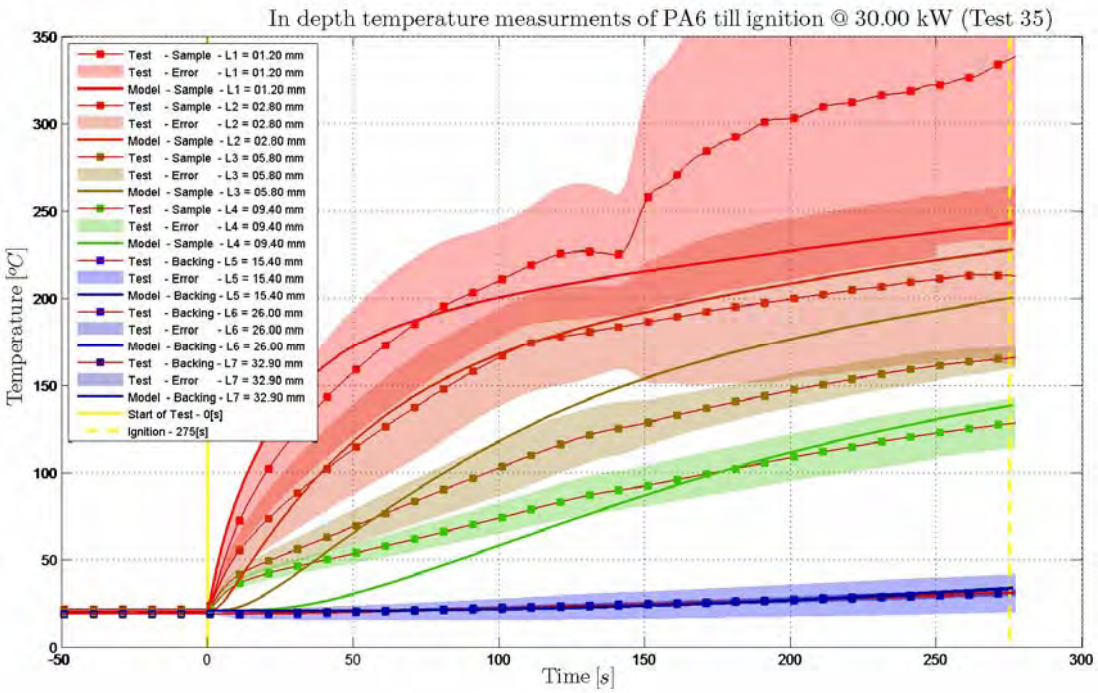

Figure 220 In-depth temperature "Test to Model" error comparison of PA6 *without* the independently obtained intrinsic material properties (Test 35)

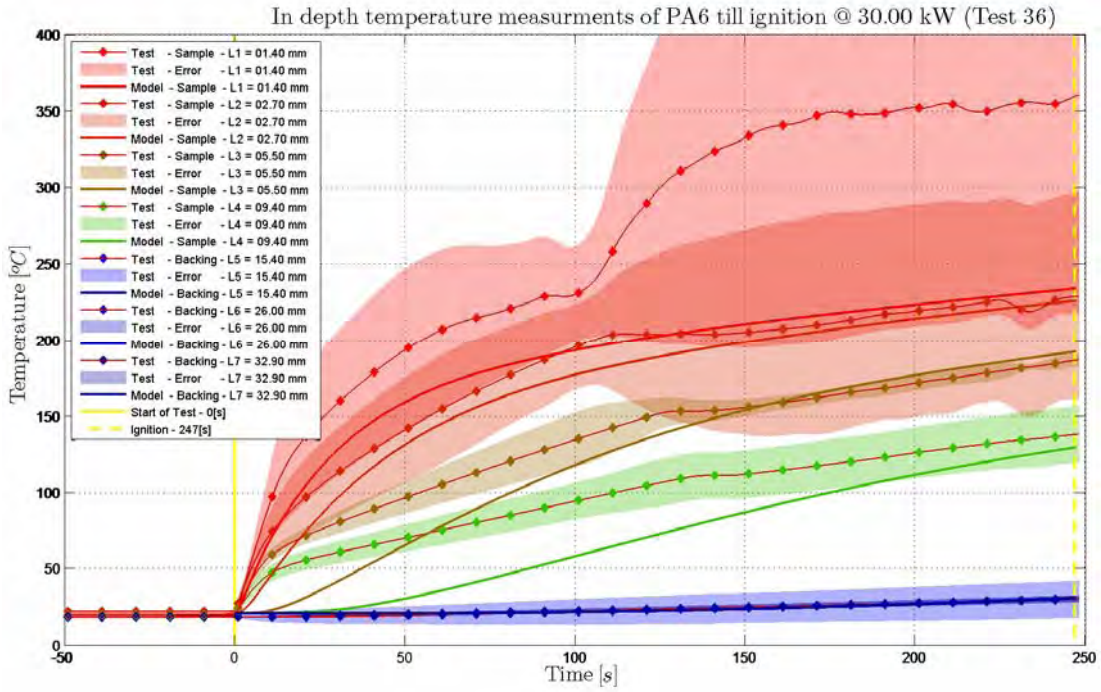

Figure 221 In-depth temperature "Test to Model" error comparison of PA6 *without* the independently obtained intrinsic material properties (Test 36)

With the independently obtained intrinsic material properties

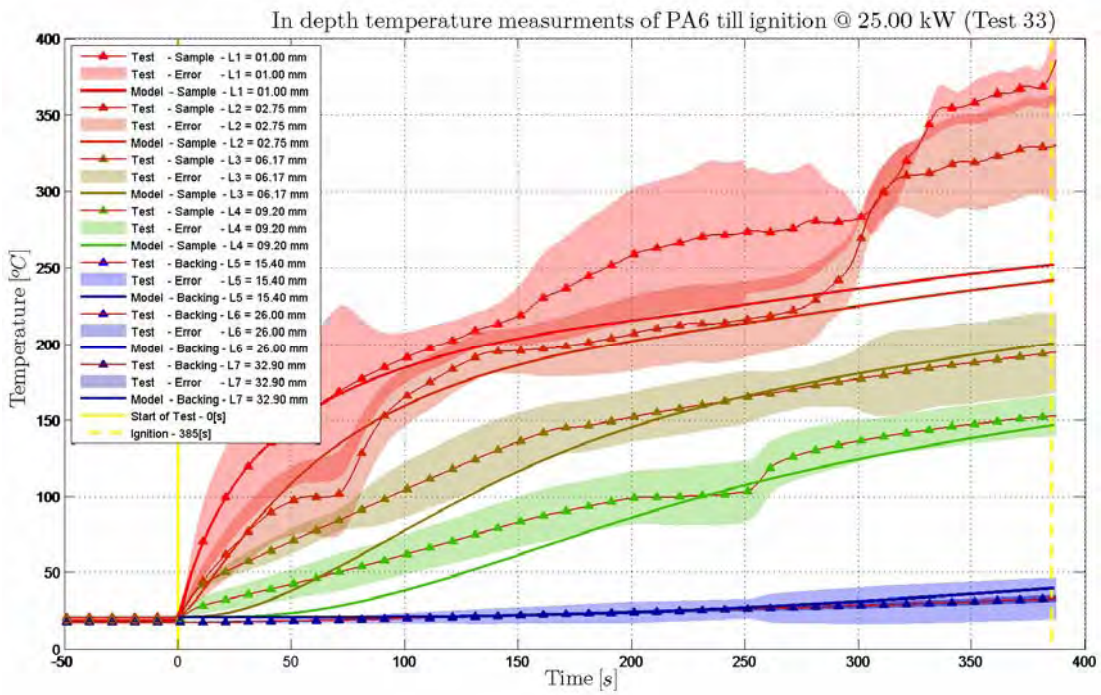

Figure 222 In-depth temperature "Test to Model" error comparison of PA6 *with* the independently obtained intrinsic material properties (Test 33)

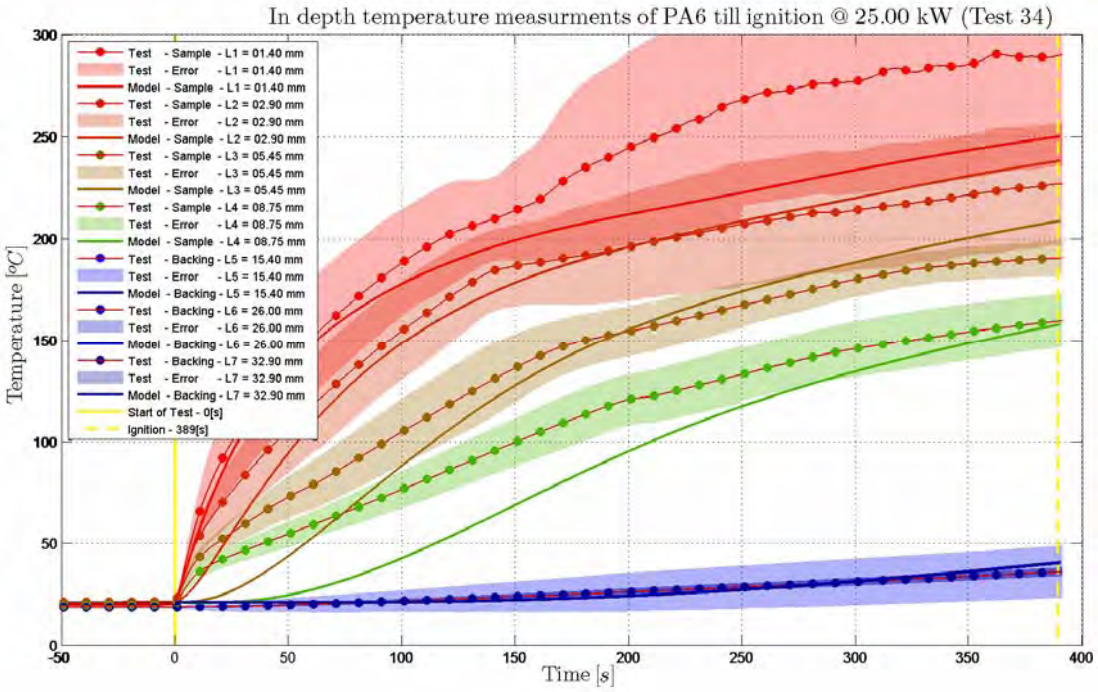

Figure 223 In-depth temperature "Test to Model" error comparison of PA6 *with* the independently obtained intrinsic material properties (Test 34)

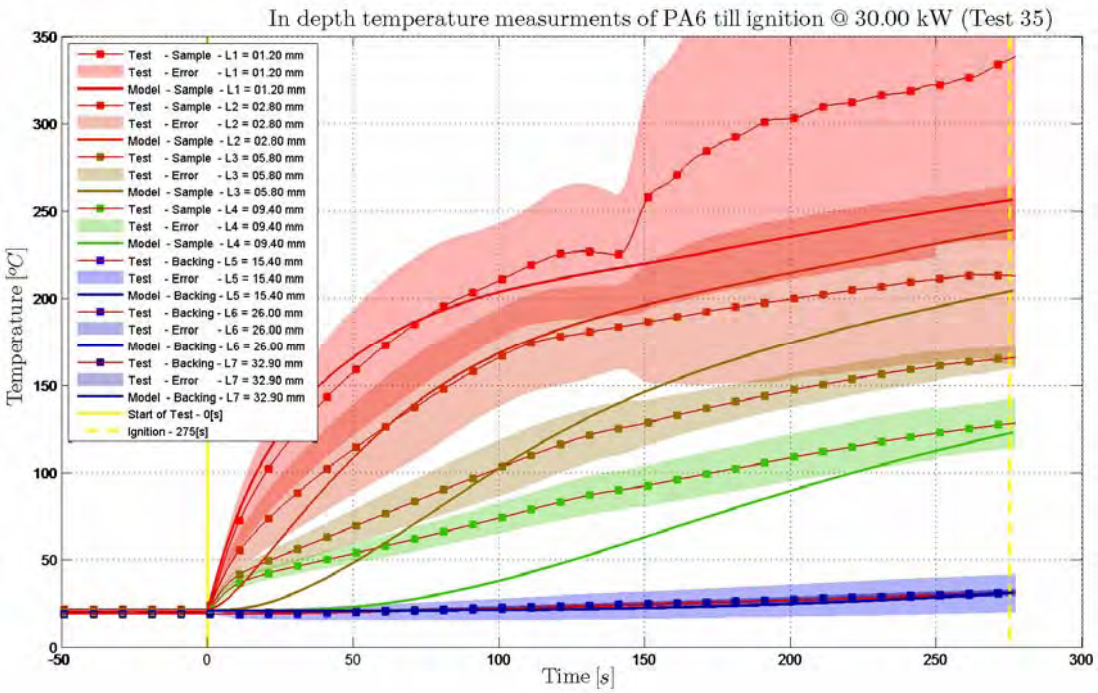

Figure 224 In-depth temperature "Test to Model" error comparison of PA6 *with* the independently obtained intrinsic material properties (Test 35)

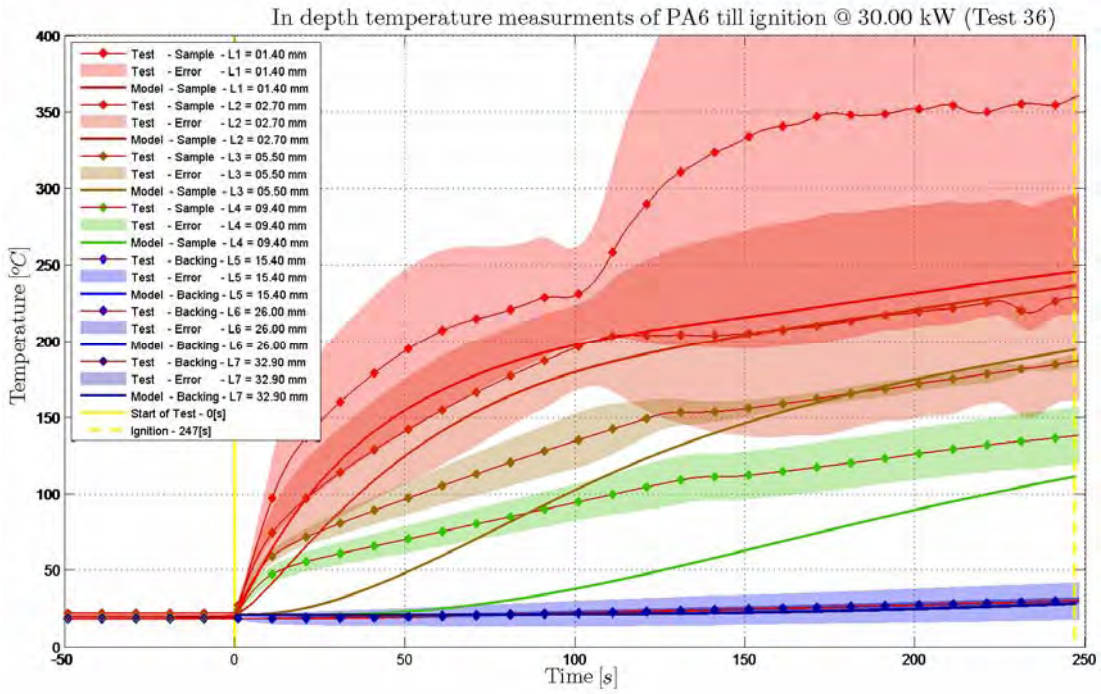

Figure 225 In-depth temperature "Test to Model" error comparison of PA6 *with* the independently obtained intrinsic material properties (Test 36)

C.1.1.2 Mass loss

Without the independently obtained intrinsic material properties

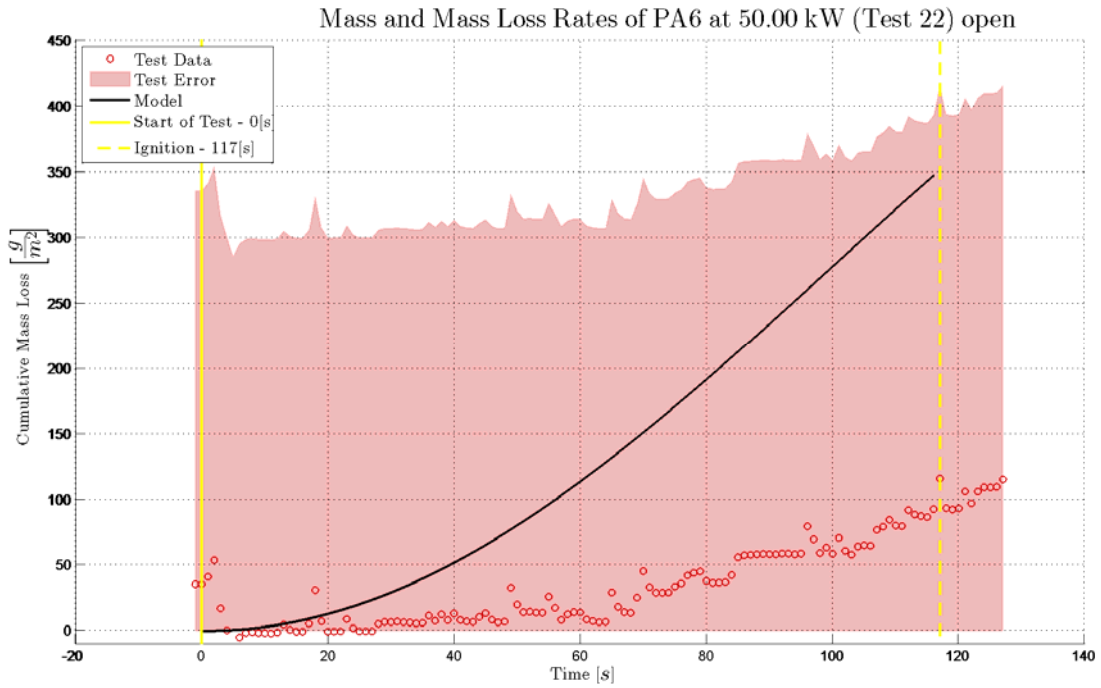

Figure 226 Cumulative mass loss "Test to Model" error comparison of PA6 *without* the independently obtained intrinsic material properties (Test 22)

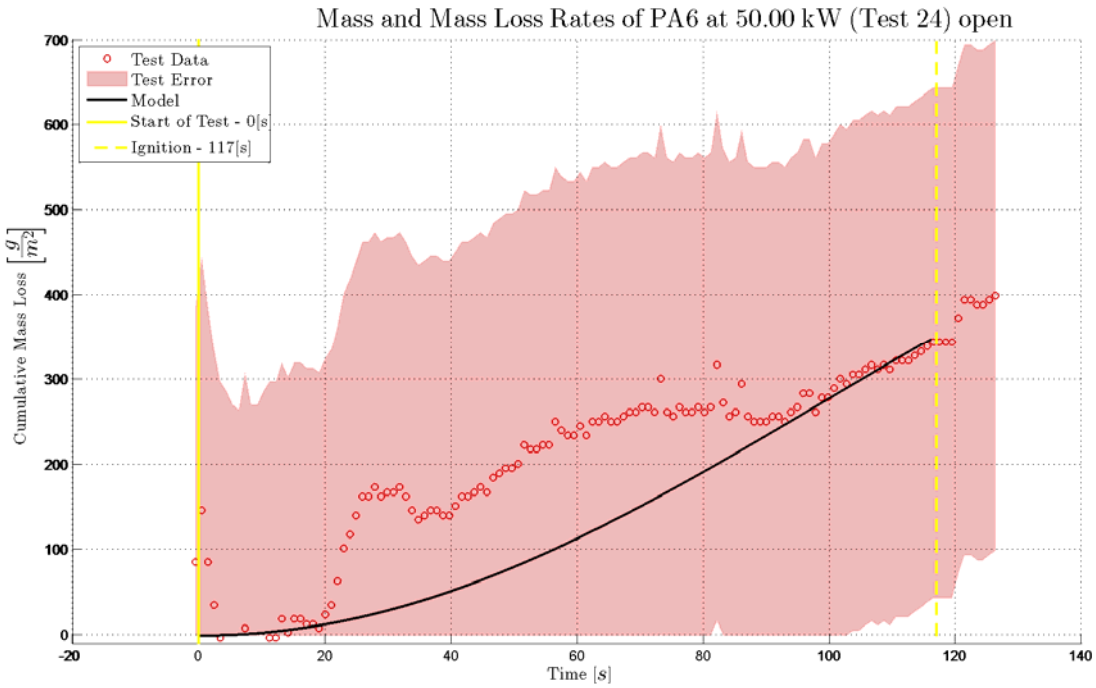

Figure 227 Cumulative mass loss "Test to Model" error comparison of PA6 *without* the independently obtained intrinsic material properties (Test 24)

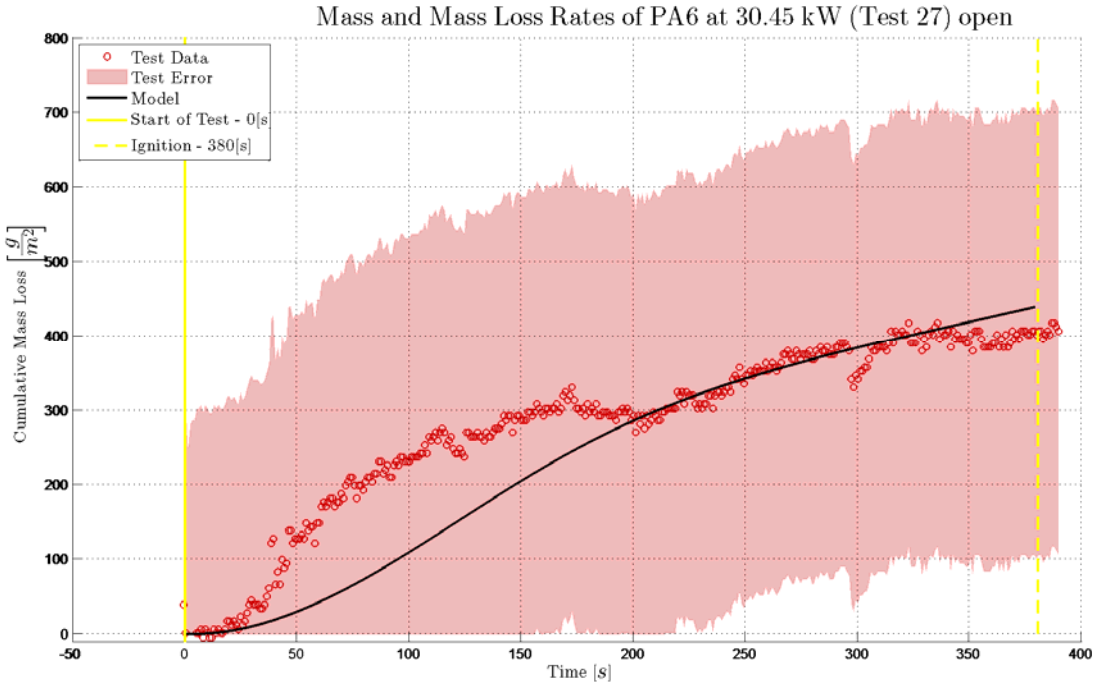

Figure 228 Cumulative mass loss "Test to Model" error comparison of PA6 *without* the independently obtained intrinsic material properties (Test 27)

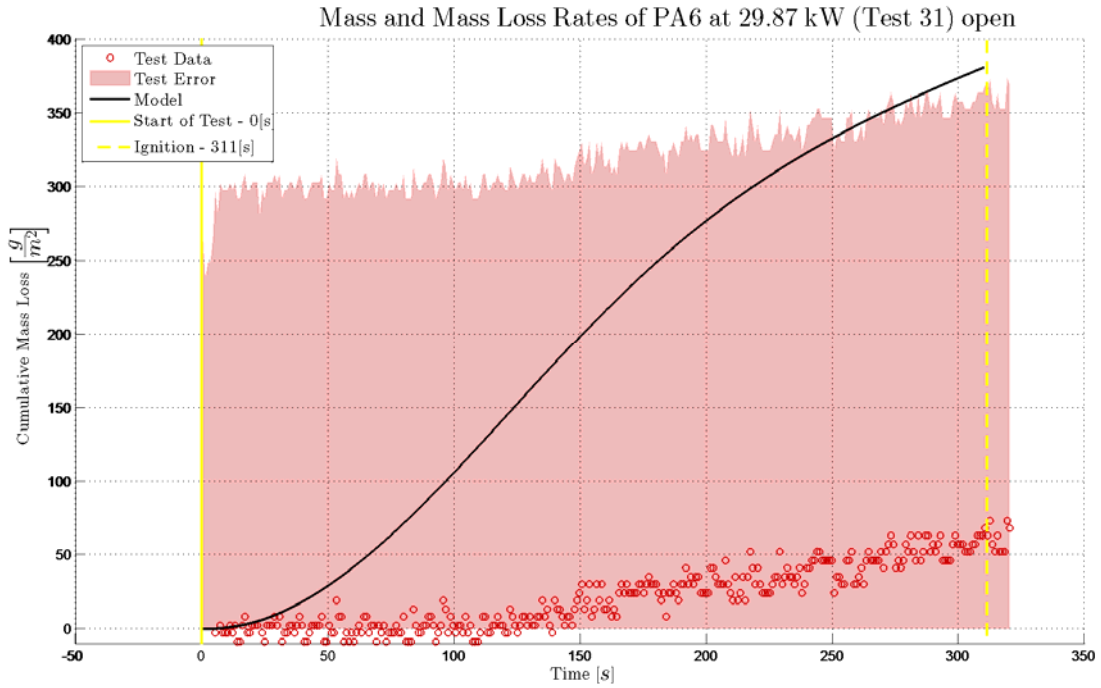

Figure 229 Cumulative mass loss "Test to Model" error comparison of PA6 *without* the independently obtained intrinsic material properties (Test 31)

With the independently obtained intrinsic material properties

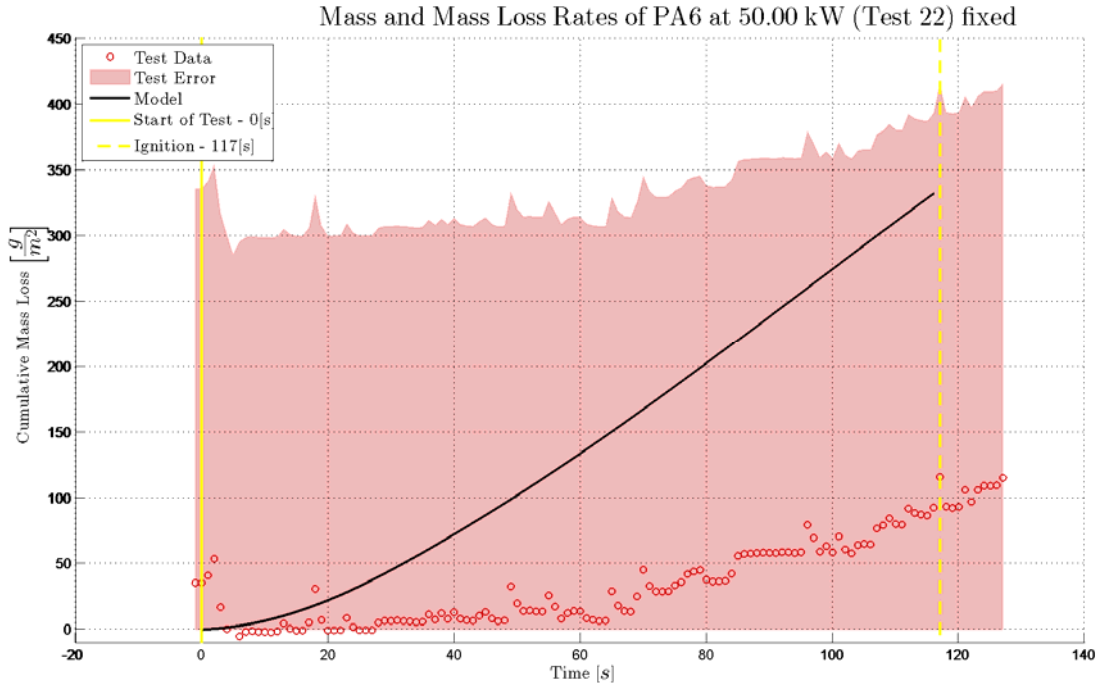

Figure 230 Cumulative mass loss "Test to Model" error comparison of PA6 *with* the independently obtained intrinsic material properties (Test 22)

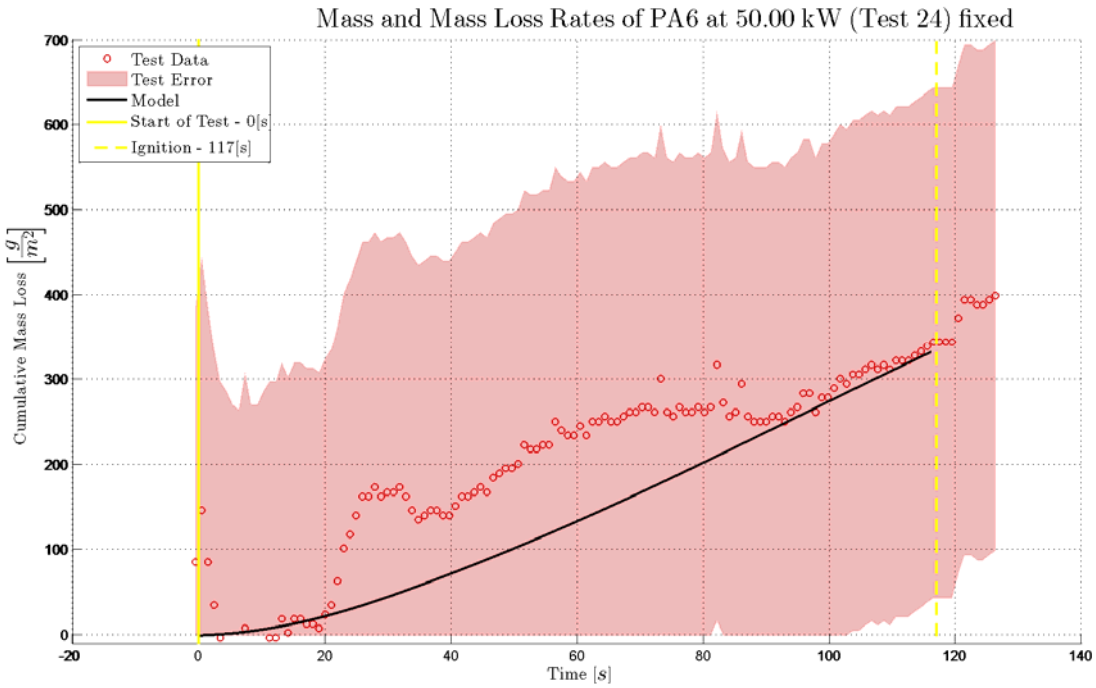

Figure 231 Cumulative mass loss "Test to Model" error comparison of PA6 *with* the independently obtained intrinsic material properties (Test 24)

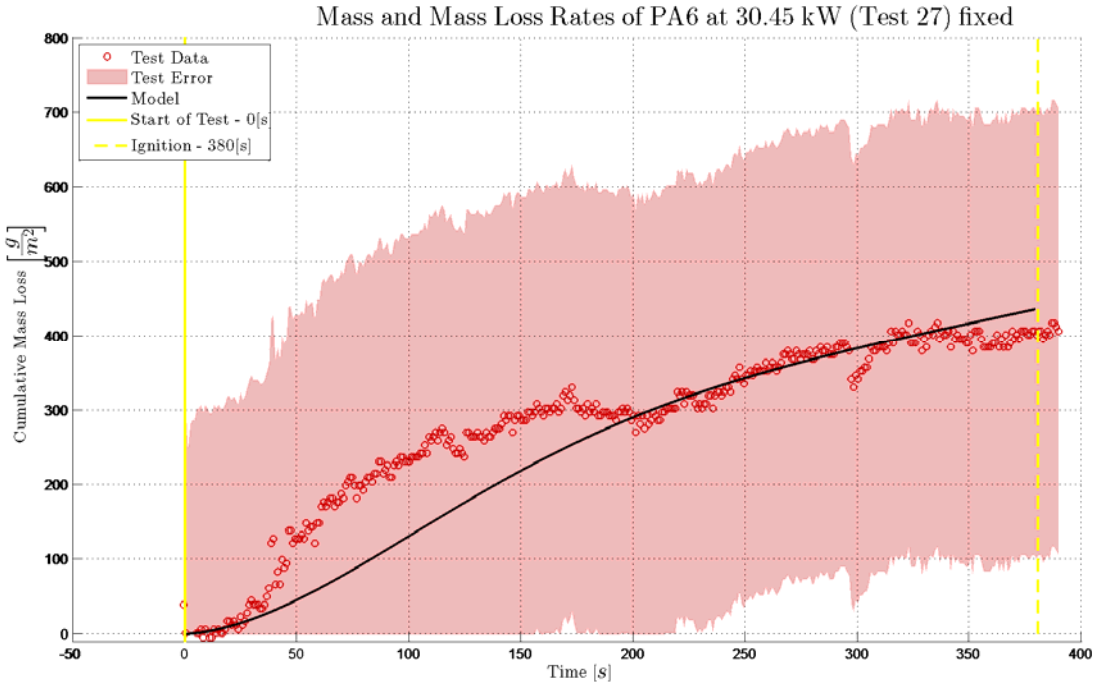

Figure 232 Cumulative mass loss "Test to Model" error comparison of PA6 *with* the independently obtained intrinsic material properties (Test 27)

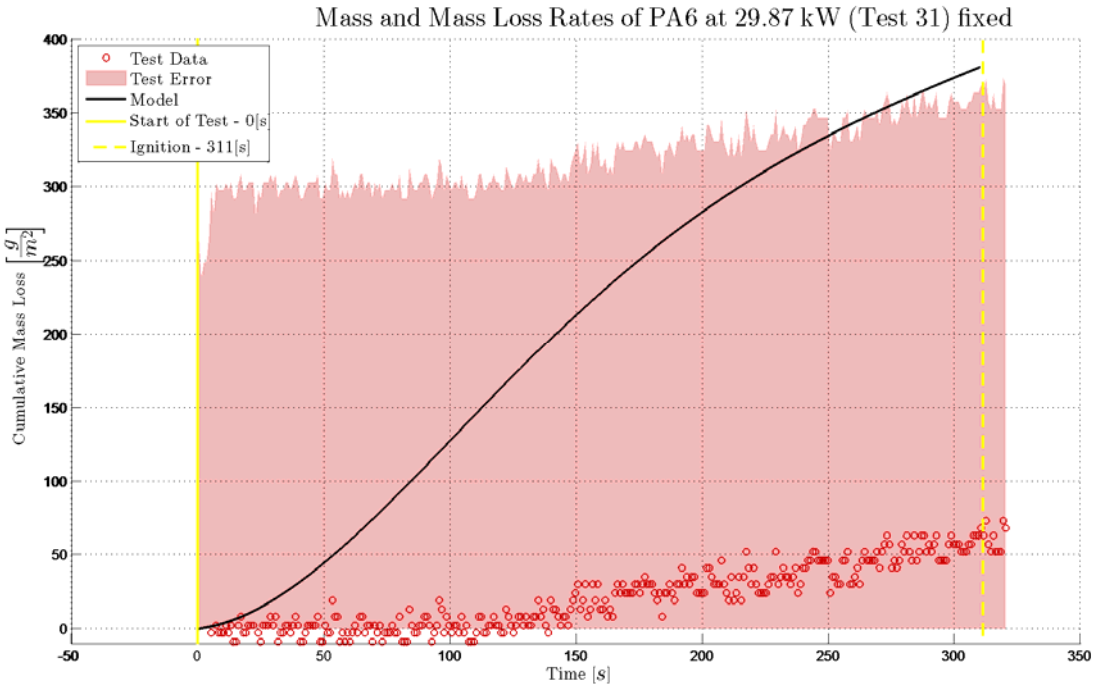

Figure 233 Cumulative mass loss "Test to Model" error comparison of PA6 *with* the independently obtained intrinsic material properties (Test 31)

C.1.2 PA6+FR

C.1.2.1 In-depth temperature

Without the independently obtained intrinsic material properties

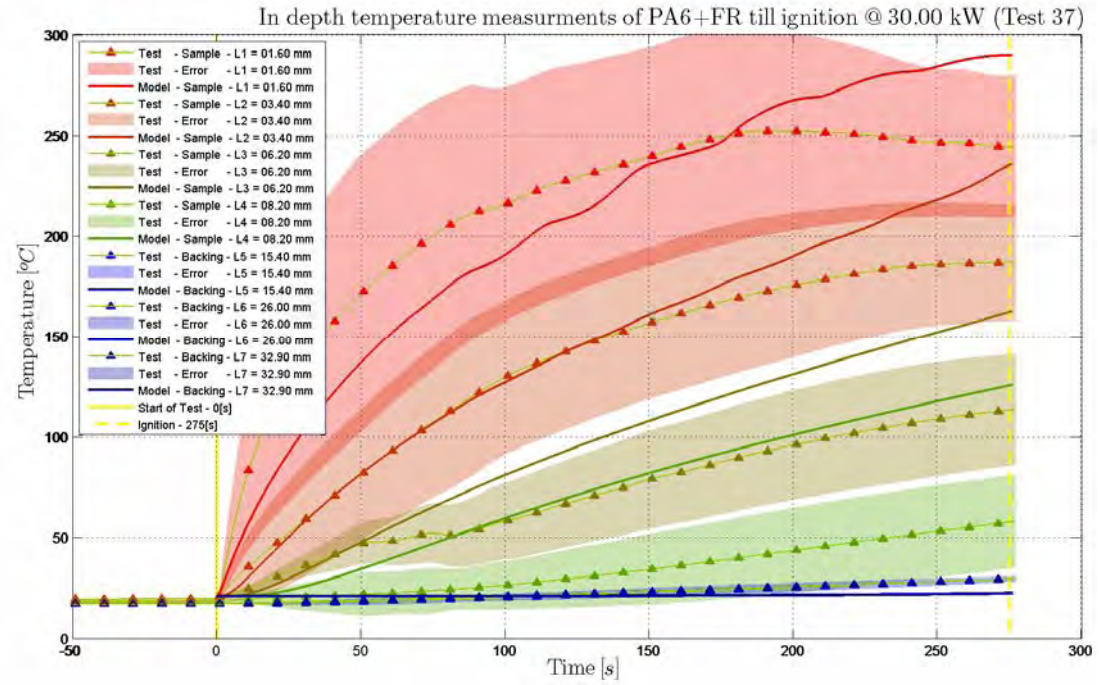

Figure 234 In-depth temperature "Test to Model" error comparison of PA6+FR *without* the independently obtained intrinsic material properties (Test 37)

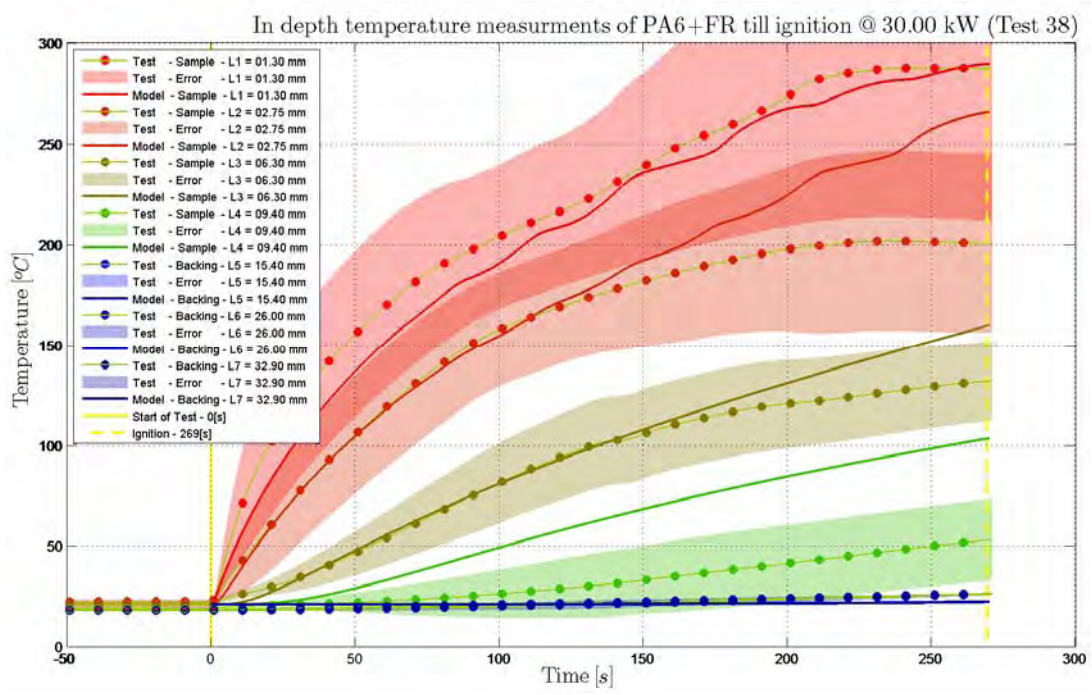

Figure 235 In-depth temperature "Test to Model" error comparison of PA6+FR *without* the independently obtained intrinsic material properties (Test 38)

With the independently obtained intrinsic material properties

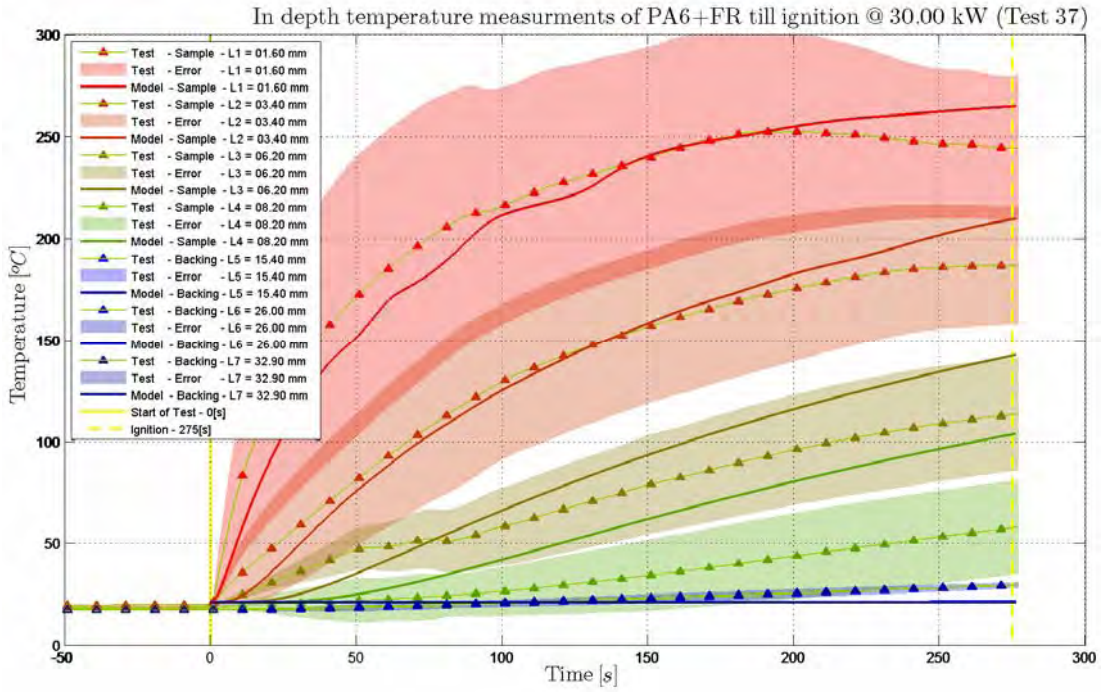

Figure 236 In-depth temperature "Test to Model" error comparison of PA6+FR *with* the independently obtained intrinsic material properties (Test 37)

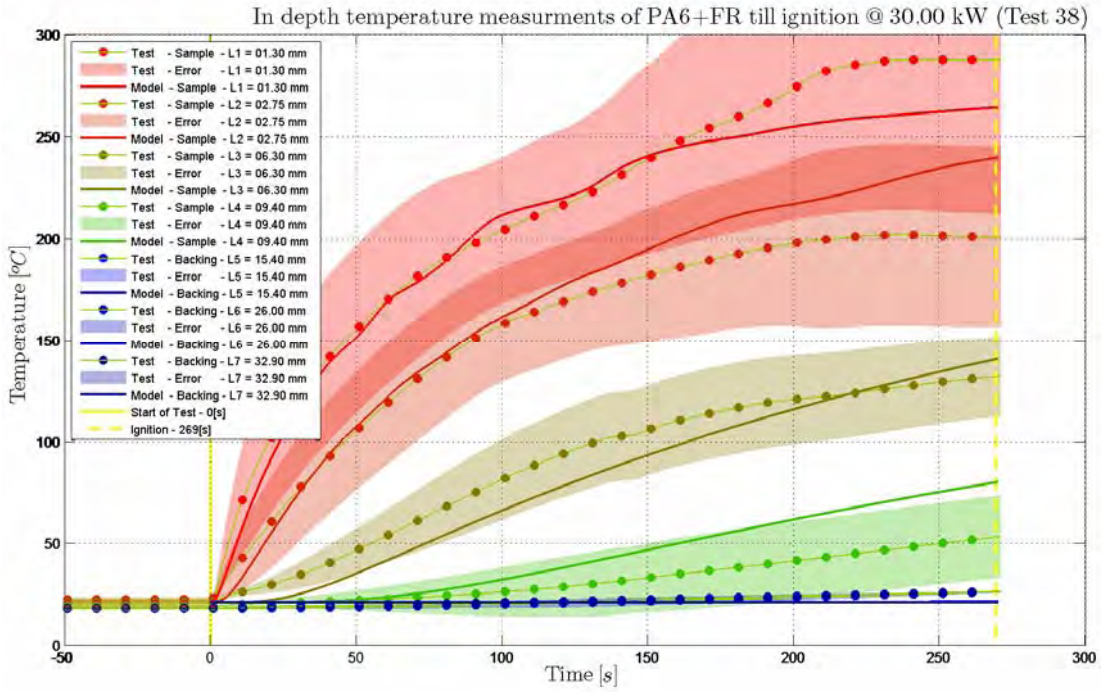

Figure 237 In-depth temperature "Test to Model" error comparison of PA6+FR *with* the independently obtained intrinsic material properties (Test 38)

C.1.2.2 Mass loss

Without the independently obtained intrinsic material properties

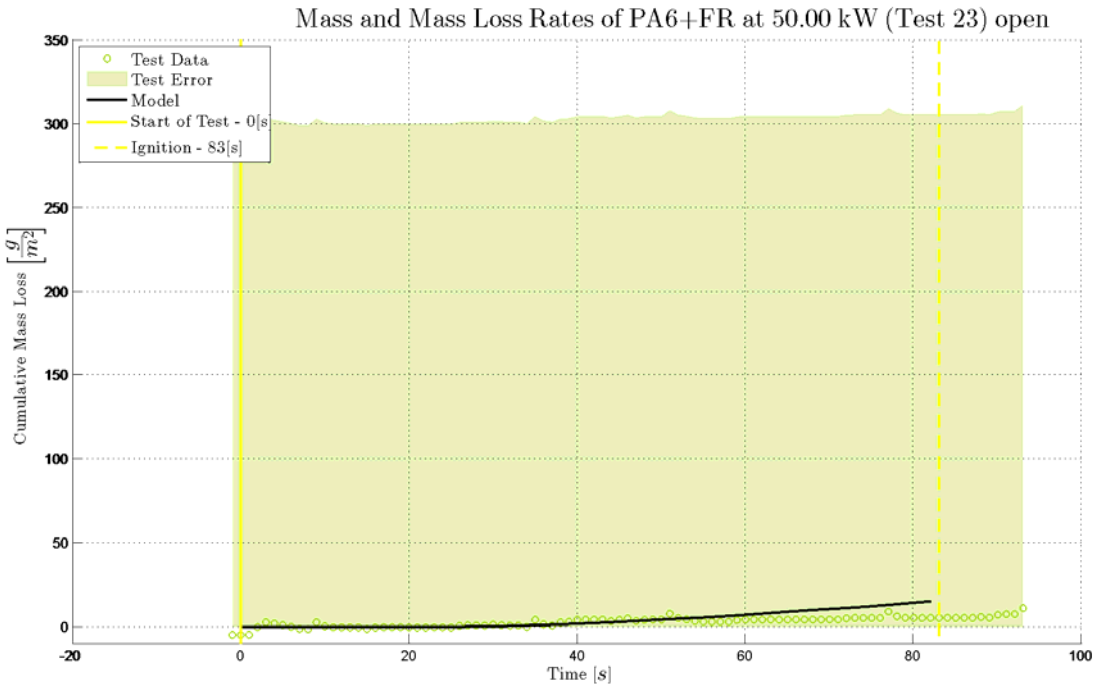

Figure 238 Cumulative mass loss "Test to Model" error comparison of PA6+FR *without* the independently obtained intrinsic material properties (Test 23)

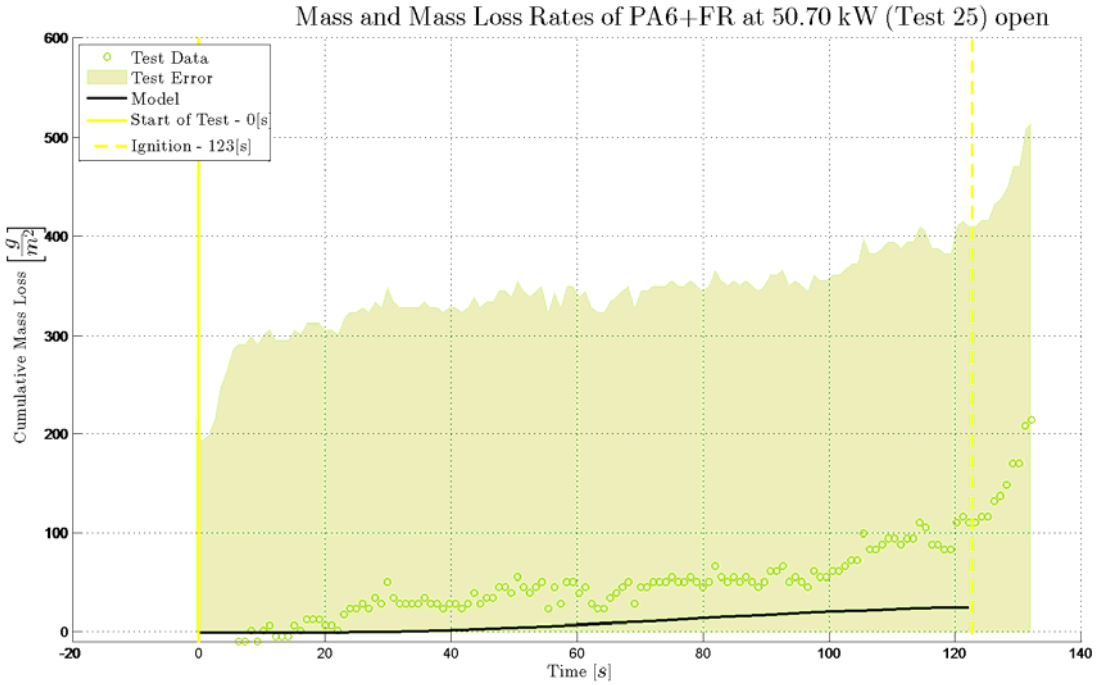

Figure 239 Cumulative mass loss "Test to Model" error comparison of PA6+FR *without* the independently obtained intrinsic material properties (Test 25)

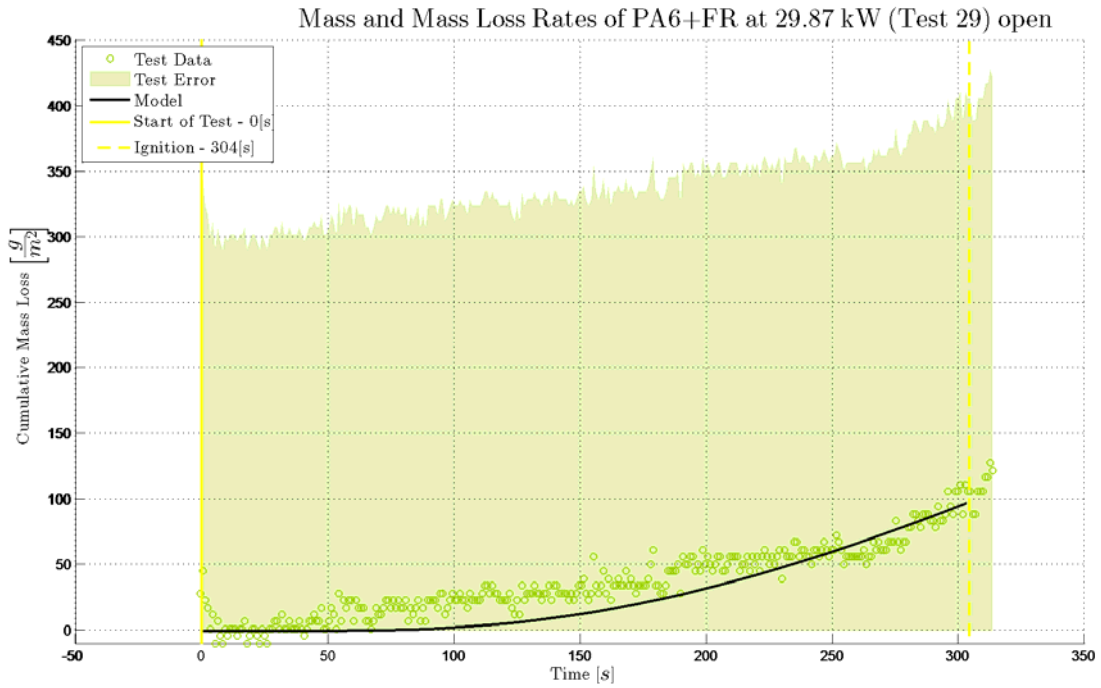

Figure 240 Cumulative mass loss "Test to Model" error comparison of PA6+FR *without* the independently obtained intrinsic material properties (Test 29)

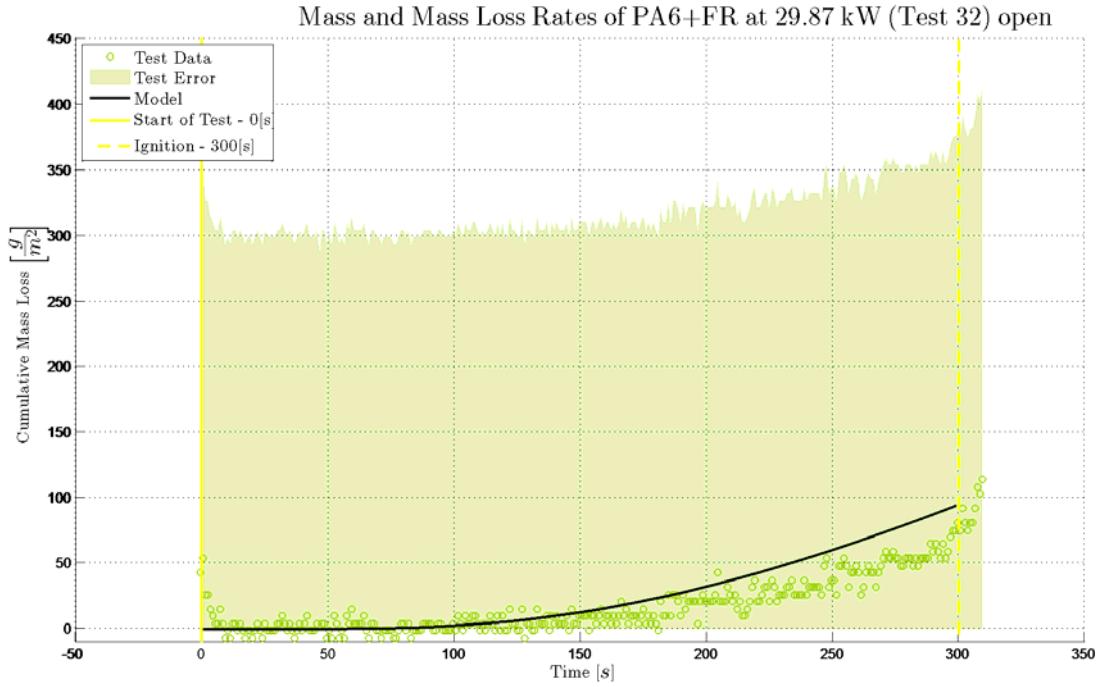

Figure 241 Cumulative mass loss "Test to Model" error comparison of PA6+FR *without* the independently obtained intrinsic material properties (Test 32)

With the independently obtained intrinsic material properties

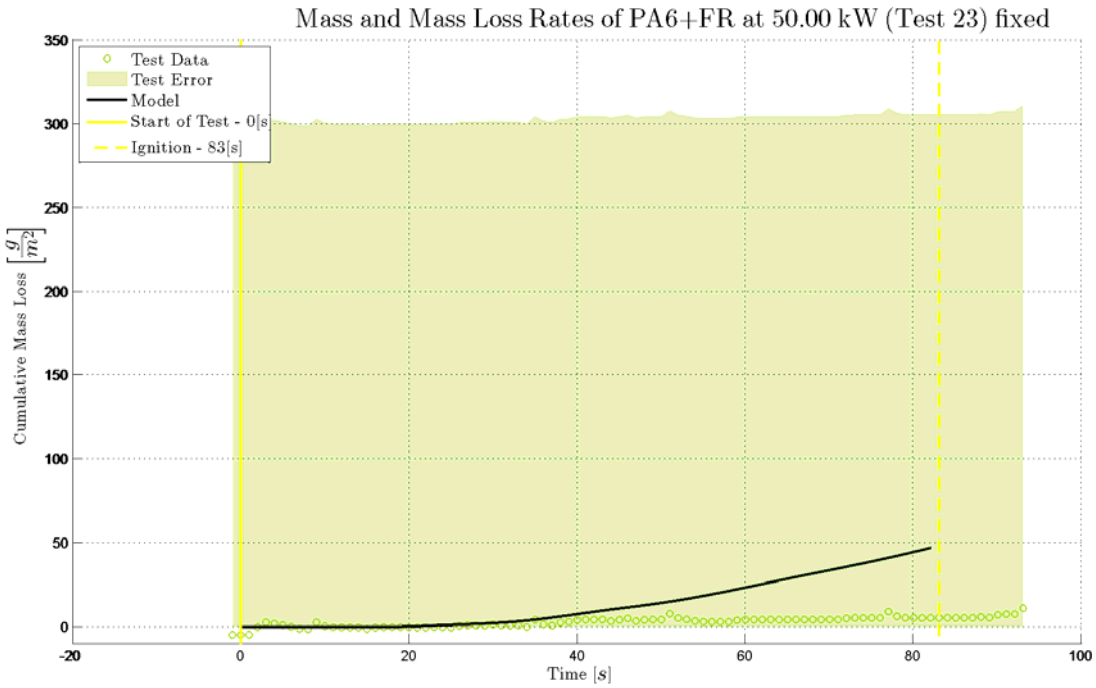

Figure 242 Cumulative mass loss “Test to Model” error comparison of PA6+FR *with* the independently obtained intrinsic material properties (Test 23)

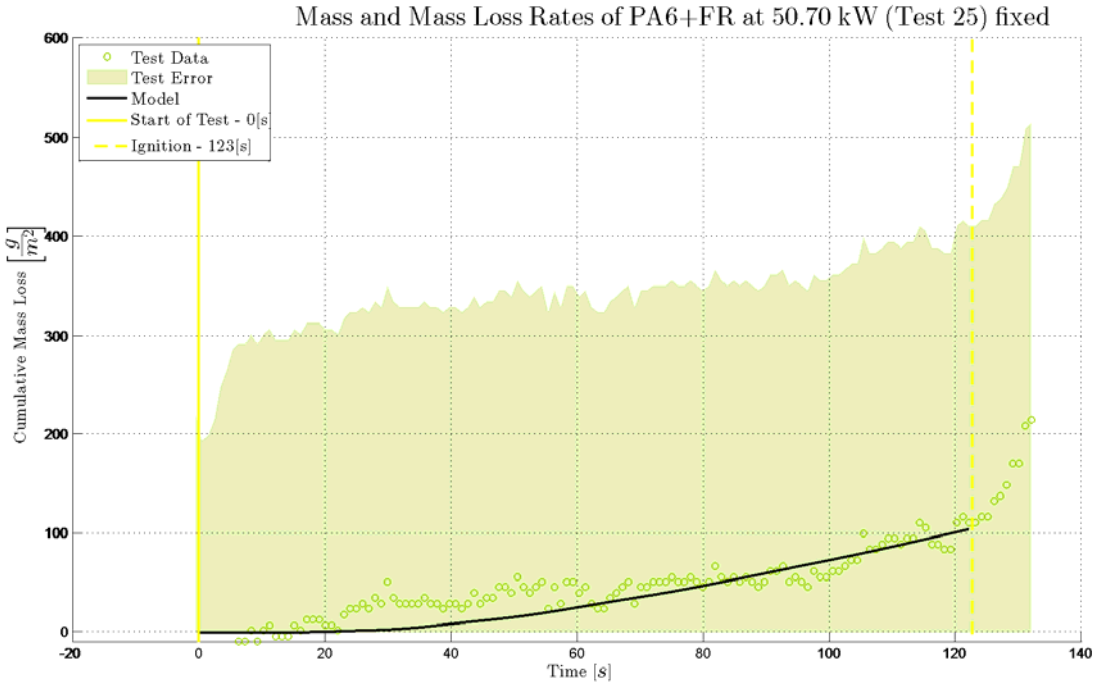

Figure 243 Cumulative mass loss “Test to Model” error comparison of PA6+FR *with* the independently obtained intrinsic material properties (Test 25)

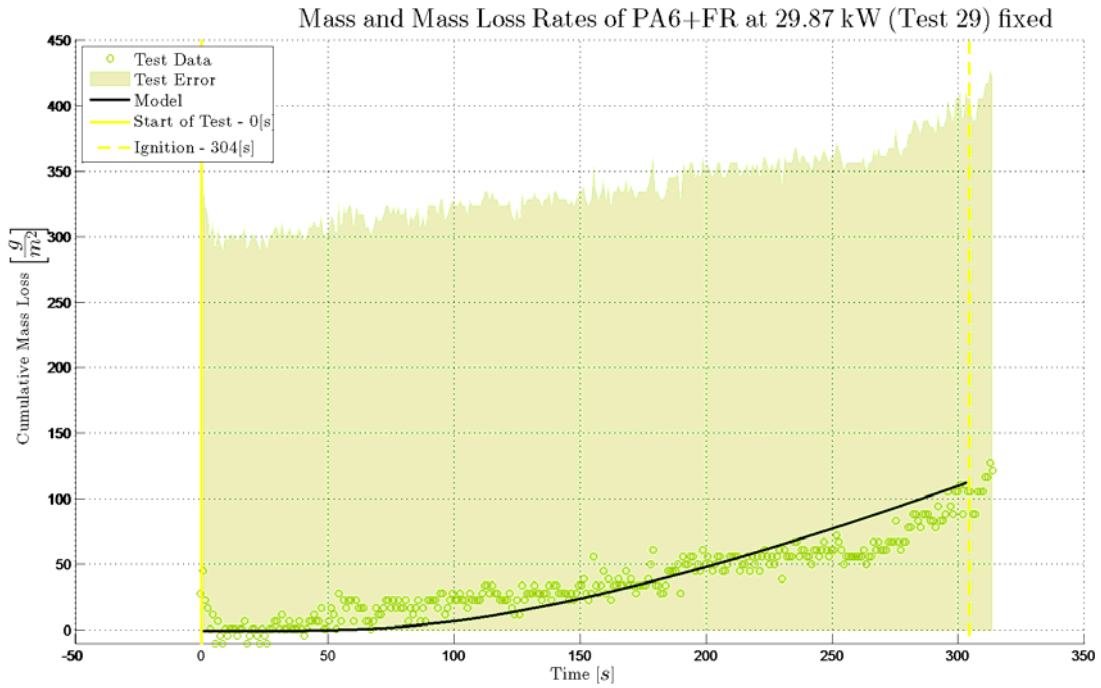

Figure 244 Cumulative mass loss "Test to Model" error comparison of PA6+FR *with* the independently obtained intrinsic material properties (Test 29)

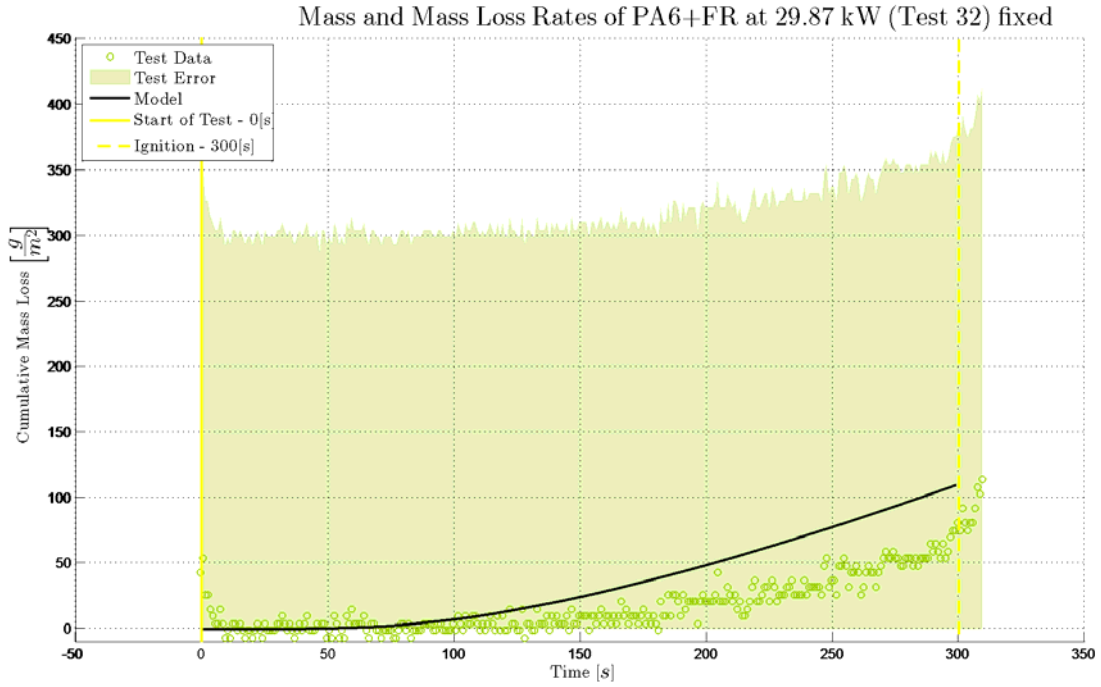

Figure 245 Cumulative mass loss "Test to Model" error comparison of PA6+FR *with* the independently obtained intrinsic material properties (Test 32)

C.1.3 PA6+NC

C.1.3.1 In-depth temperature

Without the independently obtained intrinsic material properties

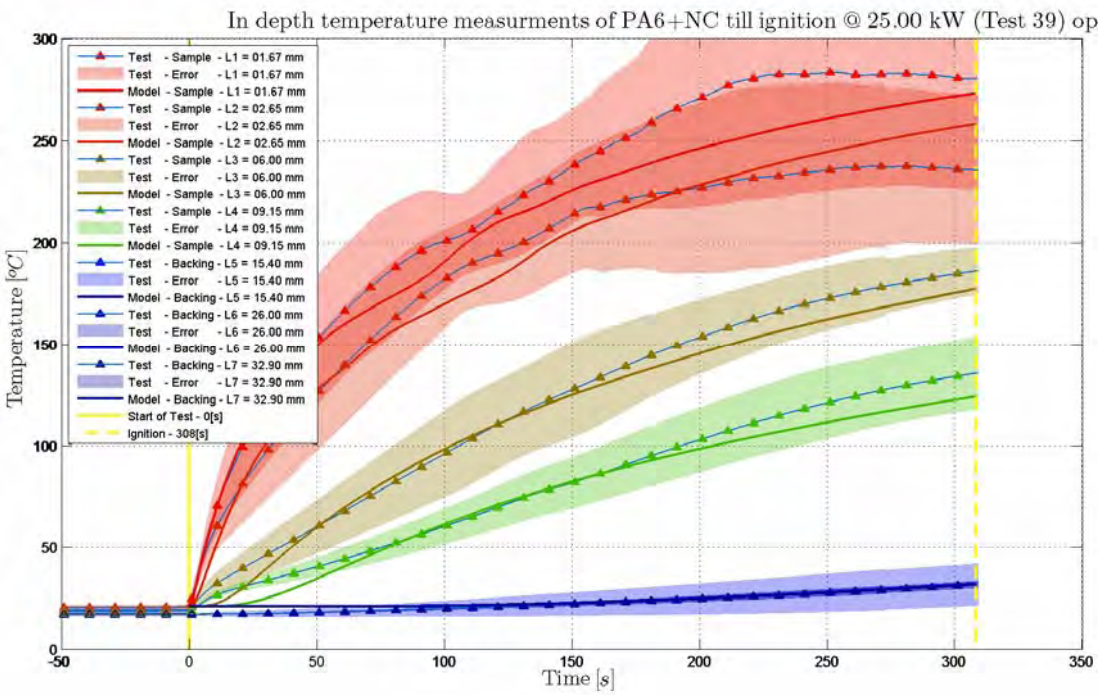

Figure 246 In-depth temperature “Test to Model” error comparison of PA6+NC *without* the independently obtained intrinsic material properties (Test 39)

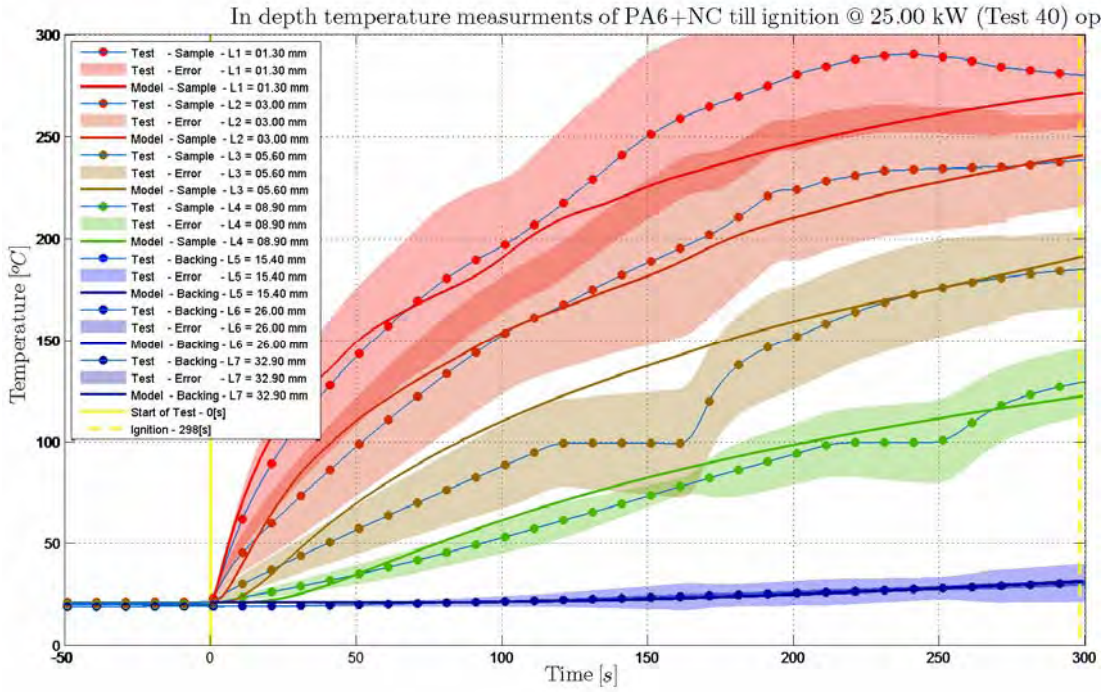

Figure 247 In-depth temperature "Test to Model" error comparison of PA6+NC *without* the independently obtained intrinsic material properties (Test 40)

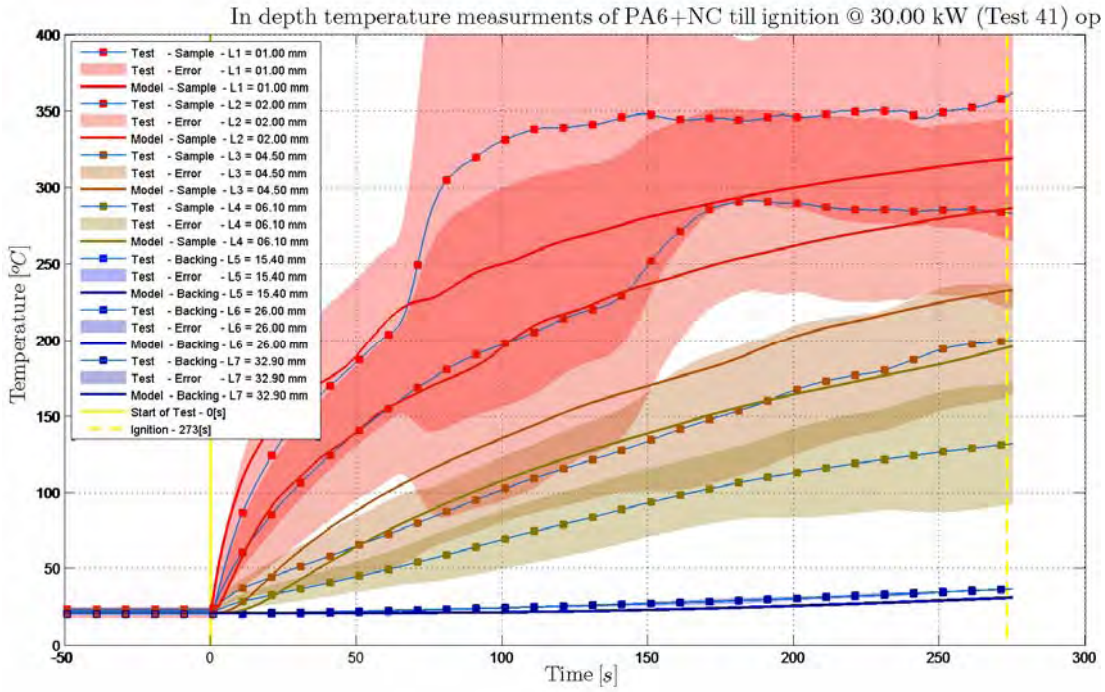

Figure 248 In-depth temperature "Test to Model" error comparison of PA6+NC *without* the independently obtained intrinsic material properties (Test 41)

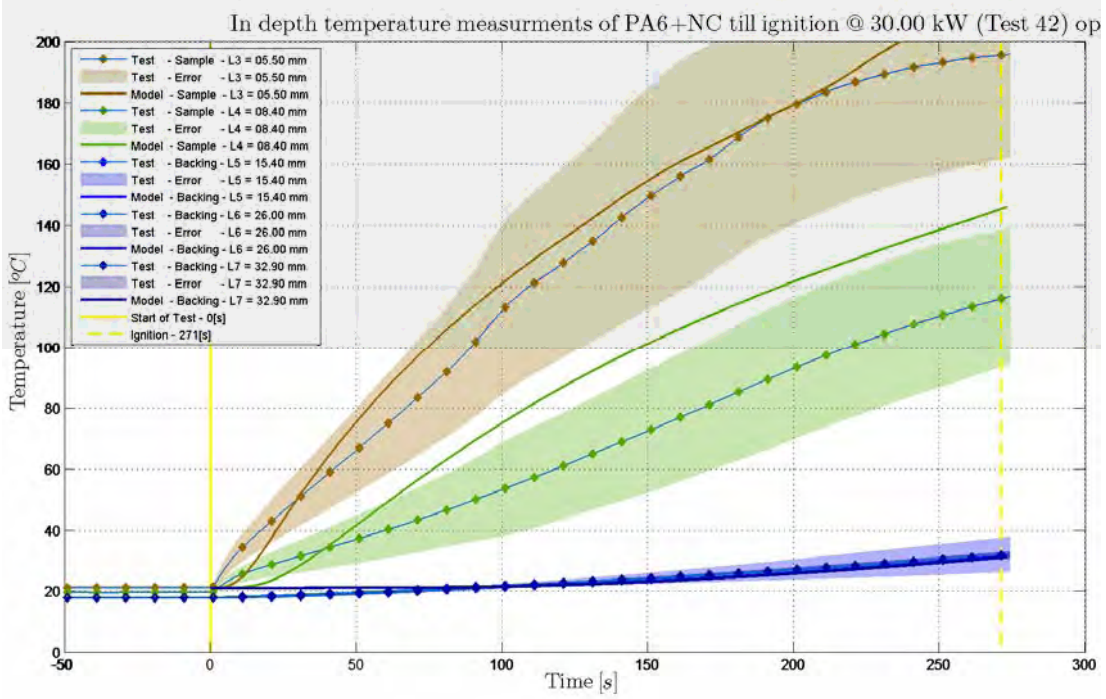

Figure 249 In-depth temperature "Test to Model" error comparison of PA6+NC *without* the independently obtained intrinsic material properties (Test 42)

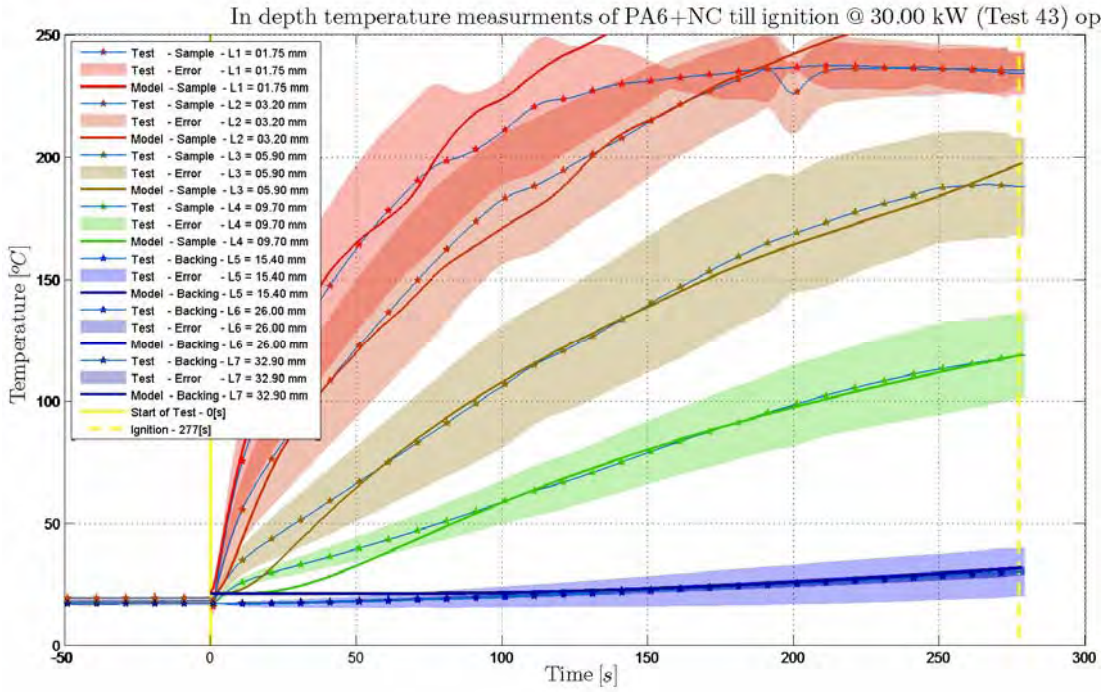

Figure 250 In-depth temperature "Test to Model" error comparison of PA6+NC *without* the independently obtained intrinsic material properties (Test 43)

With the independently obtained intrinsic material properties

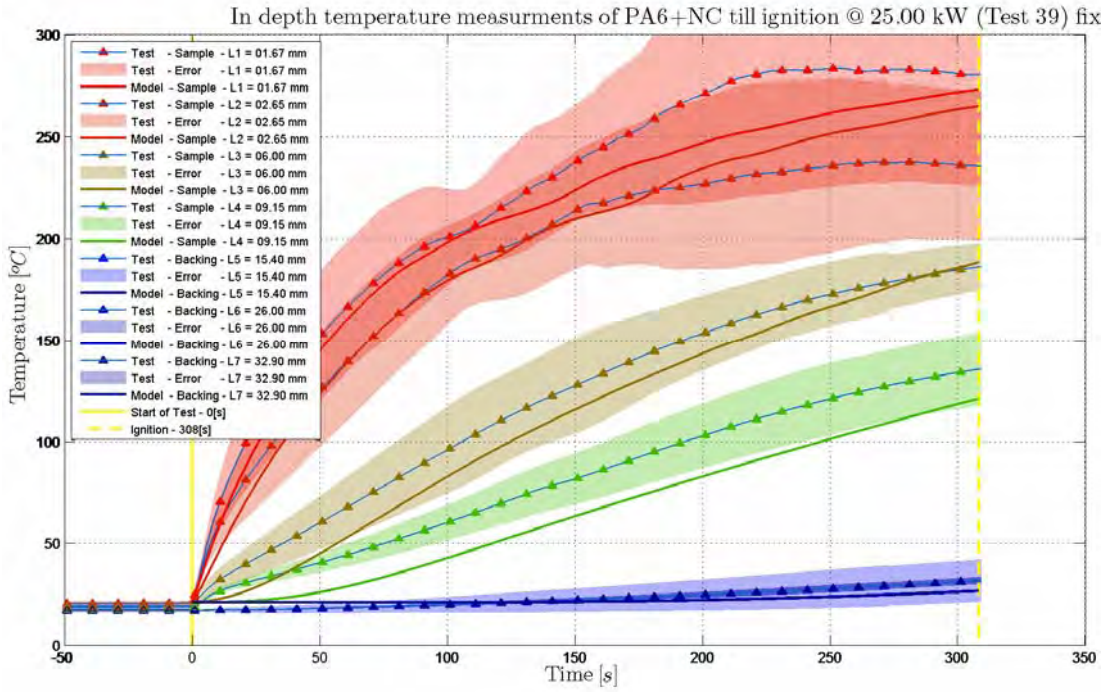

Figure 251 In-depth temperature "Test to Model" error comparison of PA6+NC *with* the independently obtained intrinsic material properties (Test 39)

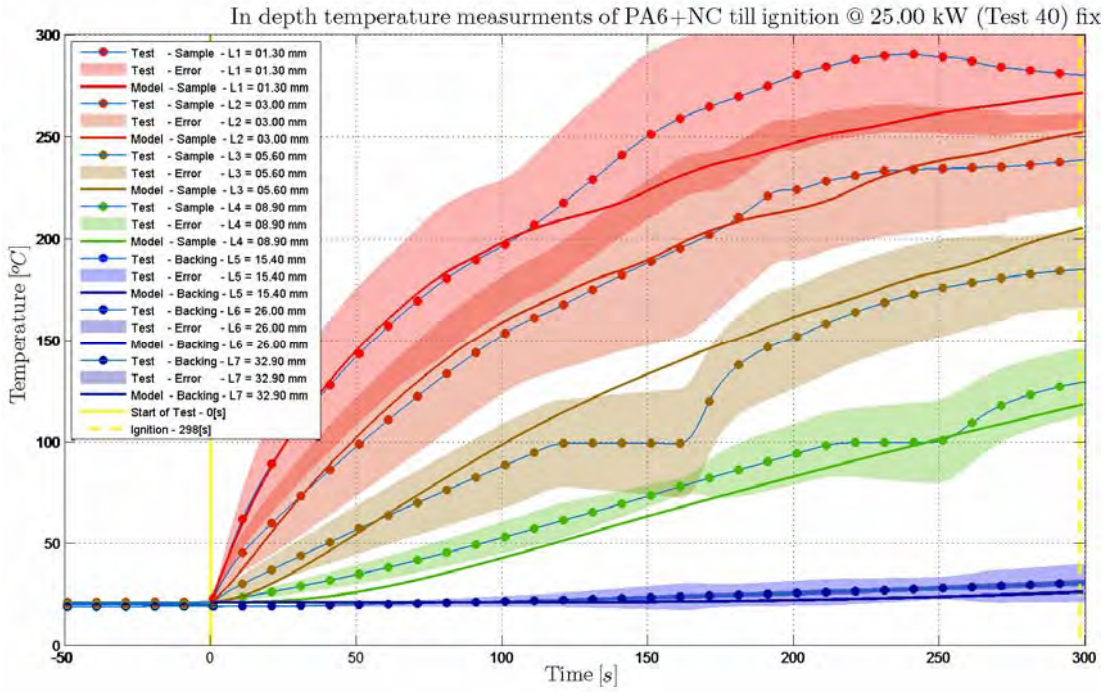

Figure 252 In-depth temperature "Test to Model" error comparison of PA6+NC *with* the independently obtained intrinsic material properties (Test 40)

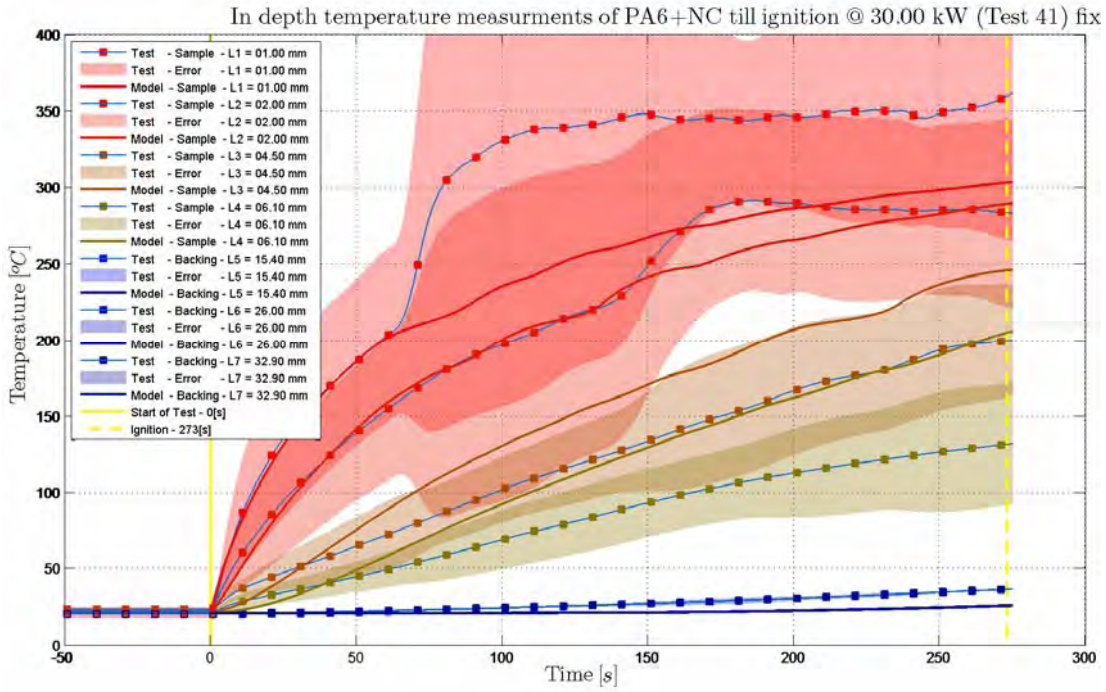

Figure 253 In-depth temperature "Test to Model" error comparison of PA6+NC *with* the independently obtained intrinsic material properties (Test 41)

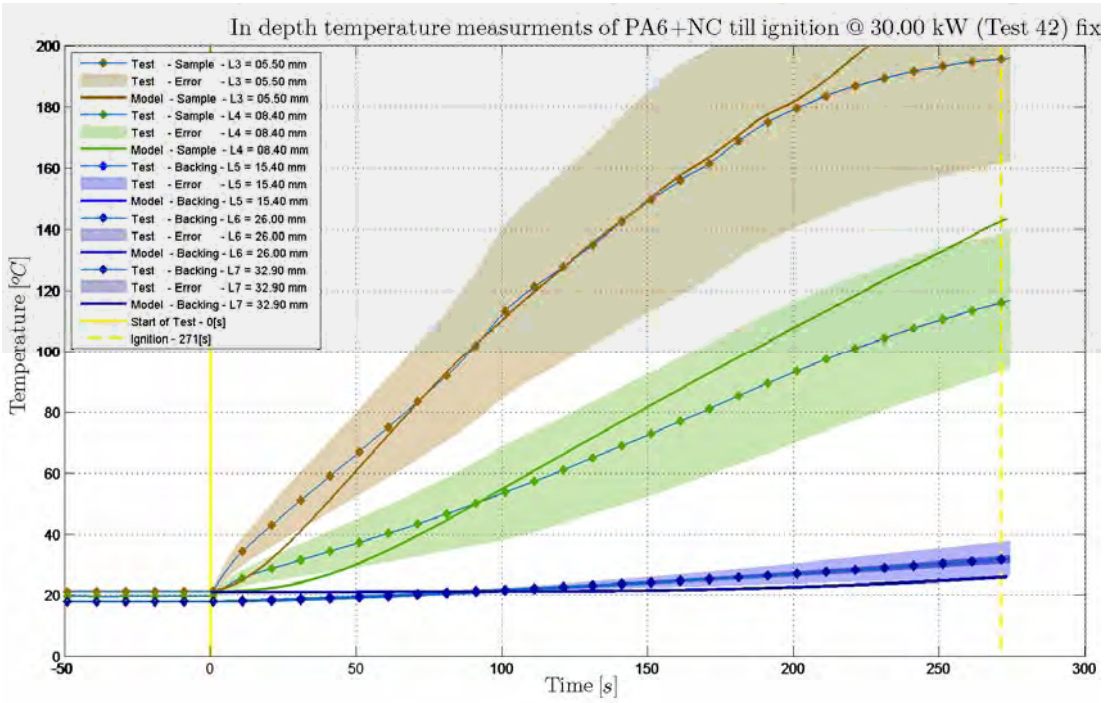

Figure 254 In-depth temperature "Test to Model" error comparison of PA6+NC *with* the independently obtained intrinsic material properties (Test 42)

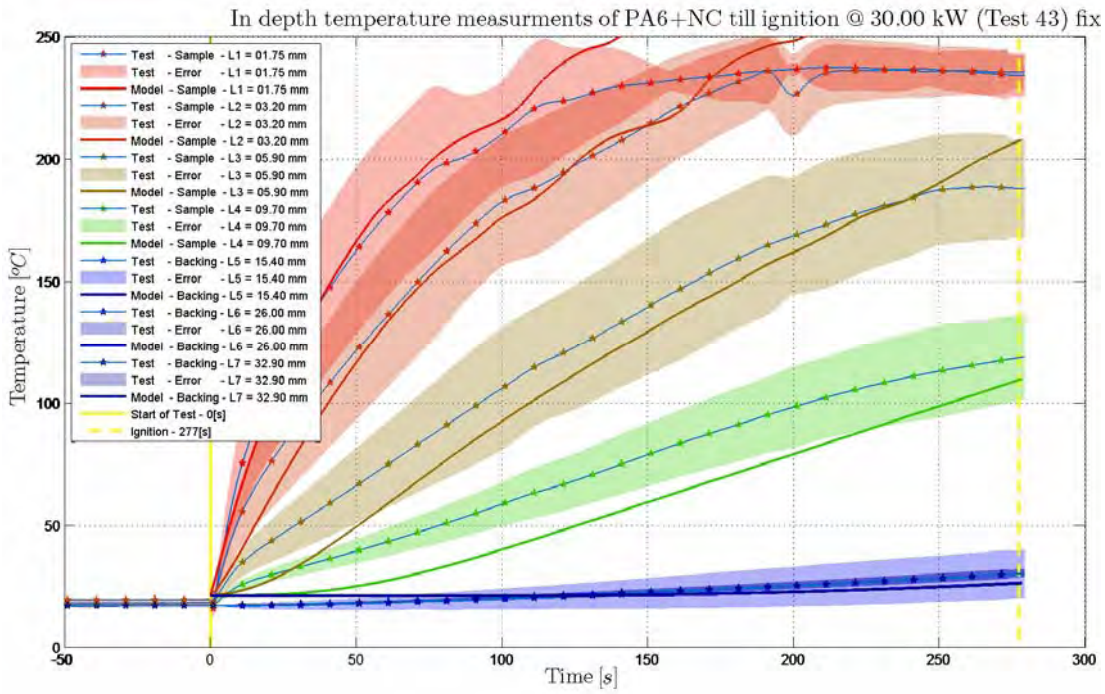

Figure 255 In-depth temperature "Test to Model" error comparison of PA6+NC *with* the independently obtained intrinsic material properties (Test 43)

C.1.3.2 Mass loss

Without the independently obtained intrinsic material properties

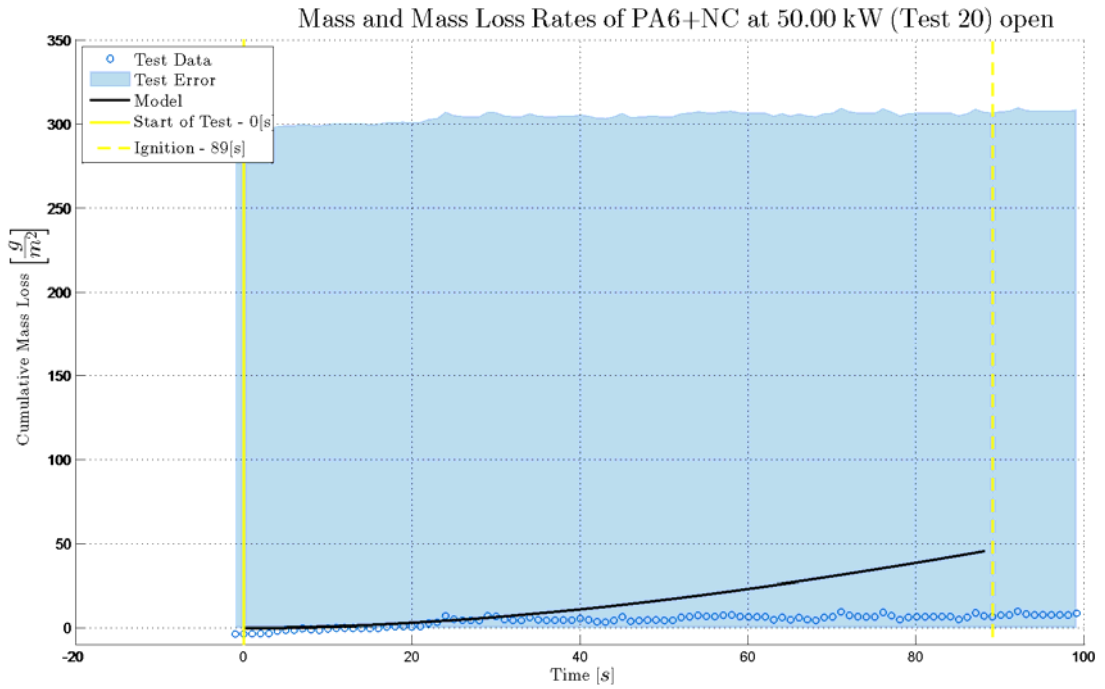

Figure 256 Cumulative mass loss "Test to Model" error comparison of PA6+NC *without* the independently obtained intrinsic material properties (Test 20)

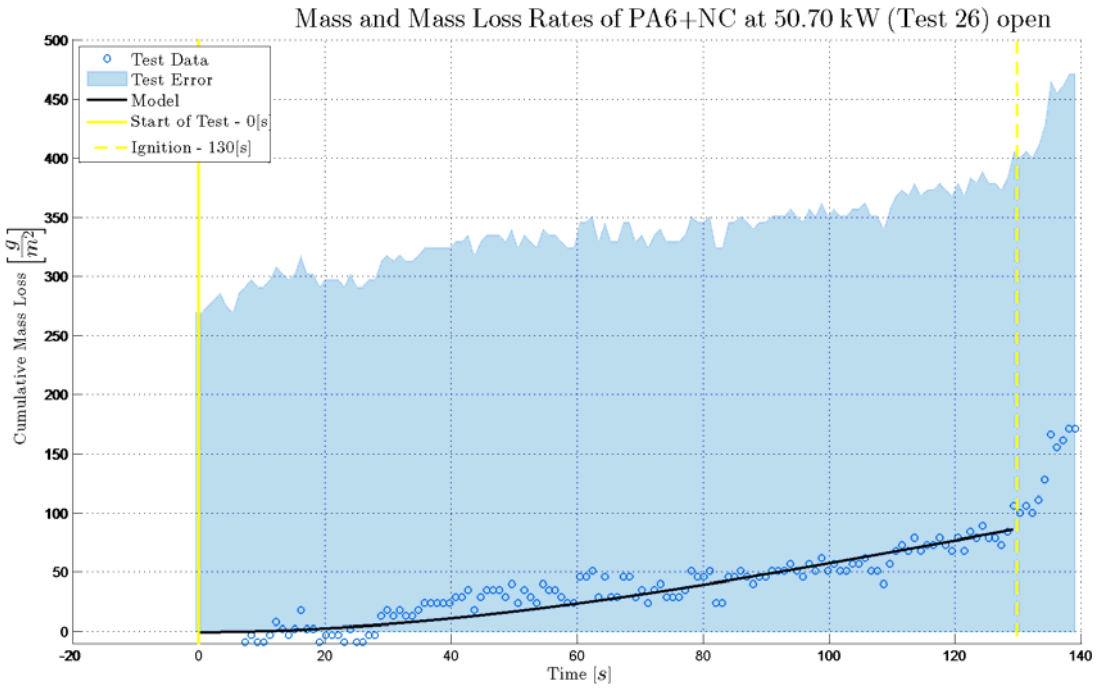

Figure 257 Cumulative mass loss "Test to Model" error comparison of PA6+NC *without* the independently obtained intrinsic material properties (Test 26)

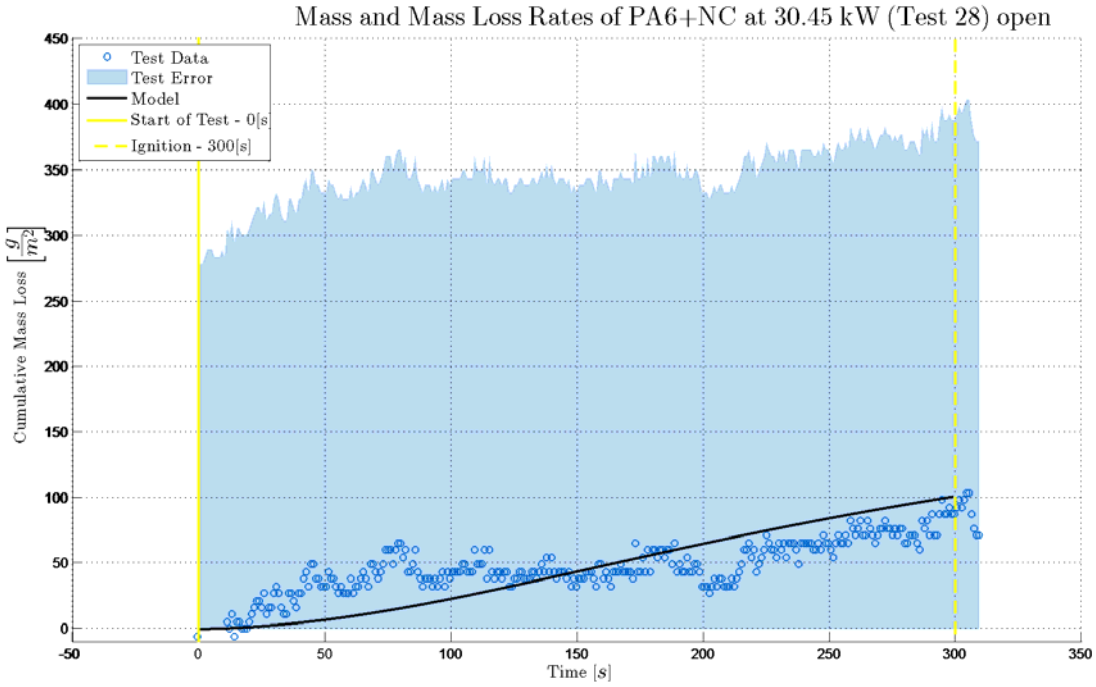

Figure 258 Cumulative mass loss "Test to Model" error comparison of PA6+NC *without* the independently obtained intrinsic material properties (Test 28)

With the independently obtained intrinsic material properties

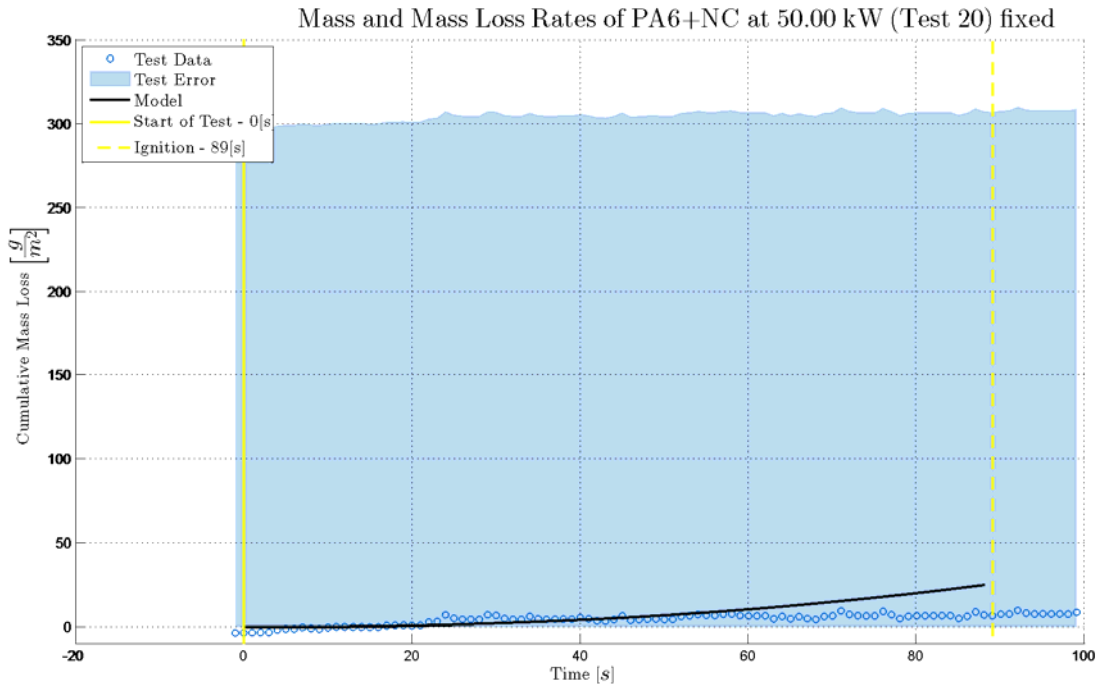

Figure 259 Cumulative mass loss "Test to Model" error comparison of PA6+NC *with* the independently obtained intrinsic material properties (Test 20)

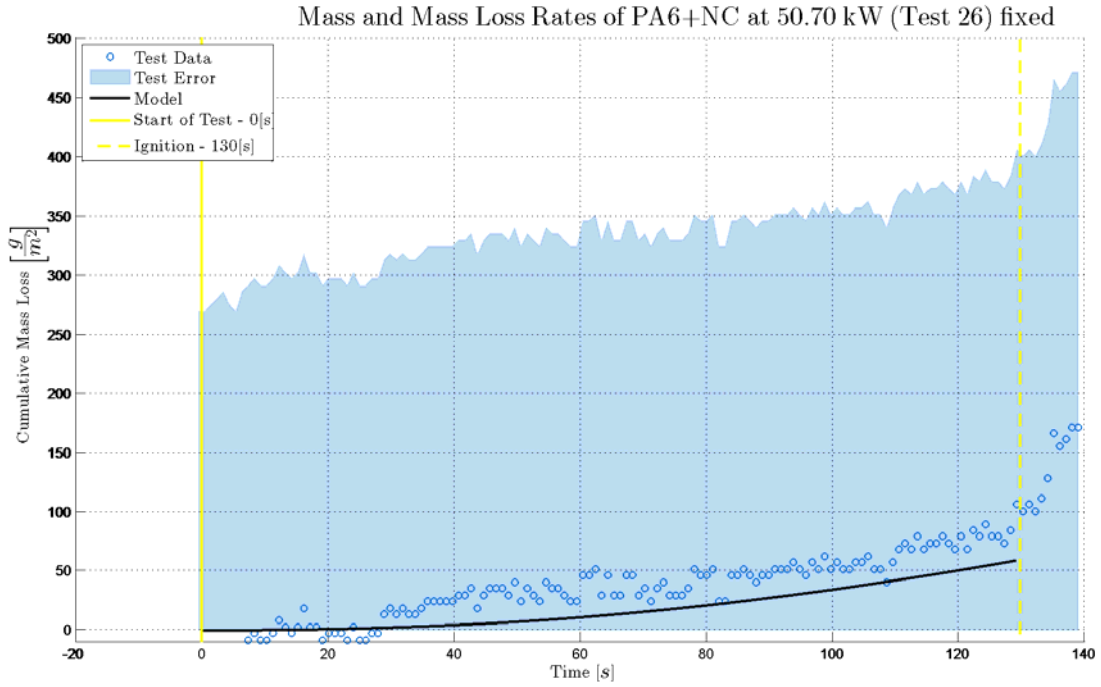

Figure 260 Cumulative mass loss "Test to Model" error comparison of PA6+NC *with* the independently obtained intrinsic material properties (Test 26)

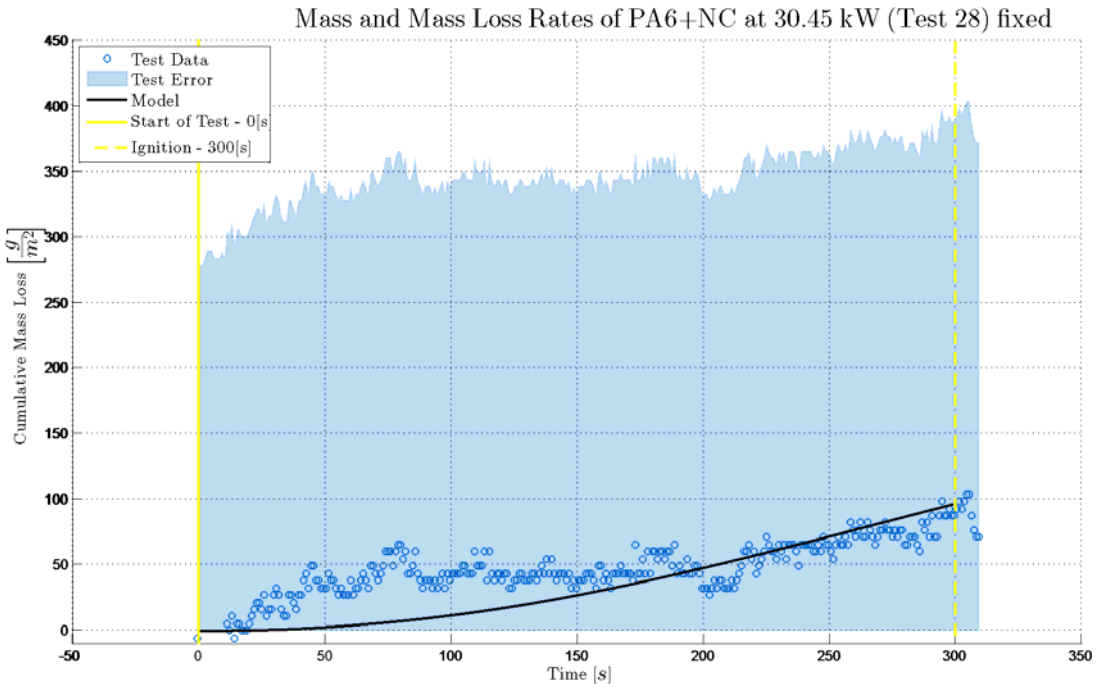

Figure 261 Cumulative mass loss “Test to Model” error comparison of PA6+NC *with* the independently obtained intrinsic material properties (Test 28)

C.1.4 PA6+NC+FR

C.1.4.1 In-depth temperature

Without the independently obtained intrinsic material properties

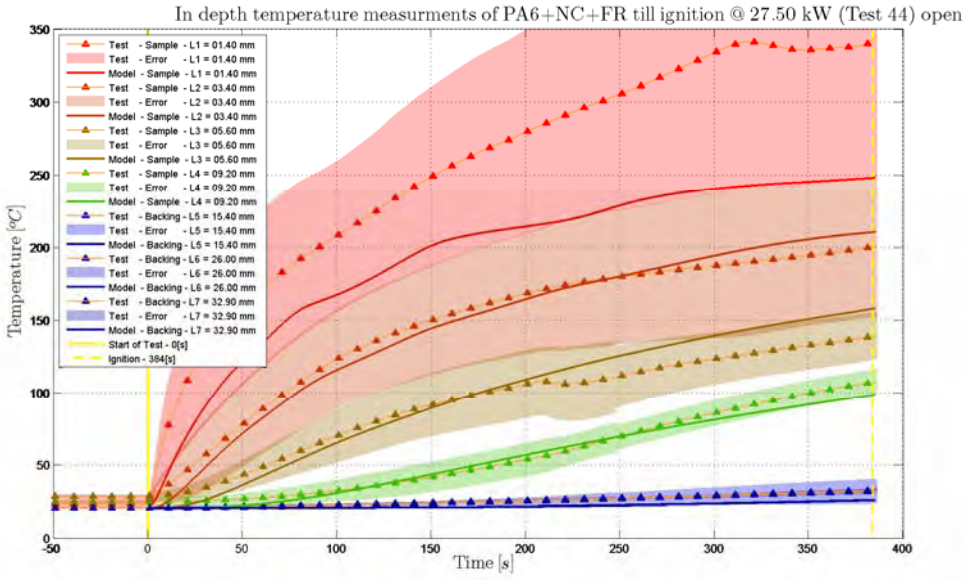

Figure 262 In-depth temperature "Test to Model" error comparison of PA6+NC+FR *without* the independently obtained intrinsic material properties (Test 44)

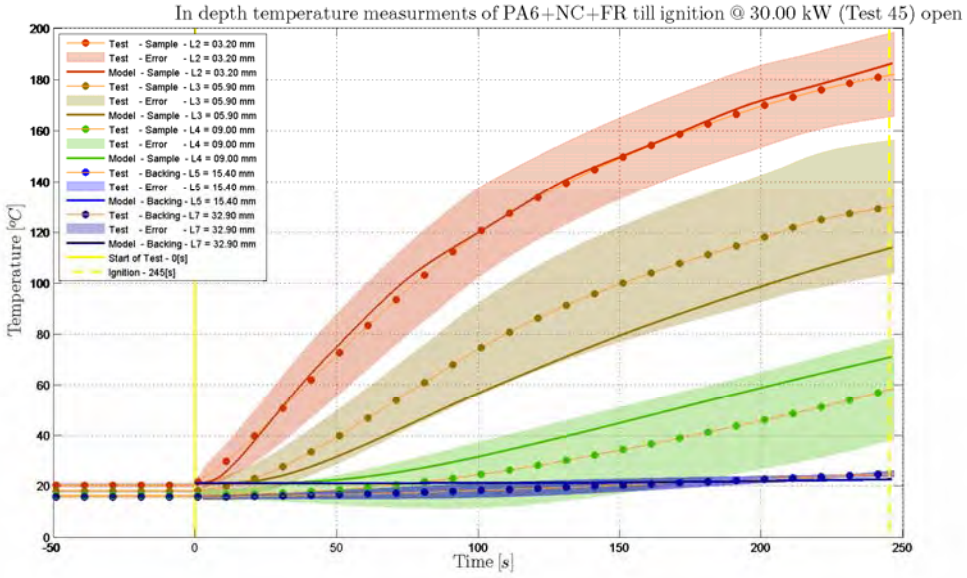

Figure 263 In-depth temperature "Test to Model" error comparison of PA6+NC+FR *without* the independently obtained intrinsic material properties (Test 45)

With the independently obtained intrinsic material properties

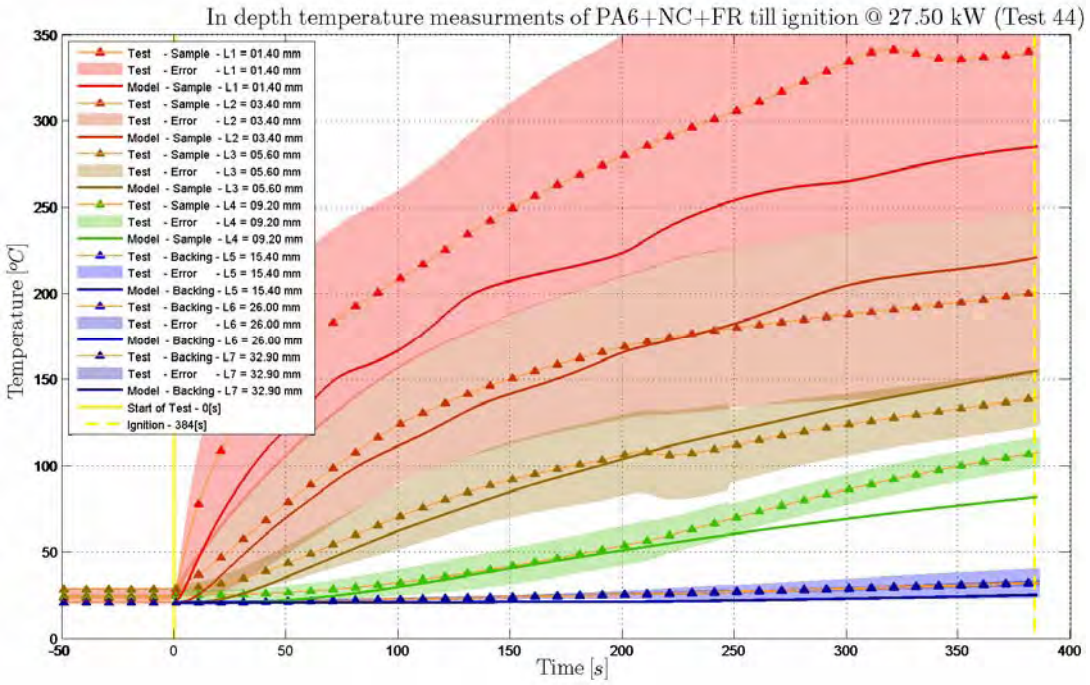

Figure 264 In-depth temperature "Test to Model" error comparison of PA6+NC+FR *with* the independently obtained intrinsic material properties (Test 44)

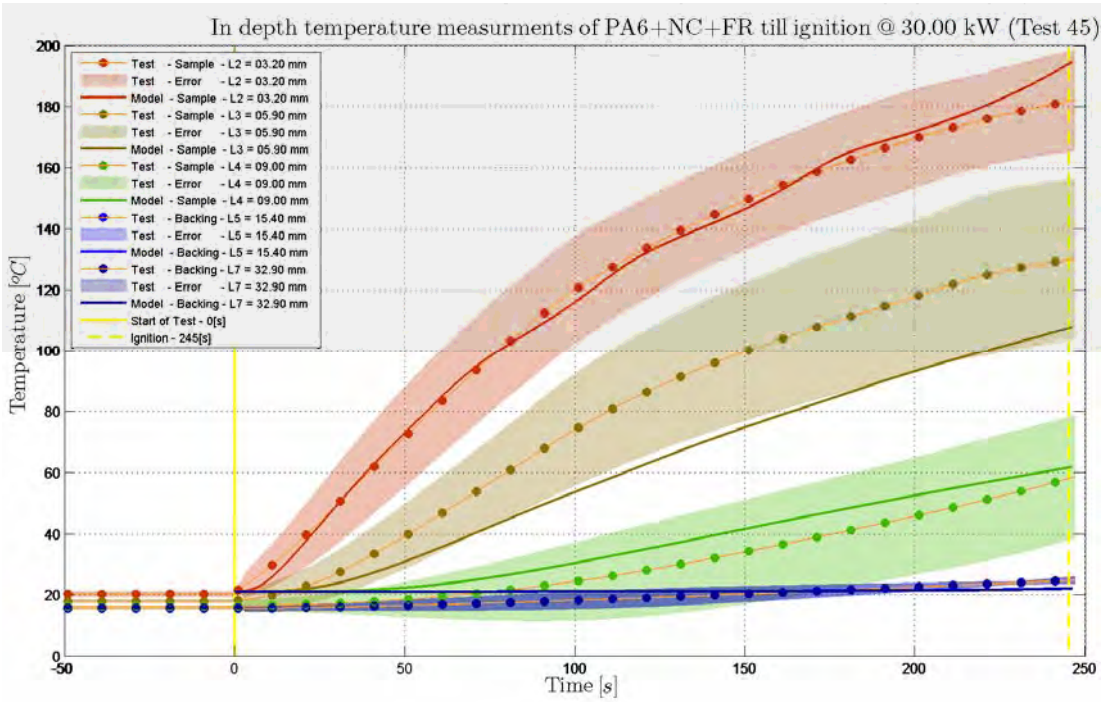

Figure 265 In-depth temperature "Test to Model" error comparison of PA6+NC+FR *with* the

C.1.4.2 Mass loss

Without the independently obtained intrinsic material properties

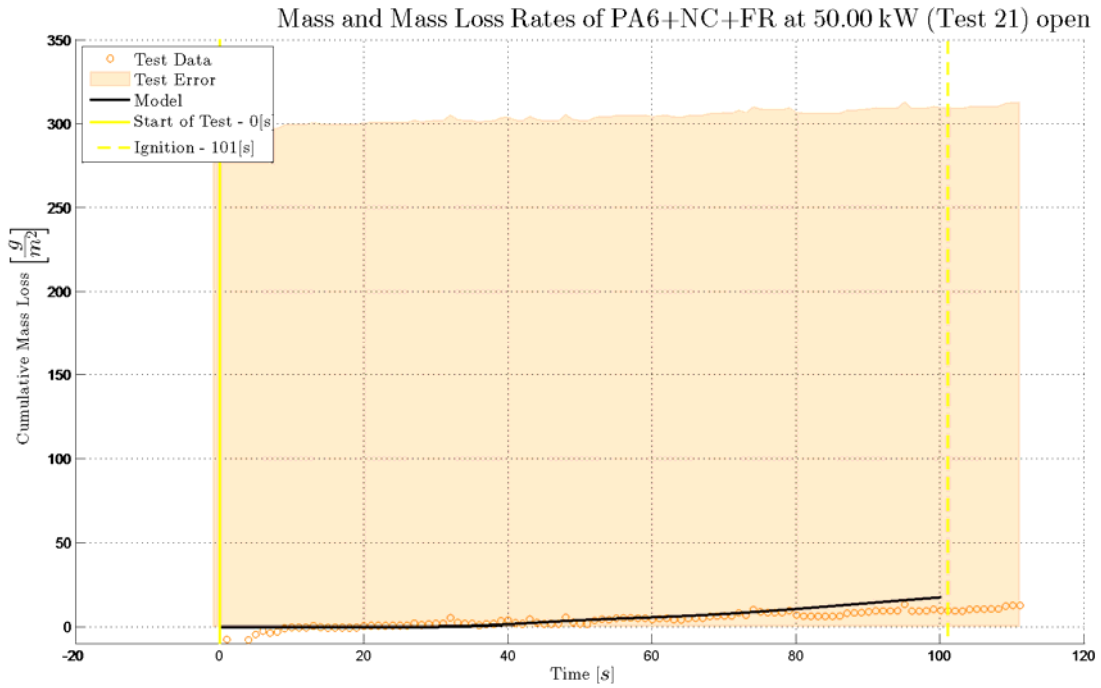

Figure 266 Cumulative mass loss "Test to Model" error comparison of PA6+NC+FR *without* the independently obtained intrinsic material properties (Test 21)

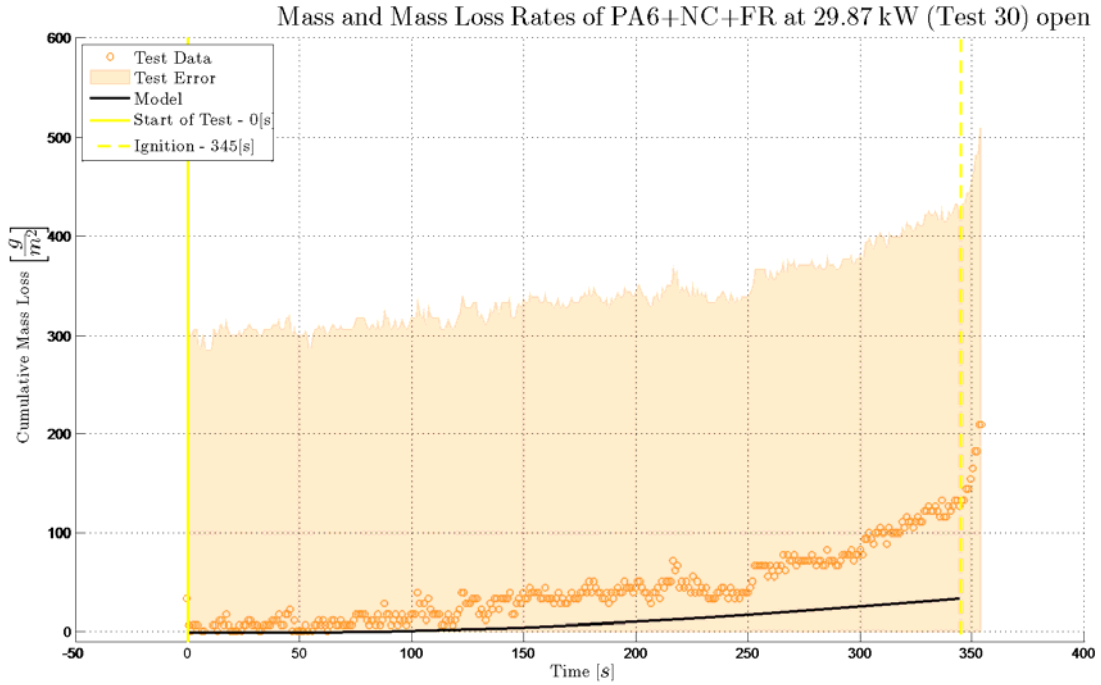

Figure 267 Cumulative mass loss "Test to Model" error comparison of PA6+NC +FR *without* the independently obtained intrinsic material properties (Test 30)

With the independently obtained intrinsic material properties

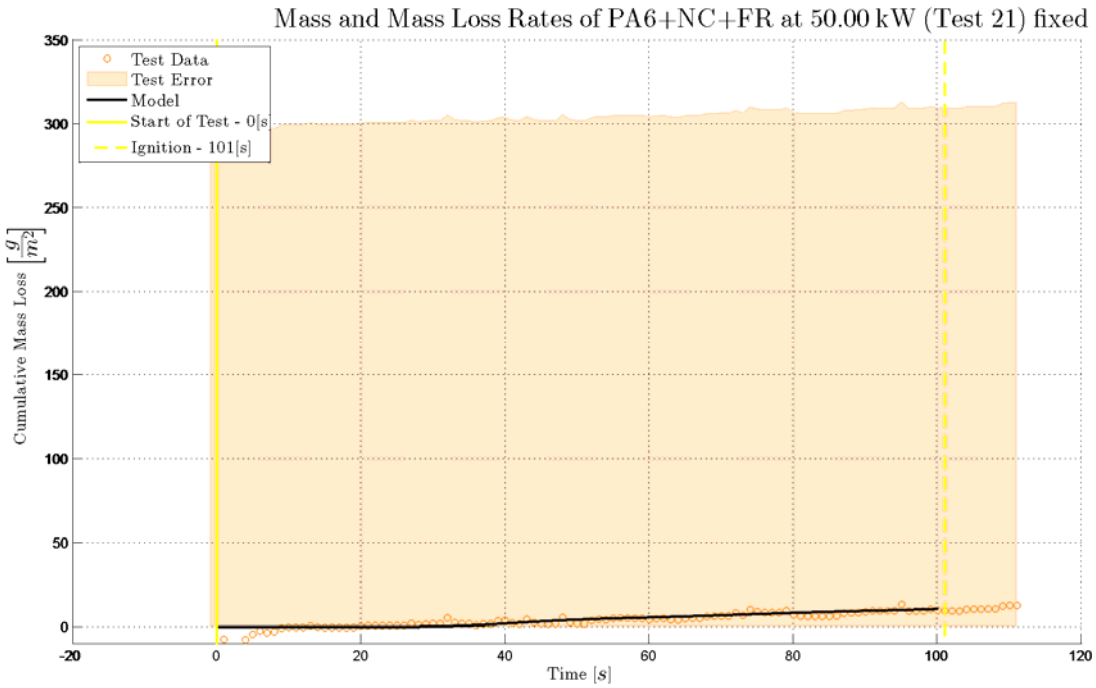

Figure 268 Cumulative mass loss "Test to Model" error comparison of PA6+NC +FR *with* the independently obtained intrinsic material properties (Test 21)

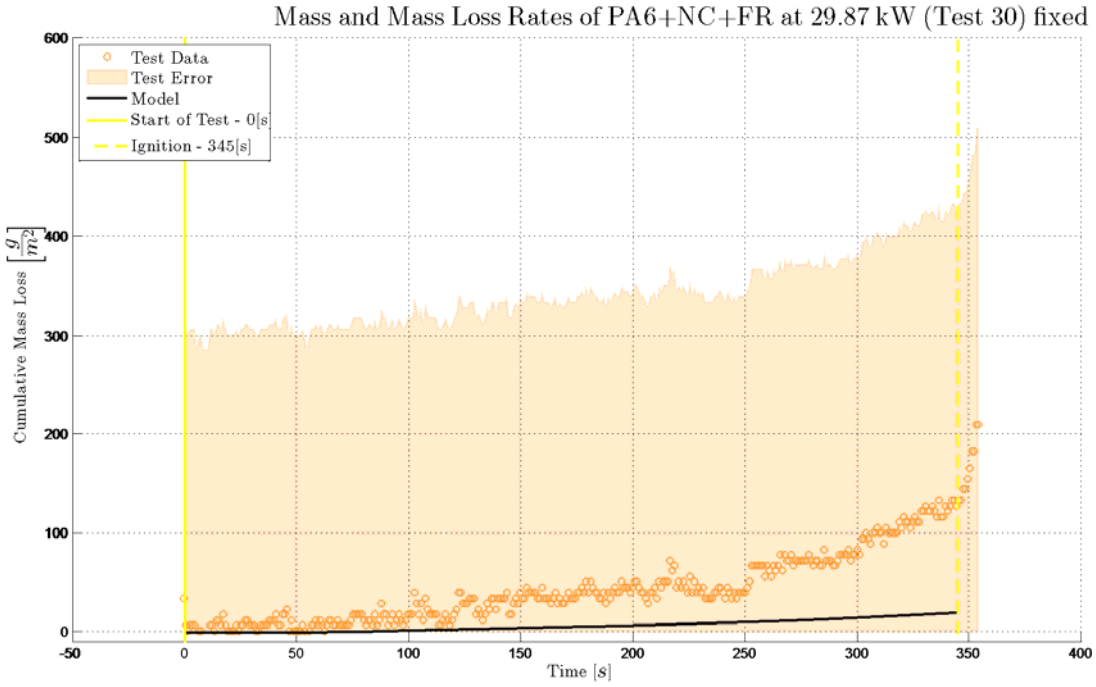

Figure 269 Cumulative mass loss "Test to Model" error comparison of PA6+NC +FR *with* the independently obtained intrinsic material properties (Test 30)

C.2 Result classification

Test data

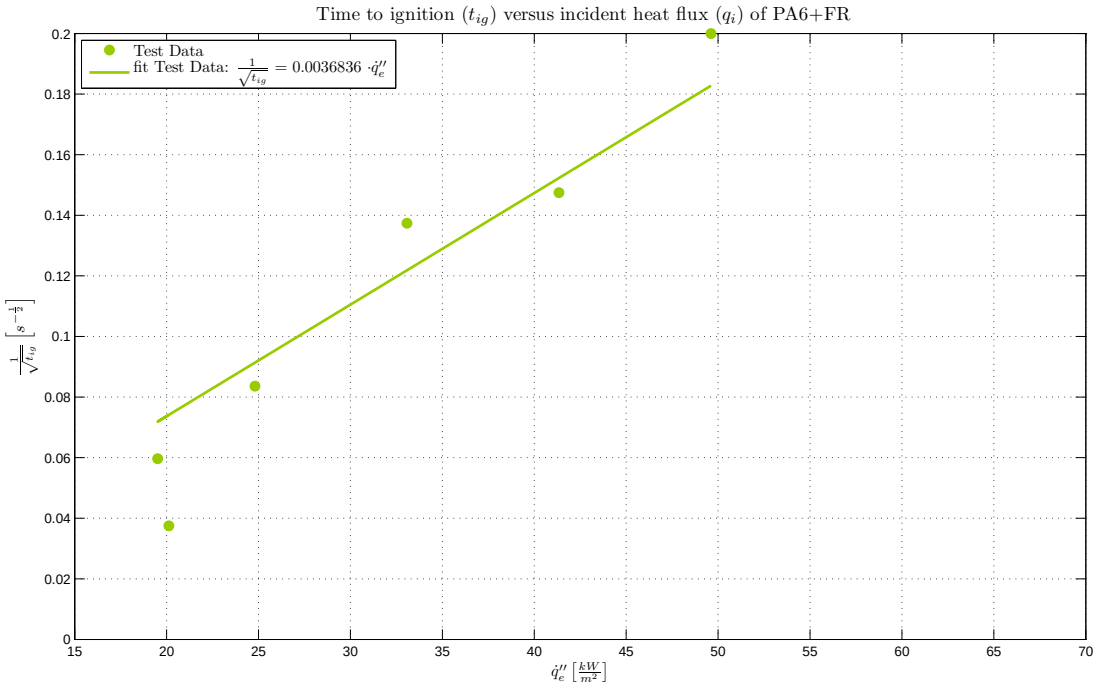

Figure 270 Time to ignition (t_{ig}) versus incident heat flux (q_i) of PA6+FR

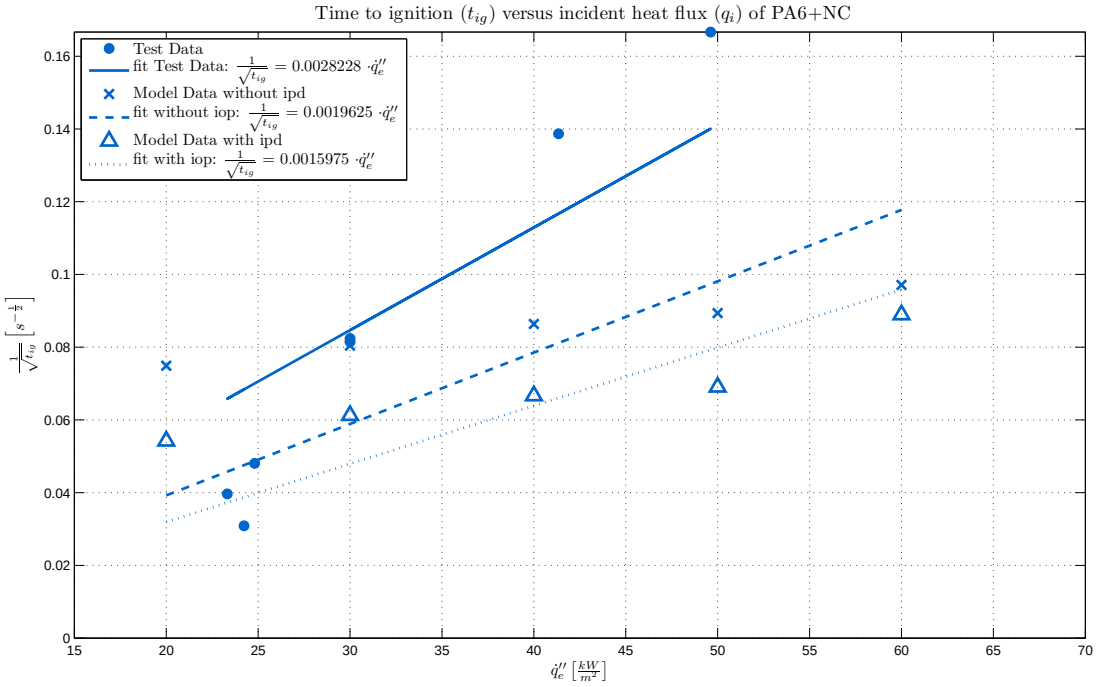

Figure 271 Time to ignition (t_{ig}) versus incident heat flux (q_i) of PA6+NC

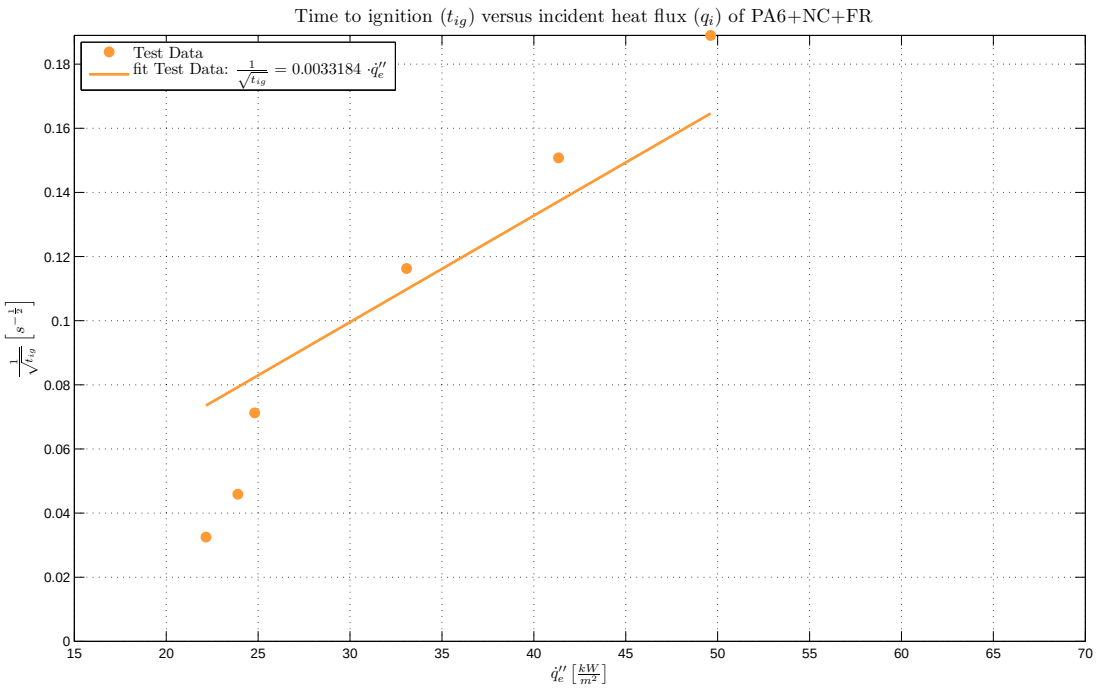

Figure 272 Time to ignition (t_{ig}) versus incident heat flux (q_i) of PA6+NC+FR

C.3 Constant heat flux in the Cone

C.3.1 Determining the temperature dependant parameter of the convective heat transfer coefficient for gpyro

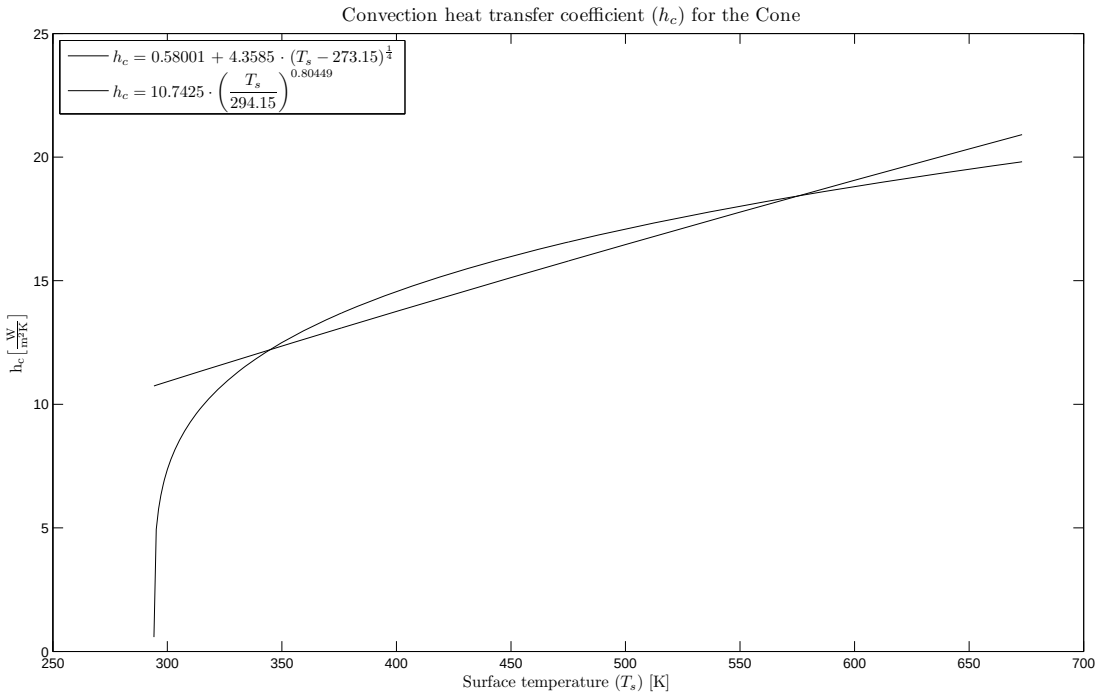

Figure 273 gpyro temperature dependant: convective heat transfer coefficient h_c (T) for the Cone

C.3.2 PA6

C.3.2.1 In-depth temperature comparison

Without the independently obtained intrinsic material properties

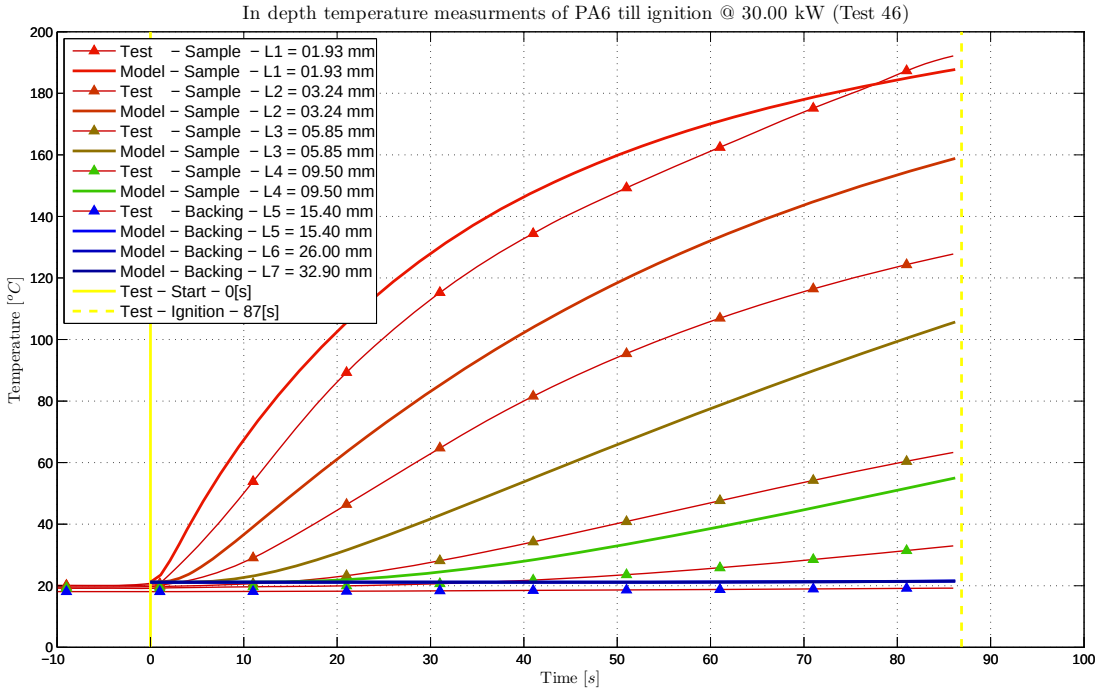

Figure 274 In-depth temperature "Cone Test to Model Data" comparison of PA6 with parameters obtained from FPA experiments *not using* the independently obtained intrinsic material properties (Test 46)

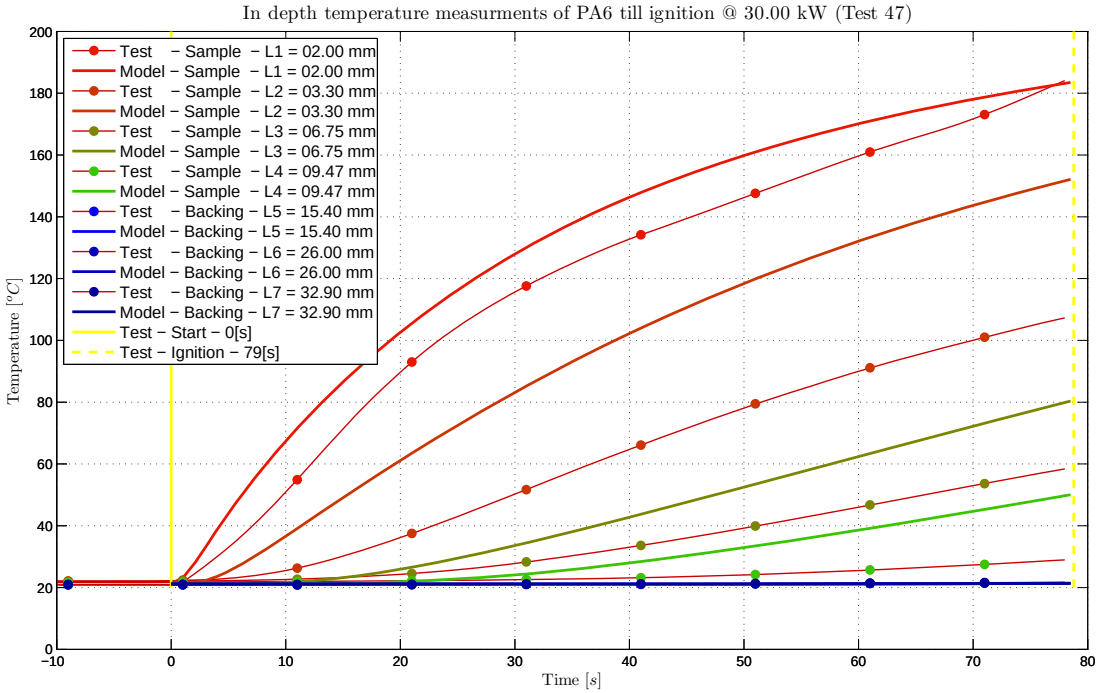

Figure 275 In-depth temperature "Cone Test to Model Data" comparison of PA6 with parameters obtained from FPA experiments *not using* the independently obtained intrinsic material properties (Test 47)

With the independently obtained intrinsic material properties

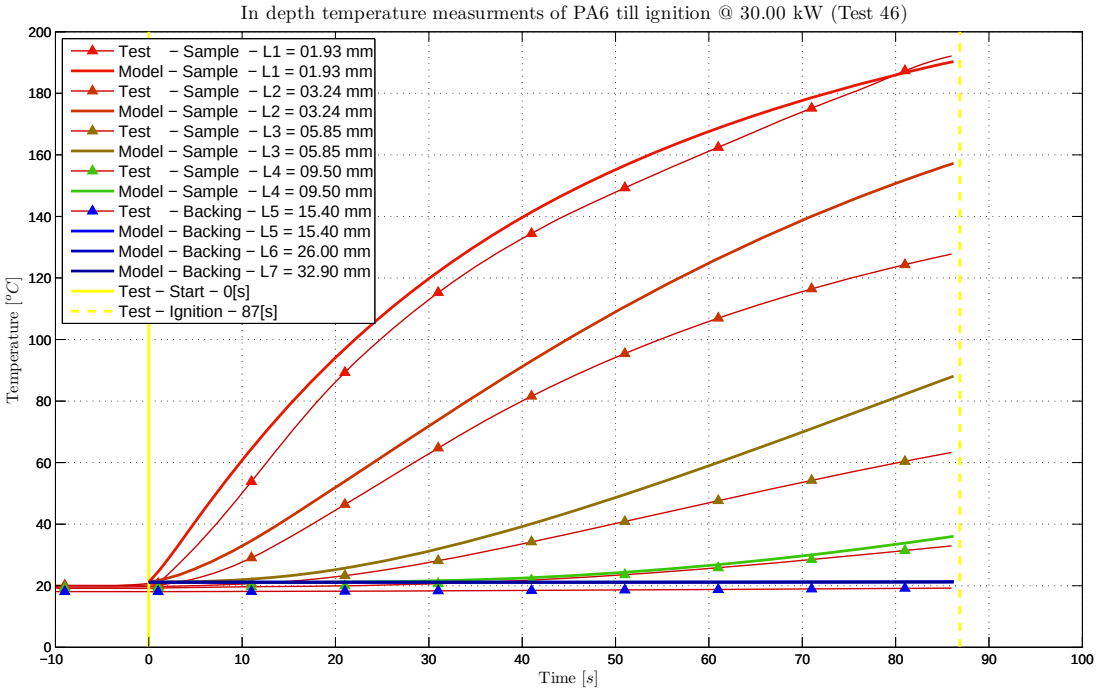

Figure 276 In-depth temperature "Cone Test to Model Data" comparison of PA6 with parameters obtained from FPA experiments *using* the independently obtained intrinsic material properties (Test 46)

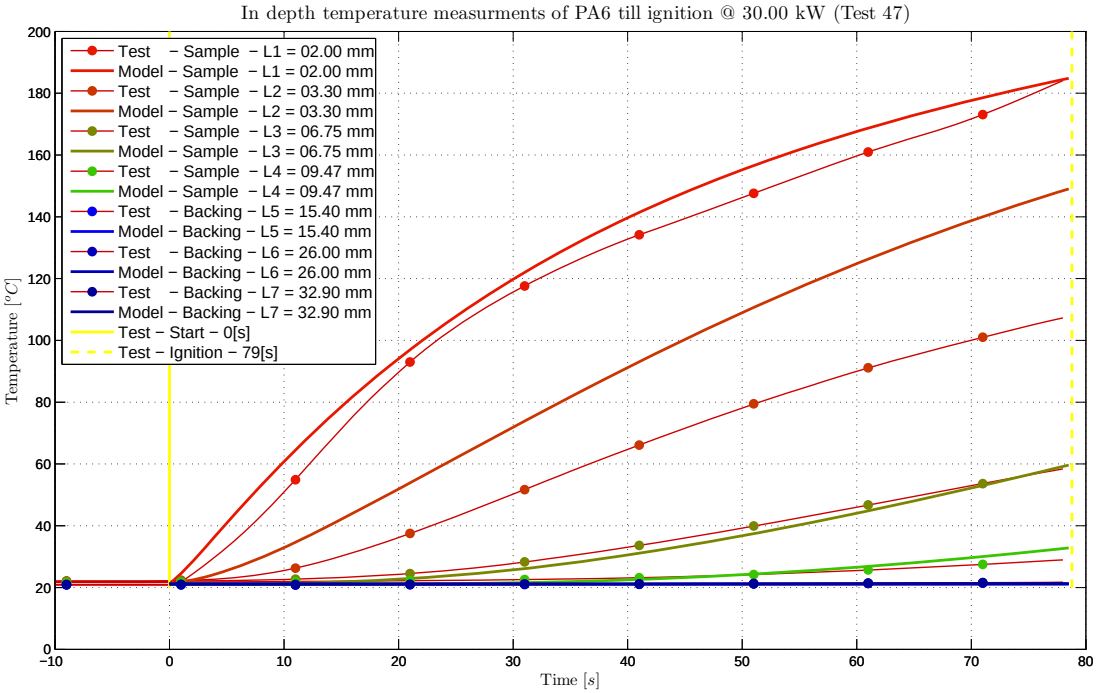

Figure 277 In-depth temperature "Cone Test to Model Data" comparison of PA6 with parameters obtained from FPA experiments *using* the independently obtained intrinsic material properties (Test 47)

C.3.2.2 Mass loss comparison

Without the independently obtained intrinsic material properties

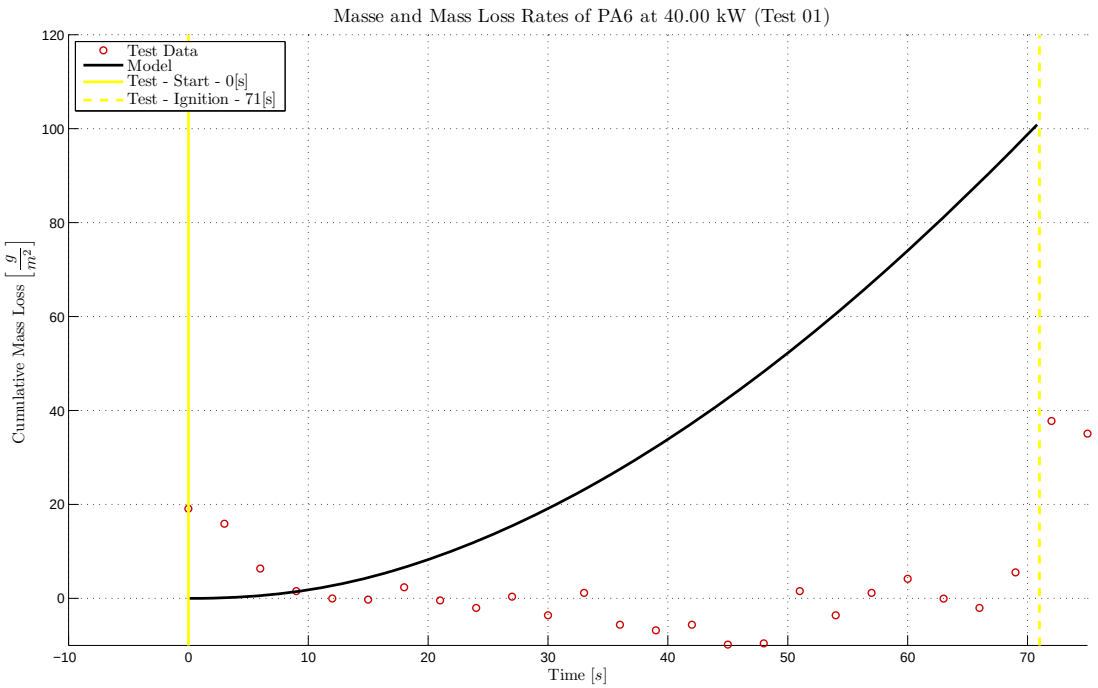

Figure 278 Mass loss "Cone Test to Model Data" comparison of PA6 with parameters obtained from FPA experiments *not using* the independently obtained intrinsic material properties (Test 01)

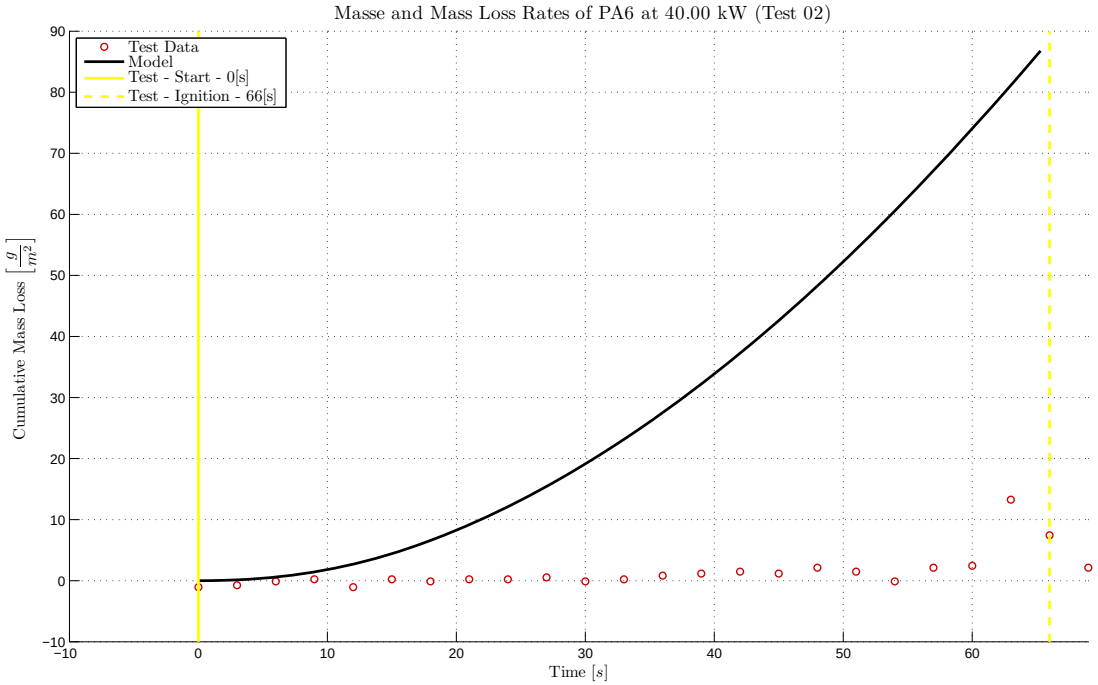

Figure 279 Mass loss "Cone Test to Model Data" comparison of PA6 with parameters obtained from FPA experiments *not using* the independently obtained intrinsic material properties (Test 02)

With the independently obtained intrinsic material properties

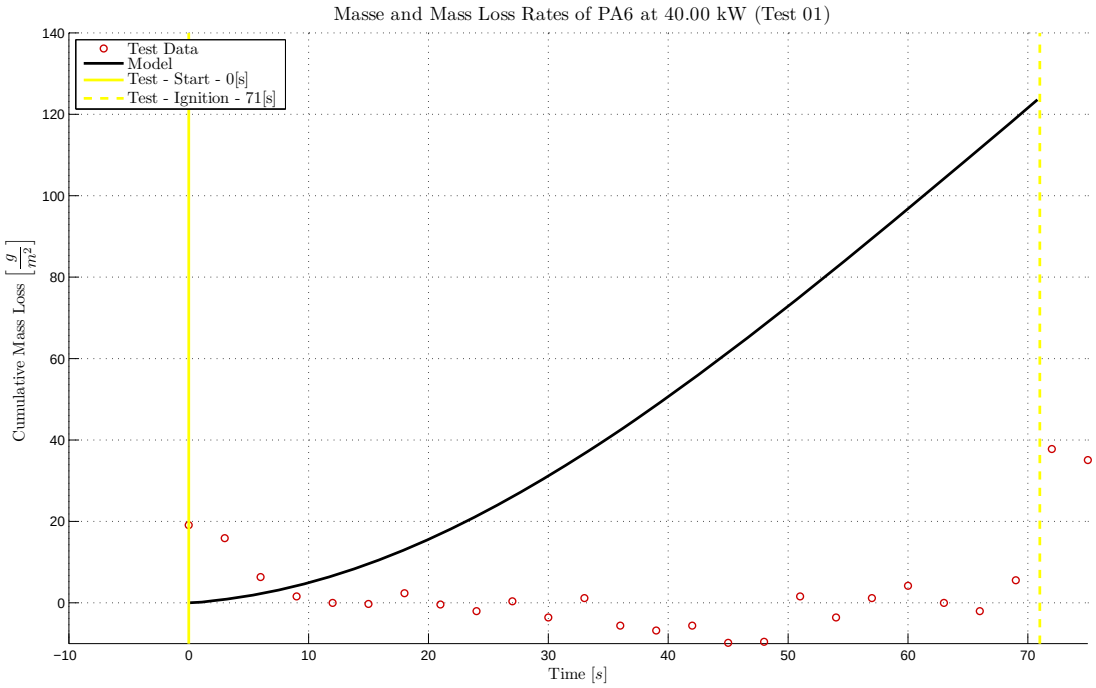

Figure 280 Mass loss "Cone Test to Model Data" comparison of PA6 with parameters obtained from FPA experiments *using* the independently obtained intrinsic material properties (Test 01)

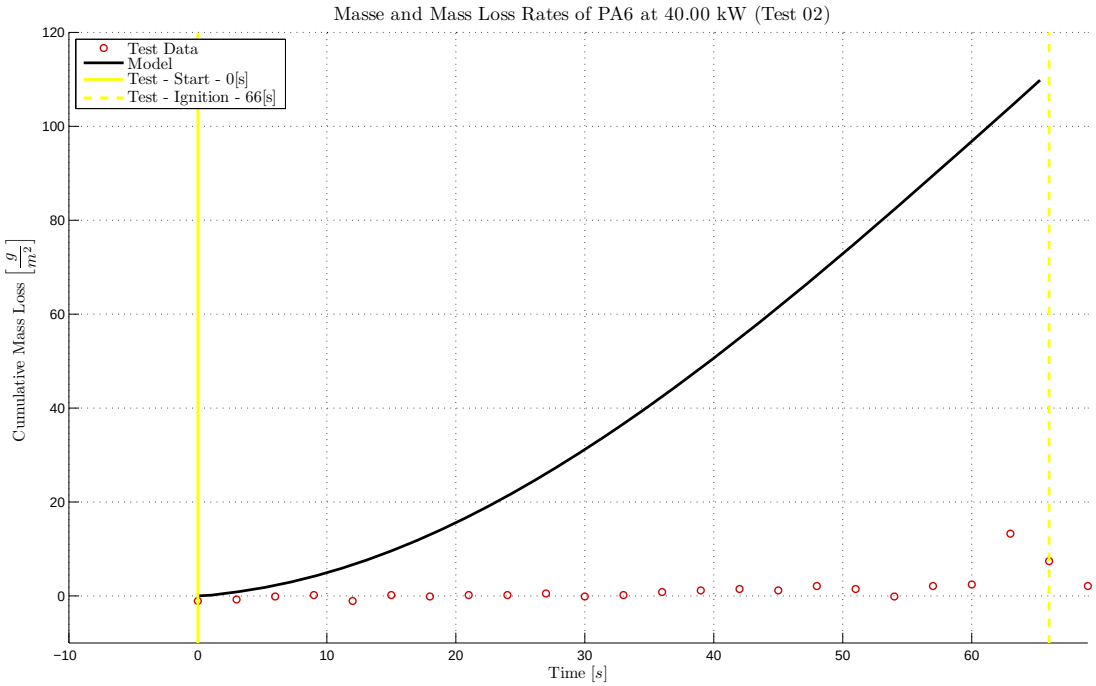

Figure 281 Mass loss "Cone Test to Model Data" comparison of PA6 with parameters obtained from FPA experiments *using* the independently obtained intrinsic material properties (Test 02)

C.3.3 PA6 + NC

C.3.3.1 In-depth temperature comparison

Without the independently obtained intrinsic material properties

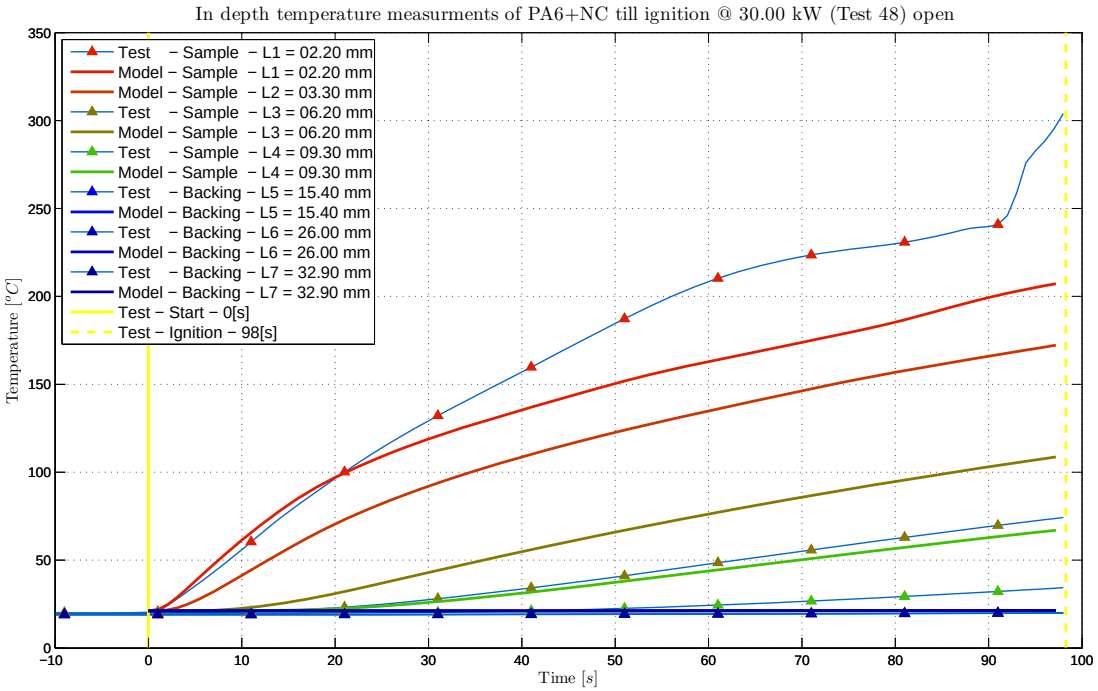

Figure 282 In-depth temperature “Cone Test to Model Data” comparison of PA6+NC with parameters obtained from FPA experiments *not using* the independently obtained intrinsic material properties (Test 48)

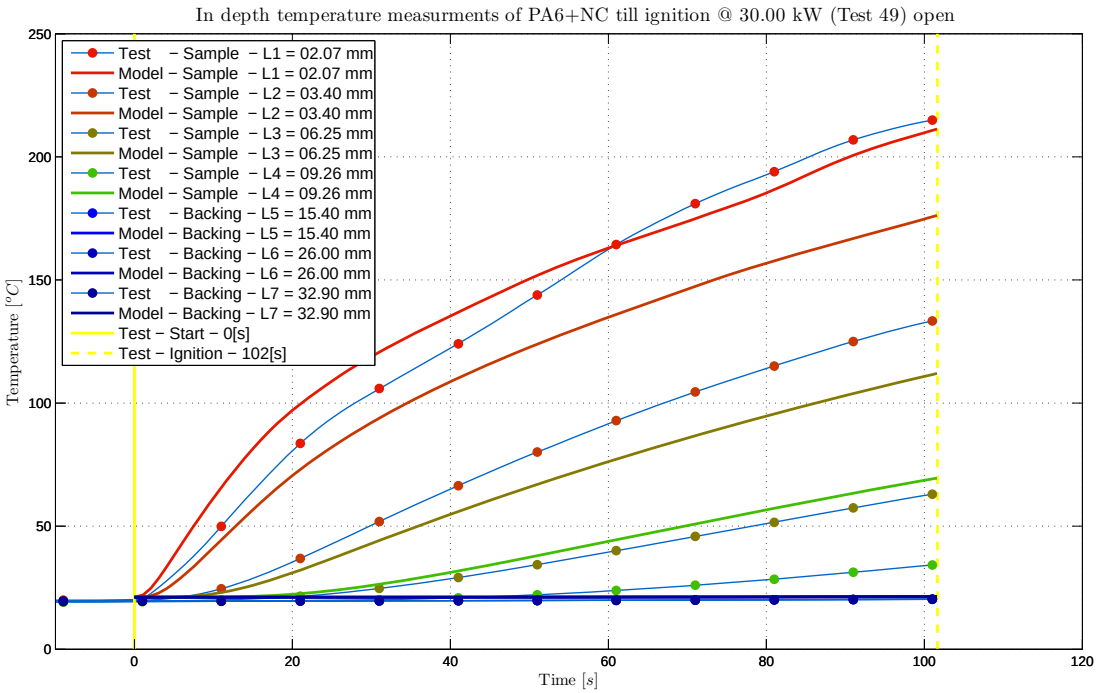

Figure 283 In-depth temperature "Cone Test to Model Data" comparison of PA6+NC with parameters obtained from FPA experiments *not using* the independently obtained intrinsic material properties (Test 49)

With the independently obtained intrinsic material properties

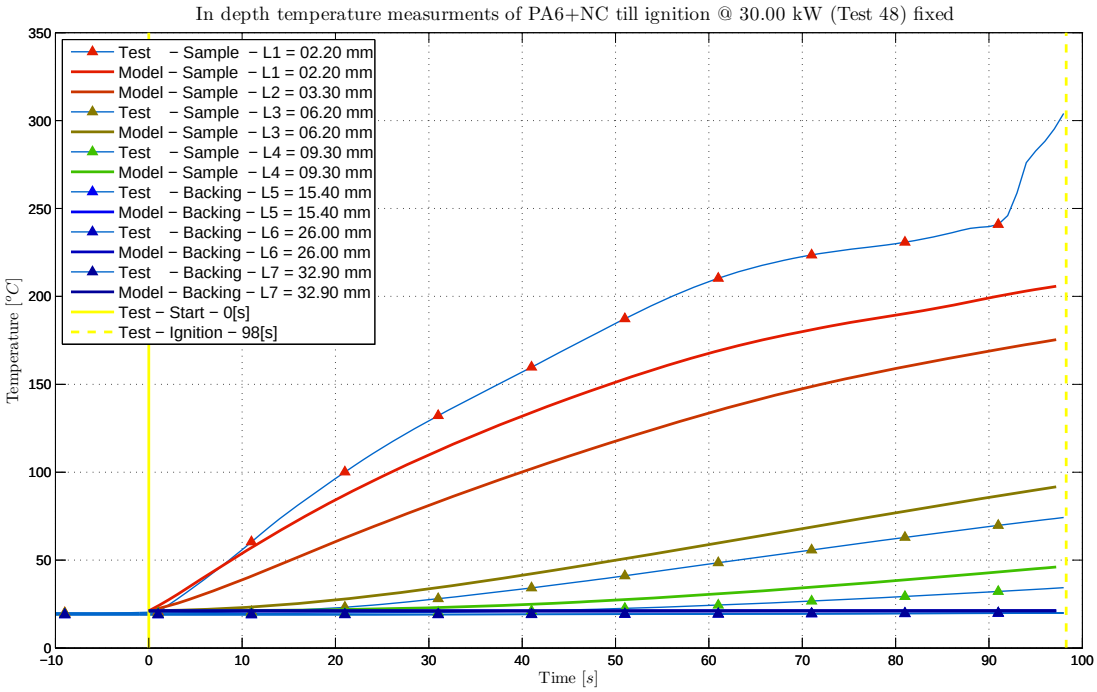

Figure 284 In-depth temperature "Cone Test to Model Data" comparison of PA6+NC with parameters obtained from FPA experiments *using* the independently obtained intrinsic material properties (Test 48)

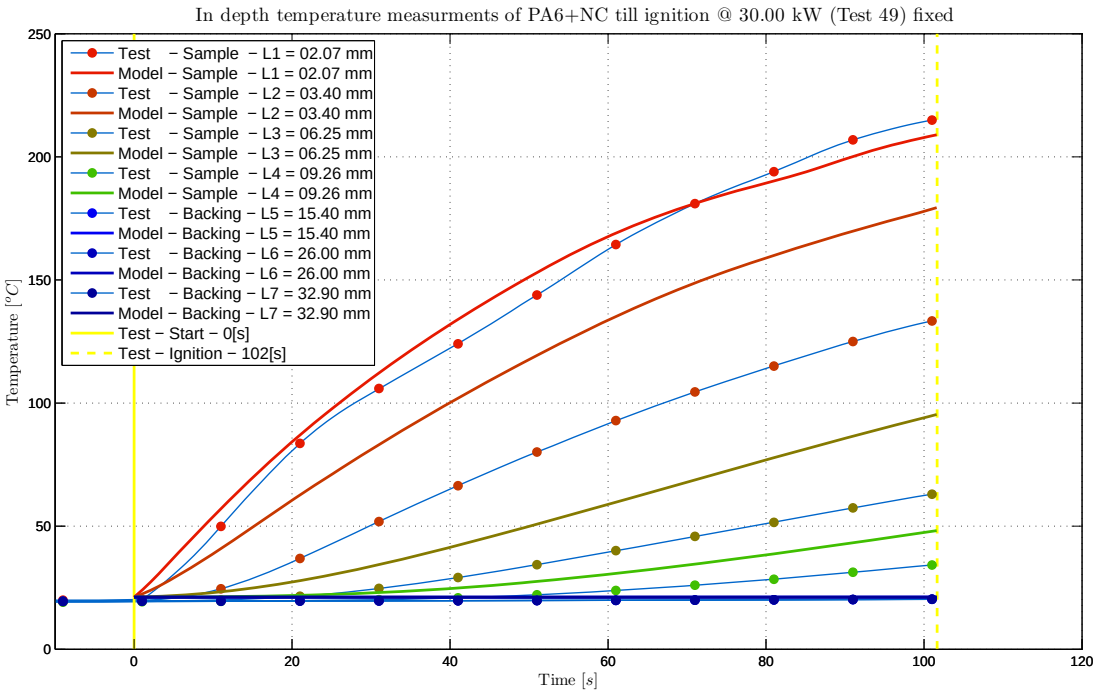

Figure 285 In-depth temperature “Cone Test to Model Data” comparison of PA6+NC with parameters obtained from FPA experiments *using* the independently obtained intrinsic material properties (Test 49)

C.3.3.2 Mass loss comparison

Without the independently obtained intrinsic material properties

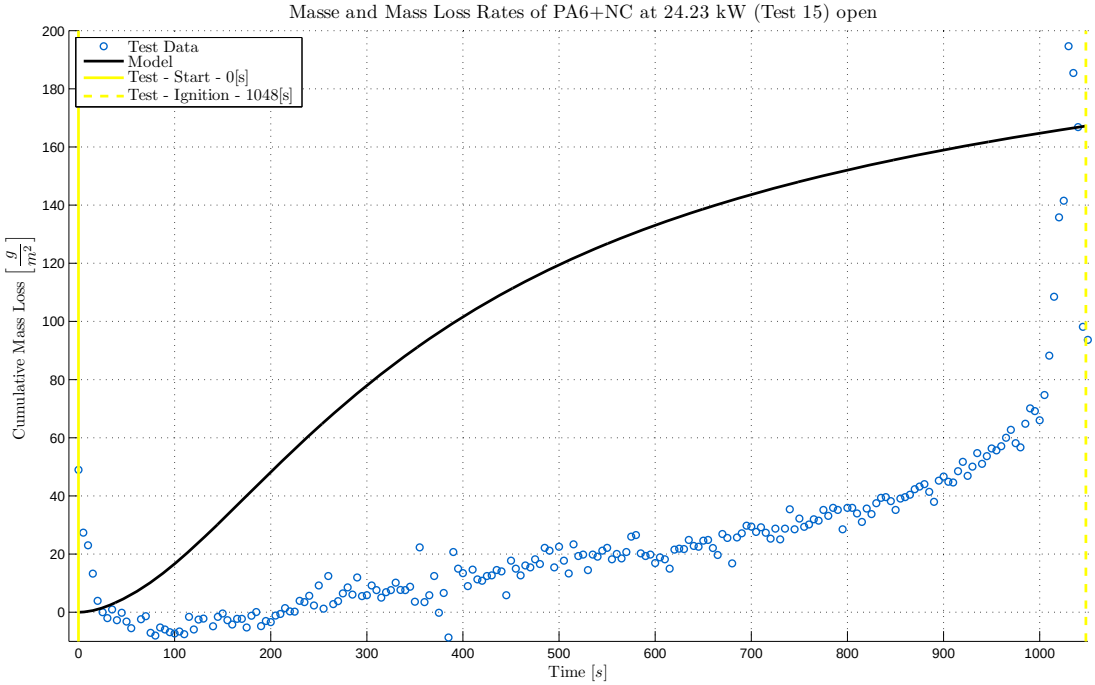

Figure 286 Mass loss "Cone Test to Model Data" comparison of PA6+NC with parameters obtained from FPA experiments *not using* the independently obtained intrinsic material properties (Test 15)

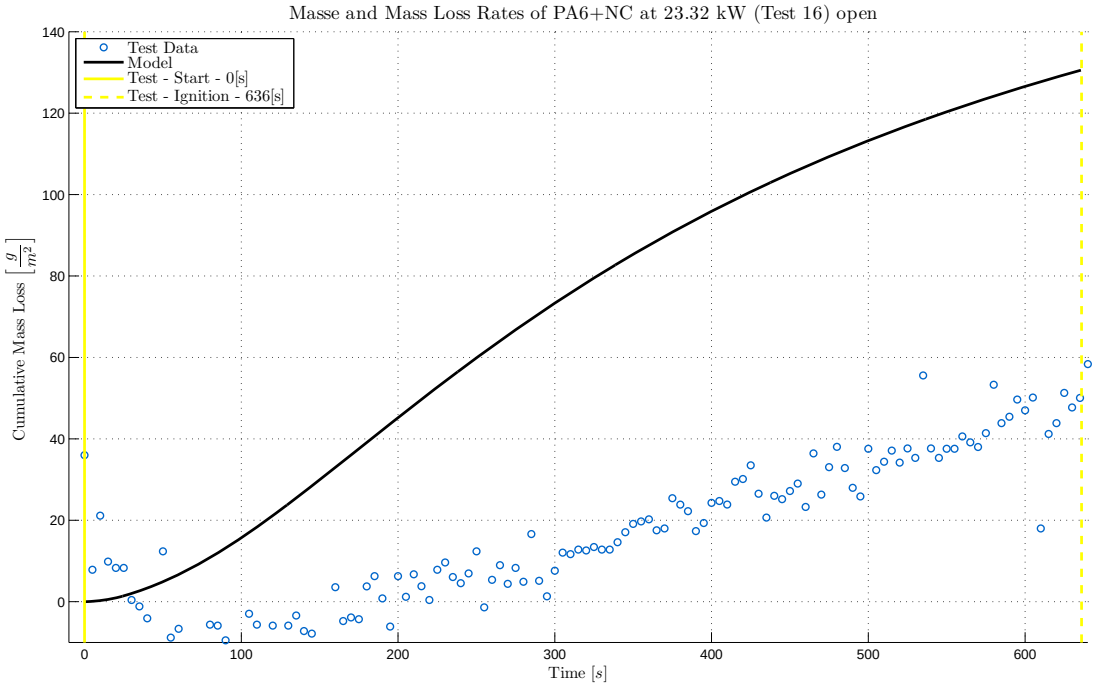

Figure 287 Mass loss "Cone Test to Model Data" comparison of PA6+NC with parameters obtained from FPA experiments *not using* the independently obtained intrinsic material properties (Test 16)

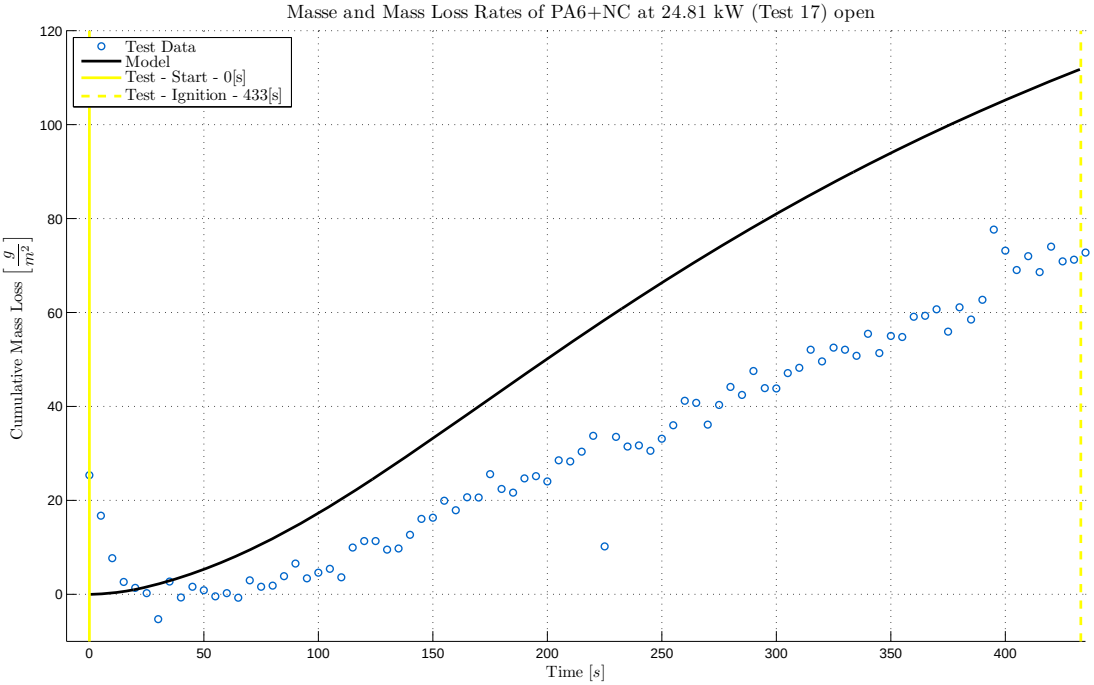

Figure 288 Mass loss "Cone Test to Model Data" comparison of PA6+NC with parameters obtained from FPA experiments *not using* the independently obtained intrinsic material properties (Test 17)

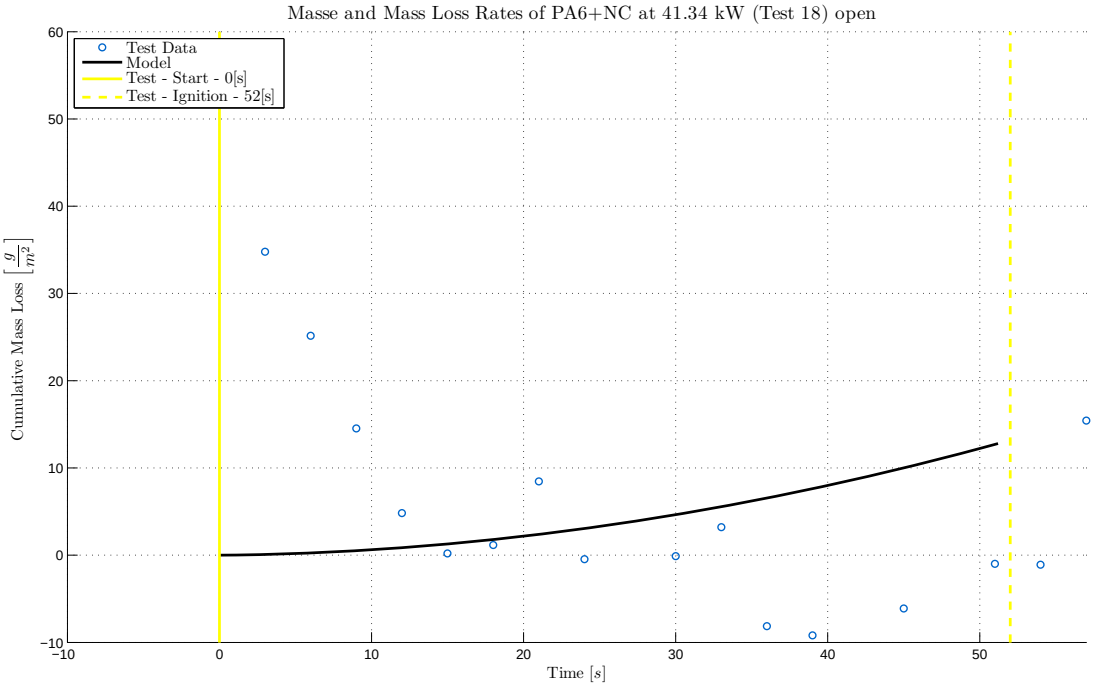

Figure 289 Mass loss "Cone Test to Model Data" comparison of PA6+NC with parameters obtained from FPA experiments *not using* the independently obtained intrinsic material properties (Test 18)

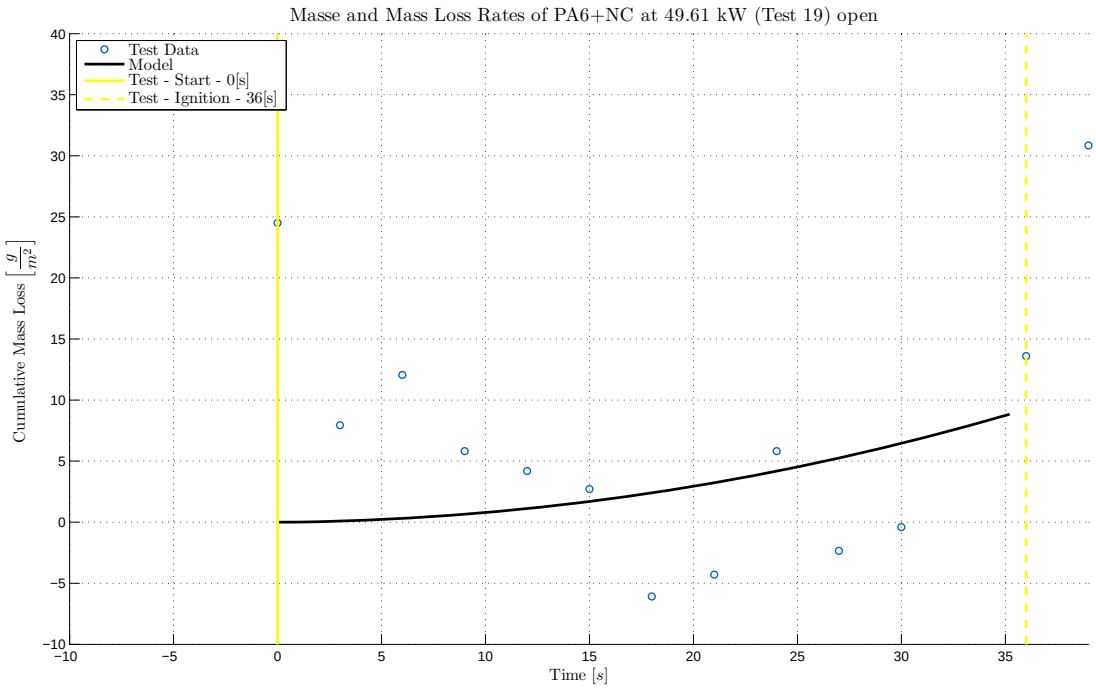

Figure 290 Mass loss "Cone Test to Model Data" comparison of PA6+NC with parameters obtained from FPA experiments *not using* the independently obtained intrinsic material properties (Test 19)

With the independently obtained intrinsic material properties

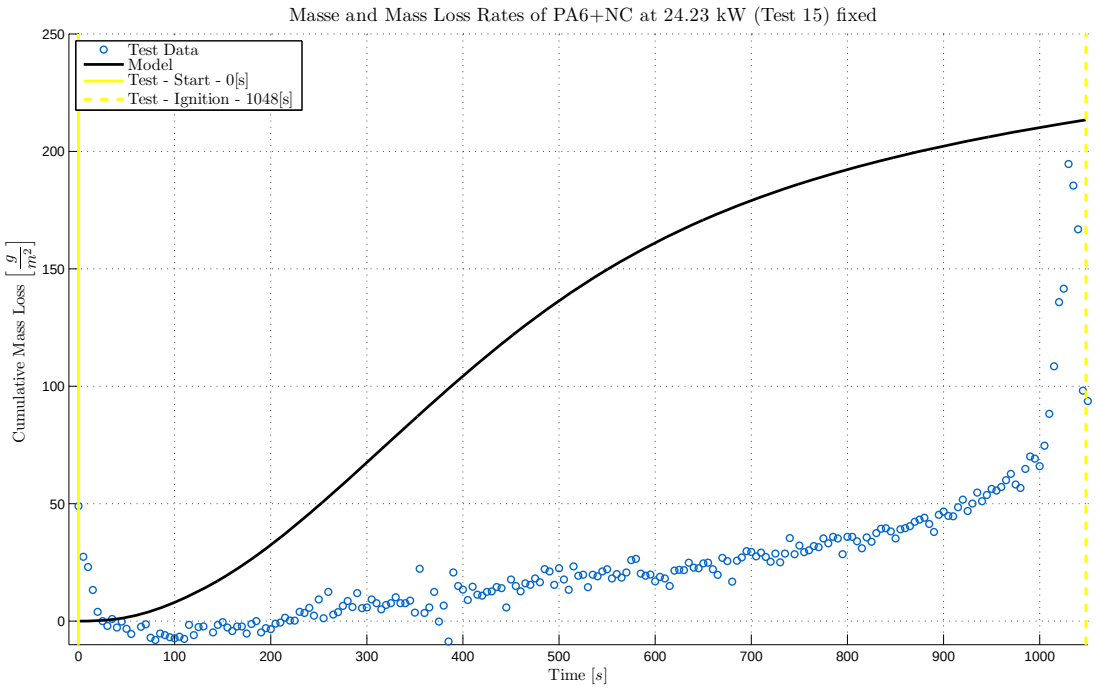

Figure 291 Mass loss "Cone Test to Model Data" comparison of PA6+NC with parameters obtained from FPA experiments *using* the independently obtained intrinsic material properties (Test 15)

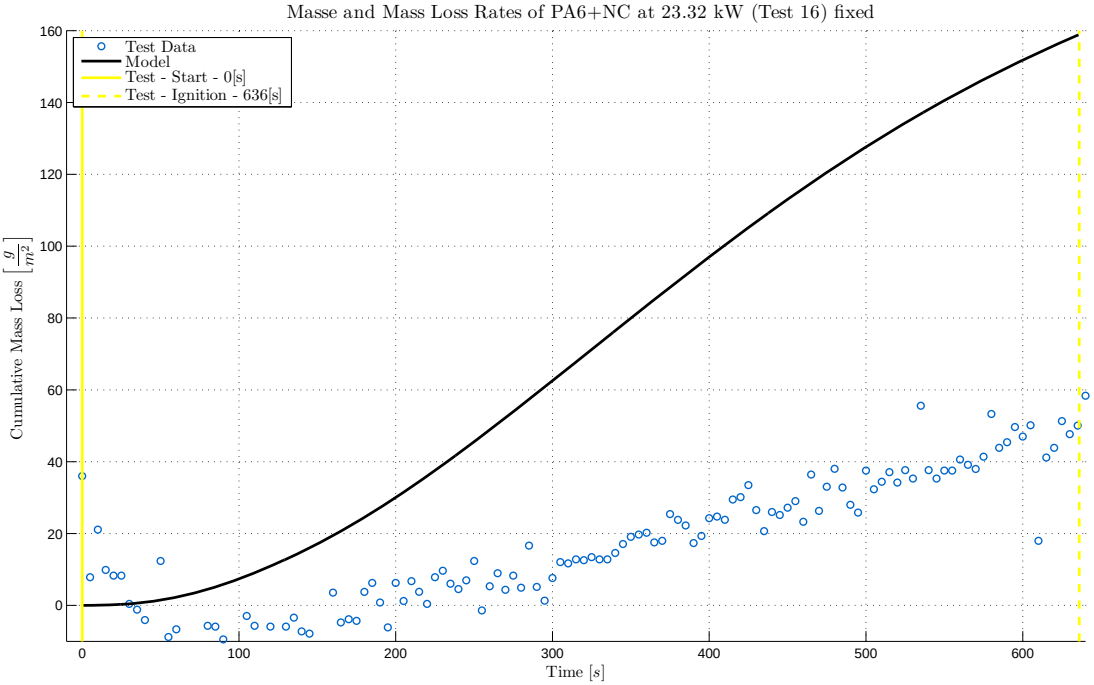

Figure 292 Mass loss "Cone Test to Model Data" comparison of PA6+NC with parameters obtained from FPA experiments *using* the independently obtained intrinsic material properties (Test 16)

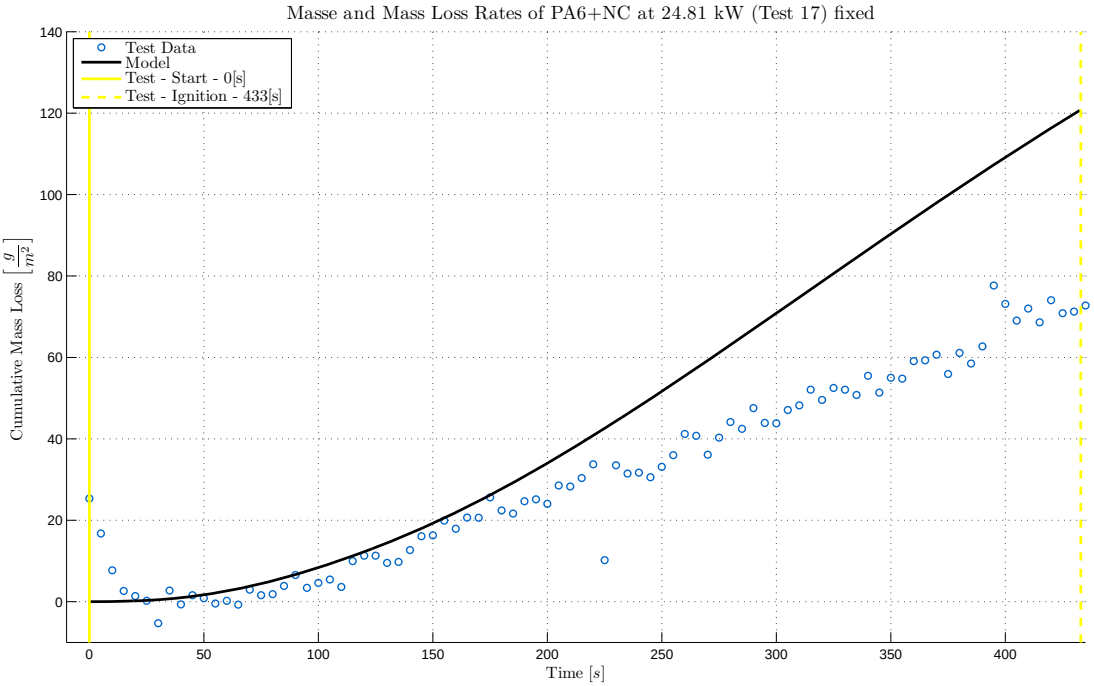

Figure 293 Mass loss "Cone Test to Model Data" comparison of PA6+NC with parameters obtained from FPA experiments *using* the independently obtained intrinsic material properties (Test 17)

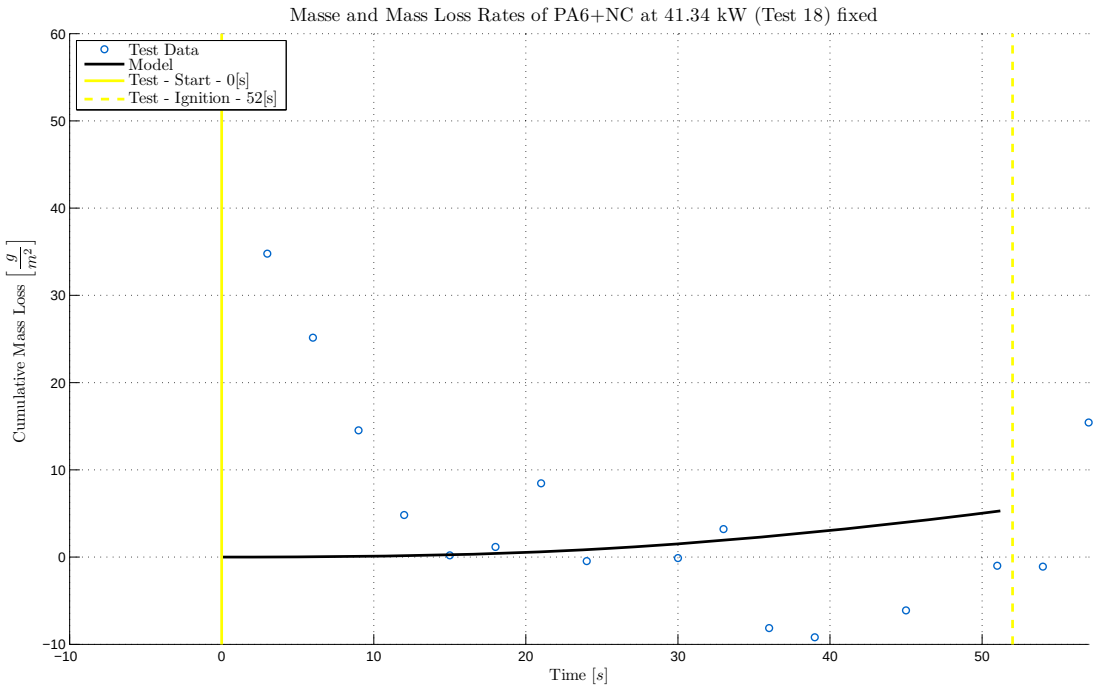

Figure 294 Mass loss "Cone Test to Model Data" comparison of PA6+NC with parameters obtained from FPA experiments *using* the independently obtained intrinsic material properties (Test 18)

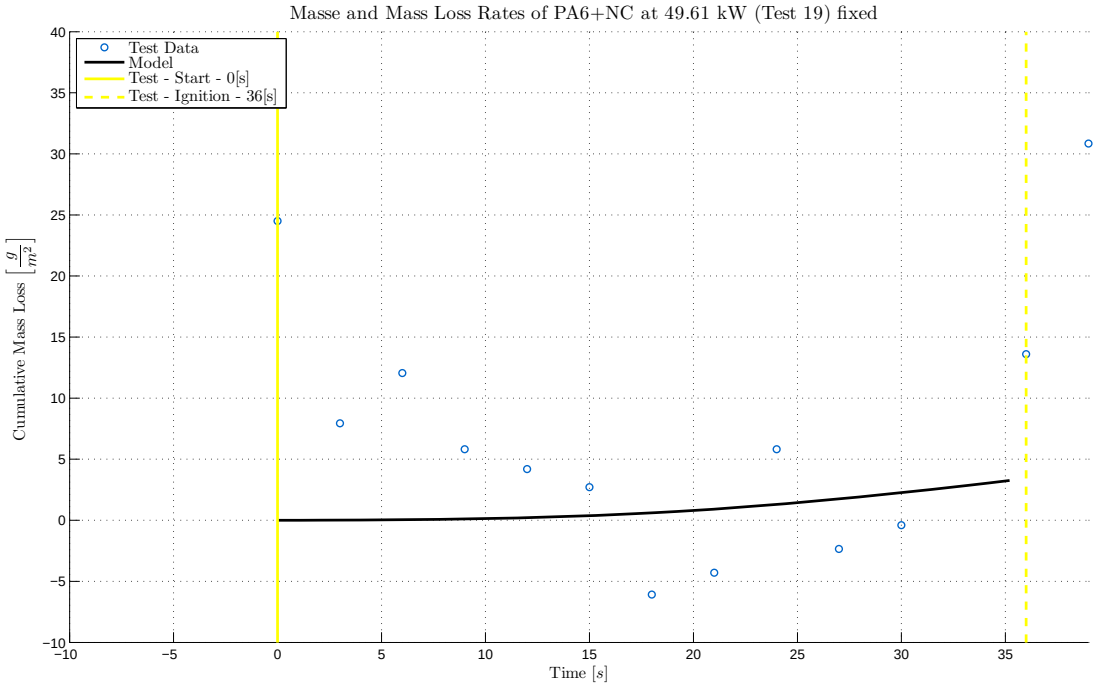

Figure 295 Mass loss "Cone Test to Model Data" comparison of PA6+NC with parameters obtained from FPA experiments *using* the independently obtained intrinsic material properties (Test 19)

C.4 Ramped heat flux in the FPA

C.4.1 PA6

C.4.1.1 In-depth temperature comparison

Without the independently obtained intrinsic material properties

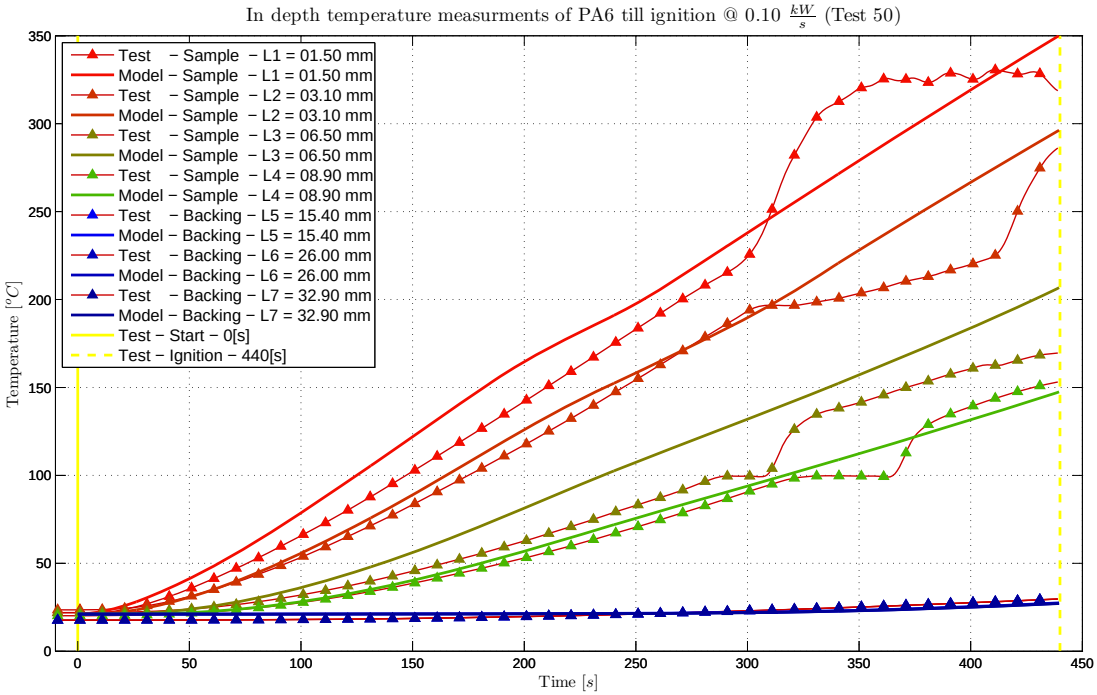

Figure 296 In-depth temperature “ramped FPA Test to Model Data” comparison of PA6 with parameters obtained from FPA experiments *not using* the independently obtained intrinsic material properties (Test 50)

With the independently obtained intrinsic material properties

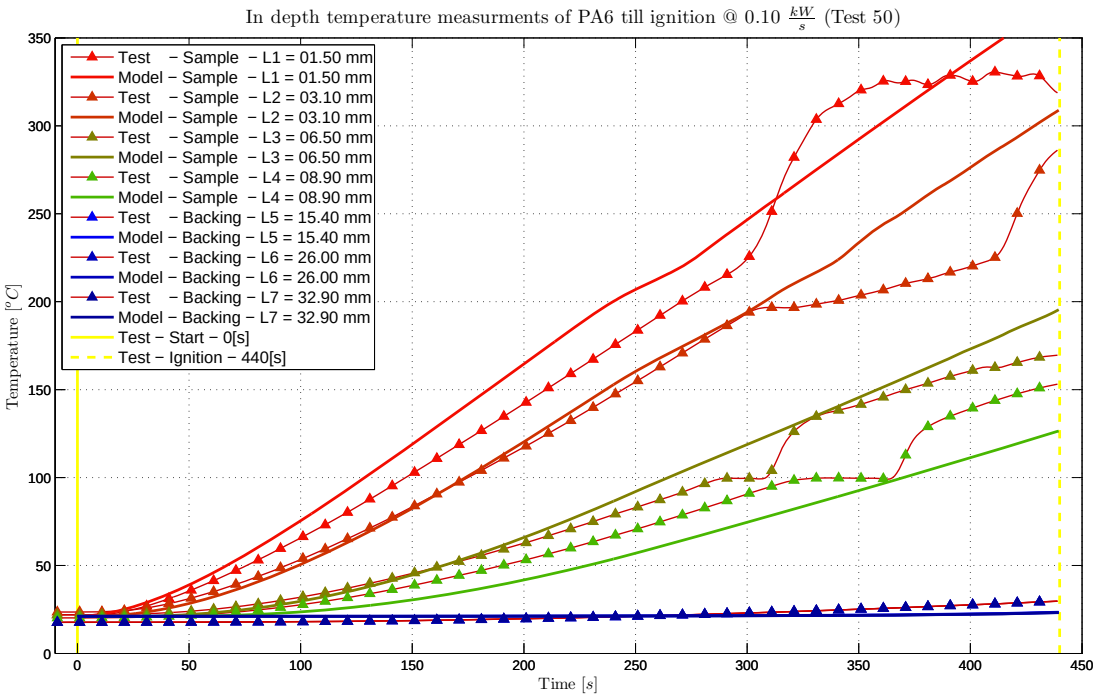

Figure 297 In-depth temperature “ramped FPA Test to Model Data” comparison of PA6 with parameters obtained from FPA experiments *using* the independently obtained intrinsic material properties (Test 50)

C.4.2 PA6+NC

C.4.2.1 In-depth temperature comparison

Without the independently obtained intrinsic material properties

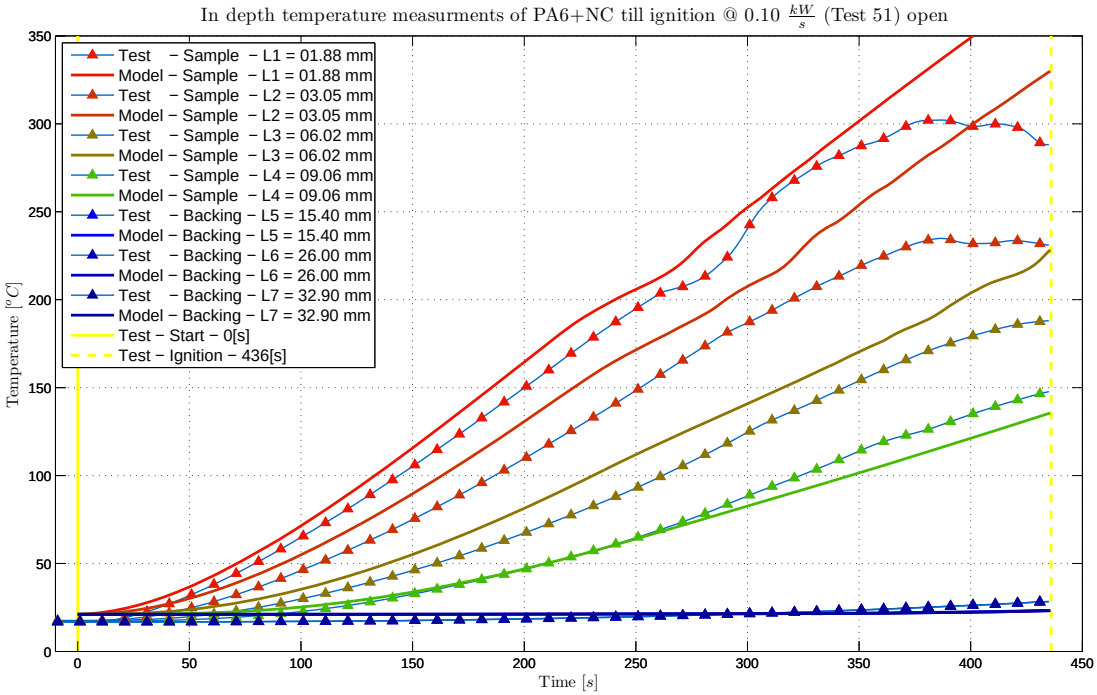

Figure 298 In In-depth temperature "ramped FPA Test to Model Data" comparison of PA6+NC with parameters obtained from FPA experiments *not using* the independently obtained intrinsic material properties (Test 51)

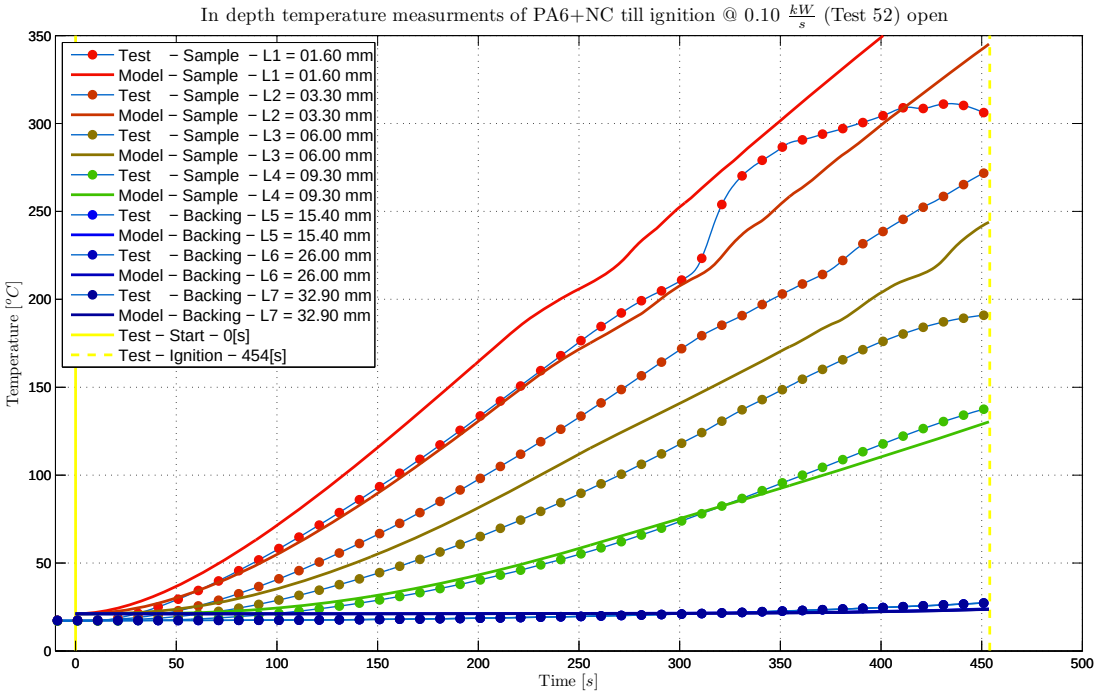

Figure 299 In In-depth temperature "ramped FPA Test to Model Data" comparison of PA6+NC with parameters obtained from FPA experiments *not using* the independently obtained intrinsic material properties (Test 52)

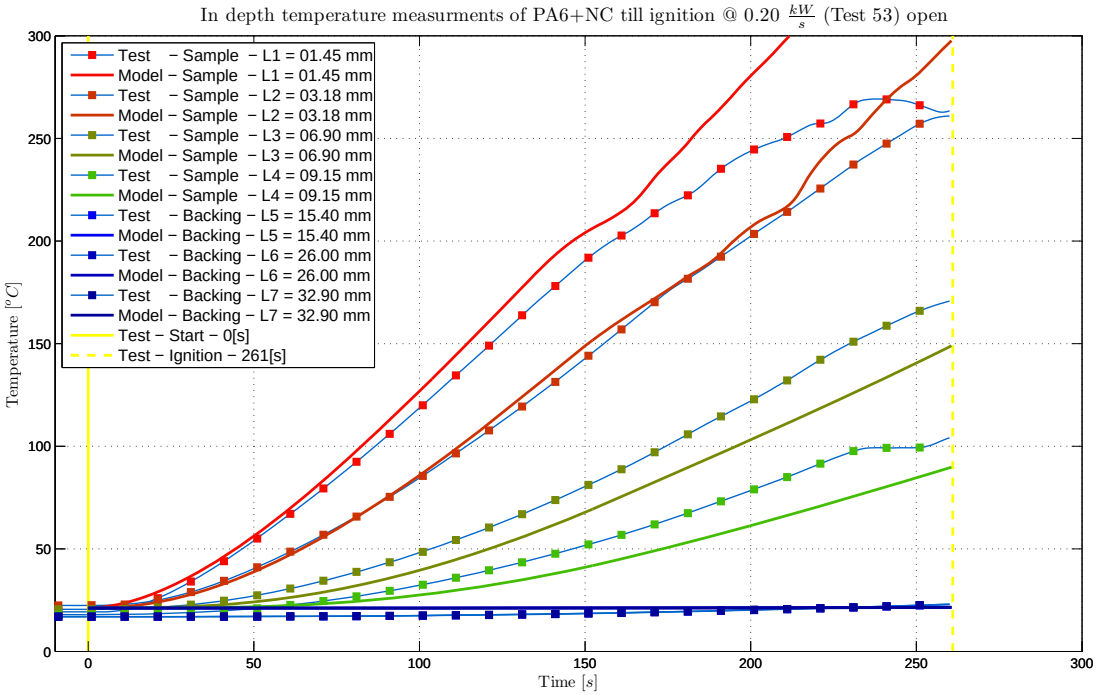

Figure 300 In In-depth temperature "ramped FPA Test to Model Data" comparison of PA6+NC with parameters obtained from FPA experiments *not using* the independently obtained intrinsic material properties (Test 53)

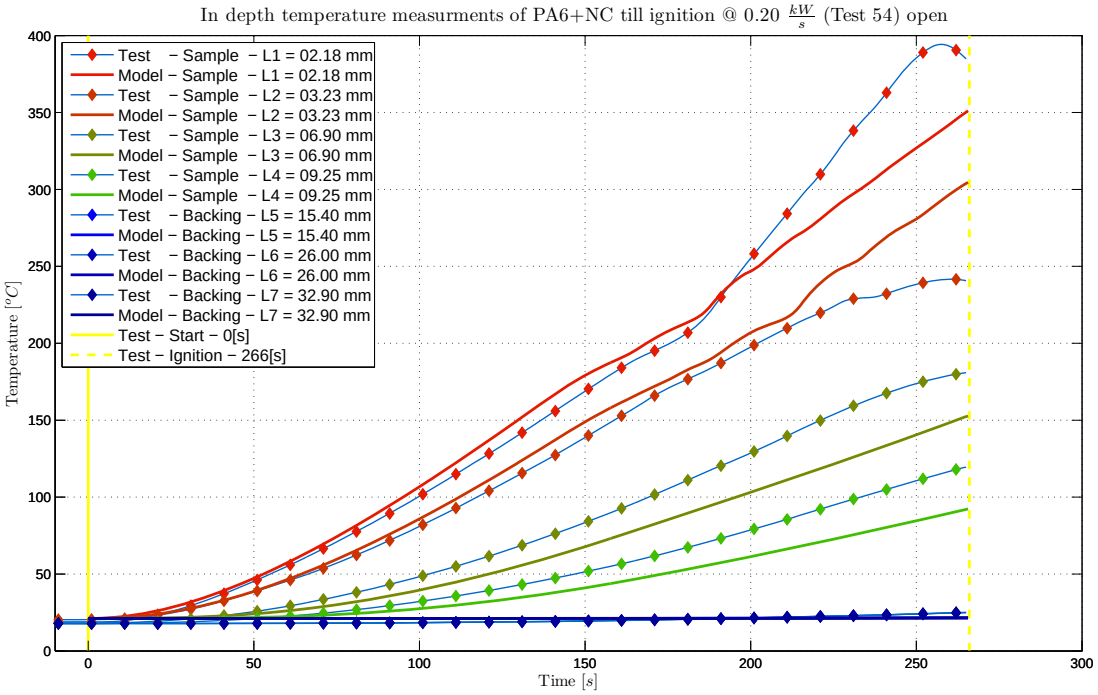

Figure 301 In In-depth temperature "ramped FPA Test to Model Data" comparison of PA6+NC with parameters obtained from FPA experiments *not using* the independently obtained intrinsic material properties (Test 54)

With the independently obtained intrinsic material properties

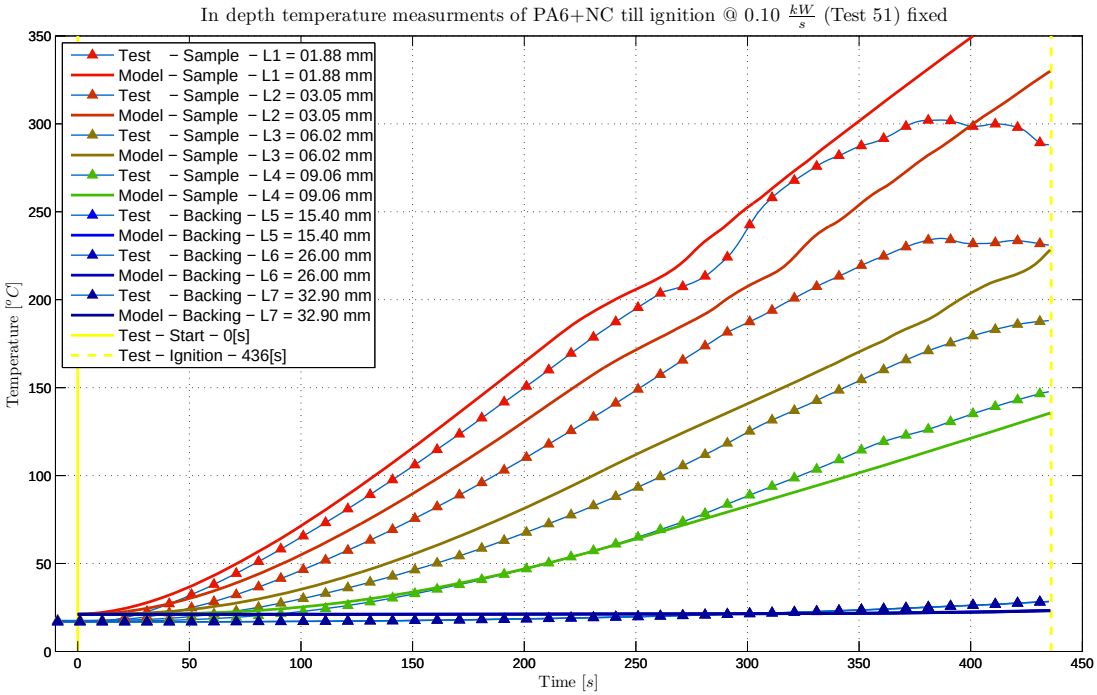

Figure 302 In-depth temperature "ramped FPA Test to Model Data" comparison of PA6+NC with parameters obtained from FPA experiments *using* the independently obtained intrinsic material properties (Test 51)

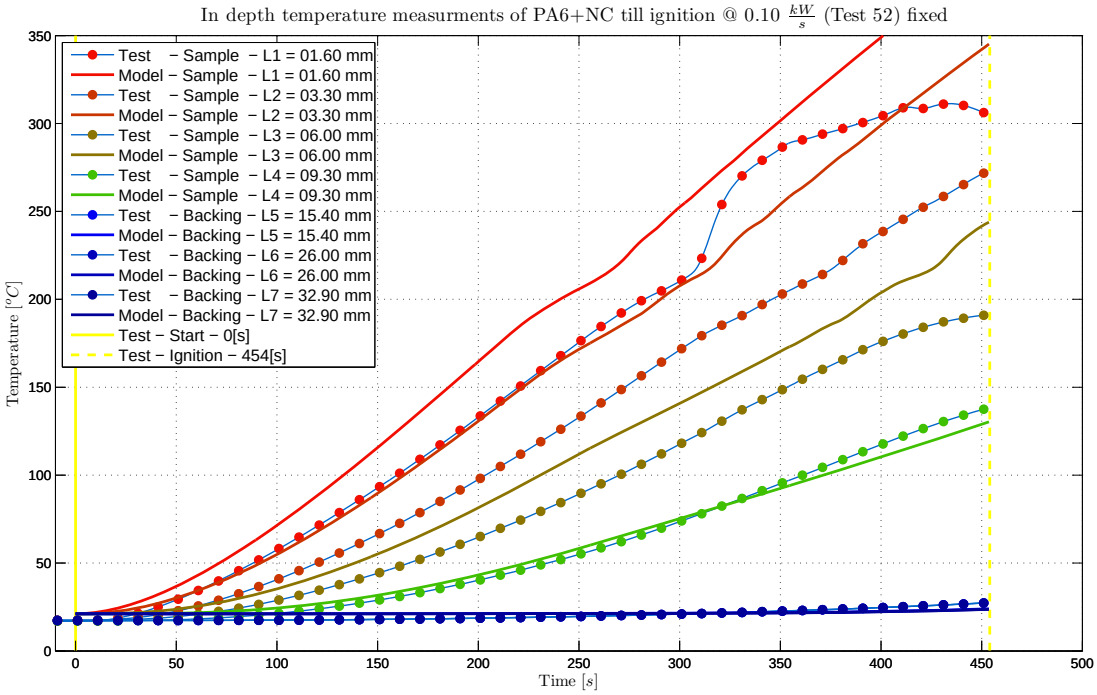

Figure 303 In-depth temperature "ramped FPA Test to Model Data" comparison of PA6+NC with parameters obtained from FPA experiments *using* the independently obtained intrinsic material properties (Test 52)

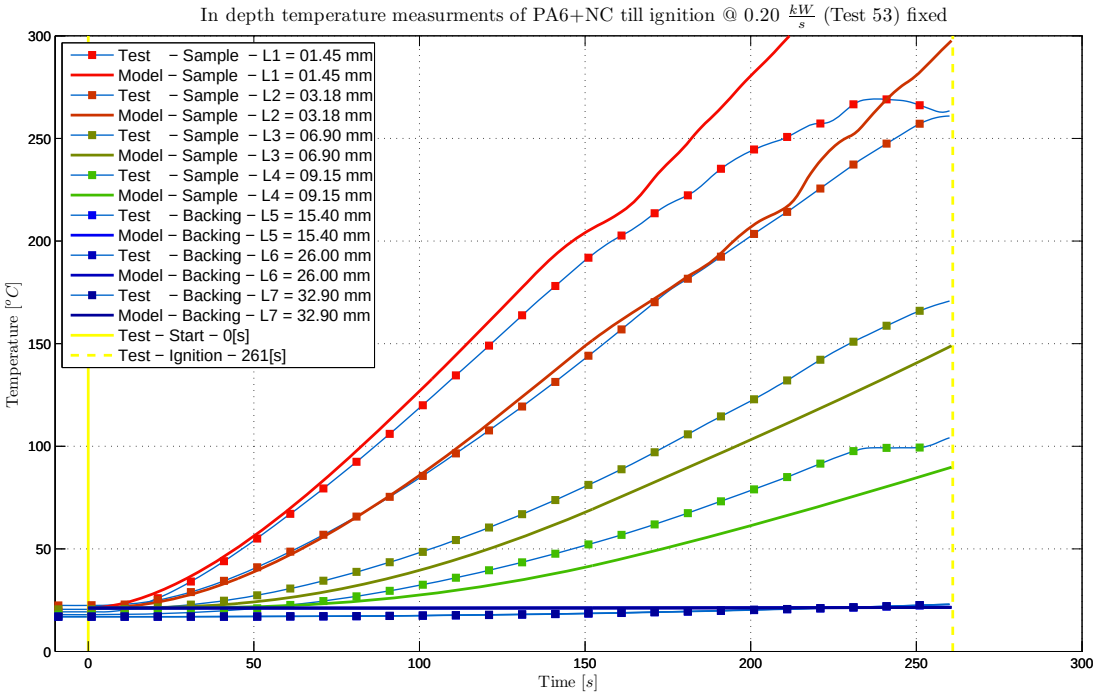

Figure 304 In-depth temperature "ramped FPA Test to Model Data" comparison of PA6+NC with parameters obtained from FPA experiments *using* the independently obtained intrinsic material properties (Test 53)

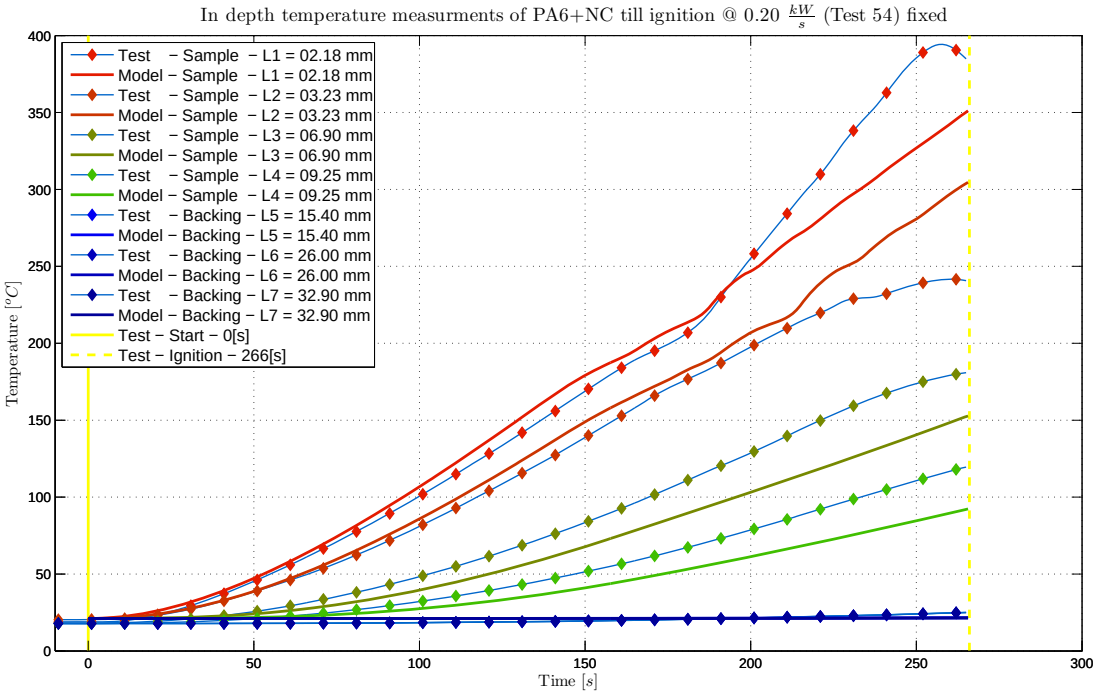

Figure 305 In-depth temperature "ramped FPA Test to Model Data" comparison of PA6+NC with parameters obtained from FPA experiments *using* the independently obtained intrinsic material properties (Test 54)